Fermilab-Pub-00/297
November 2000

QCD and Weak Boson Physics in Run II

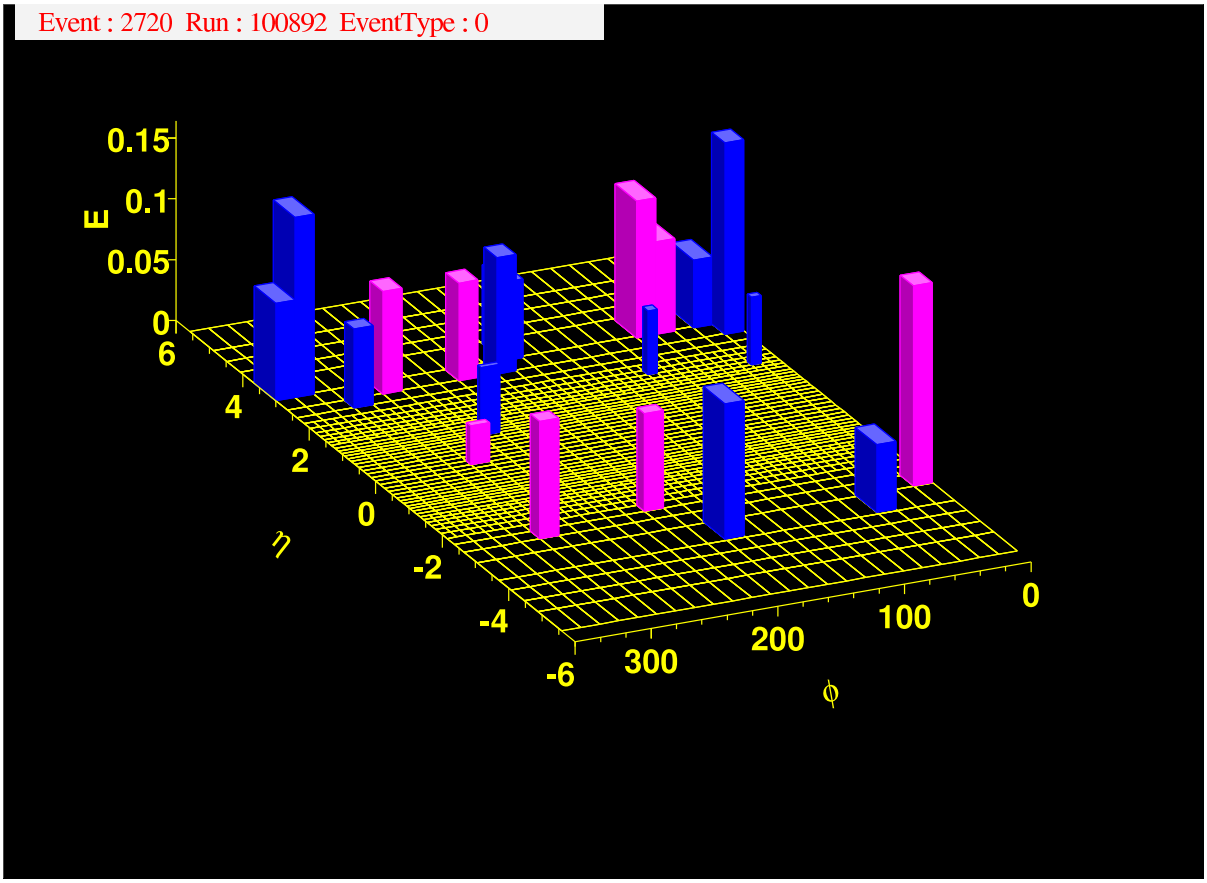

Fermilab, March – November 1999

Editors: U. Baur, R.K. Ellis and D. Zeppenfeld

Foreword

The Workshop on "QCD and Weak Boson Physics in Run II", the proceedings of which are presented here, took place at Fermilab from March to November 1999. It was promoted and financially supported by the Fermilab Theory Group and the Fermilab Directorate.

The specific goal of the Workshop was to promote QCD and weak boson physics studies for the upcoming Run II of the Tevatron. Organization of the Workshop began in the Fall of 1998 with the formation of six working groups: QCD tools for heavy flavors and new physics searches, jet physics, precision measurements, photons and weak bosons, parton distribution functions, and diffractive physics and color coherence. In each Group, theorists together with experimentalists from CDF and DØ acted as Conveners.

The first general meeting took place March 4 – 6, 1999. A second meeting was held on June 3 and 4, 1999, and the concluding general meeting was held November 4 – 6, 1999. These general meetings and a number of additional meetings of the individual working groups brought together a significant number of theorists and experimentalists from both inside and outside Fermilab, who have contributed to the Working Group discussions and many of whom presented talks at the plenary meetings. The detailed program of the general meetings can be found at Workshop homepage, `http://www-theory.fnal.gov/people/ellis/QCDWB/QCDWB.html`, together with electronic versions of the individual chapters of this report. Several working group reports, and a large fraction of individual contributions to the reports of the parton distribution functions and the diffractive physics working groups are also available via the Los Alamos archive.

Without the active participation of both the experimental and the theoretical community the Workshop would not have succeeded. We thank all our colleagues who invested much time and effort in these studies for their absolutely essential contributions. Particular thanks are due the members of the CTEQ Collaboration for their strong involvement in the Workshop, and to the members of both CDF and DØ for enthusiastically contributing in addition to the heavy load of getting the detectors ready for Run II. Special thanks go to Cynthia Sazama and Patti Poole for their invaluable help in the organization and the running of the Workshop.

Ulrich Baur
Keith Ellis
Dieter Zeppenfeld
Editors

Working Groups and Conveners

1. **QCD Tools for Heavy Flavors and New Physics Searches**

   R.K. Ellis
   R. Field
   S. Mrenna
   G. Snow

2. **Jet Physics**

   G. Blazey
   B. Flaugher
   W. Giele
   G. Sterman

3. **Precision Measurements**

   R. Brock
   J. Erler
   Y.K. Kim
   W. Marciano

4. **Photons and Weak Bosons**

   U. Baur
   E.L. Berger
   T. Diehl
   D. Errede

5. **Parton Distribution Functions**

   L. de Barbaro
   S. Keller
   S. Kuhlmann
   H. Schellman
   W.K. Tung

6. **Diffractive Physics and Color Coherence**

   M. Albrow
   A. Brandt
   A. Mueller
   C. Schmidt

Contents

Report of the QCD Tools Working Group

Convenors: Keith Ellis (FNAL), Rick Field (Florida), Stephen Mrenna (Davis) and Greg Snow (Nebraska)

Working Group Members: C. Balázs (Hawaii), E. Boos (Moscow), J. Campbell (FNAL), R. Demina (Kansas State), J. Huston (MSU), C-Y.P. Ngan (MIT), A. Petrelli (ANL), I. Puljak (LNPHE), T. Sjöstrand (Lund), J. Smith (Stony Brook), D. Stuart (FNAL), K. Sumorok (MIT)

We report on the activities of the "QCD Tools for heavy flavors and new physics searches" working group of the Run II Workshop on QCD and Weak Bosons. The contributions cover the topics of improved parton showering and comparisons of Monte Carlo programs and resummation calculations, recent developments in PYTHIA, the methodology of measuring backgrounds to new physics searches, variable flavor number schemes for heavy quark electro-production, the underlying event in hard scattering processes, and the Monte Carlo MCFM for NLO processes.

1. Overview

The task of the "QCD Tools for heavy flavors and new physics searches working group" was to evaluate the status of the tools – invariably computer programs that simulate physics processes at colliders – that are being used to estimate signal and background rates at the Tevatron, and to isolate areas of concern. The contributions presented here cover several topics related to that endeavor. It is hoped that the next period of data-taking at the Tevatron will reveal indirect or direct evidence of physics beyond the Standard Model. The precise measurement of the W boson mass M_W and its correlation with the top quark mass m_t is one example of an indirect probe of the Standard Model. The production of a light Higgs boson in association with a W or Z boson is an obvious example of a direct one. While both measurements are related to electroweak symmetry breaking, it requires a quantitative understanding of perturbative and non–perturbative QCD to interpret data.

Because of the importance of the M_W measurement, and since gauge boson production in association with jets is a serious background in many new physics searches, much effort was devoted to understanding gauge boson production processes. It is well known that the emission of many soft gluons has a profound effect on the kinematics of gauge boson production. Two calculational methods have been used to compare "theory" with data: (1) analytic resummation of several series of important logarithms, and (2) parton showering based on DGLAP–evolved parton distribution functions. Here, there are reports on our understanding of both, and improvements. Note also that diboson production is often a background too.

In the Standard Model, and its minimal supersymmetric extension, the mechanism that generates mass for the electroweak gauge bosons also generates fermion mass. From an agnostic point of view, the fact that the W and Z bosons and the top quark have roughly similar masses, and these masses are quite disparate from, say, the electron or neutrino masses, is some evidence that heavy flavor is related to electroweak symmetry breaking. Many of the search strategies for Run II rely on tagging c and b quarks or τ leptons. For this reason, there are several contributions regarding issues of determining backgrounds in Run II.

2. Performing parton showering at Next-to-Leading-Order Accuracy

by S. Mrenna

2.1. Introduction

In the near future, experiments at the Tevatron will search for evidence of physics that supersedes the standard model. Important among the tools that will be used in these searches are showering event generators or showering Monte Carlos (SMC's). Among the most versatile and popular of these are the Monte Carlos HERWIG[1], ISAJET[2], and PYTHIA[3]. SMC's are useful because they accurately describe the emission of multiple soft gluons, which is, in effect, an all orders problem in QCD. However, they only predict total cross sections to a leading order accuracy, and, thus, can demonstrate a sizeable dependence on the choice of scale used for the parton distribution functions (PDF's) or coupling constants (particularly α_s). Also, in general, they do not translate smoothly into kinematic configurations where only one, hard parton is emitted. In distinction to SMC's are certain analytic calculations which account for multiple soft gluon emission and higher order corrections to the hard scattering. These resummation calculations, however, integrate out the kinematics of the soft gluons, and, thus, are limited in their predictive power. They

can, for example, describe the kinematics of a heavy gauge boson produced in hadron collision, but cannot predict the number or distribution of jets that accompany it. However, searches for new physics, either directly or indirectly through measurements of precision electroweak observables, often demand detailed knowledge of kinematic distributions and jet activity. Furthermore, W+jets (and Z+jets) processes are often backgrounds to SUSY or technicolor signatures, and we demand a reliable prediction of their properties. Here, we report on recent progress in improving the predictive power of showering Monte Carlos by incorporating the positive features of the analytic resummation calculations into the showering algorithms. In the ensuing discussion, we focus on the specific example of W boson production at a hadron collider, when the W decays leptonically. The results apply equally well to γ^*, Z and Higgs bosons (or any heavy, color–singlet particle) produced in hadron collisions.

2.2. Parton Showers

SMC's are based on the factorization theorem [4], which, roughly, states that physical observables in QCD are the product of short–distance functions and long–distance functions. The short–distance functions are calculable in perturbation theory. The long–distance functions are fit at a scale, but their evolution to any other scale is also calculable in perturbation theory.

A standard application of the factorization theorem is to describe W boson production at a $p\bar{p}$ collider at a fixed order in α_s. The production cross section is obtained by convoluting the partonic subprocesses evaluated at the scale Q with the PDF's evaluated at Q. The partons involved in the hard collision must be sufficiently virtual to be resolved inside the proton, and a natural choice for the scale Q is $Q = M_W$ [5]. However, the valence quarks in the proton have virtualities at a much lower scale Q_0 of the order of 1 GeV. The connection between the partons at the low scale Q_0 and those at the high scale Q is described by the DGLAP evolution equations [6]. The DGLAP equations include the most important kinematic configurations of the splittings $a \to bc$, where a, b and c represent different types of partons in the hadron (q, g, etc.). Starting from a measurement of the PDF's at a low scale Q_0, a solution of the DGLAP equations yields the PDF's at the hard scale Q. Equivalently, starting with a parton c involved in a hard collision, it is also possible to determine probabilistically which splittings generated c. In the process of evolving parton c back to the valence quarks in the proton, a number of spectator partons (e.g. parton b in the branching $a \to bc$) are resolved. These partons constitute a shower of soft and/or collinear jets that accompany the W–boson, and influence its kinematics.

The shower described above occurs with unit probability and does not change the total cross section for W–boson production calculated at the scale Q [7]. The showering can be attached to the hard–scattering process based on a probability distribution *after* the hard scattering has been selected. Once kinematic cuts are applied, the transverse momentum and rapidity of the W–boson populate regions never accessed by the differential partonic cross section calculated at a fixed order. This is consistent, since the fixed–order calculation was inclusive (i.e., $p\bar{p} \to W + X$) and was never intended to describe the detailed kinematics of the W–boson in isolation. The parton shower, in effect, resolves the structure of the inclusive state of partons denoted as X. In practice, the fixed order partonic cross section (without showering) can still be used to describe properties of the decay leptons as long as the observable is well defined (e.g., the number of leptons with central rapidity and high transverse momentum, but not the distribution of transverse momentum of the W).

Here, we focus on the case of initial state gluon radiation. More details can be found in Ref. [8], for example. Showering of the parton b with momentum fraction x resolved at the scale $Q^2 = e^t$ is driven by a Sudakov form factor $\exp(-S)$, such as[9]

$$\exp\left(-\int_{t'}^{t}\int_{\frac{x}{1-\epsilon}}^{\frac{x}{x+\epsilon}} dt''dz\frac{\alpha_s(z,t'')}{2\pi}\hat{P}_{a\to bc}(z)\frac{x' f_a(x',t')}{x f_b(x,t')}\right), \quad x' = x/z, \quad (1)$$

which is implemented in PYTHIA, and the formally equivalent expression[10]

$$\frac{\Delta(t')}{f_b(x,t')}\frac{f_a(x,t)}{\Delta(t)}, \quad \Delta(t') = \exp\left(-\int_{t_0}^{t'}\int_{\epsilon}^{1-\epsilon} dt''dz\frac{\alpha_s(z,t'')}{2\pi}\hat{P}_{a\to bc}(z)\right),$$

which is implemented in HERWIG. In the above expressions, t_0 is a cutoff scale for the showering, $\hat{P}$ is a DGLAP splitting function, and f_i is a parton distribution function. The Sudakov form factor presented here is a solution of the DGLAP equation, and gives the probability of evolving from the scale $Q^2 = e^t$ to $Q'^2 = e^{t'}$ with no resolvable branching. The Sudakov form factor contains all the information necessary to reconstruct a shower, since it encodes the change in virtuality of a parton until a resolvable showering occurs. A parton shower is then an iterative

solution of the equation $r = \exp(-S)$, where r is a random number uniformly distributed in the interval $[0, 1]$, until a solution for Q' is found which is below a cutoff. For consistency, the cutoff should represent the lowest scale of resolvable emission Q_0. The evolution proceeds backwards from a large, negative scale $-|Q^2|$ to a small, negative cutoff scale $-|Q_0^2|$.

After choosing the change in virtuality, a particular backwards branching and the splitting variable z are selected from the probability function based on their relative weights (a summation over all possible branchings $a \to bc$ is implied in these expressions). The details of how a full shower is reconstructed in the PYTHIA Monte Carlo, for example, can be found in Ref. [3]. The structure of the shower can be complex: the transverse momentum of the W–boson is built up from a whole series of splittings and boosts, and is known only at the end of the shower, after the final boost.

The SMC formulation outlined above is fairly independent of the hard scattering process considered. Only the initial choice of partons and possibly the high scale differs. Therefore, this formalism can be applied universally to many different scattering problems. In effect, soft and collinear gluons are not sensitive to the specifics of the hard scattering, only the color charge of the incoming partons.

2.3. Analytic Resummation

At hadron colliders, the partonic cross sections can receive substantial corrections at higher orders in α_s. This affects not only the total production rate, but also the kinematics of the W boson. At leading order (α_s^0), the W–boson has a $\delta(Q_T^2)$ distribution in Q_T^2. At next–to–leading order, the real emission of a single gluon generates a contribution to $d\sigma/dQ_T^2$ that behaves as $Q_T^{-2}\alpha_s(Q_T^2)$ and $Q_T^{-2}\alpha_s(Q_T^2)\ln(Q^2/Q_T^2)$ while the leading order, soft, and virtual corrections are proportional to $-\delta(Q_T^2)$. At higher orders, the most singular terms follow the pattern of $\alpha_s(Q_T^2)^n \sum_{m=0}^{2n-1} \ln^m(Q^2/Q_T^2) = \alpha_s^n L^m \equiv V^n$. The logarithms arise from the incomplete cancellation of the virtual and real QCD corrections, but this cancellation becomes complete for the integrated spectrum, where the real gluon can become arbitrarily soft and/or collinear to other partons. The pattern of singular terms suggest that perturbation theory should be performed in powers of V^n instead of α_s^n. This reorganization of the perturbative series is called resummation.

The first studies of soft gluon emission resummed the leading logarithms [11,12], leading to a suppression of the cross section at small Q_T. The suppression underlies the importance of including sub–leading logarithms [13]. The most rigorous approach to the problem of multiple gluon emission is the Collins–Soper–Sterman (CSS) formalism for transverse momentum resummation [14], which resums all of the important logarithms. This is achieved after a Fourier transformation with respect to Q_T in the variable b, so that the series involving the delta function and terms V^n simplifies to the form of an exponential. Hence, the soft gluon emission is resummed or exponentiated in this b–space formalism. Despite the successes of the b–space formalism, there are drawbacks: the soft gluon dynamics are integrated out, and the Sudakov form factor is a Fourier transform.

The CSS formalism was used by its authors to predict both the total cross section to NLO and the kinematic distributions of the W–boson to all orders [15] at hadron colliders. A similar treatment was presented using the AEGM formalism [16], that does not involve a Fourier transform, but is evaluated directly in transverse momentum Q_T space. When evaluated at NLO, the two formalisms are equivalent to NNNL order in α_s, and agree with the fixed order calculation of the total cross section [17]. A more detailed numerical comparison of the two predictions can be found in Ref. [18].

Recently, the AEGM formalism has been re-investigated, and an approximation to the b–space formalism has been developed in Q_T–space which retains its predictive features [19] (see also the recent eprint [20]). This formulation *does* have a simple, physical interpretation, and can be used to develop an alternate algorithm for parton showering which *includes* higher–order corrections to the hard scattering. For this reason, we focus on the Q_T–space formalism. To NNNL accuracy, the Q_T space expression agrees exactly with the b–space expression, and has the form [19]:

$$\frac{d\sigma(h_1h_2 \to V^{(*)}X)}{dQ^2\,dQ_T^2\,dy} = \frac{d}{dQ_T^2}\widetilde{W}(Q_T, Q, x_1, x_2) + Y(Q_T, Q, x_1, x_2). \quad (3)$$

In this expression, Q, Q_T and y describe the kinematics of the boson V, the function Y is regular as $Q_T \to 0$ and corrects for the soft gluon approximation, and the function $\widetilde{W}$ has the form:

$$\widetilde{W} = e^{-S(Q_T,Q)}H(Q,y) \times \Big(C \otimes f\Big)(x_1, Q_T)\Big(C \otimes f\Big)(x_2, Q_T), \quad (4)$$

where

$$S(Q_T, Q) = \int_{Q_T^2}^{Q^2} \frac{d\bar{\mu}^2}{\bar{\mu}^2}\left[\ln\frac{Q^2}{\bar{\mu}^2}A\big(\alpha_s(\bar{\mu})\big) + B\big(\alpha_s(\bar{\mu})\big)\right], \quad (5)$$

and

$$\left(C_{jl} \otimes f_{l/h_1}\right)(x_1,\mu) = \int_{x_1}^{1} \frac{d\xi_1}{\xi_1} C_{jl}(\frac{x_1}{\xi_1}, Q_T) f_{l/h_1}(\xi_1, Q_T). \quad (6)$$

H is a function that describes the hard scattering, and A, B, and C are calculated perturbatively in powers of α_s:

$$(A,B,C) = \sum_{n=0}^{\infty} \left(\frac{\alpha_s(\mu)}{\pi}\right)^n (A,B,C)^{(n)}$$

(the first non–zero terms in the expansion of A and B are for $n = 1$). The functions $C^{(n)}$ are the Wilson coefficients, and are responsible for the change in the total production cross section at higher orders. In fact, $(C \otimes f)$ is simply a redefinition of the parton distribution function obtained by convoluting the standard ones with an ultraviolet–safe function.

Ignoring Y and other kinematical dependence, Eq. (3) can be rewritten as:

$$\frac{d\sigma(h_1h_2 \to WX)}{dQ_T^2} = \sigma_1 \left(\frac{d}{dQ_T^2}\left[e^{-S(Q_T,Q)}\ R\right]\right), \quad (7)$$

where

$$R = \frac{(C\otimes f)(x_1,Q_T)(C\otimes f)(x_2,Q_T)}{(C\otimes f)(x_1,Q)(C\otimes f)(x_2,Q)} \quad (8)$$

and

$$\sigma_1 = \kappa \int \frac{dx_1}{x_1}(C\otimes f)(x_1,Q)(C\otimes f)(x_2,Q).$$

The factor σ_1 is the total cross section to a fixed order, while the rest of the function yields the probability that the W–boson has a transverse momentum Q_T.

At leading order, the expression for the production of an on–shell W–boson simplifies considerably to:

$$\frac{d\sigma(h_1h_2 \to WX)}{dQ_T^2} = \sigma_0 \frac{d}{dQ_T^2}\left(e^{-S(Q_T,Q)} \frac{f(x_1,Q_T)f(x_2,Q_T)}{f(x_1,Q)f(x_2,Q)}\right), \quad (9)$$

$$\sigma_0 = \kappa \int \frac{dx_1}{x_1} f(x_1,Q) f(x_2,Q),$$

where κ contains physical constants and we ignore the function Y for now. The expression contains two factors, the total cross section at leading order σ_0, and a cumulative probability function in Q_T^2 that describes the transverse momentum of the W–boson. The term $e^{-S/2} f(x,Q_T)/f(x,Q)$ is of the same form as the Sudakov form factor of Eq. (2) and, hence, to that of Eq. (1).

2.4. A modified showering algorithm

The primary result of this analysis is to exploit the expression for the differential cross section, which has the form of a leading order cross section times a backwards evolution, to incorporate NLO corrections to the parton shower. We generalize the function $\Delta(t)/f(x,t) \times f(x,t')/\Delta(t')$ of the standard backwards showering algorithm to $\sqrt{\widetilde{W}}$ (the square root appears because we are considering the evolution of each parton line individually).

To implement this modification in a numerical program, like PYTHIA, we need to provide the new, modified PDF (mPDF) based on the Wilson coefficients. At leading order, the only Wilson coefficient is $C_{ij}^{(0)} = \delta_{ij}\delta(1-z)$, and we reproduce exactly the standard showering formulation. For W–boson production at NLO, the Wilson coefficients C are:

$$C_{jk}^{(1)} = \delta_{jk}\left\{\frac{2}{3}(1-z) + \frac{1}{3}(\pi^2-8)\delta(1-z)\right\}, \quad (10)$$

$$C_{jg}^{(1)} = \frac{1}{2}z(1-z). \quad (11)$$

To NLO, the convolution integrals become:

$$(C\otimes f_i)(x,\mu) = f_i(x,\mu)\left(1 + \frac{\alpha_s(\mu)}{\pi}\frac{1}{3}(\pi^2-8)\right) + \frac{\alpha_s(\mu)}{\pi}\int_x^1 \frac{dz}{z}\left[\frac{2}{3}(1-z)f_i(x/z,\mu) + \frac{1}{2}(1-z)f_g(x/z,\mu)\right],$$

and $f_g(x,\mu)$ is unchanged. The first term gives the contribution of an unevolved parton to the hard scattering, while the other two contain contributions from quarks and gluons with higher momentum fractions that split $q \to qg$ and $g \to q\bar{q}$, respectively.

We are assuming that the Sudakov form factor used in the analytic expressions and in the SMC are equivalent. In fact, the integration over the quark splitting function in $\Delta(Q)$ yields an expression similar to the analytic Sudakov:

$$\int_{z_m}^{1-z_m} dz C_F\left(\frac{1+z^2}{1-z}\right) = C_F\left(\ln\left[\frac{1-z_m}{z_m}\right]^2 - 3/2(1-2z_m)\right) \simeq A^{(1)}\ln(Q^2/Q_T^2) + B^{(1)}, \quad (13)$$

where $z_m = \frac{Q_T}{(Q+Q_T)}$ is an infrared cutoff, terms of order z_m and higher are neglected, and the z dependence of the running coupling has been ignored

[21]. Note that the coefficients $A^{(1)}$ (C_F) and $B^{(1)}$ ($-3/2C_F$) are universal to $q\bar{q}$ annihilation into a color singlet object, just as the showering Sudakov form factor only knows about the partons and not the details of the hard scattering. For gg fusion, only the coefficient $A^{(1)}$ (3) is universal. In general, at higher orders, the analytic Sudakov is sensitive to the exact hard scattering process.

While the Sudakov form factors are similar, there is no one–to–one correspondence. First, the Q_T–space Sudakov form factor is expressed directly in terms of the Q_T of the heavy boson, while, in the SMC's, the final Q_T is built up from a series of branchings. Secondly, the integral on the left of Eq. (13) is positive (provided that $z_m < \frac{1}{2}$), while the analytic expression on the right can become negative. This is disturbing, since it means sub-leading logarithms (proportional to B) are dominating leading ones. In the exact SMC Sudakov, the kinematic constraints guarantee that $\Delta(Q) < 1$. In this sense, the Sudakov in the SMC is a more exact implementation of the analytic one. Nonetheless, the agreement apparent between the analytic and parton shower expressions is compelling enough to proceed assuming the two Sudakov form factors are equivalent.

2.5. Hard Emission Corrections

The SMC and resummation formalisms are optimized to deal with kinematic configurations that have logarithmic enhancements L. For large $Q_T \simeq Q$, there are no such enhancements, and a fixed order calculation yields the most accurate predictions. The region of medium Q_T, however, is not suited to either particular expansion, in $\alpha_s^n L^m$ or α_s^n.

The problem becomes acute for SMC's. In the standard implementation of SMC's, the highest Q_T is set by the maximum virtuality allowed, $Q = M_W$ in our example, so that the region $Q_T \geq Q$ is never accessed. However, at $Q_T \geq Q$, the fixed order calculation is preferred and yields a non–zero result, so there is a discontinuity between the two predictions. This behavior does not occur in the analytic resummation calculations, because contributions to the cross section that are not logarithmically enhanced as $Q_T \to 0$ are added back order–by–order in α_s. This procedure corrects for the approximations made in deriving the exponentiation of soft gluon emission. The correction is denoted Y. If the coefficients A and B are calculated to high–enough accuracy, one sees a relatively smooth transition between Eq. (3) and the NLO prediction at $Q_T = Q$. In the Q_T–space calculation, this matching between the two calculations at $Q_T = Q$ is guaranteed at any order. The function Y has the form

$$Y(Q_T, Q, x_1, x_2) = \int_{x_1}^1 \frac{d\xi_1}{\xi_1} \int_{x_2}^1 \frac{d\xi_2}{\xi_2} \sum_{n=1}^{\infty} \left[\frac{\alpha_s(Q)}{\pi}\right]^n f_a(\xi_1, Q)\, R_{ab}^{(n)}(Q_T, Q, \frac{x_1}{\xi_1}, \frac{x_2}{\xi_2})\, f_b(\xi_2, Q). \quad (14)$$

For W or Z boson production, the $a = q, b = \bar{q}$ component of R at first order in α_s is

$$R_{q\bar{q}}^{(1)} = C_F \frac{(\hat{t}-Q^2)^2 + (\hat{u}-Q^2)^2}{\hat{t}\hat{u}} \delta(\hat{s}+\hat{t}+\hat{u}-Q^2) - \frac{1}{Q_T^2} \hat{P}_{q\to q}(z_B)\delta(1-z_A) - (A \leftrightarrow B). \quad (15)$$

The invariants $\hat{s}, \hat{t}$ and $\hat{u}$ are defined in terms of z, Q, Q_T:

$$\begin{aligned} \hat{t}/Q^2 &= 1 - 1/z_B \sqrt{1 + Q_T^2/Q^2}, \\ \hat{u}/Q^2 &= 1 - 1/z_A \sqrt{1 + Q_T^2/Q^2}. \end{aligned} \quad (16)$$

The term in R proportional to the delta function is simply the squared matrix element for the hard emission, while the terms proportional to Q_T^{-2} are the asymptotic pieces from $\widetilde{W}$.

We would like to include similar corrections into the SMC. However, this is not entirely straightforward. Though it is not obvious from Eq. (14), the ($a = g, b =$ q+permutations) components are negative for $Q_T < Q$, though the sum Y is positive. Retaining negative weights in an intermediate part of the calculation is not a problem in principle. We can artificially force the negative weights to be positive, and then include the correct sign of the weight when filling histograms, for example. However, this would involve some modification to the PYTHIA code used in this study.

A pragmatic approach is to ignore the negative weights entirely, and multiply the exact W+parton cross sections by a factor so that their sum reproduces the Q_T distribution and normalization of the analytic Y piece. For the Tevatron in Run I, we find that the multiplicative factor $f_{\rm COR} = \frac{1}{2}(Q_T/50)^2 \times (1 + Q_T/25)$ reproduces the correct behavior for $Q_T < 50$ GeV. For $Q_T \geq 50$ GeV, the uncorrected W+ parton cross sections are employed. Since the matching between the "resummed" and "fixed order" calculations is now occurring at $Q_T = 50$ GeV instead of $Q_T = M_W$, we further limit the maximum virtuality of showering to 50 GeV. This is in accord with the fact that the "resummed" part of the analytic calculation becomes negative around $Q_T = 50$ GeV. This choice does have some effect on the overall normalization of the parton showering component.

At this point, it is useful to compare the scheme outlined above to other approaches at improving the showering algorithm. One scheme is based on phase–space splitting of a NLO matrix element into a piece with LO kinematics and another with exclusive NLO kinematics [23,24]. The separation depends on an adjustable parameter that splits the phase space. In the approach of Ref. [23], the separation parameter is tuned so that the contribution with LO kinematics vanishes. The resultant showering of the term with exclusive NLO kinematics can generate emissions which are harder than the first "hard" emission, which is not consistent. More seriously, physical observables are sensitive to the exact choice of the separation parameter (see the discussion in Ref. [22] regarding Q_T^{sep}). Furthermore, the separation parameter must be retuned for different processes and different colliders. This scheme is guaranteed to give the NLO cross section before cuts, but does not necessarily generate the correct kinematics.

The other scheme is to modify the showering to reproduce the hard emission limit [25,26]. While this can be accomplished, it does so at the expense of transferring events from low Q_T to high Q_T. There is no attempt to predict the absolute event rate, but only to generate the correct event shapes. In some implementations, the high scale of the showering is increased to the maximum virtuality allowed by the collider energy. This is contrary to the analytic calculations, where the scale $Q = M_W$, for example, appears naturally (in the choice of constants C_1, C_2 and C_3 which eliminate potentially large logarithms). This scheme will generate the correct hard limit, but will not generate the correct cross section in the soft limit.

2.6. Numerical results

For our numerical results, we predict the Q_T distribution of W and Z bosons produced at the Tevatron in Run I. The modified PDF (mPDF) was calculated using CTEQ4M PDF's. These distributions are in good agreement with analytic calculations, but the shape and overall normalization cannot be predicted accurately by the standard showering algorithm. Some of the alternative showering algorithms reproduce the shape, but not the overall normalization. Secondly, we discuss jet properties for the same processes, which are not significantly altered from the predictions of the standard showering algorithm. These cannot be predicted by analytic calculations.

In Fig. 1(a), the transverse momentum of the W boson (solid line) as predicted by the algorithm outlined above is shown in comparison to DØ data[27] (crosses). The theoretical distribution has been passed through the CMS detector simulation.[1] As in analytic calculations, the position of the peak in the Q_T distribution from parton showering depends on non–perturbative physics [29]. In PYTHIA, this is implemented through a Gaussian smearing of the transverse momentum of the incoming partons. To generate this plot, we have changed the default Gaussian width from .44 GeV to 2.0 GeV, which is more in accord with other analyses. This is the value used in all subsequent results. Because of the necessity of reconstructing the missing E_T in W boson decays to leptons, the smearing of the Q_T distribution is significant, and the agreement between the prediction and data is not a rigorous test of the modified showering algorithm. Fig. 1(b) shows the comparison of the CDF Drell–Yan data [28] near the Z^0 peak to the modified showering prediction. While there is a problem with the overall normalization, the shape agreement is very good. We note that there is also a problem with the overall normalization of the analytic resummation predictions.[2]

Given all the effort necessary to improve the showering, it is reasonable to ask if the similar results would have been obtained by simply renormalizing the usual predictions to the NLO rate, i.e. using PYTHIA but applying a constant K–factor at the end. In W boson production, the relative size of the Q_T distributions vary by as much as 10% in the important regions of small and medium Q_T. Of course, the effect is much larger for the large Q_T region where there is almost no rate from the standard parton showering. If one is worried about precision measurements or is applying kinematic cuts that bias the large Q_T region, then standard parton showering can yield misleading results. In most cases, however, it appears to be perfectly reasonable to renormalize the parton showering results to the total NLO cross section. We have also checked if our new showering algorithm has an impact on jet properties. For W and Z boson production, there are only minor differences, which is expected since the Wilson coefficients for W and Z boson production are nearly unity. In general, we do not expect any major changes from using the modified PDF's, since the showering depends on the ratio of the modified PDF's evaluated at two different scales, which is not as sensitive to the overall normalization of the PDF.

2.7. Conclusions

We have presented a modified, parton showering algorithm that produces the total cross section and

[1] Special thanks go to Cecilia Gerber, for making the code portable, and to Michael Seymour for explaining how to properly use it.

[2] Csaba Balazs, private communication.

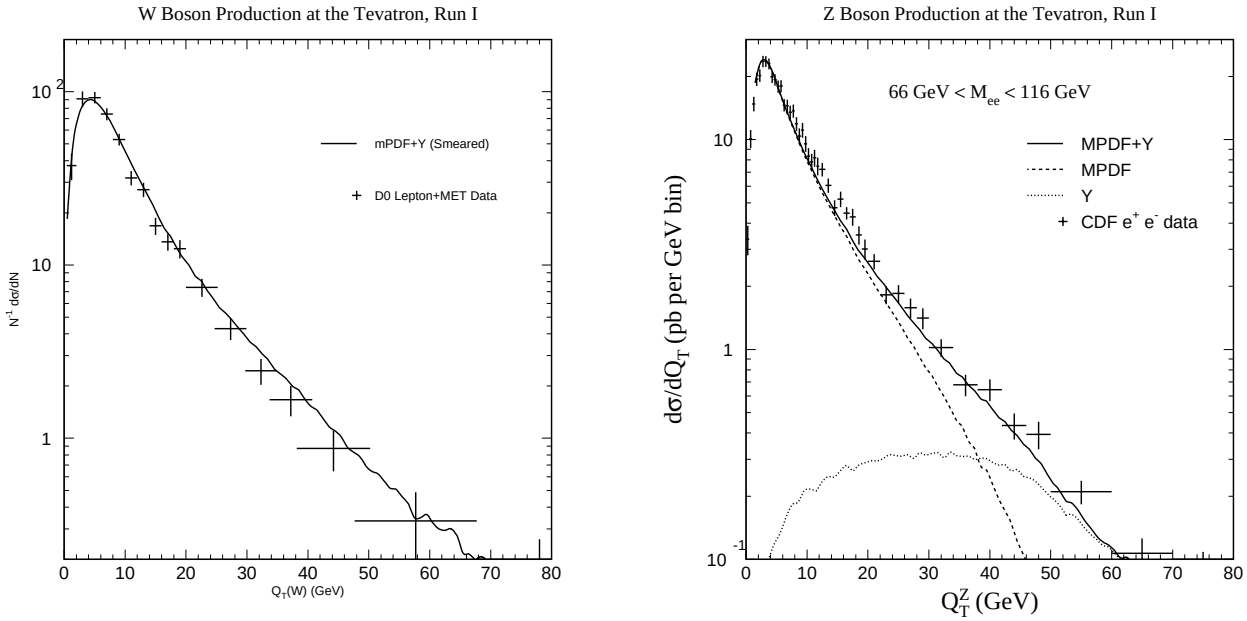

Figure 1. (a) The prediction of the W boson transverse momentum distribution in Run I at the Tevatron (solid line) compared to the DØ data. The prediction includes the effects of the modified parton distribution functions, the correction to the hard scattering process, and a primordial k_T of 2.0 GeV; (b) The prediction of the Z boson transverse momentum distribution in Run I at the Tevatron (solid line) compared to the CDF data. The prediction includes the effects of the modified parton distribution functions, the correction to the hard scattering process, and a primordial k_T of 2.0 GeV.

the event shapes beyond the leading order. These modifications are based on the Q_T–space resummation. The parton showering itself is modified by using a new PDF (called mPDF) which encodes some information about the hard scattering process. Simultaneously, the explicit, hard emission is included, but only after subtracting out the contribution already generated by the showering: this correction is called Y. The presence of Y yields a smooth transition from the parton showering to single, hard emission. We modified the PYTHIA Monte Carlo to account for these corrections, and presented comparisons with Run I W and Z boson data.

The scheme works well for the cases considered in this study, and the correct cross sections, transverse momentum distributions, and jet properties are generated. We have compared our kinematic distributions to the case when the results of the standard showering are multiplied by a constant K–factor to reproduce the NLO cross section. We find variations on the order of 10% for small and medium transverse momentum.

There are several effects which still need study. We have not included the exact distributions for the decay of the leptons [30] for W and Z production, which are resummed differently. It is straightforward to include such effects. In the theoretical discussion and numerical results, we have focussed on initial state radiation, but our results should apply equally well for final state radiation. The situation is certainly simpler, since final state radiation does not require detailed knowledge of the fragmentation functions. Also, the case when color flows from the initial state to the final state requires study. A resummed calculation already exists for the case of deep inelastic scattering [31], and much theoretical progress has been made for heavy quark production [32]. We believe that the modified showering scheme outlined in this study generalizes beyond NLO, just as the analytic calculations can be calculated to any given order. For example, we could include hard W + 2 jet corrections [33] to Y. For consistency, however, higher order terms (A and B) may also need to be included in the Sudakov form factor.

The modified PYTHIA subroutines used in this study and an explanation of how to use them are available at the following URL:
`moose.ucdavis.edu/mrenna/shower.html`.

Acknowledgements I thank C–P Yuan and

T. Sjöstrand for many useful discussions and encouragement in completing this work. This work was supported by United States Department of Energy and the Davis Institute for High Energy Physics.

3. Recent Progress in PYTHIA

by T. Sjöstrand

3.1. Introduction

A general-purpose generator in high-energy physics should address a number of physics aspects, such as:

- the matrix elements for a multitude of hard subprocesses of interest,
- the convolution with parton distributions to obtain the hard-scattering kinematics and cross sections,
- resonance decays that (more or less) form part of the hard subprocess (such as W, Z, t or h),
- initial- and final-state QCD and QED showers (or, as an alternative, higher-order matrix elements, including a consistent treatment of virtual-correction terms),
- multiple parton–parton interactions,
- beam remnants,
- hadronization,
- decay chains of unstable particles, and
- general utility and analysis routines (such as jet finding).

However, even if a Monte Carlo includes all the physics we currently know of, there is no guarantee that not some important aspect of the physics is missing. Certain assumptions and phenomenological models inside the program are not well tested and will not necessarily hold when extrapolated to different energy regimes. For example, the strong-interaction dynamics in QCD remains unsolved and thereby unpredictable in an absolute sense.

The PYTHIA 6.1 program was released in March 1997, as a merger of JETSET 7.4, PYTHIA 5.7 [3] and SPYTHIA [34]. It addresses all of the aspects listed above. The current subversion is PYTHIA 6.136, which contains over 50,000 lines of Fortran 77 code. The code, manuals and sample main programs may be found at
`http://www.thep.lu.se/~torbjorn/Pythia.html` .

The two other programs of a similar scope are HERWIG[1] [3] and ISAJET[2] [4]. For parton-level processes, many more programs have been written. The availability of several generators provides for useful cross-checks and a healthy competition. Since the physics of a complete hadronic event is very complex and only partially understood from first principles, one should not prematurely converge on one single approach.

[3] `http://hepwww.rl.ac.uk/theory/seymour/herwig/`
[4] `ftp://penguin.phy.bnl.gov/pub/isajet`

3.2. PYTHIA 6.1 Main News

Relative to previous versions, the main news in PYTHIA 6.1 includes

- a renaming of the old JETSET program elements to begin with `PY`, therefore now standard throughout,
- new SUSY processes and improved SUSY simulation relative to SPYTHIA, and new PDG codes for sparticles,
- new processes for Higgs (including doubly-charged in left–right symmetric models), technicolor, ... ,
- several improved resonance decays, including an alternative Higgs mass shape,
- some newer parton distributions, such as CTEQ5 [35],
- initial-state showers matched to some matrix elements,
- new options for final-state gluon splitting to a pair of c/b quarks and modified modeling of initial-state flavor excitation,
- an energy-dependent $p_{\perp\min}$ in multiple interactions,
- an improved modeling of the hadronization of small-mass strings, of importance especially for c/b, and
- a built-in package for one-dimensional histograms (based on GBOOK).

Some of these topics will be further studied below. Other improvements, of less relevance for $\overline{p}p$ colliders, include

- improved modeling of gluon emission off c/b quarks in e^+e^-,
- color rearrangement options for W^+W^- events,
- a Bose-Einstein algorithm expanded with new options,
- a new alternative baryon production scheme [36],
- QED radiation off an incoming muon,
- a new machinery to handle real and virtual photon fluxes, cross sections and parton distributions [37], and
- new standard interfaces for the matching to external generators of two, four and six fermions (and of two quarks plus two gluons) in e^+e^-.

The current list of over 200 different subprocesses covers topics such as hard and soft QCD, heavy flavors, DIS and $\gamma\gamma$, electroweak production of γ^*/Z^0 and $W^\pm$ (singly or in pairs), production of a light or a heavy Standard Model Higgs, or of various Higgs states in

supersymmetric (SUSY) or left–right symmetric models, SUSY particle production (sfermions, gauginos, etc.), technicolor, new gauge bosons, compositeness, and leptoquarks.

Needless to say, most users will still find that their particular area of interest is not as well addressed as could be wished. In some areas, progress will require new ideas, while lack of time and manpower is the limiting factor in others.

3.3. Matching To Matrix Elements

The matrix-element (ME) and parton-shower (PS) approaches to higher-order QCD corrections both have their advantages and disadvantages. The former offers a systematic expansion in orders of α_s, and a powerful machinery to handle multiparton configurations on the Born level, but loop calculations are tough and lead to messy cancellations at small resolution scales. Resummed matrix elements may circumvent the latter problem for specific quantities, but then do not provide exclusive accompanying events. Parton showers are based on an improved leading-log (almost next-to-leading-log) approximation, and so cannot be accurate for well separated partons, but they offer a simple, process-independent machinery that gives a smooth blending of event classes (by Sudakov form factors) and a natural match to hadronization. It is therefore natural to try to combine these descriptions, so that ME results are recovered for widely separated partons while the PS sets the subjet structure.

For final-state showers in $Z^0 \to q\overline{q}$, corrections to the showering were considered quite a while ago [38], e.g. by letting the shower slightly overpopulate the $q\overline{q}g$ phase space and then using a Monte Carlo veto technique to reduce down to the ME level. This approach easily carries over to showers in other color-singlet resonance decays, although the various relevant ME's have not all been implemented in PYTHIA so far.

A similar technique is now available for the description of initial-state radiation in the production of a single color-singlet resonance, such as $\gamma^*/Z^0/W^\pm$ [39]. The basic idea is to map the kinematics between the PS and ME descriptions, and to find a correction factor that can be applied to hard emissions in the shower so as to bring agreement with the matrix-element expression. Some simple algebra shows that, with the PYTHIA shower kinematics definitions, the two $q\overline{q}' \to gW^\pm$ emission rates disagree by a factor

$$R_{q\overline{q}'\to gW}(\hat{s},\hat{t}) = \frac{(\mathrm{d}\hat{\sigma}/\mathrm{d}\hat{\mathrm{t}})_{\mathrm{ME}}}{(\mathrm{d}\hat{\sigma}/\mathrm{d}\hat{\mathrm{t}})_{\mathrm{PS}}} = \frac{\hat{t}^2+\hat{u}^2+2m_W^2\hat{s}}{\hat{s}^2+m_W^4} \ ,$$

which is always between 1/2 and 1. The shower can therefore be improved in two ways, relative to the old description. Firstly, the maximum virtuality of emissions is raised from $Q^2_{\max} \approx m_W^2$ to $Q^2_{\max} = s$, i.e. the shower is allowed to populate the full phase space. Secondly, the emission rate for the final (which normally also is the hardest) $q \to qg$ emission on each side is corrected by the factor $R(\hat{s},\hat{t})$ above, so as to bring agreement with the matrix-element rate in the hard-emission region. In the backwards evolution shower algorithm [9], this is the first branching considered.

The other possible $\mathcal{O}(\alpha_s)$ graph is $qg \to q'W^\pm$, where the corresponding correction factor is

$$R_{qg\to q'W}(\hat{s},\hat{t}) = \frac{(\mathrm{d}\hat{\sigma}/\mathrm{d}\hat{\mathrm{t}})_{\mathrm{ME}}}{(\mathrm{d}\hat{\sigma}/\mathrm{d}\hat{\mathrm{t}})_{\mathrm{PS}}} = \frac{\hat{s}^2+\hat{u}^2+2m_W^2\hat{t}}{(\hat{s}-m_W^2)^2+m_W^4} \ ,$$

which lies between 1 and 3. A probable reason for the lower shower rate here is that the shower does not explicitly simulate the s-channel graph $qg \to q^* \to q'W$. The $g \to q\overline{q}$ branching therefore has to be preweighted by a factor of 3 in the shower, but otherwise the method works the same as above. Obviously, the shower will mix the two alternative branchings, and the correction factor for a final branching is based on the current type.

The reweighting procedure prompts some other changes in the shower. In particular, $\hat{u} < 0$ translates into a constraint on the phase space of allowed branchings.

Our published comparisons with data on the W $p_\perp$ spectrum show quite a good agreement with this improved simulation [39]. A worry was that an unexpectedly large primordial $k_\perp$, around 4 GeV, was required to match the data in the low-$p_{\perp W}$ region. However, at that time we had not realized that the data were not fully unsmeared. The required primordial $k_\perp$ is therefore likely to drop by about a factor of two [40].

It should be noted that also other approaches to the same problem have been studied recently. The HERWIG one requires separate treatments in the hard- and soft-emission regions [41]. Another, more advanced PYTHIA-based one [42], also addresses the next-to-leading order corrections to the total W cross section, while the one outlined above is entirely based on the leading-order total cross section. There is also the possibility of an extension to Higgs production [43].

Summarizing, we now start to believe we can handle initial- and final-state showers, with next-to-leading-order accuracy, in cases where these can be separated by the production of color singlet resonances — even if it should be realized that much work remains to cover the various possible cases. That still does not address the big class of QCD processes where the initial- and final-state radiation does not factorize. Possibly, correction factors to showers could be found also here. Alternatively, it may become necessary to start

showers from given parton configurations of varying multiplicity and with virtual-correction weights, as obtained from higher-order ME calculations. So far, PYTHIA only implements a way to start from a given four-parton topology in e^+e^- annihilation, picking one of the possible preceding shower histories as a way to set constraints for the subsequent shower evolution [44]. This approach obviously needs to be extended in the future, to allow arbitrary parton configurations. Even more delicate will be the consistent treatment of virtual corrections [45], where much work remains.

3.4. Charm And Bottom Hadronization

Significant asymmetries are observed between the production of D and $\overline{D}$ mesons in $\pi^- p$ collisions, with hadrons that share some of the π^- flavor content very much favored at large x_F in the π^- fragmentation region [46]. This behavior was qualitatively predicted by PYTHIA; in fact, the predictions were for somewhat larger effects than seen in the data. The new data has allowed us to go back and take a critical look at the uncertainties that riddle the heavy-flavor description [47]. Many effects are involved, and we limit ourselves here to mentioning only one.

A hadronic event can be subdivided into sets of partons that form separate color singlets. These sets are represented by strings, that e.g. stretch from a quark end via a number of intermediate gluons to an antiquark end. The string has a mass, which can be calculated from the energy-momentum of its partons. Three different mass regions for the strings may be distinguished in the process of hadronization.

1. *Normal string fragmentation.* This is the ideal situation, when each string has a large invariant mass, and the standard iterative fragmentation scheme [48] works well. In practice, this approach can be used for all strings with a mass above a cut-off of a few GeV.
2. *Cluster decay.* If a string is produced with a small invariant mass, then it is possible that only two-body final states are kinematically accessible. The traditional iterative Lund scheme is then not applicable. We call such a low-mass string a cluster, and treat it separately. In recent program versions, the modeling has been improved to give a smooth match onto the standard string scheme in the high-cluster-mass limit.
3. *Cluster collapse.* This is the extreme case of the above situation, where the string mass is so small that the cluster cannot decay into even two hadrons. It is then assumed to collapse directly into a single hadron, which inherits the flavor content of the string endpoints. The original continuum of string/cluster masses is replaced by a discrete set of hadron masses. Energy and momentum then cannot be conserved inside the cluster, but must be exchanged with other objects within the local neighborhood. This description has also been improved.

Because the mass of the charm and bottom partons are not negligible in the fragmentation process, the improved treatment of low-mass systems will have relatively more impact on charm and bottom hadronization. In general, flavor asymmetries are predicted to be smaller for bottom than for charm, and smaller at higher energies (except possibly at very large rapidities). Therefore, we do not expect any spectacular effects at the Tevatron. However, other nontrivial features of fragmentation may persist at higher energies, like a non-negligible systematic shift between the rapidity of a heavy quark parton and that of the hadron produced from it [47]. The possibility of such effects should be considered whenever trying to relate heavy flavor measurements to parton level calculations.

3.5. Multiple Interactions

Because of the composite nature of hadrons, several parton pairs may interact in a typical hadron–hadron collision [49]. Over the years, evidence for this mechanism has accumulated, such as the recent direct observation by CDF [50]. However, the occurrence of two hard interactions in one hadronic collision is just the tip of the iceberg. In the PYTHIA model, most interactions are at lower $p_\perp$, where they are not visible as separate jets but only contribute to the underlying event structure. As such, they are at the origin of a number of key features, like the broad multiplicity distributions, the significant forward–backward multiplicity correlations, and the pedestal effect under jets.

Since the perturbative jet cross section is divergent for $p_\perp \to 0$, it is necessary to regularize it, e.g. by a cut-off at some $p_{\perp\min}$ scale. That such a regularization should occur is clear from the fact that the incoming hadrons are color singlets — unlike the colored partons assumed in the divergent perturbative calculations — and that therefore the color charges should screen each other in the $p_\perp \to 0$ limit. Also other damping mechanisms are possible [51]. Fits to data typically give $p_{\perp\min} \approx 2$ GeV, which then should be interpreted as the inverse of some color screening length in the hadron.

One key question is the energy-dependence of $p_{\perp\min}$; this may be relevant e.g. for comparisons of jet rates at different Tevatron energies, and even more for any extrapolation to LHC energies. The problem actually is more pressing now than at the time of our original study [49], since nowadays parton distributions are

known to be rising more steeply at small x than the flat $xf(x)$ behavior normally assumed for small Q^2 before HERA. This translates into a more dramatic energy dependence of the multiple-interactions rate for a fixed $p_{\perp\min}$.

The larger number of partons also should increase the amount of screening, as confirmed by toy simulations [52]. As a simple first approximation, $p_{\perp\min}$ is assumed to increase in the same way as the total cross section, i.e. with some power $\epsilon \approx 0.08$ [53] that, via reggeon phenomenology, should relate to the behavior of parton distributions at small x and Q^2. Thus the new default in PYTHIA is

$$p_{\perp\min} = (1.9\ \mathrm{GeV}) \left(\frac{s}{1\ \mathrm{TeV}^2} \right)^{0.08} .$$

3.6. Interconnection Effects

The widths of the W, Z and t are all of the order of 2 GeV. A Standard Model Higgs with a mass above 200 GeV, as well as many supersymmetric and other "Beyond the Standard Model" particles would also have widths in the multi-GeV range. Not far from threshold, the typical decay times $\tau = 1/\Gamma \approx 0.1\,\mathrm{fm} \ll \tau_{\mathrm{had}} \approx 1\,\mathrm{fm}$. Thus hadronic decay systems overlap, between a resonance and the underlying event, or between pairs of resonances, so that the final state may not contain independent resonance decays.

So far, studies have mainly been performed in the context of W pair production at LEP2. Pragmatically, one may here distinguish three main eras for such interconnection:

1. Perturbative: this is suppressed for gluon energies $\omega > \Gamma$ by propagator/timescale effects; thus only soft gluons may contribute appreciably.
2. Non-perturbative in the hadroformation process: normally model-led by a color rearrangement between the partons produced in the two resonance decays and in the subsequent parton showers.
3. Non-perturbative in the purely hadronic phase: best exemplified by Bose–Einstein effects.

The above topics are deeply related to the unsolved problems of strong interactions: confinement dynamics, $1/N_{\mathrm{C}}^2$ effects, quantum mechanical interferences, etc. Thus they offer an opportunity to study the dynamics of unstable particles, and new ways to probe confinement dynamics in space and time [54,55], *but* they also risk to limit or even spoil precision measurements.

It is illustrative to consider the impact of interconnection effects on the W mass measurements at LEP2. Perturbative effects are not likely to give any significant contribution to the systematic error, $\langle \delta m_W \rangle \lesssim 5$ MeV [55]. Color rearrangement is not understood from first principles, but many models have been proposed to model effects [55–57], and a conservative estimate gives $\langle \delta m_W \rangle \lesssim 40$ MeV. For Bose–Einstein again there is a wide spread in models, and an even wider one in results, with about the same potential systematic error as above [58,59,57]. The total QCD interconnection error is thus below m_π in absolute terms and 0.1% in relative ones, a small number that becomes of interest only because we aim for high accuracy.

A study of $e^+e^- \to t\bar{t} \to bW^+\bar{b}W^- \to b\bar{b}\ell^+\nu_\ell\ell'^-\overline{\nu}'_\ell$ near threshold gave a realistic interconnection uncertainty of the top mass of around 30 MeV, but also showed that slight mistreatment of the combined color and showering structure could blow up this error by a factor of ten [60]. For hadronic top decays, errors could be much larger.

The above numbers, when applied to hadronic physics, are maybe not big enough to cause an immediate alarm. The addition of a colored underlying event — with a poorly-understood multiple-interaction structure as outlined above — has not at all been considered so far, however, and can only make matters worse in hadronic physics than in e^+e^-. This is clearly a topic for the future, where we should be appropriately humble about our current understanding, at least when it comes to performing precision measurements.

QCD interconnection may also be at the root of a number of other, more spectacular effects, such as rapidity gaps and the whole Pomeron concept [61], and the unexpectedly large rate of quarkonium production [62].

3.7. The Future: On To C++

Finally, a word about the future. PYTHIA continues to be developed. On the physics side, there is a need to increase the support given to different physics scenarios, new and old, and many areas of the general QCD machinery for parton showers, underlying events and hadronization require further improvements, as we have seen.

On the technical side, the main challenge is a transition from Fortran to C++, the language of choice for Run II (and LHC). To address this, the PYTHIA 7 project was started in January 1998, with L. Lönnblad bearing the main responsibility. A similar project, but more ambitious and better funded, is now starting up for HERWIG, with two dedicated postdoc-level positions and a three-year time frame.

For PYTHIA, what exists today is a strategy document [63], and code for the event record, the particle object, some particle data and other data base handling, and the event generation handler structure. All of this is completely new relative to the Fortran version, and is intended to allow for a much more

general and flexible formulation of the event generation process. The first piece of physics, the string fragmentation scheme, is being implemented by M. Bertini, and is nearing completion. The subprocess generation method is being worked on for the simple case of $e^+e^- \to Z^0 \to q\overline{q}$. The hope is to have a "proof of concept" version soon, and some of the current PYTHIA functionality up and running by the end of 2000. It will, however, take much further effort after that to provide a program that is both more and better than the current PYTHIA 6 version. It is therefore unclear whether PYTHIA 7 will be of much use during Run II, except as a valuable exercise for the future.

4. A Comparison of the Predictions from Monte Carlo Programs and Transverse Momentum Resummation

by C. Balázs, J. Huston, I. Puljak, S. Mrenna

4.1. Introduction

Monte Carlo programs including parton showering, such as PYTHIA[3], HERWIG[1] and ISAJET[2], are commonly used by experimentalists, both as a way of comparing experimental data to theoretical predictions, and also as a means of simulating experimental signatures in kinematic regimes for which there is no experimental data (such as that appropriate to the LHC). The final output of the Monte Carlo programs consists of the 4-vectors of a set of stable particles (e.g., e, μ, π, γ); this output can either be compared to reconstructed experimental quantities or, when coupled with a simulation of a detector response, can be directly compared to raw data taken by the experiment, and/or passed through the same reconstruction procedures as the raw data. In this way, the parton shower programs can be more useful to experimentalists than analytic calculations performed at high orders in perturbation theory. Indeed, almost all of the physics plots in the ATLAS physics TDR [108] involve comparisons to PYTHIA(version 5.7).

Here, we are concerned with the predictions of parton shower Monte Carlo programs and those from certain analytic calculations which resum logarithms associated with the transverse momentum of partons initiating the hard scattering. Most analytic calculations of this kind are either based on or originate from the formalism developed by J. Collins, D. Soper, and G. Sterman (CSS), which we choose as the analytic "benchmark" of this section. Both the parton showering and analytic calculations describe the effects of multiple soft gluon emission from the incoming partons, which can have a profound effect on the kinematics of gauge or Higgs bosons and their decay products produced in hadronic collisions. This may have an impact on the signatures of physics processes at both the trigger and analysis levels, and thus it is important to understand the reliability of such predictions. The best method for testing the reliability is a direct comparison of the predictions to experimental data. If no experimental data is available, then some understanding of the reliability may by gained by simply comparing the predictions of different calculational methods.

4.2. Parton Showering and Resummation

Parton showering is the *backwards* evolution of an initial hard scattering process, involving only a few partons at a high scale $Q^2_{\rm max}$ reflecting large virtuality, into a complicated, multi-parton configuration at a much lower scale $Q^2_{\rm min}$ typical of hadronic binding energies. In practice, one does not calculate the probability of arriving at a specific multi-parton configuration all at once. Instead, the full shower is constructed in steps, with evolution down in virtuality Q^2 with no parton emission, followed by parton emission, and then a further evolution downward with no emission, etc., until the scale $Q^2_{\rm min}$ is reached. The essential ingredient for this algorithm is the probability of evolving down in scale with no parton emission or at least no resolvable parton emission. This can be derived from the DGLAP equation for the evolution of parton distribution functions. One finds that the probability of no emission P equals $1-\exp(-S)$, where S is the Sudakov form factor, a function of virtuality and the momentum fraction x carried by a parton.

A key ingredient in the parton showering algorithm is the conservation of energy-momentum at every step in the cascade. The transverse momentum of the final system partly depends on the opening angle between the mother and daughter partons in each emission. Furthermore, after each emission, the entire multi-parton system is boosted to the center-of-mass frame of the two virtual partons, until at the end of the shower one is left with two primordial partons which are on the mass shell and essentially parallel with the incoming hadrons. These boosts also influence the final transverse momentum.

Parton showering resums primarily the leading logarithms – those resummed by the DGLAP equations – which are universal, i.e. process independent, and depend only on the given initial state. In this lies one of the strengths of the parton shower approach, since it can be incorporated into a wide variety of physical processes. An analytic calculation, in comparison, can resum many other types of potentially large logarithms, including process dependent ones. For example, the CSS formalism in principle sums all of the logarithms with Q^2/p_T^2 in their arguments, where, for

the example of Higgs boson production, Q is the four momentum of the Higgs boson and p_T is its transverse momentum. All of the "dangerous logs" are included in the Sudakov exponent, which can be written in impact parameter (b) space as:

$$\mathcal{S}(Q,b) = \int_{1/b^2}^{Q^2} \frac{d\overline{\mu}^2}{\overline{\mu}^2} \left[A\left(\alpha_s(\overline{\mu})\right) \ln\left(\frac{Q^2}{\overline{\mu}^2}\right) + B\left(\alpha_s(\overline{\mu})\right) \right],$$

with the A and B functions being free of large logarithms and calculable in fixed–order perturbation theory:

$$\begin{aligned} A\left(\alpha_s(\bar{\mu})\right) &= \sum_{n=1}^{\infty} \left(\frac{\alpha_s(\bar{\mu})}{\pi}\right)^n A^{(n)}, \\ B\left(\alpha_s(\bar{\mu})\right) &= \sum_{n=1}^{\infty} \left(\frac{\alpha_s(\bar{\mu})}{\pi}\right)^n B^{(n)}. \end{aligned} \tag{17}$$

These functions contain an infinite number of coefficients, with the $A^{(n)}$ being universal to a given initial state, while the $B^{(n)}$ are process dependent. In practice, the number of towers of logarithms included in the Sudakov exponent depends on the level to which a fixed order calculation was performed for a given process. For example, if only a next-to-leading order calculation is available, only the coefficients $A^{(1)}$ and $B^{(1)}$ can be included. If a NNLO calculation is available, then $A^{(2)}$ and $B^{(2)}$ can be extracted and incorporated into a resummation calculation, and so on. This is the case, for example, for Z^0 boson production. So far, only the $A^{(1)}$, $A^{(2)}$ and $B^{(1)}$ coefficients are known for Higgs production, but the calculation of $B^{(2)}$ is in progress [109]. If we try to interpret parton showering in the same language, then we can say that the parton shower Sudakov exponent always contains a term analogous to $A^{(1)}$. It was shown in Reference [110] that a suitable modification of the Altarelli-Parisi splitting function, or equivalently the strong coupling constant α_s, also effectively approximates the $A^{(2)}$ coefficient.[5]

In contrast with parton showering, analytic resummation calculations integrate over the kinematics of the soft gluon emission, with the result that they are limited in their predictive power. While the parton shower maintains an exact treatment of the branching kinematics, the original CSS formalism imposes no kinematic penalty for the emission of the soft gluons, although an approximate treatment of this can be incorporated into a numerical implementation, like ResBos [111]. Neither parton showering nor analytic resummation reproduces kinematic configurations where one hard parton is emitted at large p_T. In the parton shower, matrix element corrections can be imposed [39,41], while, in the analytic resummation calculation, matching is necessary.

With the appropriate input from higher order cross sections, a resummation calculation has the corresponding higher order normalization and scale dependence. The normalization and scale dependence for the Monte Carlo, though, remains that of a leading order calculation – though see Ref. [42] and the related contribution to these proceedings for an idea of how to include these at NLO. The parton showering occurs with unit probability after the hard scattering, so it does not change the total cross section.[6]

Given the above discussion, one quantity which should be well-described by both calculations is the shape of the transverse momentum (p_T) distribution of the final state electroweak boson in a subprocess such as $q\overline{q} \to WX$, ZX or $gg \to HX$, where most of the p_T is provided by initial state parton showering. The parton showering supplies the same sort of transverse kick as the soft gluon radiation in a resummation calculation. Indeed, very similar Sudakov form factors appear in both approaches, with the caveats about the $A^{(n)}$ and $B^{(n)}$ terms mentioned previously.

At a point in its evolution corresponding to a virtuality on the order of a few GeV, the parton shower is stopped and the effects of gluon emission at softer scales must be parameterized and inserted by hand. Typically, a Gaussian probability distribution function is used to assign an extra "primordial" k_T to the primordial partons of the shower (the ones which are put on the mass shell at the end of the backwards showering). In `PYTHIA`, the default is a constant value of k_T. Similarly, there is a somewhat arbitrary division between perturbative and non-perturbative regions in a resummation calculation. Sometimes the non-perturbative effects are also parametrized by Gaussian distributions in b or Q_T space. In general, the value for the non-perturbative $\langle k_T \rangle$ needed in a Monte Carlo program will depend on the particular kinematics being investigated. In the case of the resummation calculation the non-perturbative physics is determined from fits to fixed target data and then automatically evolved to the kinematic regime of interest.

A value for the average non-perturbative k_T of greater than 1 GeV does not imply that there is an anomalous intrinsic k_T associated with the parton size; rather this amount of $\langle k_T \rangle$ needs to be supplied to provide what is missing in the truncated parton

[5] This is rigorously true only for the high parton x or $\sqrt{\tau}$ region.

[6] Technically, one could add the branching for $q \to q$+Higgs in the shower, which would have the capability of increasing somewhat the Higgs cross section; however, the main contribution to the higher order K-factor comes from the virtual corrections and the 'Higgs Bremsstrahlung' contribution is negligible.

shower. If the shower is cut off at a higher virtuality, more of the "non-perturbative" k_T will be needed.

4.3. Z^0 Boson Production at the Tevatron

The 4-vector of a Z^0 boson, and thus its transverse momentum, can be measured with great precision in the e^+e^- decay mode. Resolution effects are relatively minor and are easily corrected for. Thus, the Z^0 p_T distribution is a great testing ground for both the resummation and Monte Carlo formalisms for soft gluon emission. The corrected p_T distribution for Z^0 bosons in the low p_T region for the CDF experiment[7] is shown in Figure 2, compared to both the resummed prediction from ResBos, and to two predictions from PYTHIA (version 6.125). One PYTHIA prediction uses the default (rms)[8] value of intrinsic k_T of 0.44 GeV and the second a value of 2.15 GeV per incoming parton.[9] The latter value was found to give the best agreement between PYTHIA and the data.[10] All of the predictions use the CTEQ4M parton distributions [112]. The shift between the two PYTHIA predictions at low p_T is clearly evident. As might have been expected, the high p_T region (above 10 GeV) is unaffected by the value of the non-perturbative k_T. Note the k_T imparted to the incoming partons at their lowest virtuality, Q_0, is greatly reduced in its effect on the Z^0 p_T distribution. This dilution arises because the center-of-mass energy of the "primordial" partons is typically much larger than that of the original hard scattering. Therefore, the transverse β of the boost applied to the Z^0 boson to transform it to the frame where the "primordial" partons have transverse momentum k_T is small.

As an exercise, one can transform the resummation formula in order to bring it to a form where the non-perturbative function acts as a Gaussian type smearing term. Using the Ladinsky-Yuan parameterization [114] of the non-perturbative function in ResBos leads to an rms value for the effective k_T smearing parameter, for Z^0 production at the Tevatron, of 2.5 GeV. This is similar to that needed for PYTHIA and HERWIG to describe the Z^0 production data at the Tevatron.

In Figure 2, the normalization of the resummed prediction has been rescaled upwards by 8.4%. The PYTHIA prediction was rescaled by a factor of 1.3-1.4 (remember that this is only a leading order comparison) for the shape comparison.

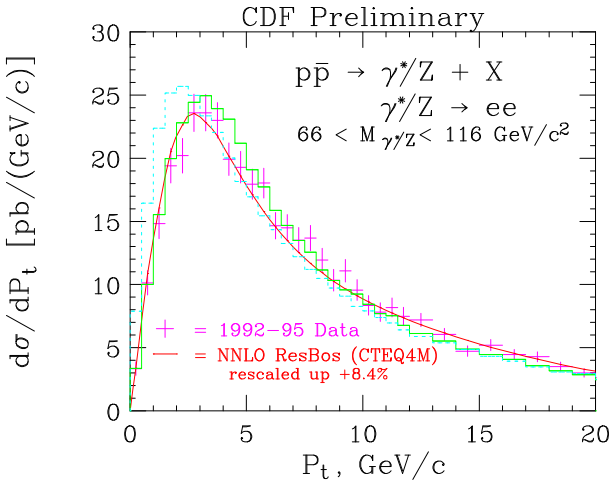

Figure 2. The Z^0 p_T distribution (at low p_T) from CDF for Run 1 compared to predictions from ResBos and from PYTHIA. The two PYTHIA predictions use the default (rms) value for the non-perturbative k_T (0.44 GeV) and the value that gives the best agreement with the shape of the data (2.15 GeV).

As stated previously, the resummed prediction correctly describes the shape of the Z^0 p_T distribution at low p_T, although there is still a noticeable difference in shape between the Monte Carlo and the resummed prediction. It is interesting to note that if the process dependent coefficients ($B^{(1)}$ and $B^{(2)}$) were not incorporated into the resummation prediction, the result would be an increase in the height of the peak and a decrease in the rate between 10 and 20 GeV, leading to a better agreement with the PYTHIA prediction [115].

The PYTHIA and ResBos predictions both describe the data well over a wider p_T range than shown in the figure. Note especially the agreement of PYTHIA with the data at high p_T, made possible by explicit matrix element corrections (from the subprocesses $q\overline{q} \rightarrow Z^0 g$ and $gq \rightarrow Z^0 q$) to the Z^0 production process.[11]

[7] We thank Willis Sakumoto for providing the figures for Z^0 production as measured by CDF

[8] For a Gaussian distribution, $k_T^{rms} = 1.13\langle k_T \rangle$.

[9] A previous publication [39] indicated the need for a substantially larger non-perturbative $\langle k_T \rangle$, of the order of 4 GeV for the case of W production at the Tevatron. The data used in the comparison, however, were not corrected for resolution smearing, a fairly large effect for the case of $W \rightarrow e\nu$ production and decay.

[10] A similar conclusion has been reached for comparisons of the CDF Z^0 p_T data with HERWIG. [113]

[11] Slightly different techniques are used for the matrix element corrections by PYTHIA [39] and by HERWIG [41]. In PYTHIA, the parton shower probability distribution is applied over the whole phase space and the exact matrix element corrections are applied only to the branching closest to the hard scatter. In HERWIG, the corrections are generated separately for the regions of phase space unpopulated by HERWIG (the 'dead zone') and the populated region. In the dead zone, the radiation is generated according to a distribution using the first order matrix element calculation, while the algorithm for the already populated region applies matrix element corrections whenever a branching is capable of being 'the hardest so far'.

4.4. Diphoton Production

Most of the comparisons between resummation calculations/Monte Carlos and data have been performed for Drell-Yan production, i.e. $q\overline{q}$ initial states. It is also interesting to examine diphoton production at the Tevatron, where a large fraction of the contribution at low diphoton mass is due to gg scattering. The prediction for the di-photon k_T distribution at the Tevatron, from PYTHIA (version 6.122), is shown in Figure 3, using the experimental cuts applied in the CDF analysis [116].

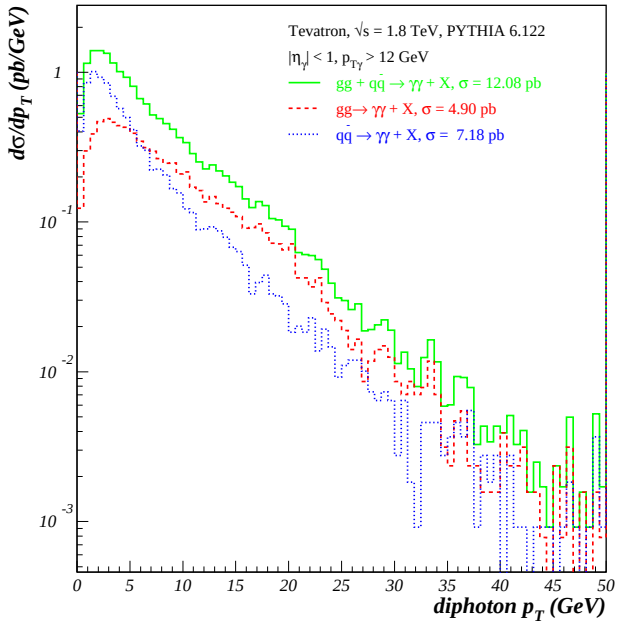

Figure 3. A comparison of the PYTHIA predictions for di-photon production at the Tevatron for the two different subprocesses, $q\overline{q}$ and gg. The same cuts are applied to PYTHIA as in the CDF di-photon analysis.

It is interesting to note that about half of the di-photon cross section at the Tevatron is due to the gg subprocess, and that the di-photon p_T distribution is noticeably broader for the gg subprocess than the $q\overline{q}$ subprocess. The gg subprocess predictions in ResBos agree well with those from PYTHIA while the $q\overline{q}$ p_T distribution is noticeably broader in ResBos. The latter behavior is due to the presence of the Y piece (fixed-order corrections) in ResBos at moderate p_T, and the matching of the $q\overline{q}$ cross section to the fixed order $q\overline{q} \to \gamma\gamma g$ at high p_T. The corresponding matrix element correction is not in PYTHIA. It is interesting to note that the PYTHIA and ResBos predictions for $gg \to \gamma\gamma$ agree in the moderate p_T region, even though the ResBos prediction has the Y piece present and is matched to the matrix element piece $gg \to \gamma\gamma g$ at high p_T, while there is no such matrix element correction for PYTHIA. This shows that the Y piece correction is not important for the gg subprocess, which is the same conclusion that was reached in Ref. [117]. This is probably a result of steep decline in the gg parton-parton with increasing partonic center of mass energy, $\sqrt{\hat{s}}$. This falloff tends to suppress the size of the Y piece since the production of the di-photon pair at higher p_T requires larger x_1, x_2 values. In the default CSS formalism, there is no such kinematic penalty in the resummed piece since the soft gluon radiation comes for "free." (Larger x_1 and x_2 values are not required.)

A comparison of the CDF di-photon data to NLO [118] and resummed (ResBos) QCD predictions has been performed, but the analysis is still in progress, so the results are not presented here. The transverse momentum distribution, in particular, is sensitive to the effects of the soft gluon radiation and better agreement can be observed with the ResBos prediction than with the NLO one. A much more precise comparison with the effects of soft gluon radiation will be possible with the 2 fb^{-1} or greater data sample that is expected for both CDF and DØ in Run 2.

4.5. Higgs Boson Production

A comparison of the two versions of PYTHIA and of ResBos is shown in Figure 4 for the case of the production of a Higgs boson with mass 100 GeV at the Tevatron with center-of-mass energy of 2.0 TeV. The same qualitative features are observed at the LHC: the newer version of PYTHIA agrees better with ResBos in describing the low p_T shape, and there is a falloff at high p_T unless the hard scale for showering is increased. The default (rms) value of the non-perturbative k_T (0.44 GeV) was used for the PYTHIA predictions. Note that the peak of the resummed distribution has moved to $p_T \approx 7$ GeV (compared to about 3 GeV for Z^0 production at the Tevatron). This is due primarily to the larger color factors associated with initial state gluons ($C_A = 3$) rather than quarks ($C_F = 4/3$).

The newer version of PYTHIA agrees well with ResBos at low to moderate p_T, but falls below the resummed prediction at high p_T. This is easily understood: ResBos switches to the NLO Higgs + jet matrix element at high p_T while the default PYTHIA can

generate the Higgs p_T distribution only by initial state gluon radiation, using as default a maximum scale equal to the Higgs boson mass. High p_T Higgs boson production is another example where a $2 \to 1$ Monte Carlo calculation with parton showering can not completely reproduce the exact matrix element calculation without the use of matrix element corrections. The high p_T region is better reproduced if the maximum virtuality Q^2_{max} is set equal to the collider center-of-mass energy, s, rather than subprocess $\hat{s}$. This is equivalent to applying the parton shower to all of phase space. However, the consequence is that the low p_T region is now depleted of events, since the parton showering does not change the total production cross section. The appropriate scale to use in PYTHIA (or any Monte Carlo) depends on the p_T range to be probed. If matrix element information is used to constrain the behavior, the correct high p_T cross section can be obtained while still using the lower scale for showering. The incorporation of matrix element corrections to Higgs production (involving the processes $gq \to qH$, $q\overline{q} \to gH$, $gg \to gH$) is the next logical project for the Monte Carlo experts, in order to accurately describe the high p_T region.

The older version of PYTHIA produces too many Higgs events at moderate p_T (in comparison to ResBos) at both the Tevatron and the LHC. Two changes have been implemented in the newer version. The first change is that a cut is placed on the combination of z and Q^2 values in a branching: $\hat{u} = Q^2/z - \hat{s}(1-z) < 0$, where $\hat{s}$ refers to the subsystem of the hard scattering plus the shower partons considered to that point. The association with $\hat{u}$ is relevant if the branching is interpreted in terms of a $2 \to 2$ hard scattering. This requirement is not fulfilled when the Q^2 value of the space-like emitting parton is little changed and the z value of the branching is close to unity. This affects mainly the hardest emission (largest Q^2). The net result of this requirement is a substantial reduction in the total amount of gluon radiation [119]. Such branchings are kinematically allowed, but since matrix element corrections would assume initial state partons to have $Q^2 = 0$, a non-physical $\hat{u}$ results (and thus no possibility to impose matrix element corrections). The correct behavior is beyond the predictive power of leading log Monte Carlos.

In the second change, the parameter for the minimum gluon energy emitted in space-like showers is modified by an extra factor roughly corresponding to the $1/\gamma$ factor for the boost to the hard subprocess frame [119]. The effect of this change is to increase the amount of gluon radiation. Thus, the two effects are in opposite directions but with the first effect being dominant.

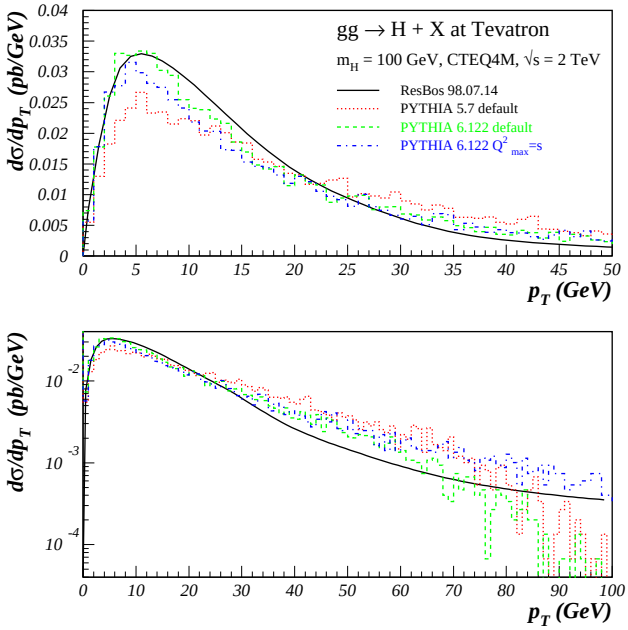

Figure 4. A comparison of predictions for the Higgs p_T distribution at the Tevatron from ResBos and from two recent versions of PYTHIA. The ResBos and PYTHIA predictions have been normalized to the same area.

This difference in the p_T distribution between the two versions of PYTHIA could have an impact on the analysis strategies for Higgs searches at the LHC. For example, for the CMS detector, the higher p_T activity associated with Higgs production in version 5.7 would have allowed for a more precise determination of the event vertex from which the Higgs (decaying into two photons) originated. Vertex pointing with the photons is not possible in CMS, and the large number of interactions occurring with high intensity running will mean a substantial probability that at least one of the interactions will produce jets at low to moderate E_T. [120] In principle, this problem could affect the p_T distribution for all PYTHIA processes. In practice, the effect has manifested itself only in gg initial states, due to the enhanced branching probability.

As an exercise, an 80 GeV W and an 80 GeV Higgs were generated at the Tevatron using PYTHIA5.7 [121]. A comparison of the distribution of values of $\hat{u}$ and the virtuality Q for the two processes indicates a greater tendency for the Higgs virtuality to be near the

maximum value and for there to be a larger number of Higgs events with positive $\hat{u}$ (than W events).

4.6. Comparison with HERWIG

The variation between versions 5.7 and 6.1 of PYTHIA gives an indication of the uncertainties due to the types of choices that can be made in Monte Carlos. The requirement that $\hat{u}$ be negative for all branchings is a choice rather than an absolute requirement. Perhaps the better agreement of version 6.1 with ResBos is an indication that the adoption of the $\hat{u}$ restrictions was correct. Of course, there may be other changes to PYTHIA which would also lead to better agreement with ResBos for this variable.

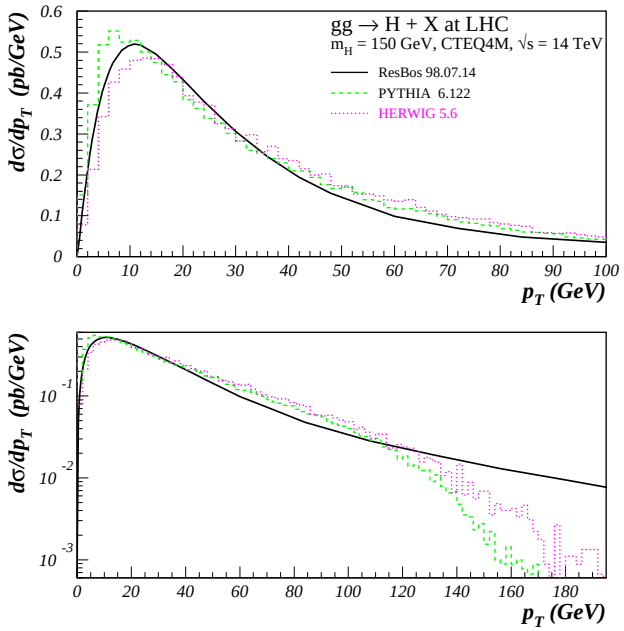

Figure 5. A comparison of predictions for the Higgs p_T distribution at the LHC from ResBos, two recent versions of PYTHIA and HERWIG. The ResBos, PYTHIA and HERWIG predictions have been normalized to the same area.

Since there are a variety of choices that can be made in Monte Carlo implementations, it is instructive to compare the predictions for the p_T distribution for Higgs boson production from ResBos and PYTHIA with that from HERWIG (version 5.6, also using the CTEQ4M parton distribution functions). The HERWIG prediction is shown in Figure 5 along with the PYTHIA and ResBos predictions, all normalized to the ResBos prediction. [12] In all cases, the CTEQ4M parton distribution was used. The predictions from HERWIG and PYTHIA 6.1 are very similar, with the HERWIG prediction matching the ResBos shape somewhat better at low p_T.

4.7. Non-perturbative k_T

A question still remains as to the appropriate value of non-perturbative k_T to input in the Monte Carlos to achieve a better agreement in shape, both at the Tevatron and at the LHC. Figure 6 compares the ResBos and PYTHIA predictions for the Higgs boson p_T distribution at the Tevatron. The PYTHIA prediction (now version 6.1 alone) is shown with several values of non-perturbative k_T. Surprisingly, no difference is observed between the predictions with the different values of k_T, with the peak in PYTHIA always being somewhat below that of ResBos. This insensitivity can be understood from the plots at the bottom of the two figures which show the sum of the non-perturbative initial state k_T (k_{T1}+k_{T2}) at Q_0 and at the hard scatter scale Q. Most of the k_T is radiated away, with this effect being larger (as expected) at the LHC. The large gluon radiation probability from a gluon-gluon initial state (and the greater phase space available at the LHC) lead to a stronger degradation of the non-perturbative k_T than was observed with Z^0 production at the Tevatron.

4.8. Conclusions

An understanding of the signature for Higgs boson production at either the Tevatron or LHC depends upon the understanding of the details of soft gluon emission from the initial state partons. This soft gluon emission can be modeled either in a Monte Carlo or in a k_T resummation program, with various choices possible in both implementations. A comparison of the two approaches is useful to understand the strengths and weaknesses of each. The data from the Tevatron that either exists now, or will exist in Run 2, will be extremely useful to test both approaches.

Acknowledgements

We would like to thank Claude Charlot, Gennaro Corcella, Willis Sakumoto, Torbjorn Sjöstrand and Valeria Tano for useful conversations and for providing some of the plots.

5. MCFM: a parton-level Monte Carlo at NLO Accuracy

by John Campbell and R.K. Ellis

[12] The normalization factors (ResBos/Monte Carlo) are PYTHIA (both versions)(1.61) and HERWIG (1.76).

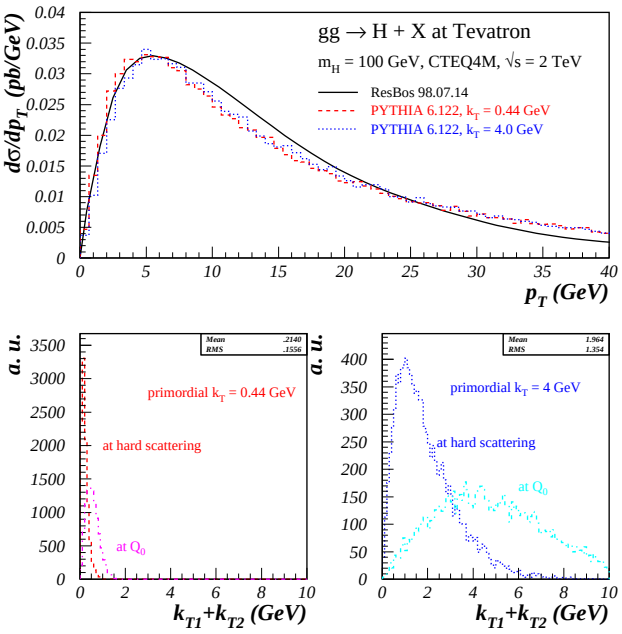

Figure 6. (top) A comparison of the PYTHIA predictions for the p_T distribution of a 100 GeV Higgs at the Tevatron using the default (rms) non-perturbative k_T (0.44 GeV) and a larger value (4 GeV), at the initial scale Q_0 and at the hard scatter scale. Also shown is the ResBos prediction (bottom) The vector sum of the intrinsic k_T (k_{T1}+k_{T2}) for the two initial state partons at the initial scale Q_0 and at the hard scattering scale for the two values of intrinsic k_T.

5.1. Introduction

In Run II, experiments at the Tevatron will be sensitive to processes occurring at the femtobarn level. Of particular interest are processes which involve heavy quarks, leptons and missing energy, since so many of the signatures for physics beyond the standard model produce events containing these features. We have therefore written the program MCFM [123,79] which calculates the rates for a number of standard model processes. These processes are included beyond the leading order in the strong coupling constant where possible; in QCD this is the first order in which the normalization of the cross sections is determined. Because the program produces weighted Monte Carlo events, we can implement experimental cuts allowing realistic estimates of event numbers for an ideal detector configuration. MCFM is expected to give more reliable results than parton shower Monte Carlo programs, especially in phase space regions with well separated jets. On the other hand it gives little information about the phase space regions which are dominated by multiple parton emission. In addition, because the final state contains partons rather than hadrons, a full detector simulation cannot be performed directly using the output of MCFM.

The processes already included in MCFM at NLO are as follows ($H_1, H_2 = p$ or $\bar{p}$),

- $H_1 + H_2 \to W^{\pm}$
- $H_1 + H_2 \to Z$
- $H_1 + H_2 \to W^{\pm} + 1$ jet
- $H_1 + H_2 \to Z + 1$ jet
- $H_1 + H_2 \to W^{\pm} + H$
- $H_1 + H_2 \to Z + H$
- $H_1 + H_2 \to W^{+}W^{-}$
- $H_1 + H_2 \to W^{\pm}Z$
- $H_1 + H_2 \to ZZ$
- $H_1 + H_2 \to W^{+} + g^{*}(\to b\bar{b})$, massless b-quarks
- $H_1 + H_2 \to Z + g^{*}(\to b\bar{b})$, massless b-quarks
- $H_1 + H_2 \to H \to W^{+}W^{-}, ZZ$ or $t\bar{t}$
- $H_1 + H_2 \to \tau^{+} + \tau^{-}$.

The decays of vector bosons and/or Higgs bosons are included. We have also included the leptonic decays of the τ-lepton. As described below the implementation of NLO corrections requires the calculation of both the amplitude for real radiation and the virtual corrections to the Born level process. We have extensively used the one loop results of Bern, Dixon, Kosower *et al.* [124], [125] to obtain the virtual corrections to above processes.

A future development path for the program would be to include the following processes at NLO:

- $H_1 + H_2 \to W^{\pm} + 2$ jets
- $H_1 + H_2 \to Z + 2$ jets .

In addition there are an number of processes which we have included only at leading order. This restriction to leading order is both a matter of expediency and because the theoretical framework for including radiative corrections to processes involving massive particles is not yet complete.

- $H_1 + H_2 \to t + \bar{t}$
- $H_1 + H_2 \to t + \bar{t} + 1$ jet
- $H_1 + H_2 \to t + \bar{b}$
- $H_1 + H_2 \to t + \bar{b} + 1$ jet
- $H_1 + H_2 \to t + \bar{t} + H$
- $H_1 + H_2 \to t + \bar{t} + Z$

H, Z and top quark decays are included.

5.2. General structure

In order to evaluate the strong radiative corrections to a given process, we have to consider Feynman diagrams describing real radiation, as well as the diagrams involving virtual corrections to the tree level graphs. The corrections due to real radiation are dealt with using a subtraction algorithm[126] as formulated by Catani and Seymour [127]. This algorithm is based on the fact that the singular parts of the QCD matrix elements for real emission can be singled out in a process-independent manner. By exploiting this observation, one can construct a set of counter-terms that cancel all non-integrable singularities appearing in real matrix elements. The NLO phase space integration can then be performed numerically in four dimensions.

The counter-terms that were subtracted from the real matrix elements have to be added back and integrated analytically over the phase space of the extra emitted parton in n dimensions, leading to poles in $\epsilon = (n-4)/2$. After combining those poles with the ones coming from the virtual graphs, all divergences cancel, so that one can safely perform the limit $\epsilon \to 0$ and carry out the remaining phase space integration numerically.

As an example of this procedure we consider the production of an on-shell W boson decaying to a lepton-antilepton pair.

$$q(p_1) + \bar{q}(p_2) \to W^+(\nu(p_3) + e^+(p_4)),$$
$$p_1 + p_2 = p_3 + p_4, \quad (p_3 + p_4)^2 = M_W^2. \quad (18)$$

In this case, the W boson rapidity distribution is calculable analytically in $O(\alpha_s)$ [128,129]. Fig. 7 shows the result calculated in the $\overline{MS}$ scheme. The virtual corrections to (18) are of the Drell-Yan type and are well known [128]. They are expressible as an overall factor multiplying the lowest order matrix element squared,

$$\sigma^{\rm V} = \sigma^{\rm LO} \times \frac{\alpha_s C_F}{2\pi} \left(\frac{4\pi\mu^2}{Q^2}\right)^{\epsilon} \frac{1}{\Gamma(1-\epsilon)} \left[-\frac{2}{\epsilon^2} - \frac{3}{\epsilon} - 6 + \pi^2\right] \quad (19)$$

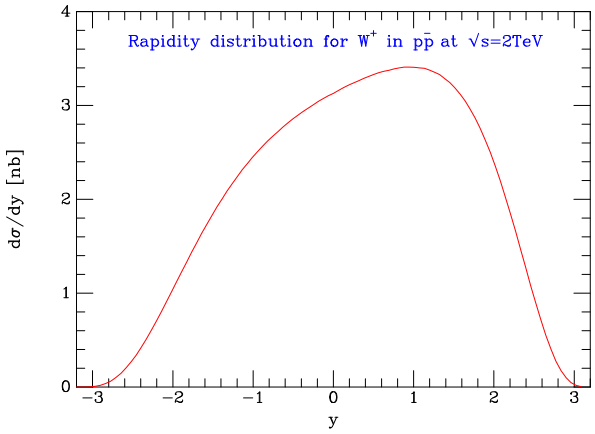

Figure 7. The rapidity distribution for W^+ production in $p\bar{p}$ collisions at $\sqrt{s} = 2$TeV.

and must be combined with the real radiation contribution. For example, gluon radiation from the $q\bar{q}$ initial state yields the subprocess

$$q(p_1) + \bar{q}(p_2) \to W(\nu(p_3) + e^+(p_4)) + g(p_5),$$
$$p_1 + p_2 = p_3 + p_4 + p_5. \quad (20)$$

To eliminate the singular part of this subprocess, we generate a counter event with the kinematics of the $2 \to 2$ process as follows

$$q(x_a p_1) + \bar{q}(p_2) \to W(\nu(\tilde{p}_3) + e^+(\tilde{p}_4)),$$
$$x_a p_1 + p_2 = \tilde{p}_3 + \tilde{p}_4 \quad (21)$$

where a Lorentz transformation has been performed on all j final state momenta

$$\tilde{p}_j^{\mu} = \Lambda_{\nu}^{\mu} p_j^{\nu}, \quad j = 3, 4 \quad (22)$$

such that $\tilde{p}_j^{\mu} \to p_j$ for p_5 collinear or soft. Thus the energy of the emitted gluon p_5 is absorbed by p_1, and the momentum components are absorbed by the transformation of the final state vectors. The phase space has a convolution structure,

$$d\Phi^{(3)}(p_5, p_4, p_3; p_2, p_1) = \int_0^1 dx\, d\Phi^{(2)}(\tilde{p}_4, \tilde{p}_3; p_2, p_1) \times [dp_5(p_1, p_2, x)] \quad (23)$$

where

$$[dp_5(p_1, p_2, x)] = \frac{d^d p_5}{(2\pi)^{d-1}} \delta^+(p_5^2)\Theta(x)\Theta(1-x)\delta(x - x_a) \quad (24)$$

This phase space may be used to integrate out the dipole term $D^{15,2}$, which is chosen to reproduce the singularities in the real matrix elements as the gluon (5) becomes soft or collinear to the quark (1),

$$D^{15,2} = \frac{4\pi\alpha_s C_F \mu^{2\epsilon}}{p_1 \cdot p_5}\left(\frac{2}{1-x_a} - 1 - x_a\right) \qquad (25)$$

Performing the integration yields,

$$\int_0^1 dx\, D^{15,2}\,[dp_5(p_1,p_2,x)] = \frac{\alpha_s C_F}{2\pi}\left(\frac{4\pi\mu^2}{2p_1\cdot p_2}\right)^{\epsilon}\frac{1}{\Gamma(1-\epsilon)}\times \left[-\frac{1}{\epsilon}p_{qq}(x) + \delta(1-x)\left(\frac{1}{\epsilon^2}+\frac{3}{2\epsilon}-\frac{\pi^2}{6}\right) + 2(1+x^2)\left[\frac{\log(1-x)}{1-x}\right]_+\right] \qquad (26)$$

with the Altarelli-Parisi function $p_{qq}(x)$ given by

$$p_{qq}(x) = \frac{2}{(1-x)_+} - 1 - x + \frac{3}{2}\delta(1-x) \qquad (27)$$

In order to obtain the complete counter-term, one must add the (identical) contribution from the dipole configuration $D^{25,1}$ that accounts for the gluon becoming collinear with the anti-quark. In a more complicated process, we would sum over a larger number of distinct dipole terms involving partons both in the initial and final states. In this simple case, we find the total counter-term contribution to the $q\bar{q}$ cross-section to be

$$\sigma^{\rm CT} = \frac{\alpha_s C_F}{2\pi}\left(\frac{4\pi\mu^2}{Q^2}\right)^{\epsilon}\frac{1}{\Gamma(1-\epsilon)}\times\left[-\frac{2}{\epsilon}p_{qq}(x) + \delta(1-x)\left(\frac{2}{\epsilon^2}+\frac{3}{\epsilon}-\frac{\pi^2}{3}\right) - 2p_{qq}(x)\log x + 4(1+x^2)\left[\frac{\log(1-x)}{1-x}\right]_+\right]$$

where each of these terms leads to a different type of contribution in MCFM. The first term, proportional to $p_{qq}(x)$, is canceled by mass factorization, up to some additional finite ($\mathcal{O}(\epsilon^0)$) pieces. The terms multiplying the delta-function $\delta(1-x)$ manifestly cancel the poles generated by the virtual graphs, given in equation (19), leaving an additional π^2 contribution. The remaining terms, which don't have the structure of the virtual contribution, are collected together and added separately in MCFM.

In Fig. 8 we have plotted the three contributions to the W rapidity calculated using MCFM. The three contributions are a) the contribution of (real-counterterm) [the lower curve], b) the contribution of leading order + virtual + integrated counter-term [the upper-most curve] and c) the total contribution. All three terms have been normalized to the $O(\alpha_s)$ rapidity distribution shown in Fig. 7. We see that (b), the leading order term, combined with the virtual correction and the results from the counterterm provides the largest contribution to the cross section. The total contribution is a horizontal line at unity, showing the agreement between MCFM and the analytically calculated result. Only at the boundaries of the phase space at large y can the contribution of the real emission minus the counterterm become sizeable.

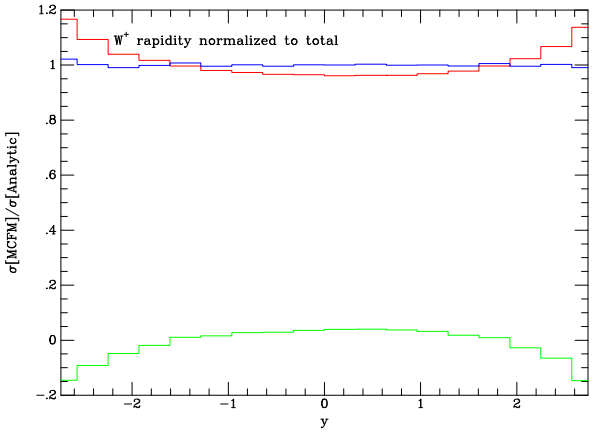

Figure 8. The ratio of the contributions to the rapidity distribution of W^+ production

5.3. Examples of MCFM results

We first detail the input parameters used in our phenomenological estimates. The electroweak theory is specified by four numbers, $M_W, M_Z, \alpha(M_Z)$, and G_F, the values of which are given in Table 1, together with other necessary constants. Other derived parameters are e, g_W and $\sin^2\theta_W$ which, when defined as below, are effective parameters including the leading effects of top quark loops[130]. We use the the first of the MRS99 parton distributions[131] which has $\alpha_S(M_Z) = 0.1175$.

$$\begin{aligned} e^2 &= 4\pi\alpha(M_Z) \\ g_W^2 &= 4\sqrt{2}G_F M_W^2 \\ \sin^2\theta_W &= \frac{e^2}{g_W^2} \end{aligned} \qquad (28)$$

Table 2 shows the production cross sections for di-boson production calculated using MCFM for $p\bar{p}$ collisions at $\sqrt{s} = 2$ TeV and for pp collisions at $\sqrt{s} = 14$ TeV. The next-to-leading order corrections vary between approximately 30% and 50% of leading

Table 1
Input parameters

M_Z, Γ_Z	91.187, 2.49 GeV
M_W, Γ_W	80.41, 2.06 GeV
m_t, Γ_t	175, 1.4 GeV
$\alpha(M_Z)$	$1/128.89$
G_F	1.16639×10^{-5}
$\sin^2\theta_W$	0.228534483
V_{ud}	0.97500
V_{us}	0.22220
V_{cd}	0.22220
V_{cs}	0.97500
Higgs mass (GeV)	BR($H \to b\bar{b}$)
100	0.8119
110	0.7697
120	0.6778
130	0.5254

Table 2
Diboson cross sections (in pb) at the Tevatron and the LHC

$\sqrt{s}$	$\sigma(W^+W^-)$	$\sigma(W^+Z)$	$\sigma(W^-Z)$	$\sigma(ZZ)$
2 TeV ($p\bar{p}$)	12.2	2.02		1.75
14 TeV (pp)	103.6	27.2	17.7	16.7

order and are almost entirely due to the virtual graphs. The numbers here are slightly different than the results in [79], because of the different choices made both for the input EW parameters and parton distributions as detailed above.

Much effort has been devoted to the study of Higgs production at the Tevatron at $\sqrt{s} = 2$ TeV. These studies indicate that, given enough luminosity, a light Higgs boson can be discovered at the Tevatron using the associated production channels WH and ZH. In this report we present results of an analysis that incorporates as many of the backgrounds as possible at next-to-leading order for the WH channel. Whilst we use no detector simulation and do not attempt to include non-physics backgrounds, the results presented here can provide a normalization for more detailed studies. This is of importance since more detailed studies are often performed using shower Monte Carlo programs which can give misleading results for well separated jets.

In particular, we will consider the light Higgs case ($M_H < 130$ GeV) in the channel $p\bar{p} \to b\bar{b}\nu e^+$. In addition to the usual cuts on rapidity and transverse momentum,

$$\begin{aligned} |y_b|, |y_{\bar{b}}| &< 2 , \\ |y_e| &< 2.5 , \\ |p_b^T|, |p_{\bar{b}}^T| &> 15 \text{ GeV} , \\ |p_e^T|, |p_\nu^T| &> 20 \text{ GeV} , \end{aligned} \tag{29}$$

we also impose isolation cuts,

$$R_{b\bar{b}}, R_{eb}, R_{e\bar{b}} > 0.7 , \tag{30}$$

as well as a cut on the scattering angle of the $b\bar{b}$ system [132] (the Higgs scattering angle) in the Collins-Soper frame [133],

$$|\cos\theta_{b\bar{b}}| < 0.8 . \tag{31}$$

Note that imposing the cut on $\cos\theta_{b\bar{b}}$ requires knowledge of the longitudinal component of a neutrino momentum. Our results for the signal, backgrounds and significance are shown in Table 3, where we use $\epsilon_{b\bar{b}} = 0.45$ and integrate the cross-sections over a $b\bar{b}$ mass range appropriate for the Higgs mass under consideration,

$$|M_H - M_{b\bar{b}}| < \sqrt{2}\sigma_M, \sigma_M = 0.1 M_H. \tag{32}$$

From this table, one can see that, even with a fairly restrictive set of cuts, the Wg^* process in particular provides a challenging background. This is further emphasized in Figure 9, where the cross-sections for $M_H = 110$ GeV are presented in 5 GeV bins across the entire $m_{b\bar{b}}$ spectrum. The signal, the two largest backgrounds and the sum of all the backgrounds including top quark production are plotted separately, as well as the totals with and without the Higgs signal. The sharp peak of the Higgs signal becomes only a small shoulder in the total distribution.

5.4. Conclusions

We have introduced the program MCFM, which calculates the rates for a number of standard model processes that are particularly relevant in Run II. These calculations are performed in fixed-order perturbation theory, mainly at next-to-leading order in the strong coupling, and as such differ from other approaches such as parton shower Monte Carlos. As illustrations of the use of MCFM, we have presented total di-boson cross-sections and a primitive study (lacking detector effects and non-physics backgrounds) of WH production as a search for a light Higgs. Such calculations can be used to provide normalizations for more detailed studies in the future.

6. Experimental handles on the backgrounds to new physics searches

by Regina Demina

Table 3
Signal, backgrounds (in fb) and significance for the W-channel at $\sqrt{s} = 2$ TeV

M_H [GeV]	Scale	100	110	120	130
$W^{\pm}H(\to b\bar{b})$	m_H	8.8	6.4	4.2	2.5
$W^{\pm}g^*(\to b\bar{b})$	$(m_W + 100\text{ GeV})/2$	25.7	22.7	18.5	15.5
$W^{\pm}Z(\to b\bar{b})$	$(m_W + 100\text{ GeV})/2$	6.7	4.3	2.0	1.0
$t(\to bW^+)\bar{t}(\to \bar{b}W^-_{\text{lept}})$	100 GeV	3.3	3.7	3.9	3.9
$t(\to bW^+)\bar{t}(\to \bar{b}W^-_{\text{hadr}})$	100 GeV	0.3	0.4	0.5	0.6
$W^{\pm *}(t(\to bW^+)\bar{b})$	100 GeV	5.1	5.8	6.0	6.0
$q't(\to bW^+)$	100 GeV	0.3	0.4	0.5	0.6
Total B	-	41.4	37.3	31.4	27.6
S/B	-	0.21	0.17	0.13	0.09
$S/\sqrt{B}$	-	1.37	1.05	0.75	0.48

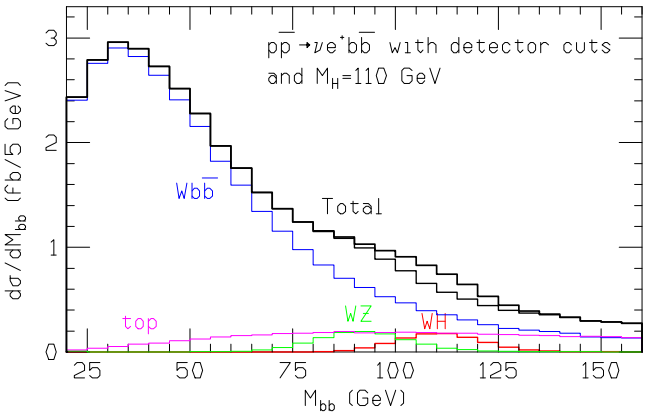

Figure 9. Signal and backgrounds for WH. 'top' represents the sum of all the backgrounds including a top quark.

6.1. Introduction

Significant work has been done in the course of the SUSY/Higgs [64] and Strong Dynamics [65] Workshops to understand the Tevatron discovery potential for new physics. Several promising signatures have been identified and the discovery reach has been estimated. In these studies, it was assumed that the systematic error on the signal and background normalization is similar in size to the statistical error, which is about 10%. Thus, the systematic error of each individual background process must be kept under 5%. Though it is probably a reasonable assumption, this will not happen automatically and dedicated studies are needed to achieve this goal. In this paper, we review the most important backgrounds to new physics and ways to estimate them in signal-depleted control samples.

6.2. New physics signatures

Associated vector boson and heavy flavor jets production is probably the most promising signature for new physics searches at the Tevatron. Standard Model (SM) Higgs boson [66], Supersymmetry [67], technicolor and topcolor [68] and even extra-dimension [69] signatures may appear in these channels.

Tables 4 and 5, show examples of new physics processes that can produce $W + 2$ jet and $W + 3$ or more jet signatures. From the experimental point of view, a "W" is usually a high p_T lepton accompanied by a significant missing energy (e.g. CDF Run I cuts are $P_T(e, \mu) > 20$ GeV/c, $\not\!\!E_T > 20$ GeV [70]). In that sense, the supersymmetric partner of W – $\widetilde{\chi}_1^+$ – looks like a W, except its transverse mass will be inconsistent with the W hypothesis, but this will become obvious only when significant statistics is accumulated. Some models predict special features, like resonance behavior in the $b\bar{b}$ invariant mass, while others do not.

Table 6 presents new physics processes that can produce $Z + 2$ jet signatures. Here we assume that the Z decays to a pair of leptons. Usually, a Z mass window cut is applied. In that sense, the supersymmetric partner of the Z – $\widetilde{\chi}_2^0$ – looks like a Z in only some regions of SUSY parameter space. If the Z decays to a pair of neutrinos, it produces missing energy. In this case, all the processes presented in Table 6 produce a $\not\!\!E_T + 2$ jet signature. Table 7 shows additional new physics processes that result in a $\not\!\!E_T$ signature. As we see, these channels are very important for new physics searches, and the Standard Model backgrounds to these signatures must be thoroughly understood before any claims of discovery are made.

6.3. Backgrounds to new physics

The $W(Z)b\bar{b}$ signature was studied in the course of the SUSY/Higgs Workshop for the Higgs discovery

#	Process	Model	Special features
1	$WH, H \to b\bar{b}$	SM Higgs	Resonance in $M_{b\bar{b}}$
2	$\rho_T^{\pm} \to W^{\pm}\pi_T^0, \pi_T^0 \to b\bar{b}$	Technicolor	Resonance in $M_{Wb\bar{b}}$ and $M_{b\bar{b}}$
3	$\rho_T^0 \to W^{\pm}\pi_T^{\mp}, \pi_T^{\pm} \to c\bar{b}$	Technicolor	Resonance in $M_{Wc\bar{b}}$ and $M_{c\bar{b}}$
4	$\widetilde{\chi}_1^+\widetilde{\chi}_2^0, \widetilde{\chi}_1^+ \to \ell\nu\widetilde{\chi}_1^0, \widetilde{\chi}_2^0 \to b\bar{b}\widetilde{\chi}_1^0$	SUSY	$M_T(\ell \not\!\!E_T)$ inconsistent with W
5	$t\bar{t}, t \to bW, \bar{t} \to \bar{\tilde{t}}\widetilde{\chi}_1^0, \bar{\tilde{t}} \to c\widetilde{\chi}_1^0$	SUSY	$M_T(\ell \not\!\!E_T)$ inconsistent with W

Table 4
Potential new physics signatures in the $W + 2$ jet channel. From the experimental point of view, a "W" is a high p_T lepton accompanied by significant missing energy (e.g., CDF cuts are $p_T(e, \mu) > 20$ GeV/c, $\not\!\!E_T > 20$ GeV). In that sense, $\widetilde{\chi}_1^+$ looks like a "W."

#	Process	Model	Special features
1	$t\bar{t}, t \to bW, \bar{t} \to \bar{\tilde{t}}\widetilde{\chi}_1^0, \bar{\tilde{t}} \to \bar{b}\widetilde{\chi}_1^-$	SUSY	$M_T(\ell \not\!\!E_T)$ inconsistent with W
2	$\tilde{t}\bar{\tilde{t}}, \tilde{t} \to b\widetilde{\chi}_1^+$	SUSY	$M_T(\ell \not\!\!E_T)$ inconsistent with W
3	$\tilde{t}\bar{\tilde{t}}, \tilde{t} \to b\ell\tilde{\nu}$	SUSY	$M_T(\ell \not\!\!E_T)$ inconsistent with W
4	$\widetilde{g}\widetilde{g}, \widetilde{g} \to t\bar{\tilde{t}}$	SUSY	$M_T(\ell \not\!\!E_T)$ inconsistent with W
5	$Z'(V_8, \eta_t) \to t\bar{t}$	Topcolor	Resonance in $M_{t\bar{t}}$

Table 5
Potential new physics signatures in the $W + 3$ or more jet channel.

#	Process	Model	Special features
1	$ZH, H \to b\bar{b}$	SM Higgs	Resonance in $M_{b\bar{b}}$
2	$\rho_T^+ \to Z\pi_T^+, \pi_T^+ \to c\bar{b}$	Technicolor	Resonance in $M_{Zc\bar{b}}$ and $M_{c\bar{b}}$
3	$\widetilde{\chi}_1^+\widetilde{\chi}_2^0, \widetilde{\chi}_1^+ \to c\bar{s}\widetilde{\chi}_1^0, \widetilde{\chi}_2^0 \to \ell^+\ell^-\widetilde{\chi}_1^0$	SUSY	$M_{\ell\ell}$ inconsistent with Z, extra $\not\!\!E_T$
4	$\tilde{b}\bar{\tilde{b}}, \tilde{b} \to b\widetilde{\chi}_1^0, \bar{\tilde{b}} \to \bar{b}\widetilde{\chi}_2^0, \widetilde{\chi}_2^0 \to \ell\ell\widetilde{\chi}_1^0$	SUSY	extra $\not\!\!E_T$

Table 6
Potential new physics signatures in the $Z + 2$ jet channel. From the experimental point of view, a "Z" is two high p_T leptons, usually with a Z mass window cut. In that sense, $\widetilde{\chi}_2^0$ looks like a "Z" only in some regions of SUSY parameter space.

#	Process	Model	Special features
1	$\tilde{t}\bar{\tilde{t}}, \tilde{t} \to c\widetilde{\chi}_1^0$	SUSY	2 charm jets and $\not\!\!E_T$
1	$\tilde{b}\bar{\tilde{b}}, \tilde{b} \to b\widetilde{\chi}_1^0$	SUSY	2 bottom jets and $\not\!\!E_T$
3	$LQ_2LQ_2, LQ_2 \to c\nu$	Leptoquarks	2 charm jets and $\not\!\!E_T$
3	$LQ_3LQ_3, LQ_3 \to b\nu$	Leptoquarks	2 bottom jets and $\not\!\!E_T$

Table 7
Potential new physics signatures in the $\not\!\!E_T + 2$ jet channel. This does not include processes complementary to those in Table 6, where a Z decays to a pair of neutrinos $Z \to \nu\bar{\nu}$, thus producing missing energy.

potential estimate [66]. The $\not\!\!E_T$+heavy flavor (c/b) signature was studied in the CDF stop/sbottom search [71]. We use these analyses as examples in our discussion.

$W(Z)b\bar{b}$ signature

Selection and sample composition

The $Wb\bar{b}$ ($Z(\to \nu\bar{\nu})b\bar{b}$) selection criteria and the resultant sample composition are summarized in Fig. 10

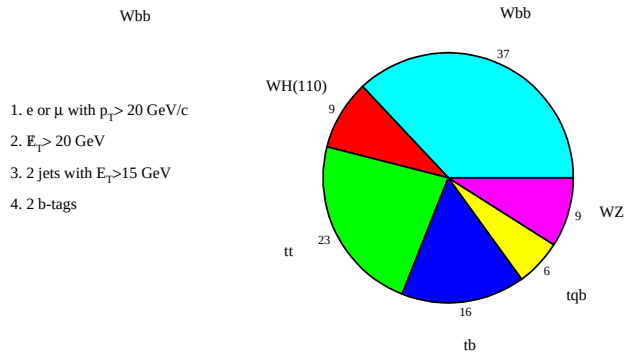

Figure 10. Selection cuts and composition of the $Wb\bar{b}$ sample.

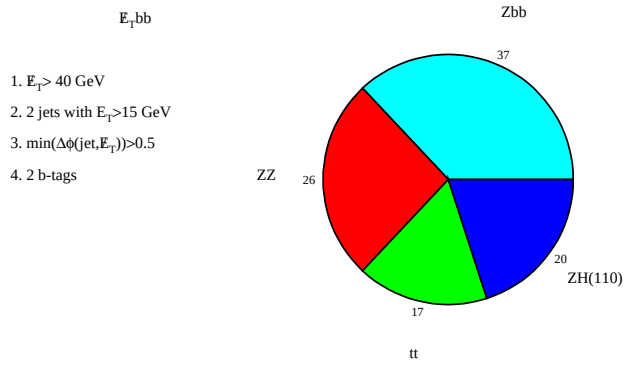

Figure 11. Selection cuts and composition of the $\not\!\!E_T b\bar{b}$ sample.

(Fig. 11). The dominant contribution to both samples is QCD production of a vector boson accompanied by two b-jets.

QCD $W(Z)b\bar{b}$ production. Experimental studies of gluon splitting to heavy flavor.

Diagrams of QCD associated production of $W(Z)$ and heavy flavor jets are presented in Figure 12. The leading contribution is $W(Z)$+gluon production with subsequent gluon splitting to a $b\bar{b}$ or $c\bar{c}$ pair, shown in Figure 12(a).

Though a next-to-leading-order calculation of the QCD $Wb\bar{b}$ production exists [72], even the authors themselves recommend that it should be tested experimentally. This is a particularly hard task in the presence of a potential signal contribution. In the case of the Higgs search, an invariant mass of two b-jets could be used as an additional handle, since gluon splitting contributes mainly to the low part of the $M_{b\bar{b}}$ spectrum, while the Higgs is a resonance at 110-130 GeV/c^2. This is not the case for some other potential signal process, e.g. process 5 in Table 4.

The probability for a gluon to split to two heavy flavor jets can be studied experimentally in different samples. The signal contamination becomes negligible, if the presence of a vector boson is not required.

Three heavy flavor production mechanisms can be isolated – direct production, final state gluon splitting and initial state gluon splitting, also called flavor excitation. Diagrams of these processes are presented in Figure 13.

Though direct production is the lowest order process, it is responsible for the production of only $\sim$ 20% of heavy flavor jets with energy above 20 GeV; about 35% are produced by flavor excitation and 45% by gluon splitting. The relative contribution of different processes changes after b-tagging is applied. Tagging is usually more efficient on directly produced jets, which tend to be back-to-back in the azimuthal plane. Heavy flavor quarks produced from gluon splitting are not well separated, and are often assigned to the same jet. Thus the relative contribution of gluon splitting to the double-tagged jet sample is quite low. Flavor excitation involves an initial state gluon splitting to two heavy flavor quarks, one of which undergoes hard scattering. The other quark, being a part of the proton remnant, is often outside the detector acceptance. Thus, the contribution of flavor excitation to the double-tagged sample is significantly depleted. An analysis of the angular correlation between two heavy flavor tagged jets can be used to isolate the gluon-splitting component in heavy flavor production, as depicted in Fig. 14.

Different methods can be used to tag heavy flavor jets.

1. Impact parameter or secondary vertex tagging (JETPROB or SECVTX in CDF jargon) [70] are the ones most commonly used. These samples have relatively high statistics. Using the same tagging method for the background and the signal sample eliminates the systematic uncertainty. The main disadvantage of these methods is the relatively low purity of these samples – contamination from c-jets and mistags is non-negligible. Usually, to get a stable fit, the b/c ratio has to be fixed to the one predicted by Monte Carlo, which is not without its own uncertainty.

2. One of the heavy flavor jets is tagged by the presence of a high p_T > 8 GeV/c lepton – electron or muon – and JETPROB or SECVTX

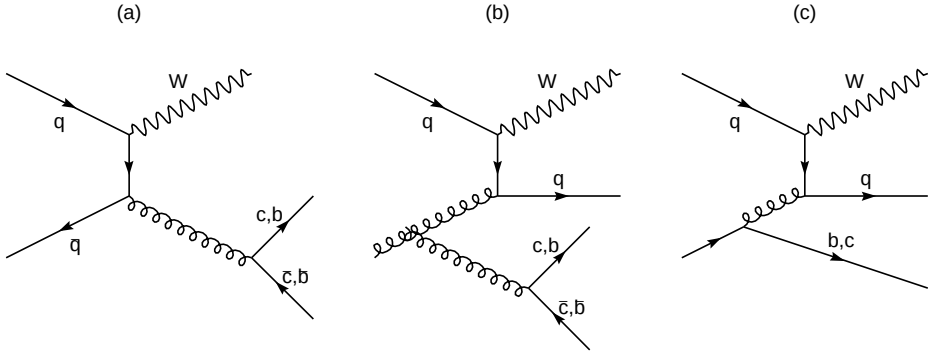

Figure 12. Diagrams of QCD associated production of $W(Z)$ and heavy flavor jets.

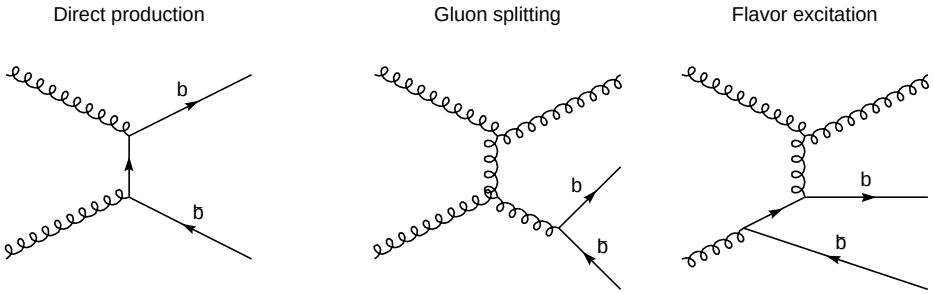

Figure 13. Diagrams of QCD heavy flavor production.

tags another jet [73]. These samples have high statistics as well, but again suffer from charm and mistag contamination. Nonetheless, it is an interesting independent study.

3. Both heavy flavor jets can be tagged by leptons. In this case it is possible to go lower in lepton momentum, usually $p_T > 3$ GeV/c [74]. Compared to the first two cases, these studies probe a lower energy region, where the direct production mechanism dominates. Thus not much information about gluon splitting probability can be gained.

4. Study #2 can be modified to increase the purity by reconstructing exclusive or semi-exclusive final states in one of the jets:

   (a) Reconstructing a decay chain $D^* \rightarrow D^0\pi, D^0 \rightarrow Ke(\mu)\nu$ can isolate the charm contribution [75]. The presence of a high p_T lepton guarantees that the contribution from $b \rightarrow c$ decay is at the order of 10% or lower. Studying the angular correlation between D^* jet and an impact parameter tagged jet isolates the gluon splitting to charm contribution. This probability can then be applied to study #2 to extract the probability of gluon splitting to b-quarks.

   (b) A similar trick can be used to isolate the b-contribution in the lepton sample. Promising decay chains are [76]: $B \rightarrow \ell\nu D^*$, $D^* \rightarrow D^0\pi$, $D^0 \rightarrow K\pi$ or $K3\pi$; $B \rightarrow \ell\nu D^+$, $D^+ \rightarrow K\pi\pi$; $B \rightarrow \ell\nu D^0$, $D^0 \rightarrow K\pi$; and $B \rightarrow J/\Psi K$.

In Table 8, we present the number of events in each of the discussed samples collected in Run I and expected in Run II and associated statistical uncertainty on the gluon splitting probability.

Run I numbers are based on CDF results. In Run II, both CDF and DØ will have similar tracking and vertexing capabilities, thus these numbers are applicable to both detectors. Statistics in Run II is increased by a factor of 40, where 20 is gained from the luminosity increase and 2 from increased acceptance of the silicon microvertex detectors. The tagging efficiency increase is not taken into account. With these dedicated studies, the statistical uncertainty on the probability of gluon splitting to heavy flavor quarks can be significantly reduced in Run II, and will become adequate to the needs of new physics searches.

#	Sample	N(Run I)	$\sigma(g \to Q\bar{Q})$ Run I	N(Run II)	$\sigma(g \to Q\bar{Q})$ Run II
1	Double tagged jets	700	20%	28000	3.2%
2	Muon+JETPROB tag	2620	16%	104800	2.5%
3	$c \to D^* \to D^0(\to K\ell\nu)\pi$	18000	15%	720000	2.4%
4	$B \to D^*\ell\nu \to D^0(\to K\pi/K3\pi)\ell\nu\pi$	1700	n.a.	68000	n.a.
5	$B \to D^+(\to K\pi\pi)\ell\nu$	1900	n.a.	76000	n.a.
6	$B \to D^0(\to K\pi)\ell\nu$	2700	#4-#7	108000	#4-#7
7	$B \to J/\Psi K^{(*)}$	1300	23%	52000	3.6%

Table 8
Data samples for heavy flavor production study. Numbers in samples #1 and #2 are double tags, while in samples #3-#7 numbers of exclusively reconstructed events are shown, without requiring a tag on the opposite side.

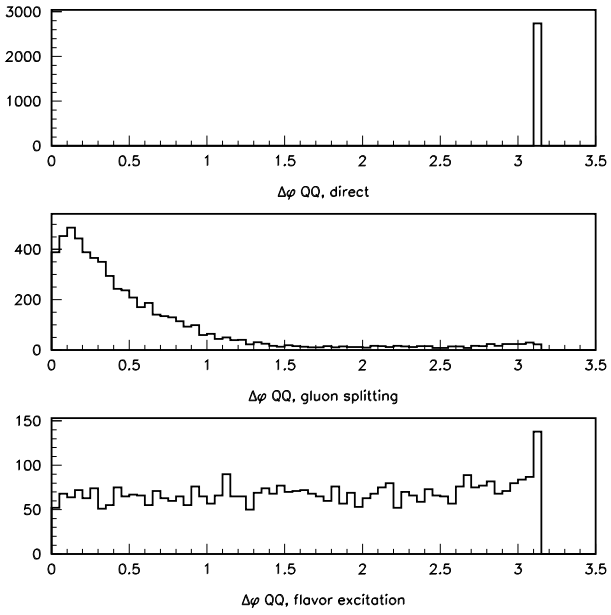

Figure 14. Distribution $\Delta\phi$ between two b-quarks from Monte Carlo events.

Top, single top and diboson production

Other backgrounds to new physics searches are top pair [77], single top [78] and diboson [79] production. The theoretical predictions for these backgrounds are more reliable, because they do not involve gluon radiation and splitting, yet they still have to be tested experimentally. This is more or less a straightforward task for top pair and diboson production, where final states can be exclusively identified. It is less so for single top production, where the final state is exactly the same – $Wb\bar{b}$ – as in new physics channels in Table 4. Additional mass constraints, e.g. on the Wb mass can be used to isolate this process, but it is not at all obvious that adequate uncertainty can be reached for this channel.

Missing energy and heavy flavor signatures

Here, we summarize the selection criteria and composition of the missing energy and heavy flavor sample used for top squark searches [71]:

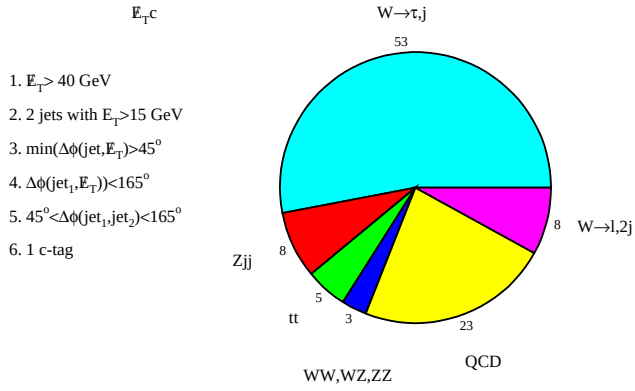

Figure 15. Selection cuts and composition of $\not\!\!E_T c$ sample.

More than 50% of the background is composed of $W(\to \tau\nu) + 1$ jet events.

$W + c$ production

The leading order production process for $W(\to \tau\nu)+$ 1 jet, where this jet is identified as charm, is $sg \to Wc$. The main uncertainty of the production rate for this process comes from the PDF of sea s quarks $f_s(x)$, which is measured by NuTeV [80] in the neutrino scattering process $\nu_\mu s \to \mu c$.

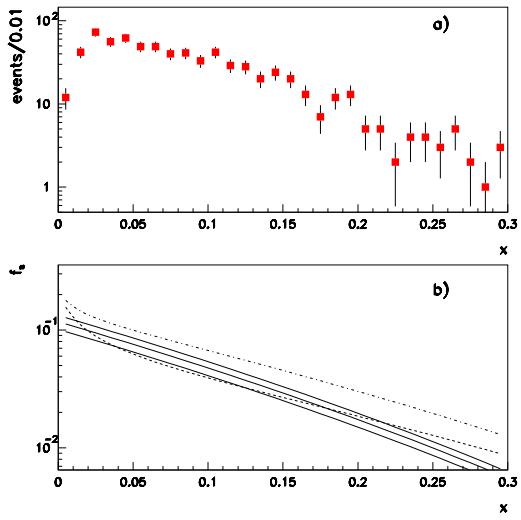

Figure 16. (a) Distribution in x of sea s-quarks that contribute to $sg \to Wc$ production at the Tevatron, generated with PYTHIA 6.1+CTEQ4LO. Selection cuts have been applied. (b) Solid lines represent $f_s(x)$ and its uncertainty, as measured by NuTeV. It is compared to GRV94LO (dashed line) and CTEQ4LO (dot-dashed line) strange sea distributions.

Figure 16 (a) shows the distribution in x of sea s-quarks that contribute to $sg \to Wc$ production at the Tevatron after the selection cuts from Figure 15 have been applied. Figure 16 (b) shows the $f_s(x)$ and its uncertainty measured by NuTeV. As we see, the region of NuTeV sensitivity is relevant for Tevatron studies. The overall uncertainty on $f_s(x)$ is 13.5%. $f_s(x)$ measured by NuTeV is in a good agreement with the results of CCFR [81], which has an uncertainty of 10.5%.

Since these uncertainties are dominated by the experimental statistics, we can hope that the combined result will have an uncertainty near 8.5%. The strange sea parton density function was also measured by the CHARM II [82] and CDHS [83] experiments. Combination of results of all four experiments is certainly desirable, but non–trivial, since somewhat different techniques where used in each analysis.

In Figure 16(b), $f_s(x)$ measured by NuTeV is compared to the one provided by the GRV94LO [84] and CTEQ4LO [85] PDF's, which are shown by dashed and dot-dashed lines, respectively. None of the PDF's provide an adequate description of the strange sea data. In the Tevatron search experiments, the systematic uncertainty on the background due to PDF's was typically estimated by switching from one PDF to another. In this case, the systematic uncertainty on the number of Wc events that pass our cuts is 36%. If instead of CTEQ4LO, $f_s(x)$ measured by NuTeV were used, the number of expected Wc events would go down by 30%. This is within the estimated uncertainty, but clearly the uncertainty has been overestimated. The correct uncertainty to use is 13.5%, or 8.5%, when the results of NuTeV and CCFR will be combined. This is a significant reduction compared to 36%, yet it is still not down to the desirable level of 5%. We can probably do better by studying Wc production when the W is identified by its decay to a muon or an electron. The expected number of events in the $Wc, W \to \ell\nu(\ell = e, \mu)$ channel is about 2800, after applying the cuts listed in Figure 15, which corresponds to the statistical uncertainty for this background of about 2%. The systematic uncertainty on missing energy and charm identification are common to the two channels, and the difference is in lepton vs. tau identification uncertainty, which can be expected to be below 5% with Run II statistics.

QCD background

The next dominant background in the $\not\!\!E_T c$ channel is QCD multijet production, where missing energy comes from jet energy mis-measurement. This background is the toughest one to estimate, because it involves multiple gluon radiation and splitting. Not only the overall rate, but also the angular correlation between jets may not be predicted reliably. To isolate this component, the usual trick is to apply all the signal selection cuts except tagging, subtract other known backgrounds and call the rest "QCD." The tagging probability derived from an independent jet sample is then applied to estimate the QCD contribution to the tagged sample [86]. One obvious drawback is that the heavy flavor fraction can change after the cuts are applied. Another is that the signal contribution is not always negligible even before tagging, and to some extent, it may be normalized away.

Other backgrounds in the $\not\!\!E_T c$ channel.

Other backgrounds in the $\not\!\!E_T c$ channel are top pair production, di-bosons, $Z+$ jets and $W+$ jets, where leptons were not identified. The discussion of these processes in Section 6.3 applies to the $\not\!\!E_T c$ channel as well.

7. Variable flavor number schemes for heavy quark electroproduction

by J. Smith

Heavy quark production has been a major topic of investigation at hadron-hadron, electron-proton and electron-positron colliders. Here a review is given of some topics which are of interest primarily for electron-proton colliders. We concentrate on this reaction because a theoretical treatment can be based on the operator product expansion, and also because data are available for deep-inelastic charm production at HERA. How all this relates to Fermilab experiments will be discussed at the end.

In QCD perturbation theory, one needs to introduce a renormalization scale and a mass factorization scale to perform calculations. We choose both equal to μ^2, which will be a function of Q^2 and the square of the mass of the charm quark m^2. At small μ^2, where kinematic effects due to quark masses are important, the best way to describe charm quark production is via heavy quark pair production from light quark u, d, s and gluon initial states. The mass m only appears in the heavy quark coefficient functions (or partonic cross sections) like $H_{i,g}^{\mathrm{S},(2)}(z, Q^2, m^2, \mu^2)$, etc., [87]. Here the superscripts refer to their flavor decomposition and the order in perturbation theory, while the subscripts refer to the projection $i = 2, L$ and the partonic initial state. The arguments refer to the partonic Bjorken variable $z = Q^2/(s + Q^2)$ and to the fact that these functions depend upon invariants and scales. The renormalization necessary to calculate these NLO expressions follows the CWZ method [88]. The symbol H refers to those coefficient functions which are derived from Feynman diagrams where the virtual photon couples to a heavy quark line. Analytic expressions for these functions are not known, but numerical fits are available in [89]. Asymptotic expressions in the limit $Q^2 \gg m^2$ are available in [90]. These contain terms like $\ln^2(Q^2/m^2)$ and $\ln(Q^2/m^2)\ln(Q^2/\mu^2)$ multiplied by functions of z; they are manifestly singular in the limit that $m \to 0$.

There are other heavy quark coefficient functions such as $L_{i,q}^{\mathrm{NS},(2)}(z, Q^2, m^2)$, which arise from tree diagrams where the virtual photon attaches to the an initial state light quark line, so the heavy-quark is pair produced via virtual gluons. Analytic expressions for these functions are known for all z, Q^2 and m^2, which, in the limit $Q^2 \gg m^2$ contain powers of $\ln(Q^2/m^2)$ multiplied by functions of z. The three-flavor light mass $\overline{\mathrm{MS}}$ parton densities can be defined in terms of matrix elements of operators and are now available in parton density sets. This is a fixed order perturbation theory (FOPT) description of heavy quark production with three-flavor parton densities. Due to the work in [87], the perturbation series is now known up to second order. In regions of moderate scales and invariants, this NLO description is well defined and can be combined with a fragmentation function to predict exclusive distributions [91] for the outgoing charm meson, the anti-charm meson and the additional parton. This NLO massive charm approach agrees well with the recent D-meson inclusive data in [92] and [93]. The charm quark structure functions in this NLO description will be denoted $\boldsymbol{F_{i,c}^{\mathrm{EXACT}}(x, Q^2, m^2, n_f = 3)}$.

A different description, which should be more appropriate for large scales where terms in m^2 are negligible, is to represent charm production by a parton density $f_c(x, \mu^2)$, with a boundary condition that the density vanishes at small values of μ^2. Although at first sight these approaches appear to be completely different, they are in fact intimately related. It was shown in [94] that the large terms in $\ln(Q^2/m^2)$ which arise when $Q^2 \gg m^2$, can be resummed to all orders in perturbation theory. In this reference, all the two-loop corrections to the matrix elements of massive quark and massless gluon operators in the operator product expansion were calculated. These contain the same type of logarithms mentioned above multiplied by functions of z (which is the last Feynman integration parameter). After operator renormalization and suitable reorganization of convolutions of the operator matrix elements (OME's) and the coefficient functions, the expressions for the infrared-safe charm quark structure functions $F_{i,c}(x, Q^2, m^2, \Delta)$ take on a simple form. After resummation, they are convolutions of light-mass, four-flavor parton coefficient functions, commonly denoted by expressions like $\mathcal{C}_{i,g}^{\mathrm{S},(2)}(Q^2/\mu^2)$ (available in [95], [96]), with four-flavor light-parton densities, which also include a charm quark density $f_c(x, \mu^2)$. Since the corrections to the OME's contain terms in $\ln(Q^2/m^2)$ and $\ln(m^2/\mu^2)$ as well as non-logarithmic terms, it is simplest to work in the $\overline{\mathrm{MS}}$ scheme with the scale $\mu^2 = m^2$ for $Q^2 \leq m^2$ and $\mu^2 = m^2 + Q^2(1 - m^2/Q^2)^2/2$ for $Q^2 > m^2$ and discontinuous matching conditions on the flavor densities at $\mu^2 = m^2$. Then all the logarithmic terms vanish at $Q^2 = \mu^2 = m^2$ and the non-logarithmic terms in the OME's are absorbed into the boundary conditions on the charm density, the new four-flavor gluon density and the new light-flavor u,d,s densities. The latter are convolutions of the previous three-flavor densities with the OME's given in the Appendix of [94].

The above considerations lead to a precise description through order α_s^2 of how, in the limit $m \to 0$, to re-express the $F_{i,c}^{\mathrm{EXACT}}(x, Q^2, m^2)$ written in terms of convolutions of heavy quark coefficient functions with three-flavor light parton densities into a description in terms of four-flavor light-mass parton coefficient functions convoluted with four-flavor parton densities. This procedure leads to the so-called

zero-mass variable-flavor-number scheme (ZM-VFNS) for $F_{i,c}(x,Q^2,\Delta)$ where the m dependent logarithms are absorbed into the new four-flavor densities. To implement this scheme, one has to be careful to use inclusive quantities which are collinearly finite in the limit $m \to 0$ and Δ is an appropriate parameter which enables us to do this. In the expression for $F_{i,c}$ there is a cancellation of terms in $\ln^3(Q^2/m^2)$ between the two-loop corrections to the light quark vertex function (the Sudakov form factor) and the convolution of the densities with the soft part of the $L_{2,q}$-coefficient function. This is the reason for the split of $L_{i,q}$ into soft and hard parts, via the introduction of a constant Δ. Details and analytic results for $L_{i,c}^{\rm SOFT}$ and $L_{i,c}^{\rm HARD}$ are available in [97]. All this analysis yielded and used the two-loop matching conditions on variable-flavor parton densities across flavor thresholds, which are special scales where one makes transitions from say a three-flavor massless parton scheme to a four-flavor massless parton scheme. The threshold is a choice of μ which has nothing to do with the actual kinematical heavy flavor pair production threshold at $Q^2(x^{-1}-1) = 4m^2$. In [94],[98] it was shown that the $F_{i,c}^{\rm EXACT}(x,Q^2,m^2,n_f = 3)$ tend numerically to the known asymptotic results in $F_{i,c}^{\rm ASYMP}(x,Q^2,m^2,n_f=3)$, when $Q^2 \gg m^2$, which also equal the ZM-VFNS results. The last description is good for large (asymptotic) scales and contains a charm density $f_c(x,\mu^2)$ which satisfies a specific boundary condition at $\mu^2 = m^2$. We denote the charm quark structure functions in this description by $\boldsymbol{F_{i,c}^{\rm PDF}(x,Q^2,n_f=4)}$.

For moderate values of Q^2, a third approach has been introduced to describe the charm components of $F_i(x,Q^2)$. This is called a variable flavor number scheme (VFNS). A first discussion was given in [99], where a VFNS prescription called ACOT was given in lowest order only. A proof of factorization to all orders was recently given in [100] for the total structure functions $F_i(x,Q^2)$, but the NLO expressions for $F_{i,c}(x,Q^2,m^2)$ in this scheme were not provided. An NLO version of a VFNS scheme has been introduced in [97] and will be called the **CSN** scheme. A different approach, also generalized to all orders, was given in [94],[98], which is called the **BMSN** scheme. Finally another version of a VFNS was presented in [101], which is called the TR scheme. The differences between the various schemes can be attributed to two ingredients entering the construction of a VFNS. The first one is the mass factorization procedure carried out before the large logarithms can be resummed. The second one is the matching condition imposed on the charm quark density, which has to vanish in the threshold region of the production process. All VFNS approaches require two sets of parton densities. One set contains three-flavor number densities whereas the second set contains four-flavor number densities. The sets have to satisfy the $\overline{\rm MS}$ matching relations derived in [94]. Appropriate four-flavor densities have been constructed in [97] starting from the three-flavor LO and NLO sets of parton densities recently published in [102].

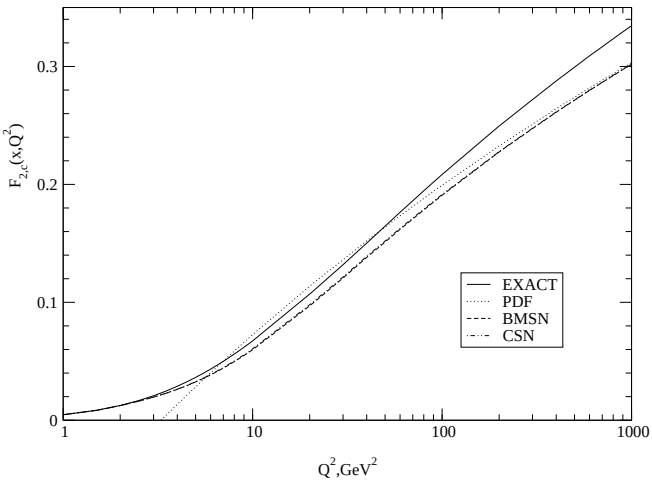

Figure 17. The charm quark structure functions $F_{2,c}^{\rm EXACT}(n_f = 3)$ (solid line) $F_{2,c}^{\rm CSN}(n_f = 4)$, (dot-dashed line) $F_{2,c}^{\rm BMSN}(n_f = 4)$, (dashed line) and $F_{2,c}^{\rm PDF}(n_f = 4)$, (dotted line) in NNLO for $x = 0.005$ plotted as functions of Q^2.

Since the formulae for the heavy quark structure functions are available in [97], we only mention a few points here. The BMSN scheme avoids the introduction of any new coefficient functions other than those above. Since the asymptotic limits for $Q^2 \gg m^2$ of all the operator matrix elements and coefficient functions are known, we define (here Q refers to the heavy charm quark)

$$\begin{aligned} F_{i,Q}^{\rm BMSN}(x,Q^2,m^2,\Delta,n_f=4) = \\ F_{i,Q}^{\rm EXACT}(x,Q^2,m^2,\Delta,n_f=3) \\ - F_{i,Q}^{\rm ASYMP}(x,Q^2,m^2,\Delta,n_f=3) \\ + F_{i,Q}^{\rm PDF}(x,Q^2,m^2,\Delta,n_f=4)\,. \end{aligned} \quad (33)$$

The scheme for $F_{i,Q}^{\rm CSN}$ introduces a new heavy quark OME $A_{QQ}^{{\rm NS},(1)}(z,\mu^2/m^2)$ [103] and coefficient functions

$H_{i,Q}^{\mathrm{NS},(1)}(z,Q^2/m^2)$ [104] because it requires an incoming heavy quark Q, which did not appear in the NLO corrections in [87]. The CSN coefficient functions are defined via the following equations. Up to second order we have

$$\mathcal{C}_{i,q,Q}^{\mathrm{CSN,SOFT,NS},(2)}\Big(\Delta,\frac{Q^2}{m^2},\frac{Q^2}{\mu^2}\Big)=A_{qq,Q}^{\mathrm{NS},(2)}\Big(\frac{\mu^2}{m^2}\Big)\mathcal{C}_{i,q}^{\mathrm{NS},(0)}$$
$$-\beta_{0,Q}\ln\left(\frac{\mu^2}{m^2}\right)\times\mathcal{C}_{i,q}^{\mathrm{NS},(1)}\Big(\frac{Q^2}{\mu^2}\Big)-\mathcal{C}_{i,q}^{\mathrm{VIRT,NS},(2)}(\frac{Q^2}{m^2})$$
$$-L_{i,q}^{\mathrm{SOFT,NS},(2)}\Big(\Delta,\frac{Q^2}{m^2},\frac{Q^2}{\mu^2}\Big),\quad(34)$$

with the virtual term the second order Sudakov form factor. The other CSN coefficient functions are defined

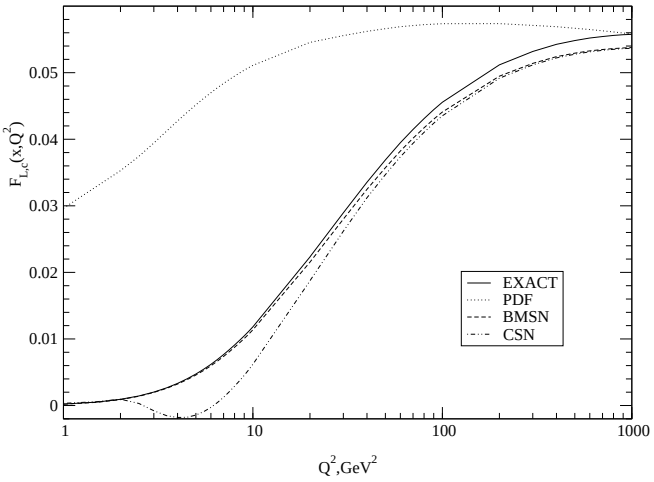

Figure 18. The charm quark structure functions $F_{L,c}^{\mathrm{EXACT}}(n_f=3)$ (solid line) $F_{L,c}^{\mathrm{CSN}}(n_f=4)$, (dot-dashed line) $F_{L,c}^{\mathrm{BMSN}}(n_f=4)$, (dashed line) and $F_{L,c}^{\mathrm{PDF}}(n_f=4)$, (dotted line) in NNLO for $x=0.005$ plotted as functions of Q^2.

by equations like (we only give one of the longitudinal terms for illustration)

$$\mathcal{C}_{L,g}^{\mathrm{CSN,S},(1)}\Big(\frac{Q^2}{m^2},\frac{Q^2}{\mu^2}\Big)=$$
$$H_{L,g}^{\mathrm{S},(1)}\Big(\frac{Q^2}{m^2}\Big)-A_{Qg}^{\mathrm{S},(1)}(\frac{\mu^2}{m^2})\,\mathcal{C}_{L,Q}^{\mathrm{CSN,NS},(0)}\Big(\frac{Q^2}{m^2}\Big),\quad(35)$$

with $\mathcal{C}_{L,Q}^{\mathrm{CSN,NS},(0)}=4m^2/Q^2$. The CSN and BMSN schemes are designed to have the following two properties. First of all, suppressing unimportant labels,

$$F_{i,Q}^{\mathrm{CSN}}(n_f=4)=F_{i,Q}^{\mathrm{BMSN}}(n_f=4)$$
$$=F_{i,Q}^{\mathrm{EXACT}}(n_f=3)\quad\text{for}\quad Q^2\le m^2\,.\quad(36)$$

Since $f_Q(m^2)^{\mathrm{NNLO}}\neq 0$ (see [94]) this condition can be only satisfied when we truncate the perturbation series at the same order. The second requirement is that

$$\lim_{Q^2\gg m^2}F_{i,Q}^{\mathrm{BMSN}}(n_f=4)=\lim_{Q^2\gg m^2}F_{i,Q}^{\mathrm{CSN}}(n_f=4)$$
$$=\lim_{Q^2\gg m^2}F_{i,Q}^{\mathrm{PDF}}(n_f=4)\,.\quad(37)$$

The only differences between the two schemes arises from terms in m^2 so they may not be equal just above $Q^2=m^2$. This turns out to be the case for the longitudinal structure function, which is more sensitive to mass effects.

Figure 17 shows NNLO results for the Q^2 dependence of $F_{2,c}^{\mathrm{EXACT}}(n_f=3)$, $F_{2,c}^{\mathrm{CSN}}(n_f=4)$, $F_{2,c}^{\mathrm{BMSN}}(n_f=4)$, and $F_{2,c}^{\mathrm{PDF}}(n_f=4)$ at $x=0.005$. Note that the results satisfy the requirements in Eqs. (36) and (37). The ZM-VFNS description is poor at small Q^2. Figure 18 shows the results for $F_{L,c}^{\mathrm{EXACT}}(n_f=3)$, $F_{L,c}^{\mathrm{CSN}}(n_f=4)$, $F_{L,c}^{\mathrm{BMSN}}(n_f=4)$, and $F_{L,c}^{\mathrm{PDF}}(n_f=4)$ at $x=0.005$. We see that the CSN result is negative and therefore unphysical for $2.5<Q^2<6$ $(\mathrm{GeV}/c)^2$ which is due to the term in $4m^2/Q^2$ and the subtraction in Eq. (35).

One way this research work is of relevance to Fermilab experiments is that it produces more precise ZM-VFNS parton densities. Such densities are used extensively to predict cross sections at high energies, for example for single top quarks. Therefore the previous work on four-flavor parton densities has been extended in [105] to incorporate the two-loop discontinuous matching conditions across the bottom flavor threshold at $\mu=m_b$ and provided a set of five-flavor densities, which contains a bottom quark density $f_b(x,\mu^2)$. The differences between the five-flavor densities and those in [106] and [35] are also discussed. Results for deep-inelastic electroproduction of bottom quarks will be presented in [107].

8. The Underlying Event in Hard Scattering Processes

by Rick Field and David Stuart

8.1. Introduction

The total proton-antiproton cross section is the sum of the elastic and inelastic cross sections. The inelastic cross section consists of a single-diffractive, double-diffractive, and a "hard core" component, where the

"hard core" is everything else. "Hard core" does not necessarily imply "hard scattering." A "hard scattering" collision, such as that illustrated in Fig. 19(a), is one in which a "hard" (i.e. large transverse momentum) 2-to-2 parton-parton subprocess has occurred. "Soft" hard core collisions correspond to events in which no "hard" interaction has occurred. When there is no large p_T subprocess in the collision, one is not probing short distances and it probably does not make any sense to talk about partons. The QCD "hard scattering" cross section grows with increasing collider energy and becomes a larger and larger fraction of the total inelastic cross section. In this analysis, we used the CDF Min-Bias trigger data sample in conjunction with the JET20 trigger data sample to study the growth and development of "charged particle jets" from $p_T(\text{jet}) = 0.5$ to 50 GeV. We compared several "local" jet observables with the QCD "hard scattering" Monte-Carlo models of HERWIG[1], ISAJET[2], and PYTHIA[3].

A "hard scattering" event, like that illustrated in Fig. 19(a) consists of large-p_T outgoing hadrons that originate from the large-p_T partons (*i.e.,* outgoing hard scattering "jets") and also hadrons that originate from the break-up of the proton and antiproton (*i.e.,* the "beam-beam remnants"). The "underlying event" is an interesting object that is not very well understood. In addition to beam-beam remnants, it may contain hadrons resulting from initial-state radiation. Also, it is possible that multiple parton scattering occurs in hadron-hadron collisions as illustrated in Fig. 19(b). This is a controversial issue, but the underlying event might also contains hadrons that originate from multiple parton interactions. PYTHIA, for example, uses multiple parton interactions as a way to enhance the activity of the underlying event [3].

In this analysis, we studied a variety of "global" observables to probe the growth and structure of the underlying event. We find that the underlying "hard scattering" event is not the same as a "soft" $p\bar{p}$ collision. For the same available energy, the underlying event in a hard scattering is considerably more active (*i.e.,* higher charged particle density and more p_T) than a "soft" collision. This is not surprising since a violent hard scattering has occurred! We find that none of the QCD Monte-Carlo models (*with their default parameters*) describe correctly all the properties of the underlying event.

8.2. Data Selection and Monte-Carlo Models

(1) Data Selection

The CDF detector, described in detail in Ref. [122], measures the trajectories and transverse momenta, p_T, of charged particles in the pseudorapidity region $|\eta| <$ 1.1 with the central tracking chamber (CTC), silicon vertex detector (SVX), and vertex time projection chamber (VTX), which are immersed in a 1.4 T solenoidal magnetic field. In this analysis we consider only charged particles measured in the central tracking chamber (CTC) and use the two trigger sets of data listed in Table 9. The minimum bias (min-bias) data were selected by requiring that at least one particle interacted with the forward beam-beam counter BBC ($3.4 < \eta < 5.9$) *and/or* the backward BBC ($-5.9 < \eta < -3.4$). The min-bias trigger selects predominately the "hard core" component of the inelastic cross section.

Charged particle tracks are found with high efficiency as long as the density of particles is not high. To remain in a region of high efficiency, we consider only charged particles with $p_T > 0.5$ GeV and $|\eta| < 1$. The observed tracks include some fake tracks that result from secondary interactions between primary particles, including neutral particles, and the detector material. There are also particles originating from other $p\bar{p}$ collisions. To reduce the contribution from these sources, we consider only tracks which point to the primary interaction vertex within 2 cm along the beam direction and 1 cm transverse to the beam direction. Detector simulations indicate that this impact parameter cut is very efficient and that the number of fake tracks is about 3.5% when a 1 cm impact parameter cut is applied in conjunction with a 2 cm vertex cut. Without the impact parameter cut the number of fake tracks is approximately 9%.

This dependence of the number of fake tracks on the CTC impact parameter cut provides a method of estimating systematic uncertainties due to fakes. Every data point P on every plot in this analysis was determined three times by using a 2 cm vertex cut in conjunction with three different CTC d_0 cuts; a 1 cm CTC d_0 cut (P), a 0.5 cm CTC d_0 cut (P_1), and no CTC d_0 cut (P_2). The 1 cm cut determined the value of the data point, P, and the difference between the 0.5 cm cut value and no cut value of the data point determined the systematic error of the data point as follows: sys-error $= P|P_2 - P_1|/P_1$ This systematic error was then added in quadrature with the statistical error. We do not correct the data for the CTC track-finding efficiency. Instead, the theoretical Monte-Carlo model predictions are corrected.

(2) QCD "Hard Scattering" Monte-Carlo Models

The "hard" scattering QCD Monte-Carlo models used in this analysis are listed in Table 10. The QCD perturbative 2-to-2 parton-parton differential cross section diverges as the p_T of the scattering, p_T^{hard},

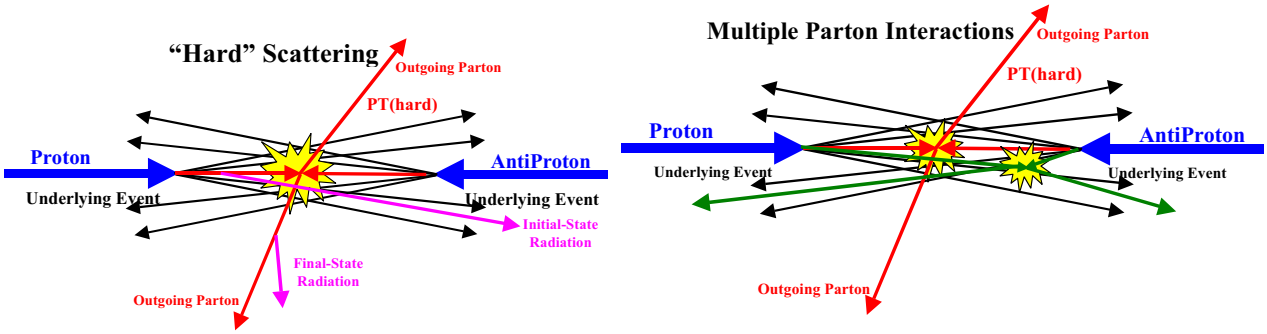

Figure 19. (a) Illustration of a $p\bar{p}$ collision in which a "hard" 2-to-2 parton scattering with transverse momentum, p_T(hard), has occurred. The resulting event contains particles that originate from the two outgoing partons (plus final-state radiation) and particles that come from the breakup of the p and $\bar{p}$ (*i.e.,* "beam-beam remnants"). The "underlying event" consists of the beam-beam remnants plus initial-state radiation; (b) Illustration of a $p\bar{p}$ collision in which a multiple parton interaction has occurred. In addition to the "hard" 2-to-2 parton scattering with transverse momentum, p_T(hard), there is an additional "semi-hard" parton-parton scattering that contributes particles to the "underlying event." For PYTHIA, we include the contributions from multiple parton scattering in the beam-beam remnant component.

Table 9
Data sets and selection criterion used in this analysis.

CDF Data Set	Trigger	Events	Selection
Min-Bias	Min-Bias Trigger	626,966	zero or one vertex in $\|z\| < 100$ cm $\|z_c - z_v\| < 2$ cm, $\|$CTC $d_0\| < 1$ cm $p_T^{\rm track} > 0.5$ GeV, $\|\eta\| < 1$
JET20	Calorimeter Tower cluster with $E_T > 20$ GeV	78,682	zero or one vertex in $\|z\| < 100$ cm $\|z_c - z_v\| < 2$ cm, $\|$CTC $d_0\| < 1$ cm $p_T^{\rm track} > 0.5$ GeV, $\|\eta\| < 1$

Table 10
Theoretical QCD "hard" scattering Monte-Carlo models studied in this analysis. In all cases we take p_T(hard) > 3 GeV.

Monte-Carlo Model	Subprocess	Comments
HERWIG 5.9	QCD 2-to-2 parton scattering IPROC = 1500	Default values for all parameters
ISAJET 7.32	QCD 2-to-2 parton scattering TWOJET	Default values for all parameters
PYTHIA 6.115	QCD 2-to-2 parton scattering MSEL = 1	Default values for all parameters: PARP(81) = 1.4
PYTHIA 6.125	QCD 2-to-2 parton scattering MSEL = 1	Default values for all parameters: PARP(81) = 1.9
PYTHIA No MS	QCD 2-to-2 parton scattering MSEL = 1	Default values for all parameters: MSTP(81) = 0

goes to zero (see Fig. 19). One must set a minimum $p_T^{\rm hard}$ large enough so that the resulting cross section is not larger that the total "hard core" inelastic cross section, and also large enough to ensure that QCD perturbation theory is applicable. In this analysis we take $p_T^{\rm hard} > 3\,{\rm GeV}$.

Each of the QCD Monte-Carlo models handle the "beam-beam remnants" in a similar fashion. A hard scattering event is basically the superposition of a hard parton-parton interaction on top of a "soft" collision. HERWIG[1] assumes that the underlying event is a soft collision between the two "beam clusters." ISAJET[2] uses a model similar to the one it uses for soft "min-bias" events (*i.e.,* "cut Pomeron"), but with different parameters, to describe the underlying beam-beam remnants. PYTHIA[3] assumes that each incoming beam hadron leaves behind a "beam remnant," which do not radiate initial state radiation, and simply sail through unaffected by the hard process. However, unlike HERWIG and ISAJET, PYTHIA also uses multiple parton interactions to enhance the activity of the underlying event as illustrated in Fig. 19.

In this analysis we examine two versions of PYTHIA, PYTHIA 6.115 and PYTHIA 6.125 both with the default values for all the parameters. The default values of the parameters are different in version 6.115 and 6.125. In particular, the effective minimum p_T for multiple parton interactions, PARP(81), changed from 1.4 GeV in version 6.115 to 1.9 GeV in version 6.125. Increasing this cut-off decreases the multiple parton interaction cross section which reduces the amount of multiple parton scattering. For completeness, we also consider PYTHIA with no multiple parton scattering (MSTP(81)=0).

Since ISAJET employs "independent fragmentation" it is possible to trace particles back to their origin and divide them into three categories: particles that arise from the break-up of the beam and target (*beam-beam remnants*), particles that arise from initial-state radiation, and particles that result from the outgoing hard scattering jets plus final-state radiation. The "hard scattering component" consists of the particles that arise from the outgoing hard scattering jets plus initial and final-state radiation (*sum of the last two categories*). Particles from the first two categories (*beam-beam remnants plus initial-state radiation*) are normally what is referred to as the underlying event (see Fig. 19). Of course, these categories are not directly observable experimentally. Nevertheless, it is instructive to examine how particles from various origins affect the experimental observables.

Since HERWIG and PYTHIA do not use independent fragmentation, it is not possible to distinguish particles that arise from initial-state radiation from those that arise from final-state radiation, but we can identify the beam-beam remnants. When, for example, a color string breaks into hadrons it is not possible to say which of the two partons producing the string was the parent. For HERWIG and PYTHIA, we divide particles into two categories: particles that arise from the break-up of the beam and target (*beam-beam remnants*), and particles that result from the outgoing hard scattering jets plus initial and final-state radiation (*hard scattering component*). For PYTHIA, we include particles that arise from multiple parton interactions in the beam-beam remnant component.

(3) Method of Comparing Theory with Data

Our philosophy in comparing the theory with data in this analysis is to select a region where the data is very "clean." The CTC efficiency can vary substantially for very low p_T tracks and in dense high p_T jets. To avoid this we have considered only the region $p_T > 0.5\,{\rm GeV}$ and $|\eta| < 1$ where the CTC efficiency is high and stable (estimated to be 92% efficient) and we restrict ourselves to jets less than 50 GeV. The data presented here are uncorrected. Instead the theoretical Monte-Carlo predictions are corrected for the track finding efficiency and have an error (*statistical plus systematic*) of about 5%. The errors on the (*uncorrected*) data include both statistical and correlated systematic uncertainties.

In comparing the QCD "hard scattering" Monte-Carlo models with the data, we require that the Monte-Carlo events satisfy the CDF min-bias trigger and we apply an 8% correction for the CTC track finding efficiency. The corrections are small. On the average, 8 out of every 100 charged particles predicted by the theory are removed from consideration. Requiring the theory to satisfy the min-bias trigger is important when comparing with the Min- Bias data, but does not matter when comparing with the JET20 data since essentially all high p_T jet events satisfy the min-bias trigger.

8.3. The Evolution of Charge Particle "Jets" from 0.5 to 50 GeV

We define charged particle "jets" and examine the evolution of these "jets" from $p_T^{\rm jet} = 0.5$ to 50 GeV. As illustrated in Fig. 20, "jets" are defined as "circular regions" ($R = 0.7$) in η-ϕ space and contain charged particles from the underlying event as well as particles which originate from the fragmentation of high p_T outgoing partons (see Fig. 19). Also, every charged particle in the event is assigned to a "jet," with the possibility that some "jets" might consist of just one charged particle. We adapt a very simple jet definition since we will be dealing with "jets" that consist of

only a few low p_T charged particles. The standard jet algorithm based on calorimeter clustering is not applicable at low p_T.

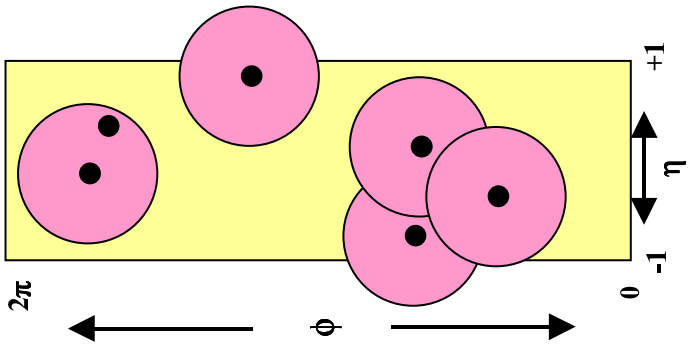

Figure 20. Illustration of an event with six charged particles ($p_T > 0.5\,\text{GeV}$ and $|\eta| < 1$) and five charged "jets" (circular regions in η-ϕ space with $R = 0.7$).

(1) Jet Definition (charged particles)

We define jets as circular regions in η-ϕ space with "distance" $R = \sqrt{(\Delta\eta)^2 + (\Delta\phi)^2}$. Our jet algorithm is as follows:

- Order all charged particles according to their p_T.
- Start with the highest p_T particle and include in the "jet" all particles within $R = 0.7$.
- Go to the next highest p_T particle (*not already included in a "jet"*) and add to the "jet" all particles (*not already included in a "jet"*) within $R = 0.7$.
- Continue until all particles are in a "jet."

We consider all charged particles ($p_T > 0.5\,\text{GeV}$ and $|\eta| < 1$) and allow the jet radius to extend outside $|\eta| < 1$. Fig. 20 illustrates an event with six charged particles and five jets. We define the p_T of the jet to be the *scalar* p_T sum of all the particles within the jet (*i.e.,* it is simply the scalar p_T sum within the circular region).

We know that the simple charged particle jet definition used here is not theoretically favored since if applied at the parton level it is not infrared safe. Of course, all jet definitions (*and in fact all observables*) are infrared safe at the hadron level. We have done a detailed study comparing the nave jet definition used here with a variety of more sophisticated charge particle jet definitions. This analysis will be presented in a future publication. Some of the observables presented here do, of course, depend on one's definition of a jet and it is important to apply the same definition to both the theory and data.

(2) Charged Jet Multiplicity versus p_T(jet#1)

Fig. 21 shows the average number of charged particles ($p_T > 0.5\,\text{GeV}$ and $|\eta| < 1$) within jet#1 (*leading charged jet*) as a function of p_T(jet#1). The solid points are Min-Bias data and the open points are the JET20 data. The JET20 data connect smoothly to the Min-Bias data and allow us to study observables over the range $0.5 < p_T(\text{jet\#1}) < 50\,\text{GeV}$. There is a small overlap region where the Min-Bias and JET20 data coincide. The errors on the data include both statistical and correlated systematic uncertainties, however, the data have not been corrected for efficiency. Fig. 21 shows a sharp rise in the leading charged jet multiplicity at low p_T(jet#1) and then a flattening out and a gradual rise at high p_T(jet#1). The data are compared with the QCD "hard scattering" Monte-Carlo predictions of HERWIG 5.9, ISAJET 7.32, and PYTHIA 6.115. The theory curves are corrected for the track finding efficiency and have an error (*statistical plus systematic*) of around 5%.

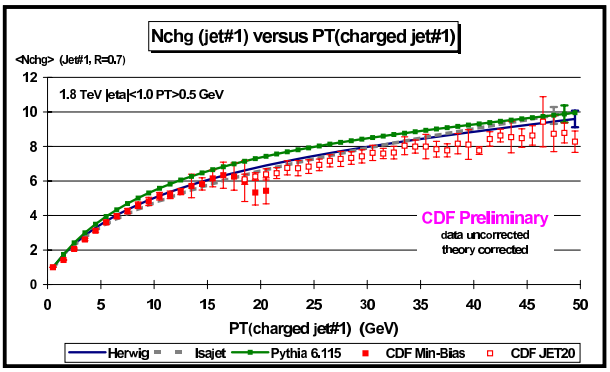

Figure 21. The average number of charged particles ($p_T > 0.5\,\text{GeV}$ and $|\eta| < 1$) within the leading charged jet ($R = 0.7$) as a function of the p_T of the leading charged jet. The solid (open) points are Min-Bias (JET20) data. The errors on the (*uncorrected*) data include both statistical and correlated systematic uncertainties. The QCD "hard scattering" theory curves (HERWIG 5.9, ISAJET 7.32, PYTHIA 6.115) are corrected for the track finding efficiency and have an error (*statistical plus systematic*) of around 5%.

(3) Charged Jet "Size" versus p_T(jet#1)

Although the charged particle jets are defined as circular regions in η-ϕ space with $R = 0.7$, this is not the "size" of the jet. The "size" of a jet can be defined in two ways: size according to particle number and size according to p_T. The first corresponds to the radius in η-ϕ space that contains 80% of the charged particles in the jet, and the second corresponds to the radius in η-ϕ space that contains 80% of the jet p_T. The data on the average "jet size" of the leading charge particle jet are compared with the QCD "hard scattering" Monte-Carlo predictions of HERWIG 5.9, ISAJET 7.32, and PYTHIA 6.115 in Fig. 22. A leading 20 GeV charged jet has 80% of its charged particles contained, on the average, within a radius in η-ϕ space of about 0.33, and 80% of its p_T contained, on the average, within a radius of about 0.20. Fig. 22 clearly illustrates the "hot core" of jets. The radius containing 80% of the p_T is smaller than the radius that contains 80% of the particles. Furthermore, the radius containing 80% of the p_T decreases as the overall p_T of the jet increases due to limited momentum perpendicular to the jet direction.

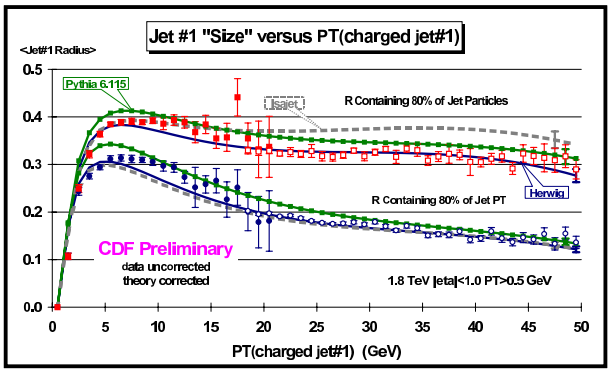

Figure 22. The average radius in η-ϕ space containing 80% of the charged particles (and 80% of the charged p_T) as a function of the p_T of the leading charged jet. The errors on the (*uncorrected*) data include both statistical and correlated systematic uncertainties. The QCD "hard scattering" theory curves (HERWIG 5.9, ISAJET 7.32, PYTHIA 6.115) are corrected for the track finding efficiency and have an error (*statistical plus systematic*) of around 5%.

8.4. The Overall Event Structure as a Function of p_T(jet#1)

In the previous section, we studied "local" leading jets observables. The QCD Monte-Carlo models did not have to describe correctly the entire event in order to fit the observable. They only had to describe correctly the properties of the leading charge particle jet, and all the models fit the data fairly well (*although not perfectly*). Now we will study "global" observables, where to fit the observable the QCD Monte-Carlo models will have to describe correctly the entire event structure.

(1) Overall Charged Multiplicity versus p_T(jet#1)

Figure 23 shows the average number of charged particles in the event with $p_T > 0.5$ GeV and $|\eta| < 1$ (*including jet#1*) as a function of p_T(jet#1) (*leading charged jet*) for the Min-Bias and JET20 data. Again the JET20 data connect smoothly to the Min-Bias data, and there is a small overlap region where the Min-Bias and JET20 data coincide. Figure 23 shows a sharp rise in the overall charged multiplicity at low p_T(jet#1) and then a flattening out and a gradual rise at high p_T(jet#1) similar to Fig. 21. We would like to investigate where these charged particles are located relative to the direction of the leading charged particle jet.

(2) Correlations in $\Delta\phi$ relative to p_T(jet#1)

As illustrated in Fig. 24, the angle $\Delta\phi$ is defined to be the relative azimuthal angle between charged particles and the direction of the leading charged particle jet. We label the region $|\phi - \phi_{\rm jet\#1}| < 60°$ as "toward" jet#1 and the region $|\phi - \phi_{\rm jet\#1}| > 120°$ is as "away" from jet#1. The "transverse" to jet#1 region is defined by $60° < |\phi - \phi_{\rm jet\#1}| < 120°$. Each region, "toward," "transverse," and "away" covers the same range $|\Delta\eta| \times |\Delta\phi| = 2 \times 120°$. The "toward" region includes the particles from jet#1 as well as a few particles from the underlying event. As we will see, the "transverse" region is very sensitive to the underlying event. The "away" region is a mixture of the underlying event and the "away-side" hard scattering jet.

Figure 25 shows the data on the average number of charged particles ($p_T > 0.5$ GeV and $|\eta| < 1$) as a function of p_T(jet#1) for the three regions. Each point corresponds to the "toward," "transverse," or "away" $\langle N_{chg} \rangle$ in a 1 GeV bin. The solid points are Min-Bias data and the open points are JET20 data. The data in Fig. 25 define the average event "shape." For example, for an "average" $p\bar{p}$ collider event at 1.8 TeV with p_T(jet#1) = 20 GeV there are, on the average,

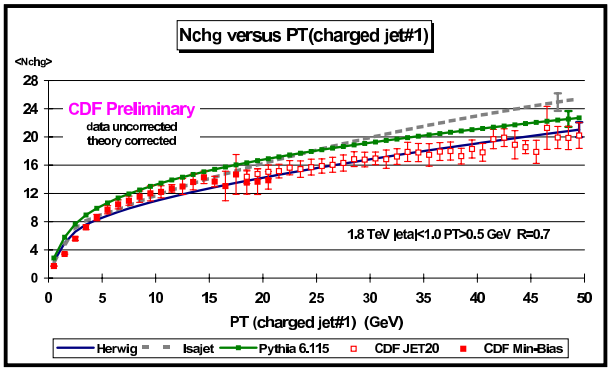

Figure 23. The average total number of charged particles in the event ($p_T > 0.5\,\text{GeV}$ and $|\eta| < 1$ including jet#1) as a function of the p_T of the leading charged jet. The solid (open) points are the Min- Bias (JET20) data. The errors on the (*uncorrected*) data include both statistical and correlated systematic uncertainties. The QCD "hard scattering" theory curves (HERWIG 5.9, ISAJET 7.32, PYTHIA 6.115) are corrected for the track finding efficiency and have an error (*statistical plus systematic*) of around 5%.

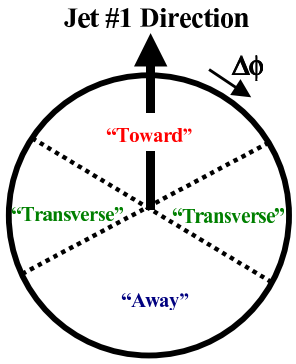

Figure 24. Illustration of correlations in azimuthal angle $\Delta\phi$ relative to the direction of the leading charged jet in the event, jet#1. The angle $\Delta\phi = \phi - \phi_{\text{jet}\#1}$ is the relative azimuthal angle between charged particles and the direction of jet#1. The region $|\Delta\phi| < 60°$ is referred to as "toward" jet#1 (*includes particles in jet#1*) and the region $|\Delta\phi| > 120°$ is called "away" from jet#1. The "transverse" to jet#1 region is defined by $60° < |\Delta\phi| < 120°$. Each region, "toward," "transverse," and "away" covers the same range $|\Delta\eta| \times |\Delta\phi| = 2 \times 120°$.

8.7 charged particles "toward" jet#1 (*including the particles in jet#1*), 2.5 "transverse" to jet#1, and 4.9 "away" from jet#1.

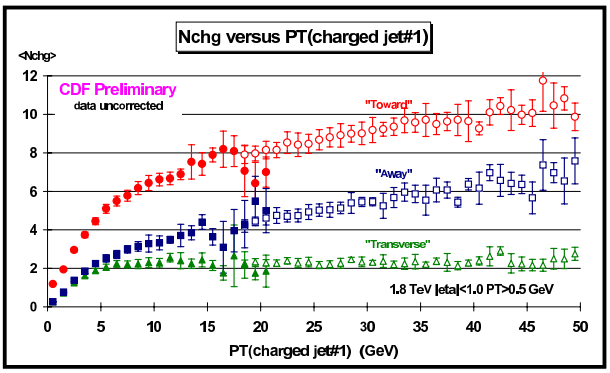

Figure 25. The average number of "toward" ($|\Delta\phi| < 60°$), "transverse" ($60° < |\Delta\phi| < 120°$), and "away" ($|\Delta\phi| > 120°$) charged particles ($p_T > 0.5\,\text{GeV}$ and $|\eta| < 1$ including jet#1) as a function of the p_T of the leading charged jet. Each point corresponds to the $\langle N_{chg} \rangle$ in a 1 GeV bin. The solid (open) points are the Min-Bias (JET20) data. The errors on the (*uncorrected*) data include both statistical and correlated systematic uncertainties. The "toward," "transverse," and "away" regions are defined in Fig. 24.

Figure 26 shows the data on the average *scalar* p_T sum of charged particles ($p_T > 0.5\,\text{GeV}$ and $|\eta| < 1$) as a function of p_T(jet#1) for the three regions. Here each point corresponds to the "toward," "transverse," or "away" $\langle p_{T\,sum} \rangle$ in a 1 GeV bin. In Fig. 27, data on $\langle N_{chg} \rangle$ as a function of p_T(jet#1) for the three regions are compared with the QCD "hard scattering" Monte-Carlo predictions of HERWIG 5.9, ISAJET 7.32, and PYTHIA 6.115. The QCD Monte-Carlo models agree qualitatively (*but not precisely*) with the data. We will now examine more closely these three regions.

(3) The "Toward" and "Away" Region versus p_T(jet#1)

Figure 28 shows the data from Fig. 25 on the average number of "toward" region charged particles compared with the QCD "hard scattering" Monte-Carlo predictions of HERWIG 5.9, ISAJET 7.32, and PYTHIA 6.115. This plot is very similar to the average number of charged particles within the leading jet shown in Fig. 21. At p_T(jet#1) = 20 GeV, the "toward" region contains, on the average, about 8.7 charged particles with about 6.9 of these charged

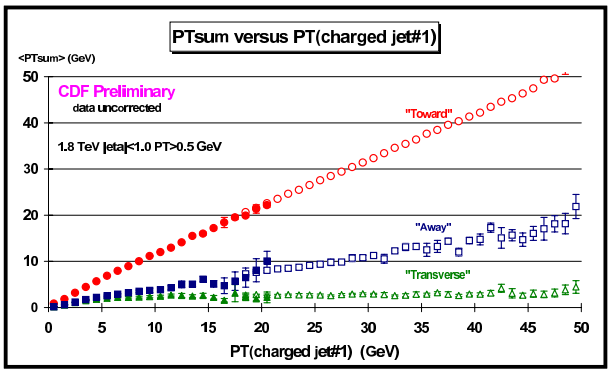

Figure 26. The average *scalar* p_T sum of "toward" ($|\Delta\phi| < 60°$), "transverse" ($60° < |\Delta\phi| < 120°$), and "away" ($|\Delta\phi| > 120°$) charged particles ($p_T > 0.5$ GeV and $|\eta| < 1$ including jet#1) as a function of the p_T of the leading charged jet. Each point corresponds to the $\langle PT_{sum} \rangle$ in a 1 GeV bin. The solid (open) points are the Min-Bias (JET20) data. The errors on the (*uncorrected*) data include both statistical and correlated systematic uncertainties. The "toward," "transverse," and "away" regions are defined in Fig. 24.

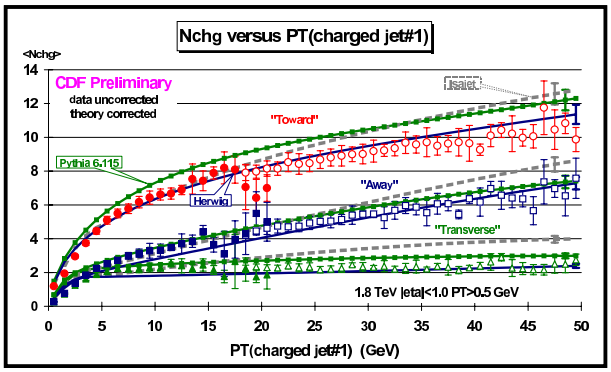

Figure 27. Data from Fig. 25 on the average number of "toward" ($|\Delta\phi| < 60°$), "transverse" ($60° < |\Delta\phi| < 120°$), and "away" ($|\Delta\phi| > 120°$) charged particles ($p_T > 0.5$ GeV and $|\eta| < 1$ including jet#1) as a function of the p_T of the leading charged jet compared to QCD "hard scattering" Monte-Carlo predictions of HERWIG 5.9, ISAJET 7.32, and PYTHIA 6.115. The errors on the (*uncorrected*) data include both statistical and correlated systematic uncertainties. The theory curves are corrected for the track finding efficiency and have an error (*statistical plus systematic*) of around 5%.

particles belonging to jet#1. As expected, the toward region is dominated by the leading jet. This is seen clearly in Fig. 29 where the predictions of ISAJET for the "toward" region are divided into three categories: charged particles that arise from the break-up of the beam and target (*beam-beam remnants*), charged particles that arise from initial-state radiation, and charged particles that result from the outgoing jets plus final-state radiation. For p_T(jet#1) values below 5 GeV the "toward" region charged multiplicity arises mostly from the beam-beam remnants, but as p_T(jet#1) increases the contribution from the outgoing jets plus final-state radiation quickly begins to dominate. The bump in the beam-beam remnant contribution at low p_T(jet#1) is caused by leading jets composed almost entirely from the remnants.

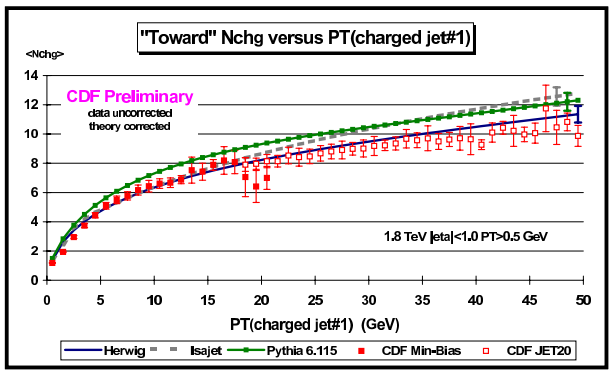

Figure 28. Data from Fig. 25 on the average number of charged particles ($p_T > 0.5$ GeV and $|\eta| < 1$) as a function of p_T(jet#1) (*leading charged jet*) for the "toward" region " defined in Fig. 24 compared with the QCD "hard scattering" Monte-Carlo predictions of HERWIG 5.9, ISAJET 7.32, and PYTHIA 6.115. Each point corresponds to the "toward" $\langle N_{chg} \rangle$ in a 1 GeV bin. The errors on the (*uncorrected*) data include both statistical and correlated systematic uncertainties. The theory curves are corrected for the track finding efficiency and have an error (*statistical plus systematic*) of around 5%.

Fig. 30 shows the data from Fig. 25 on the average number of "away" region charged particles compared with the QCD "hard scattering" Monte-Carlo predictions of HERWIG 5.9, ISAJET 7.32, and PYTHIA 6.115. In Fig. 21 the data from Fig. 26 on the average *scalar* p_T sum in the "away" region is compared to the QCD Monte-Carlo predictions. The "away" region is a mixture of the underlying event

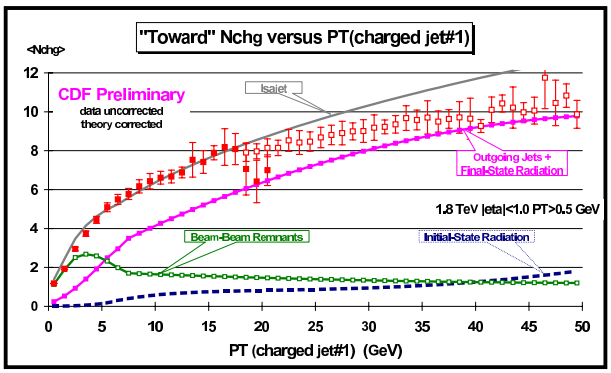

Figure 29. Data from Fig. 25 on the average number of charged particles ($p_T > 0.5\,\text{GeV}$ and $|\eta| < 1$) as a function of p_T(jet#1) (*leading charged jet*) for the "toward" region defined in Fig. 24 compared with the QCD "hard scattering" Monte-Carlo predictions of ISAJET 7.32. The predictions of ISAJETare divided into three categories: charged particles that arise from the break-up of the beam and target (*beam-beam remnants*), charged particles that arise from initial-state radiation, and charged particles that result from the outgoing jets plus final-state radiation (see Fig. 19). The errors on the (*uncorrected*) data include both statistical and correlated systematic uncertainties. The theory curves are corrected for the track finding efficiency and have an error (*statistical plus systematic*) of around 5%.

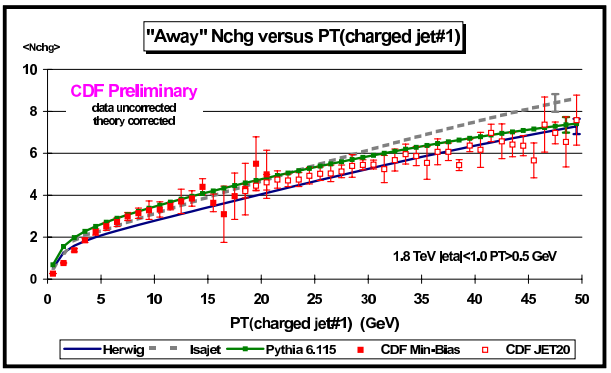

Figure 30. Data from Fig. 25 on the average number of charged particles ($p_T > 0.5\,\text{GeV}$ and $|\eta| < 1$) as a function of p_T(jet#1) (*leading charged jet*) for the "away" region defined in Fig. 24 compared with the QCD "hard scattering" Monte-Carlo predictions of HERWIG 5.9, ISAJET 7.32, and PYTHIA 6.115. The errors on the (*uncorrected*) data include both statistical and correlated systematic uncertainties. The theory curves are corrected for the track finding efficiency and have an error (*statistical plus systematic*) of around 5%.

and the "away-side" outgoing "hard scattering" jet. This can be seen in Fig. 32 where the predictions of ISAJET for the "away" region are divided into three categories: beam-beam remnants, initial-state radiation, and outgoing jets plus final-state radiation. Here the underlying event plays a more important role since the "away-side" outgoing "hard scattering" jet is sometimes outside the regions $|\eta| < 1$. For the "toward" region the contribution from the outgoing jets plus final state-radiation dominates for p_T(jet#1) values above about 5 GeV, whereas for the "away" region this does not occur until around 20 GeV.

Both the "toward" and "away" regions are described fairly well by the QCD "hard scattering" Monte-Carlo models. These regions are dominated by the outgoing "hard scattering" jets and as we saw in Section C the Monte-Carlo models describe the leading outgoing jets fairly accurately. We will now study the "transverse" region which is dominated by the underlying event.

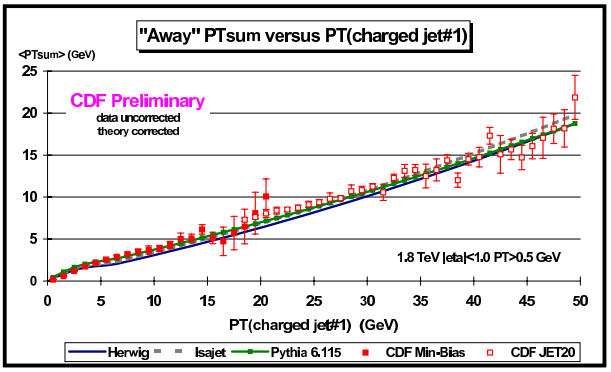

Figure 31. Data from Fig. 26 on the average *scalar* p_T sum of charged particles (($p_T > 0.5\,\text{GeV}$ and $|\eta| < 1$) as a function of p_T(jet#1) (*leading charged jet*) for the "away" region defined in Fig. 24 compared with the QCD "hard scattering" Monte-Carlo predictions of HERWIG 5.9, ISAJET 7.32, and PYTHIA 6.115. The errors on the (*uncorrected*) data include both statistical and correlated systematic uncertainties. The theory curves are corrected for the track finding efficiency and have an error (*statistical plus systematic*) of around 5%.

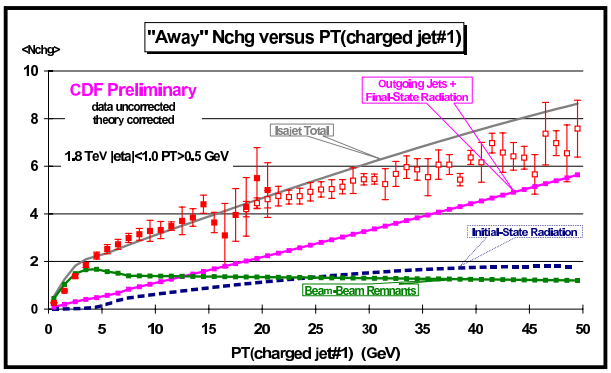

Figure 32. Data from Fig. 25 on the average number of charged particles ($p_T > 0.5\,\text{GeV}$ and $|\eta| < 1$) as a function of $p_T(\text{jet}\#1)$ (*leading charged jet*) for the "away" region defined in Fig. 24 compared with the QCD "hard scattering" Monte-Carlo predictions of ISAJET 7.32. The predictions of ISAJETare divided into three categories: charged particles that arise from the break-up of the beam and target (*beam-beam remnants*), charged particles that arise from initial-state radiation, and charged particles that result from the outgoing jets plus final-state radiation (see Fig. 19). The errors on the (*uncorrected*) data include both statistical and correlated systematic uncertainties. The theory curves are corrected for the track finding efficiency and have an error (*statistical plus systematic*) of around 5%.

8.5. The "Transverse" Region and the Underlying Event

Fig. 25 shows that there is a lot of activity in the "transverse" region. If we suppose that the "transverse" multiplicity is uniform in azimuthal angle ϕ and pseudo-rapidity η, the observed 2.3 charged particles at $p_T(\text{jet}\#1) = 20\,\text{GeV}$ translates to 3.8 charged particles per unit pseudo-rapidity with $p_T > 0.5\,\text{GeV}$ (multiply by 3 to get 360°, divide by 2 for the two units of pseudo-rapidity, multiply by 1.09 to correct for the track finding efficiency). We know that if we include all p_T that there are roughly 4 charged particles per unit rapidity in a "soft" $p\bar{p}$ collision at 1.8 TeV, and the data show that in the underlying event of a "hard scattering" there are about 3.8 charged particles per unit rapidity in the region $p_T > 0.5\,\text{GeV}$! If one includes all p_T values then the underlying event has a charge particle density that is at least a factor of two larger than the 4 charged particles per unit rapidity seen in "soft" $p\bar{p}$ collisions at this energy. As can be seen in Fig. 25, the charged particle density in the "transverse" region is a function of $p_T(\text{jet}\#1)$ and rises very rapidity at low $p_T(\text{jet}\#1)$ values. The "transverse" charged multiplicity doubles in going from $p_T(\text{jet}\#1) = 1.5\,\text{GeV}$ to $p_T(\text{jet}\#1) = 2.5\,\text{GeV}$ and then forms an approximately constant "plateau" for $p_T(\text{jet}\#1) > 6\,\text{GeV}$.

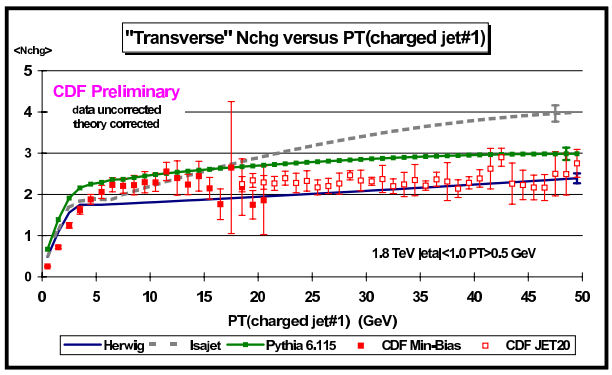

Figure 33. Data from Fig. 25 on the average number of charged particles ($p_T > 0.5\,\text{GeV}$ and $|\eta| < 1$) as a function of $p_T(\text{jet}\#1)$ (*leading charged jet*) for the "transverse" region defined in Fig. 24 compared with the QCD "hard scattering" Monte-Carlo predictions of HERWIG 5.9, ISAJET 7.32, and PYTHIA 6.115. The errors on the (*uncorrected*) data include both statistical and correlated systematic uncertainties. The theory curves are corrected for the track finding efficiency and have an error (*statistical plus systematic*) of around 5%.

Fig. 33 and Fig. 34 compare the "transverse" $\langle N_{chg}\rangle$ and the "transverse" $\langle p_{T\,sum}\rangle$, respectively, with the QCD "hard scattering" Monte-Carlo predictions of HERWIG 5.9, ISAJET 7.32, and PYTHIA 6.115. Fig. 35 and Fig. 36 compare the "transverse" $\langle N_{chg}\rangle$ and the "transverse" $\langle PT_{sum}\rangle$, respectively, with three versions of PYTHIA(6.115, 6.125, and no multiple scattering, see Table 10). PYTHIA with no multiple parton scattering does not have enough activity in the underlying event. PYTHIA 6.115 fits the "transverse" $\langle N_{chg}\rangle$ the best, but overshoots slightly the "toward" $\langle N_{chg}\rangle$ in Fig. 28. ISAJET has a lot of activity in the underlying event, but gives the wrong $p_T(\text{jet}\#1)$ dependence. Instead of a "plateau," ISAJET predicts a rising "transverse" $\langle N_{chg}\rangle$ and gives too much activity at large $p_T(\text{jet}\#1)$ values. HERWIG does not have enough "transverse" $\langle PT_{sum}\rangle$.

We expect the "transverse" region to be composed predominately from particles that arise from the break-

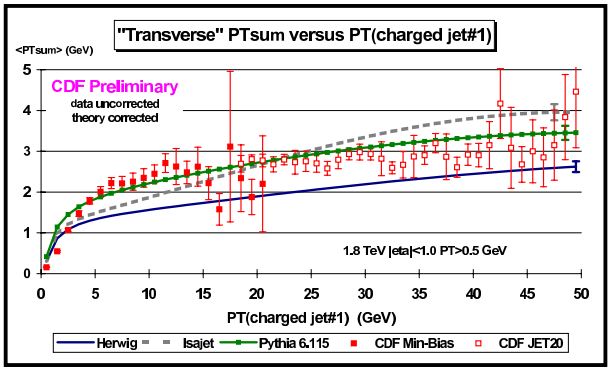

Figure 34. Data from Fig. 26 on the average *scalar* p_T sum of charged particles ($p_T > 0.5\,\text{GeV}$ and $|\eta| < 1$) as a function of p_T(jet#1) (*leading charged jet*) for the "transverse" region defined in Fig. 24 compared with the QCD "hard scattering" Monte-Carlo predictions of HERWIG 5.9, ISAJET 7.32, and PYTHIA 6.115. The errors on the (*uncorrected*) data include both statistical and correlated systematic uncertainties. The theory curves are corrected for the track finding efficiency and have an error (*statistical plus systematic*) of around 5%.

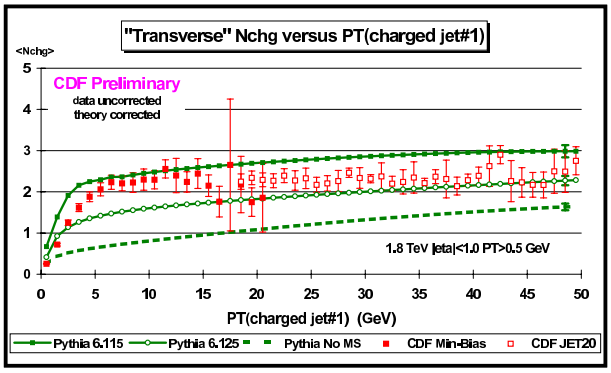

Figure 35. Data from Fig. 35 on the average number of charged particles ($p_T > 0.5\,\text{GeV}$ and $|\eta| < 1$) as a function of p_T(jet#1) (*leading charged jet*) for the "transverse" region defined in Fig. 24 compared with the QCD "hard scattering" Monte-Carlo predictions of PYTHIA 6.115, PYTHIA 6.125, and PYTHIA with no multiple parton scattering (No MS). The errors on the (*uncorrected*) data include both statistical and correlated systematic uncertainties. The theory curves are corrected for the track finding efficiency and have an error (*statistical plus systematic*) of around 5%.

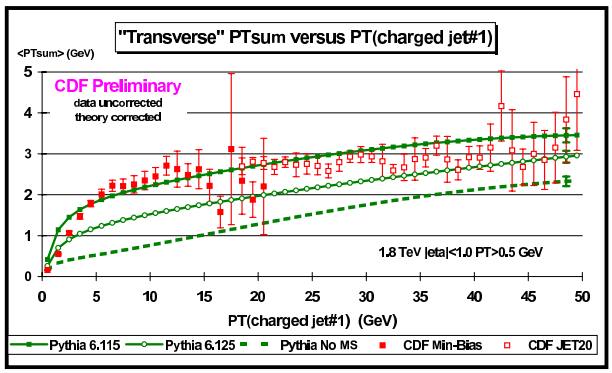

Figure 36. Data from Fig. 26 on the average *scalar* p_T sum of charged particles ($p_T > 0.5\,\text{GeV}$ and $|\eta| < 1$) as a function of p_T(jet#1) (*leading charged jet*) for the "transverse" region defined in Fig. 24 compared with the QCD "hard scattering" Monte-Carlo predictions of PYTHIA 6.115, PYTHIA 6.125, and PYTHIA with no multiple parton scattering (No MS). The errors on the (*uncorrected*) data include both statistical and correlated systematic uncertainties. The theory curves are corrected for the track finding efficiency and have an error (*statistical plus systematic*) of around 5%.

up of the beam and target and from initial-state radiation. This is clearly the case as can be seen in Fig. 37 where the predictions of ISAJET for the "transverse" region are divided into three categories: beam-beam remnants, initial- state radiation, and outgoing jets plus final-state radiation. It is interesting to see that it is the beam-beam remnants that are producing the approximately constant "plateau". The contributions from initial-state radiation and from the outgoing hard scattering jets both increase as p_T(jet#1) increases. In fact, for ISAJET it is the sharp rise in the initial-state radiation component that is causing the disagreement with the data for p_T(jet#1) $> 20\,\text{GeV}$.

As we explained in Section B, for HERWIG and PYTHIA it makes no sense to distinguish between particles that arise from initial-state radiation from those that arise from final-state radiation, but one can separate the "hard scattering component" from the beam-beam remnants. For PYTHIA the beam-beam remnants include contributions from multiple parton scattering as illustrated in Fig. 19. Fig. 38 and Fig. 39 compare the "transverse" $\langle N_{chg} \rangle$ with the QCD "hard scattering" Monte-Carlo predictions of HERWIG 5.9 and PYTHIA 6.115, respectively. Here the predictions are divided into two categories: charged particles that arise from the break-up of the beam and target (*beam-*

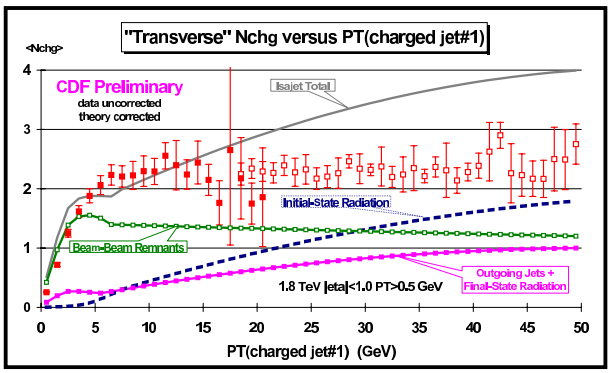

Figure 37. Data from Fig. 25 on the average number of charged particles ($p_T > 0.5\,\text{GeV}$ and $|\eta| < 1$) as a function of p_T(jet#1) (*leading charged jet*) for the "transverse" region defined in Fig. 24 compared with the QCD "hard scattering" Monte-Carlo predictions of ISAJET 7.32. The predictions of ISAJETare divided into three categories: charged particles that arise from the break-up of the beam and target (*beam-beam remnants*), charged particles that arise from initial-state radiation, and charged particles that result from the outgoing jets plus final-state radiation (see Fig. 19). The errors on the (*uncorrected*) data include both statistical and correlated systematic uncertainties. The theory curves are corrected for the track finding efficiency and have an error (*statistical plus systematic*) of around 5%.

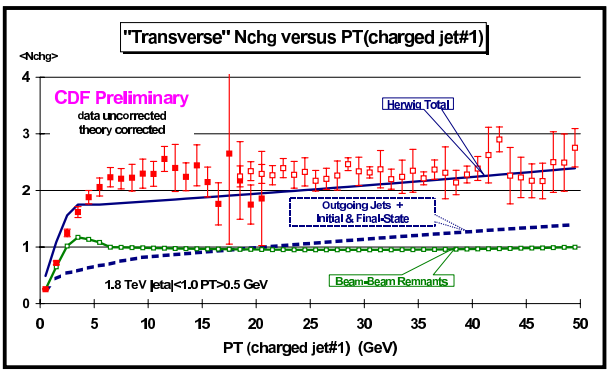

Figure 38. Data from Fig. 25 on the average number of charged particles ($p_T > 0.5\,\text{GeV}$ and $|\eta| < 1$) as a function of p_T(jet#1) (*leading charged jet*) for the "transverse" region defined in Fig. 24 compared with the QCD "hard scattering" Monte-Carlo predictions of HERWIG 5.9. The predictions of HERWIG are divided into two categories: charged particles that arise from the break-up of the beam and target (*beam-beam remnants*), and charged particles that result from the outgoing jets plus initial and final-state radiation (*hard scattering component*) (see Fig. 19). The errors on the (*uncorrected*) data include both statistical and correlated systematic uncertainties. The theory curves are corrected for the track finding efficiency and have an error (*statistical plus systematic*) of around 5%.

beam remnants), and charged particles that result from the outgoing jets plus initial and final-state radiation (*hard scattering component*). As was the case with ISAJET the beam-beam remnants form the approximately constant "plateau" and the hard scattering component increase as p_T(jet#1) increases. However, the hard scattering component of HERWIG and PYTHIA does not rise nearly as fast as the hard scattering component of ISAJET. This can be seen clearly in Fig. 40 where we compare directly the hard scattering component (*outgoing jets plus initial and final-state radiation*) of the "transverse" $\langle N_{chg} \rangle$ from ISAJET 7.32, HERWIG 5.9, and PYTHIA 6.115. PYTHIA and HERWIG are similar and rise gently as p_T(jet#1) increases, whereas ISAJETproduces a much sharper increase as p_T(jet#1) increases.

There are two reasons why the hard scattering component of ISAJET is different from HERWIG and PYTHIA. The first is due to different fragmentation schemes. ISAJET uses independent fragmentation, which produces too many soft hadrons when partons begin to overlap. The second difference arises from the way the QCD Monte-Carlo produce "parton showers". ISAJET uses a leading-log picture in which the partons within the shower are ordered according to their invariant mass. Kinematics requires that the invariant mass of daughter partons be less than the invariant mass of the parent. HERWIG and PYTHIA modify the leading-log picture to include "color coherence effects" which leads to "angle ordering" within the parton shower. Angle ordering produces less high p_T radiation within a parton shower which is what is seen in Fig. 40. Without further study, we do not know how much of the difference seen in Fig. 40 is due to the different fragmentation schemes and how much is due to the color coherence effects.

The beam-beam remnant contribution to the "transverse" $\langle N_{chg} \rangle$ is different for each of the QCD Monte-Carlo models. This can be seen in Fig. 41 where we compare directly the beam-beam remnant component of the "transverse" $\langle N_{chg} \rangle$ from ISAJET 7.32, HERWIG 5.9, PYTHIA 6.115, and PYTHIA with no multiple parton interactions. Since we are considering

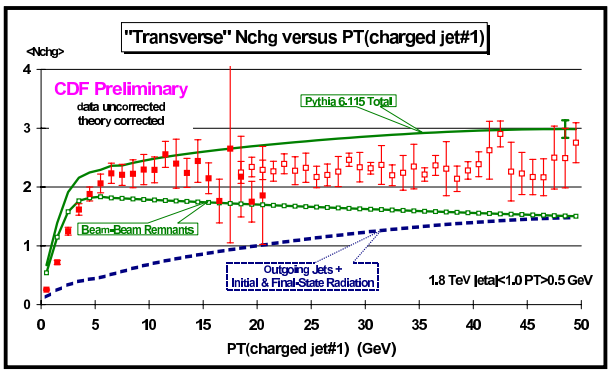

Figure 39. Data from Fig. 25 on the average number of charged particles ($p_T > 0.5\,\text{GeV}$ and $|\eta| < 1$) as a function of p_T(jet#1) (*leading charged jet*) for the "transverse" region defined in Fig. 24 compared with the QCD "hard scattering" Monte-Carlo predictions of PYTHIA 6.115. The predictions of PYTHIA are divided into two categories: charged particles that arise from the break-up of the beam and target (*beam-beam remnants*), and charged particles that result from the outgoing jets plus initial and final-state radiation (*hard scattering component*). For PYTHIA, the beam-beam remnants include contributions from multiple parton scattering (see Fig. 19). The errors on the (*uncorrected*) data include both statistical and correlated systematic uncertainties. The theory curves are corrected for the track finding efficiency and have an error (*statistical plus systematic*) of around 5%.

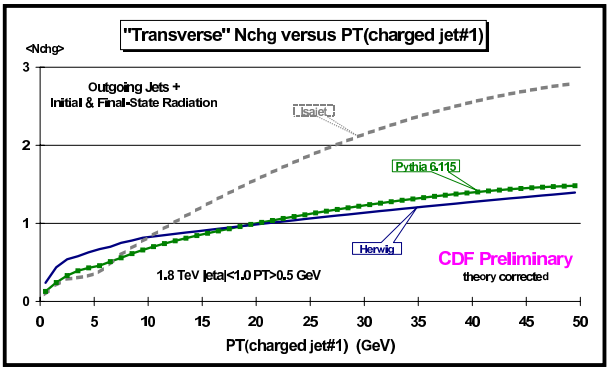

Figure 40. QCD "hard scattering" Monte-Carlo predictions from HERWIG 5.9, ISAJET 7.32, and PYTHIA 6.115 of the average number of charged particles ($p_T > 0.5\,\text{GeV}$ and $|\eta| < 1$) as a function of p_T(jet#1) (*leading charged jet*) for the "transverse" region defined in Fig. 24 arising from the outgoing jets plus initial and finial-state radiation (*hard scattering component*). The curves are corrected for the track finding efficiency and have an error (*statistical plus systematic*) of around 5%.

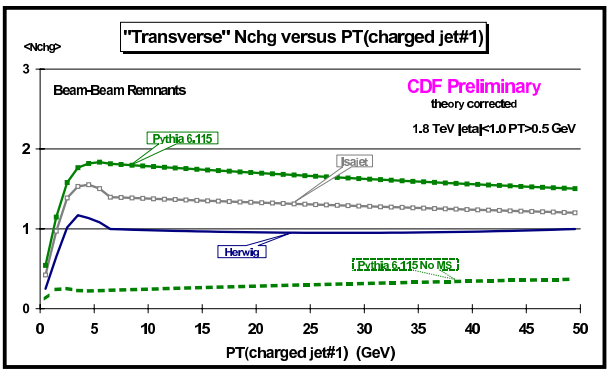

Figure 41. QCD "hard scattering" Monte-Carlo predictions from HERWIG 5.9, ISAJET 7.32, PYTHIA 6.115, and PYTHIA with no multiple parton scattering (No MS) of the average number of charged particles ($p_T > 0.5\,\text{GeV}$ and $|\eta| < 1$) as a function of p_T(jet#1) (*leading charged jet*) for the "transverse" region defined in Fig. 7 arising from the break-up of the beam and target (*beam-beam remnants*). For PYTHIA the beam-beam remnants include contributions from multiple parton scattering (see Fig. 19). The curves are corrected for the track finding efficiency and have an error (*statistical plus systematic*) of around 5%.

only charged particles with $p_T > 0.5\,\text{GeV}$, the height of the "plateaus" in Fig. 41 is related to the p_T distribution of the beam-beam remnant contributions. A steeper p_T distribution means less particles with $p_T > 0.5\,\text{GeV}$. PYTHIA uses multiple parton scattering to enhance the underlying event and we have included these contributions in the beam-beam remnants. For PYTHIA the height of the "plateau" in Fig. 41 can be adjusted by adjusting the amount of multiple parton scattering. HERWIG and ISAJET do not include multiple parton scattering. For HERWIG and ISAJET the height of the "plateau" can be adjusted by changing the p_T distribution of the beam-beam remnants.

8.6. Summary and Conclusions

For $p\bar{p}$ collisions at 1.8 TeV min-bias does not necessarily imply "soft" physics. There is a lot of QCD "hard scattering" in the Min-Bias data. We have studied both "local" leading jet observables and "global" observables where to fit the data the QCD

Monte-Carlo models have to correctly describe the entire event structure. Our summary and conclusions are as follows.

The Evolution of Charge Particle Jets

Charged particle jets are "born" somewhere around p_T(jet) of about 2 GeV with, on the average, about 2 charged particles and grow to, on the average, about 10 charged particles at 50 GeV. The QCD "hard scattering" models describe quite well (*although not perfectly*) "local" leading jet observables such as the multiplicity distribution of charged particles within the leading jet, the "size" of the leading jet, the radial flow of charged particles and p_T around the leading jet direction, and the momentum distribution of charged particles within the leading jet. In fact, the QCD "hard" scattering Monte-Carlo models agree as well with 2 GeV charged particle jets as they do with 50 GeV charged particle jets! The charge particle jets in the Min-Bias data are simply the extrapolation (*down to small* p_T) of the high p_T jets observed in the JET20 data. For a fixed p_T(hard), the QCD "hard" scattering cross section grows with increasing collider energy. As the center-of-mass energy of a $p\bar{p}$ collision grows, "hard" scattering becomes a larger and larger fraction of the total inelastic cross section. At 1.8 TeV "hard scattering" makes up a sizable part of the "hard core" inelastic cross section and a lot of min-bias events have 2 TeV or 3 GeV jets.

The "Underlying Event"

A hard scattering collider event consists of large p_T outgoing hadrons that originate from the large p_T partons (*outgoing jets*) and also hadrons that originate from the break-up of the proton and antiproton (*beam-beam remnants*). The "underlying event" is formed from the beam-beam remnants, initial-state radiation, and possibly from multiple parton interactions. Our data show that the charged particle multiplicity and scalar p_T sum in the "underlying event" grows very rapidly with the transverse momentum of the leading charged particle jet and then forms an approximately constant "plateau" for p_T(jet#1) > 6 GeV. The height of this "plateau" is at least twice that observed in "soft" collisions at the same corresponding energy.

None of the QCD Monte-Carlo models we examined correctly describe all the properties of the underlying event seen in the data. HERWIG 5.9 and PYTHIA 6.125 do not have enough activity in the underlying event. PYTHIA 6.115 has about the right amount of activity in the underlying event, but as a result produces too much overall charged multiplicity. ISAJET 7.32 has a lot of activity in the underlying event, but with the wrong dependence on p_T(jet#1). Because ISAJET uses independent fragmentation and HERWIG and PYTHIA do not, there are clear differences in the hard scattering component (*mostly initial-state radiation*) of the underlying event between ISAJET and the other two Monte-Carlo models. Here the data strongly favor HERWIG and PYTHIA over ISAJET.

The beam-beam remnant component of both ISAJET 7.32 and HERWIG 5.9 has the wrong p_T dependence. ISAJET and HERWIG both predict too steep of a p_T distribution. PYTHIA does a better job, but is still slightly too steep. It is, of course, understandable that the Monte-Carlo models might be somewhat off on the parameterization of the beam-beam remnants. This component cannot be calculated from perturbation theory and must be determined from data. With what we have learned from the data presented here, the beam-beam remnant component of the QCD "hard scattering" Monte-Carlo models can be tuned to better describe the overall event in $p\bar{p}$ collisions.

REFERENCES

1. G. Marchesini, B.R. Webber, G. Abbiendi, I.G. Knowles, M.H. Seymour and L. Stanco, Comput. Phys. Commun. 67 (1992) 465.
2. F.E. Paige, S.D. Protopescu, H. Baer and X. Tata, hep-ph/9810440.
3. T. Sjöstrand, Comput. Phys. Commun. **82** (1994) 74.
4. G. Bodwin, Phys. Rev. **D31** (1985) 2616;
   J.C. Collins, D.E. Soper, G. Sterman, Nucl. Phys. **B261** (1985) 104.
5. M. Bengtsson, T. Sjöstrand and M. van Zijl, Z. Phys. **C32** (1986) 67.
6. V.N. Gribov and L.N. Lipatov, Sov. J. Nucl. Phys. **15** (1972) 438;
   G. Altarelli and G. Parisi, Nucl. Phys. **B126** (1977) 298;
   Yu.L. Dokshitzer, Sov. Phys. JETP **46** (1977) 641.
7. R. Odorico, Nucl. Phys. **B172** (1980) 157.
8. R.K. Ellis, W.J. Stirling and B. Webber, "QCD and Collider Physics," Cambridge University Press (UK) 1996.
9. T. Sjöstrand, Phys. Lett. **157B** (1985) 321.
10. G. Marchesini and B.R. Webber, Nucl. Phys. **B238** (1984) 1;
    B.R. Webber, Ann. Rev. Nucl. Part. Sci. **36** (1986) 253.
11. Y.I. Dokshitzer, D.I. D'Yakonov, S.I. Troyan, Phys. Lett. **B79** (1978) 269.
12. G. Parisi, R. Petronzio, Nucl. Phys. **B154** (1979) 427.
13. S.D. Ellis, N. Fleishon, and W.J. Stirling, Phys.

Rev. **D24** (1981) 1386.
14. J. Collins, D. Soper, Nucl. Phys. **B193** (1981) 381; Erratum **B213** (1983) 545; **B197** (1982) 446.
15. J. Collins, D. Soper, G. Sterman, Nucl. Phys. **B250** (1985) 199.
16. G. Altarelli, R.K. Ellis, M. Greco, G. Martinelli, Nucl. Phys. **B246** (1984) 12.
17. G. Altarelli, R.K. Ellis, G. Martinelli, Z. Phys. **C27** (1985) 617.
18. P.B. Arnold, R.P. Kauffman, Nucl. Phys. **B349** (1991) 381.
19. R.K. Ellis, S. Veseli, Nucl. Phys. **B511** (1998) 649.
20. A. Kulesza and W.J. Stirling, eprint [hep-ph/9902234].
21. J. Kodaira and L. Trentadue, Phys. Lett. **112B** (1982) 66.
22. C. Balázs, C.P. Yuan, Phys. Rev. **D56** (1997) 5558.
23. H. Baer and M.H. Reno, Phys. Rev. **D44** (1991) 3375, **D45** (1992) 1503.
24. J. André and T. Sjöstrand, Phys. Rev. **D57** (1998) 5767;
    G. Ingelman, in *Physics at HERA*, Vol. 3, p. 1366;
    M.H. Seymour, Zeit. Phys. **C56** (1992) 161.
25. M. Bengtsson and T. Sjöstrand, Phys. Lett. **B185** (1987) 435;
    G. Gustafson and U. Pettersson, Nucl. Phys. **B306** (1988) 746;
    L. Lönnblad, Comput. Phys. Commun. **71** (1992) 15;
    M.H. Seymour, preprint LU TP 94-12, International Conference on High Energy Physics, Glasgow, U.K., 20–27 July 1994; Nucl. Phys. **B436** (1995) 443;
    G. Corcella and M.H. Seymour, Phys. Lett. **B442** (1998) 417.
26. G. Miu, eprint [hep-ph/9804317];
    G. Miu and T. Sjöstrand, eprint [hep-ph/9912455]
27. DØ Collaboration, S. Abachi *et al.*, Phys. Rev. Lett. **80** (1998) 5498.
28. CDF Collaboration, T. Affolder *et al.*, Phys. Rev. Lett. **84** (2000) 845.
29. S. Frixione, M.L. Mangano, P. Nason and G. Ridolfi, Nucl. Phys. **B431** (1994) 453;
    L. Apanasevich *et al.*, eprint [hep-ph/9808467].
30. C. Balázs, J.W. Qui, C.–P. Yuan, Phys. Lett. **B355** (1995) 548.
31. R. Meng, F.I. Olness, D.E. Soper, Phys. Rev. **D54** (1996) 1919.
32. N. Kidonakis, G. Sterman, Nucl. Phys. **B505** (1997) 321;
    R. Bonciani, S. Catani, M. Mangano, P. Nason, Nucl. Phys. **B529** (1998) 424;
    N. Kidonakis, G. Oderda, G. Sterman, Nucl. Phys. **B531** (1998) 365;
    S. Catani, M. Mangano, P. Nason, JHEP 9807: **024** (1998).
33. P.B. Arnold, M.H. Reno, Nucl. Phys. **B319** (1989) 37; Erratum **B330** (1990) 284.
34. S. Mrenna, Comput. Phys. Commun. **101** (1997) 232.
35. H.L. Lai, J. Huston, S. Kuhlmann, J. Morfín, F. Olness, J. Owens, J. Pumplin, W.K. Tung, hep-ph/9903282.
36. P. Edén and G. Gustafson, Z. Phys. **C75** (1997) 41.
37. C. Friberg and T. Sjöstrand, LU TP 99–11 and hep-ph/9907245, to appear in Eur. Phys. J. C.
38. M. Bengtsson and T. Sjöstrand, Phys. Lett. **B185** (1987) 435; G. Gustafson and U. Pettersson, Nucl. Phys. **B306** (1988) 746; M.H. Seymour, Comput. Phys. Commun. **90** (1995) 95.
39. G. Miu and T. Sjöstrand, Phys. Lett. **B449** (1999) 313.
40. J. Huston, these proceedings.
41. G. Corcella and M.H. Seymour, RAL-TR-1999-051 and hep-ph/9908388.
42. S. Mrenna, UCD-99-4 and hep-ph/9902471.
43. S. Mrenna, in preparation.
44. J. André and T. Sjöstrand, Phys. Rev. **D57** (1998) 5767.
45. C. Friberg and T. Sjöstrand, in 'Monte Carlo Generators for HERA Physics', eds. A.T. Doyle, G. Grindhammer, G. Ingelman and H. Jung, DESY-PROC-1999-02, p. 181.
46. WA82 Collaboration, M. Adamovich et al., Phys. Lett. **B305** (1993) 402; E769 Collaboration, G.A. Alves et al., Phys. Rev. Lett. **72** (1994) 812; E791 Collaboration, E.M. Aitala et al., Phys. Lett. **B371** (1996) 157.
47. E. Norrbin and T. Sjöstrand, Phys. Lett. **B442** (1998) 407, in preparation.
48. B. Andersson, G. Gustafson, G. Ingelman and T. Sjöstrand, Phys. Rep. **97** (1983) 31; T. Sjöstrand, Nucl. Phys. **B248** (1984) 469.
49. T. Sjöstrand and M. van Zijl, Phys. Rev. **D36** (1987) 2019.
50. CDF collaboration, F. Abe et al., Phys. Rev. Lett. **79** (1997) 584.
51. G. Gustafson and G. Miu, LU TP 99–43.
52. J. Dischler and T. Sjöstrand, in preparation.
53. A. Donnachie and P.V. Landshoff, Phys. Lett. **B296** (1992) 227.
54. G. Gustafson, U. Pettersson and P. Zerwas, Phys. Lett. **B209** (1988) 90.
55. T. Sjöstrand and V.A. Khoze, Z. Phys. **C62** (1994) 281, Phys. Rev. Lett. **72** (1994) 28.
56. G. Gustafson and J. Häkkinen, Z. Phys. **C64**

(1994) 659; L. Lönnblad, Z. Phys. **C70** (1996) 107; Š. Todorova–Nová, DELPHI Internal Note 96-158 PHYS 651; J. Ellis and K. Geiger, Phys. Rev. **D54** (1996) 1967, Phys. Lett. **B404** (1997) 230; B.R. Webber, J. Phys. **G24** (1998) 287.
57. J. Häkkinen and M. Ringnér, Eur. Phys. J. **C5** (1998) 275.
58. L. Lönnblad and T. Sjöstrand, Phys. Lett. **B351** (1995) 293, Eur. Phys. J. **C2** (1998) 165.
59. S. Jadach and K. Zalewski, Acta Phys. Pol. **B28** (1997) 1363; V. Kartvelishvili, R. Kvatadze and R. Møller, Phys. Lett. **B408** (1997) 331; K. Fiałkowski and R. Wit, Acta Phys. Pol. **B28** (1997) 2039, Eur. Phys. J. **C2** (1998) 691; Š. Todorova–Nová and J. Rameš, hep-ph/9710280.
60. V.A. Khoze and T. Sjöstrand, Phys. Lett. **B328** (1994) 466.
61. A. Edin, G. Ingelman and J. Rathsman, Z. Phys. **C75** (1997) 57.
62. A. Edin, G. Ingelman and J. Rathsman, Phys.Rev. **D56** (1997) 7317.
63. L. Lönnblad, Comput. Phys. Commun. **118** (1999) 213.
64. `http://fnth37.fnal.gov/susy.html`
65. `http://runIIcomputing.fnal.gov/strongdynamics/web/strongdynamics.html`
66. `http://fnth37.fnal.gov/higgs/draft.html`
67. `http://fnth37.fnal.gov/sugra.html`
68. `http://b0nd10.fnal.gov/~regina/tcolor.html`
69. `http://www-theory.fnal.gov/people/bdob/dimensions.html`
70. F. Abe et al., "Evidence for top quark production in $p\bar{p}$ collisions at $\sqrt{s} = 1.8$ TeV," Phys. Rev. **D50** (1994) 2966.
71. F. Abe et al., "Search for Scalar Top and Scalar Bottom in $p\bar{p}$ collisions at $\sqrt{s} = 1.8$ TeV," hep-ex/9912018, submitted to Phys. Rev. Lett.
72. J.M. Campbell, R.K. Ellis (Fermilab) This proceedings.
73. F. Abe et al., "Measurement of Correlated $\mu - \bar{b}$ Jet Cross Sections in $p\bar{p}$ Collisions at $\sqrt{s} = 1.8$ TeV," Phys. Rev. **D53** (1996) 1051.
74. F. Abe et al., "A Measurement of the Bottom Quark Production Cross Section in 1.8 TeV $p\bar{p}$ Collisions Using Semileptonic Decay Muons," Phys. Rev. Lett. **71** (1993) 2396.
75. T. Nakaya, "Measurement of the D^* + (2010) production cross section in $p\bar{p}$ collisions at $\sqrt{s} =$ 1.8 TeV," report CDF-ANAL-BOTTOM-CDFR-5025.
76. F. Abe et al., "Measurement of the B0 anti-B0 Oscillation Frequency Using pi-B Meson Charge-Flavor Correlations in $p\bar{p}$ Collisions at $\sqrt{s} = 1.8$ TeV," Phys. Rev. Lett. **80** (1998) 2057; F. Abe et al., "A Measurement of the B Meson and b Quark Cross Section at $\sqrt{s} = 1.8$ TeV Using the Exclusive Decay $B^0 \to J/\Psi K^*(892)$," Phys. Rev. **D50** (1994) 4252; F. Abe et al., "A Measurement of the B Meson and b Quark Cross Section at $\sqrt{s} = 1.8$ TeV Using the Exclusive Decay $B^+ \to J/\Psi K^+$," Phys. Rev. Lett. **68** (1992) 3403.
77. `http://www-theory.fnal.gov/people/ellis/Talks/top.ps.gz`
78. See the references at `http://www-d0.fnal.gov/~heinson/thinkshop/singletop_papers_thinkshop.html`
79. J.M. Campbell, R.K. Ellis, Phys. Rev. **D60** (1999) 113006.
80. T.Adams et al., in Proceedings of the 33rd Rencontres de Moriond, QCD and Hadronic Interactions, (to be published), hep-ex/9906037.
81. S.A.Rabinowitz et al., Phys. Rev. Lett. **70** (1993) 134.
82. P. Vilain et al., Eur. Phys. J. **C11** (1999) 19.
83. H. Abramowicz et al., Z. Phys. **C15** (1982) 19.
84. M. Gluck, E. Reya, A. Vogt, "Dynamic parton distributions of the proton and small-x physics," Z. Phys. **C67** (1995) 433.
85. H.L. Lai, et al., "Improved Parton Distributions from Global Analysis of Recent Deep Inelastic Scattering and Inclusive Jet Data," Phys. Rev. **D55** (1997) 1280.
86. F. Abe et al., "Search for New Particles Decaying into $b\bar{b}$ and Produced in Association with W Bosons Decaying into $e\nu$ and $\mu\nu$ at the Tevatron," Phys. Rev. Lett. **79** (1997) 3819.
87. E. Laenen, S. Riemersma, J. Smith and W.L. van Neerven, Nucl. Phys. **B392** (1993) 162; ibid. (1993) 229.
88. J. Collins, F. Wilczek and A. Zee, Phys. Rev. D**18** (1978) 242.
89. S. Riemersma, J. Smith and W.L. van Neerven, Phys. Lett. **B347** (1995) 43.
90. M. Buza, Y. Matiounine, J. Smith, R. Migneron and W.L. van Neerven, Nucl. Phys. **B472** (1996) 611.
91. B.W. Harris and J. Smith, Nucl. Phys. **B452** (1995) 109.
92. J. Breitweg et al. (ZEUS Collaboration), Phys. Lett. **B407** (1997) 402, hep-ex/9908012.
93. C. Adloff et al. (H1-collaboration), Nucl. Phys. **B545** (1999) 21.
94. M. Buza, Y. Matiounine, J. Smith, W.L. van Neerven, Eur. Phys. J. **C1** (1998) 301.
95. W.L. van Neerven and E.B. Zijlstra, Phys. Lett. **B272** (1991) 127, E.B. Zijlstra and W.L. van Neerven, Phys. Lett. **B273** (1991) 476, Nucl. Phys. **B383** (1992) 525.

96. P.J. Rijken and W.L. van Neerven, Phys. Rev. **D51** (1995) 44.
97. A. Chuvakin, J. Smith and W.L. van Neerven, hep-ph/9910250.
98. M. Buza, Y. Matiounine, J. Smith, W.L. van Neerven, Phys. Lett. **B411** (1997) 211; W.L. van Neerven, Acta Phys. Polon. **B28** (1997) 2715;
W.L. van Neerven in *Proceedings of the 6th International Workshop on Deep Inelastic Scattering and QCD "DIS98"* edited by GH. Coremans and R. Roosen, (World Scientific, 1998), p. 162-166, hep-ph/9804445;
J. Smith in *New Trends in HERA Physics*, edited by B.A. Kniehl, G. Kramer and A. Wagner, (World Scientific, 1998), p. 283, hep-ph/9708212.
99. M.A.G. Aivazis, J.C. Collins, F.I. Olness and W.-K. Tung, Phys. Rev. D**50** (1994) 3102; F. Olness and S. Riemersma, Phys. Rev. D**51** (1995) 4746.
100. J.C. Collins, Phys. Rev. D**58** (1998) 0940002.
101. R.S. Thorne and R.G. Roberts, Phys. Lett. **B421** (1998) 303; Phys. Rev. **D57** (1998) 6871.
102. M. Glück, E. Reya and A. Vogt, Eur. Phys. J. **C5** (1998) 461.
103. W.L. van Neerven and J.A.M. Vermaseren, Nucl. Phys. **B238** (1984) 73; See also S. Kretzer and I. Schienbein, Phys. Rev. **D58** (1998) 094035.
104. F.A. Berends, G.J.J. Burgers and W.L. van Neerven, Nucl. Phys. **B297** (1988) 429 ; Erratum ibid. Nucl. Phys. **B304** (1988) 921.
105. A. Chuvakin, J. Smith, hep-ph/9911504.
106. A.D. Martin, R.G. Roberts, W.J. Stirling and R. Thorne, Eur. Phys. J. **C4** (1998) 463.
107. A. Chuvakin, J. Smith and W.L. van Neerven, in preparation.
108. ATLAS Detector and Physics Performance Technical Design Report, CERN/LHCC/99-14.
109. C. Schmidt, private communication.
110. S. Catani and B.R. Webber, *Nucl. Phys.* **B349** (1991) 635.
111. C. Balazs and C. P. Yuan, Phys. Rev. **D56**, 5558 (1997) hep-ph/9704258; C. Balazs and C. P. Yuan, hep-ph/0001103.
112. H.L. Lai, J. Huston, S. Kuhlmann, F. Olness, J. Owens, D. Soper, W.K. Tung, H. Weerts, *Phys. Rev.* **D55** (1997) 1280.
113. G. Corcella, talk at the LHC workshop, October 1999.
114. G. Ladinsky, C.P. Yuan, *Phys. Rev.* **D50** (1994) 4239.
115. C. Balazs, J. Collins and D. Soper, these proceedings.
116. F. Abe et al., *Phys. Rev. Lett.* **70** (1993) 2232; T. Takano, Ph.D. thesis, U. Tsukuba (1998); CDF Collaboration, paper in preparation.
117. C. Balazs, P. Nadolsky, C. Schmidt and C.–P. Yuan, hep-ph/9905551.
118. P. Aurenche, A. Douri, R. Baier, M. Fontannaz, *Z. Phys.* **C29** (1985) 423; B. Bailey, J. Owens, J. Ohnemus, *Phys. Rev.* **D46** (1992) 2018; T. Binoth, J.P. Guillet, E. Pilon, M. Werlen, hep-ph/9911340.
119. PYTHIA manual update for version 6.1.
120. D. Denegri, private communication.
121. S. Mrenna, talk at the Run 2 workshop, Nov 1999, Fermilab; C. Balazs, J. Huston, S. Mrenna, I. Puljak, Proceedings of the Run 2 Workshop.
122. F. Abe et al., Nucl. Instrum. Methods, **A271** (1988) 387.
123. R.K. Ellis and Sinisa Veseli, Phys.Rev. **D60** (1999) 011501.
124. Z. Bern, L. Dixon, D. Kosower and S. Weinzierl, Nucl. Phys. **B489** (1997) 3;
Z. Bern, L. Dixon and D. Kosower, Nucl. Phys. **B513** (1998) 3.
125. L. Dixon, Z. Kunszt and A. Signer, Nucl. Phys. **B531** (1998) 3.
126. R.K. Ellis, D.A. Ross and A.E. Terrano, Nucl. Phys. **B178** (1981) 421.
127. S. Catani and M.H. Seymour, Nucl. Phys. **B485** (1997) 291, Erratum, ibid **B510** (1997) 503.
128. G. Altarelli, R.K. Ellis and G. Martinelli, Nucl. Phys. **B157** (1979) 461.
129. J. Kubar, M. Le Bellac, J.L. Meunier, G. Plaut, Nucl. Phys.**B175** (1980) 251.
130. H. Georgi, Nucl. Phys.**B363** (1991) 301.
131. A.D. Martin, R.G. Roberts, W.J. Stirling, R.S. Thorne, eprint [hep-ph/9907231]
132. S. Kim, S. Kuhlmann and W.M. Yao, presented at 1996 DPF/DPB Summer Study on New Directions for High-energy Physics (Snowmass 96), Snowmass, CO, July 1996;
P. Agrawal, D. Bowser-Chao and K. Cheung, Phys. Rev. **D51** (1995) 6114.
133. J.C. Collins and D. Soper, Phys. Rev. **D16** (1977) 2219.

Run II Jet Physics

Gerald C. Blazey[a], Jay R. Dittmann[b], Stephen D. Ellis[c], V. Daniel Elvira[b], K. Frame[d], S. Grinstein[e], Robert Hirosky[f], R. Piegaia[e], H. Schellman[g], R. Snihur[g], V. Sorin[e], Dieter Zeppenfeld[h]

[a]Department of Physics, Northern Illinois University, DeKalb, IL 60115, USA

[b]Fermilab, P.O. Box 500, Batavia, IL 60510, USA

[c]Department of Physics, University of Washington, Box 351560, Seattle, WA 98195-1560, USA

[d]Department of Physics and Astronomy, Michigan State University, East Lansing, MI 48824, USA

[e]Depto. de Fisica, FCEyN-Universidad de Buenos Aires, Pab I, Ciudad Universitaria, (1428) Capital Federal, Argentina

[f]Department of Physics, University of Illinois at Chicago, Chicago, IL 60607, USA

[g]Physics Department, Northwestern University, Evanston, IL 60210

[h]Department of Physics, University of Wisconsin at Madison, Madison, WI 53706, USA

The Run II jet physics group includes the Jet Algorithms, Jet Shape/Energy Flow, and Jet Measurements/Correlations subgroups. The main goal of the jet algorithm subgroup was to explore and define standard Run II jet finding procedures for CDF and DØ. The focus of the jet shape/energy flow group was the study of jets as objects and the energy flows around these objects. The jet measurements/correlations subgroup discussed measurements at different beam energies; α_S measurements; and LO, NLO, NNLO, and threshold jet calculations. As a practical matter the algorithm and shape/energy flow groups merged to concentrate on the development of Run II jet algorithms that are both free of theoretical and experimental difficulties and able to reproduce Run I measurements.

Starting from a review of the experience gained during Run I, the group considered a variety of cone algorithms and K_T algorithms. The current understanding of both types of algorithms, including calibration issues, are discussed in this report along with some preliminary experimental results. The jet algorithms group recommends that CDF and DØ employ the *same* version of *both* a cone algorithm and a K_T algorithm during Run II. Proposed versions of each type of algorithm are discussed. The group also recommends the use of full 4-vector kinematic variables whenever possible. The recommended algorithms attempt to minimize the impact of seeds in the case of the cone algorithm and preclustering in the case of the K_T algorithm. Issues regarding precluster definitions and merge/split criteria require further study.

1. Prologue

The Run I jet programs at CDF and DØ made impressive measurements of the inclusive jet cross section, dijet angular and mass distributions, and triple differential cross sections. These measurements were all marked by statistical accuracy equal or superior to current theoretical accuracy [1]. However, the always compelling search for quark compositeness, the quest to improve the calculational accuracy of QCD, and the desire to fully understand the composition of the proton will certainly prompt improvements over these measurements. Without question, with $\sim 2\ fb^{-1}$, the Run II jet physics program will extend the jet measurements of Run I to even higher jet energies.

There are three issues, experimental and theoretical, that currently limit the sensitivity of compositeness searches and QCD tests: limited knowledge of the parton distribution functions (pdfs), systematic uncertainties related to jet energy calibration, and the limited accuracy of fixed order perturbative calculations due to the incomplete nature of the calculations and incomplete specification of jet finding algorithms. Inadequate knowledge of the pdfs and calibration are currently the dominant uncertainties, engendering greater than 50% uncertainties at the largest energies. The reader may refer to the chapter on Parton Distributions for a complete discussion of pdf measurements.

As mentioned, the uncertainty of NLO perturbative calculations is due in part to the inherent incompleteness of fixed order calculations. The initial meeting of the jet physics group included talks on "Leading Order (LO) Multi-jet Calculations" by Michelangelo Mangano, "Next-to-Leading Order (NLO) Multi-jet Calculations" by Bill Kilgore, "Prospects for Next-to-NLO (NNLO) Multi-jet Calculations" by Lance Dixon, "Threshold Resummations for Jet Production"

by Nicolas Kidonakis, "Different Beam Energies" by Greg Snow, and "α_S Measurements in Jet Systems" by Christina Mesropian. These attempts to improve the accuracy of perturbative calculations show the vigorous nature of ongoing efforts and should prove fruitful before the arrival of Run II data.

Jet algorithms, the other source of calculation uncertainty, start from a list of "particles" that we take to be calorimeter towers or hadrons at the experimental level, and partons in a perturbative QCD calculation. The role of the algorithm is to associate clusters of these particles into jets such that the kinematic properties of the jets (*e.g.*, momenta) can be related to the corresponding properties of the energetic partons produced in the hard scattering process. Thus the jet algorithm allows us to "see" the partons (or at least their fingerprints) in the hadronic final state.

Differences in the properties of reconstructed jets when going from the parton to the hadron or calorimeter level are a major concern for a good jet algorithm. Each particle i carries a 4-momentum p_i^μ, which we take to be massless. The algorithm selects a set of particles, which are typically emitted close to each other in angle, and combines their momenta to form the momentum of a jet. The selection process is called the "jet algorithm" and the momentum addition rule is called the "recombination scheme". Note that these two steps are logically distinct. One can, for example, use one set of kinematic variables in the jet algorithm to determine the particles in a jet and then construct a separate set of kinematic variables to characterize the jets that have been identified. This point will be important in subsequent discussions.

Historically cone algorithms have been the jet algorithm of choice for hadron-hadron experiments. As envisioned in the Snowmass algorithm [2], a cone jet of radius R consists of all of the particles whose trajectories (assuming no bending by the magnetic field of the detector) lie in an area $A = \pi R^2$ of $\eta \times \phi$ space, where η is the pseudorapidity $\eta = -\ln\tan\theta/2$. It is further required, as explained in detail below, that the axis of the cone coincides with the jet direction as defined by the E_T-weighted centroid of the particles within the cone (where E_T is transverse energy, $E_T = E\sin\theta$). In principle, one simply searches for all such "stable" cones to define the jet content of a given event.

In practice, in order to save computing time, the iterative process of searching for the "stable" cones in experimental data starts with only those cones centered about the most energetic particles in the event (the so-called "seeds"). Usually, the seeds are required to pass a threshold energy of a few hundred MeV in order to minimize computing time. The E_T-weighted centroids are calculated for the particles in each seed cone and then the centroids are used as centers for new cones in $\eta \times \phi$ space. This procedure is iterated for each cone until the cone axis coincides with the centroid. Unfortunately, nothing prevents the final stable cones from overlapping. A single particle may belong to two or more cones. As a result, a procedure must be included in the cone algorithm to specify how to split or merge overlapping cones [3].

At least part of the uncertainty associated with fixed order perturbative calculations of jet cross sections can be attributed to the difficulties encountered when this experimental jet cone algorithm, with both seeds and merging/splitting rules, is applied to theoretical calculations. (See Ref. [1] for a discussion of the CDF and DØ algorithms.) Neither issue was treated by the original Snowmass algorithm [2] that forms the basis of fixed order perturbative cone jet calculations. Current NLO inclusive jet cross section calculations (which describe either two or three final state partons) require the addition of an ad hoc parameter R_{Sep} [4]. This additional parameter is used to regulate the clustering of partons and simulate the role of seeds and merging in the experimentally applied algorithm. In essence, the jet cone algorithm, used so pervasively at hadron-hadron colliders, must be modeled in NLO calculations. This modeling results in 2–5% uncertainties as a function of jet transverse energy E_T in calculated cross sections.

Even worse, with the current cone algorithms, cross sections calculated at NNLO exhibit a marked sensitivity to soft radiation. As an illustration, consider two well-separated partons that will just fit inside, but at opposite sides, of a single cone. With only the two partons, and nothing in between to serve as a seed, the current standard cone algorithms will reconstruct the two partons as two jets. At NNLO a very soft gluon could be radiated between the two well-separated partons and serve as a seed. In this case the single jet solution, with both partons inside, will be identified by the current cone algorithm. Thus the outcome of the current cone algorithm with seeds is manifestly sensitive to soft radiation. Because of the difficulties inherent with typical usage of the cone algorithm, the jet algorithm and jet shape/energy flow subgroups decided to establish an Improved Legacy Cone Algorithm (whimsically dubbed ILCA). Ideally, the ILCA should replicate Run I cross sections within a few percent, but not have the same theoretical difficulties.

Inspired by QCD, a second class of jet algorithms, K_T algorithms, has been developed. These algorithms successively merge pairs of "particles" in order of increasing relative transverse momentum. They typically contain a parameter, D (also called R),

that controls termination of merging and characterizes the approximate size of the resulting jets. Since a K_T algorithm fundamentally merges nearby particles, there is a close correspondence of jets reconstructed in a calorimeter to jets reconstructed from individual hadrons, leptons and photons. Furthermore, every particle in an event is assigned to a unique jet. Most importantly, K_T jet algorithms are, by design, infrared and collinear safe to all orders of calculation. The algorithms can be applied in a straightforward way to fixed–order or resummed calculations in QCD, partons or particles from a Monte Carlo event generator, or energy deposited in a detector [5].

However, until recently, a full program for the calibration of K_T algorithms at hadron-hadron colliders had not been developed. This was due mostly to difficulties with the subtraction of energy from spectator fragments and from the pile-up of multiple hadron-hadron interactions. Since the K_T jets have no fixed shape, prescriptions for dealing with the extra energy have been difficult to devise and the use of K_T algorithms at hadron-hadron colliders has been limited. Also, as with the issue of seeds in the case of the cone algorithm, there is a practical question of minimizing the computing time required to apply the K_T algorithm. Typically this is treated in a preclustering step where the number of "particles" is significantly reduced before the K_T algorithm is applied. A successful K_T algorithm must ensure that any preclustering step does not introduce the sort of extra difficulty found with seeds.

Buoyed by the successful use of K_T algorithms at LEP and HERA, eager to benefit from their theoretical preciseness, and reassured by recent success with calibration, the jet physics group decided to specify a standard K_T algorithm for Run II.

2. Attributes of the Ideal Algorithm

Although it provided a good start, the Snowmass algorithm has proved to be incomplete. It does not address either the phenomena of merging and splitting or the role of the seed towers with the related soft gluon sensitivity. Also, jet energy and angle definitions have varied between experiments. To treat these issues, the group began discussions with the following four general criteria:

1. *Fully Specified*: The jet selection process, the jet kinematic variables and the various corrections (*e.g.*, the role of the underlying event) should be clearly and completely defined. If necessary, preclustering, merging, and splitting algorithms must be completely described.
2. *Theoretically Well Behaved*: The algorithm should be infrared and collinear safe with no ad hoc clustering parameters.
3. *Detector Independence*: There should be no dependence on cell type, numbers, or size.
4. *Order Independence*: The algorithms should behave equally at the parton, particle, and detector levels.

The first two criteria should be satisfied by every algorithm; however, the last two can probably never be exactly true, but should be approximately correct.

2.1. Theoretical Attributes of the Ideal Algorithm

The initial efforts of the algorithm working group were focused on extending and illuminating the list of desirable features of an "ideal" jet algorithm. From the "theoretical standpoint" the following features are desirable and, for the most part, necessary:

1. *Infrared safety:* The algorithm should not only be infrared safe, in the sense that any infrared singularities do not appear in the perturbative calculations, but should also find solutions that are insensitive to soft radiation in the event. As illustrated in Fig. 1, algorithms that look for jets only around towers that exhibit some minimum energy activity, called seed towers or just seeds, can be quite sensitive to soft radiation. The experimental cone algorithms employed in previous runs have such seeds.
2. *Collinear safety:* The algorithm should not only be collinear safe, in the sense that collinear singularities do not appear in the perturbative calculations, but should also find jets that are insensitive to any collinear radiation in the event.

   A) Seed-based algorithms will in general break collinear safety until the jets are of sufficiently large E_T that splitting of the seed energy between towers does not affect jet finding (See Fig. 2). This was found to be the case for jets above 20 GeV in the DØ data, where jets were found with 100% efficiency using a seed tower threshold of 1.0 GeV [6]. The collinear dependence introduced via the seed threshold is removed when the jets have sufficient E_T to be reconstructed with 100% efficiency.

   B) Another possible collinear problem can arise if the algorithm is sensitive to the E_T ordering of particles. An example would be an algorithm where a) seeds are treated in order of decreasing

E_T and b) a seed is removed from the seed list when it is within a jet found using a seed that is higher on the list. For such an algorithm consider the configuration illustrated in Fig. 3. The difference between the two situations is that the central (hardest) parton splits into two almost collinear partons. The separation between the two most distant partons is more than R but less than $2R$. Thus all of the partons can fall within a single cone of radius R around the central parton(s). However, if the partons are treated as seeds and analyzed with the candidate algorithm suggested above, different jets will be identified in the two situations. On the left, where the single central parton has the largest E_T, a single jet containing all three partons will be found. In the situation on the right, the splitting of the central parton leaves the right-most parton with the largest E_T. Hence this seed is looked at first and a jet may be found containing only the right-most and two central partons. The left-most parton is a jet by itself. In this case the jet number changes depending on the presence or absence of a collinear splitting. This signals an incomplete cancellation of the divergences in the real and virtual contributions to this configuration and renders the algorithm collinear unsafe. While the algorithm described here is admittedly an extreme case, it is not so different from some schemes used in Run I. Clearly this problem should be avoided by making the selection or ordering of seeds and jet cones independent of the E_T of individual particles.

3. *Invariance under boosts:* The algorithm should find the same solutions independent of boosts in the longitudinal direction. This is particularly important for $p\overline{p}$ collisions where the center-of-mass of the individual parton-parton collisions is typically boosted with respect to the $p\overline{p}$ center-of-mass. This point was emphasized in conversations with the Jet Definition Group Les Houches [7].[1]

4. *Boundary Stability:* It is desirable that the kinematic variables used to describe the jets exhibit kinematic boundaries that are insensitive to the details of the final state. For example, the scalar E_T variable, explained in more detail in the next section, has a boundary that is sensitive to the number of particles present and their relative angle (*i.e.*, the boundary is sensitive to the mass of the jet). The bound $E_T^{max} = \sqrt{s}/2$ applies only for collinear particles and massless jets. In the case of massive jets the boundary for E_T is larger than $\sqrt{s}/2$. Boundary stability is essential in order to perform soft gluon summations.

5. *Order Independence:* The algorithm should find the same jets at parton, particle, and detector level. This feature is clearly desirable from the standpoint of both theory and experiment.

6. *Straightforward Implementation:* The algorithm should be straightforward to implement in perturbative calculations.

[1]The Les Houches group discussed jet algorithms for both the Tevatron and LHC, and they sharpened their algorithm requirements by also requiring boundary stability (the kinematic boundary for the one jet inclusive jet cross section should be at the same place, $E_T = \sqrt{s}/2$, independent of the number of final state particles), suitability for soft gluon summations of the theory, and simplicity and elegance.

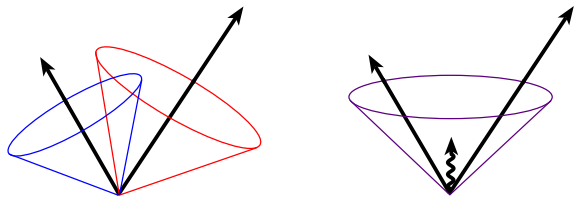

Figure 1. An illustration of infrared sensitivity in cone jet clustering. In this example, jet clustering begins around seed particles, shown here as arrows with length proportional to energy. We illustrate how the presence of soft radiation between two jets may cause a merging of the jets that would not occur in the absence of the soft radiation.

2.2. Experimental Attributes of the Ideal Algorithm

Once jets enter a detector, the effects of particle showering, detector response, noise, and energy from additional hard scatterings from the same beam crossing will subtly affect the performance of even the most ideal algorithm. It is the goal of the experimental groups to correct for such effects in each jet analysis. Ideally the algorithm employed should not cause the corrections to be excessively large. From an "experimental standpoint" we add the following criteria for a desirable jet algorithm:

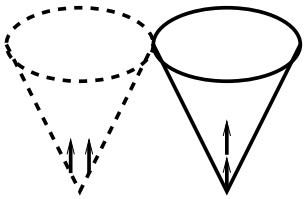

Figure 2. An illustration of collinear sensitivity in jet reconstruction. In this example, the configuration on the left fails to produce a seed because its energy is split among several detector towers. The configuration on the right produces a seed because its energy is more narrowly distributed.

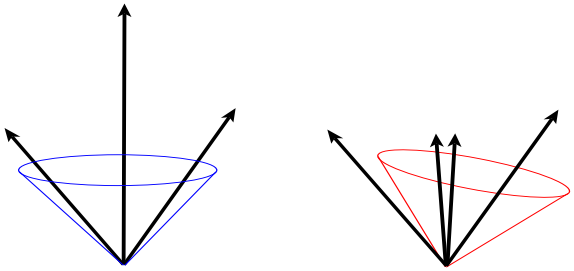

Figure 3. Another collinear problem. In this case we illustrate possible sensitivity to E_T ordering of the particles that act as seeds.

1. *Detector independence:* The performance of the algorithm should be as independent as possible of the detector that provides the data. For example, the algorithm should not be strongly dependent on detector segmentation, energy response, or resolution.

2. *Minimization of resolution smearing and angle biases:* The algorithm should not amplify the inevitable effects of resolution smearing and angle biases.

3. *Stability with luminosity:* Jet finding should not be strongly affected by multiple hard scatterings at high beam luminosities. For example, jets should not grow to excessively large sizes due to additional interactions. Furthermore the jet angular and energy resolutions should not depend strongly on luminosity.

4. *Efficient use of computer resources:* The jet algorithm should provide jet identification with a minimum of computer time. However, changes in the algorithm intended to minimize the necessary computer resources, *e.g.*, the use of seeds and preclustering, can lead to problems in the comparison with theory. In general, it is better to invest in more computer resources instead of distorting the definition of the algorithm.

5. *Maximal reconstruction efficiency:* The jet algorithm should efficiently identify all physically interesting jets (*i.e.*, jets arising from the energetic partons described by perturbative QCD).

6. *Ease of calibration:* The algorithm should not present obstacles to the reliable calibration of the final kinematic properties of the jet.

7. *Ease of use:* The algorithm should be straightforward to implement with typical experimental detectors and data.

8. *Fully specified:* Finally, the algorithm must be **fully specified**. This includes specifications for clustering, energy and angle definition, and all details of jet splitting and merging.

These experimental requirements are primarily a matter of optimization under real-life conditions and will, in general, exhibit complicated sensitivities to running conditions. They have a strong bearing on the ease with which quality physics measurements are achieved. Many of the details necessary to fully implement the jet algorithms have neither been standardized nor widely discussed and this has sometimes led to misunderstandings and confusion. The remainder of this chapter describes the cone and K_T algorithms discussed and recommended by the QCD at Run II Jets Group.

3. Cone Jet Algorithms

3.1. Introduction

This section should serve as a guide for the definition of common cone jet algorithms for the Tevatron and possibly future experiments. Section 3.2 reviews the features of previously employed cone algorithms. Section 3.3 describes a seedless cone algorithm. Section 3.4 gives a description of seed-based cone algorithms and discusses the need for adding midpoints between seeds as alternate starting points for clustering. Finally, in Section 3.5, we offer a detailed proposal for a common cone jet algorithm in Run II analyses.

3.2. Review of Cone Algorithms

Cone algorithms form jets by associating together particles whose trajectories (*i.e.*, towers whose centers) lie within a circle of specific radius R in $\eta \times \phi$ space. This 2-dimensional space is natural in $p\overline{p}$ collisions where the dynamics are spread out in the longitudinal direction. Starting with a trial geometric center (or axis) for a cone in $\eta \times \phi$ space, the energy-weighted centroid is calculated including contributions from all particles within the cone. This new point in $\eta \times \phi$ is then used as the center for a new trial cone. As this calculation is iterated the cone center "flows" until a "stable" solution is found, *i.e.*, until the centroid of the energy depositions within the cone is aligned with the geometric axis of the cone. This leads us to our initial cone algorithm based on the Snowmass scheme [2] of scalar E_T-weighted centers. The particles are specified by massless 4-vectors $(E^i = |\mathbf{p}^i|, \mathbf{p}^i)$ with angles $\left(\phi^i, \theta^i, \eta^i = -\ln\left(\tan(\theta^i/2)\right)\right)$ given by the direction from the interaction point with unit vector $\hat{\mathbf{p}}^i = \mathbf{p}^i/E^i$. The scalar E_T for each particle is $E_T^i = E^i \sin(\theta^i)$. For a specified geometric center for the cone $\left(\eta^C, \phi^C\right)$ the particles i within the cone satisfy

$$i \subset C \quad : \quad \sqrt{\left(\eta^i - \eta^C\right)^2 + \left(\phi^i - \phi^C\right)^2} \leq R. \tag{1}$$

In the Snowmass algorithm a "stable" cone (and potential jet) satisfies the constraints

$$\eta^C = \frac{\sum_{i\subset C} E_T^i \eta^i}{E_T^C}, \quad \phi^C = \frac{\sum_{i\subset C} E_T^i \phi^i}{E_T^C} \tag{2}$$

(*i.e.*, the geometric center of the previous equation is identical to the E_T-weighted centroid) with

$$E_T^C = \sum_{i\subset C} E_T^i \; . \tag{3}$$

Naively we can simply identify these stable cones, and the particles inside, as jets, $J = C$. (We will return to the practical issues of the impact of seeds and of cone overlap below.)

To complete the jet finding process we require a recombination scheme. Various choices for this recombination step include:

1. *Original Snowmass scheme:* Use the stable cone variables:

$$E_T^J = \sum_{i\subset J=C} E_T^i = E_T^C \; , \tag{4}$$

$$\eta^J = \frac{1}{E_T^J} \sum_{i\subset J=C} E_T^i \eta^i \; , \tag{5}$$

$$\phi^J = \frac{1}{E_T^J} \sum_{i\subset J=C} E_T^i \phi^i \; . \tag{6}$$

2. *Modified Run I recombination schemes:* After identification of the jet as the contents of the stable cone, construct more 4-vector-like variables:

$$E_x^i = E_T^i \cdot \cos(\phi^i) \; , \tag{7}$$

$$E_y^i = E_T^i \cdot \sin(\phi^i) \; , \tag{8}$$

$$E_z^i = E^i \cdot \cos(\theta^i) \; , \tag{9}$$

$$E_{x,y,z}^J = \sum_{i\subset J=C} E_{x,y,z}^i \; , \tag{10}$$

$$\theta^J = \tan^{-1}\left(\frac{\sqrt{(E_x^J)^2 + (E_y^J)^2}}{E_z^J}\right) . \tag{11}$$

A) In Run I, DØ used the scalar E_T^J sum as defined in Eq. 4 but used the following definitions for η^J and ϕ^J:

$$\eta^J = -\ln\left(\tan\left(\frac{\theta^J}{2}\right)\right) \; , \tag{12}$$

$$\phi^J = \tan^{-1}\left(\frac{E_y^J}{E_x^J}\right) . \tag{13}$$

B) In Run I, CDF used the angular definitions in Eqs. 12–13 and also replaced the Snowmass scheme E_T^J with:

$$E_T^J = E^J \cdot \sin(\theta^J), \quad E^J = \sum_{i\subset J} E^i \; . \tag{14}$$

Note that in the Snowmass scheme the designation of the centroid quantities η^J and ϕ^J of Eqs. 5 and 6 as a pseudorapidity and an azimuthal angle is purely convention. These quantities only approximate the true kinematic properties of the massive cluster that is the jet. They are, however, approximately equal to the "real" quantities, becoming exact in the limit of small jet mass ($M^J << E_T$). Further these quantities transform simply under longitudinal boosts (*i.e.*, η^J boosts additively while ϕ^J is invariant) guaranteeing that the jet structure determined with the Snowmass algorithm is boost invariant. It is also worthwhile noting that the Snowmass η^J is a better estimator of the "true" jet rapidity (y^J) defined below than the "true" jet pseudorapidity defined in Eq. 12. The latter quantity does not boost additively (for $M^J > 0$) and is not a good variable for systematic studies.

While the scalar sum E_T is invariant under longitudinal boosts, it is not a true energy variable. This feature leads to difficulty in resummation calculations: the kinematic boundary of the jet E_T shifts away from $\sqrt{s}/2$ appropriate for two parton kinematics when

additional final state partons are included and the jet acquires a nonzero mass. On the other hand the Snowmass variables have the attractive feature of simplicity, involving only arithmetic rather than transcendental relationships. An alternate choice, which we recommend here, is to use full 4-vector variables for the jets.

3. *E–Scheme, or 4-vector recombination:*

$$p^J = (E^J, \mathbf{p}^J) = \sum_{i \subset J = C} (E^i, p_x^i, p_y^i, p_z^i) \,, \quad (15)$$

$$p_T^J = \sqrt{(p_x^J)^2 + (p_y^J)^2} \,, \quad (16)$$

$$y^J = \frac{1}{2} \ln \frac{E^J + p_z^J}{E^J - p_z^J} \,, \quad \phi^J = \tan^{-1} \frac{p_y^J}{p_x^J} \,. \quad (17)$$

Note that in this scheme one does *not* use the scalar E_T variable. The 4-vector variables defined above manifestly display the desired Lorentz properties. Phase space boundaries will exhibit the required stability necessary for all-order resummations. While the structure of analytic fixed order perturbative calculations is simpler with the Snowmass variables, NLO cross section calculations are now also possible with Monte Carlo programs [8–11]. Such programs are fully flexible with respect to the choice of variables and the 4-vector variables pose no practical problems. It is also important to recall that, at least at low orders in perturbation theory, it is not possible for energy to be conserved in detail in going from the parton level to the hadron level. At the parton level the jet will almost surely be a cluster of partons with non-zero color charge. At the hadron level the cluster will be composed of color-singlet hadrons. The transition between the two levels necessarily involves the addition (or subtraction) of at least one colored parton carrying some amount (presumably small) of energy.

One can also employ these true 4-vector variables, rather than the E_T-weighted centroid, in the jet algorithm to find stable cones. While this choice will complicate the analysis, replacing simple arithmetic relationships with transcendental relationships, the group recommends that this possibility be investigated. The goal is to have a uniform set of kinematic variables with appropriate Lorentz properties throughout the jet analysis.

At this point it might seem that a simple and straightforward jet definition would arise from just the choice of a cone size and a recombination scheme. The algorithm would then be used to scan the detector and simply find all stable cones. In practice, this naive algorithm was found to be incomplete. To keep the time for data analysis within reasonable bounds the concept of the seed was introduced. Instead of looking "everywhere" for stable cones, the iteration process started only at the centers of seed towers that passed a minimum energy cut (how could a jet not have sizeable energy deposited near its center?). Additionally, in Run I both CDF and DØ reduced the number of seed towers used as starting points by consolidating adjacent seed towers into single starting points. (The actual clustering was always performed on calorimeter towers.) These types of procedures, however, create the problems illustrated in Figs. 1, 2 and 3, introducing sensitivity to soft emissions and the possibility of collinear sensitivity.

The naive Snowmass algorithm also does not address the question of treating overlapping stable cones. It is quite common for two stable cones to share some subset (but not all) of their particles. While not all particles in the final state need to be assigned to a jet, particles should not be assigned to more than one jet. Hence there must be a step between the stable cone stage and the final jet stage where either the overlapping cones are merged (when there is a good deal of overlap) or the shared particles are split between the cones. Typically cones whose shared energy is larger than a fixed fraction (*e.g.*, $f = 50\%$) of the energy in the lower energy cone are merged. For the cases with shared energy below this cut, the shared particles are typically assigned to the cone that is closer in $\eta \times \phi$ space. As suggested earlier, the detailed properties of the final jets will depend on the merge/split step and it is essential that these details be spelled out in the algorithm. We provide examples in the following sections.

3.3. Cone Jets without Seeds

Since many of the issues outlined in the previous section arise from the use of seed towers to define the starting point in the search for stable cones, it is worthwhile to consider the possibility of a seedless cone algorithm. A seedless algorithm is infrared insensitive. It searches the entire detector and finds all stable cones (or proto-jets[2]), even if these cones do not have a seed tower at their center. Collinear sensitivity is also removed, because the structure of the energy depositions within the cone is unimportant. In this section we present a preliminary study of such an algorithm.

3.3.1. Seedless Jet Clustering

We give an example of a seedless algorithm in the flowchart in Fig. 4. The basic idea [12] follows from the concept of "flowing" cone centers mentioned earlier.

[2]At the clustering stage we refer to stable cones as proto-jets. These may be promoted to jets after surviving the splitting and merging stage.

The location of a stable cone will act as an attractor towards which cones will flow during the iteration process. If the process starts close to such a stable center, the flow steps will be small. Starting points further from a stable center will exhibit larger flow steps towards the stable center during the iteration. Starting points outside of the region of attraction will again exhibit small flow steps. The method starts by looping through *all* detector towers[3] in some appropriate fiducial volume. For each tower k, with center $\overrightarrow{k} = \left(\eta^k, \phi^k\right)$, we define a cone of size R centered on the tower

$$\overrightarrow{C^k} = \left(\eta^{C^k} = \eta^k, \phi^{C^k} = \phi^k\right),$$
$$i \subset C^k : \sqrt{\left(\eta^i - \eta^{C^k}\right)^2 + \left(\phi^i - \phi^{C^k}\right)^2} \leq R. \quad (18)$$

For each cone we evaluate the E_T-weighted centroid

$$\overrightarrow{\bar{C}^k} = \left(\bar{\eta}^{C^k}, \bar{\phi}^{C^k}\right), \quad (19)$$
$$\bar{\eta}^{C^k} = \frac{\sum_{i \subset C^k} E_T^i \eta^i}{E_T^{C^k}}, \; \bar{\phi}^{C^k} = \frac{\sum_{i \subset C^k} E_T^i \phi^i}{E_T^{C^k}}, \quad (20)$$
$$E_T^{C^k} = \sum_{i \subset C^k} E_T^i . \quad (21)$$

Note that, in general, the centroid $\overrightarrow{\bar{C}^k}$ is not identical to the geometric center $\overrightarrow{C^k}$ and the cone is not stable. While this first step is resource intensive, we simplify the subsequent analysis with the next step. If the calculated centroid of the cone lies outside of the initial tower, further processing of that cone is skipped and the cone is discarded. The specific exclusion distance used in this cut is a somewhat arbitrary parameter and could be adjusted to maximize jet finding efficiency and minimize the CPU demand of the algorithm. All cones that yield a centroid within the original tower become preproto-jets. For these cones the process of calculating a new centroid about the previous centroid is iterated and the cones are allowed to "flow" away from the original towers. This iteration continues until either a stable cone center is found or the centroid migrates out of the fiducial volume. The surviving stable cones constitute the list of proto-jets. Note that the tower content of a cone will vary as its center moves within the area of a single tower. For a cone of radius R and tower dimension Δ (in either η or ϕ) the minimum change in the cone center location for which the tower content in the cone changes by at least one tower is characterized by $\Delta^2/2R$. This distance is of order 0.007 for $\Delta = 0.1$ and $R = 0.7$ (*i.e.*, 10% of a tower width if the diameter of the cone, $2R$, is ten times a tower width).

[3]While the algorithm may be run on individual detector cells, we do not believe that cell-level clustering is within the CPU means of current experiments for the largest expected data samples.

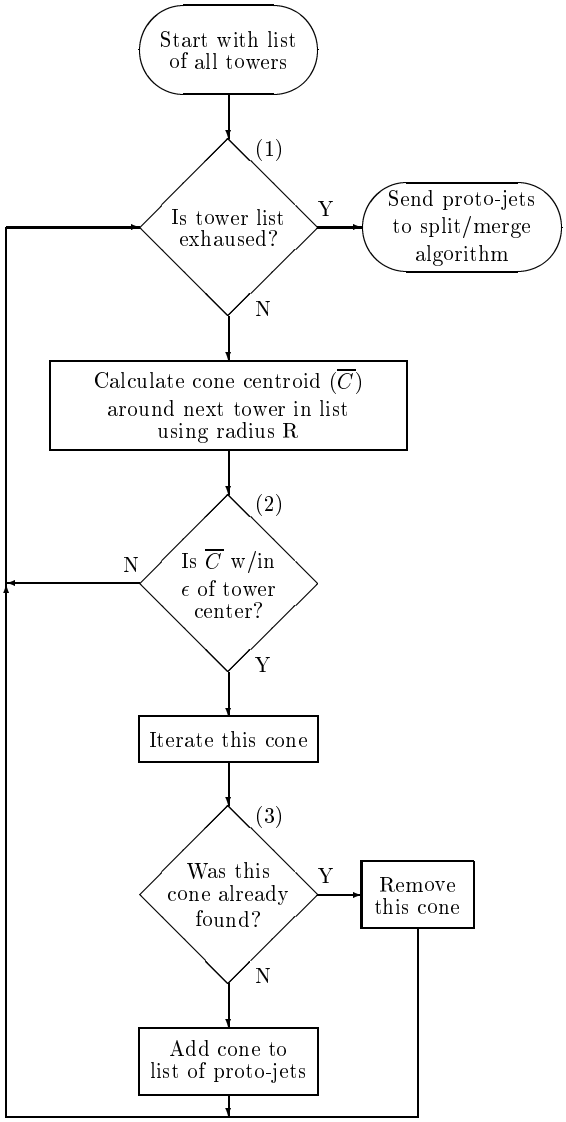

Figure 4. A seedless clustering algorithm.

An even more streamlined option would be to keep only those cones that yield a stable cone center without leaving the original tower. Since a trial cone is originally placed at the center of every tower, the only distinct stable cone centers missed by this (much!) faster algorithm correspond to very limited regions of attraction (less than the area of a tower). Such situations can arise in only two cases. One possibility is that there are two (or more) stable directions within a single tower. The second possibility is that

there is a stable direction within a tower but it is not found starting at the tower center. While both of these scenarios arise in analyses of realistic data, they do not constitute cause for concern. Proto-jets with directions that are nearly collinear (*i.e.*, that lie within a single tower) will have nearly the same tower content and be merged with little impact on the final jet properties. Isolated stable directions with very small regions of attraction (the second case) are most likely fluctuations in the background energy level and not the fingerprints of real emitted partons. In any case the stable cone centers not found by the streamlined algorithm invariably correspond to low E_T proto-jets and are well isolated from large E_T proto-jet directions (otherwise they would be attracted into the larger E_T jet). Thus the leading E_T jets (after merging and splitting) found by either the original seedless algorithm or the streamlined version are nearly identical.

For practical use it may also be necessary to apply some minimum E_T threshold to the list of proto-jets. Ideally such a threshold would be set near the noise level of the detector. However, a higher setting might be warranted to reduce the sensitivity of the algorithm to energy depositions by multiple interactions at high luminosities (see Section 3.3.4 for details of seedless clustering at the detector level).

In general, a number of overlapping cones, where towers are shared by more than one cone, will be found after applying the stable cone finding procedure. As noted earlier, the treatment of proto-jets with overlapping regions can have significant impact on the behavior of the algorithm.

3.3.2. Splitting and Merging Specifications

A well-defined algorithm must include a detailed prescription for the splitting and merging of proto-jets with overlapping cones. We provide an outline of a splitting and merging algorithm in Fig. 5. It is important to note that the splitting and merging process does not begin until all stable cones have been found. Further, the suggested algorithm always works with the highest E_T proto-jet remaining on the list and the ordering of the list is checked after each instance of merging or splitting. If these conditions are not met, it is difficult to predict the behavior of the algorithm for multiply split and/or merged jets and similar lists of proto-jets can lead to distinctly different lists of jets. This undesirable situation does not arise with the well- ordered algorithm in Fig. 5. While there will always be some order dependence in a splitting and merging scheme when treating multiply overlapping jets, we recommend fixing this order by starting with the highest E_T proto-jet and working down in the E_T ordered list. In this way the action of the algorithm is to prefer cones of maximal E_T. Note that, after a merging or splitting event, the E_T ordering on the list of remaining proto-jets can change, since the survivor of merged jets may move up while split jets may move down. Once a proto-jet shares no towers with any of the other proto-jets, it becomes a jet and is not impacted by the subsequent merging and splitting of the remaining proto-jets. As noted earlier and illustrated in Fig. 5, the decision to split or merge a pair of overlapping proto-jets is based on the percentage of transverse energy shared by the lower E_T proto-jet. Proto-jets sharing a fraction greater than f (typically $f = 50\%$) will be merged; others will be split with the shared towers individually assigned to the proto-jet that is closest in $\eta\times\phi$ space. This method will perform predictably even in the case of multiply split and merged jets. Note that there is no requirement that the centroid of the split or merged proto-jet still coincides precisely with its geometric center.

3.3.3. Parton Recombination

The definition of calorimeter towers, *i.e.*, a discretization of (η, ϕ) space, would be cumbersome in a theoretical calculation, and is indeed not necessary. In a theoretical calculation at fixed order, the maximal number of partons, n, is fixed. With specified parton momenta, the only possible positions of stable cones are then given by the partitions of the n parton momenta, *i.e.*, there are at most $2^n - 1$ possible locations of proto-jets. They are given by the positions of individual partons, all pairs of partons, all combinations of three partons, *etc.* In a perturbative calculation, *e.g.* via a NLO Monte Carlo program, the proto-jet selection of the seedless algorithm can then be defined as follows:

1. Make a list of centroids for all possible parton multiplets. These are derived from the coordinates of all parton momenta p_i, of all pairs of parton momenta $p_i + p_j$, of all triplets of parton momenta $p_i + p_j + p_k$, *etc.* For each centroid record which set of partons defines it.

2. Select the next centroid on the list as the center of a trial cone of radius R.
   Go to the split/merge stage if the list of cone centers is exhausted.

3. Check which partons are inside the trial cone.

4. If the parton list of the centroid and that of the trial cone disagree, discard the trial cone and go to (2). If the lists agree, add the set of partons inside the trial cone as a new entry to the list of proto-jets.

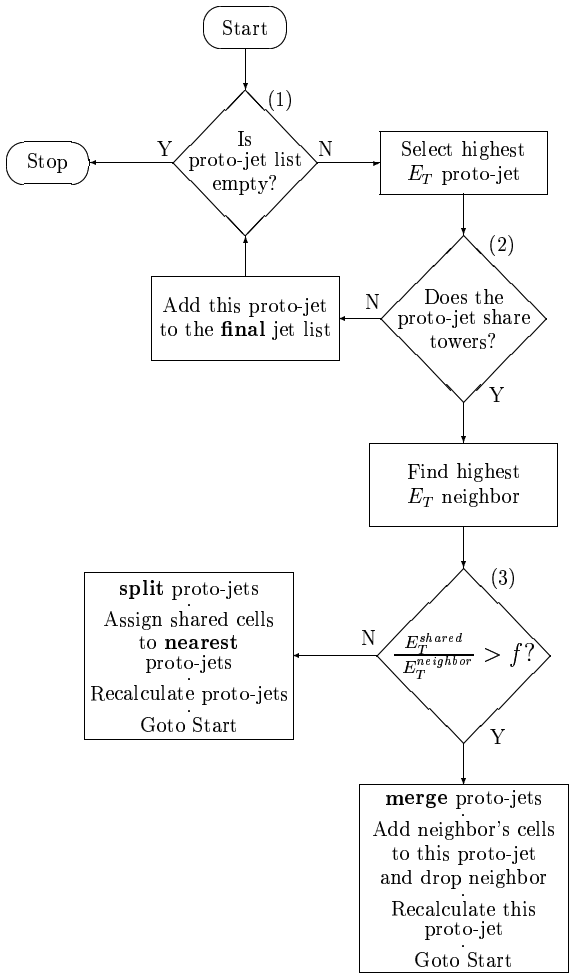

Figure 5. A fully specified splitting and merging algorithm.

As before, different proto-jets may share partons, *i.e.* they may overlap. The required split/merge step is then identical to the calorimeter-level steps (Fig. 5), with towers replaced by partons as elements of proto-jets.

In the case of analytic evaluations of the NLO perturbative jet cross section [13] the integrations over the multi-parton phase space are divided into various disjoint contributions. For a jet of fixed E_T^J, η^J and ϕ^J we have only the cases where a) one parton is in the jet direction with the jet E_T, and the other partons are excluded from nearby directions where they could fit in a jet cone with the first parton, or b) two partons fit in a single cone with their centroid properties constrained to be the jet values. The questions of overlap, splitting and merging never arise at this order for $R < \pi/3$.

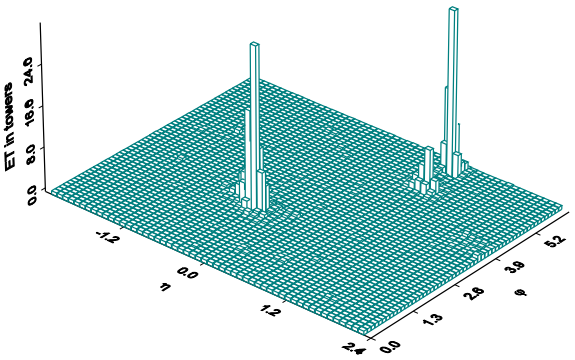

Figure 6. Calorimeter tower E_T lego plot for a simulated large-E_T jet event in the DØ Calorimeter.

3.3.4. Tests of a Seedless Algorithm

In this section we offer some insight into the performance of the seedless cone algorithm applied to a detector. We begin by examining a simulated large-E_T jet event in the DØ detector (Fig. 6). The event was chosen from a sample generated with PYTHIA [14] using a 160 GeV minimum E_T cut at the parton-level generator. After hadronization, the events were processed through a full simulation of the DØ detector. The towers in the central region ($-3.2 < \eta < 3.2$) are 0.1×0.1 in size. Fig. 6 shows the distribution of calorimeter tower E_T's for the event in the central fiducial volume ($-2.4 < \eta < 2.4$) where cones of $R = 0.7$ can be fully contained in the central region. Three jets clearly dominate the display (along with a less distinctive feature at the large η boundary near $\phi = 4$). Fig. 7 shows the E_T contained in a cone of radius 0.7 centered at each calorimeter tower, displaying the same structure for the event in a slightly different language. We can make this picture even more clear by appealing to the "flow imagery" of Section 3.3.1. We define a flow vector as the 2-dimensional vector difference between the calculated centroid for a cone centered on a tower and the geometric center of the tower ($\overrightarrow{C^k} - \overrightarrow{C^k}$ in Eqs. 18 and 19). This vector vanishes for a stable cone. This flow vector is plotted in the corresponding range of $\eta \times \phi$ in Fig. 8 for the same PYTHIA generated event.

The flow vector clearly points to the four potential jets noted above. Cones that are in the neighborhood of a potential jet exhibit flow vectors of large magnitude pointing towards the jet center. This magnitude will generally be sufficient to cause the cone to fail the second test in Fig. 4, thus preventing further iteration of the cone to define a proto-jet. The contours of Fig. 8

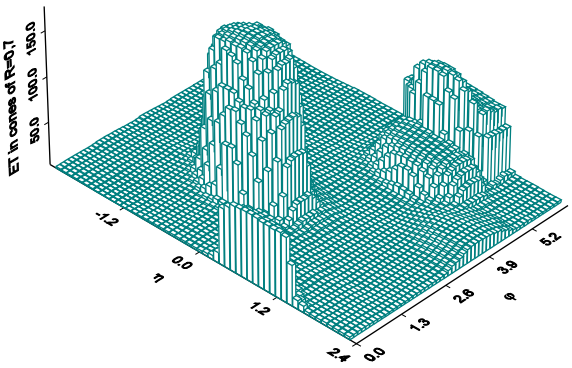

Figure 7. E_T in cones centered on each calorimeter tower (in $|\eta^{tower}| < 2.4$) for the simulated large-E_T jet event of Fig. 6.

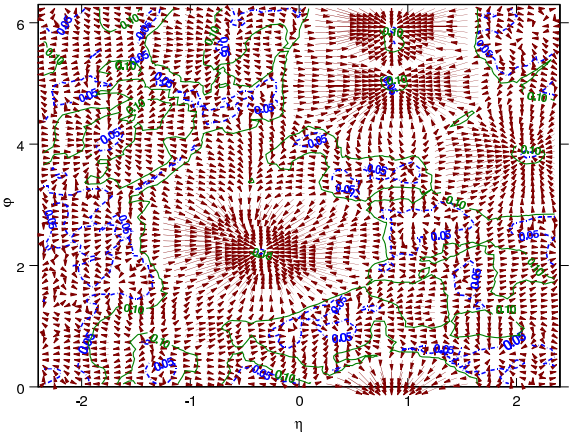

Figure 8. Energy flow for the cones in the large-E_T jet event of Figs. 6–7. The contours bound flow regions with vector magnitude < 0.1 (solid contours) and < 0.05 (dashed contours) in $\eta \times \phi$.

bound regions of flow with magnitude < 0.1 (solid contours) and < 0.05 (dashed contours) in $\eta \times \phi$, within which we expect to find the final jets. It is important to note the size of the detector regions with small flow magnitude. Regions with sufficiently small flow will pass test (2) in the clustering stage and allow the cone to undergo additional iterations. This ultimately increases processing time for clustering and complexity in splitting and merging (due to the production of many additional proto-jets). The flow magnitude cut has a natural size on the order of the detector tower size. For the DØ detector, with a typical towers size of $\eta \times \phi = 0.1 \times 0.1$, the cut would be between the two contours shown above. A too small magnitude cut will cause inefficiencies in jet finding; too large a cut will cause iterations on cones over the whole detector volume.

It is clear from Figs. 6–8 that the region of interest around the jets is much smaller than the area contained within the contours of "stable" cones. There are broad "plains" of low energy deposition where the flow vector is of small magnitude, but also of rapidly varying direction. Stable cones are found in these regions. But these presumably arise simply from local fluctuations yielding local extrema and are not expected to correspond to the fingerprints of underlying (energetic) partons. There are at least two, possibly parallel paths to follow in order to reduce the impact of these regions on the analysis, in terms of both required resources and final results.

As already noted, we can further streamline the analysis by applying the cut on the flow vector at each step in the iteration. Thus we keep only those cones that do not "flow" outside of their original tower before a stable center is reached. Such an algorithm converges rapidly to the stable cones pointed to by the largest magnitude flow vectors in Fig. 8 and efficiently eliminates most of the cones in the "plains". We do lose the stable cones that a full iteration, allowing any amount of flow, finds in the flat regions of the previous figures. However, as already emphasized, these cones do not correspond to the physics we wish to study with jet analyses. With a large savings in analysis time the streamlined algorithm finds the same leading jet properties (*e.g.*, E_T and η^J) as the more complete algorithm to a fraction of a percent. The final jets contain typically 120 to 160 towers. The differences between the leading jets found with the two algorithms arise from differences in tower content of just 1 or 2 towers (at the cone boundary).

One can also reduce the effort and the final event complexity by applying a minimum E_T cut on the cones at the proto-jet stage. An obvious choice for this minimum E_T cut would be to place it above the level of detector noise. As alluded to in Section 3.3.1, a practical cut might be placed slightly higher to reduce sensitivity to varying event pileup with changes in beam luminosity. Unfortunately, this places a rather arbitrary threshold into the algorithm from the standpoint of theoretical calculations, *i.e.* what is the 'noise' level at NLO? Additionally, such cuts will in practice be applied before final jet scale corrections. How does X GeV uncorrected in the experiment compare to X GeV at generator level? Such experiment specific considerations clearly are out of the realm of event generator design! A possible improvement would be

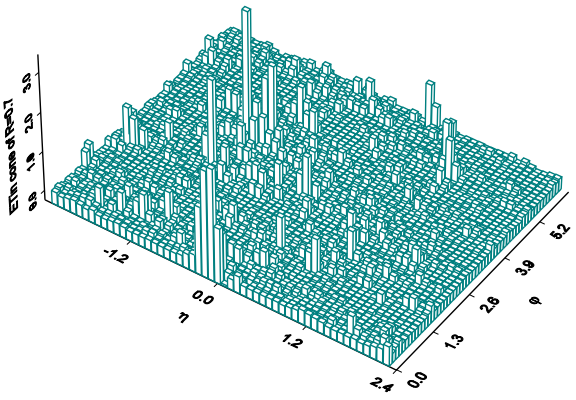

Figure 9. A sample event from data. Tower E_T lego plot for an event passing the DØ $W \to jets$ trigger.

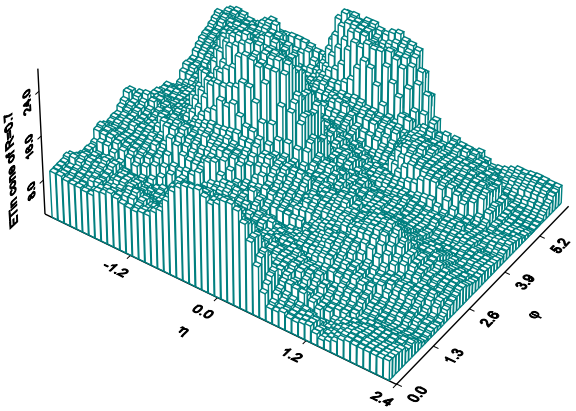

Figure 10. E_T in cones centered on each calorimeter tower (in $|\eta^T| < 2.4$) for the $W \to jets$ sample event of Fig. 9.

to set a minimum cone E_T threshold equal to some fraction of the scalar E_T in the event. In this way such effects will tend to partially cancel between generators and experiments, better relating the cut between the two levels.

We next look at an example of the seedless algorithm tested on actual calorimeter data. Fig. 9 shows the tower E_T lego plot for a DØ event passing a $W \to jets$ trigger. The trigger required at least two central jets with $E_T > 15$ GeV. These data were taken at high luminosity with an average of ∼2.8 interactions per beam crossing. The two leading jets that pass the cut are reasonably obvious (along with, perhaps, two other subleading jets) but overall this event is clearly

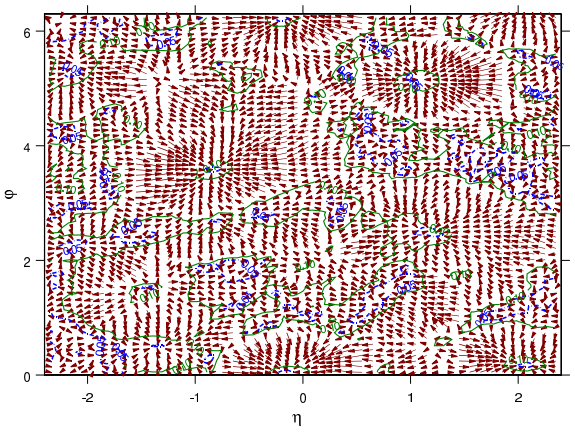

Figure 11. Energy flow for the cones in the $W \to jets$ event of Figs. 9–10. The contours bound flow regions with vector magnitude < 0.1 (solid contours) and < 0.05 (dashed contours) in $\eta \times \phi$.

noisier (more realistic) than the PYTHIA generated event. This point is illustrated also in Figs. 10 and 11, which show the cone energy and flow vectors for this event, analogous to Figs. 7 and 8. In this case the baseline energy subtraction for calorimeter cell energies in the data leads to towers with (small) negative energy deposition.

The increased level of noise and the possibility of negative tower energy results in two new issues for the jet analysis that were not observed in the analysis of the Monte Carlo data. The negative energy cells allow true stability with respect to the iteration process to be replaced by limit cycles. Iteration leads not only to cone center locations for which $\overrightarrow{C^j} - \overrightarrow{C^j} = 0$ but also, for example, to doublets of locations for which $\overrightarrow{C^1} = \overrightarrow{C^2}$ and $\overrightarrow{C^2} = \overrightarrow{C^1}$, or $\overrightarrow{C^1} - \overrightarrow{C^1} = -(\overrightarrow{C^2} - \overrightarrow{C^2})$. Thus continued iteration simply carries the cone center back and forth between location 1 ($\overrightarrow{C^1}$) and location 2 ($\overrightarrow{C^2}$). (More complex multiplets of locations with sets of 3, or even 6, 2-dimensional flow vectors summing to 0 are also observed.) The good news is that these clusters of cone centers are typically close by each other and yield essentially the same final jets, after merging, independent of where in the limit cycle the iteration process is terminated. This is guaranteed to be true for the streamlined algorithm where the entire cycle must occur within a single tower. (The $(\eta \times \phi)$ distance between two members of such a limiting cycle driven by a negative tower energy of magnitude E_N is approximately $R{\cdot}E_N/E_C$, where E_C is the total energy in the cone. This can be as small as the minimum

distance for a change of one tower in the cone as noted above, *i.e.*, 7% of a tower width.)

The noisy quality of the event leads to an even more troubling phenomenon. There are so many locally stable cone centers found in the now rapidly fluctuating "plain" region that the proto-jet list may exhibit a surprisingly large number of mutually overlapping cones. During the merging phase these can coalesce into jets with large (even leading) E_T. This issue has historically been treated by applying a minimum E_T cut to the proto-jet list before merging and splitting. With the event studied here a cut of 8 GeV (typical of values used by DØ) is not sufficient. If we keep all stable cones with $E_T > 8$ GeV, with no other cuts, as proto-jets, the merging process builds a leading jet by pulling together many cones where there is clearly no real jet. This problem does not arise in the streamlined algorithm where only stable cones that stayed within their original tower are kept. In this case the algorithm identifies the leading jets anticipated intuitively from the above figures.

3.3.5. Comments on the Seedless Clustering

We may summarize the advantages of the seedless clustering described above as follows:

1. Avoids undesirable sensitivity to soft and collinear radiation.
2. Offers increased efficiency for all physically interesting jets.
3. Offers improved treatment of limit cycles and overlapping cones.
4. "Flow cut" method offers more efficient use of computer resources than unrestricted seedless clustering.

We have not investigated further improvements in the optimization of the computational efficiency for this seedless algorithm. However, some improvement may be gained by using the fact that cones centered on adjacent towers are largely overlapping, thus reducing the number of towers to sum for each new center. Other improvements such as region of interest (ROI) clustering may also be explored.

3.4. Cone Jets with Seeds

In an actual experiment the number of calorimeter towers may be very large (order 6000 for tower sizes of $\Delta\eta \times \Delta\phi = 0.1 \times 0.1$ and an η coverage of ± 5 units of pseudorapidity). The above seedless algorithm may then be expensive computationally. The question arises whether an acceptable approximation of the seedless algorithm can be constructed, analogous to the parton-level short cut, while considering primarily those towers which have energy depositions above a minimal seed threshold for finding proto-jets.

Seed-based cone algorithms offer the advantage of being comparatively efficient in CPU time. In a typical application, detector towers are sorted according to descending E_T and only towers passing a seed cut,

$$E_T^{tower} > E_T^{seed} \,, \tag{22}$$

are used as starting points for the initial jet cones. This greatly reduces the number of cones that need to be evaluated in the initial stage. The seed threshold E_T^{seed} must be chosen low enough so that variations of E_T^{seed} lead to negligible variations in any observable under consideration. The simple seed-based algorithm is sensitive to both infrared or collinear effects. However, sensitivity to the splitting of the seed E_T between multiple towers is greatly reduced for larger E_T jets. As stated above, this is true when the jet reconstruction becomes 100% efficient (*i.e.*, around 20 GeV for jets in DØ). For fully efficient jet algorithms the collinear dependency is reduced to a second-order effect, namely, the effective number of low E_T proto-jets that may engage in splitting and merging. In a typical algorithm a minimum E_T cut may also be applied to each proto-jet to prevent excessive merging of noise and energy not associated with the hard scattering producing the jets.

3.4.1. Addition of Midpoints

The seedless algorithm discussed previously can be approximated by a seed-based algorithm with the addition of 'midpoints' in the list of starting seeds. The idea [15] is to duplicate the parton-level algorithm discussed in Section 3.3.3, but with partons replaced by seeds. By adding a starting point for clustering at the positions given by $p_i + p_j$, $p_i + p_j + p_k$ etc., the sensitivity of the algorithm to soft radiation as illustrated in Fig. 1 is essentially removed. Since widely separated seeds cannot be clustered to a proto-jet, it is sufficient to only consider those midpoints where all seeds lie within a distance

$$\Delta R < 2.0 \cdot R_{cone} \tag{23}$$

of each other.

With these changes, the resulting algorithm is quite close to those used in Run I of the Tevatron. The main change is the inclusion of midpoints of seeds (the $p_i + p_j$ pairs) and of centers of larger numbers of seeds as additional seed locations for trial cones. Two studies of the effects of adding midpoints were completed during the workshop and are summarized below. The first checks the infrared safety of the midpoint algorithm, also called the Improved Legacy Cone Algorithm (ILCA), in a Monte Carlo study. The

second tests the effect of adding midpoints on the performance of the Run I DØ cone algorithm.

3.4.2. Results from a Monte Carlo Study

The request for an infrared and collinear safe jet-algorithm is most important from the viewpoint of perturbative QCD calculations. Unsafe algorithms simply do not permit unambiguous results, once higher order corrections are considered [16,17]. Instead results will depend on the technical regularization procedure adopted in a specific calculation.

The deficiencies of an unsafe algorithm will only show up at sufficiently high order in the perturbative expansion. For example, the jet merging due to soft gluon radiation as depicted in Fig. 1 will only become a problem when three partons or more can be combined to a single jet. In hadron collider processes this first happens in, for example, the NLO corrections to three-jet production [8], where four-parton final states are included in the real emission contributions. The fourth parton is needed to provide the necessary recoil transverse momentum to the other three partons which may or may not form a single jet. The NLO three-jet Monte Carlo is very CPU intensive, however, making it a cumbersome tool to investigate jet algorithms, at present. A much faster probe is provided by the existing NLO dijet Monte Carlos in DIS [10,11].

In $ep \to ejjX$, the electron provides the necessary recoil p_T to the final-state partons. The real emission QCD corrections at $\mathcal{O}(\alpha_s^2)$ thus contain three partons which can be close together. Their merging to a single jet, with the concomitant loss of two-jet cross section, is a probe of the infrared safety of the two-jet vs. one-jet classification of partonic events. A second probe is provided by the E_T flow inside a jet, which has recently been modeled with up to three partons in a single jet, for the current jets in DIS [18].

We have investigated these issues with the MEPJET Monte Carlo [10], which calculates dijet production in DIS at NLO. The program was run in a kinematical range typical for HERA, ep collisions at $\sqrt{s} = 300$ GeV with $Q^2 > 100\ \mathrm{GeV}^2$. Reconstructed jets were required to satisfy

$$E_T > 10\ \mathrm{GeV}, \qquad -1 < y < 2, \qquad R_{jj} < 2, \tag{24}$$

where E-scheme recombination is used. Here R_{jj} is the separation of reconstructed jets in the legoplot. Following HERA practice, we use a cone size $R = 1$. Considering jets with a maximal separation of twice the cone size enhances the statistical significance of any splitting/merging effects in the Monte Carlo calculation.

With these settings two cone algorithms are considered to investigate the importance of extra midpoints in the perturbative results. The first is the seedless algorithm in its parton-level implementation as described in Section 3.3.3, which we here call the "midpoint" algorithm. In order to test the analog of tower threshold effects, only partons with $E_{T,i} > E_T^{seed}$ are considered for centers of trial cones, *i.e.*, trial cone centroids are the directions of these partons and their midpoints $p_i + p_j$ and $p_i + p_j + p_k$. The second algorithm, dubbed "no center seed" is identical, except that the midpoints are left out as trial cone centers. For both algorithms, the final splitting/merging decision is made with an E_T-fraction of $f = 0.75$ of the lower E_T proto-jet as the dividing line.

The MEPJET program is based on the phase space slicing method, with a parameter s_{min} defining the separation between three-parton final states on the one hand, and the virtual contributions plus soft and collinear real emission processes (which cancel the divergences of the virtual graphs) on the other. This dividing line is completely arbitrary and observables should not depend on it. A test of this requirement is shown in Fig. 12 where the dijet cross section within the cuts of Eq. 24 is shown as a function of s_{min}. Whereas the midpoint algorithm shows s_{min}-independence within the statistical errors of the Monte Carlo (plain symbols), leaving out the midpoints between partons leads to a pronounced decrease of the cross section as s_{min} becomes smaller. Smaller s_{min} implies that more events are generated as explicit three-parton final states. The additional soft gluons act as extra seeds that tend to merge the two jets, leaving the event classified as a one-jet event, which does not contribute to the plotted dijet cross section. The s_{min} dependence of the "no center seed" algorithm means that no perturbative prediction is possible for this algorithm: as s_{min} approaches zero, the dijet cross section diverges logarithmically as $\log s_{min}/Q^2$.

Even when fixing s_{min} to some typical soft QCD scale, like $s_{min} = 0.03\ \mathrm{GeV}^2$, the "no center seed" algorithm has fatal defects. This is demonstrated in Fig. 13 where the variation of the dijet cross section within the cuts of Eq. 24 is shown as a function of "tower threshold" transverse energy E_T^{seed}. The midpoint algorithm is almost independent of this threshold, as long as E_T^{seed} is less than about 10% of the jet transverse energy. The "no center seed" algorithm, on the other hand, shows a pronounced threshold dependence, raising the specter of substantial dependence of jet cross sections on detector thresholds, detector response to soft particles and nonperturbative effects. These effects have been discussed previously for three-jet events at the Tevatron [8,16].

Discarding the "no center seed" algorithm we turn to

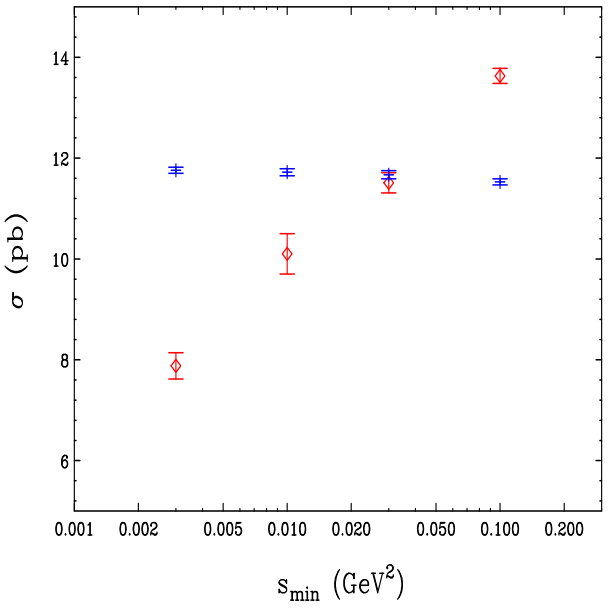

Figure 12. Dependence of the DIS dijet cross section on s_{min} for the ILCA algorithm with midpoints (plain symbols) and for the "no center seed" algorithm (diamonds).

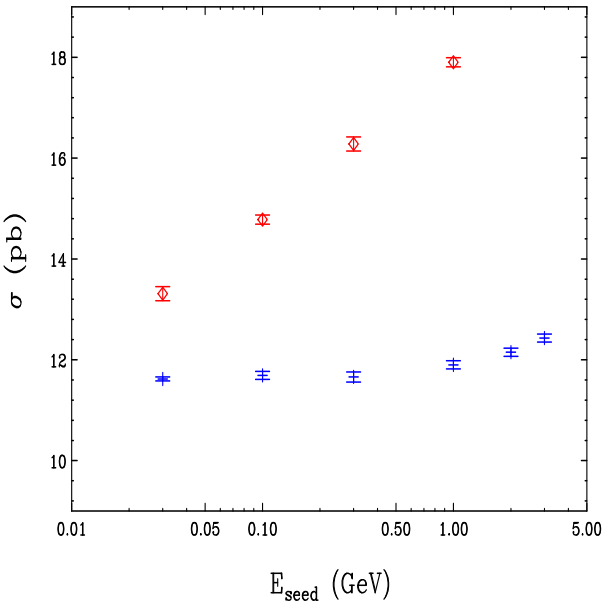

Figure 13. Dependence of the DIS dijet cross section on the seed threshold E_T^{seed} of Eq. 22. Results are shown for ILCA, with midpoints (plain symbols) and for a "no center seed" variant (diamonds).

internal E_T flow inside a single jet as another measure of the performance of jet algorithms. The differential jet shape, $\rho(r)$, is defined as $1/\Delta r$ times the average E_T fraction of a jet in a narrow ring of width Δr, a distance r from the jet axis. In Fig. 14 the differential jet shape is shown for current jets at HERA, in the phase space region

$$E_T > 14 \text{ GeV} , \qquad -1 < \eta < 2 \tag{25}$$

for DIS events with $Q^2 > 100$ GeV^2. Results are shown for the midpoint (ILCA) and the K_T algorithm (to be described later) at NLO ($\mathcal{O}(\alpha_s^2)$). The midpoint algorithm produces wider jets than the K_T algorithm with $D = R$, as is to be expected since two partons with a separation slightly less than $2R$ can be clustered by the midpoint, but not the K_T algorithm. NLO corrections are quite small for the midpoint algorithm. We have also checked that the jet shapes in the midpoint algorithm exhibit good scale dependence at NLO, similar to the K_T algorithm [18].

3.4.3. Results from Data Study

A midpoint algorithm has previously been employed by the OPAL Collaboration [19]. We now report a study performed using the DØ data. The data were acquired from a two-jet trigger sample with an average of 2.8 interactions per beam crossing. The goal of the data-based study was to test the sensitivity of DØ's Run I cone algorithm to the addition of midpoints. To facilitate a direct comparison of Run II jet results with the current data it is desirable that algorithms supported[4] for the new data produce similar results.

Details in the DØ Run I jet algorithm forced the splitting and merging of jets to occur as they are found. In effect this defines an order dependence based on the seed E_T of the jets. It was possible to test two orderings in the jet clustering. In the first case, jets were initially found around all seed towers above a 1 GeV threshold, then around all midpoints. In the second case they were first found around all midpoints between seed towers, then around the seed towers themselves. Fig. 15 shows the E_T distributions for three trials, the legacy seed, seed + midpoint, and midpoint + seed trials. Also shown are the ratios of the E_T spectra. A cone radius of 0.7 was used.

[4]While any number of jet algorithms may in principle be included in an offline analysis stream, in practice only a few algorithms will typically be fully supported by detailed energy

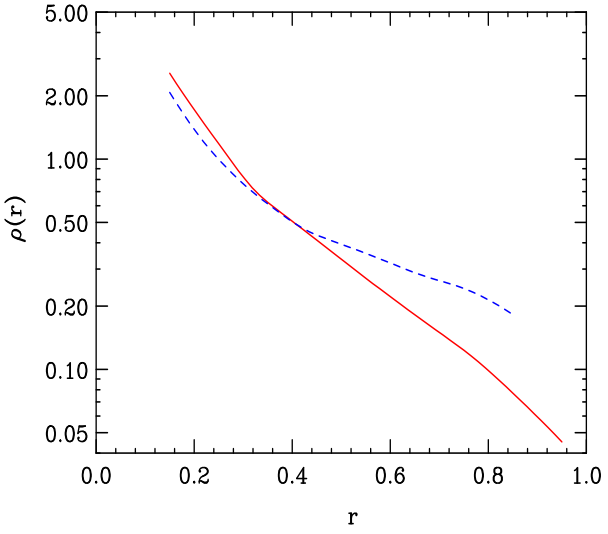

Figure 14. Jets shapes in ILCA (dashed line) compared to K_T (solid line).

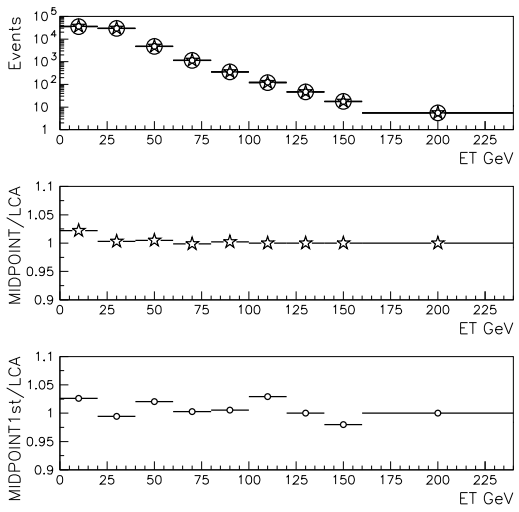

Figure 15. Jet E_T distributions and ratios. Top: Jet E_T distributions for the three algorithms overlayed. Legacy seeds (large circles), seeds + midpoints (stars), midpoints + seeds (small circles). Middle: Seeds + midpoint distribution divided by the legacy distribution. Bottom: Midpoint + seeds distribution divided by the legacy distribution.

There are two effects to observe in Fig. 15. First, the addition of midpoints tends to cause an increase in the number of low E_T jets. This is because the midpoints are effectively zero threshold seeds, therefore very soft jets that tend to fail reconstruction by falling short of the seed requirement may sometimes be reconstructed around a midpoint. Second, the results are different depending on the order in which the seeds + midpoints are used. However, we can safely conclude that the addition of midpoints has little more than a few percent effect on the experimental jet E_T distribution.

Fig. 16 shows the ratio of the leading jet for the legacy seed and midpoint + seed algorithms. Since a meaningful test requires the comparison of the same jets, the jets were also required to be matched within a radius of 0.2 (in $\Delta\eta \times \Delta\phi$) to prevent accidental comparisons of unrelated jets due to 'flipping' of the jet order between algorithms. Fig. 17 shows the fractions of isolated, merged, split, and multiply split/merged jets for the legacy seed and midpoint + seed algorithms. In each case only small variations are observed between the two algorithms, indicating that a legacy cone algorithm augmented by midpoints is an acceptable choice for comparisons to Run I physics results. In fact, Figs. 15 and 16 represent extreme deviations in jet E_T, since E_T differences are expected to be reduced after application of jet energy corrections appropriate to each algorithm.

scale, resolution, and efficiency corrections.

3.5. Proposals for Common Run II Cone Jet Algorithms

The cone algorithm starts with a cone defined in E-scheme variables as

$$i \subset C \quad : \quad \sqrt{(y^i - y^C)^2 + (\phi^i - \phi^C)^2} \leq R. \tag{26}$$

where for massless towers, particles, or partons $y^i = \eta^i$. The E-scheme centroid corresponding to this cone is given by

$$p^C = (E^C, \mathbf{p}^C) = \sum_{i \subset C} (E^i, p_x^i, p_y^i, p_z^i) \, , \tag{27}$$

$$\bar{y}^C = \frac{1}{2} \ln \frac{E^C + p_z^C}{E^C - p_z^C} \, , \quad \bar{\phi}^C = \tan^{-1} \frac{p_y^C}{p_x^C} \, . \tag{28}$$

A jet arises from a "stable" cone, for which $\bar{y}^C = y^C = y^J$ and $\bar{\phi}^C = \phi^C = \phi^J$, and the jet has kinematic

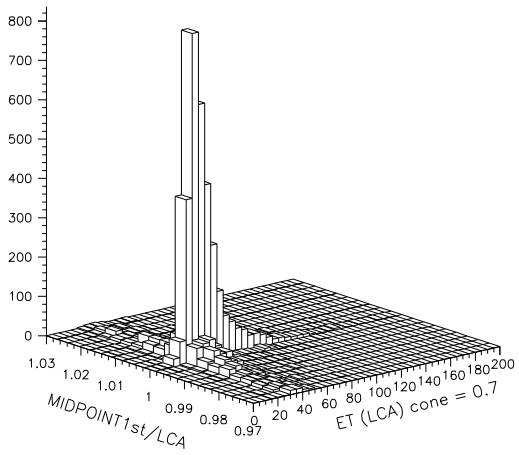

Figure 16. E_T ratios for leading jets. The ratio of leading jet E_T in the midpoint algorithm is plotted as a function of the legacy cone jet's E_T.

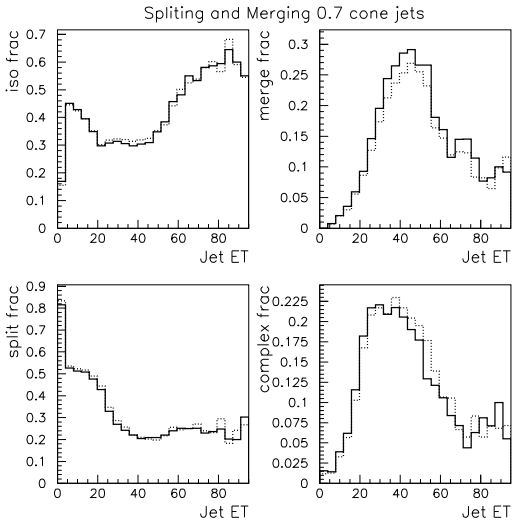

Figure 17. A view of splitting and merging fractions in the legacy seed (solid) and midpoint + seed algorithms (dotted).

properties

$$p^J = (E^J, \mathbf{p}^J) = \sum_{i \subset J = C} (E^i, p_x^i, p_y^i, p_z^i) \,, \tag{29}$$

$$p_T^J = \sqrt{(p_x^J)^2 + (p_y^J)^2} \,, \tag{30}$$

$$y^J = \frac{1}{2} \ln \frac{E^J + p_z^J}{E^J - p_z^J} \,, \quad \phi^J = \tan^{-1} \frac{p_y^J}{p_x^J} \,. \tag{31}$$

Seedless algorithm. For a seedless algorithm we recommend the streamlined jet algorithm defined in Section 3.3.1 that includes the flow cut for computational efficiency improvement and reduction of soft proto-jet construction. The clustering or jet finding should be done in terms of E-scheme variables.

Seed–based algorithm or ILCA. Backwards compatibility is important here as well as common specifications between experiments. For the Run II algorithm we recommend that jet clustering commence on each seed tower (rather than consolidated seeds as in Run I), for simplicity of the algorithm and to reduce dependencies on detector segmentation. Since the finding of proto-jets is determined by the seed threshold, it is reasonable to determine the midpoints based on the positions of the proto-jets rather than the seed list itself, as illustrated in Fig. 18. This would reduce the number of midpoints to be calculated due to the large combinatorics caused by adjacent seed towers within jet cones.

Specifications Summary We list here the precise specifications of the jet algorithms and variables:

1. R_{cone}: 0.7
2. p_T^{seed}: 1.0 GeV
3. Recombination: E-scheme
4. Midpoints: Added after cone clustering
5. Split/Merge: p_T ordered, threshold = 50% of lower p_T jet
6. Reported kinematic variables: E-scheme, either directly as $(E^J, \mathbf{p}^J)$ or as $(m^J, {p_T}^J, y^J, \phi^J)$, where m^J is the mass of the jet ($m^J = \sqrt{{E^J}^2 - {\mathbf{p}^J}^2}$).

4. K_T Jet Algorithms

4.1. Introduction

This section provides a guide for the definition of K_T jet algorithms for the Tevatron. Section 4.2 describes the recommended algorithm in detail. Section 4.3 discusses preclustering of particles, cells, or towers for both the CDF and DØ experiments. Sections 4.4 and 4.5 outline momentum calibration of the K_T algorithm and briefly describe jet resolution. Finally, in Section 4.6, we provide a few examples of the versatility of the K_T algorithm.

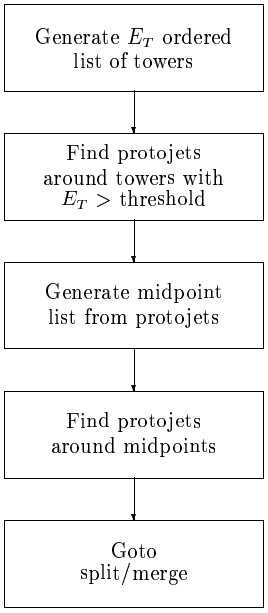

Figure 18. Method for addition of midpoints.

4.2. The Run II K_T Algorithm

In this section we propose a standard K_T jet algorithm for Run II at the Fermilab Tevatron. This proposal, based on studies of the K_T algorithm by several groups [20–22], establishes a common algorithm that satisfies the general criteria presented in Section 1.

The K_T jet algorithm starts with a list of *preclusters* which are formed from calorimeter cells, particles, or partons.[5] Initially, each precluster is assigned a vector

$$(E, \mathbf{p}) = E\,(1,\, \cos\phi \sin\theta,\, \sin\phi \sin\theta,\, \cos\theta) \tag{32}$$

where E is the energy associated with the precluster, ϕ is the azimuthal angle, and θ is the polar angle with respect to the beam axis. For each precluster, we calculate the square of the transverse momentum, p_T^2, using

$$p_T^2 = p_x^2 + p_y^2 \tag{33}$$

and the rapidity, y, using[6]

$$y = \frac{1}{2} \ln \frac{E + p_z}{E - p_z}. \tag{34}$$

[5] Preclustering is discussed in detail in Section 4.3.

[6] To avoid differences in the behavior of the algorithm due to computational precision when $|y|$ is large, we assign $y = \pm 10$ if $|y| > 10$.

A flowchart of the K_T algorithm is shown in Fig. 19. Starting with a list of preclusters and an empty list of jets, the steps of the algorithm are as follows:

1. For each precluster i in the list, define

   $$d_i = p_{T,i}^2 \,. \tag{35}$$

   For each pair (i, j) of preclusters $(i \neq j)$, define

   $$\begin{aligned} d_{ij} &= \min\left(p_{T,i}^2, p_{T,j}^2\right) \frac{\Delta\mathcal{R}_{ij}^2}{D^2} \\ &= \min\left(p_{T,i}^2, p_{T,j}^2\right) \frac{(y_i - y_j)^2 + (\phi_i - \phi_j)^2}{D^2} \end{aligned} \tag{36}$$

   where $D \approx 1$ is a parameter of the jet algorithm. For $D = 1$ and $\Delta\mathcal{R}_{ij} \ll 1$, d_{ij} is the minimal relative transverse momentum $k_\perp$ (squared) of one vector with respect to the other.

2. Find the minimum of all the d_i and d_{ij} and label it d_{min}.

3. If d_{min} is a d_{ij}, remove preclusters i and j from the list and replace them with a new, merged precluster $(E_{ij}, \mathbf{p}_{ij})$ given by

   $$E_{ij} = E_i + E_j \,, \tag{37}$$

   $$\mathbf{p}_{ij} = \mathbf{p}_i + \mathbf{p}_j \,. \tag{38}$$

4. If d_{min} is a d_i, the corresponding precluster i is "not mergable." Remove it from the list of preclusters and add it to the list of jets.

5. If any preclusters remain, go to step 1.

The algorithm produces a list of jets, each separated by $\Delta\mathcal{R} > D$. Fig. 20 illustrates how the K_T algorithm successively merges the preclusters in a simplified diagram of a hadron collision.

The K_T algorithm presented above is based on several slightly different K_T jet clustering algorithms for hadron colliders [20–22]. The main differences have to do with (1) the recombination scheme and (2) the method of terminating the clustering. The choices in the proposal above are discussed in the following paragraphs.

The recombination scheme was investigated by Catani *et al.* [20]. We elect to use the covariant E-scheme (Eqs. 37–38), which corresponds to vector addition of four-momenta, because our goals are

1. conceptual simplicity,

2. correspondence to the scheme used in the K_T algorithm for e^+e^- collisions [23],

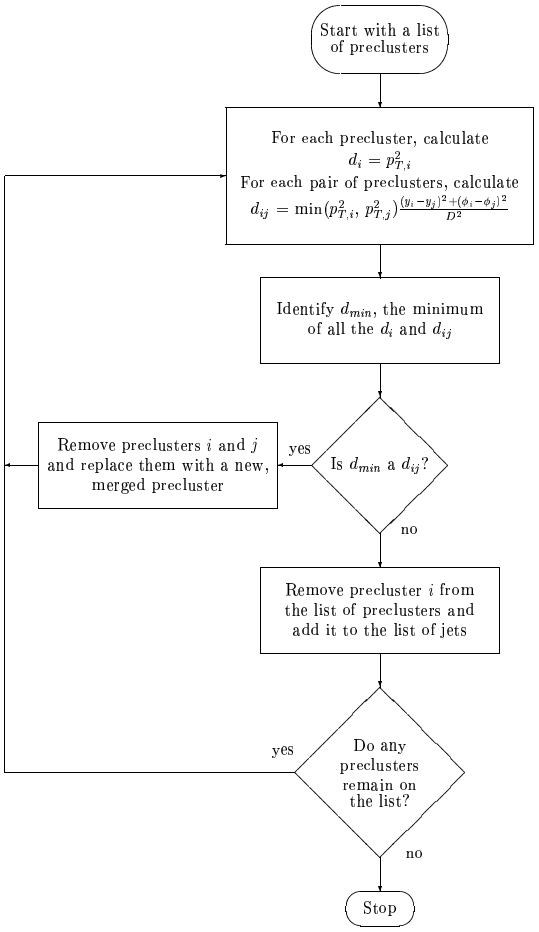

Figure 19. The K_T jet algorithm.

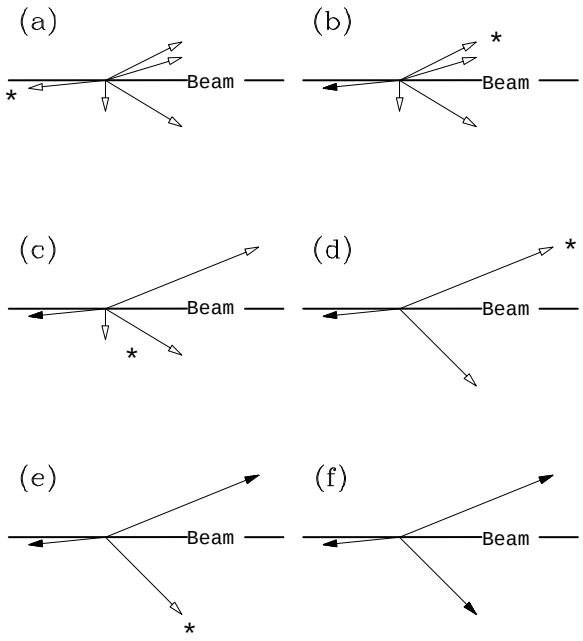

Figure 20. A simplified example of the final state of a hadron collision. The open arrows represent preclusters in the event, and the solid arrows represent the final jets reconstructed by the K_T algorithm. The six diagrams show successive iterations of the algorithm. In each diagram, either a jet is defined (when it is well separated from all other preclusters), or two preclusters are merged (when they have small relative $k_\perp$). The asterisk labels the relevant precluster(s) at each step.

3. absence of an energy defect [24], and

4. optimum suitability for the calibration method described in Section 4.4. [25]

The prescription of Catani, *et al.* [20,21] introduces a stopping parameter, d_{cut}, that defines the hard scale of the physics process and separates the event into a hard scattering part and a low-p_T part ("beam jets"). Catani *et al.* suggest two ways to use the d_{cut} parameter. First, d_{cut} can be set to a constant value *a priori*, and when $d_{min} > d_{cut}$ the algorithm stops. At this point, all previously identified jets with $p_T^2 < d_{cut}$ are classified as beam jets, and all remaining preclusters with $p_{T,i}^2 > d_{cut}$ are retained as hard final-state jets. Alternatively, an effective d_{cut} can be identified on an event-by-event basis so that clustering continues until a given number of final-state jets are reconstructed.

Unlike Catani, *et al.*, the algorithm proposed by Ellis and Soper [22] continues to merge preclusters until all jets are separated by $\Delta\mathcal{R} > D$. We have adopted this choice. Besides its simplicity, this method maintains a similarity with cone algorithms in hadron collisions. Whereas the use of d_{cut} is well suited for defining an *exclusive* jet cross section (typical of e^+e^- collisions), we desire an algorithm that defines *inclusive* jet cross sections in terms of a single angular resolution parameter D, which is similar to R for cone algorithms.

4.3. Preclustering

As described in the previous section, the input to the K_T jet algorithm is a list of vectors, or preclusters. Ideally, one should be able to apply the K_T algorithm equally at the parton, particle, and detector levels, with no dependence on detector cell type, number of cells, or size. The goal of *preclustering* is to strive for order independence and detector independence by employing well-defined procedures to remove (or re-

duce) the detector-dependent aspects of jet clustering. Practically, however, this independence is very difficult to achieve. For example, if a single particle strikes the boundary between two calorimeter towers, two clusters of energy may be measured. Conversely, two collinear particles may shower in a single calorimeter tower so that only one vector is measured experimentally. Preclustering all vectors within a radius larger than the calorimeter tower size removes this problem.

At the parton and particle levels, the simplest possible preclustering scheme is to identify each parton or particle four-vector as a precluster. Experimentally, differences between the geometries of the CDF and DØ calorimeters necessitate different preclustering schemes. In particular, the DØ discussion describes how the preclustering scheme can be used to control the number of preclusters passed to the K_T algorithm in order to keep the jet analysis computationally feasible. It can also be used to ensure that the preclusters all exhibit positive energy. Candidate schemes to achieve these goals are described in detail in the following sections. However, it is important that the preclustering scheme does not introduce the sort of problems with infrared or collinear sensitivities that we earlier discussed for the case of seeds.

4.3.1. CDF Preclustering

The CDF calorimeter system for Run II [26] consists of 1,536 towers. Each tower consists of an electromagnetic (EM) component and a hadronic (HAD) component. In order to form preclusters for input to the K_T algorithm, we propose the following:

1. Measure the amount of EM energy deposited into each calorimeter tower, E_{EM}, and form the vector $(E_{EM}, \mathbf{p}_{EM})$ where

$$p_{x,EM} = E_{EM} \cos\phi \sin\theta_{EM} \ , \tag{39}$$
$$p_{y,EM} = E_{EM} \sin\phi \sin\theta_{EM} \ , \tag{40}$$
$$p_{z,EM} = E_{EM} \cos\theta_{EM} \ . \tag{41}$$

   Likewise, measure the amount of HAD energy deposited into each calorimeter tower, E_{HAD}, and form the vector $(E_{HAD}, \mathbf{p}_{HAD})$ where

$$p_{x,HAD} = E_{HAD} \cos\phi \sin\theta_{HAD} \ , \tag{42}$$
$$p_{y,HAD} = E_{HAD} \sin\phi \sin\theta_{HAD} \ , \tag{43}$$
$$p_{z,HAD} = E_{HAD} \cos\theta_{HAD} \ . \tag{44}$$

   The angles θ_{EM}, θ_{HAD} and ϕ specify the position of the calorimeter tower components with respect to the interaction point. Note that θ_{EM} and θ_{HAD} may take on slightly different values when calculated using different interaction points along the beam axis (see Fig. 21).

2. For each calorimeter tower, calculate a vector $(E, \mathbf{p})$ by summing the vectors for the EM and HAD components:

$$(E, \mathbf{p}) = (E_{EM} + E_{HAD}, \mathbf{p}_{EM} + \mathbf{p}_{HAD}) \tag{45}$$

3. For each calorimeter tower, calculate the p_T from its associated vector using

$$\begin{aligned} p_T &= \sqrt{p_x^2 + p_y^2} \\ &= E_{EM} \sin\theta_{EM} + E_{HAD} \sin\theta_{HAD} \ . \end{aligned} \tag{46}$$

4. Assemble a list of tower vectors for which

$$p_T > p_T^{min}, \tag{47}$$

   where $p_T^{min} \approx 100$ MeV.[7] These are the preclusters for the K_T algorithm.

In designing the CDF preclustering scheme, the primary goal was simplicity. We made every attempt to maintain a close relationship between the physical calorimeter towers and the input preclusters for the K_T algorithm.

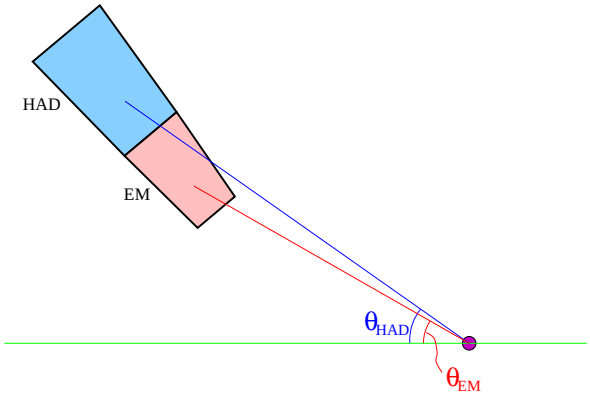

Figure 21. Schematic of a single CDF calorimeter tower.

4.3.2. DØ Preclustering

The K_T jet algorithm is an $\mathcal{O}(n^3)$ algorithm, where n is the number of vectors in the event [20]. Limited computer processing time does not allow this algorithm

[7] This p_T cut is designed to retain towers with energies well above the level of electronic noise. The exact value for this p_T cut will depend on measurements of calorimeter performance.

to run on the $\sim$ 45000 cells or even the $\sim$ 6000 towers of the DØ calorimeter. Therefore, we employ a preclustering algorithm to reduce the number of vectors input to the algorithm. Essentially, towers are merged if they are close together in $\eta \times \phi$ space, or if they have small p_T (or negative p_T, as explained below). The preclustering algorithm described below was used by the DØ experiment in Run I. We examine the effects of the Run I preclustering algorithm, and discuss possible alternatives for Run II. Although the effects of preclustering on jet observables should be small, this is analysis and detector dependent. A Monte Carlo study of preclustering effects on the jet p_T and on jet structure is also presented.

In Run I, one use of preclustering was to account for negative energy calorimeter towers [27] which can cause difficulties for the K_T algorithm. In the DØ calorimeter, we measured the difference in voltage between two readings (peak minus base), as illustrated in Fig. 22. To first order, this online baseline subtraction technique removes the effect of luminosity-dependent noise in the calorimeter, on a tower-by-tower basis. Residual fluctuations in each reading, however, sometimes lead to measured energies which are negative. One can imagine at least four ways to deal with these negative energy towers.

1. Absorb the negative energy into a precluster of towers such that the overall precluster energy is positive, as will be discussed here.

2. Add an offset to all tower energies so that there are none with negative energy. The offset could then be removed later in the analysis.

3. Ignore all towers with negative energy, *i.e.*, remove them from the jet analysis.

4. Proceed with the K_T algorithm analysis including the negative energy towers, assuming that their impact is negligible. Recall that in the cone algorithm case the negative energy towers are the source of the observed limit cycles for quasi-stable cones, which does not seem to be a serious problem.

Clearly, further studies of this issue are required. The precluster scheme can also be used to absorb low p_T towers similarly to what is done for negative energy towers.

The Run I preclustering algorithm, which is employed in the following studies, has six steps:

1. Identify each calorimeter cell with a 4-vector $(E, \mathbf{p}) = E\,(1, \cos\phi \sin\theta, \sin\phi \sin\theta, \cos\theta)$ where

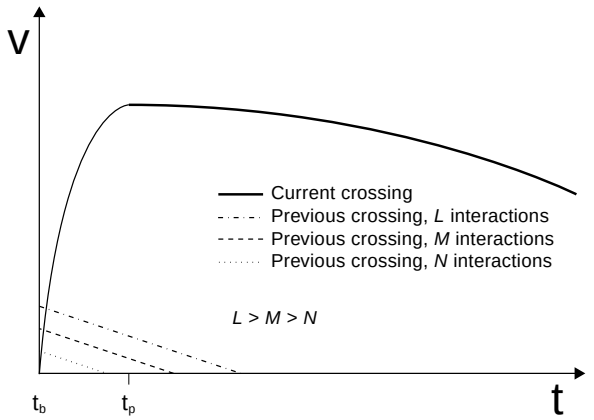

Figure 22. Schematic of voltage in a calorimeter cell as a function of time. The solid line shows the contribution for a given event (the current crossing). The cell is sampled once at t_b, just before a $p\bar{p}$ bunch crossing, to establish a base voltage. The voltage rises during the time it takes electrons to drift in the liquid argon gap ($\sim$500 ns), and reaches a peak value at $t_p \approx 2\,\mu$s, which is set by pulse-shaping amplifiers in the signal path. The cell is sampled again at t_p, and the voltage difference $\Delta V = V(t_p) - V(t_b)$ is proportional to the raw energy in the cell. Because the decay time of the signal $\tau \approx 30\,\mu$s is much larger than the accelerator bunch crossing time $t_x = 3.5\,\mu$s, $V(t_b)$ may have a contribution from a previous bunch crossing. The size of this contribution is related to the number of $p\bar{p}$ interactions in the previous crossing, which depends on the beam luminosity. The dashed lines show an example contribution from a previous bunch crossing containing three different numbers of $p\bar{p}$ interactions. The figure is not drawn to scale.

   E is the measured energy in the cell. For each cell, define

   $$p_T = \sqrt{p_x^2 + p_y^2} = E \sin\theta \tag{48}$$

   and

   $$\eta = -\ln\left(\tan\frac{\theta}{2}\right)\ . \tag{49}$$

2. Remove any calorimeter cells with $p_T < -500$ MeV. Cells with slightly negative p_T are allowed due to pileup effects in the calorimeter, but cells with highly negative p_T are very rarely observed in minimum bias events and are thus considered spurious, so they are removed.

3. For each calorimeter tower, sum the transverse

momenta of cells within that tower:

$$p_T^{tower} = \sum_{cell \in tower} p_T^{cell} \ . \quad (50)$$

4. Merge towers if they are close together in $\eta \times \phi$ space:
   (a) Form an η-ordered (from most negative to most positive) list of towers; towers with equal η are ordered from $\phi = 0$ to $\phi = 2\pi$.
   (b) Remove the first tower in the list and call it a precluster.
   (c) From the remainder of the list, find the closest tower to the precluster.
   (d) If they are within $\Delta\mathcal{R}_p = \sqrt{\Delta\eta^2 + \Delta\phi^2} = 0.2$, remove the closest tower from the list, and combine it with the existing precluster, forming a new precluster; go to 4c.
   (e) If any towers remain, go to 4b.
5. Preclusters which have negative transverse momentum $p_T = p_{T-} < 0$ are redistributed to neighboring preclusters. Given a negative p_T precluster with (p_{T-}, η_-, ϕ_-), we define a search square of size $(\eta_- \pm 0.1) \times (\phi_- \pm 0.1)$. If the vector sum of positive p_T in the search square is greater than $|p_{T-}|$, then p_{T-} is redistributed to the positive p_T preclusters in the search square. Otherwise, the search square is increased in steps of $\Delta\eta = \pm 0.1$ and $\Delta\phi = \pm 0.1$, and redistribution is again attempted. If redistribution still fails with a search square of size $(\eta_- \pm 0.7) \times (\phi_- \pm 0.7)$, the p_T of the negative momentum precluster is set to zero.
6. Preclusters which have $p_T < p_T^p = 200$ MeV are redistributed to neighboring preclusters, as in step 5. We make the additional requirement that the search square have at least three positive p_T preclusters, to reduce the overall number of preclusters. The threshold p_T^p was tuned to produce ~ 200 preclusters/event, as shown in Fig. 23, to fit processing time constraints. Next, jets are reconstructed from the preclusters.

In steps 4–6, the combination followed a Snowmass style prescription:

$$p_T = p_{T,i} + p_{T,j} \ , \quad (51)$$

$$\eta = \frac{p_{T,i}\eta_i + p_{T,j}\eta_j}{p_{T,i} + p_{T,j}} \ , \quad (52)$$

$$\phi = \frac{p_{T,i}\phi_i + p_{T,j}\phi_j}{p_{T,i} + p_{T,j}} \ . \quad (53)$$

As a minimal change to the Run I preclustering algorithm, a possible Run II preclustering proposal should instead use vector addition of four-momenta. The Run II preclustering algorithm should also use y (as defined by Eq. 34) instead of η and a true 2-vector p_T rather than the scalar p_T of Eq. 51. Generally, the definitions of variables and recombination scheme in the preclustering algorithm should match the choices used in the proposed K_T jet algorithm. All of the results presented here used the Run I preclustering algorithm.

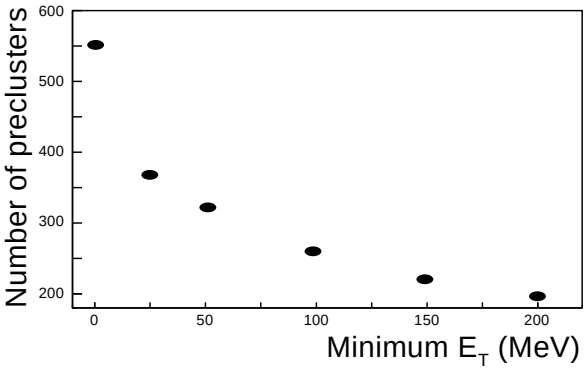

Figure 23. The number of preclusters per event, as a function of minimum precluster transverse energy E_T^p. The DØ data were preclustered with the choice $E_T^p = 200$ MeV, which produced $\sim$200 preclusters per event. With the preclusters treated as massless, E_T is the same as p_T. This identification is certainly appropriate for individual calorimeter towers.

The preclustering radius $\Delta\mathcal{R}_p$ in step 4 of the algorithm above can be used to test the sensitivity of jets to the calorimeter segmentation size, $\Delta\phi \times \Delta\eta = 0.1 \times 0.1$ (or smaller) in the DØ calorimeter. Preclustering with $\Delta\mathcal{R}_p = 0.2 > \Delta\eta$ or $\Delta\phi$ in step 4 of the algorithm mimics a coarser calorimeter. This effect was studied in a sample of HERWIG Monte Carlo QCD jet events. The jets in the hard $2 \to 2$ scattering were generated with $p_T > 50$ GeV, and at least one of the two leading order partons was required to be central ($|\eta| < 0.9$). The events were passed through a full simulation (including luminosity $\mathcal{L} \approx 5 \times 10^{30} \mathrm{cm}^{-2}\mathrm{s}^{-1}$) of the DØ detector. The MC sample is described in more detail in Section 4.4.1. Fig. 24 shows the number of preclusters with $\Delta\mathcal{R}_p = 0.2$ is $\sim$180, reduced by 37% from that obtained with $\Delta\mathcal{R}_p = 0$. Fig. 25 shows that preclustering is necessary even at the particle level in the Monte Carlo, reducing the number preclusters by 24%. Comparing Figs. 24 and 25, the number of preclusters in the detailed detector simulation is a

factor 2.4 higher than at the particle level for $\Delta\mathcal{R}_p = 0$. Most of the additional preclusters are reconstructed near the beampipe and some are due to localized deposits of low energy. With $\Delta\mathcal{R}_p = 0.2$, the number of preclusters increases only by a factor 2.0.

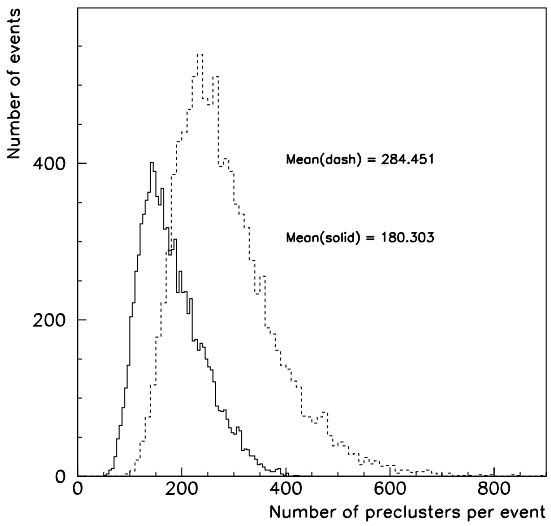

Figure 24. Distribution of the number of preclusters per event, with $\Delta\mathcal{R}_p = 0.2$ (solid), and with $\Delta\mathcal{R}_p = 0$ (dash). Taken from a sample of QCD jet events from MC data. The jets were reconstructed using the calorimeter simulation, including the luminosity simulation. The preclustering radius $\Delta\mathcal{R}_p = 0.2$ reduces the mean number of preclusters per event by 37%.

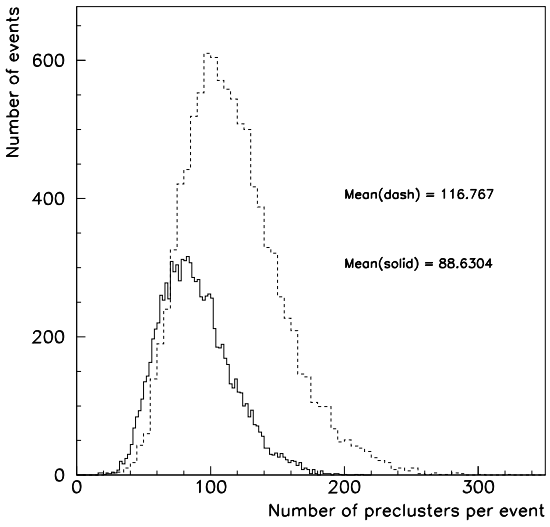

Figure 25. Same as in Fig. 24, except the jets were reconstructed in MC data at the particle level, with no calorimeter or luminosity simulation. The same preclustering radius $\Delta\mathcal{R}_p = 0.2$ reduces the mean number of preclusters per event by 24%
.

The effect of the preclustering radius $\Delta\mathcal{R}_p$ on jets and jet structure was examined next. Fig. 26 shows the comparison of the leading jet p_T with $\Delta\mathcal{R}_p = 0.2$ to that with $\Delta\mathcal{R}_p = 0$. The jets were reconstructed with the K_T jet algorithm $D = 0.5$. The preclustering radius $\Delta\mathcal{R}_p = 0.2$ (step 4 of the preclustering algorithm) reduces the mean jet p_T by 0.7 GeV. Evidently, the preclustering algorithm assigns energy differently than the K_T algorithm. It is difficult to track exactly which towers end up in each jet, in part because of the redistribution of energy in steps 5 and 6 of the preclustering algorithm. The net effect is that some energy belonging to the leading jet when $\Delta\mathcal{R}_p = 0$ is transferred to non-leading jets when $\Delta\mathcal{R}_p = 0.2$. The shift in the leading jet p_T spectrum is visible in the top panel of Fig. 26, and the ratio in the bottom panel suggests some dependence on the jet p_T. Such a shift may need to be corrected for in the Run II experimental data, but will be different due to the change in calorimeter electronics. In Run I, a correction was not explicitly applied to the experimental data for this effect. Instead, the theoretical predictions included the identical preclustering algorithm used in experimental data. Fortunately, the particle-level result for leading jet p_T is not as sensitive to $\Delta\mathcal{R}_p$. This is shown in Fig. 27. Note that even the particles in the Monte Carlo were projected into a calorimeter-like grid ($\Delta\phi \times \Delta\eta = 0.1 \times 0.1$) by the preclustering algorithm. If this were not the case, then we would expect an even larger effect than illustrated in Fig. 27.

The jet structure, however, is more sensitive to the preclustering radius $\Delta\mathcal{R}_p$. Fig. 28 shows the average subjet multiplicity, as a function of y_{cut} (see Section 4.6.1), in particle-level jets. There are more subjets in jets when $\Delta\mathcal{R}_p = 0$, compared to when $\Delta\mathcal{R}_p = 0.2$. Requiring preclusters to be separated by $\Delta\mathcal{R}_p$ affects the subjet structure below

$$\begin{aligned} y_{cut} &< \left(\frac{\Delta\mathcal{R}_p}{2D}\right)^2 \\ &< 10^{-1.4}. \end{aligned} \quad (54)$$

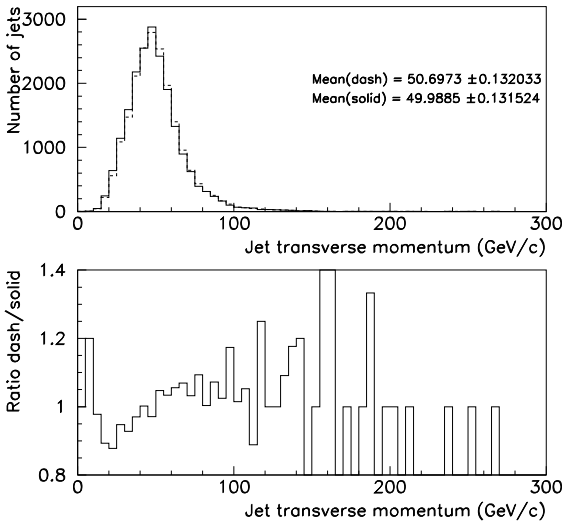

Figure 26. The top panel shows the distribution of the leading jet p_T with $\Delta\mathcal{R}_p = 0.2$ (solid), and with $\Delta\mathcal{R}_p = 0$ (dash). Measured in a sample of QCD jet events from MC data. The sample was generated with minimum parton transverse momentum $p_T^{min} = 50$ GeV. The K_T jets were reconstructed with $D = 0.5$ in the calorimeter simulation, including the luminosity simulation. The preclustering radius $\Delta\mathcal{R}_p = 0.2$ reduces the mean of the leading jet p_T by 0.7 GeV. The bottom panel shows the ratio of the histograms in the top panel.

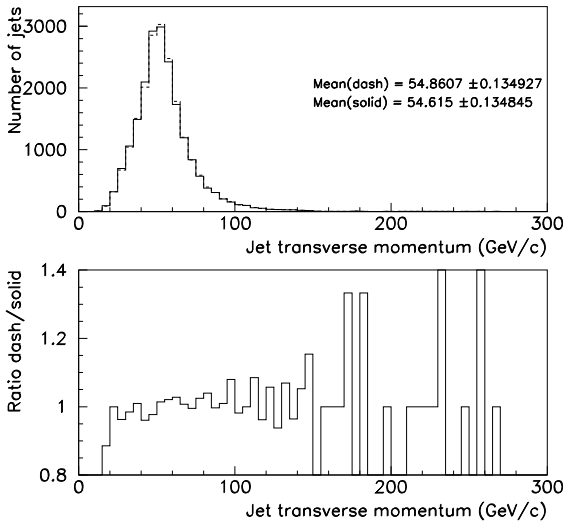

Figure 27. Same as in Fig. 26, except the jets were reconstructed in MC data at the particle level, with no calorimeter or luminosity simulation. The same preclustering radius $\Delta\mathcal{R}_p = 0.2$ reduces the mean of the leading jet p_T by 0.25 GeV. The bottom panel shows the ratio of the histograms in the top panel.

Again, the subjet multiplicity is increased even further when particles in the Monte Carlo are not projected into a calorimeter-like grid ($\Delta\phi \times \Delta\eta = 0.1 \times 0.1$). This underscores the fact that the same preclustering algorithm, as well as the same jet algorithm, must be used in any comparisons of theoretical predictions to experimental data which are sensitive to internal jet structure at the level of the detector granularity.

4.4. Momentum Calibration of K_T Jets at DØ

Jet production is the dominant process in $p\overline{p}$ collisions at $\sqrt{s} = 1.8$ TeV, and almost every physics measurement at the Tevatron involves events with jets. A precise calibration of measured jet momentum and energy, therefore, is of fundamental importance. Although the use of a K_T algorithm is well defined theoretically, questions have recently arisen regarding the performance of the algorithm in a high luminosity hadron collider environment.

The DØ Collaboration developed a method to calibrate K_T jets to a high level of accuracy. The details are discussed thoroughly in Ref. [28,29]. Here, we briefly summarize this work by the DØ Collaboration to illustrate instrumentation effects on the K_T algorithm, as well as its behavior in a high luminosity hadron collider. The K_T jets momentum scale correction is largely based on the calibration of cone jets, extensively discussed in a recent article [27]. The derivation of the momentum scale correction is performed for K_T jets with $D = 1$. The measured jet momentum, p_{jet}^{meas}, is corrected to that of the final-state particle-level jet, p_{jet}^{ptcl}, using the following relation:

$$p_{jet}^{ptcl} = \frac{p_{jet}^{meas} - p_O}{R_{jet}}, \tag{55}$$

where p_O denotes a momentum offset correction for underlying event, uranium noise, pile-up, and additional $p\overline{p}$ interactions. R_{jet} is the calorimeter momentum response to jets. Note that the equation is missing the out-of-cone showering loss factor. In cone jets, this factor corrects for the fraction of the energy of the final-state hadrons which is lost outside the cone boundaries due to calorimeter showering. This is an instrumentation effect completely unrelated to

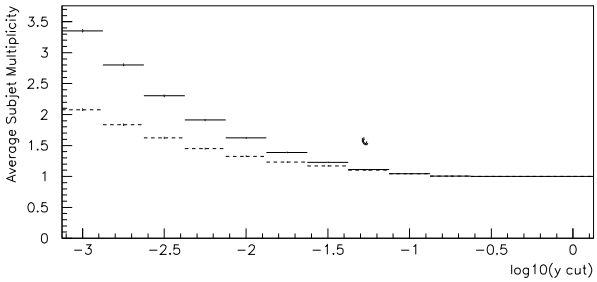

Figure 28. The average subjet multiplicity, as a function of y_{cut}, in a sample of jets reconstructed in MC data at the particle level, with no calorimeter or luminosity simulation. The solid curve shows the results with $\Delta\mathcal{R}_p = 0$, and the dashed curve shows the results with $\Delta\mathcal{R}_p = 0.2$. The preclustering radius $\Delta\mathcal{R}_p = 0.2$ reduces the average subjet multiplicity for $y_{cut} < 10^{-1.4}$.

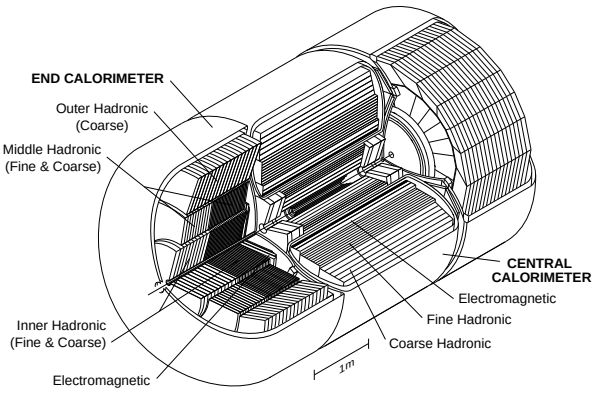

Figure 29. The DØ liquid argon calorimeter is divided physically into three cryostats, defining the central calorimeter and two end calorimeters. Plates of absorber material are immersed in the liquid argon contained by the cryostats. Each cryostat is divided into an electromagnetic, fine hadronic, and coarse hadronic section.

parton showering losses outside the cone. There is no correction for the latter. Note that the important issue here is not so much that p_O be small or that R_{jet} be near unity, but rather that these parameters can be determined with precision. This is the question to be addressed when comparing jet algorithms.

The DØ uranium-liquid argon sampling calorimeters [30] are shown in Fig. 29–30. They constitute the primary system used to identify e, γ, jets and missing transverse energy ($\vec{\not\!\!E}_T$). $\vec{\not\!\!E}_T$ is defined as the negative of the vector sum of the calorimeter cell transverse energies (E_T's). The Central (CC) and End (EC) Calorimeters contain approximately seven and nine interaction lengths of material respectively, ensuring containment of nearly all particles except high p_T muons and neutrinos. The intercryostat region (IC), between the CC and the EC calorimeters, is covered by a scintillator based intercryostat detector (ICD) and massless gaps (MG) [30]. The segmentation is $\Delta\phi\times\Delta\eta$ = 0.1 × 0.1 (or smaller).

The fractional energy resolution, σ_E/E, characterizes the suitability of the DØ calorimeter system for *in-situ* momentum calibration techniques. It is parameterized with a $\sqrt{S^2/E + C^2}$ functional form. For electrons, the sampling term, S, is 14.8 (15.7)% in the CC (EC), and the constant term, C, is 0.3% in both the CC and EC. For pions, the sampling term is 47.0 (44.6)%, and the constant term is 4.5 (3.9)% in the CC (EC). The energy response is linear to within 0.5% for electrons above 10 GeV and for pions above 20 GeV. The DØ calorimeters are nearly compensating, with an $\frac{e}{\pi}$ ratio less than 1.05 above 30 GeV. Due to the hermiticity and linearity of the DØ

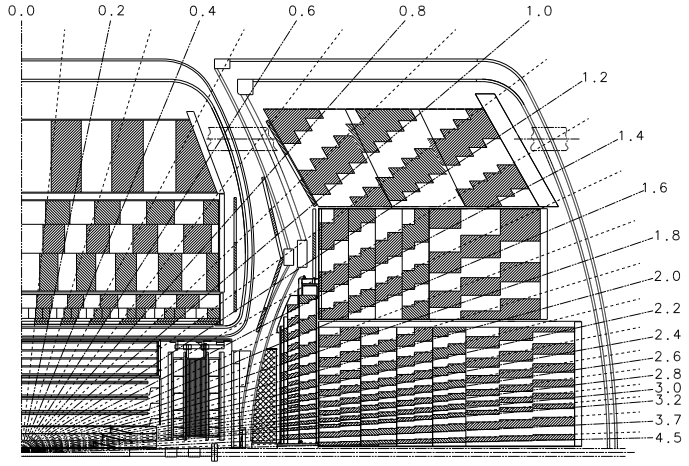

Figure 30. One quadrant of the DØ calorimeter and drift chamber, projected in the $x-z$ plane. Radial lines illustrate the detector pseudorapidity and the pseudoprojective geometry of the calorimeter towers. Each tower is of size $\Delta\eta \times \Delta\phi = 0.1 \times 0.1$.

calorimeters their response function is well described by a Gaussian distribution. These properties indicate that the DØ calorimeter system is well suited for jet and $\not\!\!E_T$ measurements and are the basis of the *in-situ* calibration method described here.

4.4.1. Offset Correction

The total offset correction is measured in transverse momentum and expressed as $p_{T,O} = O_{ue} + O_{zb}$. The first term is the contribution of the underlying event (energy associated with the spectator partons in a high p_T event). The second term accounts for uranium

noise, pile-up and energy from additional $p\overline{p}$ interactions in the same crossing. Pile-up is the residual energy from previous $p\overline{p}$ crossings as a result of the long shaping times associated with the preamplification stage in calorimeter readout cells.

To simulate the contribution of O_{zb} to jets, DØ Run I collider data taken in a random $p\overline{p}$ crossing (no trigger requirements) was overlayed on high p_T jet HERWIG [31] Monte Carlo events. Jets were matched in this sample to jets in the sample with no overlay. The contribution of uranium noise, pile-up, and multiple interactions was determined by taking the difference in p_T between matched pairs. O_{ue} was extracted in the same way from the overlap of low luminosity minimum bias data (a crossing with an inelastic collision) on Monte Carlo events. O_{ue} and O_{zb} for jets with $p_T = 30 - 50$ GeV are shown in Figs. 31 and 32. The offset is derived in the central calorimeter and extrapolated to higher η regions.

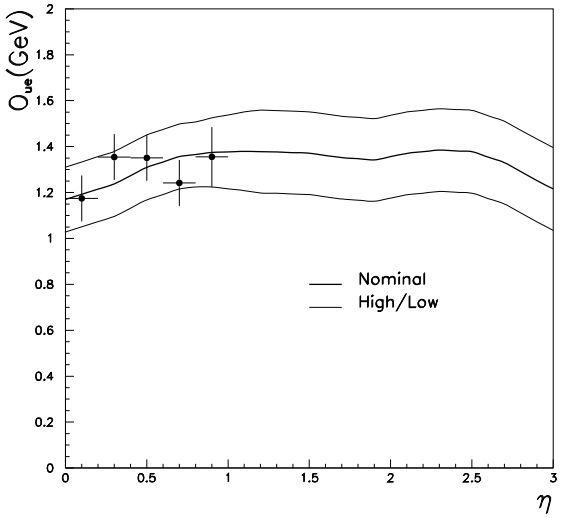

Figure 31. Physics underlying event offset O_{ue} versus η. Above $\eta = 0.9$, the result is an extrapolation.

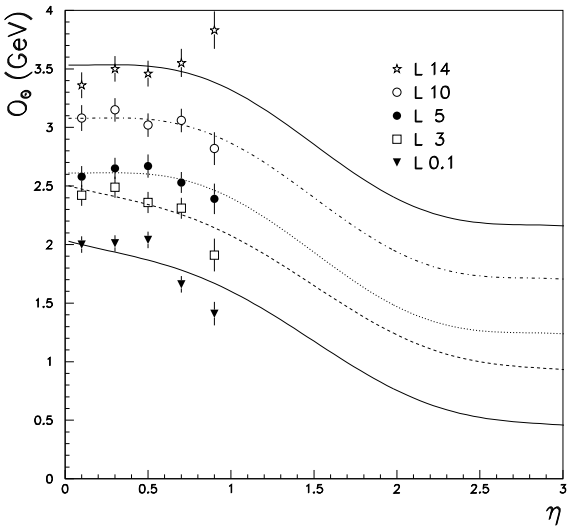

Figure 32. Offset due to uranium noise, pile-up and multiple interactions, O_{zb} versus η for different luminosities in units of 10^{30} cm^{-2}sec^{-1}. Above $\eta = 0.9$, the result is an extrapolation.

4.4.2. Response: The Missing E_T Projection Fraction Method

DØ makes a direct measurement of the jet momentum response using conservation of p_T in Run I photon-jet (γ-jet) collider events [27]. Previously, the photon energy/momentum scale was determined from the DØ $Z \to e^+e^-$, J/ψ and π° data samples, using the masses of these known resonances. In the case of a γ-jet two body process, the jet momentum response can be measured as:

$$R_{jet} = 1 + \frac{\vec{\not{E}}_T \cdot \hat{n}_{T\gamma}}{p_{T\gamma}}\,, \tag{56}$$

where $p_{T\gamma}$ and $\hat{n}$ are the transverse momentum and direction of the photon. To avoid resolution and trigger biases, R_{jet} is binned in terms of $E' = p_{T\gamma}^{meas} \cdot \cosh(\eta_{jet})$ and then mapped onto p_{jet}^{meas}. E' depends only on photon variables and jet pseudorapidity, which are quantities measured with very good precision. R_{jet} and E' depend only on the jet position, which has little dependence on the type of jet algorithm employed.

R_{jet} as a function of p_{jet}^{meas} (p_{Kt}) is shown in Fig. 33. The data is fit with the functional form $R_{jet}(P) = a + b \cdot \ln(P) + c \cdot \ln(P)^2$. R_{jet} for cone ($R = 0.7$) [27] and K_T ($D = 1$) jets are different by about 0.05. This difference does not have any physical meaning; it arises from different voltage-to-energy conversion factors at the cell level before reconstruction.

4.4.3. Tests of the Method

The accuracy of the K_T jet momentum scale correction was verified using a HERWIG γ-jet sample and a fast version (SHOWERLIB) [32] of the Run I detector simulation using GEANT [33]. A Monte Carlo jet momentum scale was derived and the corrected jet momentum compared directly to the momentum of the associated particle jet. Figure 34 shows the ratio of calorimeter and particle jet momentum before and

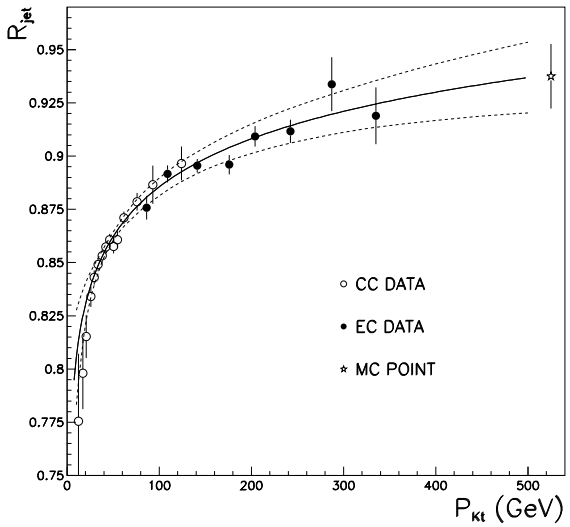

Figure 33. R_{jet} versus K_T jet momentum. The solid lines are the fit and the dashed band the error of the fit. (The three lowest points have nearly fully correlated uncertainties and are excluded from the fit.)

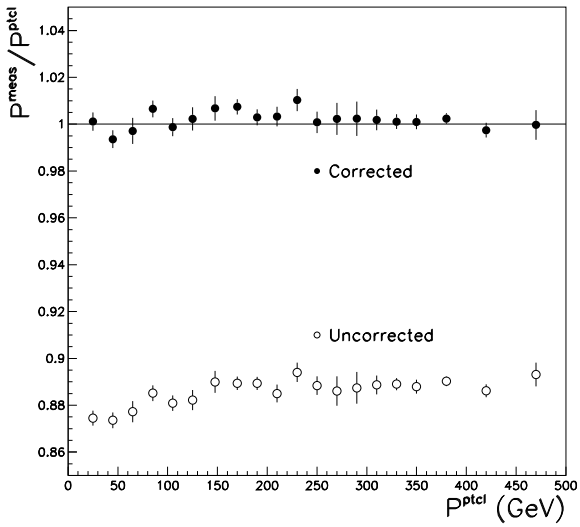

Figure 34. Monte Carlo verification test. The vertical bars are statistical errors. Systematic errors (not shown) are of the order of 0.01–0.02. The corrected $p_{jet}^{meas}/p_{jet}^{ptcl}$ ratio is consistent with unity within errors.

after the jet scale correction in the CC. The vertical bars are statistical errors. Systematic errors (not shown) are of the order of 0.01–0.02. After the jet correction is applied, the ratio versus particle jet p_T is consistent with unity within the total uncertainty.

4.4.4. Summary

DØ improved the method introduced in Ref. [27] for estimating the effects of underlying event, uranium noise, pile-up, and additional $p\overline{p}$ interactions. The offset correction is larger for K_T jets with $D = 1$ than for cone jets with $R = 0.7$ by approximately 20–30%. The uncertainty ($\sim$0.1 GeV for underlying event, and $\sim$0.2 GeV for the second offset term in the CC), however, is slightly smaller. A K_T ($D = 1$) algorithm reconstructs more energy from uranium noise, pile-up, underlying event, and multiple $p\overline{p}$ interactions than a cone algorithm ($R = 0.7$). The accuracy of the associated corrections are, however, on the same order. The missing E_T projection fraction method is well suited to calibrate K_T jets [34]. The uncertainty in R_{jet} for K_T and cone jets is about the same: (0.5–1.6%) for jet p_T = 50–450 GeV in the CC.

Overall, it may be possible to determine the jet momentum scale more accurately for K_T jets than the energy scale for cone jets, given the absence of a cone boundary in the former. The difference in precision could be large in the low p_T and high pseudorapidity range, where the cone showering correction is larger and more inaccurately determined. (The showering correction uncertainty contributes 1–3% [34] to the total error for $R = 0.7$ cone jets.)

4.5. Jet Momentum Resolutions of K_T Jets

One of the largest sources of uncertainty in jet measurements (besides the jet momentum scale) is the effect of a finite calorimeter jet momentum resolution. *A priori*, due to the absence of cone boundaries, K_T jets should be affected little by jet-to-jet fluctuations in the shower development. The jets will, of course, still be subjected to the effects of hadronization.

We compared jet energy resolutions for cone jets ($R = 0.7$) and momentum resolutions for K_T jets ($D = 1$) derived from a DØ Monte Carlo simulation using the HERWIG event generator plus the GEANT simulation of the DØ detector (Run I). The test was performed for an inclusive jet sample with average p_T = 60 GeV and 80 GeV in $|\eta| < 0.5$. Within statistical errors, σ_{p_T}/p_T for K_T jets and σ_{E_T}/E_T for cone jets are the same: 0.109 $\pm$ 0.009 and 0.105 $\pm$ 0.006 for K_T ($D = 1$) and cone ($R = 0.7$) jets at 60 GeV, and 0.10 $\pm$ 0.01 for both at 80 GeV. Preliminary measurements of K_T jet momentum resolutions and cone jet energy resolutions using Run I collider data support the previous statement. Note, however, that resolutions depend on the algorithm parameters R and D. Resolution studies for different (smaller) R and D parameters should be performed, as well as for different type of samples, for example quark or gluon enriched samples. These studies will make more clear how energy/momentum resolutions compare for cone and K_T jets.

4.6. Testing QCD with the K_T Jet Algorithm

4.6.1. Jet Structure

The subjet multiplicity is a natural observable of a K_T jet [35,36]. Subjets are defined by re-running the K_T algorithm starting with a list of preclusters in a jet. Pairs of objects with the smallest d_{ij} are merged successively until all remaining d_{ij} are larger than $y_{cut}E_T^2(jet)$, where $0 < y_{cut} < 1$ is a resolution parameter. The resolved objects are called subjets, and the number of subjets within the jet is the subjet multiplicity M. For $y_{cut} = 1$, every jet consists of a single subjet ($M = 1$). As y_{cut} decreases, the subjet multiplicity increases until every precluster becomes resolved as a separate subjet. At this level of detail the specific preclustering algorithm used clearly influences the result. A measurement of M for quark and gluon jets is a test of QCD, and may eventually be used in Run II as a discriminant variable to tag quark jets in the final state. Fig. 35 shows a preliminary measurement of M by DØ [37], using Run I data (K_T algorithm with $D = 0.5$ and $y_{cut} = 0.001$). The ratio $R = \frac{\langle M_g \rangle - 1}{\langle M_q \rangle - 1}$ is $1.91 \pm 0.04(stat) \pm 0.23(sys)$. It is well described by the HERWIG Monte Carlo, and illustrates the fact that gluons radiate more than quarks.

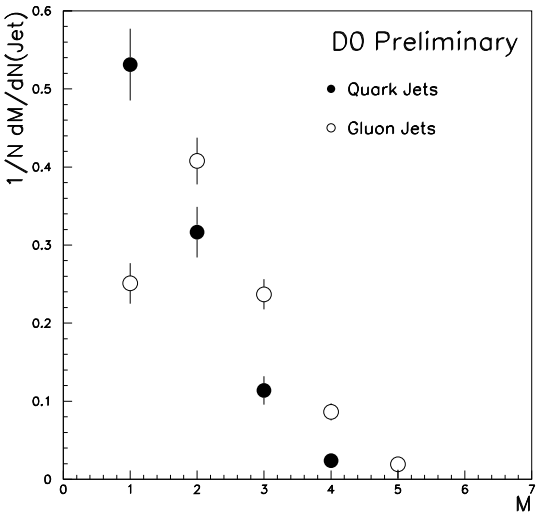

Figure 35. Subjet multiplicity for quark and gluon jets at DØ.

4.6.2. Jet Production

Jet cross section measurements have been extensively used by both Fermilab Tevatron collaborations during Run I to test perturbative (NLO) QCD predictions, to test the available parton distribution functions at the x and Q^2 ranges covered by the Tevatron, and to search for quark compositeness [38–47]. The higher center-of-mass energy and the larger data sample will allow the Tevatron experiments to extend the energy reach and precision of jet cross sections in Run II. The largest source of uncertainty in a jet cross section measurement is the jet energy (or momentum) scale. As an example, a 1% uncertainty in the jet energy calibration translates into a 5–6% (10–15%) uncertainty in the $|\eta| < 0.5$ inclusive jet cross section at 100 GeV (450 GeV). As a function of η, the jet cross section falls more quickly with transverse energy, and the cross section error is even larger.

The K_T jet algorithm may provide experimental advantages for jet production measurements. At DØ, the jet scale uncertainty for cone jets in the high E_T range is dominated by the contributions from the response and out-of-cone showering corrections. In Run II, the availability of more high E_T photon data and a more accurate determination of the position of the interaction vertex promise a reduction in the response uncertainty. Furthermore, the absence of out-of-cone showering losses in K_T jets will likely lead to improved jet cross section measurements in the forward η regions. Most of the Run I cross section results by CDF and DØ use jet energy measurements restricted to central regions ($|\eta| < 1$). A couple of exceptions to the rule are the DØ measurements of the pseudorapidity dependence of the jet cross section [45], and the test of BFKL dynamics in dijet cross sections at large pseudorapidity intervals [48].

4.6.3. Event Shapes

Event shape variables in e^+e^- and ep interactions have attracted considerable interest over the last few years [49–51]. Little attention has been paid to measurements or calculations of event shape variables at hadron colliders. An important example is thrust which is defined as:

$$T = \max_{\hat{n}} \frac{\sum_i |\vec{p_i} \cdot \hat{n}|}{\sum_i |\vec{p_i}|}, \qquad (57)$$

where the sum is over all parton, or particle momenta.

A LO jet rate calculation with two partons in the final state yields $T = 1$. A NLO calculation, with three partons in the final state would produce a deviation from $T = 1$ (LO in thrust). A NNLO prediction with four partons in the final state would then give a NLO prediction of thrust. At all orders, thrust would take values from 0.5 to unity. In other words, thrust measures the pencil-likeness of the event: $T \to 1$ for back-to-back events, and $T < 1$ as more radiation is present. The low scales introduced by soft and collinear emission in events with $T \lesssim 1$ could be the reason for the observed discrepancy between LO and NLO calculations and experimental e^+e^- data [49]. Resummation of higher-order perturbative terms could lead to a better understanding of the problem.

The simplest measurements of thrust we can perform are the thrust distributions in jet events, changing the definition of thrust to sum over all the jets in the event. In order to be able to resum logarithms of the jet resolution scale, jets must be defined using an algorithm such as the K_T algorithm [52]. The contribution of the underlying event, and multiple $p\overline{p}$ interactions in hadron colliders, introduce an experimental difficulty not present in lepton colliders. It is possible, however, to minimize these systematics by choosing carefully the variable to measure.

We can also define transverse thrust, T_T, by replacing particle momenta by transverse momenta in Eq. 57. T_T is Lorentz invariant for boosts along the beam axis, an advantage in the case of hadron colliders.

Figs. 36–38 show the difference between T_T calculated from particle-level jets (reconstructed from final-state hadrons) and T_T from calorimeter-level jets (reconstructed from cells). HERWIG was used as the generator, and SHOWERLIB [32] (a fast version of GEANT) simulated the Run I detector. In all cases jets are reconstructed with the K_T jet algorithm ($D = 1$). Fig. 36 shows a T_T distribution for events with H_T = 90–150 GeV, where H_T is the scalar sum p_T of all jets above 8 GeV. H_T was chosen instead of Q^2 as an estimator of the hard scattering energy scale of the event. All jets with $p_T > 8$ GeV contribute to T_T. The full circles are the particle-level or "true" distribution. The triangles are the distribution as seen in the calorimeter in an ideal environment with no offset (underlying event, multiple $p\overline{p}$ interactions, pile-up, or noise). The open circles are a calorimeter-level distribution which includes a random collider crossing event at a luminosity of $5 \times 10^{30}\text{cm}^{-1}\text{sec}^{-1}$. While the effect of calorimeter momentum response, resolution, and showering is minimal, the offset distorts the distribution to a large extent.

In Fig. 37, the thrust definition was modified to allow only the three leading jets (above 8 GeV) to contribute to the thrust (T_{T3}) and to H_T (now H_{T3}). The difference between the true and the fully-simulated calorimeter distribution is now much smaller. Finally, in Fig. 38, only the two leading jets contribute to the thrust (T_{T2}) for events with H_{T3} = 90–150 GeV. Now the calorimeter distribution is even closer to the true distribution. Although T_{T3} and T_{T2} are not calculated from all final-state particles (to reduce contamination), they implicitly include the information about the whole radiation pattern through the p_T and $\eta - \phi$ position of the first few leading jets.

Event shape variables, like a modified version of thrust, can be studied with precision at the Tevatron. The use of the K_T algorithm, infrared safe at all orders in perturbation theory, provides a test

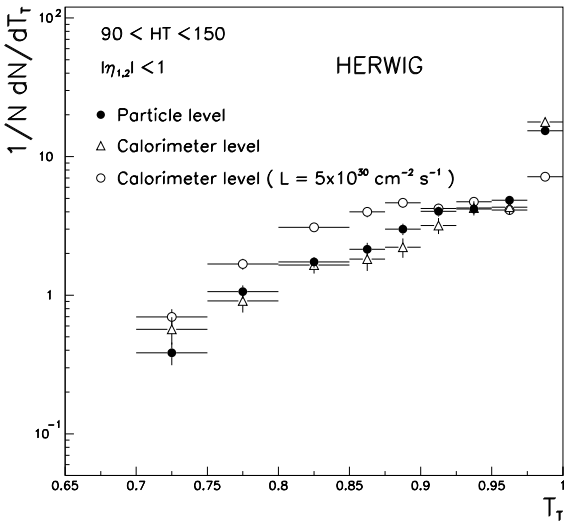

Figure 36. All jets with $p_T > 8$ GeV contribute to T_T. The full circles are the particle-level or "true" distribution. The triangles are the distribution as seen in the calorimeter in an ideal environment with no offset (underlying event, multiple $p\overline{p}$ interactions, pile-up, or noise). The open circles are a calorimeter-level distribution which includes a random crossing collider event at a luminosity of $5 \times 10^{30}\text{cm}^{-2}\text{sec}^{-1}$.

of the newly available hadronic three jet production calculations at NLO [8,53]. In the QCD calculation of the thrust variables defined in this section, there are no large logarithms in the $T \to 1$ limit. Then, it is neither possible nor necessary to resum them. However, if we redefine thrust in terms of subjets or tracks, the measurement is more interesting and resummation becomes an issue [54]. The availability of the contributions of higher-order terms through a resummation calculation would be desirable, in that case, to improve the understanding of the range $T \lesssim 1$. In Run II, both the CDF and the DØ detectors will have upgraded tracking systems. This will allow both experiments to implement improved techniques for the identification of hadrons using both the calorimeter and the tracking detectors.

The H_T dependence of $\langle 1 - T \rangle$, in the range where resummation and hadronization effects are small, could also provide a measurement of α_s.

5. Conclusions

Jet algorithms present a challenge to experimentalists and theorists alike. Although everyone "knows a jet when they see it," precise definitions are elusive and detailed. The jet working group has attempted to provide guidelines and recommendations for jet algorithm development. The end product of the year-long effort

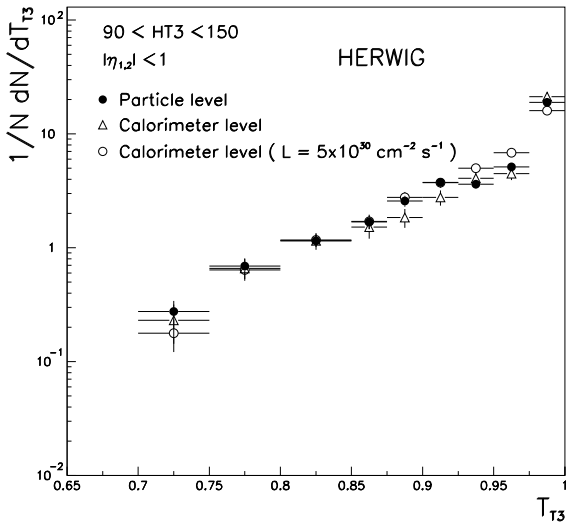

Figure 37. Same as Fig. 36 but only the three leading jets contribute to T_T, now T_{T3}. H_{T3} is the scalar sum p_T of the three leading jets in the event.

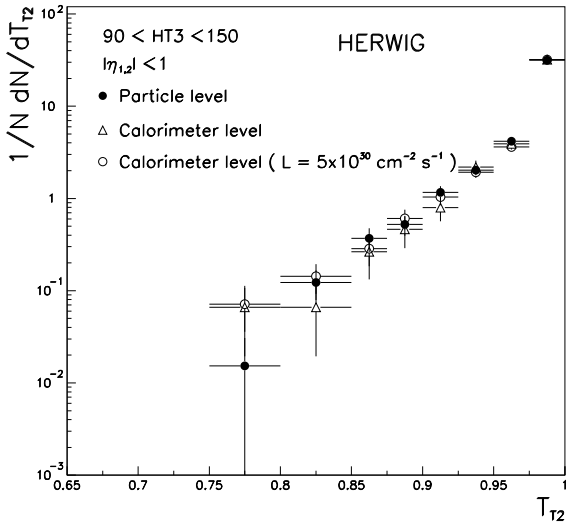

Figure 38. Same as Fig. 36 but only the two leading jets contribute to T_T, now T_{T2}. H_{T3} is the scalar sum p_T of the three leading jets in the event.

has been standardized jet cone and K_T algorithms, and the recommendation to use 4-vector, E-scheme kinematic variables. A legacy algorithm or ILCA has been suggested which will bridge the gap between past results and improved theoretical calculations. This document has addressed concerns about the use and calibration of K_T jets.

We strongly recommend that both CDF and DØ adopt standard algorithms for Run II. Since continued development is probably inevitable, we encourage continued dialogue. The usefulness of standardized algorithms, which can replicate past results and meet experimental and theoretical requirements, makes continued coordination well worth the effort.

REFERENCES

1. G.C. Blazey and B.L. Flaugher, Ann. Rev. of Nucl. and Part. Sci., Vol. 49 (1999), FERMILAB-Pub-99/038-E.
2. J.E. Huth *et al.* in *Proceedings of Research Directions For The Decade: Snowmass 1990*, July, 1990, edited by E.L. Berger (World Scientific, Singapore, 1992) p. 134.
3. B. Abbott *et al.* (DØ Collaboration), Fermilab-Pub-97-242-E (1997).
4. S.D. Ellis, Z. Kunszt, D. Soper, Phys. Rev. Lett. **69** 3615 (1992) and S. Ellis CERN-TH-6861-93, Jun 1993. 13pp. Presented at 28th Rencontres de Moriond: QCD and High Energy Hadronic Interactions, Les Arcs, France, 20-27 Mar 1993. Published in Moriond 1993: Hadronic: 235–244; hep-ph/930628. B. Abbott *et al.*, Fermilab-Pub-97-242-E (1997).
5. Y. L. Dokshitzer, G. D. Leder, S. Moretti and B. R. Webber, JHEP **9708**, 001 (1997) [hep-ph/9707323]; A. T. Pierce and B. R. Webber, Phys. Rev. **D59**, 034014 (1999) [hep-ph/9807532]; M. H. Seymour, Nucl. Phys. **B513**, 269 (1998) [hep-ph/9707338].
6. Z. Casilum and R. Hirosky, *Jet Reconstruction Efficiency*, DØ Note 3324, unpublished.
7. S. Catani et al., *Report of the QCD and standard model working group* for the Workshop *Physics at TeV Colliders*, Les Houches, France, 8-18 June 1999.
8. Z. Bern, L. Dixon, and D.A. Kosower, Ann. Rev. Nucl. Part. Sci. **46**, 109 (1996) [hep-ph/9602280]; W.B. Kilgore and W.T. Giele, Phys. Rev. **D55**, 7183 (1997); W.B. Kilgore and W.T. Giele, *Hadronic three jet production at next-to-leading order*, e-Print hep-ph/9903361.
9. H. Baer, J. Ohnemus and J. F. Owens, Phys. Lett. **B234**, 127 (1990); J. Ohnemus, Phys. Rev. **D50**, 1931 (1994) [hep-ph/9403331]; R. K. Ellis and S. Veseli, Phys. Rev. **D60**, 011501 (1999) [hep-ph/9810489]; J. M. Campbell and R. K. Ellis, Phys. Rev. **D60**, 113006 (1999) [hep-ph/9905386].
10. E. Mirkes and D. Zeppenfeld, Phys. Lett. **B380**, 205 (1996); E. Mirkes, preprint TTP-97-39 (1997) [hep-ph/9711224].
11. S. Catani and M. H. Seymour, Nucl. Phys. **B485**, 291 (1997) [hep-ph/9605323]; D. Graudenz, hep-ph/9710244; B. Potter, Comput. Phys. Commun. **119**, 45 (1999) [hep-ph/9806437].
12. Private communication from S.D. Ellis and D.E.

Soper.
13. S.D. Ellis, Z. Kunszt, and D.E. Soper, Phys. Rev.Lett. **69**, 291 (1992); *ibid.* 1496 (1992); Phys. Rev. Lett. **62**, 2121 (1990).
14. T. Sjostrand, "Pythia 5.7 and jetset 7.4 physics and manual," CERN-TH-7112-93.
15. This idea was originally suggested by S.D. Ellis, D.E. Soper and H.-C. Yang to the OPAL Collaboration. See the discussion in references [16] and [19].
16. M.H. Seymour, Nucl. Phys. **B513**, 269 (1998).
17. B. Potter and M.H. Seymour, J. Phys. **G25**, 1473 (1999).
18. N. Kauer, L. Reina, J. Repond and D. Zeppenfeld, Phys. Lett. **B460**, 189 (1999) hep-ph/9904500.
19. OPAL Collaboration, Z. Phys., C63, 197–211 (1994).
20. S. Catani, Yu.L. Dokshitzer, M.H. Seymour, and B.R. Webber, Nucl. Phys. B **406** 187 (1993).
21. S. Catani, Yu.L. Dokshitzer, and B.R. Webber, Phys. Lett. B **285** 291 (1992).
22. S.D. Ellis and D.E. Soper, Phys. Rev. **D48** 3160 (1993).
23. D. Buskulic *et al.* (ALEPH Collaboration), Phys. Lett. B **346**, 389 (1995).
24. E.W.N. Glover and D.A. Kosower, Phys. Lett. B **367** 369 (1996).
25. K.C. Frame in Proceedings of the VIII International Conference on Calorimetry in High Energy Physics, Lisbon, 1999 (to be published); Ph.D. thesis, Michigan State University 1999 (unpublished).
26. R. Blair *et al.* (CDF Collaboration), The CDF II Detector: Technical Design Report, FERMILAB-PUB-96/390-E (1996).
27. B. Abbott *et al.*, Nucl. Instr. and Meth. A (1999) 352.
28. K. Frame (DØ Collaboration). To be published in the proceedings of the Seventh International Conference on Calorimetry in High Energy Physics.
29. To be submitted to Nucl. Instr. and Meth. (in preparation).
30. S. Abachi *et al.*, Nucl. Instr. and Meth. A (1994) 185.
31. G. Marchesini and B. Webber, Nucl. Phys. B 310 (1988).
32. J. Womersley for the DØ Collaboration, presented at the International Conference on High Energy Physics, Dallas, USA (1992), FERMILAB-CONF-92-306 (unpublished).
33. DØ detector simulation packaged based on GEANT. GEANT by R. Brun and F. Carminati, CERN Program Library Long Writeup W5013 (1993).
34. A. Goussiou for the DØ Collab., FERMILAB-PUB-99/264-E (1995).
35. M. Seymour, Nucl. Phys. B **421** 545 (1994).
36. J. Forshaw and M. Seymour, JHEP **9909** 009 (1999).
37. R. Snihur (DØ Collaboration), 7th International Workshop on Deep Inelastic Scattering and QCD DESY Zeuthen, Germany 19-23 Apr 1999. Nuclear Physics B (Proc. Suppl.) 79, 494–496 (1999).
38. B. Abbott *et al.* (DØ Collaboration), Phys. Rev. Lett. **82**, 2451–2456 (1999).
39. F. Abe *et al.* (CDF Collaboration), Phys. Rev. Lett. **77**, 438 (1996).
40. B. Abbott *et al.* (DØ Collaboration), Phys. Rev. Lett. **80**, 666–671 (1997).
41. F. Abe *et al.* (CDF Collaboration), Phys. Rev. Lett. **77**, 5336–5341 (1996).
42. B. Abbott *et al.* (DØ Collaboration), Phys. Rev. Lett. **82**, 2457–2462 (1999).
43. T. Affolder *et al.* (CDF Collaboration). Submitted to Phys. Rev. D (1999).
44. J. Krane (CDF and DØ Collaborations), Iowa State University, Proceedings of DPF99.
45. L. Babukhadia (DØ Collaboration), QCD Multiparticle Production, XXIX International Symposium on Multiparticle Dynamics (ISMD99), August 9–13, 1999, Brown University, Providence. Proceedings in preparation.
46. H. Schellman (DØ Collaboration), 7th International Workshop on Deep Inelastic Scattering and QCD (DIS 99), Zeuthen, Germany, 19–23 Apr 1999. FERMILAB-CONF-99-170-E, Jun 1999.
47. F. Chlebana (CDF Collaboration), 7th International Workshop on Deep Inelastic Scattering and QCD DESY Zeuthen, Germany 19–23 Apr 1999.
48. B. Abbott *et al.* (DØ Collaboration). Submitted to Phys. Rev. Lett. (1999).
49. E. Gardi, G. Grunberg (Ecole Polytechnique). High Energy Physics International Euroconference on Quantum Chromo-Dynamics (QCD99), Montpellier, France, 7–13 Jul 1999 (hep-ph/9909226).
50. V. Antonelli, M. Dasgupta, G. Salam, BICOCCA-FT-99-32, Dec 1999. 25pp. (hep-ph/9912488).
51. G. Korchemsky, G. Sterman, Nucl. Phys. **B555**, 335–351, 1999 (hep-ph/9902341).
52. M. Seymour, CERN-TH/95-225 (hep-ph/9603281).
53. Private communication with W. Giele.
54. Private communication with M. Seymour.

Report of the Working Group on Precision Measurements

Conveners: Raymond Brock[a], Jens Erler[b], Young-Kee Kim[c], and William Marciano[d]
Working Group Members: William Ashmanskas[e], Ulrich Baur[f], John Ellison[g], Mark Lancaster[h], Larry Nodulman[i], John Rha[j], David Waters[k], John Womersley[l]

[a]Michigan State University, East Lansing, MI 48824

[b]University of Pennsylvania, Philadelphia, PA 19104

[c]University of California, Berkeley, CA 94720

[d]Brookhaven National Laboratory, Upton, NY 11973

[e]University of Chicago, Chicago, IL 60637

[f]State University of New York, Buffalo, NY 14260

[g]University of California, Riverside, CA 92521

[h]University College, London WC1E 6BT, U.K.

[i]Argonne National Laboratory, Argonne, IL 60439

[j]University of California, Riverside, CA 92521

[k]Oxford University, Oxford, OX1 3RH, U.K.

[l]Fermilab, Batavia, IL 60510

Overview

Precision measurements of electroweak quantities are carried out to test the Standard Model (SM). In particular, measurements of the top quark mass, m_{top}, when combined with precise measurements of the W mass, M_W, and the weak mixing angle, $\sin^2\bar{\theta}_W$, make it possible to derive indirect constraints on the Higgs boson mass, M_H, via top quark and Higgs boson electroweak radiative corrections to M_W. Comparison of these constraints on M_H with the mass obtained from direct observation of the Higgs boson in future collider experiments will be an important test of the SM.

In this report, the prospects for measuring the W parameters (mass and width) and the weak mixing angle in Run II are discussed, and a program for extracting the probability distribution function of M_H is described. This is done in the form of three largely separate contributions.

The first contribution describes in detail the strategies of measuring M_W and the W width, Γ_W, at hadron colliders, and discusses the statistical, theoretical and detector specific uncertainties expected in Run II. The understanding of electroweak radiative corrections is crucial for precision W mass measurements. Recently, improved calculations of the electroweak radiative corrections to W and Z boson production in hadronic collisions became available. These calculations are summarized and preliminary results from converting the theoretical weighted Monte Carlo program into an event generator are described. The traditional method of extracting M_W from the line-shape of the transverse mass distribution has been the optimal technique for the extraction of M_W in the low luminosity environment of Run I. Other techniques may cancel some of the systematic and statistical uncertainties resulting in more precise measurements for the high luminosities expected in Run II. Measuring the W mass from fits of the transverse momentum distributions of the W decay products and the ratio of the transverse masses of the W and Z bosons are investigated in some detail. Finally, the precision expected for the W mass in Run II is compared with that from current LEP II data, and the accuracy one might hope to achieve at the LHC and a future linear e^+e^- collider.

In the second contribution, a study of the measurement of the forward-backward asymmetry, A_{FB}, in

e^+e^- and $\mu^+\mu^-$ events is presented. The forward-backward asymmetry of $\ell^+\ell^-$ events in Run II can yield a measurement of the effective weak mixing angle $\sin^2\bar{\theta}_{\rm W}$ and can provide a test of the standard model γ^*/Z interference at $\ell^+\ell^-$ invariant masses well above the 200 GeV center of mass energy of the LEP collider. The asymmetry at large partonic center of mass energies can also be used to study the properties of possible new neutral gauge bosons, and to search for compositeness and large extra dimensions. Estimates of the statistical and systematic uncertainties expected in Run II for A_{FB} and $\sin^2\bar{\theta}_{\rm W}$ are given. The uncertainty for $\sin^2\bar{\theta}_{\rm W}$ is compared with the precision expected from LHC experiments, and from a linear collider operating at the Z pole.

The third contribution summarizes the features of the FORTRAN package GAPP which performs a fit to the electroweak observables and extracts the probability distribution function of M_H.

Measurement of the W Boson Mass and Width

William Ashmanskas[a], Ulrich Baur[b], Raymond Brock[c], Young-Kee Kim[d], Mark Lancaster[e], Larry Nodulman[f], David Waters[g], John Womersley[h]

[a]University of Chicago, Chicago, IL 60637

[b]State University of New York, Buffalo, NY 14260

[c]Michigan State University, East Lansing, MI 48824

[d]University of California, Berkeley, CA 94720

[e]University College, London WC1E 6BT, U.K.

[f]Argonne National Laboratory, Argonne, IL 60439

[g]Oxford University, Oxford, OX1 3RH, U.K.

[h]Fermilab, Batavia, IL 60510

We discuss the prospects for measuring the W mass and width in Run II. The basic techniques used to measure M_W are described and the statistical, theoretical and detector-related uncertainties are discussed in detail. Alternative methods of measuring the W mass at the Tevatron and the prospects for M_W measurements at other colliders are also described.

1. Introduction

Measuring the W mass, M_W, and width, Γ_W are important objectives for the Tevatron experiments in Run II. The goal for the W mass measurement at the Tevatron in Run II is determined by three factors: the direct measurement of the LEP II experiments, the indirect determination from within the Standard Model (SM), and the ultimate precision on the measured top quark mass. The expectations for LEP II appear to be an overall uncertainty of approximately ± 35 MeV/c^2 [1]. The indirect determination is at the ± 30 MeV/c^2 level and is not likely to significantly improve given the end of the LEP and SLC programs. Finally, the top quark mass precision may reach the ± 2 GeV/c^2 level, which corresponds to a parametric uncertainty of $\delta M_W = 12$ MeV/c^2 [2]. The constraint provided by a successful $\pm$ 30 MeV/c^2 W boson mass measurement per experiment per channel[1] would have an impact on electroweak global fitting comparable to that of the LEP Z asymmetries. If the ultimate precision on the M_W determination could reach $\sim \pm 30$ MeV/c^2, then the bound on the Higgs boson mass would reach approximately ± 30 GeV/c^2 [3]. With the best fit central value close to the current LEP II direct search lower limit of $M_H > 113.2$ GeV/c^2 [4], considerable pressure can be brought to bear on the SM.

This document is structured as follows. The basic techniques used to measure the W mass and width are briefly reviewed in section 2. The statistical and detector-related uncertainties affecting the W mass and width measurements are discussed in more detail in section 3 and section 4, respectively. A number of systematic uncertainties clearly do not scale statistically and these are addressed separately in section 5. The expected errors on the measured W mass in Run II using the conventional transverse mass method and the W width are summarized in section 6. Alternative methods of measuring the W mass at the Tevatron are described in section 7 and prospects for M_W measurements at other colliders are discussed in section 8. Finally, some theoretical considerations important for future W mass measurements are brought up in section 9. Section 10 concludes this document.

2. M_W and Γ_W Measurements from the M_T Lineshape

The determination of M_W depends on the two body nature of the W decay: $W \to \ell\nu_\ell$. The kinematical Jacobian peak and sharp edge at the value of $M_W/2$ is easily observed in the measurement of the transverse momentum of either of the leptons. In practice, the situation is difficult due to both challenging experimental issues and the fact that phenomenological

[1]While the measurements from the different channels and different experiments provide cross checks, the combined measurement is not expected to yield a much better precision than a single measurement because of large common uncertainties.

Table 1
Advantages and disadvantages to an M_W determination via transverse mass or lepton transverse momenta.

Measurable	p_T^W sensitivity	resolution sensitivity
M_T	small	significant
p_T^e	significant	small
p_T^ν	significant	significant

assumptions must be made in order to perform the analysis. Because the standard measurable cannot be written in closed form, an unbinned maximum likelihood calculation is required. Figure 1 shows a calculation of p_T^e (unsmeared) with $p_T^W = 0$; the effect of finite p_T^W; and the inclusion of detector smearing effects. It is apparent that p_T^e is very sensitive to the transverse motion of the W boson.

Historically, precise understanding of p_T^W has been lacking, although it is currently modeled by measurable parameters through the resummation formalism of Collins, Soper, and Sterman [5]. For this reason, the transverse mass quantity was suggested [6] and has been the traditional measurable. It is defined by

$$M_T = \sqrt{2p_T^\ell p_T^\nu (1 - \cos(\phi_{\ell,\nu}))}, \quad (1)$$

where $\phi_{\ell,\nu}$ is the angle between the charged lepton and the neutrino in the transverse plane. The observables are the lepton transverse energy or momentum $\vec{p}_T^{\,\ell}$ and the non-lepton transverse energy $\vec{u}$ (recoil transverse energy against the W), from which the neutrino momentum $\vec{p}_T^{\,\nu}$ and the transverse mass M_T are derived. Figure 2 shows that the sensitivity of M_T to p_T^W is nearly negligible. While considerably more stable to the phenomenology of the production model, the requirement that the neutrino direction be accurately measured leads to a set of experimental requirements which are difficult in practice to control. So, there are different benefits and challenges among the direct measurements of the transverse quantities, p_T^ℓ, p_T^ν, and M_T. Table 1 lists these relative pros and cons of the transverse mass and transverse momentum measurements.

Both CDF and DØ have determined the W boson mass using the transverse mass approach. The individual measurements of both experiments are shown in Table 2 and the overall combined result is

$$M_W = 80.452 \pm 0.062 \text{ GeV/c}^2. \quad (2)$$

The W boson width is precisely predicted in terms

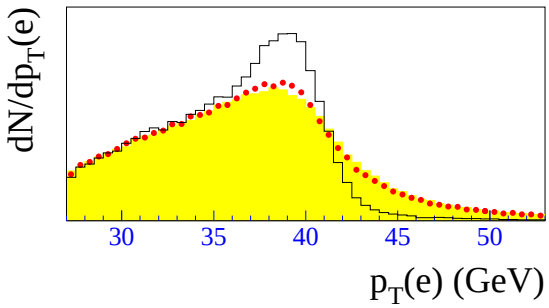

Figure 1. The effects of resolution and the finite p_T^W on p_T^e in W boson decay. The histogram shows p_T^W without detector smearing and for $p_T^W = 0$. The dots include the effects of adding finite p_T^W, while the shaded histogram includes the effects of detector resolutions. The effects are calculated for the DØ Run I detector resolutions.

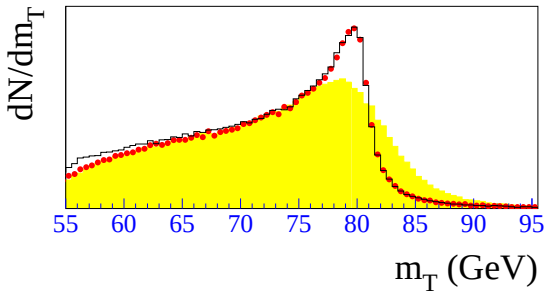

Figure 2. The effects of resolution and the finite p_T^W on M_T in $W \to e\nu$. The histogram shows M_T without detector smearing and for $p_T^W = 0$. The dots include the effects of adding finite p_T^W, while the shaded histogram includes the effects of detector resolutions. The effects are calculated for the DØ Run I detector resolutions.

of well-measured SM masses and coupling strengths:

$$\begin{aligned} \Gamma_W &= \frac{G_F M_W^3}{6\sqrt{2}\pi}\left[3 + 6\left(1 + \frac{\alpha_s(M_W)}{\pi} + \mathcal{O}(\alpha_s^2)\right)\right] \\ &\quad \times(1 + \mathcal{O}(1\%)) \\ &= 2.093 \pm 0.002 \text{ GeV} \end{aligned} \quad (3)$$

where the uncertainty is dominated by the experimental M_W precision [7,8]. The mass and width of the W boson connect both theoretically and experimentally, as Γ_W has been extracted from a lineshape analysis using techniques developed for the W mass measure-

Table 2
Tevatron results for M_W. N_W is the number of W boson events observed. Scale and non-scale systematic errors are listed separately.

Experiment	$\int \mathcal{L}dt$ pb^{-1}	N_W	M_W $\mathrm{GeV/c^2}$	$\pm$ stat $\mathrm{GeV/c^2}$	$\pm$ sys $\mathrm{GeV/c^2}$	$\pm$ scale $\mathrm{GeV/c^2}$
CDF Run 0 e	4.4	1130	79.91	0.35	0.24	0.19
CDF Run 0 μ	4.4	592	79.90	0.53	0.32	0.08
CDF Run Ia e	18.2	5718	80.490	0.145	0.130	0.120
DØ Run Ia e	12.8	5982	80.350	0.140	0.165	0.160
CDF Run Ia μ	19.7	3268	80.310	0.205	0.120	0.050
CDF Run Ib e	84	30,100	80.473	0.065	0.054	0.075
DØ Run Ib e	82	28,323	80.440	0.070	0.070	0.065
DØ Run Ib e, forward	82	11,089	80.757	0.107	0.091	0.181
CDF Run Ib μ	80	14,700	80.465	0.100	0.057	0.085

ment. Combining CDF electron and muon data from 1994–95 yields a result with 140 MeV precision [9]:

$$\Gamma_W = 2.04 \pm 0.11 \text{ (stat)} \pm 0.09 \text{ (syst) GeV}. \quad (4)$$

In this measurement, $u < 20$ GeV is required to improve the M_T resolution and to reduce backgrounds.

Figure 3 shows the dependence of the M_T spectrum on Γ_W. In the region $M_T > 100$ GeV/c^2, the lineshape is sensitive to Γ_W but relatively insensitive to uncertainties in the p_T^ν resolution. Thus, Γ_W is extracted from a fit to the region 100 GeV/c^2 $< M_T <$ 200 GeV/c^2, after signal and background templates are normalized to the data in the region 40 GeV/c^2 $< M_T <$ 200 GeV/c^2. Figure 4 shows the fits to the CDF electron and muon data. The upper limit $M_T <$ 200 GeV/c^2 is somewhat arbitrary.

The measurement of Γ_W depends on a precise determination of the transverse mass lineshape. Thus, the same error sources contribute to both the W mass and width measurement. In the following we discuss these sources, concentrating on how they impact the W mass measurement. Run II projections for the individual uncertainties contributing to the W width measurement are presented in section 6.

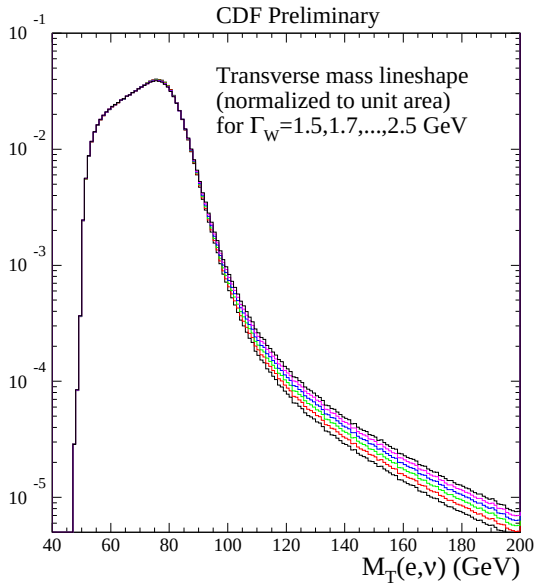

Figure 3. Dependence of the M_T spectrum on Γ_W. Each spectrum is normalized to unit area.

3. Statistical Uncertainties in the M_W Determination

In order to reach the target precision for M_W, considerable luminosity will be required. Presuming that Run II is to deliver an integrated luminosity of 2 fb^{-1}, the statistical precision on M_W can be estimated from the existing data (see Table 2). Figure 5 shows the W statistical uncertainties in these measurements as a function of $1/\sqrt{N_W}$, demonstrating a predictable extrapolation to $N_W \simeq 700,000$ which corresponds to a Run II dataset per experiment per channel. The statistical uncertainty from this extrapolation is approximately 13 MeV/c^2. For a goal of $\pm$30 MeV/c^2 overall uncertainty, this leaves 27 MeV/c^2 available in the error budget which must be accounted for by all systematic uncertainties.

4. Detector-specific Uncertainties in the M_W Determination

After the lepton energy and momentum scales, the modeling of the W recoil provided the largest systematic uncertainty in the CDF Run Ib W mass measure-

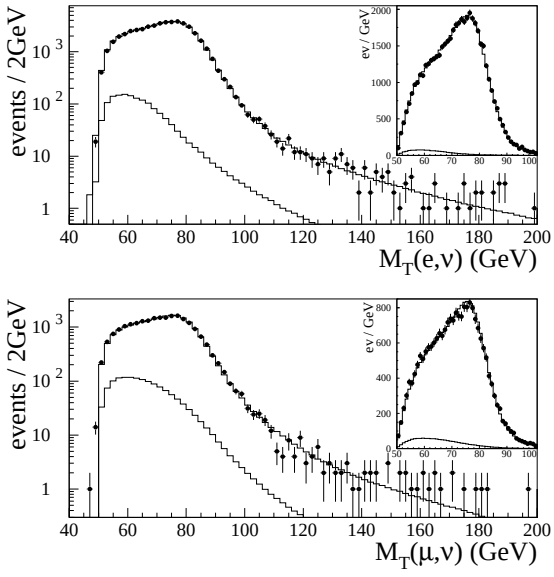

Figure 4. CDF 1994-95 e and μ data, on a semilogarithmic scale, with best fits for Γ_W. The background estimates are also shown. The insets show the Jacobian peak regions on a linear scale.

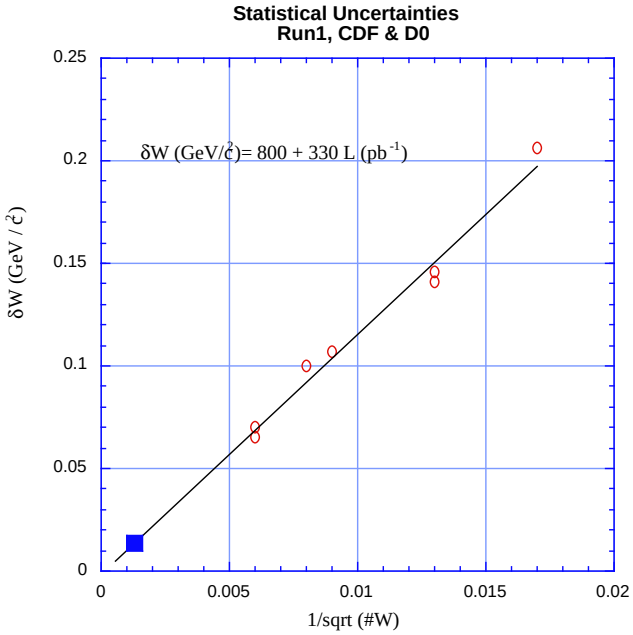

Figure 5. Statistical uncertainties in Run I M_W measurements. Each circle represents either a CDF or DØ measurement. The result of a straight line fit is shown. The shaded box is the approximate extrapolation to a 2 fb^{-1} Run II result.

ment. Since Z statistics dominates this number, it can be expected to be reduced significantly in Run II. Non-Z related recoil systematics were estimated to enter at the 10 MeV/c^2 level, which is probably indicative of the limiting size of this error. The increase in the average number of overlapping minimum bias events in Run II may seriously impact the recoil model systematics, although various detector improvements may partly compensate for this.

Much of the understanding of experimental systematics comes from a detailed study of the Z bosons and hence as luminosity improves, systematic uncertainties should diminish in kind. Certainly, the scale and resolution of the recoil energy against the W come from measurements of the Z system. Likewise, background determination, underlying event studies, and selection biases depend critically, but not exclusively, on Z boson data. Most importantly, the lepton energy and momentum scales depend solely on the Z boson datasets.

Figure 6 shows the CDF and DØ systematic uncertainties for both electrons and muons as a function of $1/\sqrt{N_W}$ and in particular the calorimeter scale uncertainties for electrons. This latter important energy scale determination is currently tied to the determination of fiducial di-lepton decay resonances, notably the Z boson, but also the J/ψ, Υ and the E/p dependence on the energy E, using electrons from W and Z decays. As the statistical precision improves, the dominant feature of the scale determination becomes its value in the region of M_W, so offsets and any low energy nonlinearities become relatively less important and hence reliance on the low mass resonances is reduced. On the other hand, for the muon momentum scale determination, where the observable is the curvature, low mass resonances are also important. Figure 6 suggests that this uncertainty is truly statistical in nature and extrapolates to approximately the 15 MeV/c^2 level. The ability to bound non-linearities using collider data may become a limiting source of error in Run II. Hence, the remaining systematic uncertainties must be controlled to a level of approximately 22 MeV/c^2 in order to reach the overall goal of $\pm$30 MeV/c^2.

Figure 6 also shows the non-scale systematic uncertainties from both the CDF and DØ electron measurements of M_W and the CDF muon measurement. Here the extrapolation is not as straightforward, but there is clearly a distinct statistical nature to these

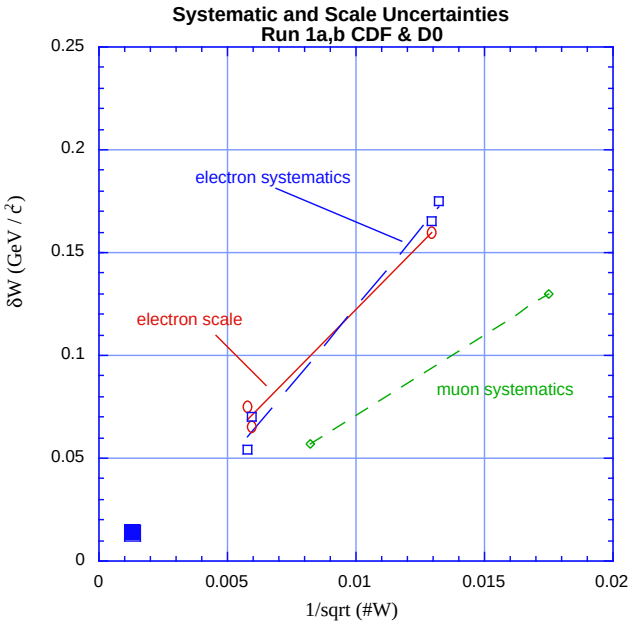

Figure 6. Systematic uncertainties for each Run I M_W measurement. The open squares are the four electron measurements from CDF and DØ, the circles are the scale uncertainties from two DØ electron measurements and the Run Ib CDF measurement, and the diamonds are the systematic uncertainties (excluding scale) for the CDF muon measurements. The large box is the position of the extrapolated statistical uncertainties to the Run II luminosity. The lines are linear fits to each set of points.

errors. That they appear to extrapolate to negative values suggests that the systematic uncertainties may contain a statistically independent component for both the muon and the electron analyses.

For both M_W and Γ_W analyses, the $Z \to \ell\ell$ data constrain both the lepton scales and resolutions and an empirical model of the hadronic recoil measurement. QED corrections are an issue in measuring the Z mass, and the discussion of these corrections should be in terms of the W/Z mass ratio. In a high-precision width measurement, more effort will also be needed to place bounds on possible tails in the lepton and recoil resolution functions. Uncertainty in the recoil measurement is predominantly statistical in how well model parameters are determined. Several cross checks which improve with statistics independently ensure the efficacy of the model.

Selection biases can be studied with various control samples, notably the second lepton originating from Z decays. The QCD background can be also studied by varying cuts and studying control samples. The background from $W \to \tau\nu$ is well understood, and the background from $Z \to \ell\ell$ will be reduced for Run II since the tracking and muon coverages are improved for both experiments.

5. Theoretical Uncertainties in the M_W Determination

The M_T lineshape simulation requires a theoretical model, as a function of Γ_W and M_W, of $\frac{d^3\sigma}{d\hat{s}\ dy\ dp_T}$, including correlations between p_T and $\hat{s}$. For producing high-statistics fitting templates, a weighted Monte Carlo generator is useful, so that M_W, Γ_W, and the p_T spectrum can be varied simply by reweighting events. Because the measurement of the recoil energy against the W, $\vec{u}$, is modeled empirically, the generator does not have to describe the recoil energy at the particle level. A detailed description of final-state QED radiation is important, because bremsstrahlung affects the isolation variables needed to select a clean W sample.

The W and Z p_T spectra are not calculable using perturbation theory at low p_T. In this region, the perturbative calculation must be augmented by a non-perturbative contribution which depends on three parameters (see section 5.2.1) which are tuned to fit the $Z \to \ell\ell$ data. Theoretical guidance is useful for choosing an appropriate set of parameters to vary. A strategy such as has been used in the CDF Run Ib analysis to use theory to extrapolate from the Z p_T distribution to the W p_T distribution seems to limit the effect of theoretical assumptions to ± 5 MeV/c^2.

The parameters of parton distribution functions are also empirical, and seldom have quoted uncertainties. PDF uncertainties seem under control for Run I data but will need improvement to avoid becoming dominant in Run II. More work is needed to determine how both to minimize the impact of PDF uncertainties (e.g. by extending the lepton rapidity coverage of the measurements as done in the DØ analysis [10]) and to evaluate the effects of PDF uncertainties in precision measurements.

To date, *ad hoc* event generators have been used in the W mass and width measurements. In Run II, these measurements will reach a precision of tens of MeV/c^2, requiring much more attention to detail in Monte Carlo calculations. Precision electroweak measurements in Run II should strive to use (possibly to develop) published, well documented Monte Carlo programs that are common to both collider experiments. In particular, the M_W and Γ_W measurements would benefit from a unified generator that incorporates state-of-the-art QED and electroweak calculations, uses a boson p_T

model tunable to Run II data, and correctly handles W bosons that are produced far off-shell.

The W width uncertainty in the M_W measurement could become significant but assuming the SM M_W-Γ_W relation, it won't be a dominant uncertainty.

5.1. Parton Distribution Functions

The transverse mass distribution is invariant under the longitudinal boost of the W boson. However, the incomplete η coverage of the detectors introduces a dependence of the measured M_T distribution on the longitudinal momentum distribution of the produced W's, determined by the PDF's. Therefore, quantifying the uncertainties in PDFs and the resulting uncertainties in the W mass measurement is crucial.

5.1.1. Constraining PDFs from the Tevatron data

The measurement of the W charge asymmetry at the Tevatron, which is sensitive to the ratio of d to u quark densities in the proton, is of direct benefit in constraining PDF effects in the W mass measurement. This has been demonstrated by the CDF experiment. Following Ref. [11], they made parametric modifications to the MRS family of PDFs. These modifications with retuned parameters are listed in Table 3 and their predictions are compared to the W lepton charge asymmetry measurement and the NMC d/u data [12] in Fig. 7. From the variation among the six reference PDFs, an uncertainty of 15 MeV/c^2 was taken which is common to the electron and muon analyses.

Since the Run Ib charge asymmetry data is dominated by statistical uncertainties, we expect a smaller uncertainty for the Run II measurement. Measurements of Drell-Yan production at the Tevatron can be used to get further constraints on PDFs.

Table 3
Reference PDFs and modifications

PDF set	Modification
MRS-T	$d/u \to d/u \times (1.07 - 0.07e^{-8x})$
MRS-R2	$d/u \to d/u + 0.11x \times (1 + x)$
MRS-R1	$d/u \to d/u \times (1.00 - 0.04e^{-\frac{1}{2}(\frac{(x-0.07)}{0.015})^2})$

5.1.2. Reducing the PDF uncertainty with a larger η coverage

Since the PDF uncertainty comes from the finite η coverage of the detectors, it is expected to decrease with the more complete rapidity coverage of the Run II detectors. The advantage of a larger rapidity coverage has been demonstrated by the DØ experiment: the uncertainty on the W mass measurement using their central calorimeter was 11 MeV/c^2, while that using both the central and end calorimeter was 7 MeV/c^2. With the upgraded calorimeters and trackers for the range $|\eta| > 1$, the CDF experiment can measure the W mass over a larger rapidity range in Run II.

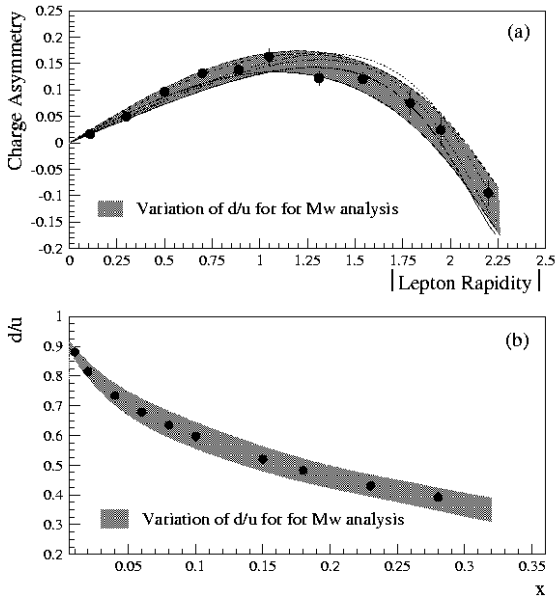

Figure 7. (a) The CDF measurement of the W lepton charge asymmetry. (b) The NMC d/u data evolved to $Q^2 = M_W^2$. The gray bands represent the range spanned by the six reference PDFs considered.

5.1.3. A Global Approach

There has been a systematic effort to map out the uncertainties allowed by available experimental constraints, both on the PDFs themselves and on physical observables derived from them. This approach will provide a more reliable estimate and may be the best course of action for precision measurements such as the W mass or the W production cross section. This has been emphasized at this workshop by the Parton Distributions Working Group [13].

5.2. W Boson Transverse Momentum

The neutrino transverse momentum is estimated by combining the measured lepton transverse momentum and the W recoil: $\vec{p}_T^{\,\nu} = -(\vec{p}_T^{\,l} + \vec{u})$. It is clear therefore that an understanding of both the underlying W boson transverse momentum distribution and the corresponding detector response, usually called the recoil model, is crucial for a precision W mass measure-

ment. For the CDF Run Ib W mass measurement, the systematic uncertainties from these two sources were estimated to be $15-20$ MeV/c^2 and $35-40$ MeV/c^2, respectively, in each channel [14].

5.2.1. Extracting the p_T^W Distribution

The strategy employed in Run I, which is expected to be used also in Run II, is to extract the underlying p_T^W distribution from the measured p_T^Z distribution (Y is the weak boson rapidity):

$$\frac{d^2\sigma}{dp_T^W\,dY} = \frac{d^2\sigma}{dp_T^Z dY} \times \frac{d^2\sigma/dp_T^W\,dY}{d^2\sigma/dp_T^Z dY}\,, \qquad (5)$$

where the ratio of the W and Z differential distributions is obtained from theory. This method relies on the fact that the observed p_T^Z distribution suffers relatively little from detector smearing effects, allowing fits to be performed for the true distribution. The CDF Run Ib data and the results of a Monte Carlo simulation using the best fit parameters are compared in Fig. 8.

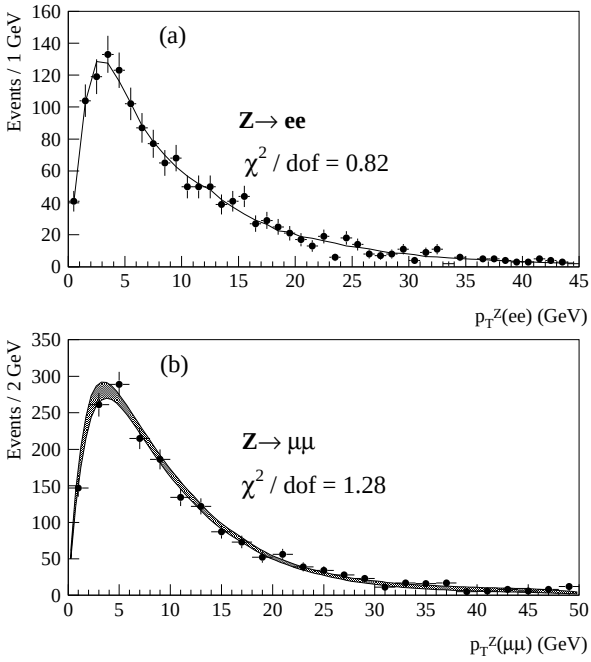

Figure 8. The observed p_T^Z distributions in the electron and muon channels using the CDF Run Ib data. Also shown are the curves for the Monte Carlo simulation using the best fit parameters for the input p_T^Z distribution.

The experimental uncertainties, as in many aspects of the W mass measurement, are dominated by the available $Z \to \ell^+\ell^-$ statistics and should scale correspondingly with the delivered luminosity in Run II. Theoretical uncertainties in the ratio of W to Z transverse momentum distributions contribute a further $\mathcal{O}(5)$ MeV/c^2 to the overall error. The two sources of uncertainty are compared for the CDF Run Ib $W \to \mu\nu$ analysis in Fig. 9.

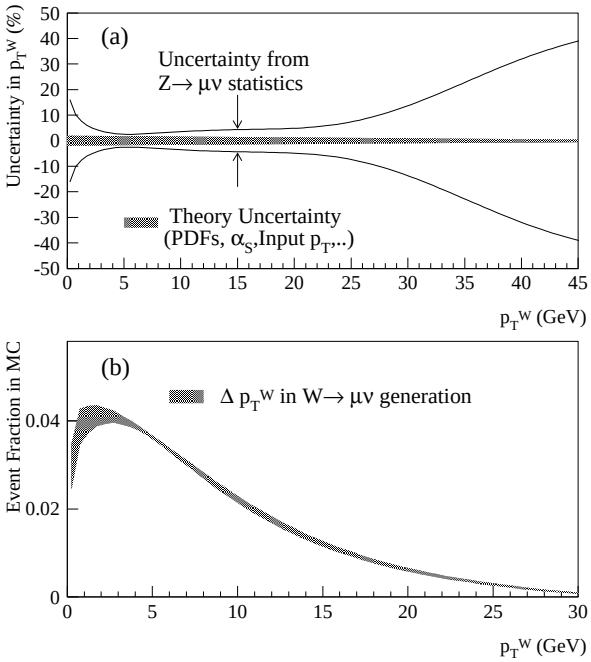

Figure 9. (a) A comparison of the two sources of uncertainty on the derived p_T^W distribution. (b) The p_T^W distribution extracted for the CDF Run Ib $W \to \mu\nu$ mass measurement.

The ratio of W to Z transverse momentum distributions used in Eq. (5) is taken from resummation calculations, which attempt to resum terms corresponding to multiple soft and collinear gluon emission to all orders. They thereby include the dominant contribution to the cross section at small boson p_T that is missing in fixed order calculations. These perturbative calculations need to be augmented by a non-perturbative contribution which, in the case of impact-parameter (b) space resummations, is typically parameterized as a Sudakov form-factor with the following form:

$$F^{NP} = \exp\left[-g_1 b^2 - g_2 b^2 \ln(Q/2Q_0) - g_1 g_3 b \ln(100 x_1 x_2)\right], \qquad (6)$$

where Q_0 is a low scale of $\mathcal{O}$(few) GeV and the parameters g_1, g_2 and g_3 must be obtained from fits to the data [15]. DØ has shown that the Run I p_T^Z data is as sensitive to g_1 and g_2 as the low-energy Drell-Yan data that has largely been used to constrain these parameters in the past [16]. The Run II data will therefore provide significant new constraints on the form of the non-perturbative contribution to the p_T^W distribution.

Moreover, recent theoretical developments in combining the advantages of $b-$space and p_T-space resummation formalisms may provide a better theoretical framework for extracting the underlying p_T^W distribution in Run II [17].

In short, the precision Z data available in Run II together with further theoretical advances will reduce in a number of ways the systematic uncertainties due to the knowledge of the p_T^W distribution, perhaps down to the level of ~ 5 MeV/c^2.

5.3. QCD Higher Order Effects

The W bosons are treated as spin-one particles and decay via the weak interaction into a charged lepton (e, μ or τ) and a neutrino. The charged leptons are produced from the W decay with an angular distribution determined by the $\mathcal{O}(\alpha_s^2)$ calculation of [18] which, for W^+ bosons with a helicity of –1 with respect to the proton direction, has the form :

$$\frac{d\sigma}{d\cos\theta_{\rm CS}} \propto 1 + a_1(p_T)\cos\theta_{\rm CS} + a_2(p_T)\cos^2\theta_{\rm CS} \qquad (7)$$

where p_T is the transverse momentum of the W and $\theta_{\rm CS}$ is the polar direction of the charged lepton with respect to the proton direction in the Collins-Soper frame [19]. a_1 and a_2 are p_T dependent parameters. For $p_T = 0$, $a_1 = 2$ and $a_2 = 1$, providing the angular distribution of a W boson fully polarized along the proton direction. For the p_T^W values relevant to the W mass analysis ($p_T^W < 30$ GeV/c), the change in W polarization as p_T^W increases only causes a modest change in the angular distribution of the decay leptons [18].

While the uncertainty associated with the change in the angular distribution of the W decay lepton due to higher order QCD corrections (a few MeV/c^2) has been negligible for the Run I measurements, it can not be ignored for the Run II measurements (see the Photon and Weak Boson Physics working group report for more details).

5.4. QED Radiative Effects

5.4.1. Introduction

The understanding of QED radiative corrections is crucial for precision W mass measurements at the Tevatron. The dominant process is final state radiation (FSR) from the charged lepton, the effect of which strongly depends on the lepton identification criteria and the energy or momentum measurement methods employed. Calorimetric energy measurements, such as those employed in the electron channel, are more inclusive than track based momentum measurements used in the muon channel and the effect of FSR is consequently reduced. In the CDF Run Ib W mass measurement the mass shifts due to radiative effects were estimated to be -65 ± 20 MeV/c^2 and -168 ± 10 MeV/c^2 for the electron and muon channels, respectively [14]. These effects will be larger in Run II due to increase in tracker material in CDF and magnetic tracking in DØ.

The Monte Carlo program used for the Run I W mass measurement incorporated a calculation of QED corrections by Berends and Kleiss [20]. This treatment, however, does not include initial state radiation (ISR) and has a maximum of one final state photon. The effect of multiple photon emission was estimated by comparing the calculation of Berends and Kleiss to `PHOTOS` [21], a universal Monte Carlo program for QED radiative corrections that can generate a maximum of two final state photons. Likewise, the effect of ISR and other missing diagrams was estimated by comparing the calculation of Berends and Kleiss to a full $\mathcal{O}(\alpha)$ calculation by Baur *et al.* [22]. The resulting systematic uncertainties on the W mass are estimated to be 20 MeV/c^2 and 10 MeV/c^2 in the electron and muon channels, respectively [14]. Clearly these systematic uncertainties become much more significant in the context of statistical uncertainties of $\mathcal{O}(10)$ MeV/c^2 expected for 2 fb^{-1} in Run II.

The next section describes in more detail the calculation by Baur *et al.*, which forms the basis for a new event generator. Some studies of the effects of QED radiation on the W mass measurement are presented in section 5.4.4. Section 5.4.5 briefly outlines some work in progress that should further reduce systematic uncertainties due to radiative corrections in Run II.

5.4.2. `WGRAD`

`WGRAD` is a program for calculating $\mathcal{O}(\alpha)$ electroweak radiative corrections to the process $q\bar{q}' \to W^\pm \to \ell^\pm\nu$, including the real photon contribution $q\bar{q}' \to \ell^\pm\nu\gamma$. Both ISR from the incoming quarks, FSR from the final state charged lepton, and interference terms are included. Many more details can be found in [22].

The most important generator level cuts are on the final state photon energy and collinearity for radiative events. The photon energy cut, controlled by the parameter δ_s, is made on the fraction of the parton's energy carried by the emitted photon in the parton-parton center of mass system: $E_\gamma^* >$

Table 4
The fraction of $q\bar{q}' \to \mu\nu(\gamma)$ events containing a final state photon for different final state photon soft and collinear cuts. Events are generated with ISR only, FSR only, and with a full treatment of QED radiation.

Photon Cuts	ISR	FSR	Full
Photon Cuts	ISR	FSR	Full
$\delta_s = 0.01, \delta_c = 0.01$	1.6%	9.4%	11.1%
$\delta_s = 0.01, \delta_c = 0.001$	2.5%	9.4%	12.0%
$\delta_s = 0.001, \delta_c = 0.001$	4.1%	15.5%	20.0%
$\delta_s = 0.001, \delta_c = 0.0001$	5.2%	15.5%	21.3%

$\delta_s\sqrt{\hat{s}}/2$. The photon collinearity cut, controlled by the parameter δ_c, is made on the angle between the charged fermion and the emitted photon in the same frame: $\cos\theta^* < 1 - \delta_c$. However, final state collinear singularities are regulated by the finite lepton masses and the above cut is only implemented for quarkonic radiation when ISR is included. The fraction of radiative events corresponding to different photon cuts is given in Table 4 for the process $q\bar{q}' \to \mu\nu(\gamma)$ at $\sqrt{s} = 2$ TeV. Loose fiducial cuts $p_T^\mu > 10$ GeV/c, $|\eta^\mu| < 2$ and $p_T^\nu > 10$ GeV/c have been applied. The inclusion of ISR increases the photon yield by around 30%, depending on the soft and collinear photon cuts applied. The fractions are significantly higher for the process $q\bar{q}' \to e\nu(\gamma)$ in the cases that FSR is included. The effect on the fitted W mass of the inclusion of ISR is examined in section 5.4.4.

5.4.3. Event Generation

WGRAD has been turned into an event generator through a suitable unweighting scheme described extensively in [23]. A significant complication is the presence of negative $q\bar{q}' \to \ell^\pm\nu$ event weights in the program which, while expected to cancel with positive $q\bar{q}' \to \ell^\pm\nu\gamma$ event weights in the calculation of physical observables, nevertheless appear separately in the unweighting procedure. The approach here has been to unweight the negative weight events in a similar manner to the positive weight events, such that the output consists of both positive and negative unit weight events. The fraction of negative weight events, plotted in Fig. 10 for the process $q\bar{q}' \to \mu\nu(\gamma)$, depends strongly on the soft and collinear photon cuts applied. It is not significantly different for $q\bar{q}' \to e\nu(\gamma)$ events. The effect of negative weights on the fitted W mass is examined in the next section.

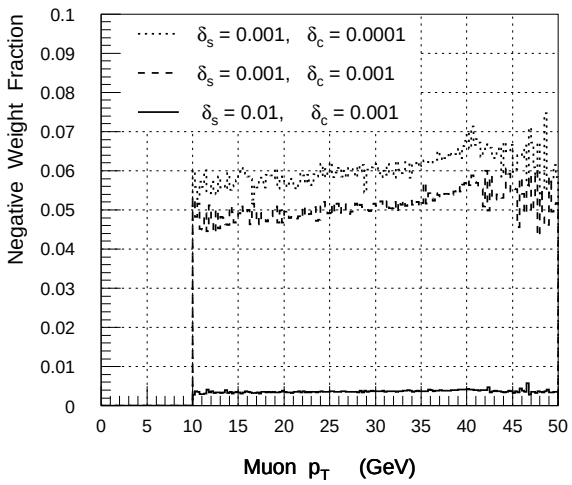

Figure 10. The negative weight fraction versus p_T^μ for different soft and collinear photon cuts.

5.4.4. The Effect of QED Radiation on the Measured W Mass

WGRAD has been used to generate large $W \to \mu\nu$ event samples for the purposes of investigating the effect of QED radiation on the measurement of the W mass. The events have been generated at $\sqrt{s} =$ 1.8 TeV in order to make use of the CDF Run I W production model and detector smearing parameterizations. The W production model, extracted from the Run I Drell-Yan data, is used to smear the true W transverse momentum. The CDF recoil model is then used to translate this into a measured $p_T(W)$, which is combined with the smeared lepton and photon momenta to form a realistic transverse mass distribution. Loose fiducial cuts $p_T^\mu > 20$ GeV/c, $|\eta^\mu| < 2$ and missing-$E_T > 20$ GeV are applied. To simulate the CDF muon identification criteria, events are rejected if a photon with $E_\gamma > 2.0$ GeV is found within an $\eta - \phi$ cone of radius 0.25 around the muon. Low energy photons inside the cone are not included in the measurement of the muon p_T, as is the case experimentally.

The unweighted event samples, all generated with $M_W = 80.4$ GeV/c^2 and $\Gamma_W = 2.1$ GeV, are divided into "data" and "Monte Carlo" sub-samples and fitted against one another in pseudo-experiments. The fit is to the transverse mass distribution in the range $50 < M_T < 100$ GeV/c^2. For a number of events in the transverse mass fit region equal to that in the CDF Run Ib $W \to \mu\nu$ analysis, the resulting statistical error is very similar.

As a cross check of this procedure, "data" and

Table 5
The results of pseudo-experiments generated by WGRAD with different treatments of QED radiative effects. Further details are given in the text.

	"Data"	"Monte Carlo"	Fit Result
(a)	FULL; $\delta_s = 0.01, \delta_c = 0.01$	FULL; $\delta_s = 0.01, \delta_c = 0.01$	80.4030 ± 0.0069 GeV/c^2
(b)	FULL; $\delta_s = 0.01, \delta_c = 0.01$	FULL no neg.; $\delta_s = 0.01, \delta_c = 0.01$	80.4027 ± 0.0069 GeV/c^2
(c)	FSR only; $\delta_s = 0.01, \delta_c = 0.01$	FULL; $\delta_s = 0.01, \delta_c = 0.01$	80.392 ± 0.006 GeV/c^2
(d)	FSR only; $\delta_s = 0.001, \delta_c = 0.001$	FULL; $\delta_s = 0.01, \delta_c = 0.01$	80.381 ± 0.006 GeV/c^2
(e)	FULL; $\delta_s = 0.001, \delta_c = 0.001$	FULL; $\delta_s = 0.01, \delta_c = 0.01$	80.389 ± 0.009 GeV/c^2
(f)	FULL no neg.; $\delta_s = 0.001, \delta_c = 0.001$	FULL; $\delta_s = 0.01, \delta_c = 0.001$	80.399 ± 0.009 GeV/c^2

"Monte Carlo" samples generated with identical cuts are fitted against one another, with the result shown in Table 5(a). It is interesting to note that if the negative weight events, which occur at the 0.2% level in the "Monte Carlo" sample, are removed, the fit result changes by less than 0.5 MeV/c^2 (Table 5(b)).

Table 5(c) shows the result of fitting "data" generated with FSR only. The shift in the fitted W mass of ≈ 8 MeV/c^2 is consistent with the estimate given in [14] of the effect of ISR on the fitted W mass, although the uncertainties here are rather large. If the soft and collinear cuts are reduced in the "data" sample, as shown in Table 5(d), the fitted W mass shifts significantly downwards. This is to be expected since the track based muon p_T measurement does not incorporate collinear photons. The setting of soft and collinear photon cuts is therefore particularly important in the generation of $W \to \mu\nu$ Monte Carlo samples.

The fits shown in Table 5(e) and (f) are performed in order to examine the effect of negative weights on the fit when, as in the case of this "data" sample, negative weights are present at the 5% level. When the negative weight events are excluded from the fit, the result changes by 10 MeV/c^2. The larger shift in the fitted W mass with respect to Table 5(b) is commensurate with the larger negative weight fraction in this sample.

5.4.5. Work in Progress

A remaining source of systematic uncertainty due to QED radiation is the effect of multiple photon emission. As discussed above, this has previously been estimated by comparing the Berends and Kleiss single photon calculation with the results of running the PHOTOS algorithm. Recently, however, complete matrix element calculations of the processes $q\bar{q}' \to \ell^{\pm}\nu\gamma\gamma$ and $q\bar{q} \to \ell^+\ell^-\gamma\gamma$ have been performed [24]. It may be possible in the future to do detailed comparisons of the results of these calculations and the PHOTOS algorithm, in order to arrive at a better constrained systematic uncertainty due to multiple photon emission.

Furthermore, a complete set of $\mathcal{O}(\alpha)$ electroweak radiative corrections to the process $q\bar{q} \to \ell^+\ell^-$, including the real photon contribution $q\bar{q} \to \ell^+\ell^-\gamma$, will soon be available. This will enable a consistent Monte Carlo description of the W data and the Z data, upon which the W mass analysis crucially depends for the understanding of gauge boson production and the calibration of the detectors.

5.4.6. Summary and Conclusions

Systematic uncertainties due to QED radiative effects currently run at the level of ≈ 20 MeV/c^2 in the electron channel and ≈ 10 MeV/c^2 in the muon channel. A large contribution to this uncertainty is the effect of ISR and interference terms, which are not present in the Berends and Kleiss calculation and the PHOTOS algorithm that have previously been used in W production Monte Carlo programs.

A full $\mathcal{O}(\alpha)$ calculation by Baur *et al.* has been used as the basis for a new event generator. The results of several pseudo-experiments generated with different treatments of QED radiative effects agree with previous estimates. They show that negative weights need to be treated carefully, especially in the case of very small soft and collinear photon cuts.

Further studies of QED radiative corrections to W production will continue as new calculations become available. It is clear, however, that the use of new programs such as WGRAD could significantly reduce systematic uncertainties due to QED radiative corrections in Run II, either through explicit corrections being applied to the extracted W mass, or through

their use in new Monte Carlo event generators. The remaining systematic uncertainties due to QED corrections might then be reduced to the level of 5 MeV/c^2 and 10 MeV/c^2 in the muon and electron channels, respectively.

6. Summary of Run II Expectations

As has been discussed in previous sections, many of the systematic uncertainties in the W mass measurement approximately scale with statistics. These are listed in Table 6 for the Run Ib CDF muon analysis and should scale to $\approx$ 20 MeV/c^2 for an integrated luminosity of 2 fb^{-1}. With reasonable assumptions for the size of non-scaling systematics such as those due to PDFs and higher order QED effects, a 40 MeV/c^2 measurement in the muon channel by each experiment seems achievable. The systematic uncertainties in the electron channel are less easy to extrapolate given the particular sensitivity to calorimeter scale non-uniformities in this channel and the extra material in the Run II tracking detectors. The detailed understanding of detector performance is of course difficult to anticipate, although it is clear that both scalable and non-scaling systematics would be easier to understand if fast Monte Carlo generators including all the relevant effects were available.

Table 6
Errors on the CDF Run Ib muon W mass which scale statistically, in MeV/c^2.

Source	error
Fit statistics	100
Recoil model	35
Momentum resolution	20
Selection bias	18
Background	25
Momentum scale	85

The individual uncertainties for the Run Ib Γ_W measurement are listed in Table 7 together with their projections for 2 fb^{-1}. All but the last three sources of error are constrained directly from collider data, and hence should scale roughly as $1/\sqrt{\mathcal{L}}$. While the last three uncertainties may decrease somewhat as new measurements and calculations become available, they will not scale statistically with the Run II dataset. Assuming no improvement in these three uncertainties, while all others scale statistically, each experiment can make a $\sim$ 40 MeV width measurement, combining e and μ channels for a 2 fb^{-1} dataset.

Table 8
Dominant uncertainties for contrasting components of the DØ M_W determination. The quantities shown are the shift in M_W for a 1σ change in the relevent parameter. The EM resolution term refers to the sampling term for the resolution function. Taken from Ref. [25].

Source	$\delta M_W(M_T)$	$\delta M_W(p_T^e)$
p_T^W	10	50
EM resolution	23	14
hadron scale	20	16
hadron resolution	25	10
backgrounds	10	20

7. Other Methods of Determining M_W at the Tevatron

While the traditional transverse mass determination has been the optimal technique for the extraction of M_W in the low-luminosity running at hadron colliders, other techniques have been or may be employed in the future. These methods may shuffle or cancel some of the systematic and statistical uncertainties resulting in more precise measurements.

7.1. Transverse Momentum Fitting

As noted above, the most obvious extensions of the traditional transverse mass approach to determining M_W are fits of the Jacobian kinematical edge from the transverse momentum of both leptons. DØ has measured M_W using all three distributions and the uncertainties are indeed ordered as one would expect: The fractional uncertainties on M_W from the DØ Run I measurements for the three methods of fitting are: 0.12% (M_T), 0.15% (p_T^e), and 0.21% (p_T^ν). As expected, the p_T^e method is slightly less precise than the transverse mass. However, for a central electron ($|\eta| < 1$), the uncertainty in the p_T^e measurement due to the p_T^W model is 5 times that in the M_T measurement. As can be seen from Table 8, this is nearly balanced by effects from electron and hadron response and resolutions which are relatively worse for M_T. Accordingly, when there are sufficient statistics to enable cuts on the measured hadronic recoil, the measurement uncertainty from the p_T^W model might be better controlled and enable the p_T^e measurement to compete favorably with the M_T measurement which relies so heavily on modeling of the hadronic recoil. In order to optimize the advantages of all three measurements, the DØ final Run I determination of M_W

Table 7
Sources of error for CDF 1994-95 Γ_W measurement and extrapolations to 2 fb^{-1}. The last three uncertainties are common to the e and μ analyses.

	CDF 1994-95 ($\rightarrow$ 2fb^{-1})	
Source	$\Delta\Gamma$ (e, MeV)	$\Delta\Gamma$ (μ, MeV)
Statistics	125 ($\rightarrow$ 30)	195 ($\rightarrow$ 45)
Lepton E or p_T non-linearity	60	5
Recoil model	60	90
W P_T	55	70
Backgrounds	30	50
Detector modeling, lepton ID	30	40
Lepton E or p_T scale	20	15
Lepton resolution	10	20
PDFs (common)	15	15
M_W (common)	10	10
QED (common)	10	10
Uncorrelated systematic	112 ($\rightarrow$ 25)	133 ($\rightarrow$ 30)
Correlated systematic	21	21
Total systematic	115 ($\rightarrow$ 33)	135 ($\rightarrow$ 37)
Total stat + syst	170 ($\rightarrow$ 45)	235 ($\rightarrow$ 60)

combined the separate results [25].

The resolution sensitivity for muon measurements is even less than that for electrons so that has the benefit of slightly favoring a transverse mass measurement with muons over that for electrons.

7.2. Ratio Method

DØ has preliminarily determined M_W by consideration of ratios of W and Z boson distributions which are correlated with M_W [26]. The principle is that one can cancel common scale factors in ratios and directly determine the quantity $r^{meas} \equiv \frac{M_W}{M_Z}$, which can be compared with the precise LEP M_Z^{LEP}. The quantities that have been considered are:

1. $r(M_T)$ and $r(p_T)$, which has the advantage of being well-studied [27]. There are challenges with this approach which will be discussed below.

2. $r(E^e)$ which has the advantage that the peak of the distribution is precisely correlated with M_W, but the disadvantage that statistical uncertainty washes out the position of that peak.

3. The difference of transverse mass distributions (not as precise as ratios).

The procedure is to compare two distributions, one for W bosons and a similarly constructed one for Z bosons, for example, $f^{W,Z}(x)$ as a function of a given variable, such as $x = M_T$ or $x = p_T^e$. Practically speaking, the Z boson decay electrons are scaled by a factor s and $f^Z(x,s)$ is compared with $f^W(x)$ as a function of x, for different trial values of s. A statistical measure (the Kolmogorov-Smirnov test) is calculated for each s and the value of the highest Kolmogorov-Smirnov probability, s^{best}, is declared to be r^{meas} and the desired mass is then extracted from $M_W = r^{meas} \times M_Z^{LEP}$. In principle, minimal Monte Carlo fitting is required, as the measurement is performed with data.

Figure 11 shows the idea with an unsmeared Z boson transverse mass distribution compared to a simulated (unsmeared) W boson distribution. Various values of s lead to various mismatches between $f^W(M_T)$ and $f^Z(M_T)$ which can be characterized by a Kolmogorov-Smirnov probability as a function of $M_W = s \times M_W^{LEP}$. This probability distribution for an ensemble of 100 Monte Carlo experiments is shown in Fig. 12 resulting in an RMS of 40 MeV/c^2.

However, there are challenges to be faced using this technique.

- Many systematic effects cancel in this method, such as electromagnetic scale, hadronic scale, angular scale, luminosity effects. However, these are first-order cancellations, some of which in the end are not sufficient: the second order effects from these quantities must be considered. Likewise, most resolutions have additive terms which do not cancel in a ratio.

- The statistical precision of the Z sample is directly propagated into the resultant overall δM_W, in contrast to the traditional approach where the Z boson statistics is a component of various of the measured resolutions.

- The detector modeling must take into account

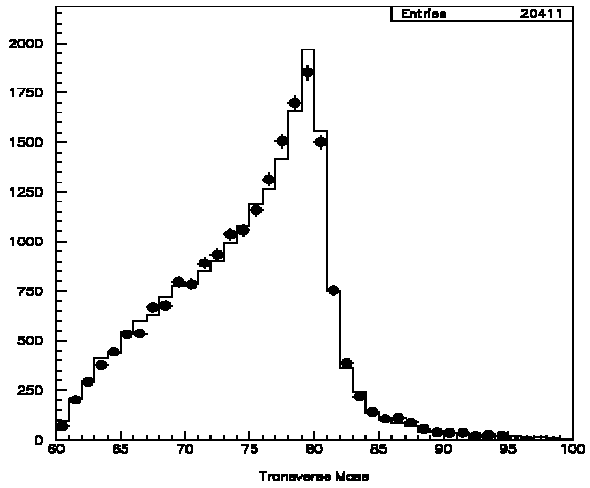

Figure 11. For unsmeared Monte Carlo events, the transverse mass of simulated W bosons (histogram) is overlayed with that of Z boson (dots) events in which the electron has been scaled by a factor which produces the best match.

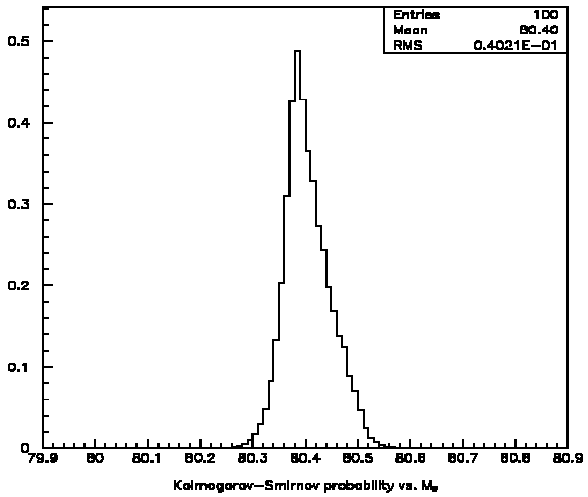

Figure 12. The Kolmogorov-Smirnov probability distribution for various scales in a comparison of W and Z boson unsmeared events corresponding to 100 experiments. The RMS is 40 MeV/c^2 for 20000 events.

small, but important differences between Z and W events such as underlying event, resolutions, efficiencies, acceptances, and the effects of the "extra" electron in Z boson events which complicates underlying event and recoil measurements.

- From the physics model, there are also differences between the two samples which must be considered, such as the fact that the production of Z and W bosons take place from the annihilation of like and unlike flavored quarks, respectively and that weak asymmetries lead to different decay angular distributions.

- Particularly difficult is the need to "extra-smear" the electrons from Z boson decays. This is due to the fact that p_T^e values for the heavier Z boson are harder, resulting in a different average resolution smearing. This same effect is true for the recoil distributions between Z and W bosons.

- Finally, the acceptances for the two bosons are different since there are potentially two opportunities to select a Z boson event at the trigger and event selection stages. Similarly, there is an acceptance difference in the opposite direction due to electrons in Z bosons being lost in cracks between the CC and EC calorimeters in the DØ detector.

An analysis from Run Ia data from the DØ experiment has been done [26]. Figure 13 shows data for the scaled comparison and the unscaled original distributions. Electrons from the W boson events were selected to have $p_T^e > 30$ GeV/c, while those from Z boson events, must satisfy $p_T^e > 34.1$ GeV/c. Electrons from the W sample and at least one electron from the Z samples were required to be in the central calorimeter. This results in 5244 W bosons and 535 Z boson events. Backgrounds are subtracted according to the traditional analysis. "Extra-smearing" is done for each accepted Z boson event (twice, for both electrons) 1000 times, using a different random seed for each smearing. Differences in the W and Z boson production mechanisms and acceptances result in an effective correction of 109 MeV/c^2, while the difference in radiative corrections results in an effective correction of -116 MeV/c^2. The magnitude of these corrections is not very different from corrections within the traditional technique and the demand on knowing the uncertainties in them is similarly stringent. Figure 14 shows the probability distribution for the result. The preliminary result from this analysis for central, Run Ia electrons is

$$M_W = 80.160 \pm 0.360 \pm 0.075 \text{ GeV/c}^2.$$

Comparison with the traditional Run Ia result from the same data is readily made, but most appreciated

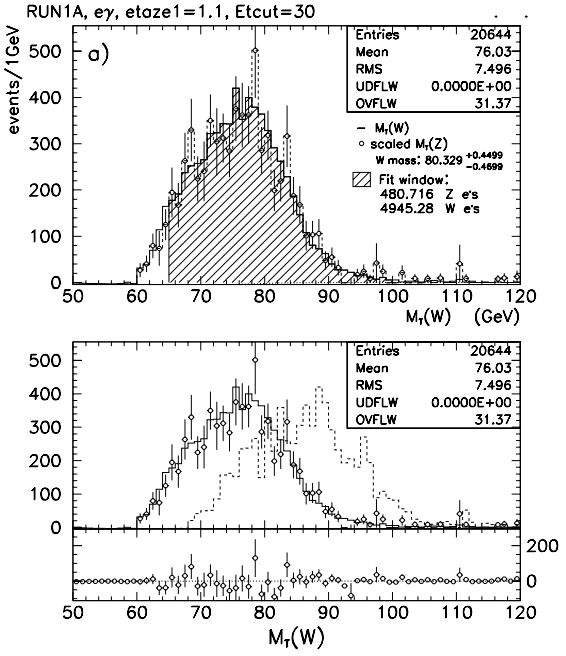

Figure 13. (a) The transverse mass distribution of W (solid) and scaled Z (dots) bosons is shown along with the hatched fit window. (b) The original distributions are shown, along with their difference. The Z distribution has been normalized to that of the W boson sample.

with a slightly different interpretation of the Run Ia uncertainties. The Run Ia result [28] from Table 2 is

$$80.350 \pm 0.140 \pm 0.165 \pm 0.160 \text{ GeV/c}^2$$

where the first error is the statistical uncertainty (from W events), the second is the systematic uncertainty and the third is the electron scale determination. It is important to note that the scale uncertainty is almost completely dominated by the Z boson statistics. Therefore, as a statistical uncertainty, it can be combined with the W uncertainty of 140 MeV/c^2 for the purposes of comparison with the ratio method. This results in an overall "statistical" uncertainty of 212 MeV/c^2. Now, the stronger systematic power of the ratio method is apparent (75 versus 165 MeV/c^2) and the poorer statistical power (360 versus 212 MeV/c^2) is also evident.

7.2.1. Prospects for Run II

This apparent systematic power of the ratio method can only fully be realized in high luminosity running, such as Run II. The ratio method analysis of the

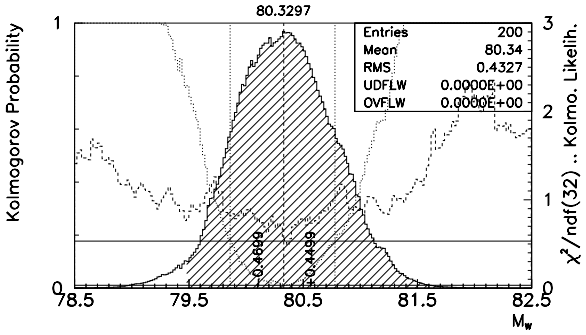

Figure 14. The Kolmogorov probability distribution (hatched) is shown as a function of the W boson mass used as a scale factor. The dotted curve is the Kolmogorov Likelihood and the dashed curve is the χ^2/ndf distribution (right axis).

DØ Run Ib data was recently completed [29]. The Run Ib sample has 82 pb^{-1} of data (1994–1995 data set), 33,137 W and 4,588 Z events (electrons in both Central and End Calorimeters of DØ) after the standard electron selection cuts. The W mass resulting from the ratio fit is $M_W = 80.115 \pm 0.211$ (stat.) $\pm$ 0.050 (syst.) GeV/c^2. The statistical uncertainty is in good agreement with an ensemble study of 50 Monte Carlo samples of the same size (80.36 ± 0.25 GeV/c^2).

Early efforts at predicting the results for a Run II sample of 100,000 W bosons is shown in Fig. 15 with full detector acceptances and resolutions taken into account. The statistical precision from this fit is of the order of 20 MeV/c^2 and the systematic uncertainties may be nearly negligible.

8. Prospects for Measuring M_W at Other Accelerators

8.1. LEP II

The prospects for determination of M_W at LEP II have become fully understood in the last year with the accumulation of hundreds of pb^{-1} at four center of mass energies. Here we review the status as of the Winter 2000 conferences and project the prospects through to the completion of electron-positron running at CERN. For a review, see Ref. [30,31].

8.1.1. Data Accumulation

The annihilation of e^+e^- into W boson pairs occurs via three diagrams: a t-channel neutrino exchange and s-channel Z or γ exchange. The final states from the decays of the two W bosons are: both W bosons decay

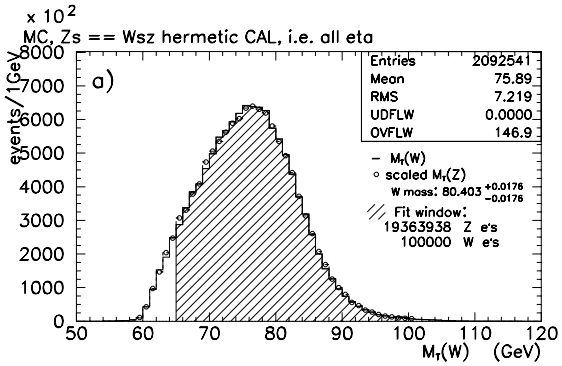

Figure 15. Same as Fig. 13a, but for 100,000 W bosons.

into hadrons ($qqqq$, "4-q" mode); one W decays into quarks, and the other into leptons (e, μ , τ and their neutrinos, "$qq\ell\nu$"); and both W bosons decay leptonically. Collectively, the latter two modes are referred to as "non-q" modes. The efficiencies and sample purities are typically quite high, as shown in Table 9.

Table 9
Efficiencies and sample purity for a representative LEP II experiment (OPAL).

Channel	ϵ (%)	purity (%)
$qqqq$	85	80
$qqe\nu$	85	80
$qq\mu\nu$	87	80-90
$qq\tau\nu$	66	80

The results by Spring 2000 come from running at center of mass energies: 172, 183, 189, and several energies between 190 GeV and 200 GeV. There is recent running above 200 GeV for a total of more than 400 pb^{-1} accumulated per experiment. M_W results are final for all four experiments for the 172 and 183 GeV sets [32–35] and preliminary for the 1998 189 GeV running [36–39]. In addition, ALEPH [40], L3 [41], and OPAL [42] have preliminary results from the collection of runs in the range from 190 GeV to 200 GeV. Table 10 shows the approximate accumulated running to date (July 2000).

There are broadly two methods employed for determining M_W at LEP II. The first method is the measurement of the threshold of the WW cross section and the second is the set of constrained fits possible

Table 10
Approximate accumulated running per experiment. The 2000 totals are current as of the first week in July 2000.

year	beam energy (GeV)	$\int \mathcal{L} dt$ (pb^{-1})
1996	80.5-86	25
1997	91-92	75
1998	94.5	200
1999	96-102	250
2000	100-104	100

for the various measured final states. The latter set of methods constitute the prominent results and employ construction of invariant masses making use of the beam constraints. There are a variety of methods, some of which make use of the constraint $M_{W_1} = M_{W_2}$ and some of which involve sophisticated multivariate analyses. The spirit of approach is much like the strategies employed in the top quark mass analyses of CDF and DØ.

The results are treated separately for the $qq\ell\nu$ and $qqqq$ final states due to the significant differences in systematic uncertainties. Typical uncertainty contributions are listed in Table 11 [43]. Many of the experimental uncertainties, such as scale, background, and Monte Carlo generation, are statistically limited. For example, there is a fixed amount of $\sqrt{s} = M_Z$ running in each running period and that contributes a statistical component to the energy scale uncertainty.

The dominant uncertainty comes from the final state effects in the $qqqq$ channel. Because the outgoing quarks can have color connections among them, the fragmentation of the ensemble of quarks into hadrons are not independent. This leads to an theoretical uncertainty called "Color Reconnection" (CR). In addition, since the hadronization regions of the W^+ and W^- overlap, coherence effects between identical low-momentum bosons originating from different W's due to Bose-Einstein (BE) correlations may be present. The combined total of these two effects is currently accepted to contribute 52 MeV/c^2 of uncertainty to the $qqqq$ results. Ultimately, the non-CR/BE uncertainty will likely be the uncertainty in modeling single-quark fragmentation and associated QCD emission effects.

8.1.2. Results, April 2000

The preliminary results for M_W from the combined data taking through 1999 running period are shown in Table 12. The combined LEP result for the $qq\ell\nu$ channels is [44]:

$$M_W^{qq\ell\nu} = 80.398 \pm 0.039 \pm 0.031 \pm 0.017 \text{ GeV}/c^2$$

Table 11
Typical systematic uncertainties on M_W for a generic LEP II experiment from data sets corresponding to the 189 GeV running. Entries are approximate and broad averages meant to give a relative sense of scale only. The Source labels are generally self-explanatory, with CR/BE standing for "Color Reconnection" and "Bose-Einstein" respectively.

Source	$qq\ell\nu$ (MeV/c^2)	$qqqq$ (MeV/c^2)
ISR	15	15
frag	25	30
4 fermion	20	20
detector	30	35
fit	30	30
bias	25	25
bckgrnd	< 5	15
MC stat	10	10
Subtotal	61	67
LEP	17	17
CR/BE		60
Total	63	85

where the first error is statistical, the second systematic, and the third the LEP energy scale. The combined preliminary result for the $qqqq$ channel is:

$$M_W^{4q} = 80.408 \pm 0.037 \pm 0.031 \pm 0.016 \pm 0.052 \text{ GeV}/c^2$$

where the first three errors are the same as for the $qq\ell\nu$ result and the fourth error is due to the combined CR/BE theoretical uncertainty. Taking into account the correlations, the combined preliminary result from constrained fitting for all channels is:

$$M_W^{4f} = 80.401 \pm 0.027 \pm 0.031 \pm 0.017 \pm 0.018 \text{ GeV}/c^2$$

where the four errors are in the same order as for the $qqqq$ result. The current overall result comes from combining the above with that from the threshold measurement of

$$M_W^{\sigma(E)} = 80.400 \pm 0.220 \pm 0.025 \text{ GeV}/c^2.$$

Here the first error is combined statistical and systematic and the second error is the error due to LEP energy scale. This results in the preliminary overall LEP II (April 2000) value of

$$M_W^{LEP} = 80.401 \pm 0.048 \text{ GeV}/c^2.$$

8.1.3. Prospects for the Future

The current results are preliminary and running is underway at this writing with the end of LEP II scheduled for the beginning of October, 2000. Eventually, the 1999 data will be fully analyzed and, with the accumulation of the final 2000 running, should result in a combined statistical and systematic uncertainty (excluding the CR/BE and LEP contributions) of approximately 35 MeV/c^2 [1]. With the overall contribution of 18 MeV/c^2 and 17 MeV/c^2 from the CR/BE and LEP errors respectively, the ultimate limit from LEP II W boson pair determination of M_W should be approximately 40 MeV/c^2.

Table 12
Preliminary LEP II results for M_W by experiment and according to reconstructed channel. The results are from the combination of 1996-1998 running (all experiments) plus preliminary results from 1999 running for ALEPH, DELPHI, L3, and OPAL.

	M_W (GeV/c^2)	
Experiment	$qq\ell\nu$	$qqqq$
ALEPH	80.435 ± 0.079	80.467 ± 0.086
DELPHI	80.230 ± 0.140	80.360 ± 0.115
L3	80.282 ± 0.102	80.489 ± 0.132
OPAL	80.483 ± 0.078	80.380 ± 0.103

8.2. LHC

It was pointed out several years ago [45] that the LHC has the potential to provide an even more precise measurement of M_W. This suggestion was based on the observations that the precision measurement of M_W at hadron colliders has been demonstrated to be possible; that the statistical power of the LHC dataset will be huge; and that triggering will not be a problem. These authors estimated that M_W could be determined to better than 15 MeV/c^2. More recently, the ATLAS collaboration has studied the question in more detail [46] and arrived at an uncertainty of 25 MeV/c^2, per experiment, in the electron channel alone.

Achieving such precision will require substantial further reduction of theoretical and systematic uncertainties, all of which must be reduced to the $\leq$ 10 MeV level. This includes the contributions from the W production model, parton distributions, and radiative decays, as well as experimental systematics such as the energy-momentum scale of the detector and any complications from underlying energy deposition even in the low luminosity running. While some have questioned whether such "heroic" progress will ever be possible, we would argue that it is futile to debate the question at this time. Rather, the best indicator of future LHC precision will be to see how well the Fermilab experiments manage to deal with the significant improvements in systematics which will be necessary in order to match the anticipated precision for m_t. The point to be made is this: should it prove

necessary to determine the W mass to a precision of 10–20 MeV/c^2, the LHC will have the *statistical power* to continue the hadron collider measurements into this domain. The success of such a program will then depend on

- Consensus in the field that such precision is needed. One such justification might be to distinguish among different models of supersymmetry-breaking using global fits including M_W, the top mass and the light Higgs mass. It is likely that a big parallel effort to push down the top mass uncertainty to the 1 GeV/c^2 level would also then be needed;
- A major, multi-year effort within the LHC experiments in order to understand their detectors and their response to leptons, missing transverse energy and recoil hadrons at the required level. This is a measurement which places heavy burdens on manpower as it requires an understanding of the detector which is more precise than for any other measurement;
- A comparable major effort to reduce the theoretical uncertainties through better calculations, through control-sample measurements, and work on parton distributions.

This is not a program that will be undertaken lightly. But should it turn out to be necessary, the experience of Run II at the Tevatron will be invaluable in carrying it out.

8.3. A Linear Collider

The W mass can be measured at a Linear Collider (LC) in W^+W^- production either in a dedicated threshold scan operating the machine at $\sqrt{s} \approx 161$ GeV, or via direct reconstruction of the W bosons in the continuum ($\sqrt{s} = 0.5-1.5$ TeV). Both strategies have been used with success at LEP II.

In the threshold region, the W^+W^- cross section is very sensitive to the W mass. The sensitivity is largest in the region around $\sqrt{s} = 161$ GeV [47] at which point the statistical uncertainty is given by

$$\delta M_W^{stat} \approx 90 \text{ MeV/c}^2 \left[\frac{\varepsilon \int \mathcal{L} dt}{100 \text{ pb}^{-1}}\right]^{-1/2}. \quad (8)$$

Here, ε is the efficiency for detecting W bosons. For $\varepsilon = 0.67$ and an integrated luminosity of 100 fb^{-1}, one finds from Eq. (8)

$$\delta M_W^{stat} \approx 3.5 \text{ MeV/c}^2. \quad (9)$$

Assuming that the efficiency and the integrated luminosity can be determined with a precision of $\Delta\varepsilon = 0.25\%$ and $\Delta\mathcal{L} = 0.1\%$, M_W can be measured with an uncertainty of [48]

$$\delta M_W \approx 6 \text{ MeV/c}^2, \quad (10)$$

provided that the theoretical uncertainty on the W^+W^- cross section is smaller than about 0.1% in the region of interest.

Presently, the W pair cross section in the threshold region is known with an accuracy of about 1.4% [49]. In order to reduce the theoretical uncertainty of the cross section to the desired level, the full $\mathcal{O}(\alpha)$ electroweak corrections in the threshold region are needed. This calculation is extremely difficult. In particular, currently no practicable solution of the gauge invariance problem associated with finite W width effects in loop calculations exists. The existing calculations which take into account $\mathcal{O}(\alpha)$ electroweak corrections all ignore non-resonant diagrams [50].

If one (pessimistically) assumes that the theoretical uncertainty of the cross section will not improve, the uncertainty of the W mass obtained from a threshold scan is completely dominated by the theoretical error, and the precision of the W mass is limited to [47]

$$\begin{aligned} \delta M_W \approx \delta M_W^{theor} &\approx 17 \text{ MeV/c}^2 \left[\frac{\Delta\sigma}{\sigma} \times 100\%\right] \quad (11) \\ &\approx 24 \text{ MeV/c}^2. \end{aligned}$$

Using direct reconstruction of W bosons and assuming an integrated luminosity of 500 fb^{-1} at $\sqrt{s} = 500$ GeV, one expects a statistical error of $\delta M_W^{stat} \approx 3.5$ MeV/c^2 [51]. Systematic errors are dominated by jet resolution effects. Using $Z\gamma$, $Z \to 2$ jet events where the photon is lost in the beam pipe for calibration, a systematic error $\delta M_W^{syst} < 10$ MeV/c^2 is expected to be achieved. The resulting overall precision of the W boson mass from direct W reconstruction at a Linear Collider operating at an energy well above the W pair threshold is

$$\delta M_W \approx 10 \text{ MeV/c}^2. \quad (12)$$

9. Theoretical Issues at high $\sqrt{s}$

Future hadron and lepton collider experiments are expected to measure the W boson mass with a precision of $\delta M_W \approx 10 - 20$ MeV/c^2. For values of δM_W smaller than about 40 MeV/c^2, the precise definition of the W mass and width become important when these quantities are extracted.

In a field theoretical description, finite width effects are taken into account in a calculation by resumming the imaginary part of the W vacuum polarization. This leads to an energy dependent width. However, the simple resumming procedure carries the risk of

breaking gauge invariance. Gauge invariance works order by order in perturbation theory. By resumming the self energy corrections one only takes into account part of the higher order corrections. Apart from being theoretically unacceptable, breaking gauge invariance may result in large numerical errors in cross section calculations.

In order to restore gauge invariance, one can adopt the strategy of finding the minimal set of Feynman diagrams that is necessary for compensating those terms caused by an energy dependent width which violate gauge invariance [52]. This is relatively straightforward for a simple process such as $q\bar{q}' \to W \to \ell\nu$ [53], but more tricky for $e^+e^- \to W^+W^- \to 4$ fermions, in particular when higher order corrections are included. The so-called *complex mass* scheme [54], which uses a constant, *ie.* an energy independent width, offers a convenient alternative. At LEP II energies, $\sqrt{s} \approx$ 200 GeV, the differences in the $e^+e^- \to 4$ fermions cross section using an energy dependent and a constant width are small. However, at Linear Collider energies, $\sqrt{s} = 0.5 - 2$ TeV, the terms associated with an energy dependent width which break gauge invariance lead to an overestimation of the cross section by up to a factor 3 [54].

For $q\bar{q}' \to W \to \ell\nu$, the parameterizations of the W resonance in terms of an energy dependent and a constant W width are equivalent. The W resonance parameters in the constant width scenario, $\overline{M_W}$ and $\overline{\Gamma_W}$, and the corresponding quantities, M_W and Γ_W, of the parameterization using an energy dependent width are related by a simple transformation [55]

$$\overline{M_W} = M_W \left(1+\gamma^2\right)^{-1/2}, \quad (13)$$

$$\overline{\Gamma_W} = \Gamma_W \left(1+\gamma^2\right)^{-1/2}, \quad (14)$$

where $\gamma = \Gamma_W/M_W$. The W mass obtained in the constant width scenario thus is about 27 MeV/c^2 smaller than that extracted using an energy dependent width.

In the past, an energy dependent W width has been used in measurements of the W mass at the Tevatron [56,57]. The Monte Carlo programs available for the W mass analysis at LEP II (see Ref. [50] for an overview) in contrast use a constant W width. Since the difference between the W mass obtained using a constant and an energy dependent width is of the same size or larger than the expected experimental uncertainty, it will be important to correct for this difference in future measurements.

10. Conclusions

The measurements of the W mass and width in Run I already represent great experimental achievements and contribute significantly to their world average determinations. Close inspection of the various systematic error sources leads us to believe that a W mass measurement in Run II at the 30 MeV/c^2 level per experiment is achievable, and this compares well to the expected uncertainty on the W mass measured at LEP II. Each experiment is expected to measure the W width to a similar precision with 2 fb^{-1} of data.

Alternative methods for determining M_W at the Tevatron have been discussed and may turn out to be more appropriate in the Run II operating environment than the traditional transverse mass fitting approach. Determination of the W mass at the LHC will be extremely challenging, using detectors that are not optimized for this measurement. A future linear collider should do significantly better. Clearly, the W mass and width measurements at the Tevatron in Run II will remain the best hadron collider determinations of these quantities for many years and will compete with the best measurements made elsewhere.

REFERENCES

1. A. Straessner, "Measurement of the Mass of the W Boson at LEP and Determination of Electroweak Parameters", XXXV$^{\text{th}}$ *Rencountres de Moriond*, Electroweak Interactions and Unified Theories, March, 2000, to be published.
2. G. Degrassi, P. Gambino, M. Passera and A. Sirlin, Phys. Lett. **B418**, 209 (1998).
3. J. Erler and P. Langacker, "Status of the Standard Model", hep-ph/9809352.
4. T. Junk, talk given at the "LEP Fest", October 2000.
5. J. Collins, D. Soper and G. Sterman, Nucl. Phys. **B 250**, 199 (1985).
6. J. Smith, W. L. van Neerven and J. A. M. Vermaseren, Phys. Rev. Lett. **50**, 1738 (1983); V. Barger, A. D. Martin and R. J. N. Phillips, Z. Phys. **C 21**, 99 (1983).
7. J. Rosner, M. Worah, T. Takeuchi, Phys. Rev. **D 49**, 1363 (1994).
8. D. Groom *et al.* (Particle Data Group), Eur. Phys. J. **C 15**, 1 (2000).
9. T. Affolder *et al.* [CDF Collaboration], hep-ex/0004017, FERMILAB-PUB-00-085-E, April 2000, to be published in Phys. Rev. Lett.
10. B. Abbott *et al.* [DØ Collaboration], Phys. Rev. Lett. **84**, 222 (2000).
11. "Parton Distributions, d/u, and Higher Twists at High x", U.K. Yang, A. Bodek and Q. Fan, Proceedings of the 33$^{\text{th}}$ Rencontres de Moriond: QCD and High-energy Hadronic Interactions, Les Arcs, France, April 1998 and UR-1518 (1998).

12. A. Arneodo *et al.*, [NMC Collaboration], Nucl. Phys. **B 487**, 3 (1997).
13. Report of the Working Group on Parton Distribution Functions, these Proceedings.
14. T. Affolder *et al.* [CDF Collaboration], hep-ex/0007044, FERMILAB-PUB-00-158-E, July 2000, to be published in Phys. Rev. **D**.
15. G. A. Ladinsky and C.-P. Yuan, Phys. Rev. **D 50**, 4239 (1994).
16. B. Abbott *et al.* [DØ Collaboration], Phys. Rev. **D 61**, 032004 (2000); F. Landry, R. Brock, G. Ladinsky, and C.P. Yuan, hep-ph/9905391 to appear in Phys. Rev **D**.
17. A. Kulesza and W. J. Stirling, J. Phys. G: Nucl. Part. Phys. **26**, 637 (2000) and references therein.
18. E. Mirkes, Nucl. Phys. **B 387**, 3 (1992).
19. J. Collins and D. Soper, Phys. Rev. **D 16**, 2219 (1977).
20. F. A. Berends *et al.*, Z. Phys. **C 27**, 155 (1985); F. A. Berends and R. Kleiss, Z. Phys. **C 27**, 365 (1985).
21. E. Barberio, Z. Wąs, Comp. Phys. Commun. **79**, 291 (1994); E. Barberio, B. van Eijk, Z. Wąs, Comp. Phys. Commun. **66**, 115 (1992).
22. U. Baur, S. Keller, D. Wackeroth, Phys. Rev. **D 59**, 013992 (1999).
23. M. Lancaster and D. Waters, CDF-Note 5240.
24. U. Baur and T. Stelzer, Phys. Rev. **D 61**, 073007 (2000).
25. B. Abbott *et al.* [D0 Collaboration], Phys. Rev. Lett. **84**, 222 (2000) and Phys. Rev. **D 62**, 092006 (2000).
26. S. Rajagopalan and M. Rijssenbeek, "Measurement of the W Mass Using the Transverse Mass Ratio of the W and Z", DØ Note 3000, June, 1996; S. Rajagopalan, "Measurement of the W Mass Using the Transverse Mass Ratio of the W and Z", Division of Particles and Fields Conference, 1996.
27. W. T. Giele and S. Keller, Phys. Rev. **D 57**, 4433 (1998).
28. Phys. Rev. Lett. **77**, 3309 (1996); Phys. Rev. **D 58**, 092003 (1998).
29. D. Shpakov, "A W Boson Mass Measurement Using the Transverse Mass Ratio of the W and Z Bosons in $p\bar{p}$ Collisions at $\sqrt{s} = 1.8$ TeV", Ph.D. Thesis, Stony Brook, August 2000.
30. "LEP W-pair Cross Section and W Mass and Width for Winter 2000 Conferences", LEP WW Working Group, LEPEWWG/WW/00-01, April, 2000.
31. "A Combination of Preliminary Electroweak Measurements and Constraints on the Standard Model", [The LEP Collaborations], CERN-EP-2000-016, January 2000.
32. R. Barate *et al.* [ALEPH Collaboration], Phys. Lett. **B 453**, 121 (1999).
33. M. Acciarri *et al.* [L3 Collaboration], Phys. Lett. **B 454**, 386 (1999).
34. P. Abreu *et al.* [DELPHI Collaboration], Phys. Lett. **B 462**, 410 (1999).
35. G. Abbiendi *et al.* [OPAL Collaboration], Phys. Lett. **B 453**, 138 (1999).
36. ALEPH Collaboration, ALEPH 99-017 CONF 99-012, CERN EP/2000-0145.
37. L3 Collaboration, L3 Note 2520.
38. DELPHI Collaboration, DELPHI 99-64 CONF 251.
39. OPAL Collaboration, Physics Note PN385.
40. ALEPH Collaboration, ALEPH 2000-018 CONF 2000-015.
41. L3 Collaboration, L3 Note 2520.
42. OPAL Collaboration, Physics Note PN422.
43. D. Glenzinski, private communication, March, 1999.
44. The quoted results are not the strict averaging of the data shown in Table 12. Rather it is a sophisticated combination, including systematic uncertainties, of 28 separate measurements including the correlations among experiments.
45. S. Keller and J. Womersley, Eur. Phys. J. **C5**, 249 (1998) [hep-ph/9711304].
46. S. Haywood *et al.*, hep-ph/0003275, Proceedings of the "1999 CERN Workshop on Standard Model Physics (and more) at the LHC", CERN Yellow Report CERN-2000-004, eds. G. Altarelli and M. Mangano.
47. W. J. Stirling, Nucl. Phys. **B 456**, 3 (1995).
48. G. Wilson, Proceedings, Linear Collider Workshop, Sitges, Spain (1999).
49. Z. Kunszt *et al.*, in *"Physics at LEP2"*, CERN Yellow report CERN-96-01, vol. 1, p. 141, hep-ph/9602352 (February 1996).
50. M. W. Grünewald *et al.*, hep-ph/0005309, to appear in the Proceedings of the 1999 LEP2-MC workshop.
51. K. Mönig and A. Tonazzo, Linear Collider Workshop, Padova, Italy, May 2000.
52. U. Baur and D. Zeppenfeld, Phys. Rev. Lett. **75**, 1002 (1995); E. N. Argyres *et al.*, Phys. Lett. **B 358**, 339 (1995); W. Beenakker *et al.*, Nucl. Phys. **B 500**, 255 (1997).
53. D. Wackeroth and W. Hollik, Phys. Rev. **D 55**, 6788 (1997).
54. A. Denner, S. Dittmaier, M. Roth and D. Wackeroth, Nucl. Phys. **B 560**, 33 (1999).
55. D. Bardin, A. Leike, T. Riemann and M. Sachwitz, Phys. Lett. **B 206**, 539 (1988).

56. F. Abe *et al.* [CDF Collaboration], Phys. Rev. Lett. **75**, 11 (1995) and Phys. Rev. **D 52**, 4784 (1995).
57. S. Abachi *et al.* [D0 Collaboration], Phys. Rev. Lett. **77**, 3309 (1996); B. Abbott *et al.* [D0 Collaboration], Phys. Rev. **D 58**, 012002 (1998); Phys. Rev. Lett. **80**, 3008 (1998); Phys. Rev. **D 58**, 092003 (1998); Phys. Rev. **D 62**, 092006 (2000) and Phys. Rev. Lett. **84**, 222 (2000).

Measurement of the Forward-Backward Asymmetry in e^+e^- and $\mu^+\mu^-$ events with DØ in Run II

Ulrich Baur[a], John Ellison[b] and John Rha[b]

[a]State University of New York, Buffalo, NY 14260

[b]University of California, Riverside, CA 92521

The forward-backward asymmetry of $\ell^+\ell^-$ events in Run II can yield a measurement of the effective weak mixing angle $\sin^2\bar{\theta}_{\rm W}$ and can provide a test of the standard model γ^*/Z interference at $\ell^+\ell^-$ invariant masses well above the 200 GeV center of mass energy of the LEP II collider. The asymmetry at large partonic center of mass energies can also be used to study the properties of possible new neutral gauge bosons. We describe an updated study of the forward-backward asymmetry and give estimates of the statistical and systematic uncertainties expected in Run II. The prospects for measuring the weak mixing angle at the LHC and a linear collider operating at $\sqrt{s} = M_Z$ are also briefly described.

1. Introduction

In this note we present an updated study of the prospects for measurement of the forward-backward asymmetry in $p\bar{p} \to \gamma^*/Z \to \ell^+\ell^-$ events. This work extends our earlier study described in the TeV2000 report [1] in several respects: (i) we include the effects of QED corrections; (ii) we include the effects of expected Run II DØ detector resolutions and efficiencies; (iii) we consider systematic errors in more detail; and (iv) we include a simulation of the muon channel process $p\bar{p} \to \gamma^*/Z \to \mu^+\mu^-$.

The forward-backward asymmetry (A_{FB}) in $p\bar{p} \to \gamma^*/Z \to \ell^+\ell^-$ events arises from the parton level process $q\bar{q} \to \gamma^*/Z \to \ell^+\ell^-$. This asymmetry depends on the vector and axial-vector couplings of the quarks and leptons to the Z boson and is therefore sensitive to the effective weak mixing angle $\sin^2\bar{\theta}_W$. The current world average value of $\sin^2\bar{\theta}_W$ from LEP and SLD asymmetry measurements is $\sin^2\bar{\theta}_W = 0.23147 \pm 0.00017$ [2]. As will be seen from our results it will be necessary to achieve high luminosity (> 10 fb^{-1}) and combine the results from the electron and muon channels and the results from DØ and CDF to achieve a precision comparable to this.

The SM tree level prediction [3] for A_{FB} as a function of $\hat{s}$ for $q\bar{q} \to \gamma^*/Z \to e^+e^-$ is shown in Fig. 1 for u and d quarks. These are the same asymmetries as encountered in the inverse e^+e^- annihilation reactions. The largest asymmetries occur at parton center-of-mass energies of around 70 GeV and above 110 GeV. At the Z-pole the asymmetry is dominated by the couplings of the Z boson and arises from the interference of the vector and axial components of its coupling. The asymmetry is proportional to the deviation of $\sin^2\bar{\theta}_W$ from $\frac{1}{4}$. At large invariant mass, the asymmetry is dominated by γ^*/Z interference and is almost constant (≈ 0.6), independent of invariant mass.

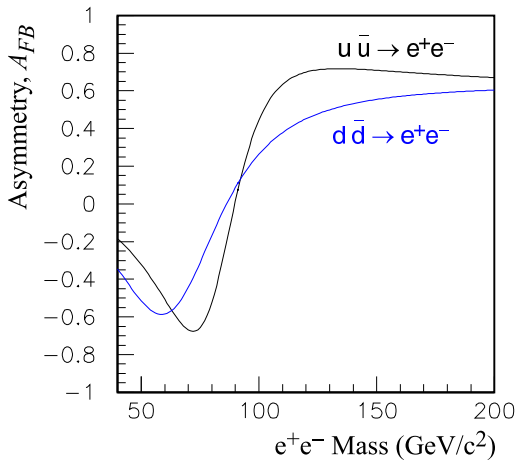

Figure 1. The standard model tree level prediction of the forward-backward asymmetry as a function of e^+e^- invariant mass for $u\bar{u} \to e^+e^-$ and $d\bar{d} \to e^+e^-$.

With sufficient statistics in Run II the forward-backward asymmetry can be used to measure $\sin^2\bar{\theta}_W$, which in turn can provide a constraint on the standard model complementary to the measurement of the W boson mass. The Tevatron also allows measurement of the asymmetry at partonic center-of-mass energies above the center of mass energy of LEP II. This measurement can be used, not only to confirm the standard model γ^*/Z interference which dominates

in this region, but also to investigate possible new phenomena which may alter A_{FB}, such as new neutral gauge bosons [4] or large extra dimensions [5].

CDF have measured the forward-backward asymmetry at the Tevatron using e^+e^- pairs in 110 pb^{-1} of data at $\sqrt{s} = 1.8$ TeV [6]. They obtain $A_{FB} = 0.070 \pm 0.016$ in the mass region 75 GeV $< m_{e^+e^-} <$ 105 GeV, and $A_{FB} = 0.43 \pm 0.10$ in the region $m_{e^+e^-} > 105$ GeV. The much larger Run II statistics will enable A_{FB} to be measured with an uncertainty reduced by over an order of magnitude.

2. Simulation

The simulations presented here use the ZGRAD Monte Carlo program [7], which includes $\mathcal{O}(\alpha)$ QED radiative corrections to the process $p\bar{p} \to \gamma^*/Z \to \ell^+\ell^-$. We simulate this process at $\sqrt{s} = 2.0$ TeV using the MRST parton distributions as our default set. Since the radiative corrections are included in ZGRAD, we denote the process of interest by $p\bar{p} \to \gamma^*/Z \to \ell^+\ell^-(\gamma)$ in the remainder of this paper. The ZGRAD program includes real and virtual corrections in the initial and final states.

In our simulations, the effects of detector resolution are modeled by smearing the 4-momenta of the particles from ZGRAD according to the estimated resolution of the Run II DØ detector. We smear the 4-momenta of electrons, positrons and photons according to the energy resolution σ_{EM} of the calorimeters, which have been parametrized using constant, sampling and noise terms as

$$\left(\frac{\sigma_{EM}}{E}\right)^2 = \begin{cases} c_{EM}^2 + \left(\frac{s_{EM}}{\sqrt{E_T}}\right)^2 + \left(\frac{n_{EM}}{E}\right)^2 \\ \qquad \textit{Central Calorimeter} \\ c_{EM}^2 + \left(\frac{s_{EM}}{\sqrt{E}}\right)^2 + \left(\frac{n_{EM}}{E}\right)^2 \\ \qquad \textit{End Calorimeters} \end{cases} \quad (1)$$

where we use the parameters relevant for the Run I detector, $c_{EM} = 0.0115$, $s_{EM} = 0.135$, and $n_{EM} = 0.43$ for the CC, and $c_{EM} = 0.0100$, $s_{EM} = 0.157$, and $n_{EM} = 0.29$ for the EC. With the addition of the 2 T solenoidal magnetic field in Run II, only minor changes in these parameters are expected. The transverse momentum of muons in the Run II detector will be measured in the central tracking system, consisting of the Central Fiber Tracker (CFT) and the Silicon Microstrip Tracker (SMT). The momentum resolution of the tracking system has been studied using the fast Monte Carlo MCFAST. From these studies the resolution in $1/p_T$ is parametrized as:

$$\sigma\left(\frac{1}{p_T}\right) = \sqrt{\left(\frac{\alpha}{L^2}\right)^2 + \left(\frac{\gamma}{p_T\sqrt{L|\sin\theta|}}\right)^2} \quad (2)$$

where

$$L = \left\{ \begin{array}{ll} 1 & 0 < \theta \le \theta_c \\ \frac{\tan\theta}{\tan\theta_c} & \theta_c < \theta < 90^\circ \end{array} \right\} . \quad (3)$$

Here $\alpha = 0.0017$ GeV^{-1}, $\gamma = 0.018$, L is the fraction of the projection of the track length in the bending plane which is measured in the Tracker, and $\theta_c \approx 23^\circ$ is the polar angle beyond which the number of CFT layers crossed by a track starts to decrease. The first term in Eq. (3) is due to the detector resolution while the second term is due to multiple scattering.

Figure 2 shows the transverse momentum resolution as a function of detector pseudorapidity $|\eta_{det}|$ for tracks with a p_T of 1, 20 and 100 GeV, while Fig. 3 shows the resolution as a function of p_T and $|\eta_{det}|$ in the form of a contour plot. For central tracks ($\eta = 0$) with $p_T = 45$ GeV, the resolution is $\sigma(p_T)/p_T = 8\%$, to be compared with the calorimeter energy resolution for 45 GeV electrons of $\sigma(E)/E = 2.5\%$.

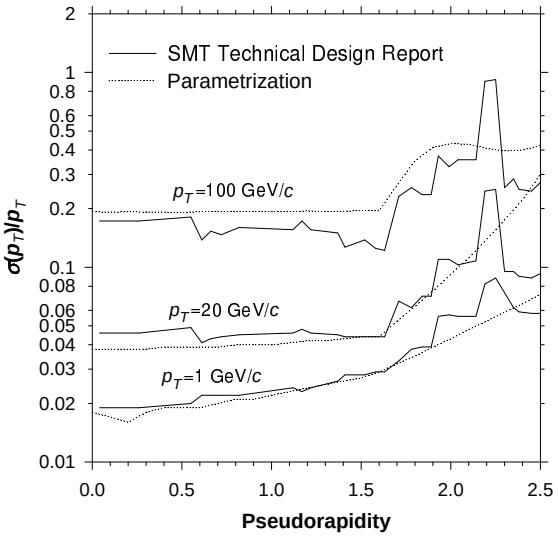

Figure 2. Parametrized transverse momentum resolution for the DØ Run II tracking system (dotted lines). The solid lines are the results of a simple Monte Carlo simulation taken from the DØ SMT Technical Design Report [8].

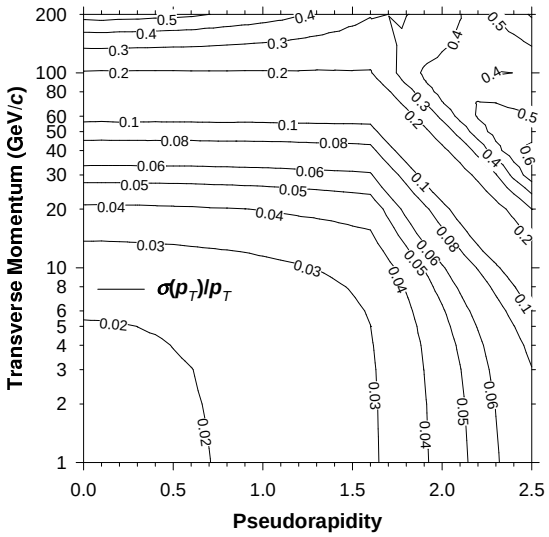

Figure 3. Transverse momentum resolution for the central tracking system plotted as a function of transverse momentum and pseudorapidity.

We assume an overall detection efficiency of 75% for e^+e^- events and 65% for $\mu^+\mu^-$ events. These efficiencies are rough estimates of the effects of trigger and particle identification efficiencies expected in Run II. The results can be updated once more realistic numbers for these efficiencies become available.

The ZGRAD program generates weighted events. Due to the occurrence of negative weights, we did not attempt to unweight the events. Thus, we work with weighted events and properly account for the weights in our calculations of the forward-backward asymmetry errors. The forward-backward asymmetry is defined by

$$A_{FB} = \frac{\sigma_F - \sigma_B}{\sigma_F + \sigma_B} \tag{4}$$

where σ_F and σ_B are the forward and backward cross sections, defined by

$$\sigma_F = \int_0^1 \frac{d\sigma}{d(cos\theta^*)} d(cos\theta^*)$$

$$\sigma_B = \int_{-1}^0 \frac{d\sigma}{d(cos\theta^*)} d(cos\theta^*) \tag{5}$$

and θ^* is the angle of the lepton in the Collins-Soper frame [9].

The statistical error on A_{FB} is given by

$$\delta A_{FB} = 2\frac{\sqrt{\sigma_B^2(\delta\sigma_F)^2 + \sigma_F^2(\delta\sigma_B)^2}}{(\sigma_F + \sigma_B)^2} \tag{6}$$

where $\delta\sigma_F$, $\delta\sigma_B$ are the uncertainties in the forward and backward cross sections. For unweighted events, this simplifies to

$$\delta A_{FB} = \frac{2}{N_F + N_B}\sqrt{\frac{N_F N_B}{N_F + N_B}} \tag{7}$$

where N_F, N_B are the numbers of forward and backward events. However, ZGRAD generates weighted events and, therefore, we use Eq. (6) where $\delta\sigma_F$ and $\delta\sigma_B$, are calculated using the appropriate event weights.

The selection cuts used in our study are summarized in Table 1. In the electron channel we require one of the electrons to be in the CC ($|\eta_{det}| < 1.0$), while the other electron may be in the CC or in the EC ($|\eta_{det}| < 1.0$ or $1.5 < |\eta_{det}| < 2.5$).

In the muon channel we require both muons to be within $|\eta_{det}| < 1.7$. In Run II the muon coverage is expected to extend up to $|\eta_{det}| = 2.0$. We chose to limit the muon acceptance to $|\eta_{det}| = 1.7$ since Monte Carlo events were already generated with this restriction and large CPU time would have been required to re-generate the events.

We account in our simulation for the granularity of the DØ calorimeter. If the photon is very close to the electron its energy will be merged with that of the electron cluster. Thus, in the simulation we combine the photon and electron 4-momenta to form an effective electron 4-momentum if the photon is within $\Delta R_{e\gamma} \equiv \sqrt{\Delta\eta_{e\gamma}^2 + \Delta\phi_{e\gamma}^2} < 0.2$. If the photon falls within $0.2 < \Delta R_{e\gamma} < 0.4$, we reject the event if $E_\gamma/(E_e + E_\gamma) > 0.15$, since the event will not pass the standard isolation criterion imposed on electrons.

If a photon is very close to a muon and it deposits sufficient energy in the calorimeter close to the muon track, the energy deposition in the calorimeter will not be consistent with the passage of a minimum ionizing muon. Therefore, in the simulation we reject events if $\Delta R_{\mu\gamma} < 0.2$ and $E_\gamma > 2$ GeV.

Table 1
Selection criteria for e^+e^- and $\mu^+\mu^-$ events.

	e^+e^-		$\mu^+\mu^-$	
Selection cut	e_1	e_2	μ_1	μ_2
p_T (GeV)	> 25	> 25	> 20	> 15
$\|\eta_{det}\|$	< 1.0	< 1.0 or $1.5 - 2.5$	< 1.7	< 1.7
$m_{\ell^+\ell^-}$ (GeV)	> 40	> 40	> 40	> 40

3. Results

The $\ell^+\ell^-$ invariant mass distributions for $p\bar{p} \to \gamma^*/Z \to \ell^+\ell^-(\gamma)$ at $\sqrt{s} = 2.0$ TeV from the ZGRAD simulations, using the MRST parton distribution functions are shown in Fig. 4. The thin line shows $d\sigma/dm_{\ell^+\ell^-}$ without any kinematic cuts applied and with no detector acceptance or resolution effects included. In order to obtain sufficient statistical precision a large number of events were generated in multiple runs covering overlapping regions of $m_{\ell^+\ell^-}$. The thick line shows $d\sigma/dm_{\ell^+\ell^-}$ after kinematic cuts and detector effects are included. The error bars represent the statistical errors only, calculated from Eq. (6), assuming an integrated luminosity of 10 fb^{-1}.

Fig. 5 shows the forward-backward asymmetry as a function of $m_{\ell^+\ell^-}$. The solid line shows A_{FB} without any kinematic cuts applied and with no detector acceptance or resolution effects included. The solid points show A_{FB} after kinematic cuts and detector effects are included. The error bars represent the statistical errors only, calculated from Eq. (6), assuming an integrated luminosity of 10 fb^{-1}. As can be seen, detector resolution and acceptance effects significantly alter the shape of the A_{FB} vs. $m_{\ell^+\ell^-}$ curve, especially at low di-lepton invariant masses. In this region, the effect of CC/EC acceptance increases A_{FB}, while restricting $\mu^+\mu^-$ events to be in the central region decreases the asymmetry. This is also true of e^+e^- events if only CC/CC events are considered. In the vicinity of the Z-pole the energy resolution is better than the p_T resolution, and hence the $A_{FB}^{e^+e^-}$ is altered less than $A_{FB}^{\mu^+\mu^-}$. In these plots the A_{FB} shown is the reconstructed A_{FB} without corrections for acceptance or resolution effects.

In order to obtain a measurement of the weak mixing angle we assume the relationship

$$A_{FB} = a + b \sin^2\bar{\theta}_W \tag{8}$$

so that the statistical error on $\sin^2\bar{\theta}_W$ is given by

$$\delta \sin^2\bar{\theta}_W = \frac{\delta A_{FB}}{b}. \tag{9}$$

The quantity b is determined by varying $\sin^2\bar{\theta}_W$ in the Monte Carlo simulations. Since A_{FB} is determined over a finite range of di-lepton invariant mass, we have investigated the effect of the lower and upper $m_{\ell^+\ell^-}$ cuts on $\delta \sin^2\bar{\theta}_W$. The optimal precision is obtained for 75 GeV $< m_{\ell^+\ell^-} <$ 105 GeV, i.e. a mass window encompassing the Z-pole. This is to be expected because the sensitivity b is maximal at the Z-pole and this region is where the cross section peaks and hence the statistical error is smallest. Thus, the

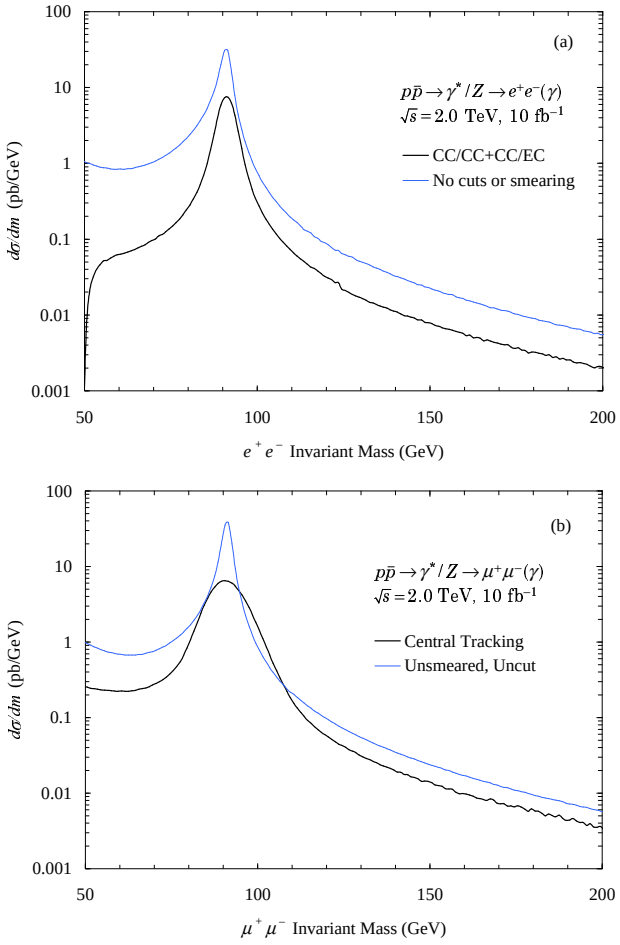

Figure 4. Invariant mass $m_{\ell^+\ell^-}$ distributions for (a) e^+e^- events and (b) $\mu^+\mu^-$ events. The thin line is the distribution obtained with no cuts or detector effects applied and the thick line is the resulting distribution after selection cuts and detector effects are included.

A_{FB} values and errors presented in the remainder of this paper are all obtained with a di-lepton invariant mass cut of 75 GeV $< m_{\ell^+\ell^-} <$ 105 GeV. Table 2 shows the resulting statistical uncertainties obtained from the electron and muon channels. The e^+e^- and $\mu^+\mu^-$ channels yield similar uncertainties on A_{FB} and $\sin^2\bar{\theta}_W$. In both channels the effect of the selection cuts is to reduce the sensitivity b from about 3.5 to about 2.8.

The effects of NLO QCD corrections to the process $p\bar{p} \to \gamma^*/Z \to \ell^+\ell^-$ are not included in ZGRAD, so we estimate these using the $\mathcal{O}(\alpha_s)$ event generator described in [7]. Using the same method as described in Section 2, we calculate the change in the forward-backward asymmetry and the shift in sensitivity due

Table 2
Uncertainties on A_{FB} and $\sin^2\bar{\theta}_W$ in the invariant mass range 75 GeV $< m_{\ell^+\ell^-} <$ 105 GeV for an integrated luminosity of 10 fb^{-1}. Also shown are the assumed event detection efficiency, the number of events passing all the cuts N_{obs}, the forward-backward asymmetry A_{FB}, and the sensitivity b.

Process	Selection cuts	Efficiency	N_{obs}	A_{FB}	δA_{FB}^{stat}	b	$\delta \sin^2\bar{\theta}_W$
$Z \to e^+e^-$	no	100%	1.78×10^6	0.0551	0.0008	3.43	0.0002
$Z \to e^+e^-$	yes	75%	3.82×10^5	0.0515	0.0014	2.78	0.0005
$Z \to \mu^+\mu^-$	no	100%	1.87×10^6	0.0534	0.0007	3.51	0.0002
$Z \to \mu^+\mu^-$	yes	65%	5.67×10^5	0.0420	0.0011	2.62	0.0004

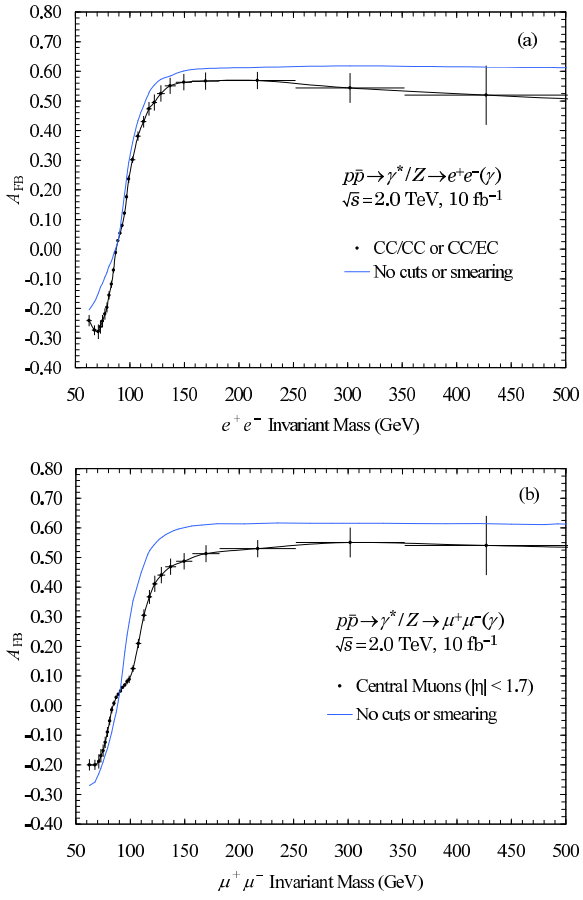

Figure 5. Forward-backward asymmetry A_{FB} vs. di-lepton invariant mass for (a) e^+e^- events and (b) $\mu^+\mu^-$ events. The solid line is the distribution obtained with no cuts or detector effects applied and the points are the resulting distribution after selection cuts and detector effects are included. The error bars represent the statistical errors for a data sample of 10 fb^{-1}.

to NLO QCD corrections. Thus, we write

$$\Delta A_{FB} = A_{FB}^{\mathcal{O}(\alpha_s)} - A_{FB}^{LO} \quad (10)$$

$$\Delta b = b^{\mathcal{O}(\alpha_s)} - b^{LO} \quad (11)$$

where LO denotes the leading-order quantities. For events generated including detector effects we find the shift in A_{FB} to be negligible for e^+e^- events and -13% for $\mu^+\mu^-$ events. The shift in sensitivity is $\Delta b/b^{LO} \approx -3.4\%$ for e^+e^- events and $\approx -25\%$ for $(\mu^+\mu^-)$ events. Thus, NLO QCD effects decrease the sensitivity to $\sin^2\bar{\theta}_W$ by 3.4% in the e^+e^- channel and 25% in the $\mu^+\mu^-$ channel.

4. Systematic Uncertainties

4.1. Parton Distribution Functions

Since the vector and axial couplings of the u and d quarks to the Z boson are different, the lepton forward-backward asymmetry is expected to depend on the ratio of the u to d quark parton distribution functions. Thus, the choice of the parton distribution functions (PDF's) will affect the measured lepton forward-backward asymmetry.

We have run simulations with six PDF's from the MRS [10] and CTEQ [11] sets to study the effect of the PDF's on the asymmetry. Fig. 6 shows the e^+e^- and $\mu^+\mu^-$ asymmetries and their statistical errors for each PDF.

The largest deviation from the MRST value for A_{FB} is 0.0018 for the e^+e^- channel and 0.0015 for the $\mu^+\mu^-$ channel. While these numbers are of the same order as the statistical error expected on A_{FB} for 10 fb^{-1}, we expect that in Run II our knowledge of the PDF's will improve considerably, e.g. from the constraints imposed by the Run II W asymmetry measurements. Thus, we expect a significantly decreased systematic error due to the uncertainty in the PDF's which will likely render it insignificant compared with the statistical error in the measurement. For example, if the PDF uncertainty scales as $1/\sqrt{N}$, the uncertainty in A_{FB} would be $\delta A_{FB} \approx 0.00018$ (0.00015) for an

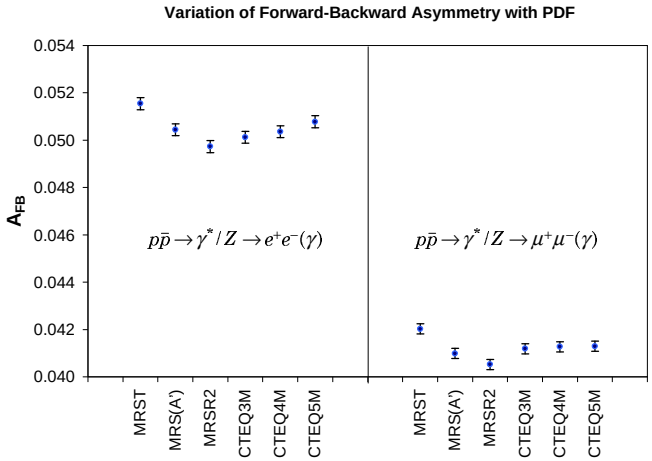

Figure 6. Variation of the forward-backward asymmetry for e^+e^- and $\mu^+\mu^-$ events, including selection cuts and detector effects.

integrated luminosity of 10 fb^{-1} in the e^+e^- ($\mu^+\mu^-$) channel.

4.2. Energy Scale Calibration Uncertainties

The energy scale uncertainty, or the uncertainty in mapping the calorimeter response to the true electron energy, affects the forward-backward asymmetry by causing a shift in the $\ell^+\ell^-$ invariant mass range over which we integrate A_{FB}. The effect is significant in the Z-pole region, but at large invariant masses A_{FB} is essentially constant and the energy scale uncertainty does not play a role. For electrons, the measured energy can be related to the true energy by

$$E_{meas} = \alpha E_{true} + \delta \tag{12}$$

where the scale factor α and offset δ are determined by calibration of the calorimeters. In Run I DØ determined $\alpha = 0.9533 \pm 0.0008$ and $\delta = -0.16^{+0.03}_{-0.21}$ GeV.

Assuming these uncertainties in α and δ, we find a systematic error of $\delta A_{FB} = 0.0002$ due to the overall energy scale uncertainty.

4.3. Uncertainty due to Backgrounds

Backgrounds are not included in the simulations above, but we can estimate the uncertainty due to backgrounds as follows. If we assume that the fraction of observed events which are due to backgrounds is $\alpha \pm \delta\alpha$, then the uncertainty in the forward-backward asymmetry will be

$$\delta A_{FB} = 2\sqrt{2}\frac{N_F N_B}{(N_F + N_B)^2}\delta\alpha \tag{13}$$

where N_F, N_B are the numbers of background-subtracted forward and backward events, and we have assumed that the background events are symmetric in $cos\theta^*$. If we assume that the error in the background fraction $\delta\alpha$ scales as the inverse of the integrated luminosity, we can extrapolate from the uncertainties in the Run I CDF and DØ data samples to estimate the error. The Run I uncertainties were $\delta\alpha \approx 0.1 - 1.0\%$. Thus, for an integrated luminosity of 10 fb^{-1}, we obtain an uncertainty on A_{FB} of $\delta A_{FB} = 0.00014$.

4.4. Summary of Uncertainties in $\sin^2\bar{\theta}_W$

Table 3 summarizes the statistical and individual systematic uncertainty estimates expected with 10 fb^{-1} of data. We estimated the uncertainties due to electron energy resolution and muon transverse momentum resolution to be negligible.

4.5. Conclusions

The measurement of the forward-backward asymmetry in e^+e^- and $\mu^+\mu^-$ events in Run II provides a means to test the standard model γ^*/Z interference at $\ell^+\ell^-$ invariant masses well above the center of mass energy of the LEP II collider. The estimated DØ precision on A_{FB} achievable with 10 fb^{-1} integrated luminosity is shown in Fig. 5.

In the vicinity of the Z-pole this measurement can also be used to determine the effective weak mixing angle $\sin^2\bar{\theta}_W$. The optimal precision on $\sin^2\bar{\theta}_W$ is obtained for 75 GeV $< m_{\ell^+\ell^-} <$ 105 GeV, i.e. a mass window encompassing the Z-pole. This is to be expected because the sensitivity b is maximal at the Z-pole and this region is where the cross section peaks and hence the statistical error is smallest. For 10 fb^{-1} we estimate that the total error on $\sin^2\bar{\theta}_W$ will be 0.0005 in the electron channel and 0.0006 in the muon channel, assuming that systematic errors scale as the inverse of the square root of the integrated luminosity. One would expect similar precision from CDF, and combining the results of the two experiments in both channels the overall uncertainty would be $\delta\sin^2\bar{\theta}_W \approx 0.00028$. Therefore, if integrated luminosities in excess of 10 fb^{-1} can be achieved in Run II, it appears that the determination of $\sin^2\bar{\theta}_W$ will have comparable precision to the current world average of the measurements from LEP and SLD.

5. Measuring A_{FB} at the LHC

At the LHC, the $Z \to \ell^+\ell^-$ cross section is approximately a factor 7 larger than at the Tevatron. However, the measurement of the forward backward asymmetry is complicated by several factors. In pp collisions, the quark direction in the initial state has to be extracted

Table 3
Summary of uncertainties on A_{FB} and $\sin^2\bar{\theta}_W$ in the invariant mass range 75 GeV $< m_{\ell^+\ell^-} <$ 105 GeV for an integrated luminosity of 10 fb^{-1}. The effects of $\mathcal{O}(\alpha)$ QED corrections and NLO QCD corrections have been taken into account.

	e^+e^-		$\mu^+\mu^-$	
Error source	δA_{FB}	$\delta \sin^2\bar{\theta}_W$	δA_{FB}	$\delta \sin^2\bar{\theta}_W$
Statistical	0.0014	0.0005	0.0011	0.0006
Systematics	0.0003	0.0001	0.0002	0.00010
PDF	0.00018	0.00007	0.00015	0.00008
EM scale	0.0002	0.00007	–	–
Backgrounds	0.00014	0.00005	0.00014	0.00007
Total uncertainty	0.0014	0.0005	0.0011	0.0006

from the boost direction of the $\ell^+\ell^-$ system with respect to the beam axis. At LHC energies, the sea-sea quark flux is much larger than at the Tevatron. As a result, the probability, f_q, that the quark direction and the boost direction of the di-lepton system coincide is rather small. The forward backward asymmetry is therefore smaller than at the Tevatron, and the sensitivity to $\sin^2\bar{\theta}_W$ at the LHC with 100 fb^{-1} per lepton channel and experiment [7,12] is similar to that estimated for the Tevatron with 10 fb^{-1} (see Sec. 4.5).

Restricting the A_{FB} measurement to events which satisfy $|y(\ell^+\ell^-)| > 1$ in addition to the $|y(\ell)| < 2.5$ cut improves the significance of the measurement by about a factor 1.5. Events with a large di-lepton rapidity originate from collisions where at least one of the partons carries a large fraction x of the proton momentum. Since valence quarks dominate at high values of x, a cut on $y(\ell^+\ell^-)$ increases f_q and thus the asymmetry. However, the gain due to the larger asymmetry is partially cancelled by the loss of statistics, leaving a modest improvement only.

In order to achieve a precision better than the current value of $\delta \sin^2\bar{\theta}_W = 1.7 \times 10^{-4}$ [13], it will be necessary to detect one of the leptons in the rapidity range up to $|y(\ell)| < 5$ at the LHC. If this can be done, one expects that the weak mixing angle can be determined with a precision of

$$\delta \sin^2\bar{\theta}_W = 1.4 \times 10^{-4}, \qquad (14)$$

per lepton channel and experiment for an integrated luminosity of 100 fb^{-1}. In order to reach the precision given in Eq. (14), a jet rejection factor of $10 - 100$ has to be achieved in the forward rapidity region $2.5 < |y(\ell)| < 5$, and the lepton acceptance times the reconstruction efficiency as a function of $y(\ell)$ has to be known to 0.1% or better [12].

For comparison, at a Linear Collider operating at $\sqrt{s} = M_Z$ with a luminosity of a few $\times 10^{33}$ cm^{-2} s^{-1}, it is expected that the weak mixing angle be determined with a precision of about $\delta \sin^2\bar{\theta}_W = 1 \times 10^{-5}$ [14].

REFERENCES

1. "Future Electroweak Physics at the Fermilab Tevatron: Report of the TeV_2000 Study Group", edited by D. Amidei and R. Brock, FERMILAB-PUB-96/082, pp.75-79 (1996).
2. J. Mnich, "Tests of the Standard Model", CERN-EP/99-143 (1999), to appear in Proceedings of the international Europhysics Conference on High Energy Physics, Tampere, Finland, 15-21 July, 1999.
3. J.L. Rosner, Phys. Lett. **B221**, 85 (1989)
4. J.L. Rosner, Phys. Rev. **D35**, 2244 (1987); J.L. Rosner, Phys. Rev. **D54**, 1078 (1996).
5. I. Antoniadis, et al., Phys. Lett. **B436**, 257 (1998); J.L. Hewett, Phys. Rev. Lett. **82**, 4765 (1999).
6. F. Abe, et al., (CDF Collaboration), Phy. Rev. Lett. **77**, 2616 (1996).
7. U. Baur, S. Keller, and W. K. Sakumoto, Phy. Rev. **D57**, 199 (1998).
8. DØ Silicon Tracker Technical Design Report, (DØ Collaboration), DØ Note 2169 (1994).
9. J.C. Collins and D.E. Soper, Phys. Rev. **D16**, 2219 (1977).
10. A.D. Martin, R.G. Roberts, W.J. Stirling, Phys. Rev. **D50**, 6734 (1994); *ibid.* **D51**, 4756 (1995); A.D. Martin, R.G. Roberts, W.J. Stirling, Phys. Lett. **B387**, 419 (1996); A.D. Martin, R.G. Roberts, W.J. Stirling, R.S. Thorne, Phys. Lett. **B443**, 301 (1998).
11. H.L. Lai et al., Phys. Rev. **D51**, 4763 (1995); *ibid.*

D55, 1280 (1997); H.L. Lai et al., Eur. Phys. J. **C12**, 375 (2000).
12. S. Haywood *et al.*, Report of the Electroweak Physics Working Group, hep-ph/0003275 (March 2000), in *Proceedings of the 1999 CERN Workshop on Standard Model Physics (and more) at the LHC* CERN Yellow Report, CERN-2000-04, eds. G. Altarelli and M. Mangano.
13. D. Abbaneo *et al.* (The LEP Electroweak Working Group), CERN-EP-2000-016 (January 2000).
14. J. Erler, S. Heinemeyer, W. Hollik, G. Weiglein and P. M. Zerwas, Phys. Lett. **B486**, 125 (2000).

Global Fits to Electroweak Data Using GAPP

J. Erler[a]

[a]Department of Physics and Astronomy, University of Pennsylvania,
Philadelphia, PA 19104-6396

At Run II of the Tevatron it will be possible to measure the W boson mass with a relative precision of about 2×10^{-4}, which will eventually represent the best measured observable beyond the input parameters of the SM. Proper interpretation of such an ultra-high precision measurement, either within the SM or beyond, requires the meticulous implementation and control of higher order radiative corrections. The FORTRAN package GAPP, described here, is specifically designed to meet this need and to ensure the highest possible degrees of accuracy, reliability, adaptability, and efficiency.

1. PRECISION TESTS

Precision analysis of electroweak interactions follows three major objectives: high precision tests of the SM; the determination of its fundamental parameters; and studies of indications and constraints of possible new physics beyond the SM, such as supersymmetry or new gauge bosons. Currently, the experimental information comes from the very high precision Z boson measurements at LEP and the SLC, direct mass measurements and constraints from the Tevatron and LEP II, and low energy precision experiments, such as in atomic parity violation, ν scattering, and rare decays. These measurements are compared with the predictions of the SM and its extensions. The level of precision is generally very high. Besides the need for high-order loop calculations, it is important to utilize efficient renormalization schemes and scales to ensure sufficient convergence of the perturbative expansions.

The tasks involved called for the creation of a special purpose FORTRAN package, GAPP, short for the *Global Analysis of Particle Properties* [1]. It is mainly devoted to the calculation of pseudo-observables, i.e., observables appropriately idealized from the experimental reality. The reduction of raw data to pseudo-observables is performed by the experimenters with available packages (e.g., ZFITTER for Z pole physics). For cross section and asymmetry measurements at LEP II (not implemented in the current version, GAPP_99.7), however, this reduction is not optimal and convoluted expressions should be used instead. GAPP attempts to gather all available theoretical and experimental information; it allows the addition of extra parameters describing new physics; it treats all relevant SM inputs as global fit parameters; and it can easily be updated with new calculations, data, observables, or fit parameters. For clarity and speed it avoids numerical integrations throughout. It is based on the modified minimal subtraction ($\overline{\rm MS}$) scheme which demonstrably avoids large expansion coefficients.

GAPP is endowed with the option to constrain nonstandard contributions to the *oblique parameters* defined to affect only the gauge boson self-energies [2] (e.g. S, T, and U); specific anomalous Z couplings; the number of active neutrinos (with standard couplings to the Z boson); and the masses, mixings, and coupling strengths of extra Z bosons appearing in models of new physics. With view on the importance of supersymmetric extensions of the SM on one hand, and upcoming experiments on the other, I also included the $b \to s\gamma$ transition amplitude, and intend to add the muon anomalous magnetic moment. In the latter case, there are theoretical uncertainties from hadronic contributions which are partially correlated with the renormalization group (RG) evolutions of the QED coupling and the weak mixing angle. These correlations will be partially taken into account by including heavy quark effects in analytical form; see Ref. [3] for a first step in this direction. By comparing this scheme with more conventional ones, it will also be possible to isolate a QCD sum rule and to rigorously determine the charm and bottom quark $\overline{\rm MS}$ masses, $\hat{m}_c$ and $\hat{m}_b$, with high precision.

2. GAPP

2.1. Basic structure

In the default running mode of the current version, GAPP_99.7, a fit is performed to 41 observables, out of which 26 are from Z pole measurements at LEP and the SLC. The Fermi constant, G_F (from the muon lifetime), the electromagnetic fine structure constant, α (from the quantum Hall effect), and the light fermion masses are treated as fixed inputs. The exception is $\hat{m}_c$ which strongly affects the RG running[1] of $\hat{\alpha}(\mu)$ for $\mu > \hat{m}_c$. I therefore treat $\hat{m}_c$ as a fit parameter

[1]Quantities defined in the $\overline{\rm MS}$ scheme are denoted by a caret.

and include an external constraint with an enhanced error to absorb hadronic threshold uncertainties of other quark flavors, as well as theoretical uncertainties from the application of perturbative QCD at relatively low energies. Other fit parameters are the Z boson mass, M_Z, the Higgs boson mass, M_H, the top quark mass, m_t, and the strong coupling constant, α_s, so that there are 37 effective degrees of freedom. Given current precisions, M_Z may alternatively be treated as an additional fixed input.

The file `fit.f` basically contains a simple call to the minimization program MINUIT [4] (from the CERN program library) which is currently used in data driven mode (see `smfit.dat`). It in turn calls the core subroutine `fcn` and the χ^2-function `chi2`, both contained in `chi2.f`. Subroutine `fcn` defines constants and flags; initializes parts of the one-loop package FF [5,6]; and makes the final call to subroutine `values` in `main.f` which drives the output (written to file `smfit.out`). In `chi2` the user actively changes and updates the data for the central values, errors, and correlation coefficients of the observables, and includes or excludes individual contributions to χ^2 (right after the initialization, `chi2 = 0.d0`). To each observable (as defined at the beginning of `chi2`) corresponds an entry in each of the fields `value, error, smval`, and `pull`, containing the central observed value, the total (experimental and theoretical) error, the calculated fit value, and the standard deviation, respectively. The function `chi2` also contains calls to various other subroutines where the actual observable calculations take place. These are detailed in the following subsections.

Another entry to GAPP is provided through `mh.f` which computes the probability distribution function of M_H. The probability distribution function is the quantity of interest within Bayesian data analysis (as opposed to point estimates frequently used in the context of classical methods), and defined as the product of a prior density and the likelihood, $\mathcal{L} \sim \exp(-\chi^2/2)$. If one chooses to disregard any further information on M_H (such as from triviality considerations or direct searches) one needs a *non-informative prior*. It is recommended to choose a flat prior in a variable defined on the whole real axis, which in the case of M_H is achieved by an equidistant scan over $\log M_H$. An *informative prior* is obtained by activating one of the approximate Higgs exclusion curves from LEP II near the end of `chi2.f`. These curves affect values of M_H even larger than the corresponding quoted 95% CL lower limit and includes an extrapolation to the kinematic limit; notice that this corresponds to a conservative treatment of the upper M_H limit.

Contour plots can be obtained using the routine `mncontours` from MINUIT. For the cases this fails, some simpler and slower but more robust contour programs are also included in GAPP, but these have to be adapted by the user to the case at hand.

2.2. $\hat{\alpha}$, $\sin^2\hat{\theta}_W$, M_W

At the core of present day electroweak analyses is the interdependence between G_F, M_Z, the W boson mass, M_W, and the weak mixing angle, $\sin^2\theta_W$. In the $\overline{\rm MS}$ scheme it can be written as [7,8],

$$\hat{s}^2 = \frac{A^2}{M_W^2(1-\Delta\hat{r}_W)}, \qquad \hat{s}^2\hat{c}^2 = \frac{A^2}{M_Z^2(1-\Delta\hat{r}_Z)}, \tag{1}$$

where,

$$A = \left[\frac{\pi\alpha}{\sqrt{2}G_F}\right]^{1/2} = 37.2805(2)\ \text{GeV}, \tag{2}$$

$\hat{s}^2$ is the $\overline{\rm MS}$ mixing angle, $\hat{c}^2 = 1-\hat{s}^2$, and where,

$$\Delta\hat{r}_W = \frac{\alpha}{\pi}\hat{\Delta}_\gamma + \frac{\hat{\Pi}_{WW}(M_W^2) - \hat{\Pi}_{WW}(0)}{M_W^2} + \text{V} + \text{B}, \tag{3}$$

and,

$$\Delta\hat{r}_Z = \Delta\hat{r}_W + (1-\Delta\hat{r}_W)\frac{\hat{\Pi}_{ZZ}(M_Z^2) - \frac{\hat{\Pi}_{WW}(M_W^2)}{\hat{c}^2}}{M_Z^2}, \tag{4}$$

collect the radiative corrections computed in `sin2th.f`. The $\hat{\Pi}$ indicate $\overline{\rm MS}$ subtracted self-energies, and V + B denote the vertex and box contributions to μ decay. Although these relations involve the $\overline{\rm MS}$ gauge couplings they employ on-shell gauge boson masses, absorbing a large class of radiative corrections [9].

$\Delta\hat{r}_W$ and $\Delta\hat{r}_Z$ are both dominated by the contribution $\hat{\Delta}_\gamma(M_Z)$ which is familiar from the RG running of the electromagnetic coupling,

$$\hat{\alpha}(\mu) = \frac{\alpha}{1-\frac{\alpha}{\pi}\hat{\Delta}_\gamma(\mu)}, \tag{5}$$

and computed in `alfahat.f` up to four-loop $\mathcal{O}(\alpha\alpha_s^3)$. Contributions from c and b quarks are calculated using an unsubtracted dispersion relation [3]. If μ is equal to the mass of a quark, three-loop matching is performed and the definition of $\hat{\alpha}$ changes accordingly. Pure QED effects are included up to next-to-leading order (NLO) while higher orders are negligible. Precise results can be obtained for $\mu < 2m_\pi$ and $\mu \geq m_c$.

Besides full one-loop electroweak corrections, $\Delta\hat{r}_W$ and $\Delta\hat{r}_Z$ include enhanced two-loop contributions of $\mathcal{O}(\alpha^2 m_t^4)$ [10] (implemented using the analytic expressions of Ref. [11]) and $\mathcal{O}(\alpha^2 m_t^2)$ [12] (available as expansions in small and large M_H); mixed electroweak/QCD corrections of $\mathcal{O}(\alpha\alpha_s)$ [13] and $\mathcal{O}(\alpha\alpha_s^2 m_t^2)$ [14]; the analogous mixed electroweak/QED corrections of $\mathcal{O}(\alpha^2)$; and fermion mass corrections also including the leading gluonic and photonic corrections.

2.3. Z decay widths and asymmetries

The partial width for $Z \to f\bar{f}$ decays is given by,

$$\Gamma_{f\bar{f}} = \frac{N_C^f M_Z \hat{\alpha}}{24\hat{s}^2\hat{c}^2}|\hat{\rho}_f|\left[1-4|Q_f|\mathrm{Re}(\hat{\kappa}_f)\hat{s}^2+8Q_f^2\hat{s}^4|\hat{\kappa}_f|^2\right]$$

$$\times\left[1+\delta_{\rm QED}+\delta_{\rm QCD}^{\rm NS}+\delta_{\rm QCD}^{\rm S}-\frac{\hat{\alpha}\hat{\alpha}_s}{4\pi^2}Q_f^2+\mathcal{O}(m_f^2)\right]. \quad (6)$$

N_C^f is the color factor, Q_f is the fermion charge, and $\hat{\rho}_f$ and $\hat{\kappa}_f$ are form factors which differ from unity through one-loop electroweak corrections [15] and are computed in `rho.f` and `kappa.f`, respectively. For $f \neq b$ there are no corrections of $\mathcal{O}(\alpha^2 m_t^4)$ and contributions of $\mathcal{O}(\alpha^2 m_t^2)$ to $\hat{\kappa}_f$ [16] and $\hat{\rho}_f$ [9] are very small and presently neglected. On the other hand, vertex corrections of $\mathcal{O}(\alpha\alpha_s)$ [17] are important and shift the extracted α_s by ~ 0.0007.

The $Z \to b\bar{b}$ vertex receives extra corrections due to heavy top quark loops. They are large and have been implemented in `bvertex.f` based on Ref. [18]. $\mathcal{O}(\alpha^2 m_t^4)$ corrections [10,11] are included, as well, while those of $\mathcal{O}(\alpha^2 m_t^2)$ are presently unknown. The leading QCD effects of $\mathcal{O}(\alpha\alpha_s m_t^2)$ [19] and all subleading $\mathcal{O}(\alpha\alpha_s)$ corrections [20] are incorporated into $\hat{\rho}_b$ and $\hat{\kappa}_b$, but not the $\mathcal{O}(\alpha\alpha_s^2 m_t^2)$ contribution which is presently available only for nonsinglet diagrams [21].

In Eq. (6), $\delta_{\rm QED}$ are the $\mathcal{O}(\alpha)$ and $\mathcal{O}(\alpha^2)$ QED corrections. $\delta_{\rm QCD}^{\rm NS}$ are the universal QCD corrections up to $\mathcal{O}(\alpha_s^3)$ which include quark mass dependent contributions due to double-bubble type diagrams [22,23]. $\delta_{\rm QCD}^{\rm S}$ are the singlet contributions to the axial-vector and vector partial widths which start, respectively, at $\mathcal{O}(\alpha_s^2)$ and $\mathcal{O}(\alpha_s^3)$, and induce relatively large family universal but flavor non-universal m_t effects [23,24]. The corrections appearing in the second line of Eq. (6) are evaluated in `lep100.f`.

The dominant massless contribution to $\delta_{\rm QCD}^{\rm NS}$ can be obtained by analytical continuation of the Adler D-function, which (in the $\overline{\rm MS}$ scheme) has a very well behaved perturbative expansion $\sim 1+\sum_{i=0} d_i a_s^{i+1}$ in $a_s = \hat{\alpha}_s(M_Z)/\pi$ (see the Appendix for details). The process of analytical continuation from the Euclidean to the physical region induces further terms which are proportional to β-function coefficients, enhanced by powers of π^2, and start at $\mathcal{O}(\alpha_s^3)$. Fortunately, these terms [25] involve only known coefficients up to $\mathcal{O}(\alpha_s^5)$, and the only unknown coefficient in $\mathcal{O}(\alpha_s^6)$ is proportional to the four-loop Adler function coefficient, d_3. In the massless approximation,

$$\begin{aligned}\delta_{\rm QCD}^{\rm NS} \;\approx\; & a_s + 1.4092 a_s^2 - (0.681+12.086)\,a_s^3 + \\ & (d_3 - 89.19)\,a_s^4 + (d_4+79.7)\,a_s^5 + \\ & (d_5 - 121 d_3 + 3316)\,a_s^6, \end{aligned} \quad (7)$$

and terms of order $a_s^7 \sim 10^{-10}$ are clearly negligible. Notice, that the $\mathcal{O}(\alpha_s^6)$ term effectively *reduces* the sensitivity to d_3 by about 18%. Eq. (7) amounts to a reorganization of the perturbative series in terms of the d_i times some function of α_s; a similar idea is routinely applied to the perturbative QCD contribution to τ decays [26].

Final state fermion mass effects [22,27] of $\mathcal{O}(m_f^2)$ (and $\mathcal{O}(m_b^4)$ for b quarks) are best evaluated by expanding in $\hat{m}_q^2(M_Z)$ thus avoiding large logarithms in the quark masses. The singlet contribution of $\mathcal{O}(\alpha_s^2 m_b^2)$ is also included.

The dominant theoretical uncertainty in the Z lineshape determination of α_s originates from the massless quark contribution, and amounts to about ± 0.0004 as estimated in the Appendix. There are several further uncertainties, all of $\mathcal{O}(10^{-4})$: from the $\mathcal{O}(\alpha_s^4)$ heavy top quark contribution to the axial-vector part of $\delta_{\rm QCD}^{\rm S}$; from the missing $\mathcal{O}(\alpha\alpha_s^2 m_t^2)$ and $\mathcal{O}(\alpha^2 m_t^2)$ contributions to the $Zb\bar{b}$-vertex; from further non-enhanced but cohering $\mathcal{O}(\alpha\alpha_s^2)$-vertex corrections; and from possible contributions of non-perturbative origin. The total theory uncertainty is therefore,

$$\Delta\alpha_s(M_Z) = \pm 0.0005, \quad (8)$$

which can be neglected compared to the current experimental error. If $\hat{m}_b$ is kept fixed in a fit, then its parametric error would add an uncertainty of ± 0.0002, but this would not change the total uncertainty (8).

Polarization asymmetries are (in some cases up to a trivial factor 3/4 or a sign) given by the asymmetry parameters,

$$A_f = \frac{1-4|Q_f|\mathrm{Re}(\hat{\kappa}_f)\hat{s}^2}{1-4|Q_f|\mathrm{Re}(\hat{\kappa}_f)\hat{s}^2+8Q_f^2\hat{s}^4|\hat{\kappa}_f|^2}, \quad (9)$$

and the forward-backward asymmetries by,

$$A_{FB}(f) = \frac{3}{4}A_e A_f. \quad (10)$$

The hadronic charge asymmetry, Q_{FB}, is the linear combination,

$$Q_{FB} = \sum_{q=d,s,b} R_q A_{FB}(q) - \sum_{q=u,c} R_q A_{FB}(q), \quad (11)$$

and the hadronic peak cross section, $\sigma_{\rm had}$, is stored in `sigmah`, and defined by,

$$\sigma_{\rm had} = \frac{12\pi\Gamma_{e^+e^-}\Gamma_{\rm had}}{M_Z^2\Gamma_Z^2}. \quad (12)$$

Widths and asymmetries are stored in the fields `gamma(f)`, `alr(f)`, and `afb(f)`. The fermion index, `f`, and the partial width ratios, `R(f)`, are defined in Table 1.

Table 1
Some of the variables used in `lep100.f`. $\Gamma_{\rm inv}$ and $\Gamma_{\rm had}$ are the invisible and hadronic decays widths, respectively.

0	ν	`gamma(0)` $= \Gamma_{\rm inv}$	`alr(0)` $= 1$
1	e	`R(1)` $= \Gamma_{\rm had}/\Gamma_{e^+e^-}$	`alr(1)` $= A_e$
2	μ	`R(2)` $= \Gamma_{\rm had}/\Gamma_{\mu^+\mu^-}$	`alr(2)` $= A_\mu$
3	τ	`R(3)` $= \Gamma_{\rm had}/\Gamma_{\tau^+\tau^-}$	`alr(3)` $= A_\tau$
4	u	`R(4)` $= \Gamma_{u\bar{u}}/\Gamma_{\rm had}$	—
5	c	`R(5)` $= \Gamma_{c\bar{c}}/\Gamma_{\rm had}$	`alr(5)` $= A_c$
6	t	`R(6)` $= 0$	—
7	d	`R(7)` $= \Gamma_{d\bar{d}}/\Gamma_{\rm had}$	—
8	s	`R(8)` $= \Gamma_{s\bar{s}}/\Gamma_{\rm had}$	`alr(8)` $= A_s$
9	b	`R(9)` $= \Gamma_{b\bar{b}}/\Gamma_{\rm had}$	`alr(9)` $= A_b$
10	had	`gamma(10)` $= \Gamma_{\rm had}$	`afb(10)` $= Q_{FB}$
11	all	`gamma(11)` $= \Gamma_Z$	—

2.4. Fermion masses

I use $\overline{\rm MS}$ masses as far as QCD is concerned, but retain on-shell masses for QED since renormalon effects are unimportant in this case. This results in a hybrid definition for quarks. Accordingly, the RG running of the masses to scales $\mu \neq \hat{m}_q$ uses pure QCD anomalous dimensions. The running masses correspond to the functions `msrun(`μ`)`, `mcrun(`μ`)`, etc. which are calculated in `masses.f` to three-loop order. Anomalous dimensions are also available at four-loop order [28], but can safely be neglected. Also needed is the RG evolution of α_s which is implemented to four-loop precision [29] in `alfas.f`.

I avoid pole masses for the five light quarks throughout. Due to renormalon effects, these can be determined only up to $\mathcal{O}(\Lambda_{\rm QCD})$ and would therefore induce an irreducible uncertainty of about 0.5 GeV. In fact, perturbative expansions involving the pole mass show unsatisfactory convergence. In contrast, the $\overline{\rm MS}$ mass is a short distance mass which can, in principle, be determined to arbitrary precision, and perturbative expansions are well behaved with coefficients of order unity (times group theoretical factors which grow only geometrically). Note, however, that the coefficients of expansions involving large powers of the mass, $\hat{m}^n$, are rather expected to be of $\mathcal{O}(n)$. This applies, e.g., to decays of heavy quarks ($n = 5$) and to higher orders in light quark mass expansions.

The top quark pole mass enters the analysis when the results on m_t from on-shell produced top quarks at the Tevatron are included. In subroutine `polemasses(nf,mpole)` $\hat{m}_q(\hat{m}_q)$ is converted to the quark pole mass, `mpole`, using the two-loop perturbative relation from Ref. [30]. The exact three-loop result [31] has been approximated (for m_t) by employing the BLM [32] scale for the conversion. Since the pole mass is involved it is not surprising that the coefficients are growing rapidly. The third order contribution is 31%, 75%, and 145% of the second order for m_t (`nf` $= 6$), m_b (`nf` $= 5$), and m_c (`nf` $= 4$), respectively. I take the three-loop contribution to the top quark pole mass of about 0.5 GeV as the theoretical uncertainty, but this is currently negligible relative to the experimental error. At a high energy lepton collider it will be possible to extract the $\overline{\rm MS}$ top quark mass directly and to abandon quark pole masses altogether.

2.5. ν scattering

The ratios of neutral-to-charged current cross sections,

$$R_\nu = \frac{\sigma^{NC}_{\nu N}}{\sigma^{CC}_{\nu N}}, \qquad R_{\bar\nu} = \frac{\sigma^{NC}_{\bar\nu N}}{\sigma^{CC}_{\bar\nu N}}, \tag{13}$$

have been measured precisely in deep inelastic ν ($\bar\nu$) hadron scattering (DIS) at CERN (CDHS and CHARM) and Fermilab (CCFR). The most precise result was obtained by the NuTeV Collaboration at Fermilab who determined the Paschos-Wolfenstein ratio,

$$R^- = \frac{\sigma^{NC}_{\nu N} - \sigma^{NC}_{\bar\nu N}}{\sigma^{CC}_{\nu N} - \sigma^{CC}_{\bar\nu N}} \sim R_\nu - r R_{\bar\nu}, \tag{14}$$

with $r = \sigma^{CC}_{\bar\nu N}/\sigma^{CC}_{\nu N}$. Results on R_ν are frequently quoted in terms of the on-shell weak mixing angle (or M_W) as this incidentally gives a fair description of the dependences on m_t and M_H. One can write approximately,

$$R_\nu = g_L^2 + g_R^2 r, \quad R_{\bar\nu} = g_L^2 + \frac{g_R^2}{r}, \quad R^- = g_L^2 - g_R^2, \tag{15}$$

where,

$$g_L^2 = \frac{1}{2} - \sin^2\theta_W + \frac{5}{9}\sin^4\theta_W, \quad g_R^2 = \frac{5}{9}\sin^4\theta_W. \tag{16}$$

However, the study of new physics requires the implementation of the actual linear combinations of effective four-Fermi operator coefficients, $\epsilon_{L,R}(u)$ and $\epsilon_{L,R}(d)$, which have been measured. With the appropriate value for the average momentum transfer, `q2`, as input, these are computed in the subroutines `nuh(q2,epsu_L,epsd_L,epsu_R,epsd_R)` (according to Ref. [33]), `nuhnutev`, `nuhccfr`, and `nuhcdhs`, all contained in file `dis.f`. Note, that the CHARM results have been adjusted to CDHS conditions [34]. While the experimental correlations between the various DIS experiments are believed to be negligible, large correlations are introduced by the physics model through charm mass threshold effects,

quark sea effects, radiative corrections, etc. I constructed the matrix of correlation coefficients using the analysis in Ref. [34],

$$\begin{array}{ccccccc} R^- & R_\nu & R_\nu & R_\nu & R_{\bar\nu} & R_{\bar\nu} & R_{\bar\nu} \end{array}$$

$$\left(\begin{array}{ccccccc} 1.00 & 0.10 & 0.10 & 0.10 & 0.00 & 0.00 & 0.00 \\ 0.10 & 1.00 & 0.40 & 0.40 & 0.10 & 0.10 & 0.10 \\ 0.10 & 0.40 & 1.00 & 0.40 & 0.10 & 0.10 & 0.10 \\ 0.10 & 0.40 & 0.40 & 1.00 & 0.10 & 0.10 & 0.10 \\ 0.00 & 0.10 & 0.10 & 0.10 & 1.00 & 0.15 & 0.15 \\ 0.00 & 0.10 & 0.10 & 0.10 & 0.15 & 1.00 & 0.15 \\ 0.00 & 0.10 & 0.10 & 0.10 & 0.15 & 0.15 & 1.00 \end{array}\right). \quad (17)$$

The effective vector and axial-vector couplings, $g_V^{\nu e}$ and $g_A^{\nu e}$, from elastic νe scattering are calculated in subroutine `nue(q2,gvnue,ganue)` in file `nue.f`. The momentum transfer, `q2`, is currently set to zero [36]. Needed is the low energy ρ parameter, `rhonc`, which describes radiative corrections to the neutral-to-charged current interaction strengths. Together with `sin2t0` (described below) it is computed in file `lowenergy.f`.

2.6. Low energy observables

The weak atomic charge, `Qw`, from atomic parity violation and fixed target ep scattering is computed in subroutine `apv(Qw,Z,AA,C1u,C1d,C2u,C2d)` where `Z` and `AA` are, respectively, the atomic number and weight. Also returned are the coefficients from lepton-quark effective four-Fermi interactions which are calculated according to [37].

These observables are sensitive to the low energy mixing angle, `sin2t0`, which defines the electroweak counterpart to the fine structure constant and is similar to the one introduced in Ref. [7]. There is significant correlation between the hadronic uncertainties from the RG evolutions of $\hat\alpha$ and the weak mixing angle. Presently, this correlation is ignored, but with the recent progress in atomic parity violation experiments it should be accounted for in the future.

An additional source of hadronic uncertainty is introduced by γZ-box diagrams which are unsuppressed at low energies. At present, this uncertainty can be neglected relative to the experimental precision.

Besides `apv`, the file `pnc.f` contains in addition the subroutine `moller` for the anticipated polarized fixed target Møller scattering experiment at SLAC. Radiative corrections are included following Ref. [38].

2.7. $b \to s\gamma$

Subroutine `bsgamma` returns the decay ratio,

$$R = \frac{\mathcal{B}(b \to s\gamma)}{\mathcal{B}(b \to ce\nu)}. \quad (18)$$

It is given by [39,40],

$$R = \frac{6\alpha}{\pi}\left|\frac{V_{ts}^* V_{tb}}{V_{cb}}\right|^2 \frac{S}{f(z)} \frac{|\bar D|^2 + A/S + \delta_{NP} + \delta_{EW}}{(1+\delta_{NP}^{SL})(1+\delta_{EW}^{SL})}, \quad (19)$$

where $|V_{ts}^* V_{tb}/V_{cb}|^2 = 0.950$ is a combination of Cabbibo-Kobayashi-Maskawa matrix elements and S is the Sudakov factor [41]. δ_{NP} and δ_{EW} are non-perturbative and NLO electroweak [42] corrections, both for the $b \to s\gamma$ and the semileptonic ($b \to ce\nu$) decay rates.

$$\bar D = C_7^0 + \frac{\hat\alpha_s(\hat m_b)}{4\pi}(C_7^1 + V), \quad (20)$$

is called the reduced amplitude for the process $b \to s\gamma$, and is given in terms of the Wilson coefficient C_7 at NLO. C_7 and the other C_i appearing below are effective Wilson coefficients with NLO RG evolution [43] from the weak scale to $\mu = \hat m_b$ understood. The NLO matching conditions at the weak scale have been calculated in Ref. [44]. $\bar D$ includes the virtual gluon corrections,

$$V = r_2 C_2^0 + r_7 C_7^0 + r_8 C_8^0, \quad (21)$$

so that it squares to a positive definite branching fraction. On the other hand, the amplitude for gluon Bremsstrahlung ($b \to s\gamma g$),

$$A = \tfrac{\hat\alpha_s(\hat m_b)}{\pi}[C_2^0(C_8^0 f_{28}(1) + C_7^0 f_{27}(1) + C_2^0 f_{22}(1)) + C_8^0(C_8^0 f_{88}(\delta) + C_7^0 f_{78}(\delta)) + (C_7^0)^2 f_{77}(\delta)], \quad (22)$$

is added linearly to the cross section. The Wilson coefficient C_2^0 is defined as in Ref. [45]. It enters only at NLO, is significantly larger than C_7^0, and dominates the NLO contributions. The parameter $0 \le \delta \le 1$ in the coefficient functions f_{ij} characterizes the minimum photon energy and has been set to $\delta = 0.9$ [41], except for the first line in Eq. (22) where $\delta = 1.0$ corresponding to the full cross section. The f_{2i} are complicated integrals which can be solved in terms of polylogarithms up to 5th order. In the code I use an expansion in $z = m_c^2/m_b^2$ and $\delta = 1.0$. Once experiments become more precise the correction to $\delta = 0.9$ should be included.

$f(z)$ is the phase space factor for the semileptonic decay rate including NLO corrections [46]. I defined the $\overline{\rm MS}$ mass ratio in $z = [\hat m_c(\hat m_b)/\hat m_b(\hat m_b)]^2$ at the common scale, $\mu = \hat m_b$, which I also assumed for the factor $\hat m_b^5$ multiplying the decay widths. Since I do not re-expand the denominator this effects the phase space function at higher orders. Using the $\mathcal{O}(\alpha_s^2)$-estimate[2]

[2] I computed the $\mathcal{O}(\alpha_s^2)$ coefficient for comparison only, and did not include it in the code.

from Ref. [47], I obtain for the semileptonic decay width,

$$\Gamma_{SL} \sim \hat{m}_b^5 f_0(z) \left[1 + 2.7\,\frac{\hat{\alpha}_s(\hat{m}_b)}{\pi} - 1.6\left(\frac{\hat{\alpha}_s}{\pi}\right)^2\right], \quad (23)$$

where $f_0(z)$ is the leading order phase space factor. It is amusing that the coefficients in Eq. (23) are comfortably (and perhaps somewhat fortuitously) small, with the $\mathcal{O}(a_s^2)$-coefficient even smaller than the one in Ref. [47] where a low scale running mass had been advocated. Moreover, using the pre-factor $\hat{m}_b^5$ in the numerator of R reduces the size of r_7 in Eq. (21) and therefore the coefficient $\kappa(\delta) = f_{77}(\delta) + r_7/2$ which multiplies the term $a_s(C_7^{0,\text{eff}})^2$. I obtain $-2.1 < \kappa(\delta) < 1.4$, while with the pole mass pre-factor M_b^5 one would have $-8.7 \leq \kappa(\delta) < -5.3$.

Acknowledgements

It is a pleasure to thank Paul Langacker and Damien Pierce for collaborations on precision analyses. I am grateful to Francesca Borzumati and Paolo Gambino for providing me with parts of their FORTRAN codes.

A. Uncertainties from perturbative QCD

Writing the perturbative expansion of some quantity in its general form for an arbitrary gauge group, it can easily be decomposed into separately gauge invariant parts. Table 2 shows for some (related) examples that after removing the group theoretical pre-factors, all coefficients, y_i, are *strictly* of order unity, and that their mean, $\bar{y}$, is very close to zero. In particular, there is no sign of factorial growth of coefficients. These observations offer a valuable tool to estimate the uncertainties associated with the truncation of the loop expansion, so I would like to make them more precise.

Assume (for simplicity) that the y_i are random draws from some normal distribution with unknown mean, μ, and variance, σ^2. One can show that the marginal distribution of μ follows a Student-t distribution with $n-1$ degrees of freedom, t_{n-1}, centered about $\bar{y}$, and with standard deviation,

$$\Delta\mu = \sqrt{\frac{\sum_i (y_i - \bar{y})^2}{n(n-3)}}. \quad (24)$$

As can be seen from the Table, μ is consistent with zero in all cases, justifying the nullification of the unknown coefficients from higher loops. I next assert that the distribution of σ, conditional on $\mu = 0$, follows a scaled inverse-χ^2 distribution with n degrees of freedom, from which I obtain the estimate,

$$\sigma = \sigma_0 \pm \Delta\sigma = \sqrt{\frac{\sum_i y_i^2}{n-2}}\left[1 \pm \sqrt{\frac{1}{2(n-4)}}\right]. \quad (25)$$

Inspection of the Table shows indeed that σ, as the typical size of a coefficient, is estimated to be $\lesssim \mathcal{O}(1)$.

I now focus on the partial hadronic Z decay width. As discussed in Section 2.3, the $\mathcal{O}(\alpha_s^3)$ term, d_2, is much smaller than the π^2 term arising from analytical continuation. This is specifically true for the relevant case of $n_f = 5$ active flavors, where large cancellations occur between gluonic and fermionic loops. Notice, that the D-function, in contrast to R_{had}, has opposite signs in the leading terms proportional to $C_A^2 C_F$ and $C_A C_F T_F n_F$. Indeed, the Adler D-function and the β-function have similar structures regarding the signs and sizes of the various terms (see Table 2), and we *do expect* large cancellations in the β-function. The reason is that it has to vanish identically in the case of $N = 4$ supersymmetry. Ignoring scalar contributions this case can be mimicked by setting $T_F n_f = 2C_A$ (there are 2 Dirac fermions in the $N = 4$ gauge multiplet) or $n_f = 12$ for QCD, which is of the right order. In fact, all known QCD β-function coefficients become very small for some value of n_f between 6 and 16. We therefore have a reason to expect that similar cancellations will reoccur in the d_i at higher orders. As a 1σ error estimate for d_3, I suggest to use the largest known coefficient (3×0.71) times the largest group theoretical pre-factor in the next order ($C_A^3 C_F$) which results in

$$d_3 = 0 \pm 77. \quad (26)$$

With Eq. (7) and $\hat{\alpha}_s(M_Z) = 0.120$ one can absorb all higher order effects into the $\mathcal{O}(\alpha_s^4)$-coefficient of R_{had}, $r_3^{\text{eff}} = -81 \pm 63$. This shifts the extracted α_s from the Z line-shape by $+0.0005$ and introduces the small uncertainty of ± 0.0004.

The argument given above does certainly not apply to the *quenched* case, $n_f = 0$, and indeed $d_2(n_f = 0)$ is about -73% of the π^2 term, i.e., large and positive. In the case of $n_f = 3$, which is of interest for the precision determination of α_s from τ decays, d_2 is about -38% of the π^2 term. If one assumes that the same is true of d_3, one would obtain $d_3(n_f = 3) = 60$. Estimates based on the principles of minimal sensitivity, PMS, or fastest apparent convergence, FAC, yield $d_3(n_f = 3) = 27.5$ [25] so there might be some indications for a positive $d_3(n_f = 3)$. In any case, all these estimates lie within the uncertainty in Eq. (26) and we will have to await the proper calculation of the $\mathcal{O}(\alpha_s^4)$-coefficient to test these hypotheses. Note, that the current τ decay analysis by the ALEPH Collaboration uses $d_3 = 50 \pm 50$ [50] which is more optimistic.

The analogous error estimate for the five-loop β-function coefficient yields,

$$\beta_4 = 0 \pm 579. \tag{27}$$

To get an estimate for the uncertainty in the RG running of $\hat{\alpha}_s$, I translate Eq. (27) into

$$\beta_3 = \beta_3 \pm \frac{\hat{\alpha}_s(\mu_0)}{\pi}\beta_4, \tag{28}$$

where μ_0 is taken to be the lowest scale involved. This overestimates the uncertainty from β_4, thereby compensating for other neglected terms of $\mathcal{O}(\alpha_s^{n+4} \ln^n \mu^2/\mu_0^2)$. For the RG evolution from $\mu = m_\tau$ to $\mu = M_Z$ this yields an uncertainty of $\Delta\alpha_s(M_Z) = \pm 0.0005$. Conversely, for fixed $\alpha_s(M_Z) = 0.120$, I obtain $\hat{\alpha}_s(\hat{m}_b) = 0.2313 \pm 0.0006$, $\hat{\alpha}_s(m_\tau) = 0.3355 \pm 0.0045$, and $\hat{\alpha}_s(\hat{m}_c) = 0.403 \pm 0.011$, where I have used $\hat{m}_b = 4.24$ GeV and $\hat{m}_c = 1.31$ GeV. For comparison, the ALEPH Collaboration quotes an evolution error of $\Delta\alpha_s(M_Z) = \pm 0.0010$ which is twice as large. I emphasize that it is important to adhere to consistent standards when errors are estimated. This is especially true in the context of a global analysis where the precisions of the observables enter as their relative weights.

REFERENCES

1. The GAPP package is available at URL: `http://www.physics.upenn.edu/~erler/electroweak`.
2. M. Peskin and T. Takeuchi, Phys. Rev. Lett. **65**, 964 (1990); D. Kennedy and P. Langacker, Phys. Rev. Lett. **65**, 2967 (1990); B. Holdom and J. Terning, Phys. Lett. **B247**, 88 (1990); G. Altarelli and R. Barbieri, Phys. Lett. **B253**, 161 (1990).
3. J. Erler, Phys. Rev. **D59**, 054008 (1999).
4. The MINUIT writeup is available at URL: `http://consult.cern.ch/writeup/minuit/`.
5. G.J. van Oldenborgh and J.A.M. Vermaseren, Z. Phys. **C46**, 425 (1990); G.J. van Oldenborgh, Comput. Phys. Commun. **66**, 1 (1991).
6. The FF package is available at URL: `http://www.xs4all.nl/~gjvo/FF.html`.
7. A. Sirlin, Nucl. Phys. **B332**, 20 (1990);
8. G. Degrassi, S. Fanchiotti, and A. Sirlin, Nucl. Phys. **B351**, 49 (1991); G. Degrassi and A. Sirlin, Phys. Rev. **D46** 3104 (1992).
9. G. Degrassi and P. Gambino, Nucl. Phys. **B567**, 3 (2000).
10. R. Barbieri *et al.* , Phys. Lett. **B288**, 95 (1992) and Nucl. Phys. **B409**, 105 (1993).
11. J. Fleischer, O.V. Tarasov, and F. Jegerlehner, Phys. Lett. **B319**, 249 (1993).
12. G. Degrassi, P. Gambino, and A. Vicini, Phys. Lett. **B383**, 219 (1996);
13. A. Djouadi and C. Verzegnassi, Phys. Lett. **B195**, 265 (1987); A. Djouadi, Nuovo Cimento **100A**, 357 (1988); B.A. Kniehl, Nucl. Phys. **B347**, 86 (1990); S. Fanchiotti, B.A. Kniehl, and A. Sirlin, Phys. Rev. **D48**, 307 (1993); A. Djouadi and P. Gambino, Phys. Rev. **D49**, 3499 (1994), **D49**, 4705 (1994), and **D53**, 4111(E) (1996).
14. K.G. Chetyrkin, J.H. Kühn, and M. Steinhauser, Phys. Lett. **B351**, 331 (1995); L. Avdeev, J. Fleischer, S. Mikhailov, and O. Tarasov, Phys. Lett. **B336**, 560 (1994) and **B349**, 597(E) (1995).
15. G. Degrassi and A. Sirlin, Nucl. Phys. **B352** 342 (1991).
16. G. Degrassi, P. Gambino, and A. Sirlin, Phys. Lett. **B394**, 188 (1997).
17. A. Czarnecki and J.H. Kühn, Phys. Rev. Lett. **77**, 3955 (1997).
18. J. Bernabeu, A. Pich, and A. Santamaria, Nucl. Phys. **B363**, 326 (1991).
19. J. Fleischer, F. Jegerlehner, P. Raczka, and O.V. Tarasov, Phys. Lett. **B293**, 437 (1992).
20. R. Harlander, T. Seidensticker, and M. Steinhauser, Phys. Lett. **B426**, 125 (1998).
21. K.G. Chetyrkin and M. Steinhauser, Eur. Phys. J. **C11**, 89 (1999).
22. K.G. Chetyrkin, J.H. Kühn, and A. Kwiatkowski, Phys. Rep. **277**, 189 (1996).
23. S.A. Larin, T. van Ritbergen, and J.A.M. Vermaseren, Nucl. Phys. **B438**, 278 (1995).
24. B.A. Kniehl and J.H. Kühn, Nucl. Phys. **B329**, 547 (1990).
25. A.L. Kataev and V.V. Starshenko, Mod. Phys. Lett. **A10**, 235 (1995).
26. F. Le Diberder and A. Pich, Phys. Lett. **B286**, 147 (1992).
27. K.G. Chetyrkin and J.H. Kühn, Phys. Lett. **B406**, 102 (1997).
28. J.A.M. Vermaseren, S.A. Larin, and T. van Ritbergen, Phys. Lett. **B405**, 327 (1997).
29. T. van Ritbergen, J.A.M. Vermaseren, and S.A. Larin, Phys. Lett. **B400**, 379 (1997).
30. N. Gray, D.J. Broadhurst, W. Grafe, and K. Schilcher, Z. Phys. **C48**, 673 (1990).
31. K. Melnikov and T. van Ritbergen, e-print `hep-ph/9912391`.
32. S.J. Brodsky, G.P. Lepage, and P.B. Mackenzie, Phys. Rev. **D28**, 228 (1983).
33. W.J. Marciano and A. Sirlin, Phys. Rev. **D22**, 2695 (1980).
34. F. Perrier, p. 385 of Ref. [35].
35. *Precision Tests of the Standard Electroweak Model*, ed. P. Langacker (World Scientific, Singa-

pore, 1995).
36. W.J. Marciano, p. 170 of Ref. [35].
37. W.J. Marciano and A. Sirlin, Phys. Rev. **D29**, 75 (1984); W.J. Marciano, p. 613 of the Proceedings of TASI 93, *The Building Blocks of Creation: from Microfermis to Megaparsecs*, eds. S. Raby and T. Walker, (World Scientific, River Edge, 1994).
38. A. Czarnecki and W.J. Marciano, Phys. Rev. **D53**, 1066 (1996).
39. C. Greub, T. Hurth, and D. Wyler, Phys. Rev. **D54**, 3350 (1996).
40. F.M. Borzumati and C. Greub, Phys. Rev. **D58**, 074004 (1998) and references therein.
41. A.L. Kagan and M. Neubert, Eur. Phys. J. **C7**, 5 (1999).
42. A. Czarnecki and W.J. Marciano, Phys. Rev. Lett. **81**, 277 (1998).
43. K. Chetyrkin, M. Misiak, and M. Münz, Nucl. Phys. **B518**, 473 (1998).
44. K. Adel and Y.P. Yao, Phys. Rev. **D49**, 4945 (1994).
45. A.J. Buras, M. Misiak, M. Münz, and S. Pokorski, Nucl. Phys. **B424**, 374 (1994).
46. Y. Nir, Phys. Lett. **B221**, 184 (1989).
47. A. Czarnecki and K. Melnikov, Phys. Rev. **D59**, 014036 (1999).
48. K.G. Chetyrkin, Phys. Lett. **B391**, 402 (1997).
49. L.R. Surguladze and M.A. Samuel, Phys. Rev. Lett. **66**, 560 (1991) and *ibid.* **66**, 2416 (1991); S.G. Gorishny, A.L. Kataev, S.A. Larin, Phys. Lett. **B212**, 238 (1988).
50. R. Barate *et al.* [ALEPH Collaboration], Eur. Phys. J. **C4**, 409 (1998).

Table 2
Coefficients ($\overline{\rm MS}$) appearing in the β-function of a simple group [29]; in non-Abelian corrections to the QED β-function (denoted $\tilde{D}$) [3,48]; in the Adler D-function [49] (rescaled by an overall factor 1/3); and in $R_{\rm had}$ (analytical continuation of D). The first four segments correspond, respectively, to the first four loop orders of non-singlet type. The fifth segment is the singlet (double triangle) contribution in $\mathcal{O}(\alpha_s^3)$. In $\tilde{D}$, D, and $R_{\rm had}$, an overall factor $\hat{\alpha}M_Z$ and the sums involving charges or Z couplings have been dropped. The completely symmetrical tensors of rank four, d_A and d_F, as well as T_F when appearing in parenthesis, apply to the β-function only. Each T_F is understood to be multiplied by the number of flavors, n_f, except for the singlet term involving the symmetrical structure constants, d.

group factor	β	$\tilde{D}$	D	$R_{\rm had}$
C_A	0.92	—	—	—
(T_F)	−0.33	−0.33	0.33	0.33
C_A^2	0.71	—	—	—
$C_A T_F$	−0.42	—	—	—
$C_F(T_F)$	−0.25	−0.25	0.25	0.25
C_A^3	0.83	—	—	—
$C_A^2 T_F$	−0.82	—	—	—
$C_A C_F(T_F)$	−0.36	−0.23	0.18	0.18
$C_A T_F^2$	0.09	—	—	—
$C_F^2(T_F)$	0.03	0.03	−0.03	−0.03
$C_F T_F(T_F)$	0.08	0.08	−0.06	−0.06
C_A^4	1.19	—	—	—
$C_A^3 T_F$	−1.67	—	—	—
$C_A^2 C_F(T_F)$	−0.23	−0.28	0.32	−0.38
$C_A^2 T_F^2$	0.50	—	—	—
$C_A C_F^2(T_F)$	−0.42	−0.07	0.51	0.51
$C_A C_F T_F(T_F)$	0.51	0.42	−0.71	−0.21
$C_A T_F^3$	0.01	—	—	—
$C_F^3(T_F)$	0.18	0.18	−0.18	−0.18
$C_F^2 T_F(T_F)$	−0.17	−0.17	0.02	0.02
$C_F T_F^2(T_F)$	0.02	0.02	0.09	−0.01
d_A^2/N_A	1.07	—	—	—
$d_A d_F/N_A$	−2.38	—	—	—
d_F^2/N_A $(T_F^2 d^2/4)$	0.50	0.50	−0.50	−0.50
$\bar{y}$	−0.02	−0.01	0.02	−0.01
$\Delta\mu$	0.17	0.09	0.11	0.09
σ_0	0.83	0.28	0.37	0.31
$\Delta\sigma$	0.13	0.07	0.09	0.08

Report of the Working Group on Photon and Weak Boson Production

Conveners: U. Baur (Buffalo), E.L. Berger (ANL), H.T. Diehl (FNAL), and D. Errede (UIUC)
Subgroup Conveners: *Photon Production:* J. Huston (MSU), J. Owens (FSU), and J. Womersley (FNAL) *Weak Boson Production:* D. Casey (MSU) and T. Dorigo (Harvard), *Diboson Production:* U. Baur (Buffalo) and H.T. Diehl (FNAL)
Contributing authors: L. Apanasevich (Rochester), M. Begel (Rochester), Y. Gershtein (Brown), M. Kelly (Michigan), S. E. Kuhlmann (ANL), S. Leone (Pisa), D. Partos (Brandeis), D. Rainwater (FNAL), W.K. Sakumoto (Rochester), G. Steinbrück (Columbia), M. Zieliński (Rochester), and V. Zutshi (Rochester)

This report discusses physics issues which can be addressed in photon and weak boson production in Run II at the Tevatron. The current understanding and the potential of Run II to expand our knowledge of direct photon production in hadronic collisions is discussed. We explore the prospects for using the W-boson cross section to measure the integrated luminosity, improving the measurement of the W and Z boson transverse momentum distributions, the $Z \to b\bar{b}$ signal, and the lepton angular distribution in W decays. Finally, we consider the prospects for measuring the trilinear gauge boson couplings in Run II.

1. Introduction

For the next few years, the Fermilab Tevatron Collider will be the high energy frontier of particle physics. The luminosity enhancement provided by the Main Injector will significantly increase the discovery reach of the Tevatron experiments over what has been achieved with Run I data. It will also move the experimental program into a regime of precision hadron collider physics. This will make it possible to address open questions of high energy physics from several complementary directions.

Understanding the mechanism of production for photons, W, and Z-bosons is important for several reasons. First of all, it provides an opportunity to directly test the Standard Model (SM). Second, photon and weak boson production often constitute an irreducible background in searches for new physics. Finally, a detailed understanding of the production mechanism for these particles is necessary to control the systematic errors in precision measurements, such as the determination of the W mass (see Ref. [1]).

In this report, we consider several aspects of the production of photons, W, and Z bosons which are of interest for Run II of the Tevatron Collider. In Sec. 2, direct photon production is discussed. A detailed overview of our current experimental and theoretical understanding of direct photon production in hadronic collisions is presented. Direct photon production has long been considered a probe of QCD and a source for extracting the gluon distribution of the proton. Unfortunately, not all existing (fixed target and Tevatron collider) datasets are consistent, and our current theoretical understanding of direct photon production, especially at small photon transverse momenta, is incomplete. Recent theoretical developments, however, offer optimism that the long-standing difficulties in direct photon production can finally be resolved. The enormous number of photon-jet events expected in Run II may help to shed light on these issues. In particular, photon – jet correlations should be helpful in sorting out the source of disagreement between theory and experiment. In addition, the kinematic reach in transverse momentum will be greatly extended in Run II.

In Sec. 3 several important topics associated with W and Z-boson production are discussed. For many measurements in Run II, knowledge of the integrated luminosity is essential. The integrated luminosity can be extracted either from the total inelastic cross section or from the cross section of a theoretically well understood process with high statistics, such as inclusive W production. Using the total inelastic cross section to determine the integrated luminosity for Run I has led to inconsistencies which may well persist in Run II. It may thus be advantageous to use the W production cross section as an alternative. In Sec. 3.1 we present a brief overview of the magnitude of the experimental uncertainties in such a measurement. The total uncertainty in the W cross section is found to be dominated by the uncertainty from the parton distribution functions, which is considered in more detail in the Report of the Working Group on Parton Distribution Functions [2].

In Sec. 3, we also consider the transverse momentum distribution of the Z boson, $Z \to b\bar{b}$ decays, and the prospects to measure the lepton angular distribution in W decays. The Z p_T distribution is of interest as a test of QCD, and as a tool for reducing uncertainties in the transverse momentum distribution of the W. This

is important for a precise determination of the mass of the W boson (see Ref. [1]). Searching for a light Higgs boson in the range between 110 GeV and 180 GeV is one of the prime objectives for Run II. $H \to b\bar{b}$ decays dominate for Higgs boson masses $M_H < 135$ GeV. The ability to separate the Higgs boson signal in the $Wb\bar{b}$ and $t\bar{t}b\bar{b}$ channels from the large QCD background depends critically on on the $b\bar{b}$ invariant mass resolution, and thus on the measured b-quark jet energies. $Z \to b\bar{b}$ decays offer a testing ground for algorithms designed to improve the jet energy measurement for b jets and are also useful as a calibration tool. The measurement of the lepton angular distributions in W decays serves as a probe of NLO QCD. The measurement carried out by DØ in Run I is statistics limited. While a QCD calculation is preferred, large deviations from QCD are not excluded. In Run II, this measurement will allow for a much improved test of the QCD prediction.

In Sec. 4 of this report, we discuss di-boson production. Vector boson pair production provides a sensitive ground for direct tests of the trilinear gauge boson couplings. A brief overview of the WWV ($V = \gamma$, Z), $Z\gamma V$ and ZZV couplings is presented and recent advances in our theoretical understanding of the NLO QCD corrections to di-boson production are described. After a brief review of the limits on trilinear couplings obtained in Run I, the prospects for strengthening existing bounds in Run II are discussed. In addition to improving the measurements of WWV and $Z\gamma V$ couplings, it will be possible to determine the ZZV couplings via ZZ production with an accuracy of about 15% in Run II, and to observe the so-called "radiation zero" in $W\gamma$ production.

2. Direct Photon Production

The use of direct photon production as an electromagnetic probe of hard scattering dynamics has a history which covers more than twenty years. As in other electromagnetic processes such as lepton pair production or deep inelastic scattering, the point-like coupling of the photon to charged particles offers some simplifications over purely hadronic probes. Compared to hadronic jet production, direct photon production offers the apparent advantages of having fewer subprocesses at lowest order and of avoiding the complications of jet definitions when measuring or calculating a cross section. This latter point means that one can extend the range of transverse momenta to smaller values for direct photons than for jets. However, in actual practice, these apparent simplifications must be tempered by having to deal with backgrounds from neutral meson decays, a lower event rate compared to jet production, and complications from photons produced during jet fragmentation, to name just a few. Nevertheless, direct photon data provide information which complements that obtained from other hard scattering processes. Furthermore, photons may be important signatures of physics beyond the SM. Therefore, it is necessary to understand the "conventional" sources of photons before one can fully exploit them in signatures designed to look for new physics.

In this Section, recent work concerning the phenomenology of initial-state gluon emission in direct-photon production in hadron collisions is reported. In Sec. 2.1, high-mass direct-photon pairs are used to explore the impact of such radiation in terms of effective parton transverse momenta, k_T. At fixed-target energies, data on high-$p_{_T}$ inclusive π^0 and $\pi^0\pi^0$ production are used to further clarify the arguments presented. We then review progress towards fully resummed QCD descriptions and present comparisons of a phenomenological k_T model to recent fixed-target and collider data. Possibilities for more extensive studies with data from Run II, and the additional information they can provide for these considerations, are explored in Sec. 2.1.5. A consistent picture of the observed deviations of NLO perturbative QCD (pQCD) calculations from inclusive direct-photon and π^0 data is now emerging, and we comment on the implications of these results for the extraction of the gluon distribution, $G(x)$, in Sec. 2.1.6.

Run II has the potential to significantly expand our knowledge of direct photon production. Issues related to our understanding of the relevant production mechanisms in the kinematic range accessible during Run II are reviewed in Sec. 2.2. In this Section, we also discuss observables which may help improve our understanding of direct photon production as well as experimental issues which can affect the quality of the data. In Sec. 2.2.4 some predictions for photon-jet correlations are presented. The potential of observables other than the usual single photon p_T distribution to help elucidate the underlying dynamics is discussed.

Run I data are available on the associated production of a γ carrying large transverse momentum along with a charm quark c whose transverse momentum balances a substantial portion of that of the photon [3]. An intriguing possibility is that the data may be used to measure the charm quark density in the nucleon as well as to probe dynamical correlations predicted by QCD. These possibilities are discussed in Ref. [4] where predictions are obtained from a full next-to-leading order perturbative QCD calculation of $p + \bar{p} \to \gamma + c + X$ at high energy. The associated production of a photon and a heavy quark is not discussed further in this report.

2.1. Present Status of Direct Photon Production in Hadronic Collisions[1]

2.1.1. Introduction

Single and double direct-photon production at high p_T have long been viewed as ideal processes for testing the formalisms of pQCD. NLO calculations are available for both processes [5–9]. While the importance of including gluon emission through the resummation formalism was recognized and available for some time for the di-photon process [10,11], it is only recently that this approach has been developed for inclusive direct-photon production [12–17]. A complete theoretical description of the direct-photon process is of special importance as it has long been expected to provide one of the best measurements of the gluon distribution in the proton. The quark–gluon Compton scattering subprocess ($gq \to \gamma q$) shown in Fig. 1 provides a major contribution to inclusive direct-photon production. The gluon distribution ($G(x)$) is relatively well constrained for $x < 0.1$ by deep-inelastic scattering (DIS) and Drell-Yan (DY) data, but less so at larger x [18]. Fixed-target direct-photon data can constrain $G(x)$ at large x, and consequently has been incorporated in several modern global parton distribution analyses [19–21]. More recently, however, both the completeness of the theoretical NLO description of the direct-photon process, and the consistency of the available data sets have been the subject of intense debate [21–27]. Direct-photon measurements in collider

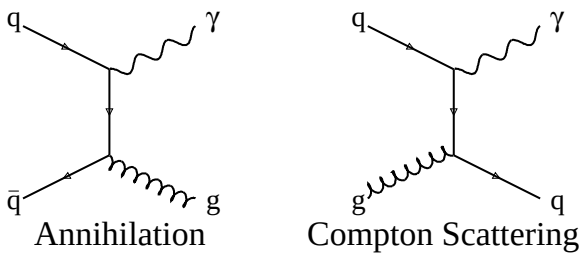

Figure 1. Leading order diagrams for direct-photon production.

data, and especially the data expected from the forthcoming Run II at the Tevatron, provide an important testing ground for novel approaches and improvements in the understanding of the direct-photon process, and therefore can help resolve the present arguments.

The understanding of single and double direct photon yields, and of the more copious high-p_T π^0 production, is of importance for searches for the Higgs in the

[1] Contributed by: L. Apanasevich, M. Begel, Y. Gershtein, J. Huston, S. E. Kuhlmann, D. Partos, J. Womersley, M. Zieliński, and V. Zutshi.

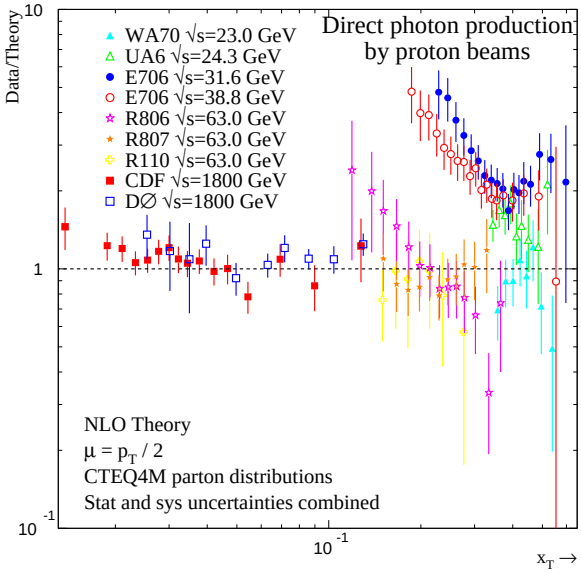

Figure 2. Comparison between proton-induced direct-photon data and NLO pQCD calculations for several experiments as a function of photon x_T ($= 2p_T/\sqrt{s}$). (The CDF and DØ data are from Run Ia, see Figs. 23 and 24 for the Run Ib update.)

$\gamma\gamma$ decay mode at the LHC. In addition, Higgs production, both at the Tevatron and the LHC, can be affected by soft-gluon emission from the initial-state partons, and separation of signal and background can benefit from a reliable resummation formalism or equivalent parton-shower Monte Carlo descriptions [28–30].

2.1.2. Parton Transverse Momentum

A pattern of deviation has been observed between measured direct-photon cross sections and NLO calculations (Fig. 2). The origin of the disagreement has been ascribed to the effect of initial-state soft-gluon radiation [23,24]. Correlations between any produced high-p_T particles probe aspects of the hard scatter not easily accessible via studies of single inclusive particle production. In particular, studies of high-mass pairs of particles such as direct photons and π^0's can be used to extract information about the transverse momentum of partons, k_T, prior to the hard scatter. Whatever the source, any transverse momentum between the partons will appear as a net p_T imbalance among the outgoing particles produced in the hard scatter, and is therefore reflected in the vector sum of the individual p_T values of the outgoing particles (Q_T). If the outgoing particles are pairs of photons or leptons, then this variable should provide a good measure of $\langle k_T \rangle$, with $\langle k_T \rangle$/parton $\approx \langle Q_T \rangle / \sqrt{2}$. When the outgoing particles

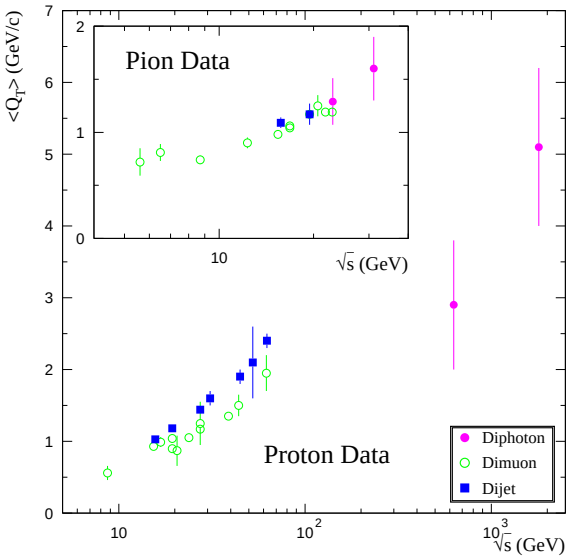

Figure 3. $\langle Q_{_T} \rangle$ of pairs of muons, photons, and jets produced in hadronic collisions versus $\sqrt{s}$.

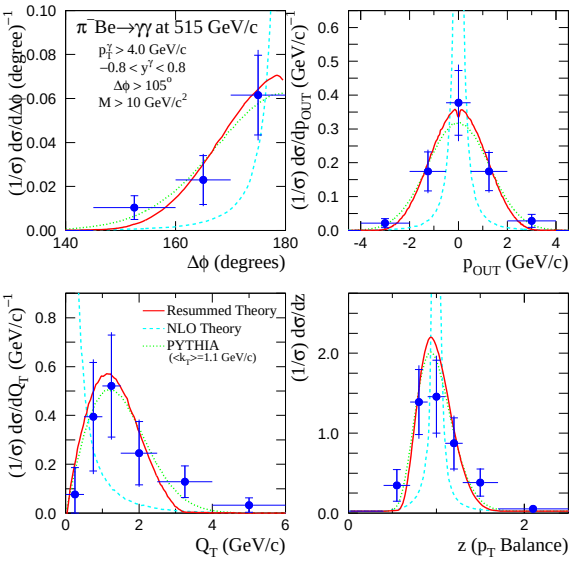

Figure 4. Diphoton $\Delta\phi$, p_{OUT}, $Q_{_T}$, and z distributions for E706 π^-Be data at $\sqrt{s} = 31.1$ GeV [31]. Overlayed on the data are the results from NLO [8] (dashed) and resummed [10] (solid) calculations. PYTHIA [37] results (dotted) with $\langle k_{_T} \rangle = 1.1$ GeV/c are also shown.

are partons, they will hadronize, but the reconstructed jets can also yield a measure of $\langle k_{_T} \rangle$.

Evidence of significant $k_{_T}$ has been found in several measurements of dimuon, diphoton, and dijet production; a collection of $\langle Q_{_T} \rangle$ measurements is displayed in Fig. 3 for a wide range of $\sqrt{s}$ [31–35]. The values of $\langle Q_{_T} \rangle$ are large, and increase with increasing $\sqrt{s}$. The dijet $k_{_T}$ measurements (Fig. 3) agree qualitatively with the dimuon and diphoton results, though they have somewhat higher mean values. Such a shift is expected since there is also potential for final-state soft-gluon emission in dijet events. The values of $\langle k_{_T} \rangle$ per parton indicated by these data are too large to be interpreted as due only to the size of the proton. From these observations, one can infer that the $\langle k_{_T} \rangle$ per parton is of order 1 GeV/c at fixed-target energies, increasing to 3 GeV/c to 4 GeV/c at the Tevatron collider, whereas $\langle k_{_T} \rangle$ would be expected to be of the order of 0.3 GeV/c to 0.5 GeV/c based solely on proton size.

The $p_{_T}$ imbalance between the outgoing particles can also be examined using kinematic variables other than $Q_{_T}$. Given some finite $k_{_T}$, the two outgoing particles no longer emerge back-to-back; the azimuthal angle between the particles, $\Delta\phi$, will differ from 180°. The transverse momentum normal to the scattering plane, p_{OUT}, and the $p_{_T}$-balance quantity,

$$z = -(\vec{p}_{_{T1}} \cdot \vec{p}_{_{T2}}/{p_{_{T2}}}^2) = (p_{_{T2}}/p_{_{T1}}) \cos\Delta\phi, \qquad (1)$$

are two useful variables, each with two possible values per pair of objects.

High-mass direct-photon pairs have been measured at the Tevatron [33,31,36]. Distributions as a function of $\Delta\phi$, p_{OUT}, $Q_{_T}$, and z for such events from E706 [31] are shown in Fig. 4. Overlayed on the data are the results from both NLO [8] and resummed [10] pQCD calculations. There are large differences in the predicted shapes. At leading order, each of these distributions would consist of a δ function. While the NLO prediction has finite width due to the radiation of a single hard gluon, the resummed theory, which also includes the effects of multiple soft-gluon emission, is in better agreement with the data. This is particularly true for $Q_{_T}$, where the NLO calculation tends towards infinity as $Q_{_T} \to 0$, while the resummed (RESBOS [10]) calculation follows the shape of the data and goes to zero. Also shown in Fig. 4 are the distributions from PYTHIA [37], where $k_{_T}$ effects are approximated by a Gaussian smearing technique. PYTHIA provides a reasonable description of the di-photon data using a value for $\langle k_{_T} \rangle$ consistent with the measurements displayed in Fig. 4. Comparisons between CDF and DØ data lead to similar conclusions [29]. There is also good agreement between the WA70 di-photon data [32] and resummed pQCD [11]. The increased statistics expected for Run II should allow for more detailed comparisons between di-photon data and theory.

Similar evidence for $k_{_T}$ effects is seen in analyses of high-mass $\pi^0\pi^0$, $\eta\pi^0$, and $\gamma\pi^0$ pairs by E706 [31].

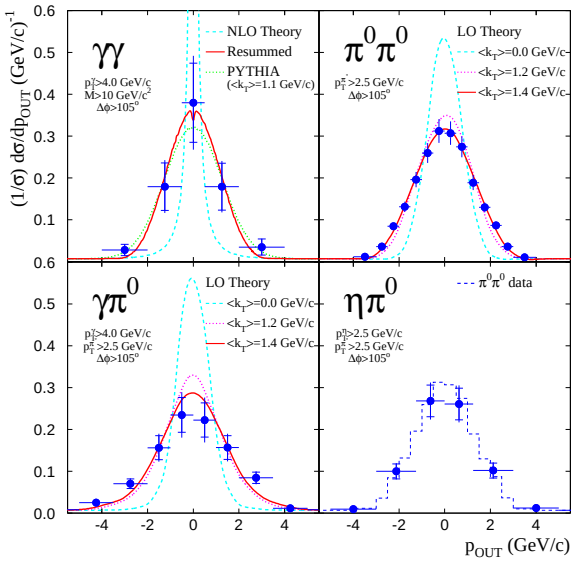

Figure 5. p_{OUT} distributions for $\gamma\gamma$, $\pi^0\pi^0$, $\gamma\pi^0$, and $\eta\pi^0$ for E706 π^-Be data at $\sqrt{s} = 31.1$ GeV [31]. Overlayed on the diphoton data are the results from NLO [8] and resummed [10] pQCD calculations. PYTHIA [37] results with $\langle k_T \rangle = 1.1$ GeV/c are also shown. Overlayed on the $\pi^0\pi^0$ and $\gamma\pi^0$ are the results from LO pQCD calculations [38] for various values of $\langle k_T \rangle$ and fixed $\langle q_T \rangle = 0.6$ GeV/c. The $\pi^0\pi^0$ data have been overlayed on the $\eta\pi^0$ data for comparison.

This is illustrated by Fig. 5 which shows a comparison of the p_{OUT} distribution from each of these samples. The LO pQCD calculation [38], which incorporates k_T effects using a Gaussian smearing technique similar to that used in PYTHIA [37], provides a reasonable characterization of k_T-sensitive variables such as $\Delta\phi$ and p_{OUT} for $\langle k_T \rangle$ similar to that measured for di-photons. The $\langle k_T \rangle$ values needed to provide good matches to the data for $\pi^0\pi^0$ and $\gamma\pi^0$ are slightly larger than for $\gamma\gamma$, but that is expected since π^0's emanate from final-state quarks and gluons that can produce additional gluon radiation. (We use $\langle q_T \rangle$=0.6 GeV/c [35] for the p_T due to fragmentation.)

2.1.3. k_T Phenomenology

Similar soft-gluon contributions are expected to be present in other hard-scattering processes, such as inclusive production of jets or direct photons [39–42]. Resummed pQCD calculations for single direct-photon production are currently under development [12–17]. Two recent independent threshold-resummed pQCD calculations for direct photons [12,13] do not include k_T effects, but exhibit less dependence on QCD scales than the NLO theory (see Figs. 6 and 7). These threshold-resummed calculations agree with the NLO

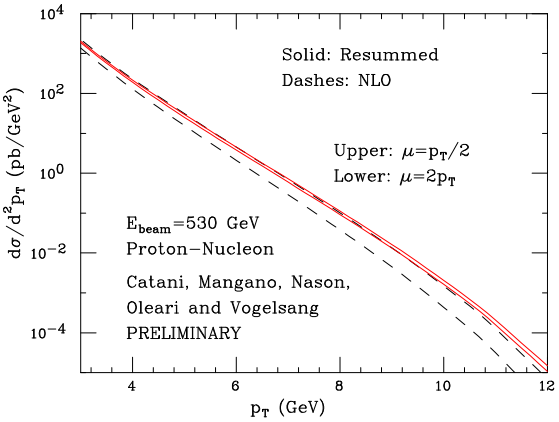

Figure 6. Comparison between a threshold resummed and a NLO theory calculation for direct-photon production for two scale choices: $p_T/2$ and $2p_T$ [12].

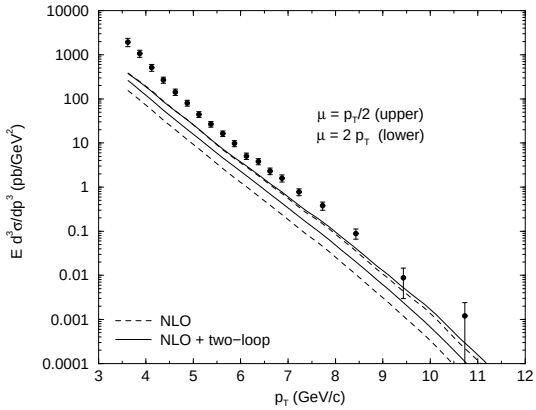

Figure 7. NLO and NNLO results for direct-photon production in hadronic collisions compared to E706 [45] pBe data at $\sqrt{s} = 31.6$ GeV [13].

prediction for the scale $\mu \approx p_T/2$ at low p_T, and show an enhancement in cross section at high p_T.

A method for simultaneous treatment of recoil and threshold corrections in inclusive single-photon cross sections has been developed [17] within the formalism of collinear factorization. This approach accounts explicitly for the recoil from soft radiation in the hard-scattering subprocess, and conserves both energy and transverse momentum for the resummed radiation. At moderate p_T, substantial enhancements from higher-order perturbative and power-law non-perturbative corrections have been found at fixed-target energies, as illustrated in Fig. 8 in a comparison with the E706 direct-photon measurement at $\sqrt{s} = 31.6$ GeV.

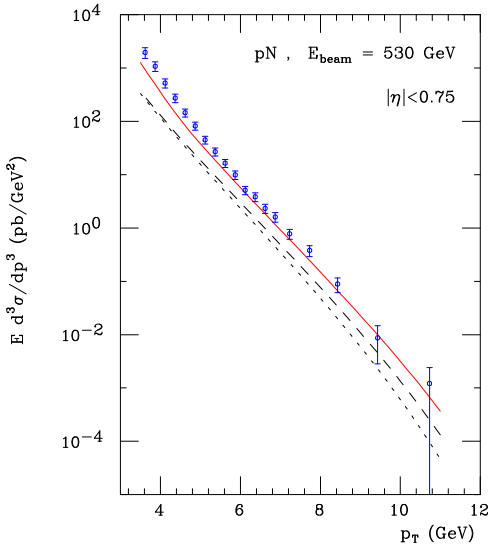

Figure 8. Direct-photon cross section for the E706 data [45]. The dotted line represents the full NLO calculation, while the dashed and solid lines respectively incorporate pure threshold resummation [12] and joint threshold and recoil resummation [17].

Although the present numerical results are only exploratory estimates of the size of expected effects, it is already clear that the phenomenological consequences are significant.

Approximate phenomenological approaches to k_T-smearing have been used in the past to investigate deviations between data and NLO pQCD. The underlying hypothesis is that the leading gluon in NLO pQCD calculations is inadequate for describing the full initial-state parton shower. Full parton shower Monte Carlos such as PYTHIA or HERWIG have been used to test this idea at collider energies [28]. We used PYTHIA v5.71 [37] and the direct photon process to extract the number of initial-state gluons as well as amount of net k_T present in initial-state gluons, after subtracting the gluon with the highest initial state p_T. The number of initial-state gluons is shown in Fig. 9, illustrating that the number is significantly larger than the NLO pQCD approximation of either 0 or 1. The net k_T present, after subtracting the highest p_T gluon, is shown in Fig. 10 for 10 GeV/c and 50 GeV/c direct photons in p$\bar{\text{p}}$ collisions at $\sqrt{s} = 1.8$ TeV. The net p_T of such remnant gluons is 2.6 GeV/c for direct photons with $p_T = 10$ GeV/c, and 5.2 GeV/c for $p_T = 50$ GeV/c.

At fixed-target energies, parton-showering models do not provide sufficient smearing because shower development is constrained by cut-off parameters that ensure the perturbative nature of the process. Since traditional NLO calculations do not account for the effects of multiple soft-gluon emission, a kinematical model was employed to incorporate k_T effects in available pQCD calculations of direct-photon (and π^0) production [24]. The relationship between this phenomenological k_T-smearing and the Collins–Soper–Sterman (CSS) resummation formalism [43,44] was considered in some detail in Ref. [29].

The same LO pQCD [38] program that successfully characterized high-mass pair production was used to generate K-factors (ratios of LO calculations for any given $\langle k_T \rangle$ to the result for k_T=0) for inclusive cross sections (Fig. 11). These K-factors were then applied

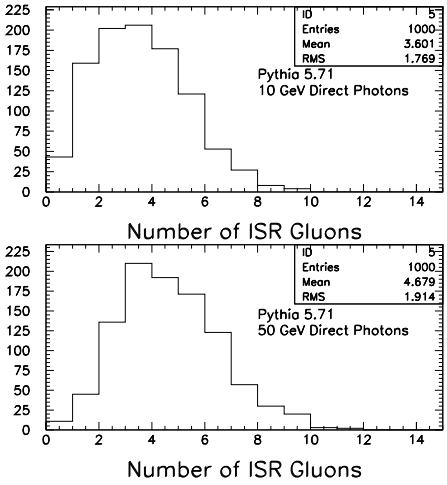

Figure 9. Number of initial-state gluons in PYTHIA from the direct-photon process at $\sqrt{s} = 1.8$ TeV.

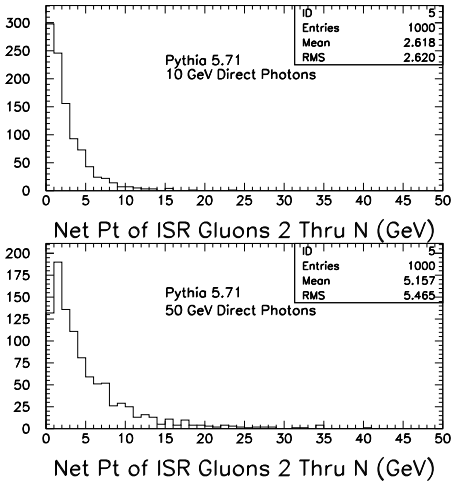

Figure 10. Net p_T due to all but the leading gluon in PYTHIA for direct-photon events.

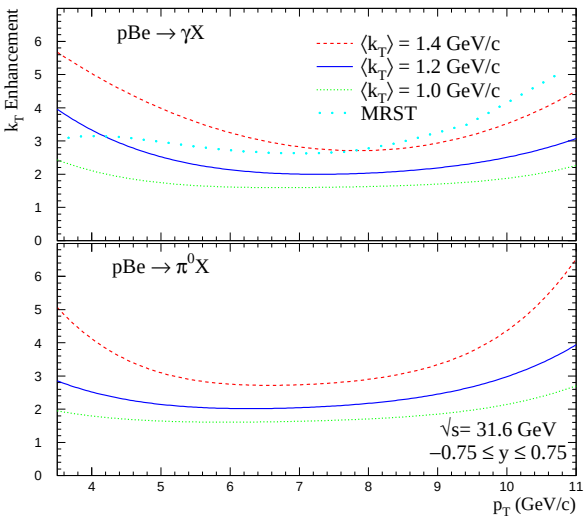

Figure 11. The variation of k_T enhancements, $K(p_T)$, for the E706 pBe data at $\sqrt{s} = 31.6$ GeV.

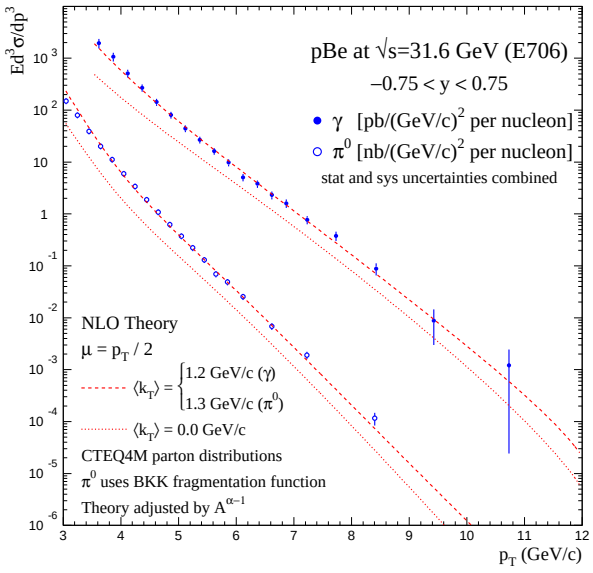

Figure 12. The photon and π^0 cross sections for E706 pBe data at $\sqrt{s} = 31.6$ GeV [45] compared to the k_T-enhanced NLO calculations.

to the NLO calculations. This procedure involves a risk of double-counting since some of the k_T-enhancements may already be contained in the NLO calculation. However, the effects of such double-counting are expected to be small [24].

As illustrated in the upper part of Fig. 11, the K-factors for direct-photon production at E706 are large over the full range of p_T, and have p_T-dependent shapes—a behavior reminiscent of that obtained from the full resummation formalism [17]. The lower part of Fig. 11 displays K-factors for π^0 production, based on the same model. The data appear to require somewhat larger values of $\langle k_T \rangle$ in the case of π^0s. At the same values of $\langle k_T \rangle$ the K-factors in π^0 production are somewhat smaller than for γ production. This is expected because π^0's originate from the fragmentation of the partons.

Figure 11 also displays the K-factor for photons used by the MRST group [21] in recent fits to parton distributions. Their result was obtained through a different technique involving analytical smearing of the parameterized photon cross section, rather than an explicit parton-level calculation. Although the correction is of similar size, it has a different p_T-dependence. It should be noted, however, that despite the similarity in the values of the K-factors used by the MRST group and the ones presented here, the $\langle k_T \rangle$ values cited by MRST are lower by a factor of 2. This difference can be traced to an erroneous relation between parameters of their analytical smearing function and the transverse momenta of partons in the hard scatter [21]. This has already been pointed out in Refs. [24,27]. The approach used here [24] is based on explicit parton kinematics and therefore does not suffer from this problem.

The treatment of k_T-enhancements proposed in Ref. [27], based on parton distributions unintegrated over the parton transverse momenta, suggests possible modifications of the above simple picture. Reference [27] imposes strong ordering of momentum transfers of emitted gluons, which prevents transverse momenta of the incoming partonic system from approaching p_T; k_T values are correlated with the scale at which the parton distributions are sampled. In their approach, the K-factors are expected to be smaller than those shown in Fig. 11, and have less p_T-dependence. Additional scrutiny of the theoretical ideas should help resolve these differences.

2.1.4. High-p_T Production Fixed Target

Invariant cross sections for inclusive direct-photon and π^0 production are displayed for the E706 pBe data at $\sqrt{s} = 31.6$ GeV in Fig. 12, with overlays from theory [45]. Discrepancies between NLO pQCD theory (dotted curves) and the data are striking. The enhancements, generated using $\langle k_T \rangle$ values consistent with the data on high-mass pairs (Fig. 5), can accommodate both the shapes and normalizations of direct-photon and π^0 inclusive cross sections.

Comparisons between direct-photon data from E706 [45], WA70 [46,47], and UA6 [48] and k_T-

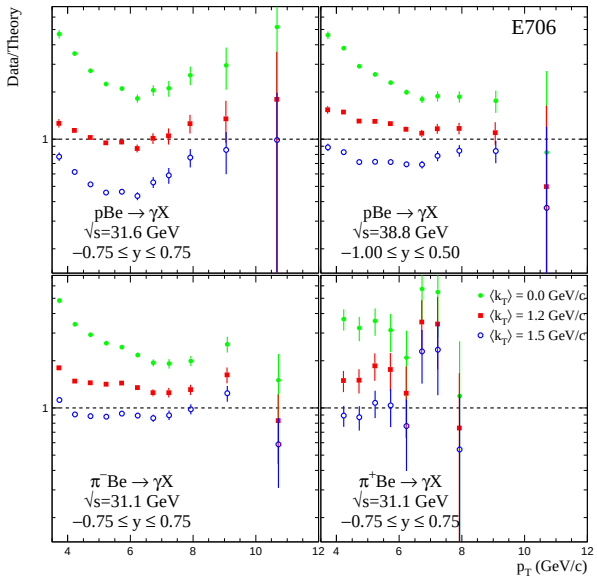

Figure 13. Comparison between the E706 direct-photon data and NLO pQCD calculations with and without k_T enhancements, for several values of $\langle k_T \rangle$.

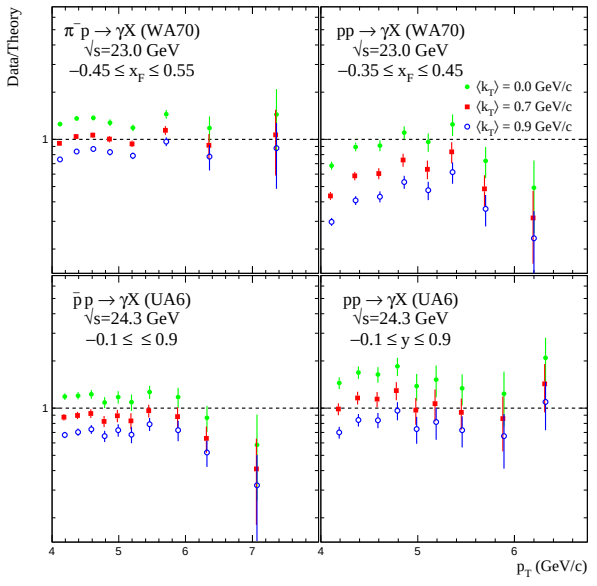

Figure 14. Comparison between the WA70 and UA6 direct-photon data and NLO pQCD calculations with and without k_T enhancements, for several values of $\langle k_T \rangle$.

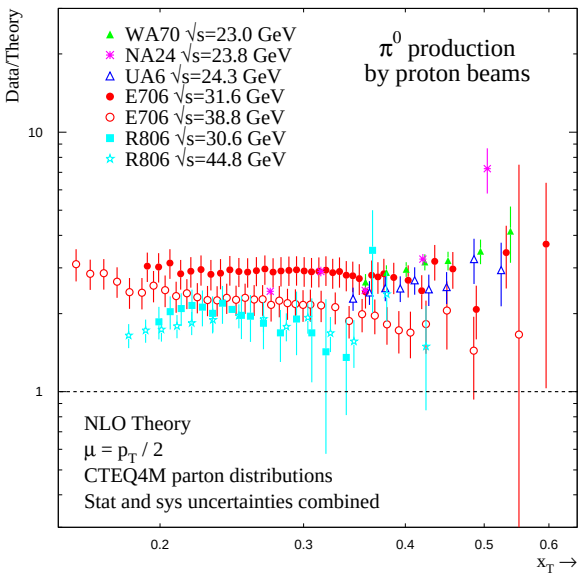

Figure 15. Comparison between proton-induced π^0 data and NLO pQCD calculations for several experiments as a function of x_T.

enhanced NLO pQCD [24] are shown in Figs. 13 and 14. The values of $\langle k_T \rangle$ were based on the data for high-mass pairs from E706 (Fig. 5), and the di-photon data from WA70 [49,32] ($\langle k_T \rangle = 0.9 \pm 0.1 \pm 0.2$ GeV/c). The center-of-mass energies for WA70 and UA6 ($\sqrt{s} \approx 24$ GeV) are smaller than those for E706. Correspondingly, $\langle k_T \rangle$ values for these experiments are expected to be slightly smaller than the values required for E706 (Fig. 3).

A recent survey of π^0 production found that current NLO pQCD calculations significantly undershoot the data [26]. A comparison between π^0 data and NLO pQCD is shown in Fig. 15 for several experiments [50]. The data are consistently a factor of 2 to 3 above theory. The above phenomenological model should also be valid for pion production. Using $\langle k_T \rangle$ similar to, but slightly higher than that for direct photons, good agreement is obtained for π^0's measured by E706 [45], WA70 [51], and UA6 [52] (Figs. 16 and 17). The k_T-enhanced predictions compare well with the π^0 cross sections, with all the E706 and UA6 direct-photon data, and with the π^- beam direct-photon cross sections of WA70.

Since k_T-smearing affects similarly direct-photon and π^0 data, the ratio of direct-photon to π^0 production should be relatively insensitive to k_T. Experimental and theoretical uncertainties also tend to cancel in such ratios. Figure 18 shows the ratios of cross-sections [50] for direct-photon to π^0 production

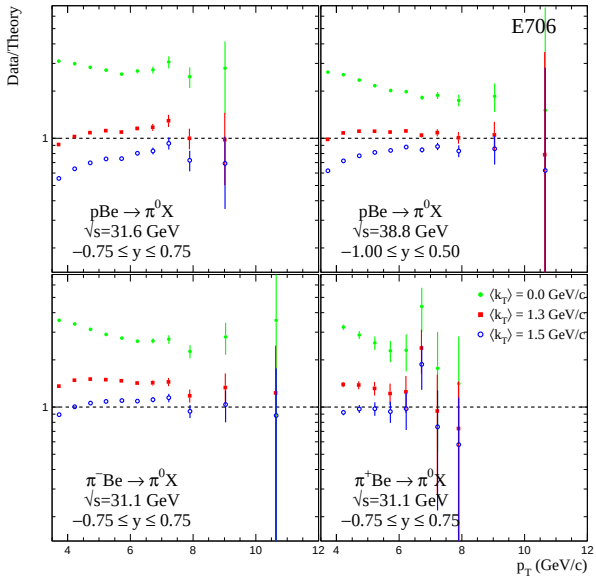

Figure 16. Comparison between the E706 π^0 data and NLO pQCD calculations with and without k_T enhancements, for several values of $\langle k_T \rangle$.

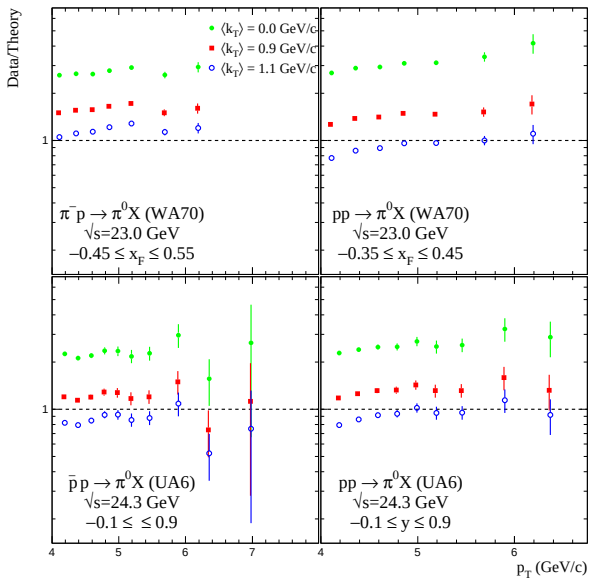

Figure 17. Comparison between the WA70 and UA6 π^0 data and an NLO pQCD calculation with and without k_T enhancements, for several values of $\langle k_T \rangle$.

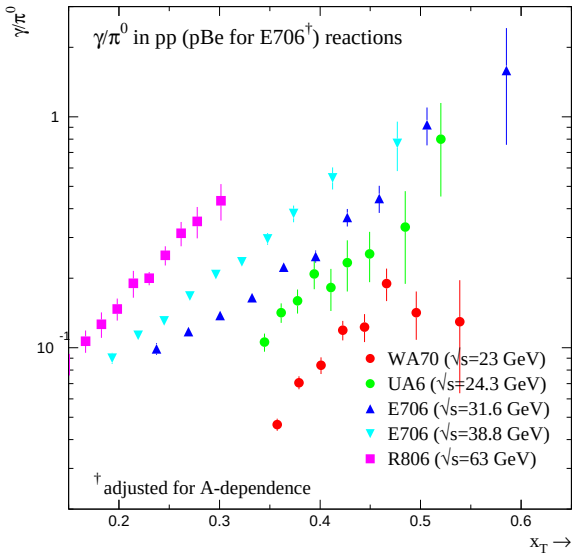

Figure 18. Ratios of direct-photon cross sections to the π^0 cross sections as a function of p_T for various experiments at several values of $\sqrt{s}$.

for WA70, UA6, E706, and R806 [53–55]. The results from WA70 (Fig. 19) and UA6 (Fig. 20), at approximately the same $\sqrt{s}$, appear to differ significantly. The ratio for NLO theory differs from that of WA70 by a factor of three, but only by $\approx 30\%$ from the UA6 data. The WA70 and UA6 π^0 results agree (Fig. 15) and most of the difference is therefore in the direct-photon cross section. Similar γ/π^0 comparisons are shown for E706 at $\sqrt{s} = 38.8$ GeV (Fig. 21) and R806 at $\sqrt{s} = 63$ GeV (Fig. 22). The same 30% level of agreement can also be found for the E706 data at $\sqrt{s} = 31.6$ GeV and the R806 data at $\sqrt{s} = 31$ GeV and 45 GeV.

The discussion of direct-photon data from fixed-target and ISR experiments [25], while rejecting the k_T interpretation for the observed deviations, pointed to limitations for the applicability of NLO calculations at lower-p_T values and to inconsistencies among experiments used in comparisons to NLO theory. Given the shortcomings of a purely NLO description, a global comparison of the available data to fully resummed theory may provide useful insights into these issues.

Run I Results

The consequences of k_T smearing are expected to depend on $\sqrt{s}$ (Fig. 3). At the Tevatron collider, where p_T is large compared to k_T, the above model of soft-gluon radiation leads to a relatively small modification of the NLO cross section. Only the lowest end of the

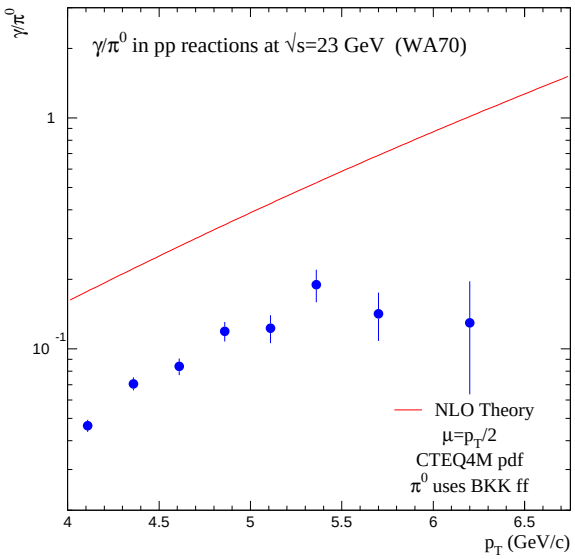

Figure 19. γ/π^0 comparison for the WA70 pp data at $\sqrt{s} = 23$ GeV. Overlayed are the results from the NLO pQCD calculations.

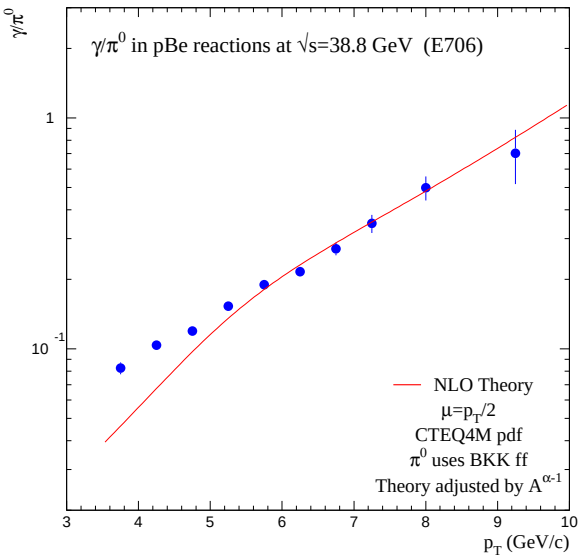

Figure 21. γ/π^0 comparison for the E706 pBe data at $\sqrt{s} = 38.8$ GeV. Overlayed are the results from the NLO pQCD calculations.

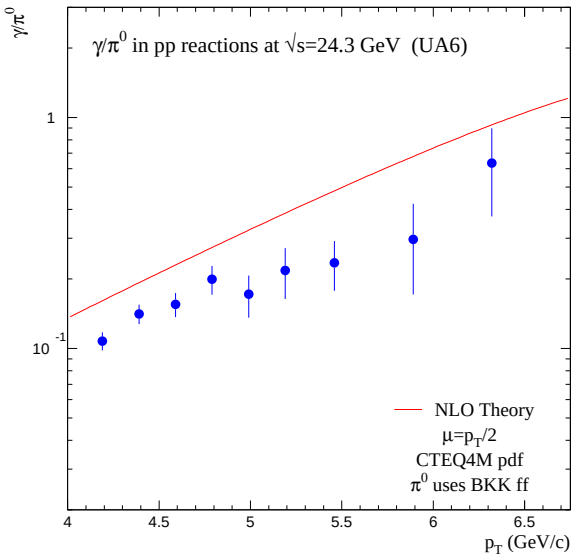

Figure 20. γ/π^0 comparison for the UA6 pp data at $\sqrt{s} = 24.3$ GeV. Overlayed are the results from the NLO pQCD calculations.

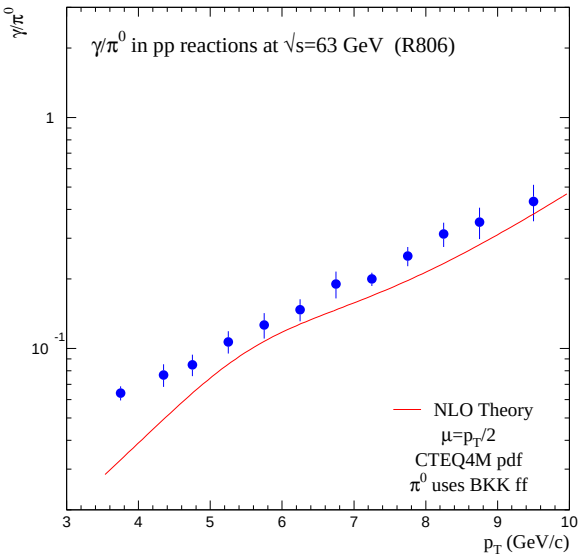

Figure 22. γ/π^0 comparison for the R806 pp data at $\sqrt{s} = 63$ GeV. Overlayed are the results from the NLO pQCD calculations.

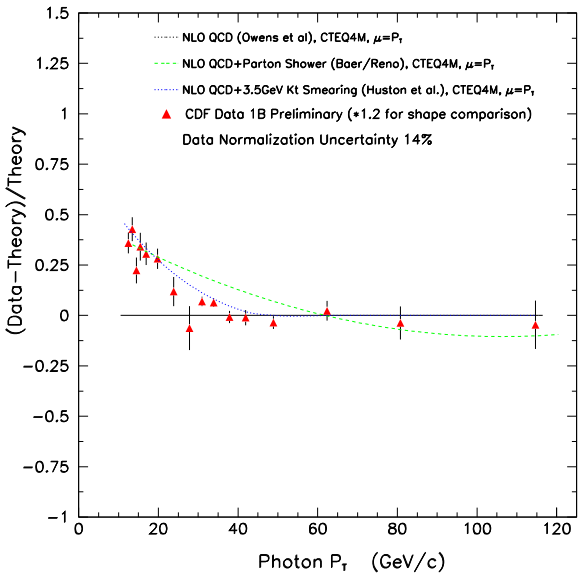

Figure 23. A comparison of the CDF isolated direct-photon data at $\sqrt{s} = 1.8$ TeV from Run Ib with a NLO pQCD prediction and two implementations of soft gluon corrections to the NLO prediction [56].

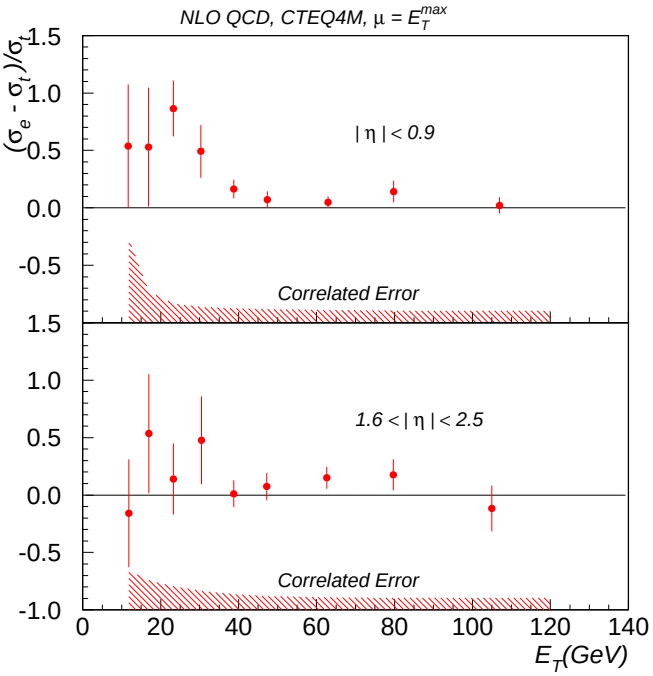

Figure 24. A comparison of the DØ isolated direct-photon data at $\sqrt{s} = 1.8$ TeV from Run Ib with a NLO pQCD calculation in both the central and forward rapidity regions [57].

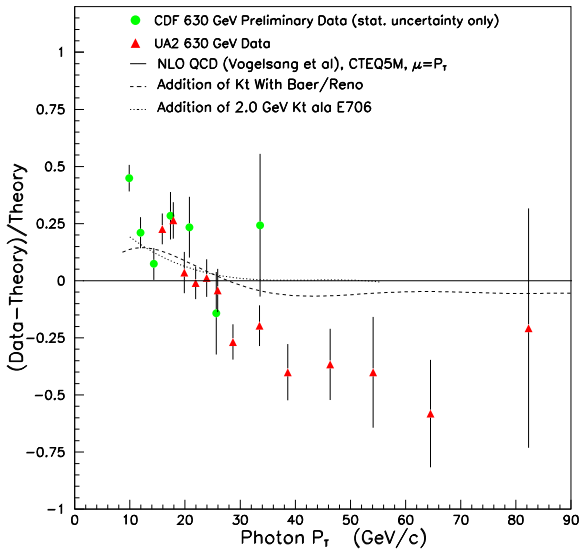

Figure 25. A comparison between CDF and UA2 data at $\sqrt{s} = 630$ GeV.

p_T spectrum is modified significantly, and the K-factor exhibits the expected $\sim 1/p_T^2$ behavior for a power correction.

A comparison of the results from Run Ib, shown in Figs. 23 and 24 [56,57], confirms the expected deviation in shape at low p_T. Using di-photons, CDF has measured $\langle k_T \rangle = 3.6 \pm 0.8$ GeV/c at $\sqrt{s} = 1.8$ TeV [33]. Employing this value, the phenomenological model adequately describes the shape of the data in Fig. 23. Also shown in this figure is an implementation of soft-gluon corrections using an enhanced parton shower [22]. The phenomenological-k_T model provides a better agreement with data than is available in the enhanced parton shower model. The agreement between the phenomenological model implementation of k_T smearing and the direct-photon data can also be seen in preliminary results from CDF at $\sqrt{s} = 630$ GeV (Fig. 25).

The CDF data in Fig. 23 have been normalized upwards by a factor of 1.2 for the benefit of a shape comparison. Without this normalization, then the CDF data lie below the NLO pQCD calculation at high p_T. Figure 25 also contains a comparison between CDF and UA2 [58,59] data at $\sqrt{s} = 630$ GeV, where a similar deficit is observed at high p_T for the UA2 data. There is currently no explanation for this effect.

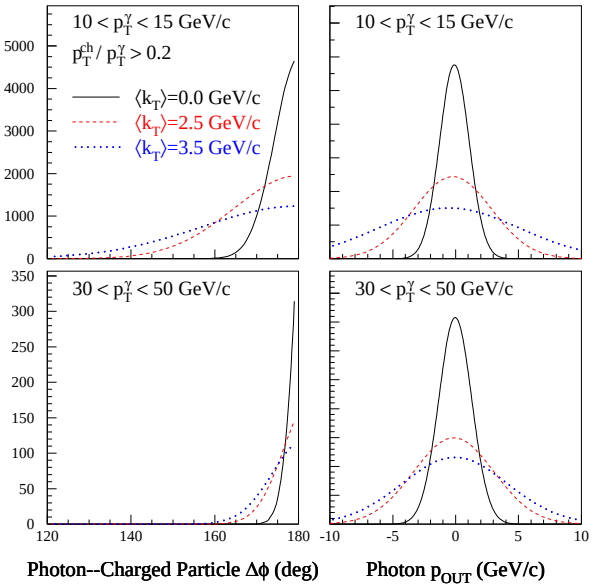

Figure 26. Left: Distributions of azimuthal angle difference $\Delta\phi$ between the direct photon and a recoil charged track for several values of k_T and for two photon p_T ranges. Right: Similar dependences for the photon p_{OUT}.

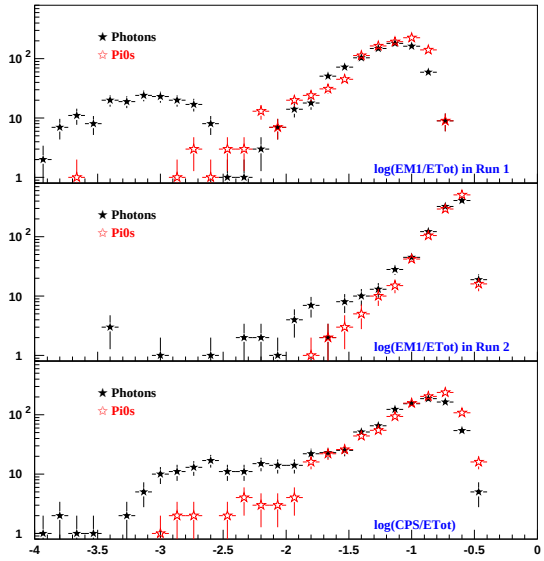

Figure 27. Comparisons of simulated discriminations between photons (solid) and π^0's (open) for the DØ detector in the Run I configuration (top, discriminant variable is $\log(E_{\rm EM1}/E_{\rm TOT})$; for the same discriminant in the Run II configuration (middle); and for the Run II configuration and $\log(E_{\rm CPS}/E_{\rm TOT})$ discriminant (bottom).

2.1.5. Expectations for Run II

k_T Studies at Low-p_T

To study the level of k_T induced by multiple gluon emissions at the collider, the experiments have employed the relatively low-statistics di-photon data. In Run II, both CDF and DØ will have precision magnetic tracking, which will permit studies of k_T effects using "two-arm" data on pairs consisting of a direct photon and a recoil charged track, in a spirit similar to that of the fixed-target investigations of $\gamma\pi^0$ and $\pi^0\pi^0$ pairs discussed before. The advantage of this approach is that it will obviate the need for jet reconstruction (difficult at low p_T), and minimize complications from jet energy scale calibration. Of course, photon+jet systems are also of interest, but may be harder to study in the range of interest for checking the effects of k_T smearing.

We simulated the expected behavior of photon–track systems using the same LO Monte Carlo [38] employed in previous fixed-target studies. The results are illustrated in Fig. 26 for $\Delta\phi$ and p_{OUT} of the photon, for two representative ranges of photon p_T that span the region where the k_T effects appear to be important in the inclusive photon cross sections from Run I. (For the measurement of p_{OUT} for photon, the scattering plane is defined by the colliding beams and the recoil track.) The sensitivity to the value of $\langle k_T\rangle$ in the range of 0 to 3.5 GeV/c is clearly seen for both variables. The $\Delta\phi$ distributions become narrower with increasing photon p_T, as expected from simple kinematic arguments. For a fixed $\langle k_T\rangle$, the width of the p_{OUT} distributions is relatively insensitive to p_T, and can therefore be particularly useful for mapping out the dependence of k_T on event kinematics (especially on the p_T of the photon). To properly interpret the widths of such distributions in terms of k_T induced by gluon-radiation, it is important to subtract the amount generated in the fragmentation of partons into the charged particles (as was done in the fixed-target analyses).

Additional handles on interpreting the data can be obtained through studies of p_T distributions of charged particles from fragmentation of partons recoiling against direct-photon triggers. In the presence of significant initial-state k_T, such distributions are expected to become softer than expected from standard fragmentation functions (determined *e.g.* from e^+e^- data), since the k_T-kick tends to increase the photon p_T while taking it away from the recoil side. This should be observed most clearly at low photon p_T's, where the effect from k_T is greatest.

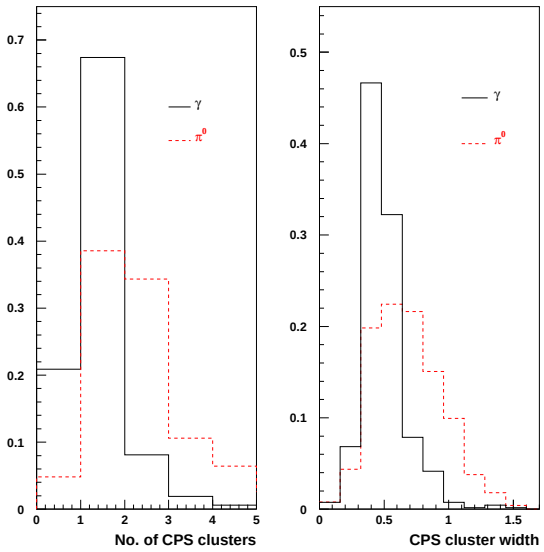

Figure 28. Additional γ *vs* π^0 discrimination with the DØ detector in Run II is possible using differences in the respective distributions for the number of reconstructed preshower clusters matched with the calorimeter shower (left) or for the width of the preshower cluster (right). Solid lines are for γ's, dashed for π^0's.

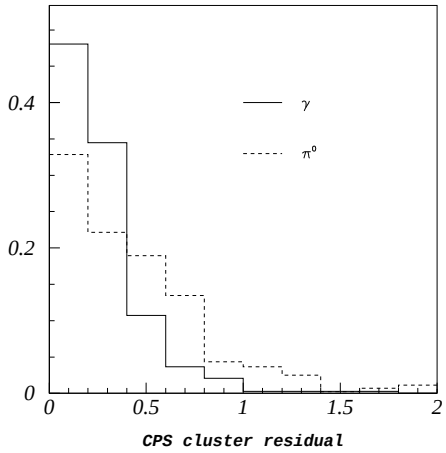

Figure 29. The residual of CPS cluster position relative to the photon or π^0 in the R-ϕ plane in the DØ detector. Clusters from π^0's have larger residuals, especially when one of the decay photons does not convert in the solenoid.

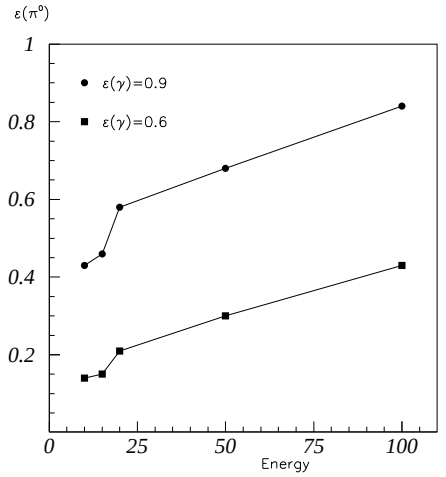

Figure 30. Efficiency for a π^0 to pass covariance matrix χ^2 cuts corresponding to photon efficiencies of 90% and 60%. (Preliminary study for the DØ detector in Run II.)

Photon Purity

The particularly interesting connection between two-arm studies and measurements of the inclusive photon cross section is mainly at relatively low p_T (10 GeV/c to 35 GeV/c), where Run I results indicate significant deviation of the cross section from expectations from NLO pQCD (Figs. 23 and 24). This is also the region of high statistics, and, consequently, where detailed studies will be possible. It is therefore important to achieve a high photon-signal purity in this region, which has proved to be difficult in Run I.

In the case of DØ, calorimeter response will be modified in Run II by the presence of a central solenoid magnet and preshower detectors [60]. The separation of photon signal and background in Run I was based on the fraction of electromagnetic energy detected in the first longitudinal layer of the calorimeter ($E_{\rm EM1}/E_{\rm TOT}$). This quantity is particularly sensitive to differences in the early stages of shower development initiated by single photons, and by photons from decays of π^0's of the same p_T. In the Run II configuration, the signal–background discrimination based on this variable is expected to deteriorate, but simulations indicate [61] that Run I performance can be recovered by using instead the fraction of energy deposited in the preshower detectors ($E_{\rm CPS}/E_{\rm TOT}$), as illustrated in Fig. 27 for photons at central rapidities. Using the fine-grained shower-profile information from the preshower strips (ca. 7 mm triangles), an additional factor of two rejection of background (while maintaining high signal-efficiencies) has been achieved in our Monte Carlo simulations [61]. As illustrated in Fig. 28, multiple preshower clusters for sufficiently large separation between photons from meson decays can be resolved, or inferred from the widths of clusters when the showers are not fully separated. Results are shown for $p_T \approx 15$ GeV/c and $\eta \approx 0.95$, where the separation

of photon signal from background is particularly difficult. Another variable useful for the discrimination is the distance in the R–ϕ plane between the detected CPS cluster and the photon position (the latter calculated from the primary vertex and the position of the calorimeter cluster) [62]. Figure 29 shows this distribution for $p_T \approx 15$ GeV/c and $\eta \approx 0.1$.

Even higher background rejection can be achieved by exploiting correlations between the calorimeter and preshower shower profiles in a covariance-matrix approach. A study was undertaken using a simplified version of the Run I covariance matrix, with added preshower variables [62]. Figure 30 shows the E_T dependence of the π^0 efficiency for χ^2 cutoffs corresponding to 90% and 60% photon efficiency.

In the central region, CDF tools for γ–background separation in Run I (shower width in the electromagnetic shower-maximum detector, and conversion in the central-preradiator detector) will remain the same. These tools provide a clear separation of the photon signal and the π^0-dominated background. The addition of a new scintillator-based endplug calorimeter with a preshower and shower-max detector will offer an extension of these tools to the forward region in Run II.

Thus, we expect a better signal purity at low p_T in Run II than was achieved in Run I, which will facilitate more precise measurements of low-p_T direct photons and di-photons.

Photons at High-p_T

At high values of p_T, separating the direct-photon signal from background and the expected reach in p_T are determined by the collected luminosity. As shown in Sec. 2.2, for the initial luminosity of 2 fb^{-1}, the inclusive direct-photon cross section measurement can be extended beyond 300 GeV/c. While the high-p_T data will permit detailed tests of perturbative QCD, it is not expected to be sensitive to differences in recent parameterizations of gluon distributions at large x (*eg.*, CTEQHJ and CTEQM). Thus, the determination of the large-x gluon distribution will have to continue to rely on direct-photon data from fixed target experiments and on jet data at the Tevatron.

2.1.6. Impact on the Gluon Distribution

The largest uncertainty in any parton distribution function (PDF) is that for the gluon distribution. At low x, the gluon can be determined indirectly from scaling violations in quark distributions, but a direct measurement is required at moderate to large x. Direct-photon production has long been regarded as potentially the most useful source of information on the large-x part of the gluon distribution. And

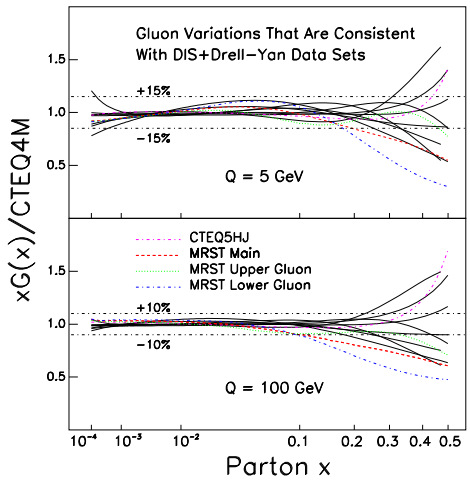

Figure 31. The ratio of gluon distributions obtained in the study in Ref. [18] to the CTEQ4M gluon at two different Q scales. All of these gluon distributions correspond to PDF's which provide a reasonably good fit to the CTEQ4 DIS/DY data set.

direct-photon data, especially from CERN fixed target experiment WA70, have been used in several global analyses [21,63]. Another process sensitive to the gluon distribution, through the gluon–gluon and gluon–quark scattering subprocesses, is jet production in hadron–hadron collisions. Precise data from Run I are available over a wide range of transverse energy and, indeed, provide a constraint on the gluon distribution in an x range from about 0.05 to 0.25. However, the low statistical power of the jet cross section at high E_T, and the dominance of the $q\bar{q}$ scattering subprocess in that kinematic region, do not provide for a similar constraint at large x.

Figure 31 shows several gluon parton distribution functions [18] that provide a reasonable fit to the DIS and DY data used in the CTEQ4 fits [19]. The excursions shown (normalized to the CTEQ4M gluon) provide an estimate of the uncertainty in the gluon distribution. The gluon distribution seems reasonably well-constrained by these data, except at large x. Also shown in Fig. 31 are the gluon distributions from CTEQ5HJ [64] (which best fits the Tevatron high-E_T jet data) and three recent MRST PDF's [21]. The MRST PDF's incorporate the WA70 direct-photon data using the k_T-enhancements described above. Nevertheless, the theoretical problems associated with direct-photon production have discouraged the CTEQ collaboration from using the direct-photon data in their recent fits [64]. The recent work on resummation offers hope that this situation will change.

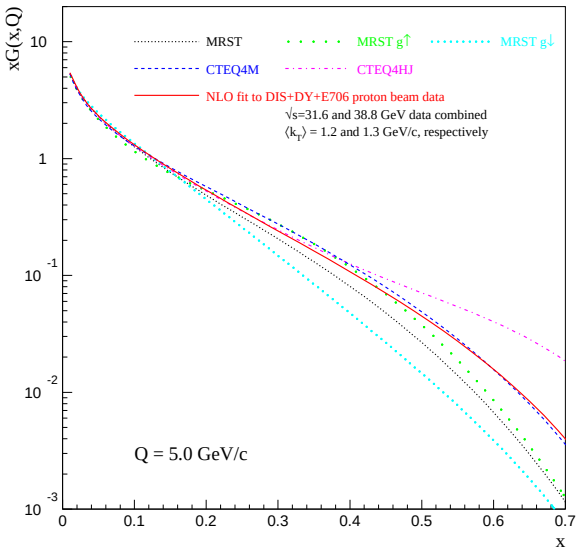

Figure 32. A comparison of the CTEQ4M, MRST, and CTEQ4HJ gluons, and the gluon distribution derived from fits that use E706 data [24]. The $g \uparrow$ and $g \downarrow$ gluon densities correspond to the maximum variation in $\langle k_T \rangle$ that MRST allowed in their fits.

The CTEQ4HJ PDF's were determined by increasing the weight for the CDF jet cross section at high E_T [19]. In the resultant fit, the increase was achieved through a significant increase in the gluon contribution at large x, without inducing serious conflicts with any of the other experiments used in the CTEQ4 data sets. This increase was allowed by the uncertainty in the gluon distribution in this x range, a flexibility not present for any of the quark distributions. Another demonstration of the uncertainty in the gluon distribution at large x can be seen in Fig. 32, where the CTEQ4HJ gluon distribution is plotted along with that of CTEQ4M and three recent MRST PDF's. At $x \approx 0.6$, there is over an order of magnitude spread between the CTEQ4HJ and the MRST $g \downarrow$ gluon distributions.

The CTEQ4HJ gluon distribution (and its successor, CTEQ5HJ) provides the best description of not only the CDF jet cross section, but that of DØ as well. At $x \approx 0.5$, corresponding roughly to $E_T \approx 450$ GeV for central η, a doubling of the gluon distribution (compared to CTEQ4M) results in only a 20% increase in the inclusive jet cross section. On the other hand, the fixed-target direct-photon yield of E706, produced mainly through gq scattering, is proportional to the gluon distribution. A fit using the E706 direct-photon data and the k_T K-factors is also shown in Fig. 32; this result is very similar to the CTEQ4M gluon. At the highest reach of the E706 data, the CTEQ4HJ gluon distribution is a factor of 4 to 5 larger than the CTEQ4M gluon. With the advent of more complete theoretical treatments [17] of direct-photon production, the E706 data should have great impact on the determination of the behavior of the gluon at large x. This would have implications not only for fixed-target direct-photon data, but also for collider physics at highest Q^2 scales.

2.1.7. Conclusions

Direct-photon physics remains a viable and interesting program for Run II of the Tevatron. The Run II measurements of single and double direct photons, and of photon and jet or single track correlations, will reach larger p_T and have improved detection efficiency at low p_T, compared to Run I. Although the data are not expected to improve directly our knowledge of the gluon distribution at intermediate and large x, it can do so by providing a testing ground for newly developed theoretical models and formalisms, and by helping clarify the currently confused role that multiple gluon emission play in direct-photon production (and other high-p_T processes). Once this physics is properly understood, the existing fixed-target data should provide one of the best constraints on the gluon distribution, as has been envisioned for a long time.

We have examined the best available experimental information on production of single and double direct photons (and mesons) at large p_T in both fixed-target and collider energy regimes. Recent theoretical developments offer optimism that the long-standing difficulties in the proper description of these processes can finally be resolved. While there is still no final consensus, the trend of recent developments has led to an increased appreciation of the importance of the effect of multiple gluon emission, and to the emergence of tools for clarifying this issue.

To summarize, measurements of the production of high-mass pairs of high-p_T particles at WA70, E706, CDF, and DØ provide consistent evidence for the presence of large k_T. NLO pQCD calculations [8], which include effects due to the radiation of a single hard gluon, compare poorly to k_T-sensitive distributions in di-photon data. `RESBOS` [10], a NLO pQCD calculation, which also includes the effects of multiple soft-gluon emission through the CSS resummation technique, compares well with the shape of the di-photon data. LO pQCD calculations [37,38] that incorporate k_T effects through Gaussian smearing techniques, provide reasonable characterizations of distributions for pairs of direct photons and mesons.

While the apparent inconsistencies between different direct-photon and π^0 data sets are not under-

stood [24–26], we found it instructive to consider results on the γ/π^0 ratio from WA70, UA6, E706, and R806. Various experimental and theoretical uncertainties tend to cancel in such a ratio, which is also relatively insensitive to $k_{_T}$-effects. We find that the ratio from theory agrees to $\approx$ 30% with data from UA6, E706, and R806 over the range 24 GeV $< \sqrt{s} <$ 63 GeV.

LO pQCD has been used to estimate the impact of $k_{_T}$ on the inclusive production of high-$p_{_T}$ direct photons and π^0's. This simple phenomenological model is able to account for differences between NLO pQCD calculations and inclusive data over a wide range in $\sqrt{s}$. While the approximate nature of such models is clear, and has been discussed in several recent papers, the emerging formalism for the full (threshold and recoil) resummation of inclusive direct-photon cross sections appears to vindicate much of the understanding of effects from multiple gluon emission that has been achieved using approximate tools. The resummation formalism can be expected to provide a solid foundation for the treatment of $k_{_T}$, at which time a global reexamination of parton distributions, with an emphasis on the determination of the gluon distribution from the direct-photon data, should become possible [65].

2.2. Direct Photon Production at the Tevatron[1]

2.2.1. Introduction

In this section we summarize features of direct photon production which are relevant in the kinematic range to be covered in Run II. In Sec. 2.2.2, a comparison between Run I data and the corresponding theoretical description is presented. Several potential problem areas are noted. Sec. 2.2.3 contains a brief description of the kinematic reach expected for Run II, based on an integrated luminosity of 2 fb^{-1}. Included here is a discussion of the sensitivity to parton distribution functions and to what extent direct photons at Run II can help constrain the gluon distribution. In Sec. 2.2.4 some predictions for photon-jet correlations are presented. The potential of observables other than the usual single photon p_T distribution to help elucidate the underlying dynamics is also discussed.

2.2.2. Comparison to Run I Data

Data for the inclusive cross section for direct photon are available over a wide range in energies from fixed target and collider experiments. By now it is well known that it has not yet been possible to simultaneously describe all of the experimental results with a next-to-leading-order (NLO) QCD calculation. A pattern of discrepancies between theory and experiment exists in both the fixed target and the collider data sets. This situation has been reviewed in [23–25]. An analysis similar to that for direct photon production in Ref. [25] has been performed for the case of π^0 production [26]. The two processes are closely related since π^0's decaying to two photons provide much of the background which must be dealt with when extracting the signal for direct photon production. Some of these issues are also dealt with in Sec. 2.1 where a detailed comparison to fixed target data is also presented. While it is clearly of interest to understand direct photon production over the entire range of available energies, this section will focus on those aspects of the data which can most directly be addressed during Run II. The first step is to examine the theoretical description of the data from Run I.

A comparison of NLO QCD predictions to the direct photon data from CDF and DØ has indicated the presence of a deviation of the data from theory at low values of transverse momentum [23,24]. This deviation decreases if the effects of soft gluon radiation are taken into account by applying a Gaussian k_T smearing model using a value of $\langle k_T \rangle$ measured in di-photon production in the two experiments.* Such a k_T treatment is phenomenologically motivated.

Recently, there has been progress in more sophisticated treatments of soft gluon radiation near threshold in the parton-parton scattering process [14,66,13]. At large values of transverse momentum for the photon, the phase space for the emission of additional gluons in the hard scattering is limited. This limitation on the emission of real gluons upsets the balance in the theoretical expressions between virtual and real emission contributions. The result is large logarithmic corrections near the threshold for the parton-parton scattering subprocesses. These large corrections can be resummed in a relatively compact formalism. The results [12,66,13] indicate that the corrections to existing next-to-leading-order calculations are large as $x_T = 2p_T/\sqrt{s}$ approaches 1. Away from the region at the edge of phase space it is observed that the corrections to the NLO results coming from the threshold resummation are relatively small over much of the x_T range covered in the fixed target experiments when the renormalization and factorization scales are chosen to be $p_T/2$ and the resummed results show an overall reduction in the sensitivity to the choices of these scales. However, the threshold resummation corrections alone are not sufficient to explain the discrepancies observed between the theoretical predictions and some of the fixed target experimental results. In addition, threshold resummation cannot explain the

[1] Contributed by: J. Huston and J.F. Owens

*The value of k_T can be directly measured in di-photon events since the photon 4-vectors can be measured precisely.

deviations observed by DØ and CDF at the low p_T end of the measured distributions.

Another approach to resumming soft gluon effects is that of Ref. [27] which uses the DDT [67] or q_T-space method. This technique has recently been applied to vector boson production [68] and compared with the impact parameter method of Ref. [44]. In Ref. [27] a parton-parton luminosity function is defined which depends on the net transverse momentum of the pair of colliding partons. The parton distributions are probed not at the scale of the hard scattering process, but instead at a scale given by q_T. This means that the scale of the parton distributions is typically somewhat smaller than, for example, the transverse momentum of the produced photon. This results in an enhancement of the cross section. In addition, the parton transverse momentum is taken into account when the final photon p_T is calculated. Some enhancement of the fixed target predictions is noted using this technique, but it is insufficient to fully describe all of the fixed target data. For the collider energy range, Ref. [27] quotes only a small effect, which does not appear to be sufficient to explain all the observed deviations. At present, the resummation is done only with the leading-log terms included. More results from this technique are anticipated as next-to-leading-log terms are included as well.

Quite recently a new formalism for simultaneously incorporating both the threshold resummation *and* the resummation of k_T (or recoil) effects has been developed [17]. This formalism possesses the desirable property of simultaneously conserving both energy and momentum in the resummation process. The initial results presented in [17] indicate that the threshold enhancement referred to above is correctly reproduced while, in addition, there is a large enhancement due to the newly included recoil effects. Detailed applications and studies of the scale dependence and the dependence on non-perturbative input parameters are expected soon.

The initial indications of discrepancies between theory and experiment in the collider data came from results taken in Run Ia. A comparison of the higher statistics results from CDF in Run Ib, shown in Fig. 23, confirms the shape deviation at low p_T and the agreement with the k_T smearing correction obtained using the Gaussian smearing model. (Also shown is an attempt to implement the soft gluon corrections using an enhanced parton shower [22]. In this case, the effect seems to drop off more slowly than the deviation observed in the data.) Note that the k_T smearing correction falls off roughly as $1/p_T^2$, as expected from a power correction type of effect. This is not true in the case of fixed target experiments, as discussed in Sec. 2.1, where the steeply falling parton distribution functions enhance the effects of the soft gluon radiation.

The DØ direct photon cross section for the central region is also consistent with such a deviation at low p_T [57], as shown in Fig. 24 while no conclusion can be reached for the DØ cross section in the forward region (see the lower half of Fig. 24 and Ref. [57]). The possibility that the discrepancy between theory and experiment may be dependent on rapidity is interesting and is one that can be investigated in more detail with the higher statistics expected from Run II.

In an attempt to achieve a better theoretical description of the data it is important to investigate what flexibility exists within the conventional QCD hard scattering NLO formalism. In order to perform perturbative QCD calculations, one must specify the renormalization and factorization scales. For the latter, there are two scales, corresponding to the factorization of collinear singularities for the initial state parton distributions and the final state fragmentation functions. For most hard scattering calculations these three scales are chosen to be proportional to the characteristic large transverse momentum - that of the photon in this case. Often, all three scales are set equal to each other. However, this latter step is not necessary and it is reasonable to ask whether or not one can describe the shapes of the CDF and DØ data in the region below $p_T = 30$ GeV by a suitable variation of all three of the scales [69]. In Fig. 33 the Run Ib CDF data are compared to several curves corresponding to different choices of the renormalization and factorization scales. One can see that it is possible to get a steepening of the slope at the low-p_T end, but only at the price of an increase in the overall normalization. Apparently, it is not possible to get both the shape and the normalization correct by such a strategy.

In Fig. 23, the CDF data has been normalized upwards by a factor of 1.2 for an easier shape comparison. If this normalization is taken out, as shown in Fig. 34, it is evident that the data fall below the NLO QCD prediction at high p_T. Also shown is a comparison to the CDF photon data taken at $\sqrt{s} = 630$ GeV and the photon data from UA2 [59] where a similar deficit is observed at high p_T. For most observables, typically, the data lie above the NLO QCD predictions so this is somewhat of an unusual situation. It is interesting to note that a measurement of the photon fraction (of the photon candidate sample) indicates that the photon fraction seems to be leveling off at approximately 80%, rather than saturating the sample at near 100% at high p_T. The latter outcome would be predicted from very basic considerations: with a fixed E_T isolation cut, jets are required to fragment into a π^0 with a higher z value as the p_T of the photon candidate increases. Such a fragmentation is suppressed by the sharp falloff

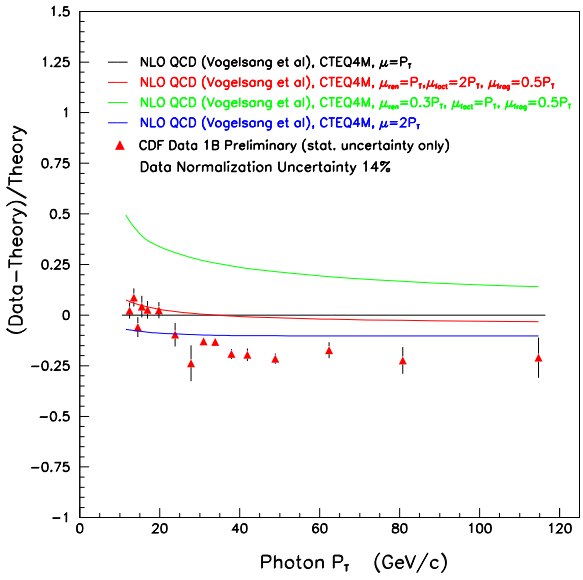

Figure 33. Comparison of the CDF Run Ib data with several NLO curves corresponding to different choices of the renormalization and factorization scales.

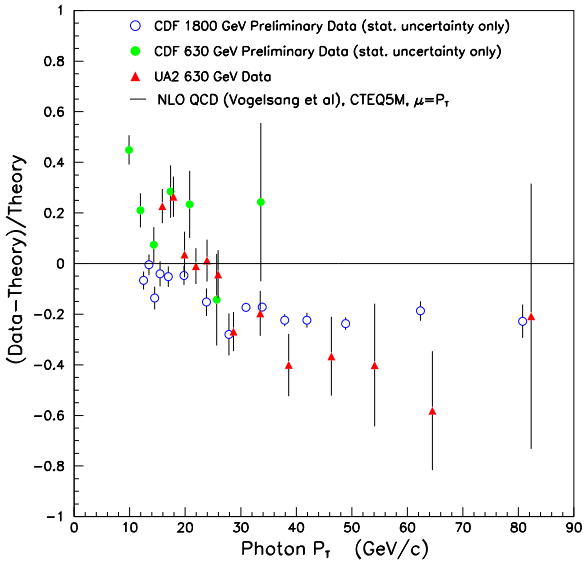

Figure 34. A comparison of the CDF photon data from Run Ib (at both $\sqrt{s} = 630$ GeV and $\sqrt{s} = 1800$ GeV) with a NLO QCD prediction and the direct photon data from UA2.

of the fragmentation function at high z. It will be interesting and important to understand this behavior. The increased statistics of Run II will allow both the low p_T and high p_T regions to be investigated more thoroughly.

2.2.3. Expectations for Run II

For the purposes of this section we shall assume an integrated luminosity for Run II of 2 fb^{-1}. As noted in Sec. 2.2.2, the data on direct photon production from Run I extend to a transverse momentum of approximately 120 GeV. The increased statistics expected from Run II greatly extend this range as shown in Figs. 35 and 36. These figures have been generated using the next-to-leading-logarithm program of [70] with the CTEQ5M [64] parton distributions and with the renormalization and factorization scales set equal to $p_T/2$. The errors shown are statistical only and the results are presented for the transverse momentum range where more than 10 events are expected in a 10 GeV bin of p_T with a total integrated luminosity of 2 fb^{-1} and 4 fb^{-1}, respectively. No efficiency/acceptance corrections, however, have been applied to these estimates. Typically, these corrections are on the order of 50%.

One can see that the range of useful statistics extends past 300 GeV in the first case and past 350 GeV in the second. This extended coverage in p_T corresponds to an increased range of sensitivity for the

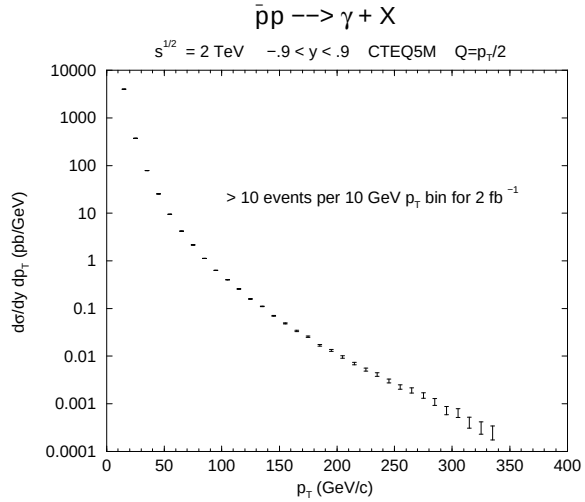

Figure 35. Direct photon p_T distribution for Run II with errors based on an integrated luminosity of 2 fb^{-1}.

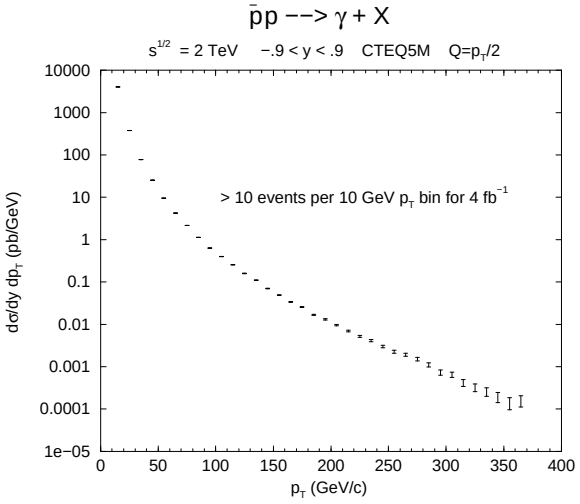

Figure 36. Direct photon p_T distribution for Run II with errors based on an integrated luminosity of 4 fb^{-1}.

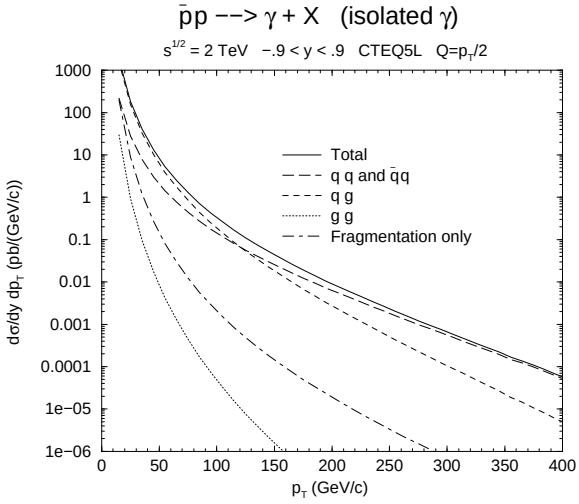

Figure 37. Contributions of the various subprocesses for direct photon production calculated in the leading-log approximation using the CTEQ5L parton distributions.

values of the parton momentum fractions of the colliding hadrons. Recall that the inclusive cross section for single photon production in the central region is sensitive to average values of the parton momentum fraction x approximately equal to $x_T = 2p_T/\sqrt{s}$. A range of x_T out to about 0.3 will be covered, corresponding to a similar range of $\langle x \rangle$ for the parton distributions. This extended range suggests that the relative ratios of the underlying subprocesses should change significantly over the p_T range to be covered. To investigate this, the inclusive cross section is displayed in Fig. 37 along with the contributions from the various parton scattering subprocesses. For ease of comparison, the same results are shown in Fig. 38 on a linear scale relative to the total rate. The results in both of these figures were generated using the leading-logarithm approximation with the CTEQ5L parton distributions. The leading-log approximation was chosen so that the separation between the point-like and fragmentation contributions would be unambiguous. Processes with two or more partons in the final state in addition to the photon can populate regions of phase space where the photon is collinear with one of the partons. These topologies correspond to the fragmentation process. Thus, the higher order terms mix the contributions from the point-like and fragmentation (or bremsstrahlung) components. One must define, through the use of appropriate experimental cuts, precisely what is meant by the bremsstrahlung component. For the purposes of the discussion being presented here the leading-log predictions are sufficient. Note that the magnitude of the next-to-leading-order corrections relative to the leading-log predictions for the choice of scale used here ($p_T/2$) is slowly varying over the kinematic region being studied, as shown in Fig. 39.

The results shown in Figs. 37 and 38 illustrate several points worth noting. First, the fragmentation component is expected to be a negligible fraction of the total rate. This is due primarily to the imposition of an isolation cut which rejects events with more than 1 GeV of hadronic energy accompanying the photon in a cone of radius 0.4 about the photon direction.[†] Such a cut is necessary experimentally in order to control the copious background to the photon signal from jets fragmenting into π^0's. This cone isolation energy is almost completely saturated by the underlying event energy accompanying the hard scatter, leaving little room for energy from the fragmentation of the jet. Note that the precise value of the fragmentation contribution relative to the total rate will vary as one includes higher order effects, but the overall contribution is still expected to be small. Next, one sees the dominance of the $qg \to \gamma q$ subprocess in the region out to about 100 GeV in p_T, *i.e.*, the range covered by the Run I data. Beyond this range the $\overline{q}q \to \gamma g$ subprocess becomes dominant.

[†]This cut was used for the CDF Run Ib direct photon measurements. The value of the isolation energy cut in Run II will have to be increased somewhat due to the contributions to the isolation energy from the larger number of minimum bias events expected in the same crossing.

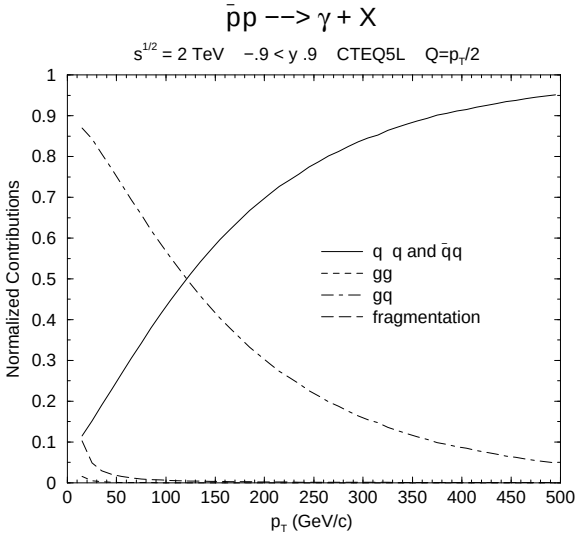

Figure 38. The same results as shown in Fig. 37 except on a linear scale and normalized to the total rate at each value of p_T.

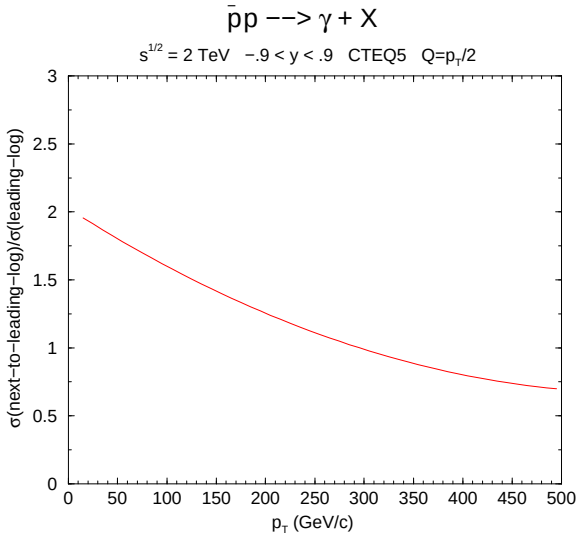

Figure 39. NLO/LO ratio for direct photon production.

Gluon-gluon initiated processes are not expected to play a significant role over the p_T range shown.

One of the classic applications of direct photon production is to provide constraints on the gluon distribution in global fits of parton distributions. The gluon distribution is especially uncertain in the region beyond $x \approx 0.15$ [18]. Run I results on high-p_T jet production from the CDF [71] and DØ [72] collaborations favor a gluon distribution which is larger at high-x than was anticipated from global fits which did not emphasize the high-p_T jet data. One such example is the CTEQ5HJ [64] set of distributions which are favored by both sets of jet data. One might hope that the direct photon data could shed some light on this issue, but such is not expected to be the case. As shown in Fig. 40, the ratio of the CTEQ5HJ and CTEQ5M predictions is consistent with unity within about 5% over the p_T range under consideration. This can be understood by referring back to Fig. 38 where it is shown that the gq subprocess decreases in importance precisely where one would like to gain a constraint on the gluon distribution.

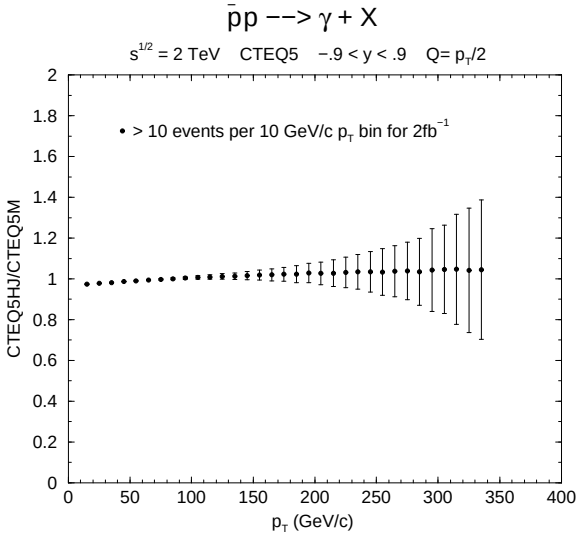

Figure 40. Ratio of the direct photon cross sections calculated with CTEQ5HJ and CTEQ5M with errors based on an integrated luminosity of 2 fb^{-1}.

2.2.4. New Measurements

As noted in the introduction, the process of direct photon production is of interest for a variety of reasons. In particular, it offers a probe of hard scattering dynamics which complements that of jet production. At this point, the comparison between theory and experiment has not reached the quantitative level that

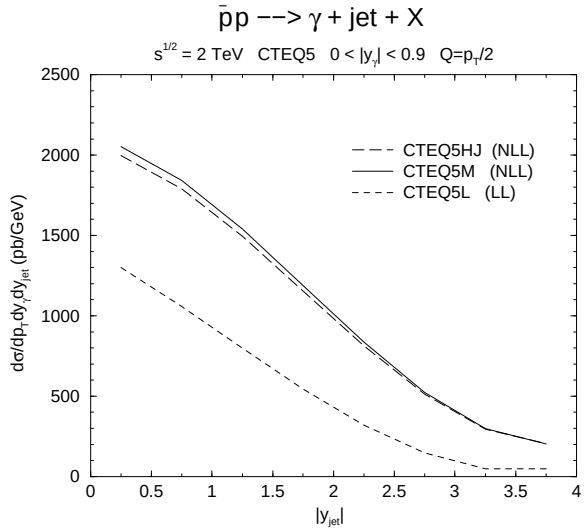

Figure 41. Jet rapidity distribution for photons in the central rapidity region calculated with the CTEQ5L, CTEQ5M, and CTEQ5HJ parton distributions with the program of Ref. [70].

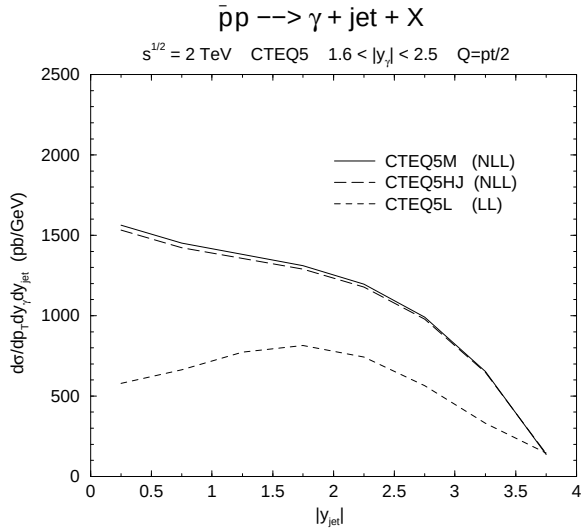

Figure 42. Jet rapidity distribution for photon in a forward rapidity region calculated with the CTEQ5L, CTEQ5M, and CTEQ5HJ parton distributions with the program of Ref. [70].

one would like, so there is clearly more to be done. Furthermore, direct photon production has the potential to provide constraints on the parton distribution functions, particularly that of the gluon. Nevertheless, the less than satisfactory description of the current data has meant that this role is, as yet, unfulfilled. Finally, one must understand conventional sources of energetic photons before being able to confidently use photons as part of the signal for new physics. With these points in mind, it is natural to ask whether there are additional observables which could help shed light on some of the theoretical problems.

To date, almost all of the experimental results for direct photon production have been for the transverse momentum distribution of the photon, *i.e.*, the single photon inclusive cross section. Clearly, there is additional information to be gained by studying the joint rapidity distributions of the photon and a jet, *e.g.*, $d\sigma/dp_T dy_\gamma dy_{jet}$ where p_T represents the transverse momentum of the photon. This observable has been measured by the CDF Collaboration [73] for photons in the the central region with 16 GeV $< p_T <$ 40 GeV. In this case the theoretical description of the jet rapidity distribution is good. However, no information is yet available for other values of photon rapidity. Some leading-log and next-to-leading-log predictions for this distribution are shown in Fig. 41 for central photons and Fig. 42 for forward photons. Notice the characteristic broadening of the jet rapidity distribution as the photon is moved forward. Note, too, the change in the ratio between the leading-log and next-to-leading-log predictions as the photon rapidity is varied. Predictions are shown for both the CTEQ5M and CTEQ5HJ parton distributions. There is only a slight difference between the two sets, due primarily to the fact that the curves were generated for $p_T > 10$ GeV. The resulting low values of x_T result in the parton distributions being probed in a region where there is little difference between the CTEQ5M and CTEQ5HJ sets. On the other hand, that means that for these distributions there will be relatively less uncertainty due to the parton distributions and that, therefore, such measurements may be useful in helping to understand the p_T region where there is a discrepancy between the existing collider data and the theoretical results. In this regard the DØ results for the inclusive photon yield shown in Fig. 24 are interesting as they may indicate that the theory/data discrepancy has some rapidity dependence. The lesson here is that photon-jet joint observables would be helpful in sorting out the source of the disagreement between theory and experiment. Note that if one wanted to increase the sensitivity to differences between parton distributions, then a larger minimum p_T cut could be employed.

As discussed in Sec. 2.2.2, there is some indication that the photon yield above a transverse momentum of about 30 GeV may actually be less than the theoretical predictions, in contrast to the situation at lower values of p_T. It was mentioned that this may be related to the observed behavior of the γ/π^0 ratio. This issue is complicated by the necessity of placing isolation cuts on the electromagnetic triggers in order to reduce the π^0 background. NLO Monte Carlo programs can simulate the effect of these isolation cuts, but the experimental dependence on the parameters of the cuts has not yet been compared to that of the theory. If the theoretical treatment of the isolation cuts is wrong, then the comparison of the NLO results to collider data must be considered suspect. In recent years the question of the theoretical treatment of such isolation cuts has been studied by several authors [74–76]. What is needed is a data set showing how the cross section depends on the cone size and the energy threshold utilized in the isolation cuts. Similar comparisons for jet production have helped refine the various jet algorithms and have been very useful in understanding issues related to the theoretical description of jets.

2.2.5. Conclusions

Run II offers many opportunities to refine our understanding of the production of photons in hard scattering processes. The kinematic reach in transverse momentum should be greatly extended and the statistical precision of the data will also be increased. While there are still problems with the theoretical description of the existing data, the Run II data have the potential to shed some light on these issues. In particular, data for photon-jet correlations and for the dependence of the cross section on the parameters of the photon isolation cuts will be helpful. A better theoretical understanding of direct photon production will enable this process to be better used in the study of large transverse momentum processes and the search for new physics.

3. Topics in Weak Boson Production[†]

The very large number of W and Z boson events CDF and DØ will collect will yield precision measurements of the W mass and width [1], which are fundamental parameters of the Standard Model and thus need to be determined with the highest possible accuracy. The Run II vector boson datasets will of course provide other important advances in the field of electroweak physics, and will be the starting point of most new physics searches; but they will also become standard tools for the understanding of many sources of systematic uncertainty in otherwise unrelated physics studies. In this Section we will give an overview of some of the additional studies it will be possible to carry out with vector bosons in Run II; for rare decays of W bosons and other topics not covered here see Ref. [77].

3.1. The W Cross Section as a Luminosity Monitor

At both DØ and CDF, the uncertainty on the total integrated luminosity is approximately 4.5% [78,79]. Though measuring the luminosity is difficult to do well, any measurement at the collider that has an absolute normalization depends on it. In several important cross section measurements made during Run I, this uncertainty contributed greatly to the overall measurement uncertainty. In particular, for both of the W and Z boson cases, the uncertainty in the luminosity measurement far outweighed the other systematic uncertainties in the measurement (see Table 1).

There is also a continuing controversy regarding the actual value of the luminosity at the two detectors at the Tevatron [78,79]. At both DØ and CDF, the integrated luminosity is normalized by the total inelastic cross section in $\overline{p}p$ collisions. CDF has made this measurement [80] and uses it to normalize their luminosity. DØ did not measure the total inelastic cross section, and chooses to normalize to the world average, which is $\sim 6.2\%$ higher than the CDF measurement [78]. This is primarily due to a 2.8 standard deviation disagreement between the CDF measurement and the E811/E710 measurements [81–84].

In the context of Run II, there are some general concerns regarding the measurement of the total integrated luminosity, particularly at high instantaneous luminosity. New luminosity monitors are being installed at each detectors as part of the modifications for Run II and CDF plans to repeat the measurement of the total inelastic cross section. However, it is not clear that this will result in a more precise determination of $\mathcal{L}$, and disagreement regarding the measured $\overline{p}p$ cross section is likely to persist. Given the high precision of the current W and Z cross section measurements, increasing precision in the matrix element calculations (now at NNLO [85]), and the expected abundance of W and Z bosons produced during Run II ($\sim 10^6$ W bosons and $\sim 10^5$ Z bosons within the fiducial volumes of each detector), we may consider using the rate of W boson production to normalize the integrated luminosity. In this subsection, we present a brief overview of the magnitude of the experimental uncertainties in the integrated luminosity using W boson production, and discuss the requirements for such a measurement to be competitive with standard luminosity measure-

[†]Contributed by: D. Casey, T. Dorigo, M. Kelly, S. Leone, W.K. Sakumoto, and G. Steinbrück

Table 1
Measurements of $\sigma(W)$ at the Tevatron. The three quoted uncertainties are statistical, systematic, and luminosity.

Detector	Channel	$\sigma(W) \cdot B$ (nb)
DØ(1A)	$W \to e\nu$	$2.28 \pm 0.02 \pm 0.08 \pm 0.10$
DØ(1A)	$W \to \mu\nu$	$2.02 \pm 0.06 \pm 0.22 \pm 0.09$
DØ(1B)	$W \to e\nu$	$2.31 \pm 0.01 \pm 0.05 \pm 0.10$
DØ(1B)	$W \to \tau\nu$	$2.22 \pm 0.09 \pm 0.10 \pm 0.10$
CDF(1A)	$W \to e\nu$	$2.49 \pm 0.02 \pm 0.08 \pm 0.09$

ments and in what context it would surpass the current precision.

3.1.1. $\sigma(W)/\mathcal{L}$ in Run I/II at DØ

As an example, we describe some details of how the Run I measurement of the cross section for W boson production at DØ would translate into a determination of the total integrated luminosity.

Reversing the relationship between the integrated luminosity ($\mathcal{L}$) and the production cross section ($\sigma(W)$) in the calculation done by DØ [78], we have the following relation:

$$\mathcal{L} = \frac{N_{cand}(1 - f_{QCD}) - N_Z}{\epsilon A(1 + \frac{A_\tau}{A})\sigma(W)} \quad (2)$$

where N_{cand} is the number of W boson candidates observed, f_{QCD} is the fraction of candidates expected from QCD multi-jet production, N_Z is the number of candidates that are Z bosons in which one of the electrons was unobserved, ϵ is the event identification efficiency, A is the geometric and fiducial acceptance, A_τ is the acceptance times branching ratio for $W \to \tau\nu$, and $\sigma(W)$ is the predicted cross section times branching ratio for producing W bosons.

Table 2 show the values of each of the quantities as measured in Run I, and the fractional uncertainty each would contribute to a measurement of $\mathcal{L}$. The total uncertainty from measured quantities alone is 2.2%. Including a 4% uncertainty in the prediction of $\sigma(W)$ increases the total uncertainty to 4.6%.

We note two things: 1) even the Run I measurement results in an uncertainty on $\mathcal{L}$ that is competitive with the directly measured result[‡] and 2) by far, the dominant uncertainty is in the prediction of $\sigma(W)$.

In preparation for Run II, both DØ and CDF are undergoing major upgrades to the detectors. For DØ, this includes the addition of a solenoid magnet and a complete replacement of the tracking system. The

[‡]Of course, we cannot reliably use the theory prediction without the experimental confirmation from Run I!

Table 2
Uncertainties on the components of the measurement of $\mathcal{L}$ if one used the components of the Run I measurement of the W production cross section by DØ.

Component	Value	Error on $\mathcal{L}$
f_{QCD}	0.064±0.014	1.5%
ϵ	0.671±0.009	1.3%
A	0.465±0.004	0.9%
N_{cand}	67078	0.4%
N_Z	621±155	0.3%
A_τ/A	0.0211±0.0021	0.2%
$\sigma(W)$	22.2±0.9 nb	4%

total luminosity is expected to increase by a factor of ~ 10. We now consider how each of the factors in Eq. 2 will be affected in Run II.

The background fraction for events from QCD multi-jet production is dominated by systematics for the detection of electrons. We do not expect the uncertainty to decrease dramatically, nor do we expect the overall background level to change much. It may be possible to reduce the backgrounds and make them easier to understand if we use the muon channel; however, no serious study has been made on the subject.

The uncertainty on the lepton identification efficiency is equal parts Z boson statistics and background subtraction statistics and will scale by $\sim 1/\sqrt{10}$ (we assume an integrated cross section of 1 fb^{-1} in this section). We expect the tracking efficiency to increase, but the efficiency of the isolation and $\not\!\!E_T$ requirements may decrease due to multiple interactions and decreased resolution due to the presence of the solenoid in the Run II detector. Speculating, these effect may balance each other, leaving an overall reduction in the uncertainty by 1/3 to 0.9%.

The geometrical and fiducial acceptance will stay approximately the same. The uncertainty is dominated by the electromagnetic energy scale (0.00319 of 0.004) whose uncertainty will be smaller in Run II due to an increased number of Z boson events and extra handles provided by a central magnetic field in the DØ detector. Scaling the rest of the uncertainties with the luminosity, we should be able to halve the uncertainty on the acceptance to 0.5%.

The uncertainties in the expected number of Z candidates and the acceptance of electrons and muons from $W \to \tau\nu$ are dominated by MC statistics and can be shrunk to a negligible value.

Finally, the number of candidates will increase by a factor of 10 just from the increased luminosity, by

Table 3
Estimated values for the uncertainties in a measurement of $\mathcal{L}$ in Run II.

Component	Error on $\mathcal{L}$
f_{QCD}	1.5%
ϵ	0.9%
A	0.5%
N_{cand}	0.08%
N_Z	0.0%
A_τ/A	0.0%
$\sigma(W)$	4%

approximately a factor 1.12 from the increase of the center of mass energy from 1.8 TeV to 2.0 TeV, and by another factor of $\sim$ 2 if one includes the muon channel, resulting in about 1.4×10^6 candidates, which translates into a statistical uncertainty of about 0.08%.

Table 3 summarizes the expected experimental uncertainties for measuring $\mathcal{L}$ in Run II at DØ. A measurement of the luminosity will be dominated by the background level and uncertainty and by the uncertainty in the prediction of the cross section. Figure 43 shows how changes in the QCD background level and uncertainty, and uncertainty in the cross section prediction, affect the overall uncertainty in the resulting luminosity. In each case, all quantities from experiment were fixed to their Run I values except the one being varied. The uncertainty on the cross section was made negligible when considering the sensitivity to the background level and uncertainty. We note that decreasing the fractional uncertainty on the QCD multi-jet background by a factor of 2 – 4 reduces the luminosity uncertainty from 2.2% to 1.7 – 1.8% – a factor of $0.3 - 0.2$. The relatively large uncertainty in the background level (20%) translates into a significant sensitivity to the background level itself. Essentially, the trade-off for loosening the selection criteria and allowing more background into the data sample is that the background must be measured much more precisely in order to maintain a small uncertainty. In Run II (as in Run I), the best strategy to minimize the effect of the background uncertainty on the total cross section measurement will be to minimize the level of the background altogether – if the background can be made negligible, the effect of the uncertainty of the background on the cross section (no matter how large) will also be negligible. The cross section uncertainty continues to dominate the situation. However, if the cross section uncertainty is kept to approximately the size of the experimental uncertainty, the resulting luminosity uncertainty is more than a factor of two better than the Run I value.

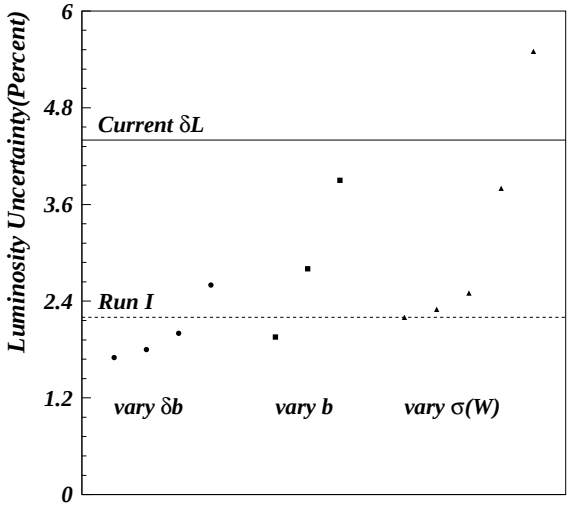

Figure 43. Impact of changing the overall background level (b), the uncertainty on the background level (δb), and the predicted $\sigma(W)$ in determining $\mathcal{L}$. Except when being varied, the experimental values are kept to the Run I determinations. Except when varying the uncertainty on the cross section, $\delta\sigma(W)$ is set to 0. The circles denote $\frac{\delta b}{b} = 0.05, 0.10, 0.15, 0.25$. The squares denote background fractions, $b = 5, 10, 15\%$. The triangles denote $\frac{\delta\sigma(W)}{\sigma(W)} = 0.001, 0.005, 0.01, 0.03, 0.05$. The solid line shows the current values of the luminosity uncertainty at $D\emptyset$ and the dashed line shows the uncertainty if the rate of W boson production was used and $\sigma(W)$ was known perfectly.

3.1.2. Counting on the Prediction for $\sigma(W)$

If one determines the integrated luminosity using the rate for W boson production, there are two fundamental issues that must be resolved. First, one must decide that the calculation for $\sigma(W)$ is reliable in itself; that it agrees with experiment. Second, one must determine the uncertainty in the calculation, since it will likely dominate the uncertainty in $\mathcal{L}$.

The first issue is likely not problematic. If all cross section measurements were normalized to a specific $\sigma(W)$ calculation, then the worst impact of a change in that calculation would be to modify all measurements in the same manner. Additionally, the advan-

tage would be that all measurements would be easy to compare, since the controversy over the measurement of the total inelastic cross section of $\overline{p}p$ collisions would be circumvented.

The problem of determining the uncertainty on the calculation is more difficult. Various *ad hoc* methods have estimated the uncertainty on $\sigma(W)$ to be $3-5\%$ [78].The uncertainty in the cross section is dominated (almost exclusively) by uncertainties in the PDF's which go into the calculation. (The uncertainties due to higher order QCD and electroweak corrections are likely much smaller than these.) Two efforts to understand the uncertainties in the PDF's quantitatively are described in the report of the Working Group on Parton Distribution Functions [2].

3.1.3. Conclusion

We have described the current expectations for measuring the integrated luminosity in Run II using the rate for W boson production. The experimental uncertainties, totaling $\sim 2.2\%$, are dominated by the uncertainty in the background from QCD multi-jet interactions. However, the total uncertainty is dominated by an ill-defined uncertainty on the prediction for the production cross section for W bosons. With sufficient progress in the continuing effort to quantify this uncertainty, we may be able to reliably determine the total integrated luminosity in Run II using the rate for W boson production to $\sim 3-4\%$.

3.2. Determination of the Weak Boson p_T Production Spectrum

During Run II at the Tevatron, CDF and DØ will obtain the largest data set of e^+e^- pairs resulting from via $p\bar{p} \to \gamma^*/Z$ to date, pushing the analysis of vector boson production characteristics over the edge from being limited by statistical uncertainties, to being limited by systematic uncertainties. The di-electron final state provides two important experimental handles. Electrons themselves are among the best-measured objects at either detector, with far better resolution in energy and position than most final-state high-p_T objects (such as jets or muons). Additionally, the di-electron final state provides complete kinematic information about the hard collision; the four-momentum of the Z/γ^* state is known unambiguously. Since the electroweak character of the decay to di-electrons is generally uncorrelated with the QCD characteristics of the production of the vector boson state, di-electron production in $p\bar{p}$ collisions via the Drell-Yan production is a sensitive probe for investigating many aspects of QCD. The rapidity (y) distribution is the Drell-Yan analog to deep inelastic scattering structure function, providing additional constraints on PDF's. The transverse momentum ($p_{\rm T}$) distribution is sensitive to predictions from standard perturbative QCD at high-$p_{\rm T}$ ($\sim Q^2$) and to predictions from soft-gluon resummation calculations at low-$p_{\rm T}$ [86,87]. Additionally, the low-$p_{\rm T}$ region is sensitive to non-perturbative effects not calculable in pQCD. These effects are included via a universal form factor, not unlike PDF's, whose parameters must tuned to data.

In addition to the intrinsic benefits of precision measurements of QCD, there are practical benefits for other measurements at the Tevatron. In the low-$p_{\rm T}$ region, where the cross section is highest, uncertainties in the phenomenology of vector boson production have contributed to the uncertainty in the measurement of the mass of the W boson ($M_{\rm W}$) [88,89]. Diboson, top quark, and Higgs boson production all have single and di-electron backgrounds from W and Z boson production that will be more constrained through a precise measurement of Z/γ^* production properties. Also, the universality of the resummation approach requires further experimental testing, with implications ranging from the impact on the precise determination of $M_{\rm W}$, to the production of Higgs bosons and di-photons [90,10].

High mass Drell-Yan e^+e^- pairs are experimentally distinctive: the electrons typically have large $E_{\rm T}$'s, are separated from each other in η and ϕ, and tend to be separated from jets and other activity in an event. In Run I, CDF and DØ collected such events with electrons in the central ($|\eta_{\rm det}| < 1.1$) and forward ($1.1 < |\eta_{\rm det}| < 2.4/2.5$) regions, providing a coverage in the e^+e^--pair rapidity of up to $|y| \sim 3$. Since the online and off-line electron identification efficiencies are comparable (for both experiments), additional off-line requirements primarily enhance the rejection of background from QCD multijet events that were mis-measured as electrons. At CDF, the most powerful discrimination is provided by tracking and precise electron shower centroid measurements. To cope with the large jet backgrounds in the forward detector region, CDF developed the SVX-Plug tracker [91] and improved the matching of tracks in the vertex tracker with calorimeter shower positions during Run I. Applying such forward tracking techniques to both e's of a pair reduced the backgrounds from about 10% to a percent or less. At DØ, the most background rejection was obtained by additional isolation and shower-shape requirements, reducing the backgrounds from $\sim 10-15\%$ to $4-7\%$, depending upon fiducial region. With the addition of central magnetic field and enhanced tracking in the Run II detector, the background is expected to be reduced even further.

To allow direct comparisons of experimental results with QCD predictions, the experimental results are fully corrected for detector acceptance, experimental

efficiencies, and detector resolution effects. For the Run I data, CDF and DØ used Monte Carlo simulations to determine the corrections for the detector efficiency, acceptance, and resolution as a function of p_T and y. CDF generated the di-electron signal using PYTHIA [92], processing them with the CDF detector simulation and reconstruction programs. Additionally, they used PHOTOS [93] to simulate final state QED radiation from the $\gamma^*/Z \to e^+e^-$ vertex. PYTHIA and the detector simulation were tuned to obtain satisfactory agreement with data [94]. DØ generated γ^*/Z events using the resummed prediction from LEGACY [95], smearing the decay electrons with a parameterized detector simulation which included final-state QED radiation corrections. The parameters and resolutions in the detector simulation were tuned to obtain agreement with data [96].

In general, the predictions for vector boson production do not yet include QED effects, therefore the experimental corrections must attempt to account for them. At a minimum, final state QED radiation must be included because the effects are large [97], and CDF and DØ included such corrections in their Run I measurements. As there is yet no numerical implementation of the QED corrections analogous to the QCD soft gluon resummation formalism, initial state QED effects have not been considered. Initial state QED radiation effects in $p_{\rm T}$ are expected to be similar to those in QCD, but since the coupling is much smaller, the $p_{\rm T}$ distribution due to QED effects should be much softer. It is expected that resummation of the initial state soft-photon emission can be implemented similarly to the soft gluon case [97].

Using 110 pb^{-1} e^+e^- data from Run I, both CDF and DØ have measured the Drell-Yan cross section $d\sigma/dp_{\rm T}$ [94,96] and CDF has measured $d\sigma/dy$ [98,99]. For both CDF and DØ, the measurement error at the peak of the $p_{\rm T}$ distribution ($\sim$ 3 GeV/c) was $\sim$ 6%. The measurement error at $|y| = 0$ was $\sim$ 5%. The combined efficiency and acceptance for these measurements was $\sim$ 33%.

The dominant systematic uncertainties in these measurements are the efficiency and background corrections. Generally, the uncertainty in shape is more problematic than the uncertainty in overall normalization. As mentioned, the level of background is expected to be reduced in Run II with the enhanced tracking available in both detectors. This will also reduce the effect of the normalization-uncertainty on the final measurement. The uncertainty in the shape of the background is dominated by statistics from events that satisfy multijet and direct-γ triggers, which also satisfy the kinematic and fiducial requirements necessary for the Z/γ^* analysis. Again, the enhanced

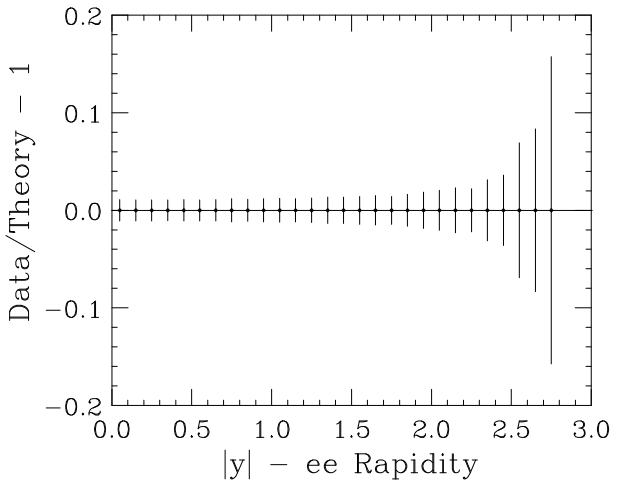

Figure 44. The expected CDF Run II measurement error on $d\sigma/dy$ of e^+e^- pairs in the mass range 66 – 116 GeV/c^2. "Data/Theory" has been arbitrarily set to unity. The error is for 2 fb^{-1}.

statistics of Run II should allow this uncertainty to by reduced. The overall electron identification efficiency is well-known in both experiments–$\delta\epsilon \sim 0.5\%$. The shape as a function of $p_{\rm T}$ is dominated by the isolation requirement being spoiled by jet activity nearby the electron cluster. Understanding this effect requires either excellent GEANT-type Monte Carlo or a great number of di-electron events from single-electron triggers, so one can investigate the effects of hadronic activity on electron isolation in an unbiased manner. We expect to see improvements in both areas in Run II, hopefully reducing the uncertainty in the shape of the efficiency as a function of $p_{\rm T}$ from $\sim 3-5\%$ to $\sim 1\%$.

The expected Run II measurement errors for the $d\sigma/dy$ and $d\sigma/dP_{\rm T}$ measurement can be estimated from the Run I measurement errors by assuming that the statistical ("Stat") and systematic ("Syst") errors scale as follows:

$$\text{Stat} \to 1/\sqrt[2]{N_{\rm ev}}$$
$$\text{Syst} \to 1/\sqrt[4]{N_{\rm ev}}$$

where $N_{\rm ev}$ is the number of events in a bin. The scaling of the systematic uncertainties should be considered a rough parameterization. Scaling the Run I uncertainties from CDF to an integrated luminosity of 2 fb^{-1}, we obtain predictions for the total measurement uncertainty in $d\sigma/dy$ (Fig. 44) and $d\sigma/dp_{\rm T}$ (Fig. 45).

With an expected precision of a few percent, the

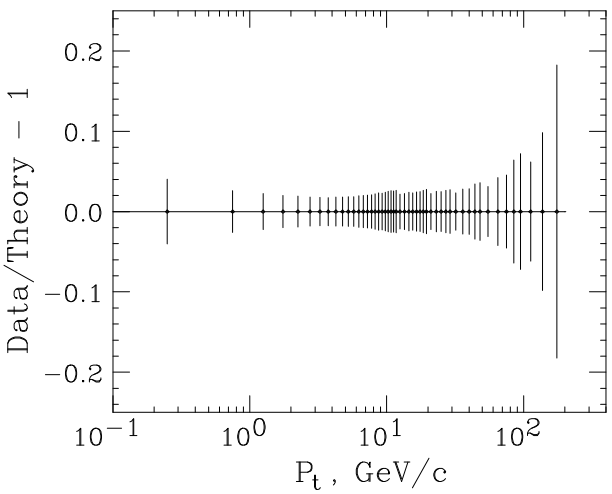

Figure 45. The expected CDF Run II measurement error on $d\sigma/dp_{\rm T}$ of e^+e^- pairs in the mass range 66 – 116 GeV/c^2. "Data/Theory" has been arbitrarily set to unity. The error is for 2 fb^{-1}.

Run II data can provide even more stringent constraints on all aspects of our understanding of Z/γ^* productions, with important implications on our understanding of resummation in pQCD, and the precision determination of $M_{\rm W}$. The precision of the Run II $d\sigma/dy$ and $d\sigma/dp_{\rm T}$ measurements will most likely be limited by systematic uncertainties from corrections to the detector acceptance/efficiency and resolution. These uncertainties will be constrained through the improved accuracy of Monte Carlo detector simulations, and the additional data available in general during Run II.

3.3. Offstream Searches for Vector Bosons

3.3.1. Introduction

Since their discovery in 1983 [100–103], W and Z bosons have been studied at hadronic colliders only via their leptonic decays. As a matter of fact the hadronic decays of these particles are generally so difficult to separate from the huge QCD backgrounds that, after the extraction of a nice mass bump in the jet-jet mass distribution by the UA2 collaboration in 1987 [104, 105], they have laid dormant for quite a while as an electroweak physics topic.

Things have started to change with the increase of collider luminosity and dataset size. During Tevatron's Run I, hadronic W decays have been successfully used by CDF and D0 in the discovery and measurement of the top quark properties both in the single lepton and fully hadronic final states, and a handful of jet-jet masses peaking at 80 GeV have been extracted from a subset of high-purity $t\bar{t}$ events (see Fig. 46). More recently, a signal of Z decays to b-quark pairs has emerged in the CDF data (Sec. 3.3.3).

With Run II sample sizes it will be possible to search for more such hadronic signals, and some of them are expected to start becoming useful tools for other physics advances. In fact, their potential as calibration tools for the jet energy measurement is high, provided that they can be collected by unbiasing triggers. This seems particularly likely in the case of $Z \to b\bar{b}$ decays, where the background has been shown to be reducible to a manageable size and the hardware tools for collecting them with good efficiency and small bandwidth concessions are now available; moreover, for b-quark jets the absolute energy scale cannot be fixed by photon-jet balancing techniques, due to the rarity of events with a photon recoiling against a single b-quark jet: a Z peak may then really be our best chance for that purpose. Hadronic W decays will also be an ideal calibration tool in $t\bar{t}$ events, but efforts need to be spent on finding their signal in independent data samples. These may be provided by diboson production processes, where triggering and background issues are less problematic.

3.3.2. Hadronic Decays of W Bosons

Searches for a W mass signal in inclusive jet triggers have been fruitless in Run I data. With respect to the lower energy $S\bar{p}pS$ collider, the Tevatron's higher center-of-mass energy is a disadvantage for once, because in the face of a four-fold increase in signal cross section the background from QCD processes increases by an order of magnitude, due to its steep behavior with respect to parton x. Moreover, no dedicated low-E_T jet triggers were devised either at CDF or DØ during Run I, given the experiments' focus on the high energy frontier; at the very end of the run, however, a sector of CDF's central tracking chamber became inoperative due to a broken wire, which allowed 1.9 pb^{-1} of data to be collected by a high-bandwidth 12 GeV dijet trigger. The data thus gathered did not allow the extraction of a W peak either, but lends itself to fruitful extrapolations to Run II.

It seems reasonable to investigate the collection of events with very low jet E_T by special low-luminosity runs, which might become an attractive option in the event of temporary inoperativeness of tracking detectors. Here we examine a scenario where CDF II or DØ gathers some 100 pb^{-1} of unprescaled data collected with a trigger requiring two calorimeter towers above 4 GeV at Level 1 and two jets with $E_T > 10$ GeV at Level 2, back-to-back in phi –about the smallest

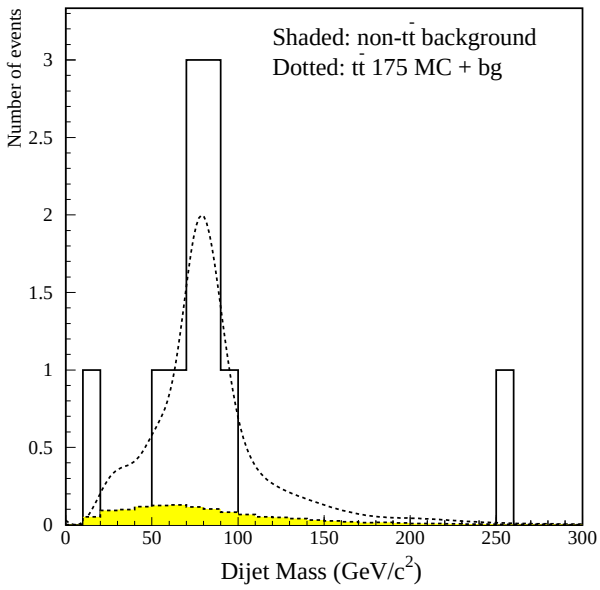

Figure 46. The jet-jet mass distribution of untagged jets in the very high purity single lepton $t\bar{t}$ candidates sample collected by CDF requiring two additional b-tagged jets.

thresholds that do not saturate the bandwidth. About two million $W/Z \to jj$ decays could be then collected, which would be reduced to 200,000 after optimized kinematic cuts requiring two central back-to-back jets and little extra-jet activity. Toy Monte Carlo studies suggest that in such a scenario the W mass could be fit with a ~ 0.5 GeV uncertainty, provided the availability of a prescaled sample with looser requirements at Level 2: this would yield an understanding of the absolute jet energy scale of the detectors to better than 1%. Such a dataset could then clearly be used also for excellent tests of optimization of jet algorithms, and thus offer benefits to any search for hadronically decaying massive objects.

3.3.3. Z Decays to b-Quark Pairs in Run I

Thanks to the several million Z decays to b-quark pairs collected by the LEP I and SLD experiments since 1992, the physics of these decays is extremely well studied and understood. At a proton-antiproton collider that particular process had not been identified before, though; therefore the extraction of a signal in Run I data was interesting in its own right. Moreover, the knowledge of how to extract a Z peak enables a careful design of a dedicated trigger for Run II, which may allow us to collect a large sample of these events, from which the mass distribution can be fit and thus insight can be obtained on the absolute energy scale for b-quark jets, substantially reducing one of the critical sources of systematic uncertainty in the top quark mass measurement.

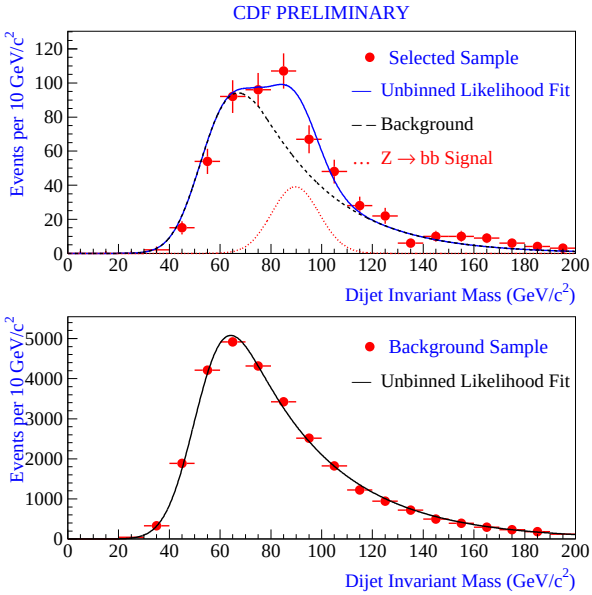

Figure 47. Top: the $Z \to b\bar{b}$ peak in the signal sample; bottom: a signal-depleted sample is used to extract the background shape.

A $Z \to b\bar{b}$ signal was extracted in Run I CDF data using kinematic tools and b-quark vertex tagging. Starting from a dataset of about five million events enriched of b-quark decays collected by a single muon trigger, a very tight kinematic selection was devised, which increased the signal to background ratio by three orders of magnitude.

The main background to the Z decay to b quarks is due to direct QCD production of a $b\bar{b}$ pair, while non-b backgrounds yielding muons can be completely eliminated by requiring the presence of a secondary vertex in each of the two jets; this cut also reduces the flavor excitation and gluon splitting contributions to b quarks in the sample quite effectively. Most of the direct $b\bar{b}$ pairs are produced at the Tevatron by a gluon fusion process, whose high color charge in the initial state and color flow topology are distinctive characteristics. To exploit the smaller probability of QCD radiation in the signal, the two leading jets were required to be back-to-back in ϕ, and the sum of all other calorime-

ter clusters in the event was required to be smaller than 10 GeV. These cuts selected 588 events, whose jet-jet mass distribution was fit to the sum of QCD background and Z decay to yield a signal of 91 ± 30 events, with a S/N ratio at the Z peak equal to 1/3; the fit resulted in a Z mass of 90.0 ± 2.4 GeV (see Fig. 47). If the same analysis should be replicated with 20 times more statistics and no detector improvements, this would yield a relative error in the b-jet energy scale smaller than 1%. The picture could be even rosier as far as statistics goes, due to the extended lepton coverage and improved silicon tracking the Run II detectors will be endowed with, but the strong bias due to the triggering lepton will make these findings of difficult use for generic b-quark jets.

Besides its possible use as a calibration tool, however, a $Z \to b\bar{b}$ peak provides a fine testing ground for algorithms designed to improve the jet energy measurement for b jets, which is one of the critical points for the discovery of an intermediate mass Higgs boson in Run II. The $b\bar{b}$ final state is the dominant one in Higgs boson decay if $M_H < 135$ GeV/c^2 [106]. Our ability to extract this particle from the large QCD background in Run II (for instance in the $Wb\bar{b}$ final state, when associated WH production is sought) will therefore depend critically on the resolution we can attain on the Higgs boson mass as reconstructed from the measured b-quark jet energies: both the possibility to see a bump in the mass spectrum of jet pairs associated to a leptonically decaying W bosons, and the alternative option of applying a mass window cut as a selection tool for these events, will strictly depend on the actual mass resolution.

The expected resolution for a generic jet-jet resonance at CDF and D0 was roughly $\sigma_{M_{jj}} = 0.1 M_{jj}$ in Run I. A relative improvement of this number by 30% would significantly extend [106] our discovery reach for the Higgs boson in Run II. In order to achieve that improvement we must study in detail the characteristics of b-quark jets emitted in the Higgs decay, and use to their utmost the large amount of available information provided by the various detector components DØ and CDF II are made up of. For example, three-dimensional tracking in the new SVX II detector may allow CDF II to infer the momentum of the escaping neutrinos in semileptonic b-quark decays, greatly improving the energy measurement of the resulting jets; this plan will work well in Run II, given the larger acceptance for charged leptons from semileptonic decays provided by the new detectors. Furthermore, the possibility of measuring track momenta to higher rapidity will allow a fruitful use of tracking information to improve the calorimetric measurement of jets.

A detailed study of the observable quantities of b-quark jets produced in $Z \to b\bar{b}$ decays followed by one semileptonic $b \to \mu X$ decay have been shown to allow a sizable reduction of the width of the reconstructed $b\bar{b}$ peak. The quantities found useful for this purpose in the CDF analysis were the muon momentum, the projection of missing transverse energy along the jet axes, and the charged fraction of the jets.

The muon momentum is needed in the correction of jets containing a semileptonic decay of b quarks, because the minimum ionizing muons do not contribute linearly to the energy measured in the calorimeter. The missing E_T, projected along the jet directions in the transverse plane, provides useful information on the amount of momentum taken away by the neutrino in the muon jet and on possible fluctuations of the energy measurement in both the muon and the away jet. The charged fraction of the jets, defined as the ratio between the total momentum of charged tracks belonging to a jet and the energy measured in the calorimeter, also helps reducing the uncertainty in the energy measurement.

By properly accounting for the value of these observables, it was possible to reduce the relative uncertainty in the dijet mass measurement, σ_M/M_{jj}, by nearly 50% (see Fig. 48).

If the alternative plan (described in the following section) based on collecting $Z \to b\bar{b}$ decays by triggering directly on secondary vertices in jets at Level 2 should fail, CDF II will anyways be able to observe a peak of several thousand events in the inclusive lepton datasets by simply replicating the Run I analysis. These peaks will not allow a precise calibration tool for inclusive b-quark jets, given the biasing semileptonic decay of one of the two jets, but they will anyways be extremely useful as a testing ground for the algorithms now under development which aim at reducing the jet energy resolution.

3.3.4. Z Decays to b-Quark Pairs in Run II

A strategy to collect $Z \to b\bar{b}$ events in Run II has been studied having in mind the CDF trigger configuration. We tried to keep the trigger requirements as simple as possible and optimize them in order to have acceptable trigger rates (less than 2% of the total bandwidth at each level) and maintain a good signal efficiency.

Most $Z \to b\bar{b}$ events should contain two reconstructable secondary vertices in the final state. In Run II it will be possible to trigger on secondary vertex information. Exploiting this feature, it should be possible to collect a sample of $Z \to b\bar{b}$ events without particular requirements on the b decay. One purpose of this dataset is to provide a sample to calibrate the calorimeter energy scale for jets containing b quarks,

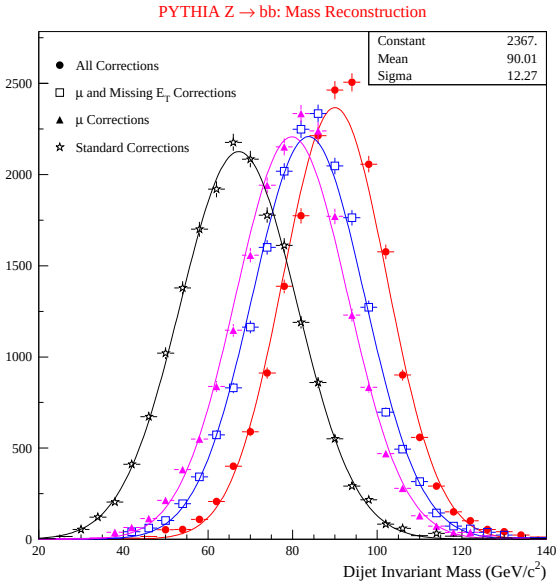

Figure 48. The four Gaussian fits show the improvement of the mass reconstruction for simulated $Z \to b\bar{b}$ events (Pythia V5.7, CDF detector simulation) when the observable characteristics of the b-quark decays are properly taken into account in the mass reconstruction.

which may limit our ability to measure the top mass. Therefore the trigger path should bias the energy scale measurement as little as possible.

At Level 1 the XFT (eXtremely Fast Tracker) information will be available: transverse momentum P_T, azimuthal angle ϕ and charge sign of particles crossing all of the Central Outer Tracker (COT) layers. We require the presence of two central high P_T tracks in opposite hemispheres. Cuts are chosen on the track P_T and $\Delta\phi$ to maximize the statistical significance $(S/\sqrt{B})$. The track P_T cuts are 6 GeV and 4 GeV, with $\Delta\phi > 150^o$.

At Level 2 the rate is reduced by requiring the tracks to have a finite impact parameter. The SVT (Silicon Vertex Tracker) processor will provide this information. The best significance is found by requiring two SVT tracks with 120 $\mu m < |d| < 1000$ μm.

The computing power of the Level 3 processors should allow the reconstruction of secondary vertices online. We require two jets, each with uncorrected $E_T > 10$ GeV in a cone of radius R = 0.7, and check that the jets contain two displaced vertices.

A summary of signal efficiency, trigger cross section and trigger rate at the three trigger levels is reported in Table 4 for a typical instantaneous luminosity $\mathcal{L} = 1.4 \cdot 10^{32}\text{cm}^{-2}\text{s}^{-1}$.

Table 4
Summary of the $Z \to b\bar{b}$ trigger efficiency, cross section, and rate at each level.

Trigger	ϵ_S (%)	σ_T	R_T (Hz)
Level 1	17.0 ± 0.2	(5.7 ± 0.3) μb	800 ± 42
Level 2	3.10 ± 0.03	(32 ± 3) nb	4.4 ± 0.4
Level 3	2.4 ± 0.1	(3.2 ± 0.9) nb	0.5 ± 0.1

Since $\sigma(p\bar{p} \to Z \to b\bar{b}X) \simeq 1$ nb, about $2 \cdot 10^6$ $Z \to b\bar{b}$ events will be produced in Run II, assuming 2 fb^{-1} of data collected in two years. We expect to collect 48,000 signal events in a total of about $6.4 \cdot 10^6$ with this trigger, corresponding to a S/B of 0.0075 and a significance $S/\sqrt{B} \simeq 19$.

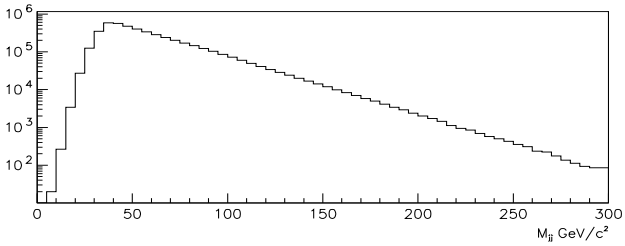

Figure 49. M_{jj} distribution expected from Run II: signal+background.

It is also advantageous to require the presence of no additional jets with $E_T > 10$ GeV in the event, either at trigger level or at a pre–analysis level. This would increase the signal fraction to 0.013 and the significance to $S/\sqrt{B} = 24$. We simulated the signal extraction procedure under these assumptions. We searched for the $Z \to b\bar{b}$ signal in the jet–jet invariant mass distribution M_{jj}. We expect to see an enhancement corresponding to the Z mass, since the statistical significance of the signal is high. Outside of the signal region the M_{jj} spectrum should be approximately described by a decreasing exponential.

The PYTHIA Monte Carlo is used to model the $Z \to b\bar{b}$ invariant mass spectrum. The background M_{jj}

distribution expected for the background is inferred from generic Run I dijet data by assuming that the request of secondary vertices does not modify its shape. The M_{jj} distributions for signal and background normalized to 2 fb^{-1} have been added (see Fig. 49).

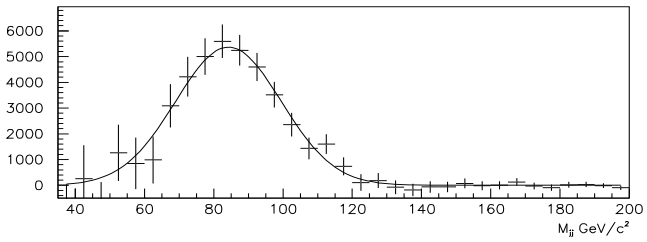

Figure 50. Background-subtracted M_{jj} distribution for Z events obtained from a pseudo-experiment.

Because of the very low S/B ratio, we cannot distinguish by eye the signal peak in Fig. 49. We conducted 1000 pseudo-experiments, varying every time the bin content according to a poissonian distribution with mean equal to the bin content itself. For each pseudo-experiment the region outside the Z peak was fitted with a decreasing exponential. The value of this function was subtracted, bin by bin, from the total spectrum. The results obtained in one of these pseudo-experiment subtractions is shown in Fig. 50, together with a gaussian fit to the excess found. With this method we typically obtain for the jet-jet invariant mass peak position $M_{meas} = 84.0$ GeV/c^2, with a statistical uncertainty of 1.5 GeV/c^2 on M_{meas}.[§]

The interval of $\pm 2\sigma$ around the Z peak (55 GeV/c^2 $< M_{jj} <$ 115 GeV/c^2) contains about 93% of the signal events and 25% of the background events. Therefore in this region $S/B = 0.05$ and the statistical significance is $S/\sqrt{B} = 44$.

The error on the Z mass can be directly translated into an error on the b-jet energy scale. Measuring the Z mass with an error of the order of 1.5 GeV/c^2 will allow to determine the b–jet absolute energy scale with an uncertainty of 1.7%.

[§]The jet energy corrections applied here are not optimized for b jets, whose higher mass and decay properties are sensibly different from those of generic light-quark and gluon jets: the invariant mass peak is thus about 7 GeV lower than the true Z mass.

3.3.5. Other Hadronic Signals

Besides its interest for the study of trilinear gauge boson couplings, discussed in Sec. 4, associated production of two vector bosons yielding a leptonic and a hadronic decay may provide additional handles for the physics of hadronic resonances, both because of the ease of collecting these events with good efficiency in high-P_T lepton triggers and because of the larger signal to background ratio with respect to single boson production processes, due mainly to the reduction of background processes with gluons in the initial state.

WW production is the best example: in a sample of 5 fb^{-1}, for instance, about 3000 $p\bar{p} \to WW \to l\nu jj$ events can be collected by applying standard cuts on the leptonic decay products and requiring two jets with uncorrected $E_T > 15$ GeV; the signal to noise ratio is then close to 1/40 before any optimized selection. Thence an observation of the W peak in the dijet mass distribution will be relatively easy to obtain. Systematic effects in the mass fits due to the low S/N ratio may make this sample of little impact as a source of knowledge of jet energy scale when compared to the high-purity $W \to jj$ samples that single lepton $t\bar{t}$ decays may provide; but the signal may still be extremely useful for the study of jet resolutions.

Another process that will be likely observed in Run II is associated WZ production with a subsequent leptonic decay of the W boson and a decay of the Z to b-quark jets. In 5 fb^{-1} about 500 such events can be collected by the lepton triggers, from where secondary vertex tagging can considerably increase the signal purity. Despite its small size, this signal may be of fundamental importance in checking systematic uncertainties in the standard model Higgs boson search, which will mainly focus on the very same dataset with very similar analysis cuts.

Finally, the possibility of collecting $Z \to b\bar{b}$ in photon triggers has been investigated. $Z\gamma$ production has a small cross section –about 2.5 pb for a photon with $E_T > 10$ GeV and two b-quark jets (see Fig. 51)– but the heavy flavor decay provides a quite distinctive signature, and the process could be easily put in evidence if a sufficiently low trigger threshold were set on the photon transverse energy, or alternatively if a γb trigger could be devised. The advantage of the process producing an additional photon over inclusive Z production lays in the suppression of the irreducible background from direct QCD $b\bar{b}$ production: since initial state photons can only be present in quark-antiquark annihilation diagrams, at Tevatron energies the $b\bar{b}\gamma$ background is suppressed by roughly an order of magnitude more than the Z signal with respect to the searches in inclusive $b\bar{b}$ samples. It is however difficult to devise an unprescaled trigger capable of a sufficient

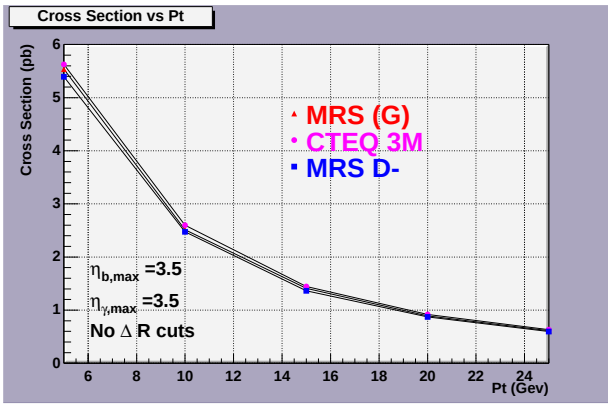

Figure 51. The cross section times branching ratio for $Z\gamma$ production with subsequent $Z \to b\bar{b}$ decay, for different choices of PDF sets, computed with the Baur-Berger-Zeppenfeld generator [107].

efficiency for the signal while maintaining the total rate at an acceptable level. In particular, a γb trigger would have to require at Level 1 both a photon candidate and one or two charged tracks; the tracks and the photon would then need to be separated in azimuthal angle, to reduce the rate of fake photon signals from QCD events. There is currently no plan to devise such a trigger in CDF II or DØ , while the lowest unprescaled photon triggers will collect events with ${E_T}^{\gamma} > 25$ GeV, where the $\gamma b\bar{b}$ cross section is only 0.6 pb. With 5 fb^{-1} it will be relatively easy to isolate a signal of one or two hundred events over a similarly sized background, but, given the small size, its exploitation appears dubious.

3.4. Lepton Angular Distributions in W Boson Decay

Next-to-leading order perturbative QCD predicts that in $W \to l\nu$ decays an angular distribution of $(1 \pm \alpha_1 \cos\theta^* + \alpha_2 \cos^2\theta^*)$ [108] should be observed, where θ^* is the polar angle of the decay lepton in the Collins-Soper frame [109]. In the presence of QCD corrections, the parameters α_1 and α_2 are functions of p_T^W, the W boson transverse momentum.

The measurement of α_2 serves as a probe of NLO QCD, using the well understood W-fermion coupling. By probing the spin structure of W production, this measurement provides another method that is independent of purely QCD analyses, while adding to the list of measurements using vector bosons to study NLO QCD. Moreover, the measurement of the angular distribution of the decay leptons is also of importance for the W mass measurements, because the next-to-leading order QCD corrections to the angular distribution are a non-negligible contribution to the W mass.

The measurement of the angular distribution of electrons from W bosons obtained with Run I data collected by DØ [110,111] is statistically limited (see Fig. 52). While a calculation that includes QCD effects is preferred over one that does not, this preference is not strong enough to exclude a p_T independent angular parameter α_2. With the next collider run starting in the near future, it is worthwhile looking at the sensitivity of this measurement in Run II. In the following discussion we will estimate the size of statistical and systematic errors to this measurement with 2 fb^{-1} in Run II.

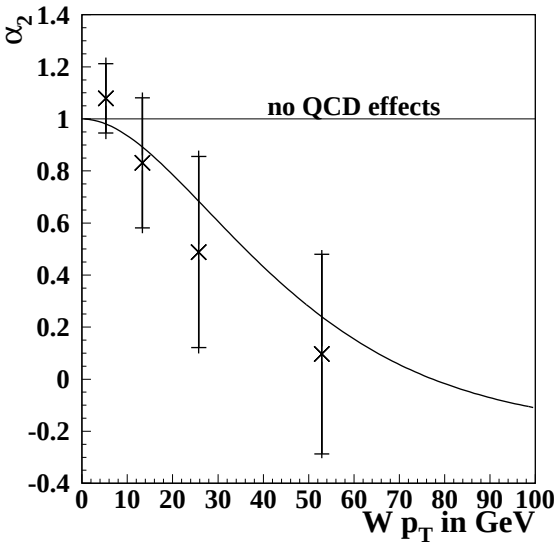

Figure 52. DØ Run I result: the measured α_2 as a function of p_T with combined statistical and systematic errors compared to the NLO QCD calculation by Mirkes (curve) and calculation in the absence of QCD effects (horizontal line). The statistical errors alone are shown as horizontal ticks.

The expected statistical errors in the determination of α_2 should simply scale like the inverse of the square root of the number of events. We consequently need to calculate the expected number of W boson events under Run II conditions. We get a factor of 57 in W

boson statistics which breaks down as follows (see [77]):

$$\frac{N_{W,RunII}}{N_{W,RunI}} = f_{lum} \times f_{2.0\,\mathrm{TeV}} \times \frac{N_e + N_\mu}{N_e} \times \frac{\epsilon_{tracking}}{\epsilon_{no\,tracking}} \quad (3)$$

where $f_{lum} = 20$ indicates the increase in luminosity, $f_{2.0TeV} = 1.2$ indicates the increase in W cross section due to the increase of the center-of-mass energy from $\sqrt{s} = 1.8$ TeV to 2 TeV, $(N_e + N_\mu)/N_e = 2$ is the additional statistics gained by including the muon channel, and

$$\frac{\epsilon_{tracking}}{\epsilon_{no\,tracking}} = \frac{0.95}{0.8} \quad (4)$$

is the increase in efficiency due to tracking capabilities of the upgraded DØ detector.

The statistical errors of the Run I measurement are therefore scaled by $1/\sqrt{57}$, as shown in Fig. 53. The

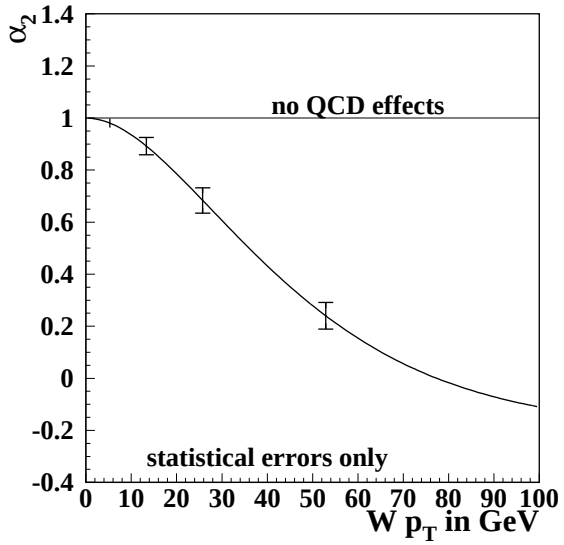

Figure 53. Estimated sensitivity of the α_2 measurement obtained by scaling statistical errors to Run II conditions.

statistical uncertainties to this measurement become quite small, and a further look at systematic errors is therefore necessary. Table 5 shows a summary of statistical and systematic errors for Run I and Run II. Since the modeling of the hadronic recoil is done from Z data, the error due to the hadronic resolution will scale with Z statistics up to a point. The estimate of this error is done by scaling the number of Z events by a factor of $\sqrt{28.5}$ (the same as for W events but excluding muons). The error on the hadronic response will also improve with increased Z statistics. Consequently, the largest errors left are the ones due to the QCD multi-jet background and the electromagnetic scale. It will be of crucial importance for this and other electroweak measurements to better estimate the QCD background. This goal can partially be reached by taking more events with a QCD monitor trigger [111]. Of course, it would be best if the QCD background fraction could be reduced even further. At this point it is not obvious if this is feasible since the current set of electron identification cuts is already very efficient in reducing this background. A Monte Carlo program that correctly models QCD multi-jet events including a realistic detector model could also help in better estimating the shape of this background. For the low p_T region, the dominant error will be the electromagnetic scale. There is however currently no good estimate by how much this error will be reduced.

Table 5
Central values and statistical errors for α_2 and systematic errors due to backgrounds, the hadronic energy scale and resolution, and the choice of α_1. All systematic errors are for Run I if not otherwise noted.

p_T [GeV]	$0-10$	$10-20$	$20-35$	$35-200$
mean p_T [GeV]	5.3	13.3	25.7	52.9
α_2, Run I	1.07 ±0.13	0.82 ±0.25	0.49 ±0.37	0.10 ±0.37
α_2, Run II	0.98	0.89	0.68	0.24
Stat. errors, e	±0.024	±0.047	±0.069	±0.069
e+μ	±0.017	±0.033	±0.049	±0.049
total syst error	±0.08	±0.09	±0.12	±0.12
QCD	±0.04	±0.05	±0.09	±0.07
Z	±0.01	±0.02	±0.02	±0.04
top	±0.00	±0.00	±0.00	±0.02
EM scale	±0.06	±0.05	±0.03	±0.04
had scale	±0.03	±0.01	±0.04	±0.04
had. resolution	±0.02	±0.02	±0.05	±0.06
had. res. Run II	±0.004	±0.004	±0.009	±0.011
α_1	±0.01	±0.05	±0.03	±0.03

In the current measurement we had to fix α_1 to the value predicted by the QCD calculation since even after summing over both W signs we are slightly sensitive to α_1 due to acceptance effects. The error due to this choice for α_1 was estimated by setting $\alpha_1 = 2.0$, the value predicted by the $V-A$ theory in the absence of QCD effects (see Table 5). This error is non-negligible. Since the central magnet in Run II will allow for sign identification of electrons, α_1 and α_2 could thus be

measured simultaneously, eliminating the need for the above assumption for α_1. This will reduce the error due to the choice of α_1. While this is a nice extension of this measurement, it is not clear at this point by how much it will numerically improve the significance of the measurement of α_2.

In the above estimate of the errors, the binning in p_T^W used for the Run I measurement was kept unchanged. With larger statistics, one would probably choose a finer binning in p_T^W, allowing for bins with larger mean p_T^W. This would increase the sensitivity in the area where the deviation of the angular distribution due to QCD effects is most pronounced.

The Monte Carlo used in the current analysis, which was originally developed for the measurement of the W mass [88] at DØ, treats hadronic jets as point particles and the hadronic recoil is treated as a single jet. This is clearly a simplification of the true processes involved and a real next-to-leading order event generator would be useful.

In addition to the experimental improvements discussed thus far, this measurement will be sensitive to W production models. These models have to be constrained by independent measurements.

To summarize, in Run II the measurement of the angular distribution of electrons from W boson decays will be systematically limited. While the recoil response and resolution will improve with increased Z statistics, the estimate of the QCD background fraction and shape becomes a limiting factor. It is difficult to estimate by how much the other dominant error, the error due to the uncertainty of the electromagnetic scale, will be reduced in Run II. Other improvements not quantified here are expected from a finer binning in p_T and sign identification of electrons.

4. Vector Boson Pair Production and Trilinear Gauge Boson Couplings – Prospects for Run II[§]

The Standard Model of electroweak interactions makes precise predictions for the couplings between gauge bosons due to the non-abelian gauge symmetry of $SU(2)_L \otimes U(1)_Y$. These self-interactions are described by the triple gauge boson (trilinear) $WW\gamma$, WWZ, $Z\gamma\gamma$, $ZZ\gamma$ and ZZZ couplings and the quartic couplings. Vector boson pair production provides a sensitive ground for *direct tests* of the trilinear couplings. Deviations of the couplings from the SM values would indicate the presence of new physical phenomena.

The purpose of this section is to present a brief overview of recent theoretical advances in understanding di-boson production in hadronic collisions, and to highlight Run II opportunities for studying the physics of vector boson pair production. Because of the large anticipated size of the data sample, $\int \mathcal{L} dt = 2$ fb^{-1}, interesting processes and final states that were not studied in Run I will become available. These are discussed, as well as prospects available in extensions of the Run I $W\gamma$, WW, and WZ analyses to Run II. This is meant to be an improvement over the forecasts of the TeV_2000 Report [77], which was written in 1995 before we had the benefit of having performed the Run Ib analyses. Indeed, some of the TeV_2000 Report's prognostications for Run II limits were achieved in Run I.

We begin with a brief summary of the trilinear gauge boson couplings and how they are parameterized. Next, we give a short description of new theoretical developments. Following that, we summarize the anomalous coupling limits obtained in Run Ia and Run Ib, and compare the Run Ib results with what we expected we would obtain, based on a simple extrapolation from Run Ia. This exercise in hindsight provides both a calibration for, and a cross-check of, the extrapolation method. The subsequent section provides expectations for anomalous coupling limits from the Run II analyses based on extrapolation of the Run I analyses to higher integrated luminosity. Next, we provide comments on some Run II analyses, and, lastly, discuss new channels and analyses which will become feasible in Run II, in particular the prospects for measuring the ZZV couplings via ZZ production.

4.1. Trilinear Couplings

The WWV ($V = \gamma$ or Z) vertices are described by a general effective Lagrangian [112,113] with two overall couplings, $g_{WW\gamma} = -e$ and $g_{WWZ} = -e \cdot \cot\theta_W$, and six dimensionless couplings g_1^V, κ_V, and λ_V ($V = \gamma$ or Z), after imposing C, P, and CP invariance. The $W_\alpha^-(q)\, W_\beta^+(\bar{q})\, V_\mu(p)$ vertex function (where all momenta are outgoing, $p + q + \bar{q} = 0$) in presence of non-standard couplings is given by:

$$\begin{aligned}\frac{\Gamma^{\alpha\beta\mu}_{WWV}}{g_{WWV}} = {} & \bar{q}^\alpha g^{\beta\mu}\left(g_1^V + \kappa_V + \lambda_V \frac{q^2}{M_W^2}\right) \\ & - q^\beta g^{\alpha\mu}\left(g_1^V + \kappa_V + \lambda_V \frac{\bar{q}^2}{M_W^2}\right) \\ & - (\bar{q}^\mu - q^\mu)\; g^{\alpha\beta}\left(g_1^V + \frac{\lambda_V}{2}\,\frac{p^2}{M_W^2}\right) \\ & + (\bar{q}^\mu - q^\mu)\,\frac{\lambda_V}{M_W^2}\; p^\alpha p^\beta \;. \end{aligned} \quad (5)$$

Here, M_W is the W-boson mass. Electromagnetic gauge invariance requires that $g_1^\gamma = 1$, which we assume throughout this paper. The SM Lagrangian is

[§]Contributed by: U. Baur, H.T. Diehl and D. Rainwater

obtained by setting $g_1^\gamma = g_1^Z = 1$, $\kappa_V = 1$ ($\Delta\kappa_V \equiv \kappa_V - 1 = 0$) and $\lambda_V = 0$.

A different set of parameters, motivated by $SU(2) \times U(1)$ gauge invariance, had been used by the LEP collaborations [114] prior to 1998. This set consists of three independent couplings $\alpha_{B\phi}$, $\alpha_{W\phi}$ and α_W: $\alpha_{B\phi} \equiv \Delta\kappa_\gamma - \Delta g_1^Z \cos^2\theta_W$, $\alpha_{W\phi} \equiv \Delta g_1^Z \cos^2\theta_W$ and $\alpha_W \equiv \lambda_\gamma$. The remaining WWZ coupling parameters λ_Z and $\Delta\kappa_Z$ are determined by the relations $\lambda_Z = \lambda_\gamma$ and $\Delta\kappa_Z = -\Delta\kappa_\gamma \tan^2\theta_W + \Delta g_1^Z$. The HISZ relations [115] which have been used by the DØ and CDF collaborations are also based on this set with the additional constraint $\alpha_{B\phi} = \alpha_{W\phi}$.

The di-boson production cross sections with non-SM couplings grow with the parton center of mass energy $\sqrt{\hat{s}}$. In order to avoid violation of S-matrix unitarity, the anomalous couplings $a = g_1^V$, $\Delta\kappa_V$, λ_V are taken as momentum dependent form factors with a scale Λ_{FF}

$$a(\hat{s}) = \frac{a}{(1 + \hat{s}/\Lambda_{FF}^2)^n} \tag{6}$$

and $n = 2$ (dipole form factor).

The $Z^\alpha(q_1)\,\gamma^\beta(q_2)\,V^\mu(P)$ ($V = \gamma$ or Z) vertices contributing to $Z\gamma$ production are described by a general vertex function [112] with eight dimensionless couplings $h_i^V (i = 1, \ldots, 4\,; V = \gamma$ or $Z)$:

$$\begin{aligned}\Gamma^{\alpha\beta\mu}_{Z\gamma V} =& \frac{P^2 - q_1^2}{M_Z^2}\left\{ h_1^V \left(q_2^\mu g^{\alpha\beta} - q_2^\alpha g^{\mu\beta}\right)\right.\\ &+ \frac{h_2^V}{M_Z^2} P^\alpha \left((P\cdot q_2)\, g^{\mu\beta} - q_2^\mu P^\beta\right)\\ &+ h_3^V \epsilon^{\mu\alpha\beta\rho} q_{2\rho}\\ &\left.+ \frac{h_4^V}{M_Z^2} P^\alpha \epsilon^{\mu\beta\rho\sigma} P_\rho q_{2\sigma}\right\}.\end{aligned} \tag{7}$$

In the SM, all h_i^V's are zero. The couplings h_1^V and h_2^V violate CP; all couplings are C-odd. The form factors for these couplings are

$$h_i^V(\hat{s}) = \frac{h_{i0}^V}{(1 + \hat{s}/\Lambda_{FF}^2)^n}\ , \tag{8}$$

where one usually assumes that $n = 3$ for $i = 1, 3$ and $n = 4$ for $i = 2, 4$ [107].

In the SM, the $\ell^+\ell^-\gamma$ final state can be produced via radiative decays of the Z boson or by production of a boson pair via t- or u-channel quark exchange. The former process is the dominant source of events with small opening angle between the photon and charged lepton and for events with a low value of photon transverse energy, E_T^γ. Events produced by the latter process have lepton-pair invariant mass, $m_{\ell\ell}$, close to M_Z and three-body invariant mass, $m_{\ell\ell\gamma}$, larger than M_Z. Anomalous $ZZ\gamma$ or $Z\gamma\gamma$ couplings would enhance the cross section for $Z\gamma$ production, particularly for high-E_T photons, relative to the SM expectations.

The most general form of the $Z^\alpha(q_1)\,Z^\beta(q_2)\,V^\mu(P)$ vertex function can be written in the form [112]

$$\begin{aligned}\Gamma^{\alpha\beta\mu}_{ZZV} =& \frac{P^2 - M_V^2}{M_Z^2}\left(i f_4^V \left(P^\alpha g^{\mu\beta} + P^\beta g^{\mu\alpha}\right)\right.\\ &\left.+ i f_5^V \epsilon^{\mu\alpha\beta\rho}\left(q_1 - q_2\right)_\rho\right).\end{aligned} \tag{9}$$

CP invariance forbids f_4^V and parity conservation requires that f_5^V vanishes. In the SM, $f_4^V = f_5^V = 0$. S-matrix unitarity requires a form factor behavior for ZZV couplings similar to that of h_1^V and h_3^V [116] (Eq. (8) with $n = 3$).

Although the WWV, $Z\gamma V$ and ZZV couplings usually are assumed to be real, they are in general complex quantities.

In theories which go beyond the SM, the WWV couplings are expected to be at most $\mathcal{O}(M_W^2/\Lambda^2)$ where $\Lambda \sim \Lambda_{FF}$ is the scale of new physics. $Z\gamma V$ and ZZV couplings are at most $\mathcal{O}(M_Z^4/\Lambda^4)$.

4.2. Recent Theoretical Developments

4.2.1. Parameterization of $Z\gamma V$ Couplings

In Ref. [117] it was pointed out that the couplings h_i^V have to be purely imaginary quantities in order to guarantee that an effective Lagrangian which would lead to a vertex function of the form of Eq. (7) is hermitian. In contrast, the WWV and ZZV couplings are normalized such that real couplings automatically correspond to a hermitian effective Lagrangian. Since one usually assumes real couplings when placing limits on anomalous vector boson self-couplings, it is useful to replace the couplings h_i^V by

$$h'^V_i = -i h_i^V \tag{10}$$

for the Run II analyses and beyond.

h'^V_i's and h_i^V's of equal magnitude result in virtually the same differential cross sections at high energies. This is illustrated in Fig. 54 for the case $|h'^Z_{30}| = |h^Z_{30}| = 0.3$. In order to simulate detector response, the following cuts have been imposed in Fig. 54:

$$p_T(\gamma) > 10 \text{ GeV}, \qquad |\eta(\gamma)| < 2.5, \tag{11}$$

$$p_T(\ell) > 20 \text{ GeV}, \qquad |\eta(\ell)| < 2.5, \tag{12}$$

$$m(\ell\ell) > 75 \text{ GeV}, \qquad m(\ell\ell\gamma) > 100 \text{ GeV}, \tag{13}$$

and

$$\Delta R(\ell\gamma) > 0.7. \tag{14}$$

The form factor scale has been chosen to be $\Lambda_{FF} = 750$ GeV.

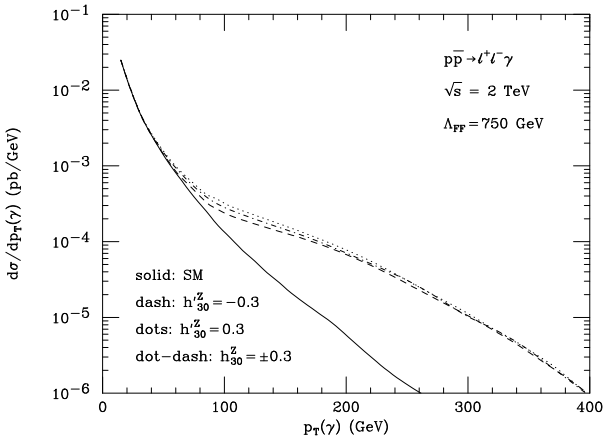

Figure 54. The photon transverse momentum distribution in $p\bar{p} \to \ell^+\ell^-\gamma$ at the Tevatron in the SM and for anomalous $ZZ\gamma$ couplings. The cuts imposed are described in the text.

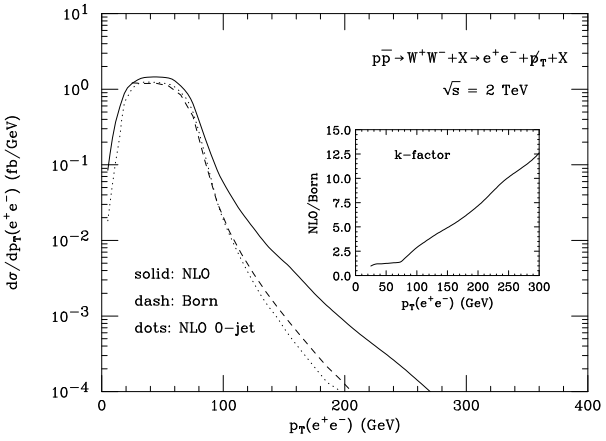

Figure 55. The e^+e^- transverse momentum distribution in $p\bar{p} \to W^+W^- + X \to e^+e^-\not{p}_T + X$ at the Tevatron in the SM. The following cuts were imposed to simulate detector response: $p_T(e) > 20$ GeV, $|\eta(e)| < 2.5$ and $\not{p}_T > 20$ GeV. For the NLO 0-jet curve (dotted line), jets with $p_T(j) > 20$ GeV and $|\eta(j)| < 3.5$ were vetoed.

Unlike for real $h^V_{3,4}$ couplings, the interference terms between the SM and the non-SM contributions do not vanish in the squared matrix element for real values of $h'^V_{3,4}$. Thus, for intermediate values of $p_T(\gamma)$, the differential cross sections for values of $h'^V_{3,4}$ of equal magnitude but opposite sign slightly differ. Since most of the sensitivity to anomalous couplings originates from the high energy domain, the limits for h'^V_i are expected to be almost identical to those obtained for h^V_i. In the following we therefore list limits only for h^V_i.

4.2.2. NLO QCD Corrections to Vector Boson Pair Production

In the Run I di-boson analyses, data were compared with leading order production calculations to extract limits on the WWV and $Z\gamma V$ couplings. The effect of higher order QCD corrections was simulated by multiplying the differential cross sections by a simple constant k-factor

$$k = 1 + \frac{8\pi}{9}\alpha_s. \qquad (15)$$

NLO calculations have shown [118] that the $\mathcal{O}(\alpha_s)$ QCD corrections in the SM depend logarithmically on $\hat{s}$ and become large at high energies, due to gluon-induced partonic subprocesses, which only enter at NLO. An example is shown in Fig. 55, where we display the transverse momentum distribution of the charged lepton pair in $p\bar{p} \to W^+W^- + X \to e^+e^-\not{p}_T + X$. NLO corrections are seen to be very large ($\mathcal{O}(10)$) at high p_T, and dramatically alter the shape of the distribution. Qualitatively this is precisely what one expects from non-standard WWV couplings. Since the real emission diagrams are responsible for the increase of the QCD corrections with p_T, a jet veto drastically reduces the size of the QCD corrections (dotted line). It should be noted that the NLO QCD corrections reduce the W^+W^- cross section when a jet veto is imposed.

With the more than 20-fold increase in statistics expected in Run II, it is clear that the QCD corrections to di-boson production must properly be taken into account when information on anomalous couplings is extracted. Over the past seven years the NLO QCD corrections to $W\gamma$ [119], $Z\gamma$ [120], WW [121] and WZ production [122] including non-standard WWV and $Z\gamma V$ couplings have been calculated using the narrow width approximation and ignoring spin correlations in the finite virtual corrections. Recently, more complete calculations have become available which properly take into account the previously ignored spin correlations. Ref. [123] also includes single resonant diagrams and finite W and Z width effects in the calculation; however, no anomalous couplings are taken into account. Refs. [124,125] use the narrow width approximation, but do include the option of non-standard WWV couplings.

The contribution of the finite virtual corrections to the NLO cross section is smaller than about 10% for all di-boson processes. The spin correlations ignored

Table 6
The $p\bar{p} \to W^+W^- + X \to e^+e^-\not{p}_T + X$ cross section for $\sqrt{s} = 2$ TeV with $p_T(e) > 20$ GeV, $|\eta(e)| < 2.5$, and $\not{p}_T > 20$ GeV. Jets are required to have $p_T(j) > 20$ GeV, $|\eta(j)| < 2.5$. Results are shown for the calculations of Ref. [121] (BHO) and Ref. [124] (DKS) with factorization scale $Q^2 = M_W^2$, and using the CTEQ4M [126] set of parton distribution functions.

	BHO σ (fb)	DKS σ (fb)
Standard Model		
Born	61.2	61.2
NLO	80.9	81.3
NLO 0-jet	65.6	65.3
$\Delta g_1^Z = 0.5$, $\lambda_Z = \lambda_\gamma = 0.1$, $\Delta\kappa_Z = \Delta\kappa_\gamma = 0.3$ $\Lambda_{FF} = 2$ TeV		
Born	82.7	82.8
NLO	106.5	107.0
NLO 0-jet	84.2	83.7

in Refs. [119–122] therefore are expected to have a rather small effect on the total cross section, as well as on most distributions. This expectation is confirmed by an explicit comparison between the calculations of Refs. [124] (DKS) and [121] (BHO) for W^+W^- production which is shown in Table 6. The two calculations are seen to agree at the 1% level.

A more detailed and careful comparison between the BHO and DKS calculations for W^+W^- and $W^\pm Z$ production at the LHC has been carried out in Ref. [127]. The WZ cross sections of the two calculations were found to agree within 1.5%, whereas in the WW case deviations of up to 3.8% were observed at NLO. Subsequently, a small error in the BHO W^+W^- code was discovered [128]. After correction of this error, the BHO and DKS calculations of W^+W^- production at the LHC agree to better than 0.5% [128].

4.3. Summary of Run Ia and Run Ib Analyses at CDF and DØ

This subsection contains a summary of the published CDF and DØ analyses. The intent is to provide an overview of the progress, a list of published papers, and tables which provide the basis for the comparison made in the next subsection.

4.3.1. $WW\gamma$ and WWZ Couplings

The DØ and CDF collaborations have performed several searches for anomalous $WW\gamma$ and WWZ couplings. Studies [129–131] of $p\bar{p} \to W\gamma + X$ have shown that the transverse energy spectrum of the photons agreed with that expected from SM production. Searches [132–134] for an excess of $p\bar{p} \to WW + X$, where the W bosons each decayed to $\ell\nu$ ($\ell = e$ or μ), yielded events which matched the SM prediction. Further, the p_T spectrum of the charged leptons agreed [134] with the prediction. Studies [135–138] of the processes $p\bar{p} \to WW + X$ and $p\bar{p} \to WZ + X$, where one W boson decayed to a lepton or anti-lepton and the corresponding anti-neutrino or neutrino and the other vector boson decayed to a quark-antiquark pair manifested as jets, yielded no excess of events and a W boson transverse energy spectrum which matched the expected background plus SM signal. Lastly, DØ studied [138] the process $p\bar{p} \to WZ + X$ where the Z boson decayed to ee and the W boson decayed to either $e\nu$ or $\mu\nu$. Limits on anomalous $WW\gamma$ and WWZ couplings were derived from each of these analyses. Several [130,132,136] of these analyses were presented in detail in Ref. [139]. The results of all of the DØ analyses were combined [138], using the maximum-likelihood method [139,140], to form the Tevatron's most restrictive limits on anomalous $WW\gamma$ and WWZ couplings.

Table 7 shows the anomalous coupling limits achieved in each of the analyses described above, the luminosity used, and the reference to the paper in which the result was published. It should be noted that many of the papers published limits under several assumptions for the relations between the coupling parameters and with several values of the form factor Λ_{FF}. Only those limits from the case $\lambda = \lambda_\gamma = \lambda_Z$ and $\Delta\kappa = \Delta\kappa_\gamma = \Delta\kappa_Z$ are listed, except for $W\gamma$ and WZ where only $WW\gamma$ and WWZ couplings, respectively, are relevant.

4.3.2. $Z\gamma V$ Couplings

The DØ and CDF collaborations have also performed several searches for anomalous $Z\gamma\gamma$ and $ZZ\gamma$ couplings. Studies [141–143] of the process $p\bar{p} \to Z\gamma + X \to \ell^+\ell^-\gamma + X$ have shown that the event yield and transverse energy spectrum of the photons agreed with that expected from SM $Z\gamma$ production, though it is noted that there were two $Z\gamma \to ee\gamma$ events with photons of E_T greater than 70 GeV, expected in only 7.3% of trial experiments.

Studies of the process $Z\gamma \to \nu\bar{\nu}\gamma$ have the advantage of the higher branching fraction for decay to neutrinos than does the charged-lepton decay mode. Furthermore, there is no final state radiation because the neutrinos are electrically neutral. However, the signal-to-background ratio is rather lower than in the charged-lepton analysis. DØ has published [144] the results of the Run Ia $Z\gamma \to \nu\bar{\nu}\gamma$ analysis. Again, the spectrum of the transverse energy of the photons, for $E_T^\gamma \geq 40$ GeV, agreed with the SM prediction.

DØ and CDF produced limits on anomalous $Z\gamma V$ ($V = Z, \gamma$) couplings using a fit to the E_T^γ spectrum.

Table 7
95% confidence level $WW\gamma$ and WWZ anomalous coupling limits achieved in Run I analyses by the DØ and CDF Collaborations.

Analysis	Ref.	Run	Lum. (pb^{-1})	Λ_{FF}	A.C. Limit (95% CL)
CDF $W\gamma \rightarrow$ $e\nu\gamma$ and $\mu\nu\gamma$	[129]	Ia	20	1.5 TeV	$-0.7 \leq \lambda \leq 0.7$ $-2.2 \leq \Delta\kappa \leq 2.3$
DØ $W\gamma \rightarrow$ $e\nu\gamma$ and $\mu\nu\gamma$	[130]	Ia	13.8	1.5 TeV	$-0.6 \leq \lambda \leq 0.6$ $-1.6 \leq \Delta\kappa \leq 1.8$
DØ $W\gamma \rightarrow$ $e\nu\gamma$ and $\mu\nu\gamma$	[131]	Ia + Ib	92.8	1.5 TeV	$-0.31 \leq \lambda \leq 0.29$ $-0.93 \leq \Delta\kappa \leq 0.94$
DØ $WW \rightarrow$ Dilepton	[132]	Ia	14	900 GeV Equal Couplings	$-2.1 \leq \lambda \leq 2.1$ $-2.6 \leq \Delta\kappa \leq 2.8$
CDF $WW \rightarrow$ Dilepton	[133]	Ia + Ib	108	1.0 TeV Equal Couplings	$-0.9 \leq \lambda \leq 0.9$ $-1.0 \leq \Delta\kappa \leq 1.3$
DØ $WW \rightarrow$ Dilepton	[134]	Ia + Ib	97	1.5 TeV Equal Coupling	$-0.53 \leq \lambda \leq 0.56$ $-0.62 \leq \Delta\kappa \leq 0.77$
CDF WW and $WZ \rightarrow$ leptons + jets	[135]	Ia	19.6	1.0 TeV Equal Couplings	$-0.81 \leq \lambda \leq 0.84$ $-1.11 \leq \Delta\kappa \leq 1.27$
DØ WW and $WZ \rightarrow$ $e\nu$jj	[136]	Ia	13.7	1.5 TeV Equal Couplings	$-0.6 \leq \lambda \leq 0.7$ $-0.9 \leq \Delta\kappa \leq 1.1$
DØ WW and $WZ \rightarrow$ $e\nu$jj	[137]	Ia + Ib	96	1.5 TeV Equal Couplings	$-0.36 \leq \lambda \leq 0.39$ $-0.47 \leq \Delta\kappa \leq 0.63$
DØ WW and $WZ \rightarrow$ $e\nu$jj	[137]	Ia + Ib	96	2.0 TeV Equal Couplings	$-0.33 \leq \lambda \leq 0.36$ $-0.43 \leq \Delta\kappa \leq 0.59$
DØ WW and $WZ \rightarrow$ $\mu\nu$jj	[138]	Ib	81	2.0 TeV Equal Couplings	$-0.43 \leq \lambda \leq 0.44$ $-0.60 \leq \Delta\kappa \leq 0.74$
DØ $WZ \rightarrow$ $ee\mu\nu$ and $eee\nu$	[138]	Ib	92	1.0 TeV	$-1.42 \leq \lambda_Z \leq 1.42$ $-1.63 \leq \Delta g_1^Z \leq 1.63$
DØ Combined	[138]	Ia + Ib	96	2.0 TeV Equal Couplings	$-0.18 \leq \lambda \leq 0.19$ $-0.25 \leq \Delta\kappa \leq 0.39$

The DØ Run Ia and Run Ib results were combined in Ref. [143]. Table 8 shows a compilation of all the Run I CDF and DØ results. The limits for h_{30}^{γ} (h_{40}^{γ}) and h_{10}^{V} (h_{20}^{V}) are almost identical to those obtained for h_{30}^{Z} (h_{40}^{Z}) and are, therefore, not shown.

4.4. Hindsight: Extrapolating Run Ia Results to Run Ib

It is interesting to see how well one can "predict" the Run Ib limits based on the Run Ia results and a simple rule for scaling the limits based on the increase in the luminosity.

The $WW\gamma$ and WWZ anomalous coupling limits should scale by

$$\left(\int \mathcal{L}dt\right)^{1/4}. \tag{16}$$

One square-root comes from the decrease in the statistical uncertainty of the cross section (as a function of E_T, for instance) and the other from the fact that the differential cross section is a quadratic function of the anomalous couplings.

The $Z\gamma\gamma$ and $ZZ\gamma$ anomalous coupling limits would also scale by the fourth-root of the ratio of the luminosities, except that the limits depend very strongly on the form-factor scale.

4.4.1. $W\gamma$

The integrated luminosity used in DØ's Run Ia + Run Ib $W\gamma$ analysis was 6.72 times larger than the Run Ia sample alone. From that we expect the combined anomalous coupling limits to be $(1/6.72)^{1/4} = 0.62$ as large as the Run Ia limits. Scaling the Run Ia results in Table 7, we would expect limits $-1.0 \leq \Delta\kappa_\gamma \leq 1.1$ and $-0.38 \leq \lambda_\gamma \leq 0.38$. Instead, from Table 7, the result was equivalent to a scaling of ~ 0.52. That does not seem very different, but it is, for it corresponds to the equivalent of a factor of two more luminosity. The difference is attributed to an improvement in technique, the use of a three-body transverse mass criteria to remove events where the photon was radiated from a charged final state lepton. It's hard to predict improvement techniques because, if such improvements were a priori known, they would most

Table 8
95% confidence level $ZZ\gamma$ and $Z\gamma\gamma$ anomalous coupling limits achieved in the Run I analyses by the DØ and CDF Collaborations.

Analysis	Ref.	Run	Lum. (pb^{-1})	Λ_{FF}	A.C. Limit (95% CL)
CDF $Z\gamma \to$	[141]	Ia	20	500 GeV	$-3.0 \le h_{30}^Z \le 3.0$
$ee\gamma$ and $\mu\mu\gamma$					$-0.7 \le h_{40}^Z \le 0.7$
DØ $Z\gamma \to$	[142]	Ia	14	500 GeV	$-1.8 \le h_{30}^Z \le 1.8$
$ee\gamma$ and $\mu\mu\gamma$					$-0.5 \le h_{40}^Z \le 0.5$
DØ $Z\gamma \to$	[143]	Ia	13	750 GeV	$-0.4 \le h_{30}^Z \le 0.4$
$\nu\bar{\nu}\gamma$					$-0.06 \le h_{40}^Z \le 0.06$
DØ $Z\gamma \to$	[144]	Ib	97	500 GeV	$-1.31 \le h_{30}^Z \le 1.31$
$ee\gamma$ and $\mu\mu\gamma$					$-0.26 \le h_{40}^Z \le 0.26$
DØ $Z\gamma \to$	[144]	Ib	97	750 GeV	$-0.69 \le h_{30}^Z \le 0.69$
$ee\gamma$ and $\mu\mu\gamma$					$-0.08 \le h_{40}^Z \le 0.08$
DØ Combined	[144]	Ia + Ib		750 GeV	$-0.36 \le h_{30}^Z \le 0.36$
					$-0.05 \le h_{40}^Z \le 0.05$

likely have been applied.

4.4.2. $WW/WZ \to e\nu$jj

We expect the Run Ia + Run Ib limits to scale by 0.61 from the ratio of the integrated luminosities. Consulting Table 7, we find that this is essentially right on the nose for the $\Lambda_{FF} = 1.5$ TeV limits. The Run Ia + Ib $\Lambda_{FF} = 2$ TeV limits, not available because of unitarity constraints in the Run Ia sample, represent a slight ($\sim 10\%$) improvement over the Run Ia + Ib $\Lambda_{FF} = 1.5$ TeV results.

4.4.3. $WW \to$ dileptons

We expect the Run Ia + Run Ib limits to scale by 0.62 from the ratio of the integrated luminosities. However, that is not what happened. An important improvement in the technique, namely a 2-D fit to the lepton E_T spectrum, plus the subsequent increase in the allowed form factor, allowed the combined results to be almost a factor of four better. Here is a case where we have already challenged the Run II limits predicted by the TeV_2000 report.

4.4.4. $Z\gamma \to ee\gamma$ and $\mu\mu\gamma$

Again, by the fourth-root rule, we expect the Run Ib limits to scale by 0.62. For $\Lambda_{FF} = 500$ GeV, we found that the h_{30}^Z results scaled by 0.72 and the h_{40}^Z by 0.52, averaging out to a scale factor of 0.62. But, because of the strong dependence on the form factor scale, the results at $\Lambda_{FF} = 750$ GeV are 3.5 and 5 times better for h_{30}^Z and h_{40}^Z, respectively.

4.5. Expectations for Run II Anomalous Coupling Limits

Having probed the usefulness and limitations of our scaling formula, we apply it to the Run I analyses to determine the limits that might be attained with 2 fb^{-1}. Of course, any projections for anomalous coupling limits are merely sensitivity estimates. Improvements in technique, such as multi-dimensional fits, or using clever projection techniques (see Ref. [145] for an example) may yield more stringent limits.

For the $W\gamma$ and WW/WZ analyses we will use an integrated luminosity scale factor $(2000/100)^{1/4} = 2.1$. The slight improvement from the $\approx 10\%$ increase in cross section available should the Tevatron operate at center of mass energy 2000 GeV is ignored. Increasing the form factor scale from 1.5 TeV to 2 TeV strengthens the limits by about 10%. The $WZ \to$ trileptons analysis will improve by about a factor of 6 because of the increased integrated luminosity and because of the improvement in limit-setting technique available by fitting the E_T spectrum of the Z bosons. Table 9 contains the expected results. In order to put these bounds into perspective, we list the most recent LEP2 (95% CL) limits from a 3-parameter fit [146], assuming $\Delta\kappa_Z = \Delta g_1^Z - \Delta\kappa_\gamma \tan^2\theta_W$ and $\lambda_Z = \lambda_\gamma$:

$$-0.073 < \Delta g_1^Z < 0.075, \quad (17)$$

$$-0.12 < \Delta\kappa_\gamma < 0.16, \quad (18)$$

$$-0.15 < \lambda_\gamma < 0.01. \quad (19)$$

It should be noted that form factor effects are *not* included in the bounds obtained at LEP2. Taking into account the form factor behavior of anomalous

Table 9
95% confidence level $WW\gamma$ and WWZ anomalous coupling limits that might be achieved by DØ or CDF in Run II.

Analysis	Lum. (pb^{-1})	Λ_{FF}	A.C. Limit (95% CL)
$W\gamma \to$	2000	1.5 TeV	$-0.14 \leq \lambda \leq 0.14$
$e\nu\gamma$ and $\mu\nu\gamma$		Equal Couplings	$-0.44 \leq \Delta\kappa \leq 0.44$
$W\gamma \to$	2000	2.0 TeV	$-0.12 \leq \lambda \leq 0.12$
$e\nu\gamma$ and $\mu\nu\gamma$		Equal Couplings	$-0.40 \leq \Delta\kappa \leq 0.40$
WW and $WZ \to$	2000	2.0 TeV	$-0.16 \leq \lambda \leq 0.17$
$e\nu$jj		Equal Couplings	$-0.20 \leq \Delta\kappa \leq 0.28$
$WZ \to$ trileptons	2000	2.0 TeV	$-0.2 \leq \lambda_Z \leq 0.2$
			$-0.3 \leq \Delta g_1^Z \leq 0.3$
Combined	2000	2.0 TeV	$-0.086 \leq \lambda \leq 0.090$
(per experiment)		Equal Couplings	$-0.12 \leq \Delta\kappa \leq 0.19$

couplings weakens the limits obtained. For a dipole form factor with $\Lambda_{FF} = 2$ TeV, this is a 2% effect.

For anomalous $Z\gamma\gamma$ and $ZZ\gamma$ couplings we forecast limits which are very similar to those given in the Tev_2000 Report. Those predictions are based on 1 fb^{-1} integrated luminosity and $\Lambda_{FF} = 1500$ GeV and are listed in Table 10. The bounds obtained for h_{10}^V (h_{20}^V) almost coincide with those found for h_{30}^V (h_{40}^V). For comparison, the most recent 95% CL limits on h_i^V from LEP2 are:

$$-0.17 < h_1^\gamma < 0.08 \qquad -0.26 < h_1^Z < 0.09, \quad (20)$$

$$-0.11 < h_2^\gamma < 0.10 \qquad -0.11 < h_2^Z < 0.16, \quad (21)$$

$$-0.027 < h_3^\gamma < 0.041 \qquad -0.29 < h_3^Z < 0.21, \quad (22)$$

$$-0.026 < h_4^\gamma < 0.022 \qquad -0.12 < h_4^Z < 0.20. \quad (23)$$

Only one coupling at a time is varied here. Correcting for form factor effects, the limits for $h_{1,3}$ ($h_{2,4}$) weaken by about 5% (7%) for $\Lambda_{FF} = 1500$ GeV.

In Run II, the Tevatron will thus be able to improve the existing bounds on anomalous $Z\gamma V$ couplings mostly for $h_{2,4}^V$. If an integrated luminosity of 10 fb^{-1} can be achieved in Run II, the limits listed in Tables 9 and 10 would improve by approximately a factor 1.5.

A few additional comments are in order at this point:

4.5.1. $WW/WZ \to e\nu$jj

Note that the expected Run II anomalous coupling limit has nearly been ruled out by the Run I combined analysis measurement. Nevertheless, if the Run II combined measurement is to scale based on the increase in the luminosity, all of the analyses must be carried out again.

4.5.2. $Z\gamma \to ee\gamma$ and $\mu\mu\gamma$

Scaling the Run I yield, totalling 29 $ee\gamma + \mu\mu\gamma$ candidates at DØ, by the increase in luminosity, one expects about 600 $ee\gamma + \mu\mu\gamma$ events per experiment. The QCD background and final state radiation background will be reduced compared to Run I through the application of a di-lepton invariant mass criteria, reducing the samples to ~ 250 events. The Run II data will settle once and for all, whether there is a bump in the $Z\gamma$ invariant mass spectrum, as is not very strongly suggested by the Run I data. That is, unless a new one crops up.

4.5.3. $Z\gamma \to \nu\bar{\nu}\gamma$

This is a powerful tool for studying $Z\gamma\gamma$ and $ZZ\gamma$ couplings because of the large (20%) branching fraction for $Z \to \nu\bar{\nu}$. However, because the Z boson is undetectable, there aren't any other kinematic handles. There are common backgrounds which produce the same signature as the signal: a photon recoiling against missing transverse energy (neutrinos). In order to reduce the backgrounds, a higher E_T^γ cut is used than in the other $Z\gamma$ analyses (40 GeV instead of 7 – 10 GeV). Understanding the normalization of the background from cosmic ray muons that happened to deposit energy in the calorimeter in such a way as to mimic a photon was the main difficulty in this analysis in Run I. This background should be more tractable in Run II using the new central and forward preshower detectors and a technique similar to that described in DØ's Run Ia publications [139,144].

4.6. New Directions in Di-boson Production for Run II

Besides improving limits from final states analyzed in Run I, a number of new channels will become accessible in Run II, either due to the increased data sample, or because of detector improvements. In addition, it will be possible to search for the so-called "radiation zero" in $W\gamma$ production. In this subsection, we first briefly describe the search for the radiation zero and the prospects for using di-boson final states involving

Table 10
95% confidence level $Z\gamma V$ anomalous coupling limits that might be achieved by DØ or CDF experiments in Run II.

Analysis	Lum. (pb^{-1})	Λ_{FF}	A.C. Limit (95% CL)
$Z\gamma \to$	1000	1.5 TeV	$-0.105 \le h_{30}^{V} \le 0.105$
$ee\gamma$			$-0.0064 \le h_{40}^{V} \le 0.0064$
$Z\gamma \to$	1000	1.5 TeV	$-0.038 \le h_{30}^{V} \le 0.038$
$\nu\nu\gamma$			$-0.0027 \le h_{40}^{V} \le 0.0027$

b-quarks. This is followed by a somewhat more detailed analysis of ZZ production, the main new di-boson channel which will become accessible in Run II.

4.6.1. Radiation Zero in $W\gamma$ Production

$W\gamma$ production is of special interest because of the "radiation zero" in the helicity amplitudes [147]. The Tev_2000 Report describes the situation very eloquently and completely. The SM helicity amplitudes of the process $q_1\bar{q}_2 \to W^{\pm}\gamma$ vanish for

$$\cos\theta^* = \frac{Q_1 + Q_2}{Q_1 - Q_2} = \pm\frac{1}{3} \tag{24}$$

where θ^* is the scattering angle of the W boson with respect to the quark (q_1) direction in the $W\gamma$ rest frame and Q_1 and Q_2 are the quark and anti-quark electric charges normalized by the proton electric charge. Anomalous couplings destroy the radiation zero as do higher-order QCD corrections, backgrounds, finite W-width effects, and events where the photon is radiated from the charged lepton instead of the W.

The trick in reconstructing θ^* is in determining the parton center-of-mass frame because there are two solutions for the z-component of the neutrino momentum. CDF discussed [148] a possible solution in selecting the minimum of the $p_z(\nu)$ solutions for $W^-\gamma$ and the maximum of the $p_z(\nu)$ solutions for $W^+\gamma$. This is correct 73% of the time because of the high W polarization at Tevatron production energies. CDF saw a hint [148] of the radiation zero in Run Ib but the signal was not definitive.

The twofold ambiguity in reconstructing $\cos\theta^*$ can be avoided by studying rapidity correlations such as $\Delta y(\gamma,\ell) = y(\gamma) - y(\ell)$, which manifests the radiation zero at $\Delta y(\gamma,\ell) \approx -0.3$ [149].

The Tevatron is operating at the ideal energy for observing the radiation zero because the zero is not smeared out by NLO processes expected from $W\gamma$ production at higher energy accelerators. Fig. 56 shows the $\Delta y(\gamma,\ell)$ distribution, together with the statistical errors for 1 fb^{-1}. The radiation zero will be observed in Run II if it is there.

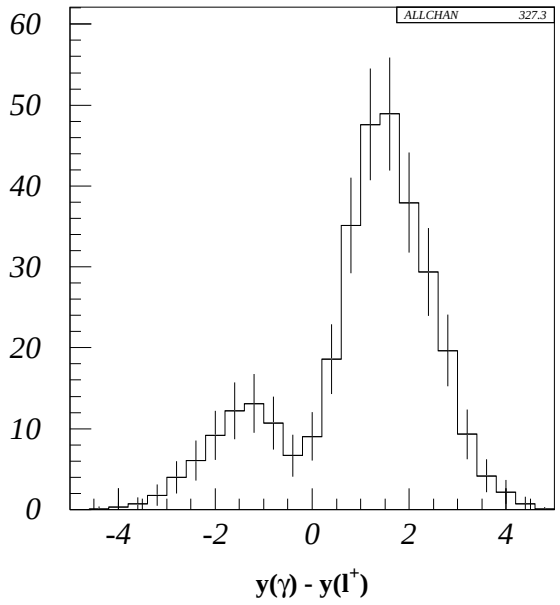

Figure 56. Simulation of the SM $\Delta y(\gamma, e)$ distribution in $p\bar{p} \to W^+\gamma \to e^+\not{p}_T\gamma$ in the DØ detector (from Ref. [77]). In addition to the standard $\not{p}_T$, electron and photon p_T and rapidity cuts, a $\Delta R(\gamma,\ell) > 0.7$ cut, and a cluster transverse mass cut of $m_T(\ell\gamma;\not{p}_T) > 90$ GeV are imposed (to reduce the $W \to e\nu\gamma$ background). The statistical error bars for an integrated luminosity of 1 fb^{-1} are also shown.

4.6.2. $WZ \to \ell\nu b\bar{b}$

This channel has not been studied in Run I. It will be examined very closely in Run II because it is a background in the search for associated Higgs boson production ($W + H^0$ where $W \to \ell\nu$ and $H^0 \to b\bar{b}$). The SM cross section for WZ production, including NLO QCD corrections, is about 3.7 pb. The branching fraction for $Z \to b\bar{b}$ is $\sim 15\%$. This is 2.5 times as much as that of $Z \to \mu\bar{\mu}$ and $Z \to e\bar{e}$ combined. So we can expect about 250 $e\nu b\bar{b} + \mu\nu b\bar{b}$ events per experiment, not counting acceptance, lepton ID, and b-tagging efficiencies, which can be expected to amount

to ~ 0.20 for such a final state. A cut on $b\bar{b}$ invariant mass will reduce the W+jets background.

This is ripe for an anomalous coupling analysis. To produce WWZ anomalous coupling limits, one can fit the E_T spectrum of the W boson and of the final-state lepton, such as was done in the Run I $WW/WZ \to \ell\nu$+jets analyses.

4.6.3. $Z\gamma \to b\bar{b}\gamma$

Scaling the Run I yield, totalling 29 $ee\gamma + \mu\mu\gamma$ candidates at DØ, by the increase in luminosity and a factor for the larger branching ratio of $Z \to b\bar{b}$ to $Z \to ee(\mu\mu)$, one might expect about 1000 $Z\gamma \to b\bar{b}\gamma$ events. Background from γjj and three jet events where a jet mimics a photon are larger than the signal and may constrain this to a limit-setting analysis (see also Sec. 3.3.5).

4.6.4. ZZ Production

For Run I, ZZ production has not been analyzed. The total cross section for $p\bar{p} \to ZZ$ at $\sqrt{s} = 2$ TeV, including NLO QCD corrections is approximately 1.5 pb. For an integrated luminosity of 2 fb^{-1} one thus expects a few $ZZ \to \ell_1^+\ell_1^-\ell_2^+\ell_2^-$ (ℓ_1, $\ell_2 = e$, μ) events, if realistic lepton p_T and pseudo-rapidity cuts are imposed. Larger event rates are expected for $ZZ \to \ell^+\ell^-\bar{\nu}\nu$, $ZZ \to \ell^+\ell^-$jj and $ZZ \to \bar{\nu}\nu$jj. These channels, however, suffer from non-trivial background contributions. In this subsection we briefly discuss the signals of anomalous ZZV couplings in the four channels, and derive sensitivity bounds on f_4^V and f_5^V which one expects to achieve with 2 fb^{-1} (Run IIa) and 10 fb^{-1} (Run IIb). More details will be given elsewhere [116].

The results reported here are based on a tree level calculation of ZZ production in the double pole approximation. Timelike photon exchange and the decays of the Z bosons, including full decay correlations and finite Z width effects, are taken into account in the calculation. To simulate detector response, we impose the following transverse momentum, pseudo-rapidity and separation cuts:

$$p_T(\ell) > 15 \text{ GeV}, \qquad |\eta(\ell)| < 2.5, \tag{25}$$

$$p_T(j) > 20 \text{ GeV}, \qquad |\eta(j)| < 2.5, \tag{26}$$

$$\Delta R(\ell j) > 0.6, \qquad \Delta R(jj) > 0.6. \tag{27}$$

In the $ZZ \to \bar{\nu}\nu$jj case, Eq. (25) is replaced by a charged lepton veto

$$p_T(\ell) < 10 \text{ GeV} \qquad \text{for} \qquad |\eta(\ell)| < 2.5. \tag{28}$$

In addition to the cuts imposed on the leptons and jets, we require

$$\not{p}_T > 20 \text{ GeV} \quad \text{for} \quad ZZ \to \ell^+\ell^-\not{p}_T, \tag{29}$$

$$\not{p}_T < 20 \text{ GeV} \quad \text{for} \quad ZZ \to \ell^+\ell^-\text{jj}, \tag{30}$$

$$\not{p}_T > 60 \text{ GeV} \quad \text{for} \quad ZZ \to \not{p}_T\text{jj} \tag{31}$$

and

$$76 \text{ GeV} < m(\ell\ell) < 106 \text{ GeV}, \tag{32}$$

$$76 \text{ GeV} < m(jj) < 106 \text{ GeV}. \tag{33}$$

Finally, in the $ZZ \to \ell^+\ell^-\bar{\nu}\nu$ case, we require that the angle in the transverse plane between a charged lepton and the missing transverse momentum is between 20° and 160° if the missing p_T is $\not{p}_T < 50$ GeV. This suppresses backgrounds from $b\bar{b}$ production and $Z \to \tau^+\tau^-$ decays to a negligible level.

Uncertainties in the energy measurements are taken into account in the numerical simulations by Gaussian smearing of the particle momenta according to the resolutions of the CDF II detector. For the form factor we use the form of Eq. (8) with $n = 3$ and $\Lambda_{FF} = 750$ GeV. We use the CTEQ4L parton distribution functions with $Q^2 = M_Z^2$. Unless stated otherwise, only one ZZV coupling at a time is chosen different from its zero SM value. For simplicity, we only consider real ZZV couplings.

$ZZ \to 4$ leptons

Similar to the WWV and $Z\gamma V$ couplings, the effects of anomalous ZZV couplings are enhanced at large energies. A typical signal of nonstandard ZZZ and $ZZ\gamma$ couplings thus will be a broad increase in the ZZ invariant mass distribution, the Z transverse momentum distribution and the p_T distribution of the Z decay leptons. This is illustrated in Fig. 57 for the $p_T(Z)$ and the $p_T(\mu)$ distributions in $p\bar{p} \to ZZ \to e^+e^-\mu^+\mu^-$. Results are shown for the SM, $f_{40}^Z = 0.3$ and $f_{50}^\gamma = -0.3$. Terms proportional to f_4^V and f_5^V in the matrix elements have identical high energy behavior. Differences in the differential cross sections at high energies between ZZZ and $ZZ\gamma$ couplings are thus controlled by the $Zf\bar{f}$ and $\gamma f\bar{f}$ couplings, and by the parton distribution functions. At the Tevatron these result in differential cross sections which differ by only a few percent for $\hat{s} \gg M_Z^2$ if $|f_i^Z| = |f_i^\gamma|$ ($i = 4, 5$). Slightly larger differences are observed at intermediate energies and transverse momenta. Since f_4^V violate CP conservation, terms in the helicity amplitudes proportional to those couplings do not interfere with the SM terms as long as f_4^V is real. Cross sections thus are independent of the sign of f_4^V.

To distinguish f_4^V and f_5^V, and to determine the sign of f_5^V, the $\Delta R(\ell_i^+\ell_i^-)$ and $\Delta\Phi(\ell_i^+\ell_i^-)$ ($i = 1, 2$) distributions may be helpful, if deviations from the SM predictions should be found in the p_T or the m_{ZZ} differential cross sections. Fig. 58 shows the $\Delta R(\mu^+\mu^-)$ and $\Delta\Phi(\mu^+\mu^-)$ distributions for $p\bar{p} \to ZZ \to e^+e^-\mu^+\mu^-$ in the SM and for non-standard ZZZ couplings. The shape of the distributions for non-zero f_4^V, $f_5^V > 0$ and

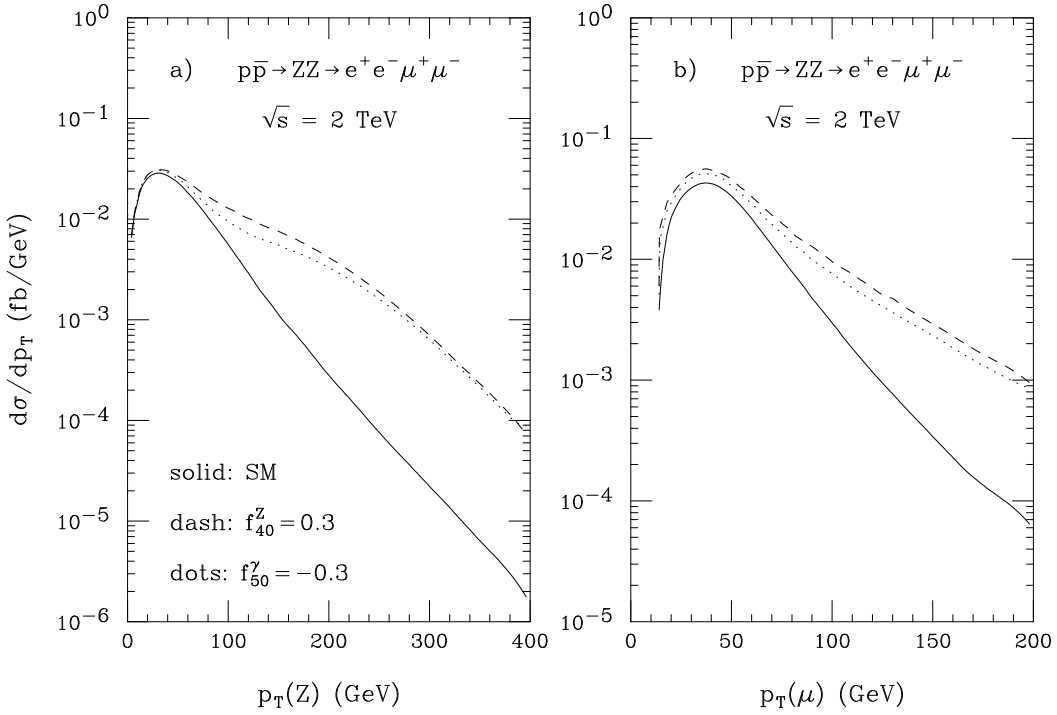

Figure 57. The $p_T(Z)$ and $p_T(\mu)$ distributions in $p\bar{p} \to ZZ \to e^+e^-\mu^+\mu^-$ in the SM and in the presence of non-standard ZZV couplings.

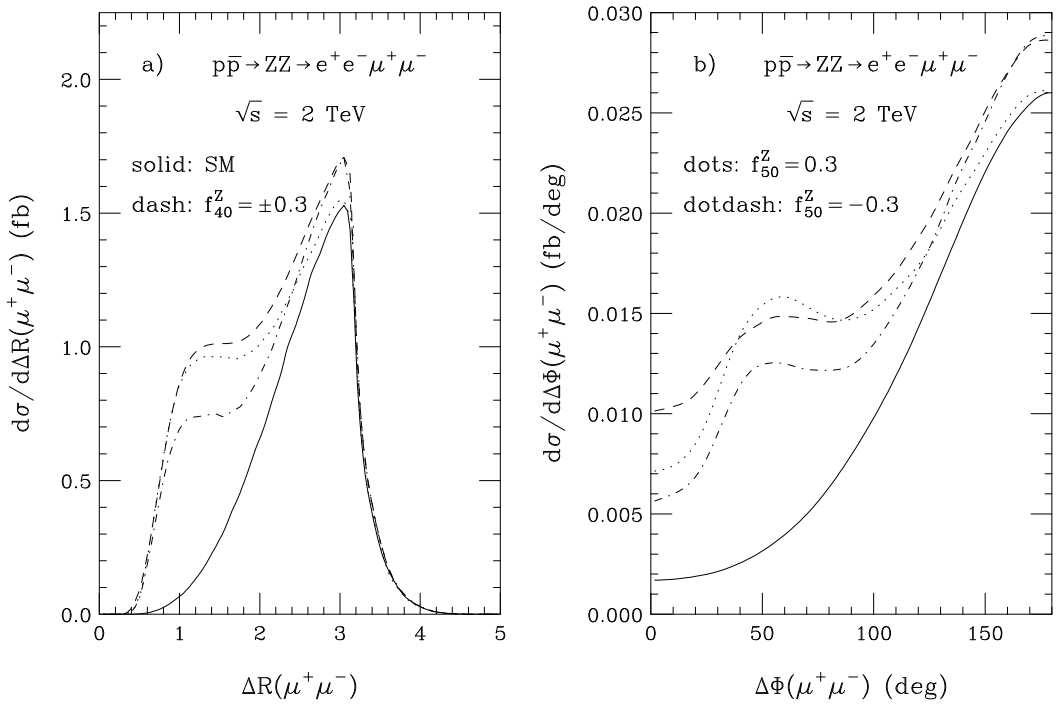

Figure 58. The $\Delta R(\mu^+\mu^-)$ and $\Delta\Phi(\mu^+\mu^-)$ distributions in $p\bar{p} \to ZZ \to e^+e^-\mu^+\mu^-$ in the SM and in the presence of non-standard ZZZ couplings.

$f_5^V < 0$ are quite different. Similar results are obtained for the corresponding distributions of the e^+e^- pair, and for the $ZZ\gamma$ couplings $f_{4,5}^\gamma$.

Anomalous couplings mostly affect the cross section at large Z-boson transverse momentum. Due to the Lorentz boost, the relative opening angle between the leptons originating from the Z decay decreases with increasing p_T. The deviations due to non-standard ZZV couplings in the $\Delta R(\ell_i^+\ell_i^-)$ and $\Delta\Phi(\ell_i^+\ell_i^-)$ distributions thus are therefore concentrated at rather small values. The SM $\Delta R(\ell_i^+\ell_i^-)$ and $\Delta\Phi(\ell_i^+\ell_i^-)$ differential cross sections are dominated by the threshold region, $\sqrt{\hat{s}} \approx 2m_Z$, where the Z boson momenta are small and the decay leptons tend to be back-to-back, *i.e.* the distributions are strongly peaked at $\Delta R \approx 3$ and $\Delta\Phi = 180°$.

Using the $\Delta R(\ell_i^+\ell_i^-)$ and $\Delta\Phi(\ell_i^+\ell_i^-)$ distributions, it may be possible to distinguish f_4^V and f_5^V and to determine the sign of f_5^V, provided a sufficient number of events are observed.

$ZZ \to \ell^+\ell^-\bar{\nu}\nu$

In contrast to the $ZZ \to 4$ leptons mode which is almost background free, there are several potentially important background processes if one of the two Z bosons decays into neutrinos. The advantage of the $ZZ \to \ell^+\ell^-\bar{\nu}\nu$ channel is its larger branching fraction. Summing over the three neutrino species, the number of $ZZ \to \ell^+\ell^-\bar{\nu}\nu$ signal events is about a factor 6 larger than the number of $ZZ \to 4$ leptons events.

The most important background processes contributing to the $ZZ \to \ell^+\ell^-\bar{\nu}\nu$ channel are $t\bar{t} \to W^+W^-b\bar{b}$, standard electroweak $W^+W^- + X$ production with $W^+W^- \to \ell^+\nu\ell^-\bar{\nu}$, and $Z(\to \ell^+\ell^-) + 1$ jet production with the jet rapidity outside the range covered by the detector and thus faking missing p_T. Our results for signal and backgrounds are summarized in Fig. 59 for the $ZZ \to e^+e^-\bar{\nu}\nu$ case.

The two most important backgrounds are $t\bar{t}$ and $W^+W^- + X$ production. If no additional cuts are imposed to suppress the $t\bar{t}$ background, its differential cross section is larger than the SM signal for e^+e^- transverse momenta as large as 200 GeV, and may thus reduce the sensitivity to anomalous ZZV couplings (see Fig. 59a). Requiring that no jets with $p_T(j) > 20$ GeV and $|\eta(j)| < 3.5$ are present almost completely eliminates the $t\bar{t}$ background. It also reduces the $W^+W^- + X$ background at large transverse momenta. As shown in Fig. 55, NLO QCD corrections strongly affect the $p_T(e^+e^-)$ distribution in $W^+W^- \to e^+\nu e^-\bar{\nu}$. The enhancement at large p_T is mostly due to real emission diagrams, leading to events which contain a hard jet.

To calculate the $Z + 1$ jet background, we have assumed that jets with a rapidity $|\eta(j)| > 3.5$ are misidentified as $\not{p}_T$. With this rather conservative assumption, the $Z+1$ jet background is much larger than the ZZ signal at small transverse momenta. Due to kinematical constraints, however, it drops rapidly with p_T. Since non-standard ZZV couplings lead to large deviations from the SM only at high transverse momentum, essentially no sensitivity is lost by requiring $p_T(\ell^+\ell^-) > 40$ GeV when testing for ZZV couplings.

$ZZ \to \ell^+\ell^- jj$ and $ZZ \to \bar{\nu}\nu jj$

The $ZZ \to \ell^+\ell^-$jj and $ZZ \to \bar{\nu}\nu$jj channels have larger branching ratios than the $ZZ \to 4$ leptons and the $ZZ \to \ell^+\ell^-\bar{\nu}\nu$ channels, but also much higher backgrounds. The main background sources are QCD $Z + 2$ jet production and $W^\pm Z$ production with the W decaying into two jets. The $p_T(\ell^+\ell^-)$ distribution for $ZZ \to \ell^+\ell^-$jj is shown in Fig. 60a. Fig. 60b shows the p_T(jj) distribution for $ZZ \to \bar{\nu}\nu$jj. In each case we display the SM cross section together with the two main backgrounds, Zjj and $W^\pm Z$ production. We also show the ZZ cross section for $f_{40}^Z = 0.3$.

The $\not{p}_T > 60$ GeV cut imposed in the $ZZ \to \not{p}_T$jj case helps to suppress the $b\bar{b}$ and $Z \to \tau^+\tau^-$ backgrounds. The "kink" in the WZ and ZZ differential cross sections at $p_T \approx 250$ GeV is due to the $\Delta R(jj) > 0.6$ cut which becomes effective only at sufficiently high transverse momenta. The $W^\pm Z$ differential cross section is very similar to that of the SM signal over most of the p_T range considered. The $\not{p}_T < 20$ GeV cut imposed in the $ZZ \to \ell^+\ell^-$jj channel effectively eliminates the $t\bar{t} \to \ell^+\nu\ell^-\bar{\nu}$jj background. The charged lepton veto (see Eq. (28)) required in the $ZZ \to \not{p}_T$jj case rejects backgrounds from $t\bar{t}$ production, $W \to \ell\nu$, and $Z \to \ell^+\ell^-$ decays. The Zjj background is uniformly about a factor 10 larger than the SM ZZ signal. It will therefore be very difficult to observe ZZ production in the semi-hadronic channels, if the SM prediction is correct. However, for sufficiently large anomalous ZZV couplings, the ZZ cross section exceeds the background at large transverse momenta. $ZZ \to \ell^+\ell^-$jj and $ZZ \to \bar{\nu}\nu$jj therefore may still be useful in obtaining limits on the ZZV couplings, similar to the semi-hadronic WW and WZ channels used by CDF and DØ in Run I to extract limits on the WWV couplings.

Sensitivity Bounds

In order to derive sensitivity limits for anomalous ZZV couplings which one can hope to achieve in Run II, we use the $p_T(\ell^+\ell^-)$ distribution for $ZZ \to$

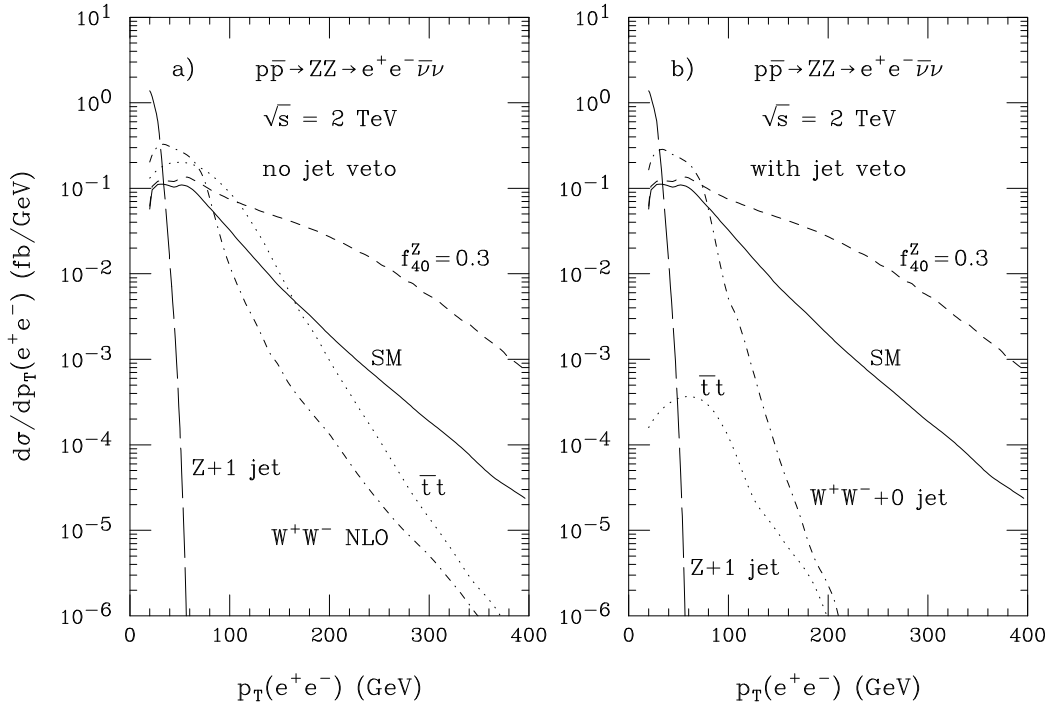

Figure 59. Transverse momentum distribution of the e^+e^- pair in $p\bar{p} \to ZZ \to e^+e^-\bar{\nu}\nu$ at the Tevatron, together with the differential cross sections from several background processes a) without and b) with a jet veto applied.

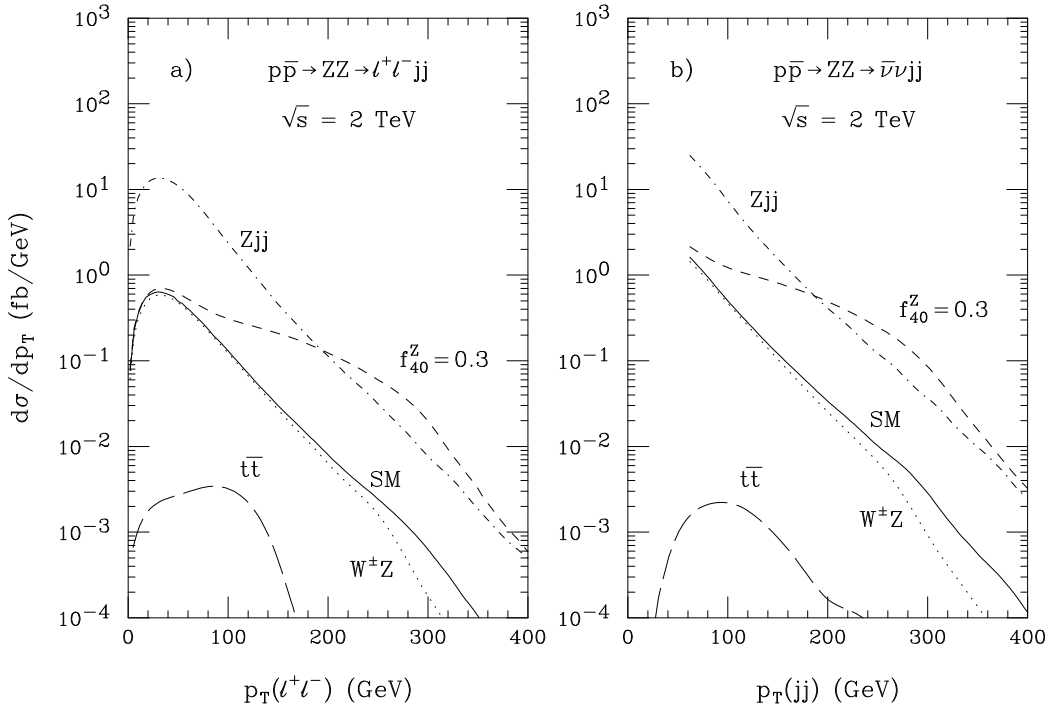

Figure 60. Transverse momentum distribution of a) the $\ell^+\ell^-$ pair in $p\bar{p} \to ZZ \to \ell^+\ell^- jj$, and b) of the jet pair in $ZZ \to \bar{\nu}\nu jj$ at the Tevatron, together with the differential cross sections from $t\bar{t}$, $W^{\pm}Z$ and $Z + 2$ jet production.

Table 11
Sensitivities achievable at 95% CL for the anomalous ZZV couplings in $p\bar{p} \to ZZ \to 4$ leptons, $p\bar{p} \to ZZ \to \ell^+\ell^-\bar{\nu}\nu$, $p\bar{p} \to ZZ \to \ell^+\ell^-$jj, and $p\bar{p} \to ZZ \to \bar{\nu}\nu$jj at the Tevatron a) for an integrated luminosity of 2 fb^{-1}, and b) for an integrated luminosity of 10 fb^{-1}.

a) $\int \mathcal{L}dt = 2$ fb^{-1}

coupling	$ZZ \to 4$ leptons	$ZZ \to \ell^+\ell^-\bar{\nu}\nu$	$ZZ \to \ell^+\ell^-$jj	$ZZ \to \bar{\nu}\nu$jj
f_{40}^Z	–	$+0.169$ -0.169	$+0.219$ -0.218	$+0.156$ -0.155
f_{40}^γ	–	$+0.175$ -0.174	$+0.222$ -0.221	$+0.157$ -0.157
f_{50}^Z	–	$+0.171$ -0.204	$+0.220$ -0.244	$+0.157$ -0.179
f_{50}^γ	–	$+0.184$ -0.202	$+0.229$ -0.241	$+0.166$ -0.174

b) $\int \mathcal{L}dt = 10$ fb^{-1}

coupling	$ZZ \to 4$ leptons	$ZZ \to \ell^+\ell^-\bar{\nu}\nu$	$ZZ \to \ell^+\ell^-$jj	$ZZ \to \bar{\nu}\nu$jj
f_{40}^Z	$+0.180$ -0.179	$+0.097$ -0.097	$+0.146$ -0.145	$+0.104$ -0.103
f_{40}^γ	$+0.185$ -0.185	$+0.100$ -0.099	$+0.148$ -0.147	$+0.104$ -0.104
f_{50}^Z	$+0.178$ -0.216	$+0.092$ -0.120	$+0.144$ -0.167	$+0.102$ -0.124
f_{50}^γ	$+0.192$ -0.213	$+0.103$ -0.115	$+0.151$ -0.163	$+0.109$ -0.118

4 leptons, $ZZ \to \ell^+\ell^-\bar{\nu}\nu$ and $ZZ \to \ell^+\ell^-$jj. For the $ZZ \to \bar{\nu}\nu$jj channel we use the p_T(jj) distribution. Other distributions, such as the ZZ invariant mass distribution (useful only for $ZZ \to 4$ leptons), or the maximum or minimum transverse momenta of the charged leptons or jets, yield similar results. In deriving our sensitivity limits, we combine channels with electrons and muons in the final state.

We calculate 95% confidence level (CL) limits performing a χ^2 test. The statistical significance is calculated by splitting the p_T distribution into a number of bins, each with more than five events typically. In each bin the Poisson statistics is approximated by a Gaussian distribution. In order to derive realistic limits, we allow for a normalization uncertainty of 30% of the SM cross section. Backgrounds in the $ZZ \to \ell^+\ell^-\bar{\nu}\nu$, $ZZ \to \ell^+\ell^-$jj and $ZZ \to \bar{\nu}\nu$jj channels are included in our calculation. In the $ZZ \to \ell^+\ell^-\bar{\nu}\nu$ case we assume that a jet veto has been imposed to reduce the $t\bar{t}$ background and require $p_T(\ell^+\ell^-) > 40$ GeV to eliminate the $Z + 1$ jet background. As before, we use a form factor of the form of Eq. (8) with $n = 3$ and $\Lambda_{FF} = 750$ GeV. Non-negligible interference effects are found between f_4^Z and f_4^γ, and between f_5^Z and f_5^γ. As a result, different anomalous contributions to the helicity amplitudes may cancel partially, resulting in weaker bounds than if only one coupling at a time is allowed to deviate from its SM value.

In Table 11 we display sensitivity limits for the Tevatron and integrated luminosities of 2 fb^{-1} and 10 fb^{-1}, taking into account the correlations between f_4^Z and f_4^γ, and between f_5^Z and f_5^γ. No limits for the $ZZ \to 4$ leptons case with 2 fb^{-1} are given. The limited number of events in this case does not allow for an analysis of the $p_T(\ell^+\ell^-)$ distribution using the method chosen here. The bounds obtained from $ZZ \to \ell^+\ell^-\bar{\nu}\nu$ and $ZZ \to \bar{\nu}\nu$jj are quite similar. The cross section for $ZZ \to \bar{\nu}\nu$jj is about a factor 10 larger than that for $ZZ \to \ell^+\ell^-\bar{\nu}\nu$, however, the large background from Zjj production considerably limits the sensitivity to ZZV couplings for $ZZ \to \bar{\nu}\nu$jj. The limits from the $ZZ \to \ell^+\ell^-$jj and $ZZ \to 4$ leptons channels are about a factor 1.5 and 2 weaker than those from $ZZ \to \ell^+\ell^-\bar{\nu}\nu$ and $ZZ \to \bar{\nu}\nu$jj.

We have not made any attempt to combine the limits from different channels. From Table 11 it is clear that

this would result in a significant improvement of the bounds.

The sensitivity limits which can be achieved at the Tevatron in Run II should be compared with the bounds from recent measurements at LEP2 [146]:

$$|f_4^Z| < 0.49 \qquad |f_4^\gamma| < 0.82 \tag{34}$$

$$|f_5^Z| < 1.1 \qquad |f_5^\gamma| < 1.1 \tag{35}$$

Only one coupling at a time is varied here. (The LEP2 limits do not contain any form factor effects. For the form and scale chosen here, form factor effects weaken the limits by about 20%.) In Run II, CDF and DØ will be able to improve these bounds by at least a factor 4 to 8.

4.6.5. Measuring Form Factors

The limits on anomalous WWV, $Z\gamma V$ and ZZV couplings all depend on the power, n, and the scale, Λ_{FF}, of the form factor. These parameters are *a priori* unknown. In Ref. [117] it was pointed out that in final states without missing transverse momentum one can in principle determine the form factor by measuring the $\sqrt{\hat{s}}$ distribution. For $W\gamma$ production, the longitudinal momentum of the neutrino can only be reconstructed with a twofold ambiguity. Selecting the minimum of the two reconstructed values of $\hat{s}$, a similar measurement can be performed in the $W\gamma$ case [125]. Alternatively, the photon p_T distribution can be used.

In Ref. [127] a detailed study of the method was performed for $W(\to e\nu, \mu\nu)\gamma$ production at the LHC. Assuming $\lambda_0^\gamma = 0.025$, $n = 2$, $\Lambda_{FF} = 2$ TeV and an integrated luminosity of 300 fb^{-1}, λ_0^γ and Λ_{FF} were reconstructed using a binned maximum likelihood fit to the $p_T(\gamma)$ distribution. The power of the form factor, $n = 2$, was not varied and no detector simulation was included in the study. The reconstructed coupling and form factor scale were determined to $\lambda_0^\gamma = 0.0295 \pm 0.0022$ and $\Lambda_{FF} = 1.67 \pm 0.22$ TeV, *ie.* they can be measured with a relative precision of about 10 – 15%. The central values of the reconstructed parameters differ by about 20% from the input parameters. Including detector response, and treating the form factor power n as an additional free parameter is expected to increase the relative error.

The study demonstrates that, due to the restricted number of events in each bin, the method will not produce competitive limits. However, if non-zero anomalous couplings are observed, the method may be useful in determining the shape of the form factor which provides indirect information on the dynamics of the underlying new physics.

At the Tevatron, the limits on the WWV couplings exhibit only a modest dependence on n and Λ_{FF}. Direct measurement of the form factor will thus be very difficult for these couplings. The situation is more promising for $Z\gamma V$ and ZZV couplings, where the sensitivity bounds depend more strongly on the form factor parameters.

Acknowledgements

We acknowledge contributions from the other members of the working group including P. Aurenche, C. Balázs, L. Dixon, S. Eno, G. Gomez, N. Kidonakis, P. Nason, J. Qiu, and G. Sterman. We also thank T. Ferbel, M. Fontannaz, G. Ginther, B. Kniehl, A. D. Martin, R. Roberts, P. Slattery, J. Stirling, R. Thorne and W.K. Tung. We also wish to thank A. Beretvas, C. Bigongiari, J. Campbell, O. Lobban, and W. Wester for their help. Special thanks go to M. Mangano for some enlightening discussions.

REFERENCES

1. R. Brock *et al.*, Report of the *Precision Measurement* Working Group.
2. L. deBarbaro *et al.*, Report of the Working Group on *Parton Distribution Functions*.
3. F. Abe *et al.* (CDF Collaboration), Phys. Rev. **D60**, 092003 (1999).
4. B. Bailey, E L. Berger, and L. E. Gordon, Phys.Rev. **D54**, 1896 (1996).
5. P. Aurenche *et al.*, Phys. Lett. **B140**, 87 (1984).
6. E.L. Berger, E. Braaten, and R.D. Field, Nucl. Phys. **B239**, 52 (1984).
7. E.L. Berger and J.W. Qiu, Phys. Rev. **D44**,2002 (1991).
8. B. Bailey, J. F. Owens, and J. Ohnemus, Phys. Rev. **D46**, 2018 (1992).
9. T. Binoth *et al.*, Eur. Phys. J. **C16**, 311 (2000).
10. C. Balázs, E.L. Berger, S. Mrenna, and C.-P. Yuan, Phys. Rev. **D57**, 6934 (1998).
11. P. Chiappetta, R. Fergani, and J. Guillet, Phys. Lett. **B348**, 646 (1995).
12. S. Catani *et al.*, JHEP **9903**, 025 (1999).
13. N. Kidonakis and J. F. Owens, Phys. Rev. **D61**, 094004 (2000).
14. E. Laenen, G. Oderda, and G. Sterman, Phys. Lett. **B438**, 173 (1998).
15. H.-L. Lai and H. nan Li, Phys. Rev. **D58**, 114020 (1998).
16. H. nan Li, Phys. Lett. **B454**, 328 (1999).
17. E. Laenen, G. Sterman, and W. Vogelsang, Phys. Rev. Lett. **84**, 4296 (2000).
18. J. Huston *et al.* (CTEQ Collaboration), Phys. Rev. **D58**, 114034 (1998).
19. H. L. Lai *et al.* (CTEQ Collaboration), Phys. Rev. **D55**, 1280 (1997).

20. M. Glück, E. Reya, and A. Vogt, Z. Phys. **C53**, 127 (1992).
21. A. D. Martin *et al.*, Eur. Phys. J. **C4**, 463 (1998).
22. H. Baer and M. Reno, Phys. Rev. **D54**, 2017 (1996).
23. J. Huston *et al.* (CTEQ Collaboration), Phys. Rev. **D51**, 6139 (1995).
24. L. Apanasevich *et al.*, Phys. Rev. **D59**, 074007 (1999).
25. P. Aurenche *et al.*, Eur. Phys. J. **C9**, 107 (1999).
26. P. Aurenche *et al.*, Eur. Phys. J. **C13**, 347 (2000).
27. M.A. Kimber, A.D. Martin, and M.G. Ryskin, Eur. Phys. J. **C12**, 655 (2000).
28. C. Balázs, J. Huston, and I. Puljak, hep-ph/0002032 (February 2000), submitted to Phys. Rev. **D**.
29. C. Balázs, Ph.D. thesis, Michigan State University, 1999.
30. S. Catani *et al.*, hep-ph/0005114 (May 2000), to appear in the Proceedings of the *Workshop on Physics at TeV Colliders* (Les Houches, 1999).
31. M. Begel, Nucl. Phys. B (Proc. Supp.) **79**, 244 (1999); Ph.D. thesis, University of Rochester, 1999.
32. E. Bonvin *et al.* (WA70 Collaboration), Phys. Lett. **B236**, 523 (1990).
33. F. Abe *et al.* (CDF Collaboration), Phys. Rev. Lett. **70**, 2232 (1993).
34. R. Barate *et al.* (WA11 Collaboration), Phys. Rev. Lett. **21**, 1541 (1979); M. J. Corden *et al.* (WA12 Collaboration), Phys. Lett. **B76**, 226 (1978); A. L. S. Angelis *et al.* (R108 Collaboration), Phys. Lett. **B97**, 163 (1980); D. Antreasyan *et al.* (R209 Collaboration), Phys. Rev. Lett. **47**, 12 (1981); J. Badier *et al.* (NA3 Collaboration), Phys. Lett. **B117**, 372 (1982); A. S. Ito *et al.* (E288 Collaboration), Phys Rev. **D23**, 604 (1981); D. Antreasyan *et al.* (E300 Collaboration), Phys. Rev. Lett. **39**, 906 (1977); M. D. Corcoran *et al.* (E395 Collaboration), Phys. Rev. **D21**, 641 (1980); K. J. Anderson *et al.* (E444 Collaboration), Phys. Rev. Lett. **42**, 944 (1979); E. Anassontzis *et al.* (E537 Collaboration), Phys. Rev. **D38**, 1377 (1988); G. Moreno *et al.* (E605 Collaboration), Phys. Rev. **D43**, 2815 (1991); S. Palestini *et al.* (E615 Collaboration), Phys. Rev. Lett. **55**, 2649 (1985); J. S. Conway *et al.*, Phys. Rev. **D39**, 92 (1989); J. Alspector *et al.* (E687 Collaboration), Phys. Lett. **B81**, 397 (1979).
35. A. L. S. Angelis *et al.* (R108 Collaboration), Phys. Lett. **B97**, 163 (1980); A. G. Clark *et al.* (R702 Collaboration), Nucl. Phys. **B160**, 397 (1979).
36. W. Chen, Ph.D. thesis, State University of New York at Stony Brook, 1997.
37. H.-U. Bengtsson and T. Sjostrand, Comput. Phys. Commun. **46**, 43 (1987), [`Pythia` v5.7].
38. J. F. Owens, Rev. Mod. Phys. **59**, 465 (1987).
39. A. P. Contogouris, S. Papadopoulos, and C. Papavassiliou, Nucl. Phys. **B179**, 461 (1981).
40. A. P. Contogouris *et al.*, Phys. Rev. **D32**, 1134 (1985).
41. M. Fontannaz and D. Schiff, Nucl. Phys. **B132**, 457 (1978).
42. R. P. Feynman, R. D. Field, and G. C. Fox, Phys. Rev. **D18**, 3320 (1978).
43. J. Collins and D. Soper, Nucl. Phys. **B193**, 381 (1981); **B213**, 545(E) (1983); **B197**, 446 (1982); J. Collins, D. Soper, G. Sterman, Phys. Lett. **B109**, 388 (1982).
44. J.C. Collins, D.E. Soper, and G. Sterman, Nucl. Phys. **B250**, 199 (1985).
45. L. Apanasevich *et al.* (E706 Collaboration), Phys. Rev. Lett. **81**, 2642 (1998).
46. M. Bonesini *et al.* (WA70 Collaboration), Z. Phys. **C37**, 535 (1988).
47. M. Bonesini *et al.* (WA70 Collaboration), Z. Phys. **C38**, 371 (1988).
48. G. Ballocchi *et al.* (UA6 Collaboration), Phys. Lett. **B436**, 222 (1998).
49. E. Bonvin *et al.* (WA70 Collaboration), Z. Phys. **C41**, 591 (1989).
50. L. Apanasevich, Ph.D. thesis, Michigan State University, 2000.
51. M. Bonesini *et al.* (WA70 Collaboration), Z. Phys. **C37**, 39 (1987).
52. J. Antille *et al.* (UA6 Collaboration), Phys. Lett. **B194**, 568 (1987).
53. E. Anassontzis *et al.* (R806 Collaboration), Z. Phys. **C13**, 277 (1982).
54. C. Kourkoumelis *et al.* (R806 Collaboration), Z. Phys. **C5**, 95 (1980).
55. M. Diakonou *et al.* (R806 Collaboration), Phys. Lett. **B91**, 296 (1980).
56. S. Kuhlmann, Nucl. Phys. B (Proc. Suppl.) **79**, 241 (1999).
57. B. Abbott *et al.* (DØ Collaboration), Phys. Rev. Lett. **84**, 2786 (2000).
58. R. Ansari *et al.* (UA2 Collaboration), Z. Phys. **C41**, 395 (1988).
59. J. Alitti *et al.* (UA2 Collaboration), Phys. Lett. **B288**, 386 (1992).
60. S. Abachi *et al* (DØ Collaboration), FERMILAB-PUB-96-357-E.
61. V. Zutshi, DØ note in preparation.
62. Y. Gershtein, DØ note in preparation.
63. H. L. Lai *et al.* (CTEQ Collaboration), Phys. Rev. **D51**, 4763 (1995).
64. H. L. Lai *et al.* (CTEQ Collaboration), Eur. Phys.

J. **C12**, 375 (2000).
65. G. Sterman and W. Vogelsang, hep-ph/0002132 (February 2000).
66. S. Catani, M.L. Mangano, and P. Nason, hep-ph/9806484, JHEP **9807**, 024 (1998).
67. Yu.L. Dokshitzer, D.I. Dyakanov, and S.I. Troyan, Phys. Rep. **58**, 269 (1980).
68. R.K. Ellis and S. Veseli, hep-ph/9706526, Nucl. Phys. **B511**, 649 (1998).
69. W. Vogelsang and A. Vogt, hep-ph/9505404, Nucl. Phys. **B453**, 334 (1995).
70. H. Baer, J. Ohnemus, and J.F. Owens, Phys. Rev. **D42**, 61 (1990).
71. F. Abe *et al.* (CDF Collaboration), Phys. Rev. Lett. **77**, 439 (1996); a paper on the Run Ib analysis is in preparation.
72. B. Abbott *et al.* (DØ Collaboration), Phys. Rev. Lett. **82**, 2451 (1999).
73. F. Abe *et al.* (CDF Collaboration), Phys. Rev. **D57**, 1359 (1998).
74. E. L. Berger, Xiao-feng Guo, and Jian-wei Qiu, hep-ph/9512281, Phys.Rev.Lett. **76**, 2234 (1996); hep-ph/9605324, Phys. Rev. **D54**, 5470 (1996).
75. P. Aurenche *et al.*, hep-ph/9606287, Phys. Rev. **D55** 1124 (1997).
76. S. Frixione, hep-ph/9801442, Phys. Lett. **B429**, 369 (1998).
77. D. Amidei *et al.*, *Future Electro-Weak Physics at the Fermilab Tevatron*, edited by D. Amidei and R. Brock, FERMILAB-Pub-96/082 (1996).
78. B. Abbott *et al.* (DØ Collaboration), Phys. Rev. **D61**, 072001 (2000).
79. D. Cronin-Hennessy, A. Beretvas, P.F. Derwent, Nucl. Instrum. Meth. **A443**, 37 (2000).
80. F. Abe *et al.* (CDF Collaboration), Phys. Rev. **D50**, 5550 (1994).
81. C. Avila *et al.* (E811 Collaboration), Phys. Lett. **B445**, 419 (1999).
82. N. Amos *et al.* (E710 Collaboration), Phys. Rev. Lett. **68**, 2433 (1992).
83. M. Albrow, A. Beretvas, L. Nodulman, and P. Giromini, CDF-PUB-4844 (1999).
84. J. Bantly, J. Krane, D. Owen, R. Partridge, and L. Paterno, Fermilab-TM-1995 (1997).
85. R. Hamberg, W.L. van Neerven, and T. Matsuura, Nucl. Phys. **B359**, 343 (1991); W.L. van Neerven and E.B. Zijlstra, Nucl. Phys. **B382**, 11 (1992).
86. For a review of resummation in transverse momentum space, see R.K. Ellis and S. Veseli, Nucl. Phys. **B511**, 649 (1998).
87. For a review of resummation in the Fourier conjugate impact parameter space, see C. Balàzs and C.-P. Yuan, Phys. Rev. **D56**, 5558 (1997).
88. B. Abbott *et al.* (DØ Collaboration), Phys. Rev. **D58**, 092003 (1998).
89. F. Abe *et al.* (CDF Collaboration), Phys. Rev. **D52**, 4784 (1995).
90. C. Balázs and C.-P. Yuan, Phys. Rev. **D59**, 114007 (1999).
91. Q. Fan and A. Bodek, Proceedings, 6^{th} *International Conference on Calorimetry in High Energy Physics* (ICCHEP 96), Rome, Italy, 8 – 14 June 1996, pp. 553 – 560.
92. T. Sjöstrand, Comput. Phys. Commun. **82**, 74 (1994).
93. E. Barberio and Z. Was, Comput. Phys. Commun. **79**, 291 (1994); E. Barberio, B. van Eijk, and Z. Was, *ibid.* **66**, 115 (1991).
94. T. Affolder *et al.*(CDF Collaboration), Phys. Rev. Lett. **84**, 845 (2000).
95. G.A. Ladinsky and C.-P. Yuan, Phys. Rev. **D50**, 4239 (1994).
96. B. Abbott *et al.* (DØ Collaboration), Phys. Rev. **D61**, 032004 (2000).
97. U. Baur, S. Keller, and W. K. Sakumoto, Phys. Rev. **D57**, 199 (1998).
98. F. Abe *et al.* (CDF Collaboration), Phys. Rev. **D59**, 052002 (1999).
99. A. Bodek *et al.* for the CDF Collaboration, *Constraints on PDF's from W and Z Rapidity Distributions at CDF*, Fermilab-Conf-99/160-E, to be published in Proceedings, 7^{th} International Conference on Deep Inelastic Scattering and QCD (DIS 99), DESY, Zeuthen, Germany, 19 – 24 April 1999.
100. G. Arnison *et al.* (UA1 Collaboration), Phys. Lett. **B122**, 103 (1983).
101. G. Arnison *et al.* (UA1 Collaboration), Phys. Lett. **B126**, 398 (1983).
102. G. Banner *et al.* (UA1 Collaboration), Phys. Lett. **B122**, 476 (1983).
103. P. Bagnaia *et al.* (UA1 Collaboration), Phys. Lett. **B129**, 130 (1983).
104. J. Alitti *et al.* (UA2 Collaboration), Phys. Lett. **B186**, 452 (1987).
105. J. Alitti *et al.* (UA2 Collaboration), Z. Phys. **C49**, 17 (1991).
106. M. Carena *et al.*, *Report of the Higgs Working Group*, Fermilab Supersymmetry/Higgs Run II Workshop (1998).
107. U. Baur and E.L. Berger, Phys. Rev. **D47**, 4889 (1993).
108. E. Mirkes, Nucl. Phys. **B387**, 3 (1992).
109. J.C. Collins and D.E. Soper, Phys. Rev. **D16**, 2219 (1977).
110. M.I. Martin, *Measurement of the Angular Distribution of the Electron from* $W \to e\nu$ *decay in* $p\overline{p}$ *at* $\sqrt{s}$*= 1.8 TeV as Function of* p_T^W, PhD thesis, Uni-

versidad de Zaragoza, Spain, 1994 (unpublished).
111. G. Steinbrück, *Measurement of the Angular Distribution of Electrons from W Boson Decays at DØ* , PhD thesis, University of Oklahoma, Norman, Oklahoma, 1999 (unpublished).
112. K. Hagiwara, R. D. Peccei, D. Zeppenfeld and K. Hikasa, Nucl. Phys. **B282**, 253 (1987).
113. U. Baur and D. Zeppenfeld, Nucl. Phys. **B308**, 127 (1988).
114. G. Gounaris *et al.*, in *Physics at LEP2*, edited by G. Altarelli, T. Sjöstrand and F. Zwirner, CERN 96-01, 525 (1996).
115. K. Hagiwara, S. Ishihara, R. Szalapski and D. Zeppenfeld, Phys. Rev. **D48**, 2182 (1993).
116. U. Baur and D. Rainwater, FERMILAB-Pub-00/153-T, to appear in Phys. Rev. D.
117. G.J. Gounaris, J.Layssac and F.M. Renard, Phys. Rev. **D61**, 073013 (2000).
118. B. Mele, P. Nason and G. Ridolfi, Nucl. Phys. **B357**, 409 (1991); S. Frixione, P. Nason and G. Ridolfi, Nucl. Phys. **B383**, 3 (1992); S. Frixione, Nucl. Phys. **B410**, 280 (1993).
119. U. Baur, T. Han, and J. Ohnemus, Phys. Rev. **D48**, 5140 (1993).
120. U. Baur, T. Han, and J. Ohnemus, Phys. Rev. **D57**, 2823 (1998).
121. U. Baur, T. Han, and J. Ohnemus, Phys. Rev. **D53**, 1098 (1996).
122. U. Baur, T. Han, and J. Ohnemus, Phys. Rev. **D51**, 3381 (1995).
123. J.M. Campbell and R.K. Ellis, Phys. Rev. **D60**, 113006 (1999).
124. L. Dixon, Z. Kunszt and A. Signer, Phys. Rev. **D60**, 114037 (1999).
125. D. DeFlorian and A. Signer, Eur. Phys. J. **C16**, 105 (2000).
126. H.L. Lai *et al* (CTEQ Collaboration), Phys. Rev. **D55**, 1280 (1997).
127. S. Haywood *et al.*, Report of the Electroweak Physics Working Group, hep-ph/0003275 (March 2000), to appear in the CERN Yellow-Report of the *1999 CERN Workshop on Standard Model Physics (and more) at the LHC*.
128. M. Dobbs, private communication.
129. F. Abe *et al.* (CDF Collaboration), Phys. Rev. Lett. **74**, 1936 (1995).
130. S. Abachi *et al.* (DØ Collaboration), Phys. Rev. Lett. **75**, 1034 (1995).
131. S. Abachi *et al.* (DØ Collaboration), Phys. Rev. Lett. **78**, 3634 (1997).
132. S. Abachi *et al.* (DØ Collaboration), Phys. Rev. Lett. **75**, 1023 (1995).
133. F. Abe *et al.* (CDF Collaboration), Phys. Rev. Lett. **78**, 4537 (1997).
134. B. Abbott *et al.* (DØ Collaboration), Phys. Rev. **D58**, 051101 (1998).
135. F. Abe *et al.* (CDF Collaboration), Phys. Rev. Lett. **75**, 1017 (1995).
136. S. Abachi *et al.* (DØ Collaboration), Phys. Rev. Lett. **77**, 3303 (1996).
137. B. Abbott *et al.* (DØ Collaboration), Phys. Rev. Lett. **79**, 1441 (1997).
138. B. Abbott *et al.* (DØ Collaboration), Phys. Rev. **D60**, 072002 (1999).
139. S. Abachi *et al.* (DØ Collaboration), Phys. Rev. **D56**, 6742 (1997).
140. B. Abbott *et al.* (DØ Collaboration), Phys. Rev. **D58**, 031102 (1998).
141. F. Abe *et al.* (CDF Collaboration), Phys. Rev. Lett. **74**, 1941 (1995).
142. S. Abachi *et al.* (DØ Collaboration), Phys. Rev. Lett. **75**, 1028 (1995).
143. B. Abbott *et al.* (DØ Collaboration), Phys. Rev. **D57**, 3817 (1998).
144. S. Abachi *et al.* (DØ Collaboration), Phys. Rev. Lett. **78**, 3640 (1997).
145. J. Papavassiliou and K. Philippides, Phys. Rev. **D60**, 113007 (1999).
146. G. Bella *et al.* (The LEP TGC Working Group), LEPEWWG/TGC/2000-01 (March 2000).
147. R.W. Brown and K.O. Mikaelian, Phys. Rev. **D19**, 922 (1979).
148. D. Benjamin, Proceedings of the *10th Topical Workshop on Proton-Antiproton Collider Physics*, Batavia, IL, May 1995, edited by R. Raja and J. Yoh, AIP Press (1996), p. 370.
149. U. Baur, S. Errede and G. Landsberg, Phys. Rev. **D50**, 1917 (1994).

Parton Distributions

Conveners: Lucy de Barbaro[a], Stephane A. Keller[b] , Steve Kuhlmann[c], Heidi Schellman[d], and Wu-Ki Tung[e].

[a]Fermi National Accelerator Laboratory, Batavia, IL 60510

[b]Theory Division, CERN, CH 1211 Geneva 23, Switzerland

[c]Argonne National Lab, Argonne, IL, 60439

[d]Northwestern University, Dept. of Physics, Evanston, IL, 60208

[e]Michigan State University, East Lansing, MI 48824

INTRODUCTION

With Run II and its large increase in integrated luminosity, the Tevatron will enter an era of high precision measurements. In this era, parton distribution function (PDF) uncertainties will play a major role.

The basic questions for PDFs at the Tevatron Run II are simple and common to all other experiment:

- What limitations will the PDFs put on physics analysis?
- What information can we gain about the PDFs?

There are some qualitative tools that exists and can be used to try to answer these questions. However, beside S. Alekhin's pioneer work [1], quantitative tools that attempt to include all sources of uncertainties are not available yet. The main focus of this working group has therefore been to investigate the different issues associated with the development of those tools, although obviously other topics have also been investigated.

We have divided this summary of activities into individual contributions:

- UNCERTAINTIES OF PARTON DISTRIBUTION FUNCTIONS AND THEIR IMPLICATION ON PHYSICAL PREDICTIONS. R. Brock *et al.* describe preliminary results from an effort to quantify the uncertainties in PDFs and the resulting uncertainties in predicted physical quantities. The production cross section of the W boson is given as a first example.
- PARTON DISTRIBUTION FUNCTION UNCERTAINTIES. Giele *et al.* review the status of their effort to extract PDFs from data with a quantitative estimate of the uncertainties.
- EXPERIMENTAL UNCERTAINTIES AND THEIR DISTRIBUTIONS IN THE INCLUSIVE JET CROSS SECTION. R. Hirosky summarizes the current CDF and D0 analysis for the inclusive jet cross sections. So far the uncertainties have been assumed to be Gaussian distributed. He investigates what information can be extracted about the shape of the uncertainties with the goal of being able to provide a way to calculate the Likelihood.
- PARTON DENSITY UNCERTAINTIES AND SUSY PARTICLE PRODUCTION. T. Plehn and M. Krämer study the current status of PDF's uncertainties on SUSY particle mass bounds or mass determinations.
- SOFT-GLUON RESUMMATION AND PDF THEORY UNCERTAINTIES. G. Sterman and W. Vogelsang discuss the interplay of higher order corrections and PDF determinations, and the possible use of soft-gluon resummation in global fits.
- PARTON DISTRIBUTION FUNCTIONS: EXPERIMENTAL DATA AND THEIR INTERPRETATION. L. de Barbaro review current issues in the interpretation of experimental data and the outlook for future data.
- HEAVY QUARK PRODUCTION. Olness *et al.* present a status report of a variety of projects related to heavy quark production.
- PARTON DENSITIES FOR HEAVY QUARKS. J. Smith compares different PDFs for heavy quarks.
- CONSTRAINTS ON THE GLUON DENSITY FROM LEPTON PAIR PRODUCTION. E. L. Berger and M. Klasen study the sensitivity of the hadroproduction of lepton pairs to the gluon density.

Note that the individual references are at the end of the corresponding contribution. The references for the introduction and the conclusion are at the end.

UNCERTAINTIES OF PARTON DISTRIBUTION FUNCTIONS AND THEIR IMPLICATIONS ON PHYSICAL PREDICTIONS

R. Brock, D. Casey, J. Huston, J. Kalk, J. Pumplin, D. Stump, W.K. Tung

Department of Physics and Astronomy, Michigan State University, East Lansing, MI 48824

Abstract

We describe preliminary results from an effort to quantify the uncertainties in parton distribution functions and the resulting uncertainties in predicted physical quantities. The production cross section of the W boson is given as a first example. Constraints due to the full data sets of the CTEQ global analysis are used in this study. Two complementary approaches, based on the Hessian and the Lagrange multiplier method respectively, are outlined. We discuss issues on obtaining meaningful uncertainty estimates that include the effect of correlated experimental systematic uncertainties and illustrate them with detailed calculations using one set of precision DIS data.

1. Introduction

Many measurements at the Tevatron rely on parton distribution functions (PDFs) for significant portions of their data analysis as well as the interpretation of their results. For example, in cross section measurements the acceptance calculation often relies on Monte Carlo (MC) estimates of the fraction of unobserved events. As another example, the measurement of the mass of the W boson depends on PDFs via the modeling of the production of the vector boson in MC. In such cases, uncertainties in the PDFs contribute, by necessity, to uncertainties on the measured quantities. Critical comparisons between experimental data and the underlying theory are often even more dependent upon the uncertainties in PDFs. The uncertainties on the production cross sections for W and Z bosons, currently limited by the uncertainty on the measured luminosity, are approximately 4%. At this precision, any comparison with the theoretical prediction inevitably raises the question: How "certain" is the prediction itself?

A recent example of the importance of PDF uncertainty is the proper interpretation of the measurement of the high-E_T jet cross-section at the Tevatron. When the first CDF measurement was published [1], there was a great deal of controversy over whether the observed excess, compared to theory, could be explained

by deviations of the PDFs, especially the gluon, from the conventionally assumed behavior, or could it be the first signal for some new physics [2].

With the unprecedented precision and reach of many of the Run I measurements, understanding the implications of uncertainties in the PDFs has become a burning issue. During Run II (and later at LHC) this issue may strongly affect the uncertainty estimates in precision Standard Model studies, such as the all important W-mass measurement, as well as the signal and background estimates in searches for new physics.

In principle, it is the uncertainties on physical quantities due to parton distributions, rather than on the PDFs themselves, that is of primary concern. The latter are theoretical constructs which depend on the renormalization and factorization schemes; and there are strong correlations between PDFs of different flavors and from different values of x, which can compensate each other in the convolution integrals that relate them to physical cross-sections. On the other hand, since PDFs are universal, if we can obtain meaningful estimates of their uncertainties based on analysis of existing data, then the results can be applied to all processes that are of interest in the future. [3,4]

One can attempt to assess directly the uncertainty on a specific physical prediction due to the full range of PDFs allowed by available experimental constraints. This approach will provide a more reliable estimate for the range of possible predictions for the physical variable under study, and may be the best course of action for ultra-precise measurements such as the mass of the W boson or the W production cross-section. However, such results are process-specific and therefore the analysis must be carried out for each case individually.

Until recently, the attempts to quantify either the uncertainties on the PDFs themselves (via uncertainties on their functional parameters, for instance) or the uncertainty on derived quantities due to variations in the PDFs have been rather unsatisfactory. Two commonly used methods are: (1) Comparing the predictions obtained with different PDF sets, *e.g.,* various CTEQ [5], MRS [6] and GRV [7] sets; (2) Within a given global analysis effort, varying individual functional parameters *ad hoc*, within limits considered to be consistent with the existing data, e.g. [8]. Neither method provides a systematic, quantitative measure of the uncertainties of the PDFs or their predictions.

As a case in point, Fig. 1 shows how the calculated value of the cross section for W boson production at the Tevatron varies with a set of historical CTEQ PDFs as well as the most recent CTEQ [5] and MRST [6] sets. Also shown are the most recent measurements from DØ and CDF[†]. While it is comforting to see that

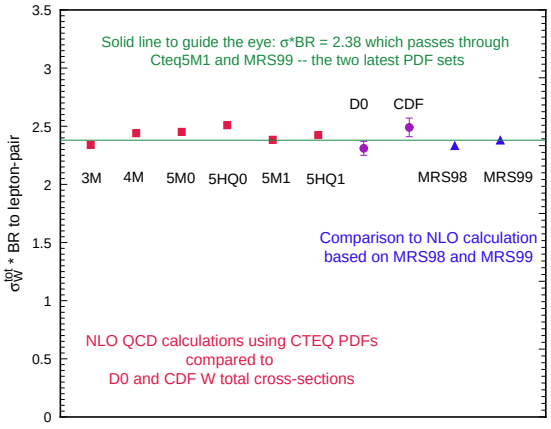

Figure 1. Predicted cross section for W boson production for various PDFs.

the predictions have remained within a narrow range, the variation observed cannot be characterized as a meaningful estimate of the uncertainty: (i) the variation with time reflects mostly the changes in experimental input to, or analysis procedure of, the global analyses; and (ii) the perfect agreement between the values of the most recent CTEQ5M1 [‡] and MRS99 sets must be fortuitous, since each group has also obtained other satisfactory sets which give rise to much larger variations of the W cross section. The MRST group, in particular has examined the range of this variation by setting a variety of parameters to some extreme values [8]. These studies are useful but can not be considered quantitative or definitive. What is needed are methods that explore thoroughly the possible variations of the parton distribution functions.

It is important to recognize all potential **sources of uncertainty** in the determination of PDFs. Focusing on some of these, while neglecting significant others, may not yield practically useful results. Sources of uncertainty are listed below:

- **Statistical uncertainties** of the experimental data used to determine the PDFs. These vary over a wide range among the experiments used in a global analysis, but are straightforward to treat.
- **Systematic uncertainties** within each data set.

[†]It is interesting to note that much of the difference between the DØ and CDF W cross sections is due to the different values of the total $p\bar{p}$ cross sections used

[‡]CTEQ5M1 is an updated version of CTEQ5M differing only in a slight improvement in the QCD evolution (cf. note added in proof of [5]). The differences are completely insignificant for our purposes. Henceforth, we shall refer to them generically as CTEQ5M. Both sets can be obtained from the web address http://cteq.org/.

There are typically many sources of experimental systematic uncertainty, some of which are highly correlated. These uncertainties can be treated by standard methods of probability theory *provided* they are precisely known, which unfortunately is often not the case – either because they may not be randomly distributed and/or because their estimation in practice involves subjective judgments.

- **Theoretical uncertainties** arising from higher-order PQCD corrections, resummation corrections near the boundaries of phase space, power-law (higher twist) and nuclear target corrections, etc.
- Uncertainties due to the **parametrization of the non-perturbative PDFs**, $f_a(x, Q_0)$, at some low momentum scale Q_0. The specific choice of the functional form used at Q_0 introduces implicit correlations between the various x-ranges, which could be as important, if not more so, than the experimental correlations in the determination of $f_a(x, Q)$ for all Q.

Since strict quantitative statistical methods are based on idealized assumptions, such as random measurement uncertainties, an important trade-off must be faced in devising a **strategy** for the analysis of PDF uncertainties. If emphasis is put on the "rigor" of the statistical method, then many important experiments cannot be included in the analysis, either because the published errors appear to fail strict statistical tests or because data from different experiments appear to be mutually exclusive in the parton distribution parameter space [4]. If priority is placed on using the maximal experimental constraints from available data, then standard statistical methods may not apply, but must be supplemented by physical considerations, taking into account experimental and theoretical limitations. We choose the latter tack, pursuing the determination of the uncertainties in the context of the current CTEQ global analysis. In particular, we include the same body of the world's data as constraints in our uncertainty study as that used in the CTEQ5 analysis; and adopt the "best fit" – the CTEQ5M1 set – as the base set around which the uncertainty studies are performed. In practice, there are unavoidable choices (and compromises) that must be made in the analysis. (Similar subjective judgments often are also necessary in estimating certain systematic errors in experimental analyses.) The most important consideration is that quantitative results must remain robust with respect to reasonable variations in these choices.

In this Report we describe preliminary results obtained by our group using the two approaches mentioned earlier. In Section 3 we focus on the error matrix, which characterizes the general uncertainties of the non-perturbative PDF parameters. In Sections 4 and 5 we study specifically the production cross section σ_W for $W^{\pm}$ bosons at the Tevatron, to estimate the uncertainty of the prediction of σ_W due to PDF uncertainty. We start in Section 2 with a review of some aspects of the CTEQ global analysis on which this study is based.

2. Elements of the Base Global Analysis

Since our strategy is based on using the existing framework of the CTEQ global analysis, it is useful to review some of its features pertinent to the current study [5].

Data selection:

Table 1 shows the experimental data sets included in the CTEQ5 global analysis, and in the current study. For neutral current DIS data only the most accurate proton and deuteron target measurements are kept, since they are the "cleanest" and they are already extremely extensive. For charged current (neutrino) DIS data, the significant ones all involve a heavy (Fe) target. Since these data are crucial for the determination of the normalization of the gluon distribution (indirectly via the momentum sum rule), and for quark flavor differentiation (in conjunction with the neutral current data), they play an important role in any comprehensive global analysis. For this purpose, a heavy-target correction is applied to the data, based on measured ratios for heavy-to-light targets from NMC and other experiments. Direct photon production data are not included because of serious theoretical uncertainties, as well as possible inconsistencies between existing experiments. Cf. [5] and [9]. The combination of neutral and charged DIS, lepton-pair production, lepton charge asymmetry, and inclusive large-p_T jet production processes provides a fairly tightly constrained system for the global analysis of PDFs. In total, there are ∼1300 data points which meet the minimum momentum scale cuts which must be imposed to ensure that PQCD applies. The fractional uncertainties on these points are distributed roughly like dF/F over the range $F = 0.003 - 0.4$.

Parametrization:

The non-perturbative parton distribution functions $f_a(x, Q)$ at a low momentum scale $Q = Q_0$ are parametrized by a set of functions of x, corresponding to the various flavors a. For this analysis, Q_0 is taken to be 1 GeV. The specific functional forms and the choice of Q_0 are not important, as long as the parametrization is general enough to accommodate the behavior of the true (but unknown) non-perturbative PDFs. The

Process	Experiment	Measurable	N_{data}
DIS	BCDMS[10]	$F_{2\ H}^{\mu}, F_{2\ D}^{\mu}$	324
	NMC [11]	$F_{2\ H}^{\mu}, F_{2\ D}^{\mu}$	240
	H1 [12]	$F_{2\ H}^{e}$	172
	ZEUS[13]	$F_{2\ H}^{e}$	186
	CCFR [14]	$F_{2\ Fe}^{\nu}, x\ F_{3\ Fe}^{\nu}$	174
Drell-Yan	E605[15]	$sd\sigma/d\sqrt{\tau}dy$	119
	E866 [16]	$\sigma(pd)/2\sigma(pp)$	11
	NA-51[17]	A_{DY}	1
W-prod.	CDF [18]	Lepton asym.	11
Incl. Jet	CDF [19]	$d\sigma/dE_t$	33
	D0[20]	$d\sigma/dE_t$	24

Table 1
List of processes and experiments used in the CTEQ5M Global analysis. The total number of data points is 1295.

CTEQ analysis adopts the functional form

$$a_0 x^{a_1}(1-x)^{a_2}(1+a_3 x^{a_4}).$$

for most quark flavors as well as for the gluon.[§] After momentum and quark number sum rules are enforced, there are 18 free parameters left over, hereafter referred to as "shape parameters" $\{a_i\}$. The PDFs at $Q > Q_0$ are determined from $f_a(x, Q_0)$ by evolution equations from the renormalization group.

Fitting:

The values of $\{a_i\}$ are determined by fitting the global experimental data to the theoretical expressions which depend on these parameters. The fitting is done by minimizing a global "chi-square" function, $\chi^2_{\rm global}$. The quotation mark indicates that this function serves as a *figure of merit* of the quality of the global fit; it does not necessarily have the full significance associated with rigorous statistical analysis, for reasons to be discussed extensively throughout the rest of this report. In practice, this function is defined as:

$$\chi^2_{\rm global} = \sum_n \sum_i w_n \left[(N_n d_{ni} - t_{ni}) / \sigma^d_{ni} \right]^2 + \sum_n \left[(1-N_n)/\sigma^N_n \right]^2 \quad (1)$$

where d_{ni}, σ^d_{ni}, and t_{ni} denote the data, measurement uncertainty, and theoretical value (dependent on $\{a_i\}$) for the $i^{\rm th}$ data point in the $n^{\rm th}$ experiment. The second term allows the absolute normalization (N_n) for each experiment to vary, constrained by the published normalization uncertainty (σ^N_n). The w_n factors are weights applied to some critical experiments with very few data points, which are known (from physics considerations) to provide useful constraints on certain unique features of PDFs not afforded by other experiments. Experience shows that without some judiciously chosen weights, these experimental data points will have no influence in the global fitting process. The use of these weighing factors, to enable the relevant unique constraints, amounts to imposing certain prior probability (based on physics knowledge) to the statistical analysis.

In the above form, $\chi^2_{\rm global}$ includes for each data point the random statistical uncertainties and the combined systematic uncertainties in uncorrelated form, as presented by most experiments in the published papers. These two uncertainties are *combined in quadrature* to form σ^d_{ni} in Eq. 1. Detailed point to point correlated systematic uncertainties are not available in the literature in general; however, in some cases, they can be obtained from the experimental groups. For global fitting, uniformity in procedure with respect to all experiments favors the usual practice of merging them into the uncorrelated uncertainties. For the study of PDF uncertainties, we shall discuss this issue in more detail in Section 5.

Goodness-of-fit for CTEQ5M:

Without going into details, Fig. 2 gives an overview of how well CTEQ5m fits the total data set. The graph is a histogram of the variable $x \equiv (d-t)/\sigma$ where d is a data value, σ the uncertainty of that measurement (statistical and systematic combined), and t the theoretical value for CTEQ5m. The curve in Fig. 2 has no adjustable parameters; it is the Gaussian with width 1 normalized to the total number of data points (1295). Over the entire data set, the theory fits the data within the assigned uncertainties σ^d_{ni}, indicating that those uncertainties are numerically consistent with the actual measurement fluctuations. Similar histograms for the individual experiments reveal various deviations from the theory, but *globally* the data have a reasonable Gaussian distribution around CTEQ5M.

3. Uncertainties on PDF parameters: The Error Matrix

We now describe results from an investigation of the behavior of the $\chi^2_{\rm global}$ function at its minimum, using the standard error matrix approach [21]. This allows us to determine which combinations of parameters are contributing the most to the uncertainty.

At the minimum of $\chi^2_{\rm global}$, the first derivatives with

[§] An exception is that recent data from E866 seem to require the ratio $\bar{d}/\bar{u}$ to take a more unconventional functional form.

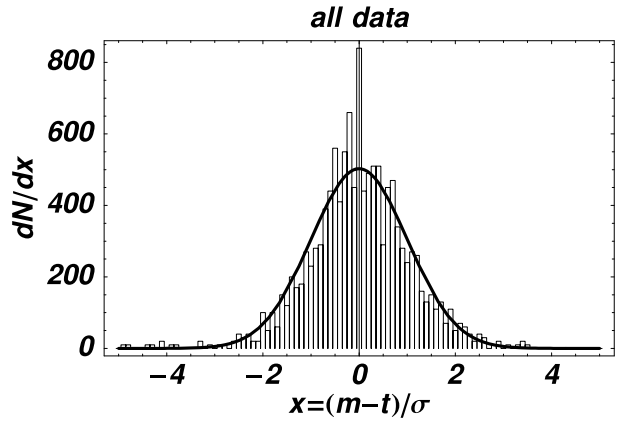

Figure 2. Histogram of the $(measurement - theory)$ for all data points in the CTEQ5m fit.

respect to the $\{a_i\}$ are zero; so near the minimum, $\chi^2_{\rm global}$ can be approximated by

$$\chi^2_{\rm global} = \chi^2_0 + \frac{1}{2}\sum_{i,j} F_{ij} y_i y_j \qquad (2)$$

where $y_i = a_i - a_{0i}$ is the displacement from the minimum, and F_{ij} is the *Hessian*, the matrix of second derivatives. It is natural to define a new set of coordinates using the complete orthonormal set of eigenvectors of the symmetric matrix F_{ij} as basis vectors. These vectors can be ordered by their eigenvalues e_i. Each eigenvalue is a quantitative measure of the uncertainties in the shape parameters $\{a_i\}$ for displacements in parameter space in the direction of the corresponding eigenvector. The quantity $\ell_i \equiv 1/\sqrt{e_i}$ is the distance in the 18 dimensional parameter space, in the direction of eigenvector i, that makes a unit increase in $\chi^2_{\rm global}$. If the only measurement uncertainty were uncorrelated gaussian uncertainties, then ℓ_i would be one standard deviation from the best fit in the direction of the eigenvector. The inverse of the Hessian is the error matrix.

Because the real uncertainties, for the wide variety of experiments included, are far more complicated than assumed in the ideal situation, the quantitative measure of a given increase in χ^2_{global} carries little true statistical meaning. However, qualitatively, the Hessian gives an analytic picture of $\chi^2_{\rm global}$ near its minimum in $\{a_i\}$ space, and hence allows us to identify the particular degrees of freedom that need further experimental input in future global analyses.

From calculations of the Hessian we find that the eigenvalues vary over a wide range. Figure 3 shows

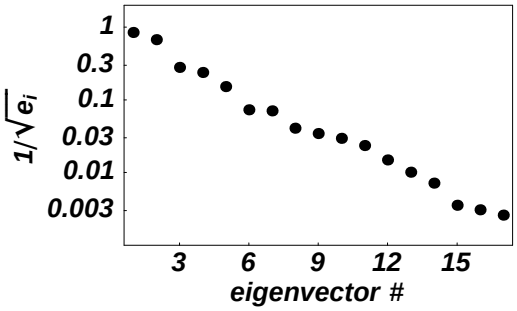

Figure 3. Plot of the eigenvalues of the Hessian. The vertical axis is $\ell_i = 1/\sqrt{e_i}$.

a graph of the eigenvalues of F_{ij}, on a logarithmic scale. The vertical axis is $\ell_i = 1/\sqrt{e_i}$, the distance of a "standard deviation" along the $i^{\rm th}$ eigenvector. These distances range over 3 orders of magnitude.Large eigenvalues of F_{ij} correspond to "steep directions" of $\chi^2_{\rm global}$. The corresponding eigenvectors are combinations of shape parameters that are well determined by current data. For example, parameters that govern the valence u and d quarks at moderate x are sharply constrained by DIS data. Small eigenvalues of F_{ij} correspond to "flat directions" of $\chi^2_{\rm global}$. In the directions of these eigenvectors, $\chi^2_{\rm global}$ changes little over large distances in $\{a_i\}$ space. For example, parameters that govern the large-x behavior of the gluon distribution, or differences between sea quarks, properties of the nucleon that are not accurately determined by current data, contribute to the flat directions. The existence of flat directions is inevitable in global fitting, because as the data improve it only makes sense to maintain enough flexibility for $f_a(x, Q_0)$ to fit the available experimental constraints.

Because the eigenvalues of the Hessian have a large range of values, efficient calculation of F_{ij} requires an adaptive algorithm. In principle F_{ij} is the matrix of second derivatives at the minimum of $\chi^2_{\rm global}$, which could be calculated from very small finite differences. In practice, small computational errors in the evaluation of $\chi^2_{\rm global}$ preclude the use of a very small step size. Coarse grained finite differences yield a more accurate calculation of the second derivatives. But because the variation of $\chi^2_{\rm global}$ varies markedly in different directions, it is important to use a grid in $\{a_i\}$ space with small steps in steep directions and large steps in flat directions. This grid is generated by an iterative procedure, in which F_{ij} converges to a good estimate of the second derivatives.

From calculations of F_{ij} we find that the minimum

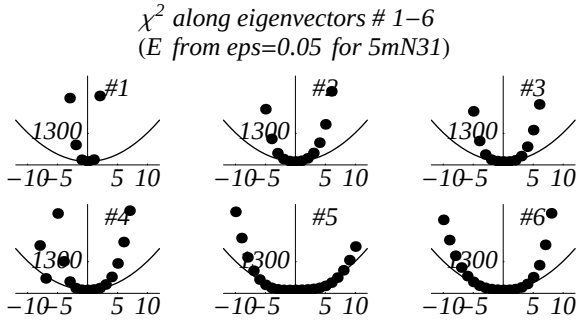

Figure 4. Value of χ^2 along the six eigenvectors with the largest eigenvalues.

of $\chi^2_{\rm global}$ is fairly quadratic over large distances in the parameter space. Figures 4 and 5 show the behavior

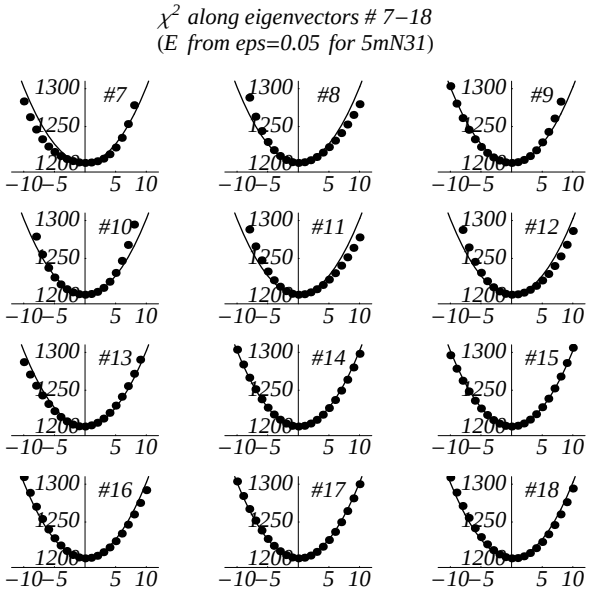

Figure 5. Value of χ^2 along the 12 eigenvectors with the smallest eigenvalues.

of $\chi^2_{\rm global}$ near the minimum along each of the 18 eigenvectors. $\chi^2_{\rm global}$ is plotted on the vertical axis, and the variable on the horizontal axis is the distance in $\{a_i\}$ space in the direction of the eigenvector, in units of $\ell_i = 1/\sqrt{e_i}$. There is some nonlinearity, but it is small enough that the Hessian can be used as an analytic model of the functional dependence of $\chi^2_{\rm global}$ on the shape parameters.

In a future paper we will provide details on the uncertainties of the original shape parameters $\{a_i\}$. But it should be remembered that these parameters specify the PDFs at the low Q scale, and applications of PDFs to Tevatron experiments use PDFs at a high Q scale. The evolution equations determine $f(x,Q)$ from $f(x,Q_0)$, so the functional form at Q depends on the $\{a_i\}$ in a complicated way.

4. Uncertainty on σ_W: the Lagrange Multiplier Method

In this Section, we determine the variation of $\chi^2_{\rm global}$ as a function of a single measurable quantity. We use the production cross section for W bosons (σ_W) as an archetype example. The same method can be applied to any other physical observable of interest, for instance the Higgs production cross section, or to certain measured differential distributions. The aim is to quantify the uncertainty on that physical observable due to uncertainties of the PDFs integrated over the entire PDF parameter space.

Again, we use the standard CTEQ5 analysis tools and results [5] as the starting point. The "best fit" is the CTEQ5M1 set. A natural way to find the limits of a physical quantity X, such as σ_W at $\sqrt{s} = 1.8\,\text{TeV}$, is to take X as one of the search parameters in the global fit and study the dependence of $\chi^2_{\rm global}$ for the 15 base experimental data sets on X.

Conceptually, we can think of the function $\chi^2_{\rm global}$ that is minimized in the fit as a function of $a_1, \ldots, a_{17}, X$ instead of $a_1, \ldots, a_{18}$. This idea could be implemented directly in principle, but a more convenient way to do the same thing in practice is through Lagrange's method of undetermined multipliers. One minimizes, with respect to the $\{a_i\}$, the quantity

$$F(\lambda) = \chi^2_{\rm global} + \lambda X(a_1, \ldots, a_{18}) \qquad (3)$$

for a fixed value of λ, the Lagrange multiplier. By minimizing $F(\lambda)$ for many values of λ, we map out $\chi^2_{\rm global}$ as a function of X. The minimum of F for a given value of λ is the best fit to the data for the corresponding value of X, *i.e.,* evaluated at the minimum.

Figure 6 shows $\chi^2_{\rm global}$ for the 15 base experimental data sets as a function of σ_W at the Tevatron. The horizontal axis is σ_W times the branching ratio for $W \to$ leptons, in nb. The CTEQ5m prediction is $\sigma_W \cdot BR_{\rm lep} = 2.374\,\text{nb}$. The vertical dashed lines are $\pm 3\%$ and $\pm 5\%$ deviations from the CTEQ5m prediction.

The two parabolas associated with points in Fig. 6 correspond to different treatments of the normalization

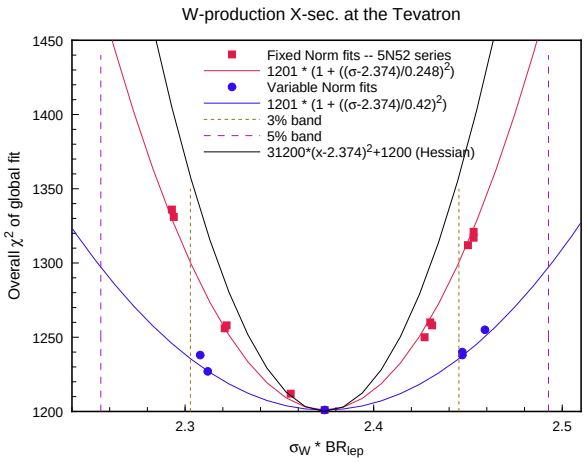

Figure 6. χ^2 of the base experimental data sets *versus* $\sigma_W \cdot BR_{\rm lep}$, the W production cross-section at the Tevatron times lepton branching ratio, in nb.

factor N_n in Eq. 1. The dots (•) are variable norm fits, in which N_n is allowed to float, taking into account the experimental normalization uncertainties, and $F(\lambda)$ is minimized with respect to N_n. The justification for this procedure is that overall normalization is a common systematic uncertainty. The boxes (□) are fixed norm fits, in which all N_n are held fixed at their values for the global minimum (CTEQ5m). These two procedures represent extremes in the treatment of normalization uncertainty. The parabolas associated with •'s and □'s are just least-square fits to the points.

The other curve in Fig. 6 was calculated using the Hessian method. The Hessian F_{ij} is the matrix of second derivatives of $\chi^2_{\rm global}$ with respect to the shape parameters $\{a_i\}$. The derivatives (first and second) of σ_W may also be calculated by finite differences. Using the resultant quadratic approximations for $\chi^2_{\rm global}(a)$ and $\sigma_W(a)$, one may minimize $\chi^2_{\rm global}$ with σ_W fixed. Since this calculation keeps the normalization factors constant, it should be compared with the fixed norm fits from the Lagrange multiplier method. The fact that the Hessian and Lagrange multiplier methods yield similar results lends support to both approaches; the small difference between them indicates that the quadratic functional approximations for $\chi^2_{\rm global}$ and σ_W are only approximations.

For the quantitative analysis of uncertainties, the important question is: How large an increase in $\chi^2_{\rm global}$ should be taken to define the likely range of uncertainty in X? There is an elementary statistical theorem that states that $\Delta\chi^2 = 1$ in a constrained fit corresponds to 1 standard deviation of the constrained quantity X. However, the theorem relies on the assumption that the uncertainties are gaussian, uncorrelated, and correctly estimated in magnitude. Because these conditions do not hold for the full data set (of ~ 1300 points from 15 different experiments), this theorem cannot be naively applied quantitatively.[¶] Indeed, it can be shown that, if the measurement uncertainties are correlated, and the correlation is not properly taken into account in the definition of $\chi^2_{\rm global}$, then a standard deviation may vary over the entire range from $\Delta\chi^2 = 1$ to $\Delta\chi^2 = N$ (the total number of data points – ~ 1300 in our case).

5. Statistical Analysis with Systematic Uncertainties

Fig. 6 shows how the fitting function $\chi^2_{\rm global}$ increases from its minimum value, at the best global fit, as the cross-section σ_W for W production is forced away from the prediction of the global fit. The next step in our analysis of PDF uncertainty is to use that information, or some other analysis, to estimate the uncertainty in σ_W. In ideal circumstances we could say that a certain increase of $\chi^2_{\rm global}$ from the minimum value, call it $\Delta\chi^2$, would correspond to a standard deviation of the global measurement uncertainty. Then a horizontal line on Fig. 6 at $\chi^2_{\rm min}+\Delta\chi^2$ would indicate the probable range of σ_W, by the intersection with the parabola of $\chi^2_{\rm global}$ versus σ_W.

However, such a simple estimate of the uncertainty of σ_W is not possible, because the fitting function $\chi^2_{\rm global}$ does not include the *correlations* between systematic uncertainties. The uncertainty σ^d_{ni} in the definition (1) of $\chi^2_{\rm global}$ combines *in quadrature* the statistical and systematic uncertainties for each data point; that is, it treats the systematic uncertainties as uncorrelated. The standard theorems of statistics for Gaussian probability distributions of random uncertainties do not apply to $\chi^2_{\rm global}$.

Instead of using $\chi^2_{\rm global}$ to estimate confidence levels on σ_W, we believe the best approach is to carry out a thorough statistical analysis, including the correlations of systematic uncertainties, on individual experiments used in the global fit for which detailed information is available. We will describe here such an analysis for the measurements of $F_2(x,Q)$ by the H1 experiment [12] at HERA, as a case study. In a future paper, we will present similar calculations for other experiments.

The H1 experiment has provided a detailed table of measurement uncertainties – statistical and systematic – for their measurements of $F_2(x,Q)$. [12] The

[¶]It has been shown by Giele *et.al.* [4], that, taken literally, only one or two selected experiments satisfy the standard statistical tests.

CTEQ program uses 172 data points from H1 (requiring the cut $Q^2 > 5\,\mathrm{GeV}^2$). For each measurement d_j (where $j = 1 \ldots 172$) there is a statistical uncertainty σ_{0j}, an uncorrelated systematic uncertainty σ_{1j}, and a set of 4 correlated systematic uncertainties a_{jk} where $k = 1 \ldots 4$. (In fact there are 8 correlated uncertainties listed in the H1 table. These correspond to 4 pairs. Each pair consists of one standard deviation in the positive sense, and one standard deviation in the negative sense, of some experimental parameter. For this first analysis, we have approximated each pair of uncertainties by a single, symmetric combination, equal in magnitude to the average magnitude of the pair.)

To judge the uncertainty of σ_W, as constrained by the H1 data, we will compare the H1 data to the global fits in Fig. 6. The comparison is based on the true, statistical χ^2, including the correlated uncertainties, which is given by

$$\chi^2 = \sum_j \frac{(d_j - t_j)^2}{\sigma_j^2} - \sum_{kk'} B_k \left(A^{-1}\right)_{kk'} B_{k'}. \tag{4}$$

The index j labels the data points and runs from 1 to 172. The indices k and k' label the source of systematic uncertainty and run from 1 to 4. The combined uncorrelated uncertainty σ_j is $\sqrt{\sigma_{0j}^2 + \sigma_{1j}^2}$. The second term in (4) comes from the correlated uncertainties. B_k is the vector

$$B_k = \sum_j \frac{(d_j - t_j)\, a_{jk}}{\sigma_j^2}, \tag{5}$$

and $A_{kk'}$ is the matrix

$$A_{kk'} = \delta_{kk'} + \sum_j \frac{a_{jk} a_{jk'}}{\sigma_j^2}. \tag{6}$$

Assuming the published uncertainties σ_{0j}, σ_{1j} and a_{jk} accurately reflect the measurement fluctuations, χ^2 would obey a chi-square distribution if the measurements were repeated many times. Therefore the chi-square distribution with 172 degrees of freedom provides a basis for calculating *confidence levels* for the global fits in Fig. 6.

Table 2 shows χ^2 for the H1 data compared to seven of the PDF fits in Fig. 6. The center row of the Table is the global best fit – CTEQ5m. The other rows are fits obtained by the Lagrange multiplier method for different values of the Lagrange multiplier. The best fit to the H1 data, *i.e.*, the smallest χ^2, is not CTEQ5m (the best global fit) but rather the fit with Lagrange multiplier 1000 for which σ_W is 0.8% smaller than the prediction of CTEQ5m. Forcing the W cross section

Lagrange multiplier	$\sigma_W \cdot B$ in nb	$\chi^2/172$	probability
3000	2.294	1.0847	0.212
2000	2.321	1.0048	0.468
1000	2.356	0.9676	0.605
0	2.374	0.9805	0.558
-1000	2.407	1.0416	0.339
-2000	2.431	1.0949	0.187
-3000	2.450	1.1463	0.092

Table 2
Comparison of H1 data to the PDF fits with constrained values of σ_W.

values away from the prediction of CTEQ5m causes an increase in χ^2 for the DIS data. At $\sqrt{s} = 1.8\,\mathrm{TeV}$, W production is mainly from $q\bar{q} \to W^+W^-$ with moderate values of x for q and $\bar{q}$, *i.e.,* values in the range of DIS experiments. Forcing σ_W higher (or lower) requires a higher (or lower) valence quark density in the proton, in conflict with the DIS data, so χ^2 increases.

The final column in Table 2, labeled "probability", is computed from the chi-square distribution with 172 degrees of freedom. This quantity is the probability for χ^2 to be greater than the value calculated from the existing data, if the H1 measurements were to be repeated. So, for example, the fit with Lagrange multiplier -3000, which corresponds to σ_W being 3.2% larger than the CTEQ5m prediction, has probability 0.092. In other words, if the H1 measurements could be repeated many times, in only 9.2% of trials would χ^2 be greater than or equal to the value that has been obtained with the existing data. This probability represents a confidence level for the value of σ_W that was forced on the PDF by setting the Lagrange multiplier equal to -3000. At the 9.2% confidence level we can say that $\sigma_W \cdot BR_{\mathrm{lep}}$ is less than 2.450 nb, based on the H1 data. Similarly, at the 21.2% confidence level we can say that $\sigma_W \cdot BR_{\mathrm{lep}}$ is greater than 2.294 nb.

Fig. 7 is a graph of χ^2/N for the H1 data compared to the PDF fits in Table 2. This figure may be compared to Fig. 6. The CTEQ5 prediction of the W production cross-section is shown as an arrow, and the vertical dashed lines are $\pm 3\%$ away from the CTEQ5m prediction. The horizontal dashed line is the 68% confidence level on χ^2/N for $N = 172$ degrees of freedom. The comparison with H1 data alone indicates that the uncertainty on σ_W is $\sim 3\%$.

There is much more to say about χ^2 and confidence levels. In a future paper we will discuss statistical calculations for other experiments in the global data

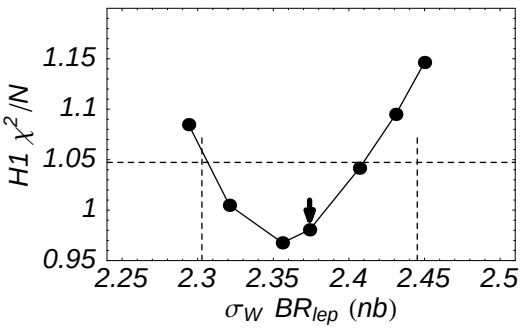

Figure 7. χ^2/N of the H1 data, including error correlations, compared to PDFs obtained by the Lagrange multiplier method for constrained values of σ_W.

set. The H1 experiment is a good case, because for H1 we have detailed information about the correlated uncertainties. But it may be somewhat fortuitous that the χ^2 per data point for CTEQ5m is so close to 1 for the H1 data set. In cases where χ^2/N is not close to 1, which can easily happen if the estimated systematic uncertainties are not textbook-like, we must supply further arguments about confidence levels. For experiments with many data points, like 172 for H1, the chi-square distribution is very narrow, so a small inaccuracy in the estimate of σ_j may translate to a large uncertainty in the calculation of confidence levels based on the absolute value of χ^2. Because the estimation of experimental uncertainties introduces some uncertainty in the value of χ^2, it is not really the *absolute* value of χ^2 that is important, but rather the *relative* value compared to the value at the global minimum. Therefore, we might study *ratios* of χ^2's to interpret the variation of χ^2 with σ_W.

6. Conclusions

It has been widely recognized by the HEP community, and it has been emphasized at this workshop, that PDF phenomenology must progress from the past practice of periodic updating of *representative* PDF sets to a systematic effort to map out the uncertainties, both on the PDFs themselves and on physical observables derived from them. For the analysis of PDF uncertainties, we have only addressed the issues related to the treatment of experimental uncertainties. Equally important for the ultimate goal, one must come to grips with uncertainties associated with theoretical approximations and phenomenological parametrizations. Both of these sources of uncertainties induce highly correlated uncertainties, and they can be numerically more important than experimental uncertainties in some cases. Only a balanced approach is likely to produce truly useful results. Thus, great deal of work lies ahead.

This report described first results from two methods for quantifying the uncertainty of parton distribution functions associated with experimental uncertainties. The specific work is carried out as extensions of the CTEQ5 global analysis. The same methods can be applied using other parton distributions as the starting point, or using a different parametrization of the non-perturbative PDFs. We have indeed tried a variety of such alternatives. The results are all similar to those presented above. The robustness of these results lends confidence to the general conclusions.

The Hessian, or error matrix method reveals the uncertainties of the shape parameters used in the functional parametrization. The behavior of $\chi^2_{\rm global}$ in the neighborhood of the minimum is well described by the Hessian if the minimum is quadratic.

The Lagrange multiplier method produces constrained fits, *i.e.,* the best fits to the global data set for specified values of some observable. The increase of $\chi^2_{\rm global}$, as the observable is forced away from the predicted value, indicates how well the current data on PDFs determines the observable.

The constrained fits generated by the Lagrange multiplier method may be compared to data from individual experiments, taking into account the uncertainties in the data, to estimate confidence levels for the constrained variable. For example, we estimate that the uncertainty of σ_W attributable to PDFs is $\pm 3\%$.

Further work is needed to apply these methods to other measurements, such as the W mass or the forward-backward asymmetry of W production in $p\bar{p}$ collisions. Such work will be important in the era of high precision experiments.

REFERENCES

1. CDF Collaboration (Abe et al.), *Phys. Rev. Lett.* **77**, (1996) 439.
2. J. Huston, E. Kovacs, S. Kuhlman, H. L. Lai, J. F. Owens, D. Soper, W. K. Tung, Phys. Rev. Lett. **77**, 444(1996); E. W. N. Glover, A. D. Martin, R. G. Roberts, and W. J. Stirling, "Can partons describe the CDF jet data?", hep-ph/9603327.
3. S. Alekhin, Eur. Phys. J. **C10**, 395 (1999) [hep-ph/9611213]; and contribution to Proceedings of *Standard Model Physics (and more) at the LHC*, 1999.
4. W. T. Giele and S. Keller, Phys. Rev. **D58**, 094023; contribution to this Workshop by W. T.

Giele, S. Keller and D. Kosower; and private communication.
5. H. L. Lai, J. Huston, S. Kuhlmann, J. Morfin, F. Olness, J. F. Owens, J. Pumplin and W. K. Tung, hep-ph/9903282, (to appear in Eur. Phys. J.); and earlier references cited therein
6. A. D. Martin and R. G. Roberts and W. J. Stirling and R. S. Thorne, Eur. Phys. J. **C4**, (1998) 463, hep-ph/9803445; and earlier references cited therein.
7. M. Gluck and E. Reya and A. Vogt, Eur. Phys. J. **C5**, (1998) 461, hep-ph/9806404.
8. A. D. Martin, R. G. Roberts, W. J. Stirling, and R. S. Thorne, "Parton Distributions and the LHC: W and Z Production", hep-ph/9907231.
9. J. Huston, et al, Phys. Rev. **D51**, (1995) 6139, hep-ph/9501230. L. Apanasevich, C. Balazs, C. Bromberg, J. Huston, A. Maul, W. K. Tung, S. Kuhlmann, J. Owens, M. Begel, T. Ferbel, G. Ginther, P. Slattery, M. Zielinski, Phys. Rev. **D59**, 074007 (1999); P. Aurenche, M. Fontannaz, J.Ph. Guillet, B. Kniehl, E. Pilon, M. Werlen, Eur. Phys. J. **C9**, 107 (1999).
10. BCDMS Collaboration (A.C. Benvenuti, *et.al.*.), Phys.Lett. **B223**, 485 (1989); and Phys. Lett.**B237**, 592 (1990).
11. NMC Collaboration: (M. Arneodo *et al.*) Phys. Lett. **B364**, 107 (1995).
12. H1 Collaboration (S. Aid *et al.*): "1993 data" Nucl. Phys. **B439**, 471 (1995); "1994 data", DESY-96-039, e-Print Archive: hep-ex/9603004; and H1 Webpage.
13. ZEUS Collaboration (M. Derrick *et al.*): "1993 data" Z. Phys. **C65**, 379 (1995) ; "1994 data", DESY-96-076 (1996).
14. CCFR Collaboration (W.C. Leung, *et al.*), Phys. Lett. **B317**, 655 (1993); and (P.Z. Quintas, *et al.*), Phys. Rev. Lett. **71**, 1307 (1993).
15. E605: (G. Moreno, *et al.*), Phys. Rev. **D43**, 2815 (1991).
16. E866 Collaboration (E.A. Hawker, *et al.*), Phys. Rev. Lett. **80**, 3175 (1998).
17. NA51 Collaboration (A. Baldit, *et al.*), Phys. Lett. **B332**, 244 (1994).
18. CDF Collaboration (F. Abe, *et al.*), Phys. Rev. Lett. **74**, 850 (1995).
19. See [1] and F. Bedeschi, talk at 1999 Hadron Collider Physics Conference, Bombay, January, 1999.
20. D0 Collaboration: B. Abbott et al., FERMILAB-PUB-98-207-E, e-Print Archive: hep-ex/9807018
21. D.E. Soper and J.C. Collins, "Issues in the Determination of Parton Distribution Functions", CTEQ Note 94/01; hep-ph/9411214.

PARTON DISTRIBUTION FUNCTION UNCERTAINTIES

Walter T. Giele[a], Stephane A. Keller[b] and David A. Kosower[c].

a) Fermi National Accelerator Laboratory, Batavia, IL 60510; b) Theory Division, CERN, CH 1211 Geneva 23, Switzerland; c) CEA–Saclay, F–91191 Gif-sur-Yvette cedex, France.

Abstract

We review the status of our effort to extract parton distribution functions from data with a quantitative estimate of the uncertainties.

1. Introduction

The goal of our work is to extract parton distribution functions (PDF) from data with a quantitative estimation of the uncertainties. There are some qualitative tools that exist to estimate the uncertainties, see e.g. Ref. [1]. These tools are clearly not adequate when the PDF uncertainties become important. One crucial example of a measurement that will need a quantitative assessment of the PDF uncertainty is the planned high precision measurement of the mass of the W-vector boson at the Tevatron. Clearly, quantitative tools along the line of S. Alekhin's pioneer work [2] are needed.

The method we have developed in Ref. [3] is flexible and can accommodate non-Gaussian distributions for the uncertainties associated with the data and the fitted parameters as well as all their correlations. New data can be added in the fit without having to redo the whole fit. Experimenters can therefore include their own data into the fit during the analysis phase, as long as correlation with older data can be neglected. Within this method it is trivial to propagate the PDF uncertainties to new observables, there is for example no need to calculate the derivative of the observable with respect to the different PDF parameters. The method also provides tools to assess the goodness of the fit and the compatibility of new data with current fit. The computer code has to be fast as there is a large number of choices in the inputs that need to be tested.

It is clear that some of the uncertainties are difficult to quantify and It might not be possible to quantify all of them. All the plots presented here are for illustration of the method only, our results are *preliminary*. At the moment we are not including all the sources of uncertainties and our results should therefore be considered as lower limits on the PDF uncertainties. Note that all the techniques we use can be found in books and papers on statistics [4] and/or in Numerical Recipes [5].

2. Outline of the Method

We only give a brief overview of the method in this section. More details are available in Ref.[3]. Our method follows the Bayesian methodology [†]. Once a set of core experiments is selected, a large number of uniformly distributed sets of parameters $\lambda \equiv \lambda_1, \lambda_2, \ldots, \lambda_{N_{par}}$ (each set corresponds to one PDF) can be generated and the probability density of the set $P(\lambda)$ calculated from the likelihood (the probability) that the predictions based on λ describe the data, see Ref. [4] and next section.

Knowing $P(\lambda)$, then for any observable x (or any quantity that depends on λ) the probability density, $P(x)$ can be evaluated, and using a Monte Carlo integration, the average value and the standard deviation of x can be calculated with the standard expressions:

$$\begin{aligned} \mu_x &= \int \left(\prod_{i=1}^{N_{par}} d\lambda_i \right) x(\lambda) P(\lambda) \\ \sigma_x^2 &= \int \left(\prod_{i=1}^{N_{par}} d\lambda_i \right) (x(\lambda) - \mu_x)^2 P(\lambda). \end{aligned} \quad (1)$$

If $P(x)$ is Gaussian distributed, then the standard deviation is a sufficient measure of the PDF uncertainties. If $P(x)$ is not Gaussian distributed, then one should refer to the distribution itself and not try to "summarize" it by a single number, all the information is in the distribution itself. The uncertainties due to the Monte Carlo can also be calculated with standard technique.

The above is correct but computationally inefficient, instead we use a Metropolis algorithm, see Ref. [5], to generate N_{pdf} unit-weighted PDFs distributed according to $P(\lambda)$. With this set of PDFs, the expressions in Eq. 1 become:

$$\begin{aligned} \mu_x &\approx \frac{1}{N_{pdf}} \sum_{j=1}^{N_{pdf}} x\left(\lambda_j\right) \\ \sigma_x^2 &\approx \frac{1}{N_{pdf}} \sum_{j=1}^{N_{pdf}} \left(x\left(\lambda_j\right) - \mu_x\right)^2 \ . \end{aligned} \quad (2)$$

This is equivalent to importance sampling in Monte Carlo integration techniques. It is very efficient because the number of PDFs needed to reach a given level of accuracy in the evaluation of the integrals is much smaller than when using a set of PDFs uniformly distributed. Given the unit-weighted set of PDFs, a new experiment can be added to the fit by assigning a weight (a new probability) to each of the PDFs, using Bayes' theorem. The above summations become weighted. There is no need to redo the whole fit *if* there is no correlation between the old and new data. If we know how to calculate $P(\lambda)$ properly, the only uncertainty in the method comes from the Monte-Carlo integrations.

[†] we also plan to present results within the "classical frequentist" framework [6]

3. Calculation of $P(\lambda)$

Given a set of experimental points $\{x^e\} = x_1^e, x_2^e, \ldots, x_{N_{obs}}^e$ the probability of a set of PDF is in fact the conditional probability of $\{\lambda\}$ given that $\{x^e\}$ has been measured, this conditional probability can be calculated using Bayes theorem:

$$P(\lambda) = P(\lambda|x^e) = \frac{P(x^e|\lambda)}{P(x^e)} P_{init}(\lambda), \quad (3)$$

where, as already mentioned, the prior distribution of the parameters, $P_{init}(\lambda)$, has been assumed to be uniform. A prior sensitivity should be performed. $P(x^e|\lambda)$ is the likelihood, the probability to observe the data given that the theory is fixed by the set of $\{\lambda\}$. $P(x^e)$ is the probability density of the data (integrated over the PDFs) and act as a normalization coefficient in Eq. 3.

If all the uncertainties are Gaussian distributed, then it is well known that:

$$P(x^e|\lambda) \approx e^{-\frac{\chi^2(\lambda)}{2}}, \quad (4)$$

where χ^2 is the *usual* chi-square:

$$\chi^2(\lambda) = \sum_{k,l}^{N_{obs}} \left(x_k^e - x_k^t(\lambda)\right) M_{kl}^{tot} \left(x_l^e - x_l^t(\lambda)\right) \ , \quad (5)$$

$x_k^t(\lambda)$ are the theory prediction for the experimental observables calculated with the parameters $\{\lambda\}$. The matrix M^{tot} is the inverse of the total covariance matrix.

When the uncertainties are not Gaussian distributed, the result is not as well known. We first present two simple examples to illustrate how the likelihood should be calculate and then give a generalization.

3.1. The simplest example

We first consider the simplest example to setup the notation, one experimental point with a statistical uncertainty:

$$x^t(\lambda) = x^e + u\Delta, \tag{6}$$

where u is a random variable that has it own distribution, f(u) (assumed to be Gaussian in this case). By convention, we take the average of u equal to 0 and its standard deviation equal to 1. Δ gives the size of the statistical uncertainty. For each experimental measurement there is a different value of u and x^e. The probability to find x^e in an element of length dx^e given that the theory is fixed by $\{\lambda\}$ is equal to the probability to find u in a corresponding element of length du[‡]:

$$P(x^e|\lambda)dx^e = f(u)du. \tag{7}$$

The variable u and the Jacobian for the change of variable from u to x^e can be extracted from Eq. 6:

$$u = \frac{x^t(\lambda) - x^e}{\Delta}; \left|\frac{du}{dx^e}\right| = \frac{1}{\Delta} \tag{8}$$

such that:

$$\begin{aligned} P(x^e|\lambda) &= \frac{f(\frac{x^t(\lambda)-x^e}{\Delta})}{\Delta} \\ &= \frac{1}{\sqrt{2\pi}\Delta} e^{-\frac{(x^t-x^e)^2}{2\Delta^2}}. \end{aligned} \tag{9}$$

This is the expected result.

3.2. A simple example

We now consider the case of one experimental point with a statistical and a systematic uncertainty:

$$x^t(\lambda) = x^e + u_1\Delta_1 + u_2\Delta_2 \tag{10}$$

Δ_1 and Δ_2 give the size of the uncertainties. u_1 and u_2 have their own distribution $f^1(u_1)$ and $f^2(u_2)$ and we use the same convention for their average and standard deviation as for u in the first example. This time for each experimental measurement, there is an infinite number of sets of u_1, u_2 that correspond to it, because there is only one equation that relate x^t, x^e and u_1 and u_2. The probability to find x^e in an element of length dx^e given that the theory is fixed by $\{\lambda\}$ is here equal to the probability to find u_1 and u_2 in a corresponding element of area $du_1\, du_2$, with an integration over one of the two variables:

$$P(x^e|\lambda)dx^e = du^1 \int du_2 f^1(u_1) f^2(u_2). \tag{11}$$

We choose to integrate over u_2. u_1 and the Jacobian for the change of variable from u_1 to x^e are given by Eq. 10:

$$u_1 = \frac{x^t - x^e - u_2\Delta_2}{\Delta_1}; \left|\frac{du_1}{dx^e}\right| = \frac{1}{\Delta_1} \tag{12}$$

such that:

$$P(x^e|\lambda) = \int du_2 f^2(u_2) \frac{f^1(\frac{x^t - x^e - u_2\Delta_2}{\Delta_1})}{\Delta_1} \tag{13}$$

If both $f^1(u_1)$ and $f^2(u_2)$ are Gaussian distribution then we recover the expected result, as in Eq 4. Note that this expected result is recovered if the uncertainties are Gaussian distributed and the relationship between the theory, the data and the uncertainties are given by Eq. 10. If that relationship is more complex there is no guarantee to recover Eq. 4. In the general case, the integral in Eq. 13 has to be done numerically.

3.3. Generalization:

We are now ready to give a generalization of the calculation of the likelihood. We are considering N_{obs} observables, and N_{unc} uncertainties (statistical and systematic) parametrized by N_{unc} random variables $\{u\} = u_1, u_2, \ldots, u_{N_{unc}}$ with their own distributions, $f^i(u_i)$.

There are N_{obs} relations between $\{x^t\}$, $\{x^e\}$ and $\{u\}$, one for each observable:

$$F_i(x_i^e, \{x^t(\lambda)\}, \{u\}) = 0. \tag{14}$$

This gives $N_{unc} - N_{obs}$ independent u_i that we choose by convenience to be the $u_i's$ corresponding to the systematic uncertainties. Without loosing generality we assume that there is one statistical uncertainty for each observable, and we organize the corresponding u_i with the same index as x_i^e, such that the last $N_{sys} (= N_{unc} - N_{obs})$ u_i are the random variables for the systematic uncertainties. For each set of measured $\{x^e\}$ there is an infinite number of $\{u\}$ sets that correspond to it.

The probability to find $\{x^e\}$ in an element of volume $\prod_{i=1}^{N_{obs}} dx_i^e$ given that the theory is fixed by $\{\lambda\}$ is equal to the probability to find the $\{u\}$ in a corresponding

[‡]the repetition of the experiment will only be distributed according to u around the true nature value of x^t. However we are trying to calculate the likelihood, the conditional probability of the data given that the true nature value of x^t is given by the value of the $\{\lambda\}$ under study

element of volume $\prod_{i=1}^{N_{unc}} dx^u$, with an integration over the independent u_i [§] :

$$P(\{x^e\}|\lambda) \prod_{i=1}^{N_{obs}} dx_i^e = (\prod_{k=1}^{N_{obs}} du_k) \int (\prod_{i=N_{obs}+1}^{N_{unc}} du_i) * \prod_{j=1}^{N_{unc}} f^j(u_j) \quad (15)$$

The values of the $\{u_i, i = 1, N_{obs}\}$ (corresponding to the statistical uncertainties) and the Jacobian, $J(u \to x^e)$, for the change of variable from those u_i to the x_i^e can be extracted from the N_{obs} relations in Eq. 14. The likelihood is then given by:

$$P(\{x^e\}|\lambda) = \int (\prod_{i=N_{obs}+1}^{N_{unc}} du_i) \prod_{j=1}^{N_{unc}} f^j(u_j) J(u \to x^e) \quad (16)$$

Often, the F_i relationship in Eq 14 have a simple dependence on $\{x^e\}$ and the $u's$ corresponding to the statistical uncertainties:

$$F_i(x_i^e, \{x^t(\lambda)\}, \{u\}) = x_i^e + u_i \Delta_i + \cdots , \quad (17)$$

where the Δ_i are the size of the statistical uncertainties. In that case, the Jacobian is simply given by:

$$J(u \to x^e) = \prod_{i=1}^{N_{obs}} \frac{1}{\Delta_i} \quad (18)$$

In most cases, the likelihood will not be analytically calculable, and has to be calculated numerically again with Monte Carlo technique.

In order to be able to calculate the likelihood we therefore need:

- the relations between $\{x^t\}$, $\{x^e\}$ and $\{u\}$ as in Eq. 14.
- the probability distribution of the random variable associated with the uncertainties: $f^i(u_i)$.

Unfortunately most of the time that information is not reported by the experimenters, and/or is not available and certainly difficult to extract from papers. It is only in the case that all the uncertainties are Gaussian distributed ¶ that it is sufficient to report the size of the uncertainties and their correlation [‖]. This is a very important issue, simply put, experiments should always provide a way to calculate the likelihood, $P(\{x^e\}|\lambda)$. This last fact was also the unanimous conclusion of a recent workshop on confidence limits held at CERN [7]. This is particularly crucial when combining different experiments together: the pull of each experiment will depend on it and, as a result, so will the central values of the deduced PDFs.

3.4. The central limit theorem

Assuming that the uncertainties are Gaussian distributed when they are not can lead to some serious problems. For example, minimizing the χ^2 constructed assuming Gaussian distribution will not even maximize the likelihood. Indeed in the general case, the usually defined χ^2 will not appear in the likelihood.

It is often assumed that the central limit theorem can be used to justify the assumption of Gaussian distribution for the uncertainties. It is therefore useful to revisit this theorem. Y is a linear combination of n independent X_i:

$$Y = \sum_i c_i X_i \quad (19)$$
$$\sigma_Y^2 = \sum_i c_i^2 \sigma_{X_i}^2$$

where the c_i are constants and the σ are the standard deviations. The theorem states that in the limit of large n the distribution of Y will be approximately Gaussian if σ_Y^2 is much larger than any component $c_i^2 \sigma_{X_i}^2$ from a non-Gaussian distributed X_i. For some examples of how large n has to be, see Ref. [4].

Here is one way the theorem could be used: If the F_i relations are given by:

$$x_i^t(\lambda) = x_i^e + \sum_{k=1}^{N_{unc}} u_k \Delta_{ik}$$

and if there is a large number of uncertainties, the u_k are independent and none of the Δ_{ik} for a non-Gaussian-like u_k dominate then we know that the sum will be approximately Gaussian distributed. One way to express this fact is simply to assume that all the uncertainties are Gaussian distributed. In this case, we recover the usual expression for the likelihood.

A direct consequence is that if there are a few uncertainties that dominate a measurement, then we certainly need to know their distribution. See Ref. [8], for an example of a non-Gaussian dominant uncertainty in a real life experiment.

[§] if there are correlations between the u_i replace $\prod_{j=1}^{N_{unc}} f^j(u_j)$ by $f(u_1, u_2, ..., u_{N_{obs}})$ the global probability distribution of the $\{u\}$

¶ or can be considered as Gaussian distributed, see later

[‖] with an explicit statement that the uncertainties can be assumed to be Gaussian distributed

3.5. Luminosity Uncertainty

We now turn to the calculation of the likelihood when there is a normalization uncertainty, like the Luminosity uncertainty. The F relation of Eq. 14 is given by:

$$\mathcal{L}\lambda = x^e + u_1\Delta_1, \tag{20}$$

where we have assumed that we are measuring the parameter directly, $x^t = \lambda$. The Luminosity, $\mathcal{L}$, has also an uncertainty:

$$\mathcal{L} = \mathcal{L}_0 + u_2\Delta_2. \tag{21}$$

We assume that both u_1 and u_2 are Gaussian distributed. Replacing Eq. 21 in Eq. 20, we obtain:

$$\mathcal{L}_0\lambda - x^e = u_1\Delta_1 - u_2\Delta_2 x^t. \tag{22}$$

This expression shows that $\mathcal{L}_0\lambda - x^e$ is the sum of two Gaussian, such that the likelihood is a Gaussian distribution with the standard deviation given by:

$$\sigma^2 = \Delta_1^2 + (\Delta_2 x^t)^2. \tag{23}$$

The systematic uncertainty due to the Luminosity uncertainty is proportional to the theory. Explicitly:

$$P(x^e|\lambda) = \frac{1}{\sqrt{2\pi}\sqrt{\Delta_1^2 + (\Delta_2\lambda)^2}} e^{-\frac{(L_0\lambda - x^e)^2}{2(\Delta_1^2 + (\Delta_2\lambda)^2)}} \tag{24}$$

This result can also be derived from the general expression of the likelihood, after doing the appropriate integral analytically.

A few remarks are in order. In this case, even though all the uncertainties are Gaussian distributed, the minimization of the χ^2 would not maximize the likelihood because the theory appears in the normalization of the likelihood. Another mistake that leads to problems in this case is to replace λ by $x^e/\mathcal{L}_0$ in the uncertainty. This mistake leads to a downwards bias. If x^e has a downward statistical fluctuation, a smaller systematic uncertainty is assigned to it, such that when it is combined with other measurements, it is given a larger weight than it should.

This example shows clearly that we have to know if the uncertainties are proportional to the theory or to the experimental value. Assuming one when the other is correct can lead to problems. It is clear that many other systematic uncertainties depend on the theory and that should also be taken into account.

4. Sources of uncertainties

There are many sources of uncertainties beside the experimental uncertainties. They either have to be shown to be small enough to be neglected or they need to be included in the PDF uncertainties. For examples: variation of the renormalization and factorization scales; non-perturbative and nuclear binding effects; the choice of functional form of the input PDF at the initial scale; accuracy of the evolution; Monte-Carlo uncertainties; and dependence on theory cut-off.

5. Current fit

Draconian measures were needed to restart from scratch and re-evaluate each issue. We fixed the renormalization and factorization scales, avoided data affected by nuclear binding and non-perturbative effects, and use a MRS-style parametrization for the input PDFs. The evolution of the PDFs is done by Mellin transform method, see Ref. [9]. All the quarks are considered massless. We imposed a positivity constraint on F2. A positivity constraint on other "observables" could also be imposed.

At the moment we are using H1 and BCDMS (proton data) measurement of F_2^p for our core set. In order to be able to use these data we have to assume that all the uncertainties are Gaussian distributed **. We then can calculate the $\chi^2(\lambda)$ and $P(\lambda)$ ($\approx \exp -\chi^2/2$) with all the correlations taken into account ††. We generated 50000 unit-weighted PDFs according to the probability function. For 532 data points, we obtained a minimum χ^2 of 530 for 24 parameters. We have plotted in Fig. 1, the probability distribution of some of the parameters. Note that the first parameter is α_s. The value is smaller than the current world average. However, it is known that the experiments we are using prefer a lower value of this parameter, see Ref. [10], and as already pointed out, our current uncertainties are lower limits. Note that the distribution of the parameter is not Gaussian, indicating that the asymptotic region is not reached yet. In this case, the blind use of the so-called chi-squared fitting method might be misleading.

From this large set of PDFs, it is straightforward to plot, for example, the correlation between different parameters and to propagate the uncertainties to other observables. In Fig. 2, the correlation between α_s and λ_g is presented. λ_g parametrizes the small Bjorken-x behavior of the gluon distribution function at the initial scale: $xg(x) \sim x^{-\lambda_g}$. The lines are constant probability density levels that are characterized by a percentage, α, which is defined such that $1-\alpha$ is the ratio of the probability density corresponding to the

** no information being given about the distribution of the uncertainties

†† here we assumed that none of the systematic uncertainties depend on the theory

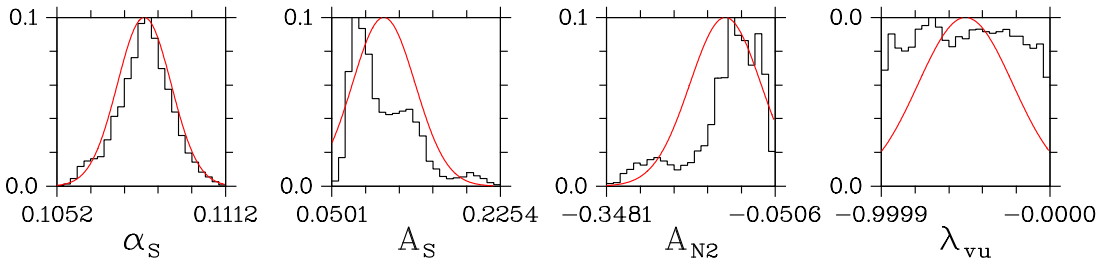

Figure 1. Plot of the distribution (black histograms) of four of the parameters. The first one is α_s, the strong coupling constant at the mass of the Z-boson. The line is a Gaussian distribution with same average and standard deviation as the histogram

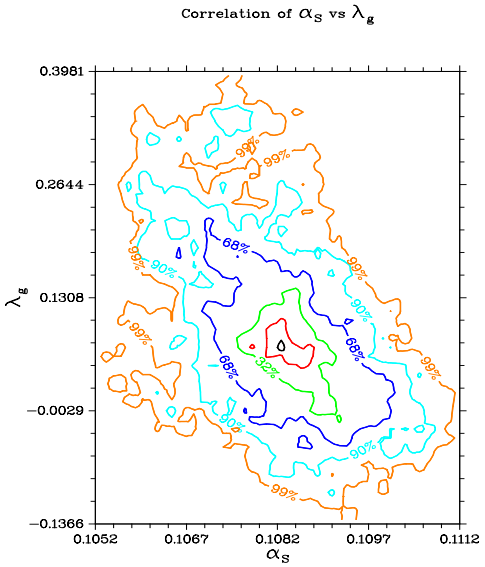

Figure 2. Correlation between two of the parameters: α_s and λ_g, see the text for their definition. Constant probability density levels are plotted.

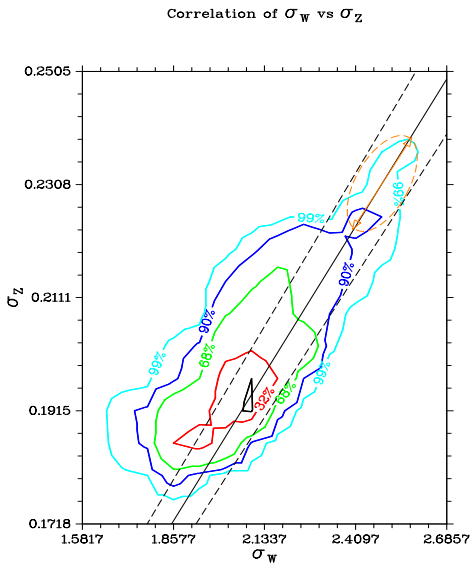

Figure 3. Correlation between the production cross sections for the W and Z vector bosons at the Tevatron, σ_W and σ_Z (in nbarns, includes leptonic branching fraction). The solid and dashed lines show the constraint due to the CDF measurement of the cross section ratio.

level to the maximum probability density.

In Fig. 3, we show the correlation between two observables, the production cross sections for the W and Z vector bosons at the Tevatron along with the experimental result from CDF. The constant probability density levels are shown. The agreement between the theory and the data is qualitatively good.

In Fig. 4, we present data-theory for the lepton charge asymmetry in W decay at the Tevatron. The data are the CDF result [11] and the theory correspond to the average value over the PDF sets for each data point, as defined in Eq. 1. The dashed line are the theory plots corresponding to the one standard deviation over the PDF sets, also defined in Eq. 1. The inner error bars are the statistical and systematic uncertainties added in quadrature[‡‡]. The outer error bar correspond to the experiment and theory uncertainties added in quadrature. The theory uncertainty is the uncertainty associated with the Monte-Carlo integration, the factorization and renormalization scale dependence are small and can be neglected. 5000 PDFs were used

[‡‡]The distribution of the uncertainties and the point to point correlation of the systematic uncertainties were not published such that we had to assume Gaussian uncertainties and no correlation

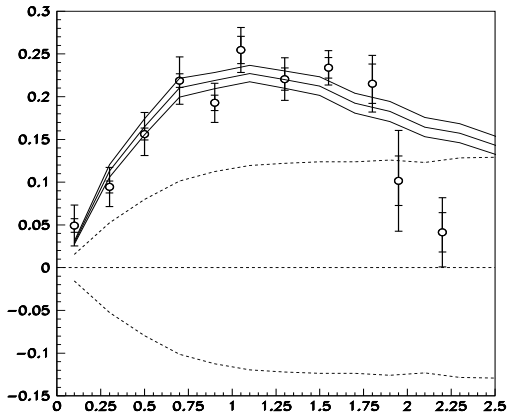

Figure 4. Data-theory for the lepton charge asymmetry in W decay at the Tevatron.

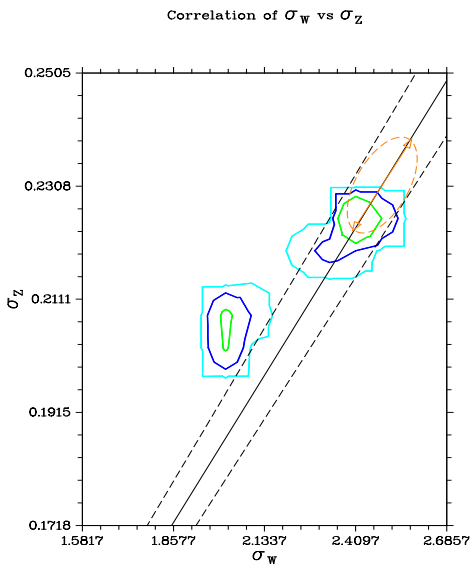

Figure 5. Same as in Fig. 3 for the weighted PDFs.

to generate this plot. It is well known that the data we have included so far in our fit mainly constraint the sum of the quark parton distribution weighted by the square of the charges. The lepton charge asymmetry is sensitive to the ratio of up-type to down-type quark and is therefore not well constraint. We can add this data set by simply weighting each PDF from our set with the likelihood of the new data. The resulting new range of the theory (calculated with weighted sums) is given by the band of solid curves in Fig 4.

The effect of the inclusion of the lepton charge asymmetry can be seen in Fig. 5, where the correlation between the W and the Z cross section is shown again but for the weighted PDFs. The agreement with the data is better than before, but the probability density has now two maxima.

It has been argued that for Run II at the Tevatron, the measurement of the number of W and Z produced could be used as a measurement of the Luminosity. That of course requires the knowledge of the cross section with a small enough uncertainties. In Fig. 6, the luminosity probability distribution is presented for the unit-weighted and weighted PDF sets along with the the luminosity used by CDF. The plot for the weighted set has also two maxima, has in Fig. 5.

5.1. Conclusions

In conclusion, we remind the reader again that all the results should be taken as illustration of the method and that not all the uncertainties have been included in the fitting.

REFERENCES

1. A. D. Martin, R. G. Roberts, W. J. Stirling, and R. S.Thorne, Eur. Phys. J. **C4** (1998) 463-496.
2. S. Alekhin, hep-ph/9611213, recently published in Eur. Phys. J. **C10** (1999) 395-403.
3. W. Giele and S. Keller, Phys. Rev. **D58** (1998) 094023.
4. see, for example, G. D'Agostini, Probability and Measurement Uncertainty in Physics - a Bayesian Primer, hep-ph/9512295; and CERN-99-03.
5. Numerical Recipes in C, Second Edition, W. H. Press, S. A. Teukolsky, W. T. Vetterling, and B. P. Flannery. Cambridge University Press.
6. R. D. Cousins and G. J. Feldman, Phys. Rev. **D57** (1998) 3873-3889.
7. Workshop on 'Confidence Limits', 17-18 January 2000, CERN, organized by F. James and L. Lyons.
8. R. Hirosky, these proceedings.
9. D. Kosower, Nucl.Phys. **B520** (1998) 263278; ibid. **B506** (1997) 439-467.
10. Fig. 21 in Ref. [1]. S.K. thanks W. J. Stirling for pointing this out.
11. CDF collaboration, Phys. Rev. Lett. 81 (1998) 5754-5759.

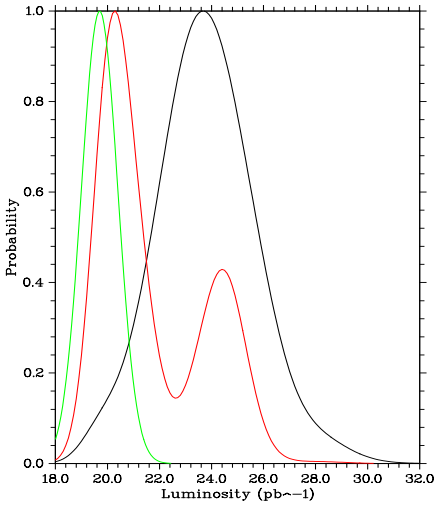

Figure 6. Probability distribution of the luminosity (run1a in pb^{-1}) for the unit-weighted (right plot) and weighted (middle plot) PDFs, compared to the value used by CDF (left plot).

EXPERIMENTAL UNCERTAINTIES AND THEIR DISTRIBUTIONS IN THE INCLUSIVE JET CROSS SECTION.

R. Hirosky
University of Illinois, Chicago, IL 60607

1. Introduction

This workshop has been an important channel of communication between those performing global parton distribution function (pdf) fits and the experimental groups who provide the data at the Tevatron. In the particular case of jets analyses we have initiated a detailed dialog on the sources and distributions of experimental uncertainties. As part of my participation in the workshop, I have used the DØ inclusive jet cross section as an example of a jet measurement with a complex ensemble of uncertainties and have provided descriptions of each component uncertainty. Such dialogs will prove crucial in obtaining the best constraints on allowable pdf models from the data.

2. Uncertainties on the CDF and DØ inclusive jet cross sections

In the first meeting we summarized the jet inclusive cross section measurements from the DØ [1] and CDF [2] experiments. In particular, we illustrated the major corrections applied to the data, namely jet E_T scale and E_T resolution corrections, as well as the derivation methods for these corrections employed by each experiment. To review these methods see [3]-[4] and references therein.

The uncertainties by component in the CDF and DØ inclusive jet cross sections are shown in Figs.1-2. Each component of the uncertainty reported for the CDF cross section is taken to be completely correlated across jet E_T, while individual components are independent of one another. The DØ uncertainties (shown here symmetrized) are also independent of one another, however each component may be either fully or partially correlated across jet E_T. In the case of the energy scale uncertainty the band shown is constructed from eight subcomponents.

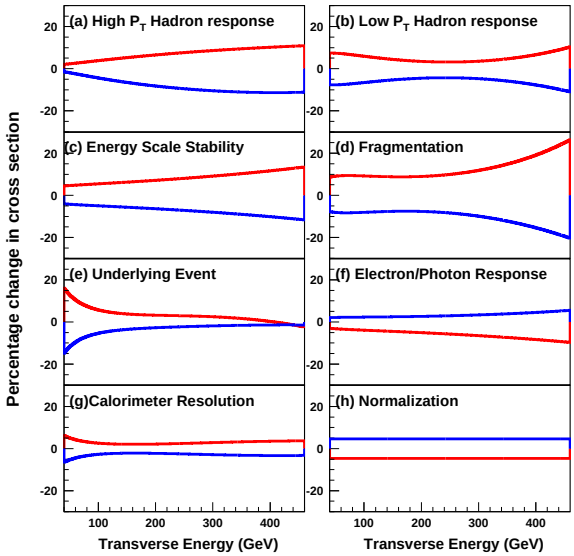

Figure 1. Uncertainties by component in the CDF inclusive jet cross section, $1/(\Delta\eta\Delta E_T)\int\int d^2\sigma/(dE_T d\eta)dE_T d\eta$, $0.1 < |\eta| < 0.7$

2.1. Comparisons with theory

The two experiments have used various means to compare their measurements to theoretical predictions. CDF has published a comparison of their cross section to a next-to-leading order (NLO) QCD calculation using a variety of pdf models by means of various normalization-insensitive, shape-dependent statistical measures [2] (Kolmogorov-Smirnov, Cramèr-VonMises, Anderson-Darling). DØ has formulated a covariance matrix using each uncertainty component in the cross section and its E_T correlation information and employed a χ^2 test to compare to NLO QCD [1].

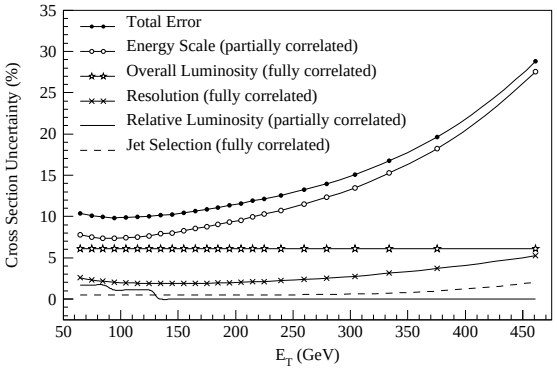

Figure 2. Uncertainties by component in the DØ inclusive jet cross section, $1/(\Delta\eta\Delta E_T)\int\int d^2\sigma/(dE_T d\eta)dE_T d\eta$, $|\eta| < 0.5$

It is difficult to generalize the various shape statistics to include non-trivial correlations in the systematic uncertainties and although correlations may be easily added to a covariant error matrix χ^2 tests can show biases when faced with correlated scale errors. Reference [6] illustrates how correlated scale errors may lead to biases in parameter estimation by noting that systematic errors reported as a fraction of the observed data can be evaluated as artificially small when applied to a point that fluctuates low. This bias may be mitigated by parameterizing the systematic scale errors as percentages of a smooth model of the data or by placing them on the smooth theory directly (see contributions to these proceedings by W. Giele, S. Keller, and D. Kosower).

Other difficulties arise in interpretation of χ^2 probabilities when uncertainties show large correlations. The probability that a prediction agrees with the data for a given χ^2 is calculated assuming that the χ^2 follows the distribution:

$$f(x;n) = \frac{(x)^{(n/2-1)}exp(x/2)}{2^{(n/2)}\Gamma(n/2)} \quad (1)$$

where n is the number of degrees of freedom of the data set. The probability of getting a worse value of χ^2 than the one obtained for the comparison is given by:

$$P(\chi^2;n) = \int_{\chi^2}^{\infty} f(x;n)dx \quad (2)$$

Hence, to verify the accuracy of the probabilities quoted in the recent DØ cross section papers (inclusive jet cross section [1] and dijet mass spectrum [7]), the χ^2 distribution may be compared to Equation 1 with the appropriate number of degrees of freedom. The χ^2 distribution for the DØ dijet mass spectrum was tested by developing a Monte Carlo program [8] that generates many trial experiments based an ansatz cross section determined from the best smooth fit to the data (with a total of 15 bins, or 15 degrees of freedom). The first step generated trials based on statistical fluctuations taking the true number of events per bin as given by the ansatz cross section. The trial spectra were then generated for each bin according to Poisson statistics. The χ^2 for each of these trials was calculated using the difference between the true and the generated values. Figure 3 (solid curve) shows the χ^2 distribution for all of the generated trials. The distribution agrees well with Equation 1 for 15 degrees of freedom. The next step assumes that the uncertainties correlated as in the measurement of the dijet mass cross section. Trial spectra are generated using these uncertainties to generate a χ^2 distribution (see the dotted curve in Fig. 3). It is clear that χ^2 distribution very similar to the curve predicted by Equation 1. Hence, any probability generated using Equation 2 will be approximately correct. The resulting χ^2 distribution was fitted by Equation 1 and the resulting fit is consistent with the distribution if 14.6 degrees of freedom are assumed.

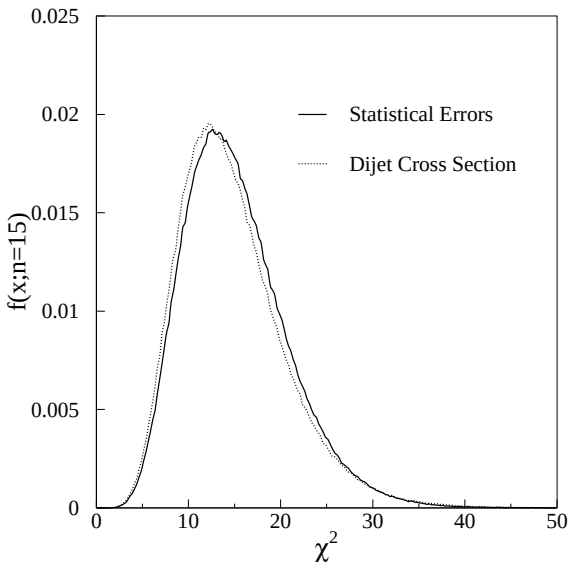

Figure 3. χ^2 distribution for random fluctuations around the nominal DØ Dijet Mass cross section. (Solid) Errors are fluctuated as uncorrelated. (Dashed) E_T correlations are included.

A similar test using the DØ inclusive jet cross section finds the distributions shown in Fig. 4. The two distributions agree well for χ^2 values below approximately 15 and then begin to diverge slowly. The distribution based on the cross section uncertainties includes a larger tail than the χ^2 distribution generated with the wholly uncorrelated uncertainties, implying that probabilities based on a χ^2 analysis will be slightly underestimated. See also the talks by B. Flaugher in this workshop for additional observations and comments on χ^2 analyses.

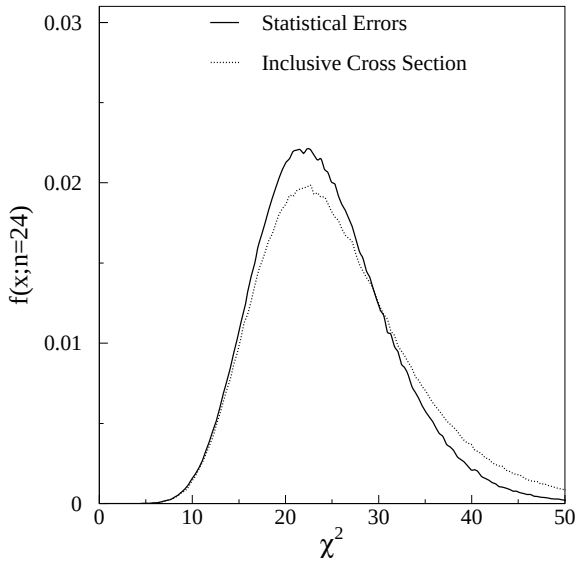

Figure 4. χ^2 distribution for random fluctuations around the nominal DØ inclusive jet cross section. (Solid) errors are fluctuated as uncorrelated. (Dashed) E_T correlations are included.

Consider an E_T-independent jet E_T scale error of 2%. What is it's effect on an inclusive jet cross section versus E_T? Jets are shifted bin-to-bin by fluctuating their E_T values within the 2% range and as a result of the steeply falling cross section, more jets from low E_T values are shifted into higher E_T bins by one extreme of this scale uncertainty than the in reverse shift for higher E_T jets. Figure. 5 shows how a flat 2% E_T scale uncertainty alters the measured cross section using a smooth fit to the DØ data as the nominal cross section model. In general the degree of this asymmetry will depend on the steepness of the measured distribution. In order to define a covariance matrix, such errors are typically symmetrized.

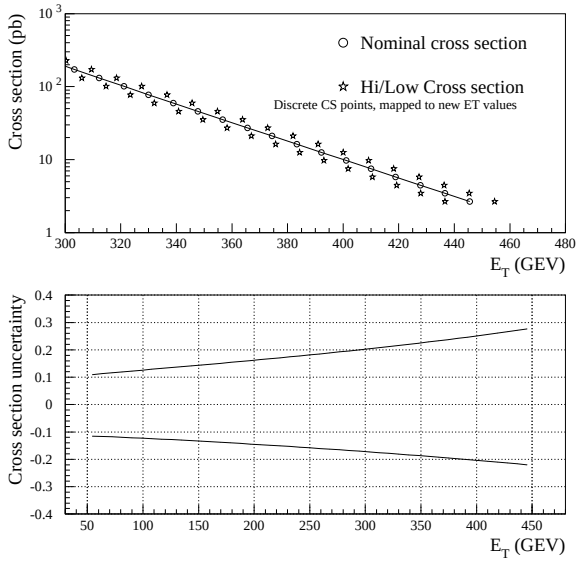

Figure 5. Example of a 2% E_T scale error propagated through an inclusive jet cross section measurement.

3. Beyond the *Normal* assumption

Independent of any difficulties due to correlated uncertainties, a χ^2 test necessarily relies on the assumption that the uncertainties follow a normal distribution. This may be a reasonable approximation in some cases. Upon close inspection we expect this assumption to be generally false for most rapidly varying observables (i.e. steeply falling cross section measurements). Perhaps, as in the most obvious case, some experimental uncertainties will simply be non-Gaussian in their distribution and furthermore symmetric uncertainties in the abscissa variable will develop into asymmetric uncertainties when propagated through to the measured distribution. The latter case is illustrated as follows.

The use of an approximate covariance matrix will also result in a loss of sensitivity when errors are shown to follow distributions with tails smaller than in a normal distribution. As an example we show a correction factor with uncertainties of this type from the DØ jet cross section analysis in Fig. 6. This figure shows the hadronic response correction for jets as a function of jet energy. The correction is derived from an analysis of $\gamma + jet$ data [4]. The bands delimit regions that contain ensembles of deviations from the nominal response within certain confidence limits. It is evident that in this case assuming the uncertainty follows a normal distribution with variance equal to the 68% limits shown will tend of underestimate the sensitivity

of the data for excluding certain classes of theories. Figure 7 shows the range of cross section uncertainty due to the response component only as a function of confidence level for several E_T values of the DØ cross section.

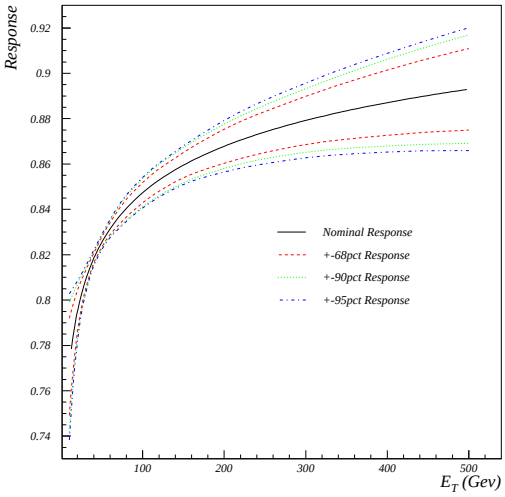

Figure 6. DØ Jet response correction versus Energy. The outer bands show the extreme deviation in response at a given confidence level as a function of jet energy.

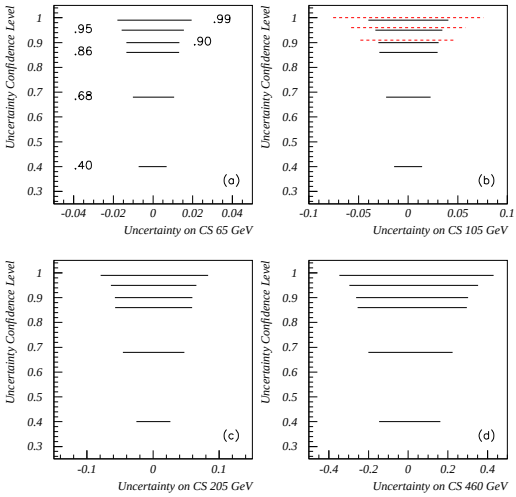

Figure 7. DØ response uncertainty propagated through the inclusive jet cross section measurement at various E_T values. The solid bands represent extreme variations at various confidence levels. The dashed bands illustrate the overestimation of these variations by using a Gaussian approximation.

4. Application to pdf constraints

In this workshop W. Giele, S. Keller, and D. Kosower have reported on a method for extracting pdf distributions with quantitative estimates of pdf uncertainties. In effect their method [5] uses a Bayesian approach that integrates sets of pdf parameterizations over properly weighted samples of experimental uncertainties to produce a set of pdf models consistent with the data within a given confidence level. The basic method may be extended to use data with arbitrary error distributions and correlations. For such methods to function reliably the experiments must be able to provide detailed descriptions of their error distributions. Giele et al. make a distinction between 'errors on the data' and 'errors on the theory' for estimation of the most likely pdf models. In this context we take only uncertainties depending directly on the number of events in a bin as 'errors on the data'. Other typical sources of uncertainty, luminosity, energy scale, resolution, etc., may be treated as 'errors on the theory' in that they are in some sense independent of the statistical precision of the data and represent how an underlying, *true*, distribution may be distorted by observation in the experiment.

As a result of these dialogs, we have revisited the DØ response uncertainty (our largest uncertainty in the inclusive jet cross section measurement) from Fig. 6 and generated a sampling of the probability density function for distributions in it parameters. This probability density function contains all the relevant information on both the shape of the uncertainty distribution and point-to-point correlations. It is clear that providing such information is a significant enhancement from traditional methods of summarizing experimental uncertainties. Optimum utilization of the data demands a detailed understanding and reporting of its associated uncertainties. Through our fruitful discussions in this workshop, we look forward to setting an example for the reporting of experimental uncertainties and to fully exploiting our cross section data in pdf analyses in the near future.

REFERENCES

1. B. Abbott *et al.*, Phys. Rev. Lett. **82**, 2451 (1999).
2. F. Abe *et al.*, Phys. Rev. Lett. **77**, 438 (1996).

3. G. Blazey and B. Flaugher, Ann. Rev. of Nucl. and Part. Sci., Vol. 49, (1999), FERMILAB-Pub-99/038-E.
4. "Determination of the Absolute Jet Energy Scale in the DØ Calorimeters", B. Abbott *et al.*, Nucl. Instrum. Methods Phys. Res. A**424**, 352 (1999); Fermilab-Pub-97/330-E; hep-ex/9805009.
5. W. Giele and S. Keller, Phys. Rev. **D58** (1998) 094023.
6. G. D'Agostini, hep-ph/9512295.
7. DØ Collaboration, B. Abbott *et al.,* Phys. Rev. Lett. **82**, 245t (1999).
8. Thanks to Iain Bertram for providing χ^2 studies with the Monte Carlo method.

PARTON DENSITY UNCERTAINTIES AND SUSY PARTICLE PRODUCTION

T. Plehn[a,†] and M. Krämer[b,‡]

a) Department of Physics, University of Wisconsin, Madison WI 53706, USA; b) Department of Physics and Astronomy, University of Edinburgh, Edinburgh EH9 3JZ, Scotland.

Abstract

Parton densities are important input parameters for SUSY particle cross section predictions at the Tevatron. Accurate theoretical estimates are needed to translate experimental limits, or measured cross sections, into SUSY particle mass bounds or mass determinations. We study the PDF dependence of next-to-leading order cross section predictions, with emphasis on a new set of parton densities [1]. We compare the resulting error to the remaining theoretical uncertainty due to renormalization and factorization scale variation in next-to-leading order SUSY-QCD.

1. Introduction

The search for supersymmetric particles is among the most important endeavors of present and future high energy physics. At the upgraded $p\bar{p}$ collider Tevatron, the searches for squarks and gluinos (and especially the lighter stops and sbottoms), as well as for the weakly interacting charginos and neutralinos, will cover a wide range of the MSSM parameter space [2,3].

The hadronic cross sections for the production of SUSY particles generally suffer from unknown theoretical errors at the Born level [4]. For strongly interacting particles the dependence on the renormalization and factorization scale has been used as a measure for this uncertainty, leading to numerical ambiguities of the order of 100%. For Drell-Yan type weak production processes the dependence on the factorization scale is mild. However, a comparison of leading and next-to-leading order predictions [5] reveals that the impact of higher-order corrections is much larger than the estimate through scale variation would have suggested. The use of next-to-leading order calculations [5–7] is thus mandatory to reduce theoretical uncertainties to a level at which one can reliably extract mass limits from the experimental data.

†Supported in part by DOE grant DE-FG02-95ER-40896 and in part by the University of Wisconsin Research Committee with funds granted by the Wisconsin Alumni Research Foundation
‡Supported in part by the EU Fourth Framework Programme 'Training and Mobility of Researchers', Network 'Quantum Chromodynamics and the Deep Structure of Elementary Particles', contract FMRX-CT98-0194 (DG 12 - MIHT)

In addition to the scale ambiguity and the impact of perturbative corrections beyond next-to-leading order, hadron collider cross section are subject to uncertainties coming from the parton densities and the associated value of the strong coupling. Previously, the only way to estimate the PDF errors was to compare the best-fit results from various global PDF analyses. Clearly, this is not a reliable measure of the true uncertainty. As a first step towards a more accurate error estimate, the widely used sets CTEQ [8] and MRST [9] now offer different variants of PDF sets, *e.g.* using different values of the strong coupling constant. In this letter we compare their predictions to the preliminary GKK parton densities [1], which provide a systematic way of propagating the uncertainties in the PDF determination to new observables.

2. Stop Pair Production

For third generation squarks the off-diagonal left-right mass matrix elements do not vanish, but lead to mixing stop (and sbottom) states. The lighter mass eigenstate, denoted as $\tilde{t}_1$, is expected to be the lightest strongly interacting supersymmetric particle. Moreover, its pair production cross section, to a very good approximation, only depends on the stop mass, in contrast to the light flavor squark production. Nevertheless, considering the different decay channels complicates the analyses [3,10]. At the Tevatron the fraction of stops produced in quark-antiquark annihilation and in gluon fusion varies strongly with the stop mass. Close to threshold the valence quark luminosity is dominant, but for lower masses a third of the hadronic cross section can be due to incoming gluons [7].

In Figure 1 we compare the total $\tilde{t}_1$-pair production cross sections for three sets of parton densities: only for incoming quarks do the CTEQ4 and MRST99 results lie on top of each other. For gluon fusion the corresponding cross sections differ by $\sim 10\%$. The GKK set centers around a significantly smaller value. This is in part due to the low average value $\langle \alpha_s(\text{GKK}) \rangle = 0.108$, which is expected to increase after including more experimental information in the GKK analysis. But even the normalized cross section σ/α_s^2 is still smaller by 35% compared to CTEQ4 and MRST99 because of the entangled fit of the strong coupling constant and the parton densities. However, the width of the Gaussian fit to the GKK results gives an uncertainty of 2% and 8% for the quark-antiquark and gluon fusion channel, similar to the difference between CTEQ4 and MRST99.

For heavier stop particles, Figure 2, the gluon luminosity is strongly suppressed due to the large final state mass, and mainly valence quarks induced processes contribute to the cross section. The Gaussian distribution of the GKK results has a width of $\sim 2\%$. The comparably large difference between CTEQ4 and MRST99 is caused by the small fraction of gluon induced processes, since the gluon flux at large values of x differs for CTEQ4 and MRST99 by approximately 40%.

3. Chargino/Neutralino Production

The production of charginos and neutralinos at the Tevatron is particularly interesting in the trilepton $\tilde{\chi}_2^0 \tilde{\chi}_1^\pm$ and the light chargino $\tilde{\chi}_1^+ \tilde{\chi}_1^-$ channels [11]. The next-to-leading order corrections to the cross sections [5] reduce the factorization scale dependence, but at the same time introduce a small renormalization scale dependence. A reliable estimate of the theoretical error from the scale ambiguity will thus only be possible beyond next-to-leading order.

The Gaussian distribution of the GKK parton densities for light chargino pairs is shown in Figure 3. For the chosen mSUGRA parameters ($m_0 = 100$ GeV, $A_0 = 300$ GeV, $m_{1/2} = 150$ GeV) the width is $\sim 2\%$, as one would expect from the quark-antiquark channel of the stop production. But in contrast to the stop production, where all quark luminosities add up, the chargino/neutralino channels can be extremely sensitive to systematic errors in different parton densities due to destructive interference between s and t channel diagrams. The total trilepton cross section for example will therefore be a particular challenge for a reliable error estimate.

4. Outlook

We have briefly reviewed the status of the theoretical error analysis of SUSY cross sections at the Tevatron. For strongly interacting final state particles, the inclusion of next-to-leading order corrections reduces the renormalization and factorization scale ambiguity to a level $\lesssim 10\%$ where the size of the PDF errors becomes phenomenologically relevant. We have compared different recent PDF sets provided by the CTEQ [8] and MRST [9] collaborations to the preliminary GKK parton densities [1]. The large spread in the cross section predictions can mainly be attributed to the low average value of the strong coupling associated with the GKK sets. We expect this spread to be reduced once more data have been included in the GKK analysis and the corresponding average value of the strong coupling becomes closer to the world average. For weak supersymmetric Drell-Yan type processes [5] the scale dependence at NLO cannot serve as a measure for the theoretical error since the renormalization

scale dependence is only introduced at NLO. The PDF induced errors for *e.g.* the case of $\tilde{\chi}_1^+\tilde{\chi}_1^-$ production are small; however, interference effects between the different partonic contributions must be taken into account.

The recently available variants of PDF sets provided by CTEQ and MRST and, in particular, the GKK parton densities allow for the first time a systematic exploration of PDF uncertainties for the prediction of SUSY particle cross sections. The preliminary GKK results do not yet allow a conclusive answer, but they point the way towards a complete and reliable error analysis in the near future.

Acknowledgments

The authors want to thank W. Beenakker, R. Höpker, M. Spira, P.M. Zerwas, and M. Klasen for the collaboration during different stages of this work. Furthermore we are grateful to S. Keller who triggered this analysis by making his preliminary set of parton densities available to us.

REFERENCES

1. W. Giele, S. Keller, D. Kosower, contributions to this volume.
2. M. Carena, R.L. Culbertson, S. Reno, H.J. Frisch, and S. Mrenna, ANL-HEP-PR-97-98, hep-ph/9712022 and references therein.
3. R. Demina, J.D. Lykken, K.T. Matchev, and A. Nomerotski, hep-ph/9910275.
4. G.L. Kane and J.P. Leveillé, Phys. Lett. **B112** (1982) 227; P.R. Harrison and C.H. Llewellyn Smith, Nucl. Phys. **B213** (1983) 223 (Err. Nucl. Phys. **B223** (1983) 542); E. Reya and D.P. Roy, Phys. Rev. **D32** (1985) 645; S. Dawson, E. Eichten and C. Quigg, Phys. Rev. **D31** (1985) 1581; H. Baer and X. Tata, Phys. Lett. **B160** (1985) 159.
5. H. Baer, B.W. Harris and M.H. Reno, Phys. Rev. **D57** (1998) 5871; W. Beenakker, T. Plehn, M. Klasen, M. Krämer, M. Spira, and P.M. Zerwas, Phys. Rev. Lett. **83** (1999) 3780.
6. W. Beenakker, R. Höpker, M. Spira, and P.M. Zerwas, Nucl. Phys. **B492** (1995) 51.
7. W. Beenakker, M. Krämer, T. Plehn, M. Spira, and P.M. Zerwas, Nucl. Phys. **B515** (1998) 3.
8. H.L. Lai, J. Huston, S. Kuhlmann, F. Olness, J. Owens, D. Soper, W.K. Tung and H. Weerts, Phys. Rev. **D55** (1997) 1280.
9. A. Martin, R.G. Roberts, W.J. Stirling, and R.S. Thorne, Eur. Phys. J. **C4** (1998) 463.
10. see *e.g.* S. Kraml, H. Eberl, A. Bartl, W. Majerotto, and W. Porod, Phys. Lett. **B386** (1996) 175; A. Djouadi, W. Hollik and C. Jünger, Phys. Rev. **D55** (1997) 6975; W. Beenakker, R. Höpker, T. Plehn, and P.M. Zerwas, Z. Phys. **C75** (1997) 349; J. Guasch, W. Hollik and J. Sola, hep-ph/0001254.
11. see *e.g.* V. Barger and C. Kao, Phys. Rev. **D60** (1999) 115015; K.T. Matchev and D.M. Pierce, Phys. Lett. **B467** (1999) 225; H. Baer, M. Drees, F. Paige, P. Quintana, and X. Tata, hep-ph/9906233.

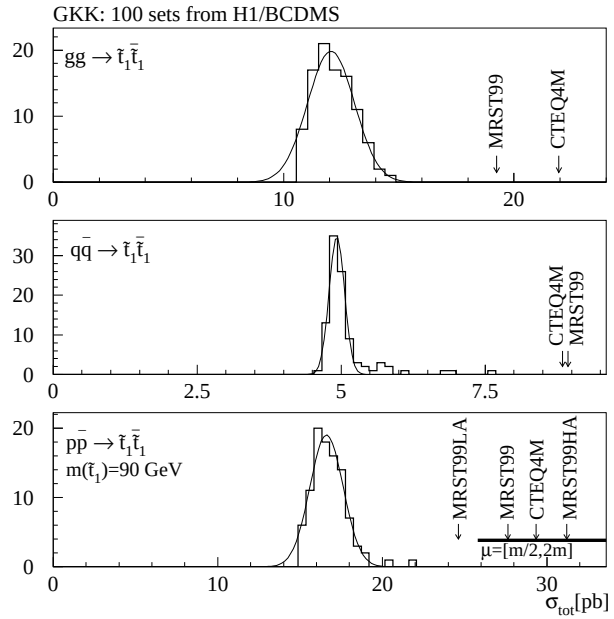

Figure 1. NLO production cross section for a light stop. The Gaussian fits the preliminary GKK parton densities. The renormalization/factorization scale is varied around the average final state mass.

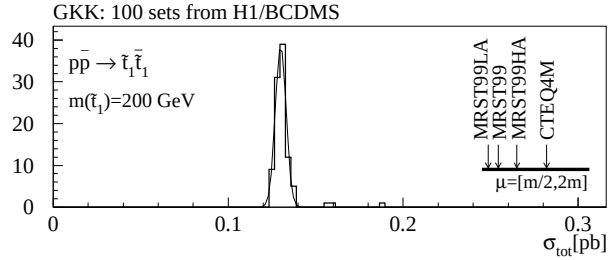

Figure 2. NLO production cross section for a heavier stop, dominated by incoming valence quarks. The Gaussian fits the preliminary GKK parton densities. The renormalization/factorization scale is varied around the average final state mass.

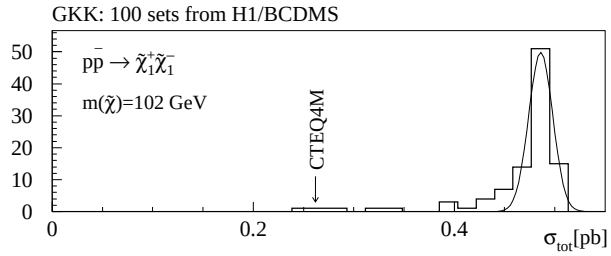

Figure 3. NLO production cross section for the chargino channel $\tilde{\chi}_1^+\tilde{\chi}_1^-$. The Gaussian fits the preliminary GKK parton densities.

SOFT-GLUON RESUMMATION AND PDF THEORY UNCERTAINTIES

George Sterman and Werner Vogelsang[†]

C.N. Yang Institute for Theoretical Physics SUNY at Stony Brook, Stony Brook, NY 11794-3840, USA.

Abstract

Parton distribution functions are determined by the comparison of finite-order calculations with data. We briefly discuss the interplay of higher order corrections and PDF determinations, and the use of soft-gluon resummation in global fits.

1. Factorization & the nlo model

A generic inclusive cross section for the process $A + B \to F + X$ with observed final-state system F, of total mass Q, can be expressed as

$$Q^4 \frac{d\sigma_{AB\to FX}}{dQ^2} = \phi_{a/A}(x_a,\mu^2) \otimes \phi_{b/B}(x_b,\mu^2) \otimes \hat{\sigma}_{ab\to FX}(z,Q,\mu)\,, \quad (1)$$

with $z = Q^2/x_a x_b S$. The $\hat{\sigma}_{ab}$ are partonic hard-scattering functions, $\hat{\sigma} = \sigma_{\rm Born} + (\alpha_s(\mu^2)/\pi)\hat{\sigma}^{(1)} + \ldots$. They are known to NLO for most processes in the standard model and its popular extensions. Corrections begin with higher, uncalculated orders in the hard scattering, which respect the form of Eq. (1). The discussion is simplified in terms of moments with respect to $\tau = Q^2/S$,

$$\tilde{\sigma}_{AB\to FX} = \int_0^1 d\tau\, \tau^{N-1}\, Q^4\, d\sigma_{AB\to FX}/dQ^2 = \sum_{a,b} \tilde{\phi}_{a/A}(N,\mu^2)\, \tilde{\sigma}_{ab\to FX}(N,Q,\mu)\, \tilde{\phi}_{b/B}(N,\mu^2)\,, \quad (2)$$

[†]This work was supported in part by the National Science Foundation, grant PHY9722101.

where the moments of the ϕ's and $\hat{\sigma}_{ab\to FX}$ are defined similarly.

Eqs. (1) and (2) are starting-points for both the determination and the application of parton distribution functions (PDFs), $\phi_{i/H}$, using 1-loop $\hat{\sigma}$'s [1–3] We may think of this collective enterprise as an "NLO model" for the PDFs, and for hadronic hard scattering in general. For precision applications we ask how well we really know the PDFs [4–6]. Partly this is a question of how well data constrain them, and partly it is a question of how well we *could* know them, given finite-order calculations in Eqs. (1) and (2). We will not attempt here to assign error estimates to theory. We hope, however, to give a sense of how to distinguish ambiguity from uncertainty, and how our partial knowledge of higher orders can reduce the latter.

2. Uncertainties, schemes & scales

It is not obvious how to quantify a "theoretical uncertainty", since the idea seems to require us to estimate corrections that we haven't yet calculated. We do not think an unequivocal definition is possible, but we can try at least to clarify the concept, by considering a hypothetical set of nucleon PDFs determined from DIS data alone [4]. To make such a determination, we would invoke isospin symmetry to reduce the set of PDF's to those of the proton, $\phi_{a/P}$, and then measure a set of singlet and nonsinglet structure functions, which we denote $F^{(i)}$. Each factorized structure function may be written in moment space as

$$\tilde{F}^{(i)}(N,Q) = \sum_a \tilde{C}_a^{(i)}(N,Q,\mu)\, \tilde{\phi}_{a/P}(N,\mu^2)\,, \quad (3)$$

in terms of which we may solve for the parton distributions by inverting the matrix $\tilde{C}$,

$$\tilde{\phi}_{a/P}(N,\mu^2) = \sum_i \tilde{C}^{-1}{}_a^{(i)}(N,Q,\mu)\; \tilde{F}^{(i)}(N,Q)\,. \quad (4)$$

With "perfect" $\tilde{F}$'s at fixed Q, and with a specific approximation for the coefficient functions, we could solve for the moment-space distributions numerically, without the need of a parameterization. In a world of perfect data, but of incompletely known coefficient functions, uncertainties in the parton distributions would be entirely due to the "theoretical" uncertainties of the C's:

$$\delta\tilde{\phi}_{a/P}(N,\mu) = \sum_i \delta\tilde{C}^{-1}{}_a^{(i)}(N,Q,\mu)\; \tilde{F}^{(i)}(N,Q)\,. \quad (5)$$

Our question now becomes, how well do we know the C's? In fact this is a subtle question, because the coefficient functions depend on choices of scheme and scale.

Factorization schemes are procedures for defining coefficient functions perturbatively. For example, choosing for F_2 the LO (quark) coefficient function in Eq. (4) defines a DIS scheme (with $\tilde{C}$ independent of μ, which is then to be taken as Q in $\tilde{\phi}$). Computing the C's from partonic cross sections by minimal subtraction to NLO defines an NLO $\overline{\rm MS}$ scheme, and so on. Once the choices of C's and μ are made, the PDF's are defined uniquely.

Evolution in an $\overline{\rm MS}$ or related scheme, enters through

$$\mu\frac{d}{d\mu}\tilde{\phi}_{a/H}(N,\mu^2) \;=\; -\Gamma_{ab}(N,\alpha_s(\mu^2))\,\tilde{\phi}_{b/H}(N,\mu^2)$$
$$\mu\frac{d}{d\mu}\tilde{C}_c^{(i)}(N,Q,\mu) \;=\; \tilde{C}_d^{(i)}(N,Q,\mu)\,\Gamma_{dc}(N,\alpha_s(\mu^2))\,. \quad (6)$$

In principle, by Eq. (6), the scale-dependence of the $C_a^{(i)}$ exactly cancels that of the PDFs in Eq. (3) and, by extension, in Eq. (1). This cancelation, however, requires that each C and the anomalous dimensions Γ be known to all orders in perturbation theory.

To eliminate μ-dependence up to order α_s^{n+1}, we need $\hat{\sigma}$ to order α_s^n and the Γ_{ab} to α_s^{n+1}. One-loop (NLO) QCD corrections to hard scattering require two-loop splitting functions, which are known. The complete form of the NNLO splitting functions, is still somewhere over the horizon [7]. Even when these are known, it will take some time before more than a few hadronic hard scattering functions are known at NNLO.

We can clarify the role of higher orders by relating structure functions at two scales,Q_0 and Q. Once we have measured $F(N,Q_0)$, we may predict $F(N,Q)$ in terms of the relevant anomalous dimensions and coefficient functions by

$$F(N,Q) \;=\; F(N,Q_0)\;\mathrm{e}^{\int_{Q_0}^{Q}\frac{d\mu'}{\mu'}\,\Gamma(N,\alpha_s(\mu'^2))} \times\left[\frac{\tilde{C}(N,Q,Q)}{\tilde{C}(N,Q_0,Q_0)}\right]. \quad (7)$$

This prediction, formally independent of PDFs *and* independent of the factorization scale, has corrections from the next, still uncalculated order in the anomalous dimension and in the ratio of coefficient functions. The asymptotic freedom of QCD gives a special role to LO: only the one-loop contribution to Γ diverges with Q in the exponent, and contributes to the leading, logarithmic scale breaking. NLO corrections already decrease as the inverse of the logarithm of Q, NNLO as two powers of the log. Thus, the theory is self-regulating towards high energy, where dependence on uncalculated pieces in the coefficients and anomalous dimensions becomes less and less important.

The general successes of the NLO model strongly suggest that relations like (7) are well-satisfied for a wide range of observables and values of N (or x) in DIS and other processes. This does not mean, however, that we have no knowledge of, or use for, information from higher orders. In particular, near $x = 1$ PDFs are rather poorly known [8]. At the same time, the ratio of C's depends on N, and if $\alpha_s \ln N$ is large, it becomes important to control higher-order dependence on $\ln N$. This is a task usually referred to as resummation, to which we now turn.

3. Resummation

Let us continue our discussion of DIS, describing what is known about the N-dependence of the coefficient functions C, as a step toward understanding the role of higher orders. Specializing again for simplicity to nonsinglet or valence, the resummed coefficient function may be written as [9,10]

$$\tilde{C}^{\rm res}(N,Q,\mu) = \tilde{C}^{\rm NLO}_{sub}(N,Q,\mu) + C_\delta^{\rm DIS}\,\mathrm{e}^{E_{\rm DIS}(N,Q,\mu)}, \quad (8)$$

where "*sub*" implies a subtraction on $\tilde{C}^{\rm NLO}$ to keep $\tilde{C}^{\rm res}$ exact at order α_s, and where $C_\delta^{\rm DIS}$ corresponds to the NLO N-independent ("hard virtual") terms. The exponent resums logarithms of N:

$$E_{\rm DIS}(N,Q,\mu) \;=\; \int_{Q^2/\bar{N}}^{\mu^2}\frac{d\mu'^2}{\mu'^2}\Big[A(\alpha_s(\mu'^2))\ln(\bar{N}\mu'^2/Q^2) + B(\alpha_s(\mu'^2))\Big], \quad (9)$$

with $\bar{N} \equiv N\mathrm{e}^{\gamma_E}$, and with

$$A(\alpha_s) \;=\; \frac{\alpha_s}{\pi}\,C_F\,\left[1+\frac{\alpha_s}{2\pi}\left(C_A\left(\frac{67}{18}-\frac{\pi^2}{6}\right)-\frac{10}{9}T_F\right)\right]$$
$$B(\alpha_s) \;=\; \frac{3}{2}C_F\frac{\alpha_s}{2\pi}\,. \quad (10)$$

Eq. (10) is accurate to leading (LL) and next-to-leading logarithms (NLL) in N in the exponent: $\alpha_s^m \ln^{m+1} N$ and $\alpha_s^m \ln^m N$, respectively. The N dependence of the ratio $\tilde{C}_2^{\rm res}(N,Q,Q)/\tilde{C}_2^{\rm NLO}(N,Q,Q)$ is shown in Fig. 1, with $Q^2 = 1$, 5, 10, 100 GeV^2. At $N = 1$ the ratio is unity. It is less than unity for moderate N, but then begins to rise, with a slope that increases strongly for small Q. At low Q^2 and large N, higher orders can be quite important. What does this mean for PDFs? We can certainly refit PDFs with resummed coefficient functions, and we see that the high moments of such PDFs are likely to be quite different from those from NLO fits.

To get a sense of how such an NLL/NLO-$\overline{\rm MS}$ scheme might differ from a classic NLO-$\overline{\rm MS}$ scheme, we resort to a model set of resummed distributions, determined

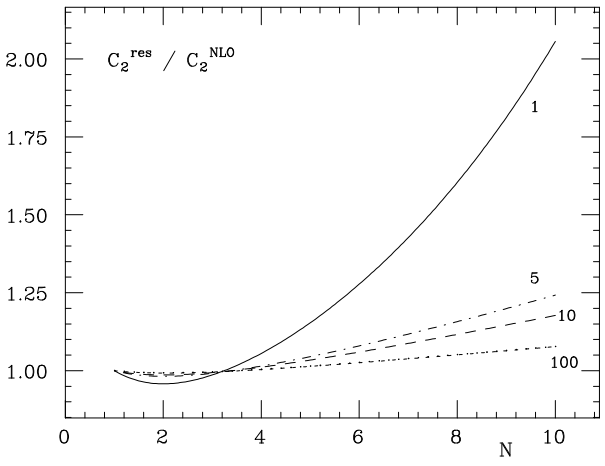

Figure 1. Ratio of Mellin-N moments of resummed and NLO $\overline{\rm MS}$-scheme quark coefficient functions for F_2. The numbers denote the value of Q^2 in GeV^2. We have chosen $\mu = Q$.

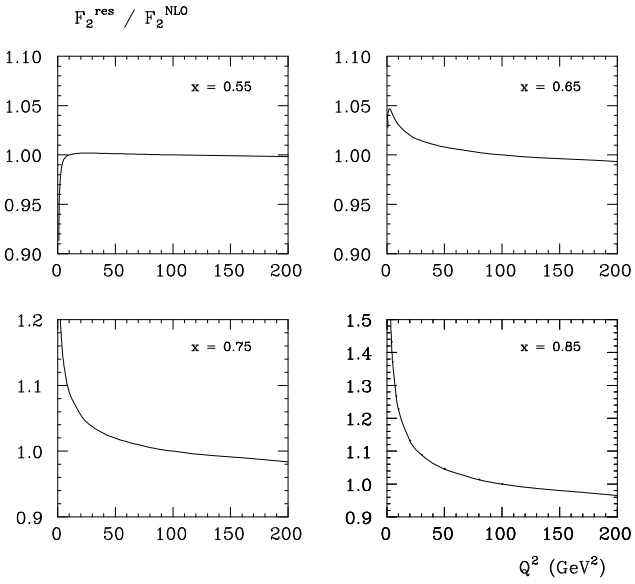

Figure 2. Ratio of the valence parts of the resummed and NLO proton structure function $F_2(x, Q^2)$, as a function of Q^2 for various values of Bjorken-x. For $F_2^{\rm res}$, the 'resummed' parton densities have been determined through Eq. (11).

as follows. We define valence PDFs in the resummed scheme by demanding that their contributions to F_2 match those of the corresponding NLO valence PDFs at a fixed $Q = Q_0$, which is ensured by

$$\tilde{\phi}^{\rm res}(N, Q_0^2) = \tilde{\phi}^{\rm NLO}(N, Q_0^2)\, \frac{\tilde{C}_2^{\rm NLO}(N, Q_0, Q_0)}{\tilde{C}_2^{\rm res}(N, Q_0, Q_0)}\,. \qquad (11)$$

Using the resummed parton densities from Eq. (11), we can generate the ratios $F_2^{\rm res}(x, Q)/F_2^{\rm NLO}(x, Q)$.

The result of this test, picking $Q_0^2 = 100$ GeV^2 is shown in Fig. 2, for the valence $F_2(x, Q)$ of the proton, with $x = 0.55$, 0.65, 0.75 and 0.85. The NLO distributions were those of [2], and the inversion of moments was performed as in [11]. The effect of resummation is moderate for most Q. At small values of Q, and large x, the resummed structure function shows a rather sharp upturn. One also finds a gentle decrease toward very large Q [12]. We could interpret this difference as the *uncertainty* in the purely NLO valence PDFs implied by resummation.

From this simplified example, we can already see that the use of resummed coefficient functions is not likely to make drastic differences in global fits to PDFs based on DIS data, at least so long as the region of small Q^2, of 10 GeV^2 or below, is avoided at very large x. At the same time, it is clear that a resummed fit will make some difference at larger x, where PDFs are not so well known. We stress that a full global fit will be necessary for complete confidence.

4. Resummed hadronic scattering

Processes other than DIS play an important role in global fits, and in any case are of paramount phenomenological interest. Potential sources of large corrections can be identified quite readily in Eq. (2). At higher orders, factors such as $\alpha_s \ln^2 N$, can be as large as unity over the physically relevant range of z in some processes. In this case, they, and their scale dependence can be competitive with NLO contributions. Since they make up well-defined parts of the correction at each higher order, however, it is possible to resum them. To better determine PDFs in regions of phase space where such corrections are important, we may incorporate resummation in the hard-scattering functions that determine PDFs.

The Drell-Yan cross section is the benchmark for the resummation of logs of $1-z$, or equivalently, logarithms of the moment variable N [9],

$$\hat{\sigma}_{q\bar{q}}^{\rm DY}(N, Q, \mu) \;=\; \sigma_{\rm Born}(Q)\, C_\delta^{\rm DY}\, {\rm e}^{E_{\rm DY}(N,Q,\mu)} + \mathcal{O}(1/N)\,. \qquad (12)$$

The exponent is given in the $\overline{\rm MS}$ scheme by

$$E_{\rm DY}(N,Q,\mu) = 2\int_{Q^2/\bar{N}^2}^{\mu^2}\frac{d\mu'^2}{\mu'^2}A(\alpha_s(\mu'^2))\ln\bar{N} + 2\int_{Q^2/\bar{N}^2}^{Q^2}\frac{d\mu'^2}{\mu'^2}A(\alpha_s(\mu'^2))\ln\left(\frac{\mu'}{Q}\right), \quad (13)$$

with A as in Eq. (10), and where we have exhibited the dependence on the factorization scale, setting the renormalization scale to Q. Just as in Eq. (10) for DIS, Eq. (13) resums all leading and next-to-leading logarithms of N.

It has been noted in several phenomenological applications that threshold resummation, and even fixed-order expansions based upon it, significantly reduce sensitivity to the factorization scale [13]. To see why, we rewrite the moments of the Drell-Yan cross section in resummed form as

$$\begin{aligned}\sigma_{AB}^{\rm DY}(N,Q) &= \sum_q \phi_{q/A}(N,\mu)\,\hat{\sigma}_{q\bar{q}}^{\rm DY}(N,Q,\mu)\,\phi_{\bar{q}/B}(N,\mu)\\ &= \sum_q \phi_{q/A}(N,\mu)\,e^{E_{\rm DY}(N,Q,\mu)/2}\sigma_{\rm Born}(Q)\,C_\delta^{\rm DY}\\ &\quad\times\phi_{\bar{q}/B}(N,\mu)\,e^{E_{\rm DY}(N,Q,\mu)/2}+\mathcal{O}(1/N)\,. \quad (14)\end{aligned}$$

The exponentials compensate for the $\ln N$ part of the evolution of the parton distributions, and the μ-dependence of the resummed expression is suppressed by a power of the moment variable,

$$\mu\frac{d}{d\mu}\left[\,\phi_{q/A}(N,\mu)\,e^{E_{\rm DY}(N,Q,\mu)/2}\,\right]=\mathcal{O}(1/N)\,. \quad (15)$$

This surprising relation holds because the function $A(\alpha_s)$ in Eq. (10) equals the residue of the $1/(1-x)$ term in the splitting function P_{qq}. Thus, the remaining N-dependence in a resummed cross section still begins at order α_s^2, but the part associated with the $1/(1-x)$ term in the splitting functions has been canceled to all orders. Of course, the importance of the remaining sensitivity to μ depends on the kinematics and the process. In addition, although resummed cross sections can be made independent of μ for all $\ln N$, they are still uncertain at next-to-next-to leading logarithm in N, simply because we do not know the function A at three loops. Notice that none of these results depends on using PDFs from a resummed scheme, because $\overline{\rm MS}$ PDFs, whether resummed or NLO, evolve the same way. The remaining, uncanceled dependence on the scales leaves room for an educated use of scale-setting arguments [14]. The connection between resummation and the elimination of scale dependence has also been emphasized in [15].

Scale dependence aside, can we in good conscience combine resummed hard scattering functions in Eq. (1) with PDFs from an NLO scheme? This wouldn't make much sense if resummation significantly changed the coefficient functions with which the PDFs were originally fit. As Fig. 2 shows, however, this is unlikely to be the case for DIS at moderate x. Thus, it makes sense to apply threshold resummation with NLO PDFs to processes and regions of phase space where there is reason to believe that logs are more important at higher orders than for the input data to the NLO fits.

At the same time, a set of fits that includes threshold resummation in their hard-scattering functions can be made [10], and their comparison to strict NLO fits would be quite interesting. Indeed, such a comparison would be a new measure of the influence of higher orders. A particularly interesting example might be to compare resummed and NLO fits using high-p_T jet data [3].

5. Power-suppressed corrections

In addition to higher orders in $\alpha_s(\mu^2)$, Eq. (1) has corrections that fall off as powers of the hard-scattering scale Q. In contrast to higher orders, these corrections require a generalization of the *form* of the factorized cross section. Often power corrections are parameterized as $h(x)/[(1-x)Q^2]$ in inclusive DIS, where they begin at twist four. In DIS, this higher twist term influences PDFs when included in joint fits with the NLO and NNLO models, and vice-versa [16–18]. As in the case with higher orders, such "power-improved" fits should be treated as new schemes.

6. Conclusions

The success of NLO fits to DIS and the studies of resummation above suggest that over most of the range of x, theoretical uncertainties of the NLO model are not severe. At the same time, to fit large x with more confidence than is now possible may require including the resummed coefficient functions.

Resummation is especially desirable for global fits that employ a variety of processes, such as DIS and high-p_T jet production, which differ in available phase space near partonic threshold. In a strictly NLO approach, uncalculated large corrections are automatically incorporated in the PDFs themselves. As a result, the NLO model cannot be expected to fit simultaneously the large-x regions of processes with differing logs of $1-x$ in their hard-scattering functions, unless these higher-order corrections are taken into account.

The results illustrated in the figures suggest that these considerations may be important in DIS with Q^2 below a few GeV^2 and at large x, where they may

have substantial effects on estimates of higher twist in DIS. In hadronic scattering, large-N ($x \to 1$) resummation, which automatically reduces scale dependence, may play an even more important role than in DIS.

Acknowledgments

We thank Andreas Vogt and Stephane Keller for useful discussions.

REFERENCES

1. A.D. Martin, R.G. Roberts, W.J. Stirling and R.S. Thorne, Eur. Phys. J. C4 (1998) 463, hep-ph/9803445; hep-ph/9906231.
2. M. Glück, E. Reya and A. Vogt, Eur Phys. J. C5 (1998) 461, hep-ph/9806404.
3. CTEQ Collaboration (H.L. Lai et al.), Eur. Phys. J. C12 (2000) 375, hep-ph/9903282.
4. S. Alekhin, Eur. Phys. J. C10 (1999) 395-403, hep-ph/9611213.
5. J. Huston *et al.*, Phys. Rev. D58 (1998) 114034, hep-ph/9801444.
6. W.T. Giele and S. Keller, Phys. Rev. D58 (1998) 094023, hep-ph/9803393; V. Periwal (1999) Phys. Rev. D59, 094006, hep-ph/9808474.
7. S.A. Larin, T. van Ritbergen and J.A.M. Vermaseren, Nucl. Phys. B427 (1994) 41; S.A. Larin, P. Nogueira, T. van Ritbergen and J.A.M. Vermaseren, Nucl. Phys. B492 (1997) 338, hep-ph/9605317.
8. S. Kuhlmann *et. al.*, hep-ph/9912283.
9. G. Sterman, Nucl. Phys. B 281 (1987) 310; S. Catani and L. Trentadue, Nucl. Phys. B 327 (1989) 323; *ibid* 353 (1991) 183.
10. S. Catani, M.L. Mangano and P. Nason, JHEP 9807 (1998) 024, hep-ph/9806484.
11. S. Catani, M.L. Mangano, P. Nason and L. Trentadue, Nucl. Phys. B478 (1996) 273, hep-ph/9604351.
12. S. Catani, hep-ph/9712442.
13. R. Bonciani, S. Catani, M.L. Mangano and P. Nason, Nucl. Phys. B 529 (1998) 424, hep-ph/9801375; N. Kidonakis and R. Vogt, Phys. Rev. D59 (1999) 074014, hep-ph/9806526; E.L. Berger and H. Contopanagos, Phys. Rev. D57 (1998) 253, hep-ph/9706206; S. Catani, M.L. Mangano, P. Nason, C. Oleari and W. Vogelsang, JHEP 9903 (1999) 025, hep-ph/9903436; E. Laenen and S.-O. Moch, Phys. Rev. D59 (1999) 034027, hep-ph/9809550; N. Kidonakis, hep-ph/9905480; N. Kidonakis and J. Owens, hep-ph/9912388.
14. P.M. Stevenson, Phys. Rev. D 23 (1981) 2916; S.J. Brodsky, G.P. Lepage and P.B. Mackenzie, Phys. Rev. D28 (1983) 228; G. Grunberg, Phys. Lett. B 95 (1984) 70.
15. C.J. Maxwell, hep-ph/9908463.
16. U.K. Yang and A. Bodek, Phys. Rev. Lett. 82 (1999) 2467, hep-ph/9809480.
17. A.L. Kateev, A.V. Kotikov, G. Parente and A.V. Sidorov, Phys. Lett. B 388 (1996) 179, hep-ph/9605367; *ibid* 417 (1998) 374, hep-ph/9706534; hep-ph/9905310.
18. W.L. van Neerven and A. Vogt, hep-ph/9907472; A. Vogt, Phys. Lett. B471 (1999) 97, hep-ph/9910545.

PARTON DISTRIBUTION FUNCTIONS: EXPERIMENTAL DATA AND THEIR INTERPRETATION

L. de Barbaro

Northwestern University, Evanston, IL, USA.

1. Introduction

The last few years have seen both new and improved measurements of deep inelastic and related hard scattering processes and invigorated efforts to test the limits of our knowledge of parton distributions (PDF) and assess their uncertainty. Recent global analysis fits to the wealth of structure functions and related data provide PDFs of substantial sophistication compared to the previous parameterizations [1][2]. The new PDF sets account for correlated uncertainty in strong coupling constant, variation from normalization uncertainty of data sets, theoretical assumptions regarding higher twists effects, initial parameterization form and starting Q_o value, etc. Range of potential variation in gluon density, strange and charm quark densities or, recently, also in d quark distribution [3] are also provided. Participants of this Workshop in the PDF group primarily concentrated on finding new ways of inclusion of systematic uncertainties associated with experimental data into the framework of global analyses. Development in likelihood calculation by Giele, Keller, and Kosower, studies by CDF and D0 collaborators, and a parallel work of CTEQ collaboration are presented in these proceedings.

New or improved results from several experiments have contributed to better knowledge of PDFs, however, there are still areas where the interpretation of experimental data is not clear. Few of these contentious issues will be discussed in this note.

2. Issues in the Interpretation of Experimental Data

2.1. Gluon distribution at moderate to high x

In principle, many processes are sensitive to the gluon distribution, but its measurement is difficult beyond x $>$ 0.2 where it becomes very small. Fermilab second generation– direct photon experiment E706, although quite challenging experimentally, was designed to constrain gluon distribution at high x. For proton-nucleon interactions in LO, direct photons are produced through Compton scattering off gluon ($gq \rightarrow \gamma q$) 90% of the time in the E706 kinematic range.

The first direct photon measurements, as well as WA70 [4] were in agreement with the NLO theory and were used in several generations of global analysis fits. However, series of revisits of theoretical issues in 1990-ties (see, e.g., discussion in [5]) pointed to a large dependence of the NLO calculation on renormalization and factorization scales and necessity to include yet-unknown photon fragmentation function in the calculations. Since the available $\sqrt(s)$ energy is low (20-40 GeV) for the fixed target experiments missing perturbation orders in the calculation are important. Moreover, as shown by the E706 analysis, the transverse momentum of initial state partons (k_T) dramatically affects the differential cross sections measured versus transverse momentum of the outgoing photon (p_T). E706 measured the so-called k_T smearing by observing kinematic imbalance in production of π^o pairs, $\pi^o\gamma$, and double-direct photons and found k_T values $\approx$ 1 GeV and increasing with $\sqrt(s)$ [6]. Similar results are obtained in dijets and Drell-Yan data. K_T is believed to arise from both soft gluon emissions and non-perturbative phenomena. NLO calculations smeared with k_T estimated from these measurements are increased by a factor of 2 to 4 (see Figure 1) and agree with the E706 direct photon and π^0 data on proton and Be targets, at $\sqrt(s)$ of 31 and 38 GeV. A strong indication of k_T effects and the need for soft gluon resummation comes also from the analysis of double direct photon production. Both the NLO resummed theory and k_T smeared NLO theory describe the double direct photon kinematics and cross section very well, in stark contrast to the "plain" NLO prediction [7].

A comparison of current gluon distribution parameterizations indicates our lack of knowledge of gluon in the moderate to high x range, (see Figure 2). The hardest gluon is the CTEQ4HJ distribution. Here the gluon distribution is forced to follow the high E_T inclusive differential jet cross section measured at CDF. Latest PDF sets by CTEQ match the WA70 direct photon data at $\sqrt(s)$=23 GeV with no k_T, and require k_T=1.1 (1.3) GeV/c for the E706 data at $\sqrt(s)$=31 (38) GeV. Due to the difficulty in reconciling this approach no direct photon data is used in the CTEQ5 global analysis. The MRST group chose a different treatment: gluon distributions are reduced at high x to accommodate some k_T smearing for both WA70 and E706 resulting in a moderately good description of the data and three PDF sets spanning the extremes (shown in Figure 2). The variety of predictions agree at low x, but differ widely at high x. The uncertainty in the k_T modeling, its unknown shape versus p_T, and potential discrepancy between WA70 and E706 measurements (see discussions in [6] and [8]) require theoretical work to help resolve this outstanding controversy. Luckily, the interest in direct photon physics and its importance

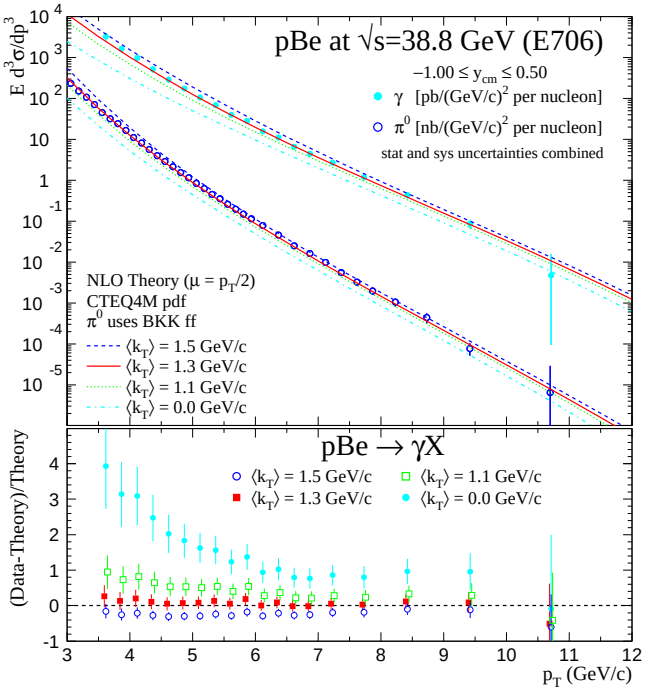

Figure 1. Data and Theory agree after k_T smearing for π^0 and γ production in pBe interactions at 800 GeV. Data-Theory/Theory comparison for various values of k_T is shown in lower insert.

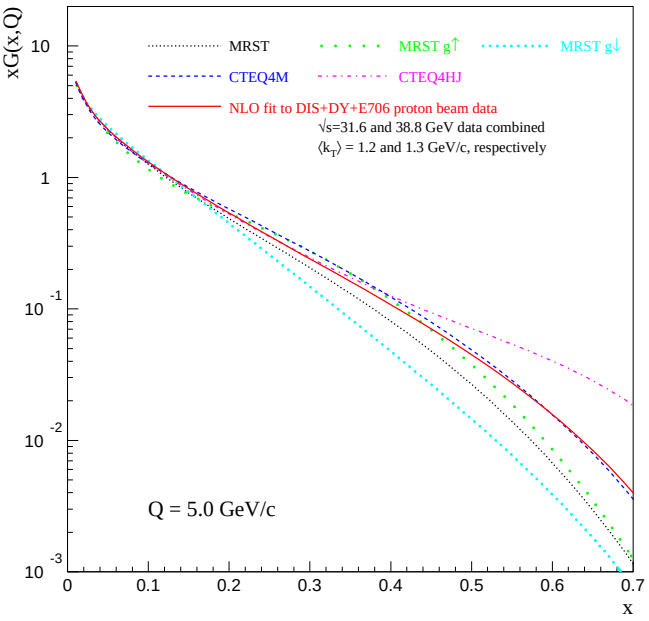

Figure 2. Recent PDF sets indicate substantial disagreement about the shape and size of gluon distribution at moderate to high x. CTEQ5 results closely follow CTEQ4M curve shown here.

for gluon determination has caught on, and 98 and 99 have seen a flurry of publications, notably: "Soft-gluon resummation and NNLO corrections for direct photon production" by N. Kidonakis, J. Owens (hep-ph/9912388), "Results in next-to-leading-log prompt-photon hadroproduction" by S. Catani, M. Mangano, C. Oleari (hep-ph/9912206), "Unintegrated parton distributions and prompt photon hadroproduction" by M. Kimber, A. Martin, M. Ryskin (DTP/99/100), "Origin of k_T smearing in direct photon production" by H. Lai, H. Li (hep-ph/9802414), "Sudakov resummation for prompt photon production in hadron collisions" by S. Catani, M. Mangano, P. Nason (hep-ph/9806484), etc. New resummation results are also expected from a group of G. Sterman and W. Vogelsang.

In addition to direct photons, the Tevatron jet and dijet measurements are also sensitive to the gluon distribution (in the moderate x region). These measurements and comparisons to theory have their own set of concerns, e.g. jet definition, which is never exactly the same in the data and in the NLO calculation or higher order correlations in the underlying event (see discussion in, e.g., [9]). The jet cross sections, strongly dominated by $q\bar{q}$ scattering, are also sensitive to changes in high x valence distributions. An unresolved issue in the jet cross section analysis is also a lack of full scaling between 630 and 1800 GeV data, predicted by QCD, and a discrepancy between the D0 and CDF measurements of this scaling ratio at lowest $x_T = E_T/\sqrt{(s)}$.

2.2. Valence distributions at high x

Apart from modifications to gluon and charm quark distributions, the valence d quark has received the biggest boost in high x region compared to previous PDF sets. The change is on the order of 30% at x=0.6 and $Q^2 = 20\text{GeV}^2$ and comes from inclusion of a new observable in the global analysis fits, namely W-lepton asymmetry measured at CDF. Precise measurement of

W-lepton asymmetry serves as an independent check on the u and d quark distributions obtained from fits to deep inelastic data. The observable is directly correlated with the slope of the d/u ratio in the x range of 0.1-0.3. The consequence of this new constraint is that the predicted F_2^n/F_2^p ratio is increased and the description of the NMC measurement of F_2^d/F_2^p is improved relative to earlier PDF sets. There remain, however, two areas of uncertainty regarding valence distributions at high x: the value of d/u ratio at x=1 and a question regarding a need for nuclear corrections to F_2^d/F_2^p NMC measurement. Deuterium is a loosely bound nucleus, of low A, and traditionally no corrections for nuclear effects have been applied. However, an analysis of SLAC F_2 data on different targets under the assumption that nuclear effects scale with the nuclear binding for all nuclei predicts nuclear correction for deuterium of 4±1% at x=0.7 [10]. There is also a lack of clarity regarding d/u value at 1. A non-perturbative QCD-motivated models of the 1970's argue that the d/u ratio should approach 0.2 at highest x, whereas any standard form of the parameterization used in global fits drive this ratio to zero. The CTEQ collaboration has performed studies of change in d/u ratio, depending on assumptions regarding nuclear effects in deuterium and the value of d/u ratio at x=1 [3]. CTEQ5UD PDF set includes nuclear corrections for deuterium in F_2^d/F_2^p; its change relative to CTEQ5 is a plausible range for d distribution uncertainty in light of this unresolved question, see Figure 3.

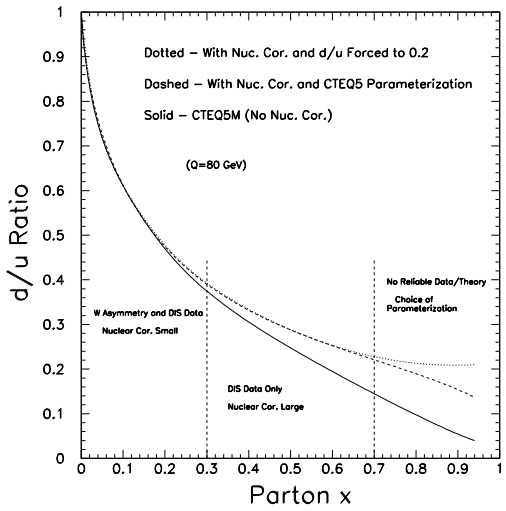

Figure 3. The d/u ratio for CTEQ5 and CTEQ5UD PDF sets, illustrating difference from nuclear correction for NMC F_2 on deuterium. The dotted and dashed lines correspond to two different assumptions regarding value of d/u at x=1.

2.3. Resolved discrepancies between PDF fits and the data

During the duration of this Workshop (March - Nov 1999), two of the outstanding discrepancies between PDF fits or two sets of the experimental data have been resolved.

One of these was the near 20% discrepancy at small x (0.007-0.1) between structure function F_2 measured in muon (NMC) and neutrino (CCFR) deep inelastic scattering [11]. For the purpose of comparison of these structure functions, NMC $F_2^{\mu p}$ was "corrected" for nuclear shadowing, measured in muon scattering, to correspond to $F_2^{\mu Fe}$, and rescaled by the 5/18 charge rule to convert from muon to neutrino F_2. On the other hand, CCFR result was obtained in the framework of massless charm quark to avoid kinematic differences between muon and neutrino scattering off the strange quark ($\nu s \to \mu c$ versus $\mu s \to \mu s$) resulting from mass of the charm. Any one of the above procedures could have had an unquantified systematic uncertainty resulting in the observed disagreement.

New analysis from CCFR, presented at this Workshop [12], indicates that the SF measured in CCFR is in agreement with the F_2 of NMC, within experimental uncertainties. The analysis used a new measurement of the difference between neutrino and antineutrino structure functions xF_3, rather than the ΔxF_3=4(s-c) parameterization used earlier. Comparison between calculations [13] indicated that there were large theoretical uncertainties in the charm production modeling for both ΔxF_3 and the "slow rescaling" correction that converts from massive to massless charm quark framework. Therefore, in the new analysis "slow rescaling" correction was not applied and ΔxF_3 and F_2 were extracted from two parameter fits to the data. The new measurement agrees well with the Mixed Flavor Scheme (MFS) for heavy quark production as implemented by MRST group. To compare with charged lepton scattering data each of the experimental results were divided by the theoretical predictions for F_2, using either light or heavy quark schemes implemented by MRST. The ratios of Data/Theory for F_2^ν (CCFR),

F_2^μ (NMC), and F_2^e (SLAC) are shown in Figure 4. Systematic errors, except for the overall normalization uncertainties, are included. The MFS MRST predictions have higher twist and target mass correction applied. Apart from resolving the NMC-CCFR discrepancy, the new measurement had also implication of ruling out one of the Variable Flavor Scheme calculations available on the market [14].

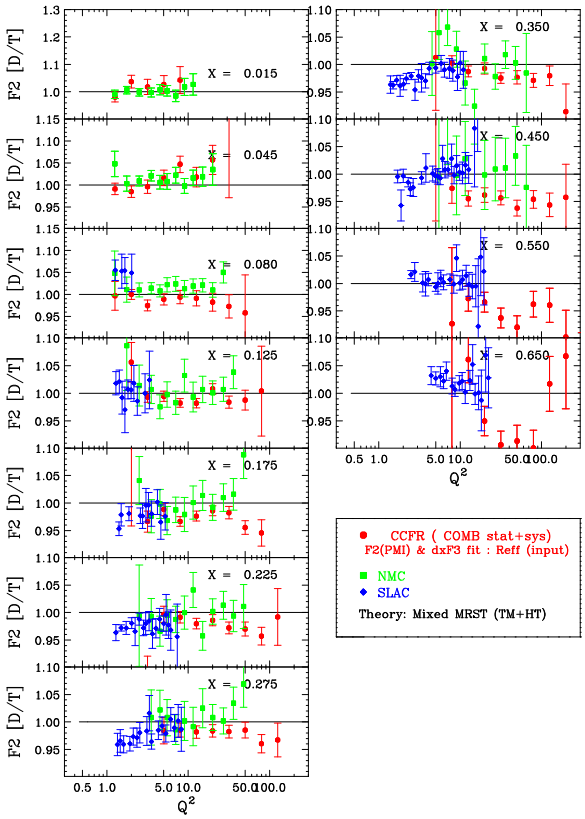

Figure 4. The ratio of the massive F_2^ν measured at CCFR to the prediction of MFS MRST prediction with target mass and higher twist corrections applied. Also shown are the ratios of $F_2\mu$ (NMC) and F_2^e (SLAC) to the MFS MRST predictions.

Another example is that of Drell-Yan production ($pd \to \mu^+\mu^-$) as measured by Fermilab experiment E772, shown in Figure 5. The MRST fits are compared to the differential cross section in $x_F = x_1 - x_2$ and in $\sqrt{\tau} = \sqrt{M^2/s}$, where x_1 and x_2 are the target and projectile fractional momenta, and M - dimuon pair mass. The discrepancy, visible at high x_F and low $\sqrt{\tau}$ was hard to reconcile, since in this kinematic region the dominant contribution to the cross section comes from $u(x_1) \times [\bar{u}(x_2) + \bar{d}(x_2)]$ evaluated at $x_1 \approx x_F$ and $x_2 \approx 0.03$, well constrained by the deep inelastic scattering data. Since then, the E772 experiment has reexamined their acceptance corrections and released an erratum to their earlier measurement [15]. The new values differ from the old ones only for large x_F and small values of mass M, and the new cross section is decreased in this region by a factor up to two.

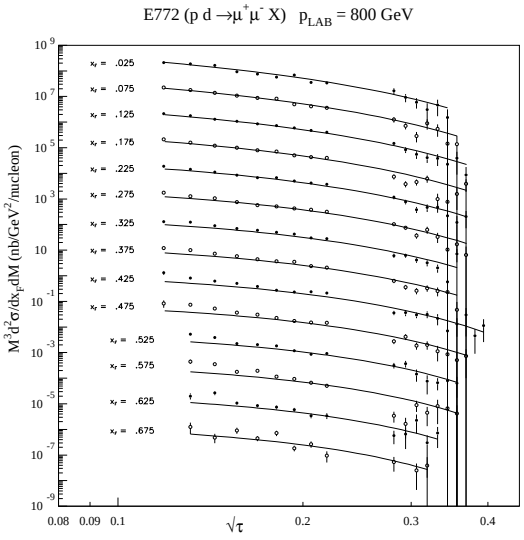

Figure 5. Drell-Yan production from E772 compared to the MRST prediction. The theory curves include K factor of 0.96 and the cross sections for different values of x_F are offset by a factor of 10. Corrected E772 data reduce the discrepancy at high x_F and low τ.

3. Outlook for New Structure Function Measurements

Measurements of neutral and charged current cross sections in positron - proton collisions at large Q^2 from the 1994-97 data have just been published by HERA experiments [16,17]. The data sample corresponds to an integrated luminosity of 35 pb^{-1}. The Q^2 evolution of the parton densities of the proton is tested over 150-30000 GeV^2, Bjorken x between 0.0032-0.65,

and yields no significant deviation from the prediction of perturbative QCD. These data samples are not yet sensitive enough to pin down the d quark distribution at high x, however, an expected 1000 pb^{-1} in positron and electron running in years 2001-2005, achievable after HERA luminosity upgrade, will have a lot to say about 20% -like effects at high x in the ratio of valence distributions[†].

HERA's 1995-1999 data sets, not yet included in the global analysis fits, were plotted against standard PDFs and showed a good agreement over the new kinematic range that these data span (extension to lower yet x and higher Q^2 compared to 1994 data) [2]. HERA's very large statistics and improved precision will allow further reduction of normalization uncertainty of PDF fits. This is important for QCD prediction like W and Z total cross sections at Tevatron - current 3% normalization uncertainty in PDFs directly translates to 3% uncertainty for these cross sections. Improvements in the measurements may need to go in hand with progress in the perturbative calculations; it is likely that NNLO analysis of deep inelastic scattering data will change the level and/or x dependence of PDFs at the percentish-type level.

One can expect continued progress in heavy quark treatment and in the theoretical understanding of soft gluon and non-perturbative effects in the direct photon production. In that case, the E706 data are sufficiently precise to severely constrain the gluon distribution.

One of the few currently active structure function – related experiments is also NuTeV (Fermilab E815). Better understanding of charm quark issues (see discussion in preceding section) and much improved calibration of NuTeV detector relative to CCFR's (with a similar statistical power of the data set) is expected to yield a more precise measurement of structure functions and differential cross section for ν and $\bar{\nu}$ interaction in Fe. Sign-selected beam and several advancements in the NLO theory of heavy quark production will allow NuTeV to improve systematic uncertainty in the new measurement of the strange seas s and $\bar{s}$.

Last but not least, Run II physics promises to be a good source of new constraints on parton distributions. W-lepton asymmetry will be measured with much improved precision and in an expanded rapidity range. New observables are proposed for further exploring collider constrains on PDFs, e.g., W and Z rapidity distributions [18]. And hopefully, many of the issues in jet measurements will be addressed and understood – they are high on J.Womersley Christmas wish-list! [19]

[†]Charge current $ep \to \nu X$ component, of the same order as the neutral current scattering at very high Q^2, directly probes u ($e^- p$) and d ($e^+ p$) distributions at high x.

REFERENCES

1. CTEQ Collaboration: H. Lai *et al.*, hep-ph/9903282 (1999).
2. MRST Collaboration: A. Martin *et al.*, Eur. Phys. J. **C4** (1998) 463, hep-ph/9803445.
   MRST Collaboration: A. Martin *et al.*, Phys. Lett. **B443** (1998) 301, hep-ph/9808371.
   MRST Collaboration: A. Martin *et al.* (1999) hep-ph/9906231.
3. S. Kuhlmann *et al.* (1999) hep-ph/9912283.
4. M. Bonesini *et al.*, Z. Phys. **C38** (1988) 371.
5. W. Vogelsang, A. Vogt, Nucl. Phys. **B453** (1995) 334, hep-ph/9505404.
6. L. Apanasevich *et al.*, hep-ex/9711017 (1997).
   L. Apanasevich *et al.*, hep-ph/9808467 (1998).
7. M. Begel for the E706 Collaboration, DPF99, to be published in the proceedings, http://home.fnal.gov/∼begel/dpf99.html.
8. P. Aurenche *et al.*, hep-ph/9811332 (1998).
9. J. Huston, ICHEP98 proceedings.
10. U. Yang, A. Bodek, Phys. Rev. Lett. **82** (1999) 2467.
    U. Yang, A. Bodek, hep-ph/9912543 (1999).
11. W. Seligman *et al.*, Phys. Rev. Lett. **79** (1997) 1213.
12. U. Yang *et al.* submitted to PRL (2000)
13. G. Kramer, B. Lampe, H. Spiesberger, Z. Phys. **C72** (1996) 99.
    R. Thorne and R. Roberts, Phys. Lett. **B421** (1998) 303.
    A. Martin *et al.* Eur. Phys. J. **C4** (1998) 463.
14. U. Yang *et al.*, DIS99, hep-ex/9906042.
15. E772 Collaboration, Erratum to Phys. Rev. **D50** (1994) 3038.
16. H1 Collaboration: C. Adloff *et al.*, submitted to Eur. Phys. J., hep-ex/9908059
17. ZEUS Collaboration, Eur. Phys. J. **C11** (1999) 3, 427
18. CDF Collaboration: A. Bodek *et al.*, DIS99, Fermilab-Conf-99/160-E.
19. J. Womersley, Fermilab-Conf-99/353.

HEAVY QUARK PRODUCTION

R. Demina[a], S. Keller[b], M. Krämer[c], S. Kretzer[d], R. Martin[e], F.I. Olness[f], R.J. Scalise[f], D.E. Soper[g], W.-K. Tung[h,i], N. Varelas[e], and U.K. Yang[j].

a) Kansas State University, Physics Department, 116 Cardwell Hall, Manhattan, KS 66506; b) Theoretical Physics Division, CERN, CH-1211 Geneva 23, Switzerland; c) Department of Physics, University of Edinburgh, Edinburgh EH9 3JZ, Scotland; d) Univ. Dortmund, Dept. of Physics, D-44227 Dortmund, Germany; e) Univ. of Illinois at Chicago, Dept. of Physics, Chicago, IL 60607; f) Southern Methodist University, Department of Physics, Dallas, TX 75275-0175; g) Institute of Theoretical Science, University of Oregon, Eugene OR 97403, USA; h) Michigan State University, Department of Physics and Astronomy, East Lansing, Michigan 48824-1116; i) Fermi National Accelerator Laboratory, Batavia, IL 60510; j) University of Chicago, Enrico Fermi Institute, Chicago, IL 60637-1434.

Abstract

We present a status report of a variety of projects related to heavy quark production and parton distributions for the Tevatron Run II.

1. Introduction

The production of heavy quarks, both hadroproduction and leptoproduction, has become an important theoretical and phenomenological issue. While the hadroproduction mode is of direct interest to this workshop,[1] we shall find that the simpler leptoproduction process can provide important insights into the fundamental production mechanisms.[2–5] Therefore, in preparation for the Tevatron Run II, we must consider information from a variety of sources including charm and bottom production at fixed-target and collider lepton and hadron facilities.

For example, the charm contribution to the total structure function F_2 at HERA, is sizeable, up to $\sim 25\%$ in the small x region.[4] Therefore a proper description of charm-quark production is required for a global analysis of structure function data, and hence a precise extraction of the parton densities in the proton. These elements are important for addressing a variety of issues at the Tevatron.

In addition to the studies investigated at the Run II workshop series, we want to call attention to the extensive work done in the *Standard Model Physics (and more) at the LHC Workshop* organized by Guido Altarelli, Daniel Denegri, Daniel Froidevaux, Michelangelo Mangano, Tatsuya Nakada which was held at CERN during the same period.* In particular, the investigations of the LHC *b-production group* (convenors: Paolo Nason, Giovanni Ridolfi, Olivier Schneider, Giuseppe Tartarelli, Vikas Pratibha) and the *QCD group* (convenors: Stefano Catani, Davison Soper, W. James Stirling, Stefan Tapprogge, Michael Dittmar) are directly relevant to the material discussed here. Furthermore, our report limits its scope to the issues discussed within the Run II workshop; for a recent comprehensive review, see Ref. [6].

2. Schemes for Heavy Quark Production

Heavy quark production also provides an important theoretical challenge as the presence of the heavy quark mass, M, introduces a new scale into the problem. The heavy quark mass scale, M, in addition to the characteristic energy scale of the process (which we will label here generically as E), will require a different organization of the perturbation series depending on the relative magnitudes of M and E. We find there are essentially two cases to consider.†

1. For the case of $E \sim M$, heavy-quark production is calculated in the so-called fixed flavor number (FFN) scheme from hard processes initiated by light quarks (u, d, s) and gluons, where all effects of the charm quark are contained in the perturbative coefficient functions. The FFN scheme incorporates the correct threshold behavior, but for large scales, $E \gg M$, the coefficient functions in the FFN scheme at higher orders in α_s contain potentially large logarithms $\ln^n(E^2/M^2)$, which may need to be resummed.[7–10]

2. For the case of $E \gg M$, it is necessary to include the heavy quark as an active parton in the proton. This serves to resum the potentially large logarithms $\ln^n(E^2/M^2)$ discussed above. The simplest approach incorporating this idea

In particular, in the Run II B-Physics workshop, the studies of *Working Group 4: Production, Fragmentation, Spectroscopy*, organized by Eric Braaten, Keith Ellis, Eric Laenen, William Trischuk, Rick Van Kooten, and Scott Menary, addressed many issues of direct interest to this subgroup. The report is in progress, and the web page is located at: http://www-theory.fnal.gov/people/ligeti/Brun2/

*The main web page is located at: http://home.cern.ch/~mlm/lhc99/lhcworkshop.html

†We emphasize that the choice of a prescription for dealing with quark masses in the hard scattering coefficients for deeply inelastic scattering is a separate issue from the choice of definition of the parton distribution functions. For all of the prescriptions discussed here, one uses the standard $\overline{\rm MS}$ definition of parton distributions.

is the so-called zero mass variable flavor number (ZM-VFN) scheme, where heavy quarks are treated as infinitely massive below some scale $E \sim M$ and massless above this threshold. This prescription has been used in global fits for many years, but it has an error of $\mathcal{O}(M^2/E^2)$ and is not suited for quantitative analyses unless $E \gg M$.

While the extreme limits $E \gg M$ and $E \sim M$ are straightforward, much of the experimental data lie in the intermediate region As such, the correct PQCD formulation of heavy quark production, capable of spanning the full energy range, must incorporate the physics of both the FFN scheme and the ZM-VFN scheme. Considerable effort has been made to devise a prescription for heavy-flavor production that interpolates between the FFN scheme close to threshold and the ZM-VFN scheme at large E.

The generalized VFN scheme includes the heavy quark as an active parton flavor and involves matching between the FFN scheme with three active flavors and a four-flavor prescription with non-zero heavy-quark mass. It employs the fact that the mass singularities associated with the heavy-quark mass can be resummed into the parton distributions without taking the limit $M \to 0$ in the short-distance coefficient functions, as done in the ZM-VFN scheme. This is precisely the underlying idea of the Aivazis–Collins–Olness–Tung (ACOT) ACOT scheme[11] which is based on the renormalization method of Collins–Wilczek–Zee (CWZ).[12] The order-by-order procedure to implement this approach has now been systematically established to all orders in PQCD by Collins.[13]

Recently, additional implementations of VFN schemes have been defined in the literature. While these schemes all agree in principle on the result summed to all orders of perturbation theory, the way of ordering the perturbative expansion is not unique and the results differ at finite order in perturbation theory. The Thorne–Roberts (TR) [14] prescription has been used in the MRST recent global analyses of parton distributions.[15] The BMSN and CNS prescriptions have made use of the $\mathcal{O}(\alpha_s^2)$ calculations by Smith, van Neerven, and collaborators[8,9] to carry these ideas to higher order. The boundary conditions on the PDF's at the flavor threshold become more complicated at this order; in particular, the PDF's are no longer continuous across the N to N+1 flavor threshold. Buza *et al.*,[8] have computed the matching conditions, and this has been implemented in an evolution program by CSN.[9] More recently, a Simplified-ACOT (SACOT) scheme inspired by the prescription advocated by Collins [13] was introduced;[16] we describe this new scheme in Sec. 4.

3. From Low To High Energy Scale

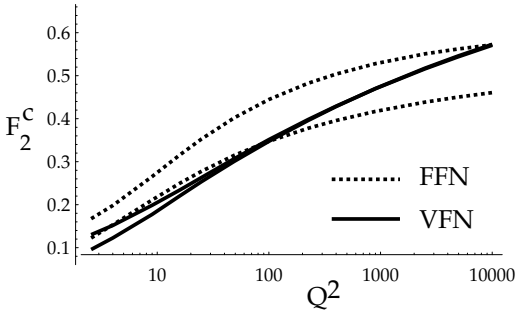

Figure 1. F_2^c for $x = 0.01$ as a function of Q^2 in GeV for two choices of μ as obtained within the $\mathcal{O}(\alpha_s^1)$ FFN and (ACOT) VFN schemes. For details, see Ref. [17].

To compare the features of the FFN scheme with the ACOT VFN scheme[‡] concretely, we will take the example of heavy quark production in DIS; the features we extract from this example are directly applicable to the hadroproduction case relevant for the Tevatron Run II. One measure we have of estimating the uncertainty of a calculated quantity is to examine the variation of the renormalization and factorization scale dependence. While this method can only provide a lower bound on the uncertainty, it is a useful tool.

In Fig. 1, we display the component of F_2^c for the $s + W \to c$ sub-process at $x = 0.01$ plotted *vs.* Q^2. We gauge the scale uncertainty by varying μ from $1/2\,\mu_0$to $2.0\,\mu_0$ with $\mu_0 = \sqrt{Q^2 + m_c^2}$. In this figure, both schemes are applied to $\mathcal{O}(\alpha_s^1)$. We observe that the FFN scheme is narrower at low Q, and increases slightly at larger Q. This behavior is reasonable given that we expect this scheme to work best in the threshold region, but to decrease in accuracy as the unresummed logs of $\ln^n(Q^2/m_c^2)$ increase.

Conversely, the ACOT VFN scheme has quite the opposite behavior. At low Q, this calculation displays mild scale uncertainty, but at large Q this uncertainty is significantly reduced. This is an indication that the resummation of the $\ln^n(Q^2/m_c^2)$ terms via the heavy quark PDF serves to decrease the scale uncertainty at a given order of perturbation theory. While these general results were to be expected, what is surprising is the magnitude of the scale variation. Even in the threshold

[‡]In this section we shall use the ACOT VFN scheme for this illustration. The conclusions extracted in comparison to the FFN scheme are largely independent of which VFN scheme are used.

region where $Q \sim m_c$ we find that the VFN scheme is comparable or better than the FFN scheme.

At present, the FFN scheme has been calculated to one further order in perturbation theory, $\mathcal{O}(\alpha_s^2)$. While the higher order terms do serve to reduce the scale uncertainty, it is only at the lowest values of Q that the $\mathcal{O}(\alpha_s^2)$ FFN band is smaller than the $\mathcal{O}(\alpha_s^1)$ VFN band. Recently, $\mathcal{O}(\alpha_s^2)$ calculations in the VFN scheme have been performed;[9] it would be interesting to extend such comparisons to these new calculations.

Let us also take this opportunity to clarify a misconception that has occasionally appeared in the literature. The VFN scheme is *not* required to reduce to the FFN scheme at $Q = m_c$. While it is true that the VFN scheme does have the FFN scheme as a limit, this matching depends on the definitions of the PDF's, and the choice of the μ scale.[§] In this particular example, even at $Q = m_c$, the resummed logs in the heavy quark PDF can yield a non-zero contribution which help to stabilize the scale dependence of the VFN scheme result.[¶]

The upshot is that even in the threshold region, the resummation of the logarithms via the heavy quark PDF's can help the stability of the theory.

4. Simplified ACOT (SACOT) prescription

We investigate a modification of the ACOT scheme inspired by the prescription advocated by Collins.[13] This prescription has the advantage of being easy to state, and allowing relatively simple calculations. Such simplicity could be crucial for going beyond one loop order in calculations.[‖]

> *Simplified ACOT (SACOT) prescription.* Set M_H to zero in the calculation of the hard scattering partonic functions $\widehat{\sigma}$ for incoming heavy quarks.

For example, this scheme tremendously simplifies the calculation of the neutral current structure function F_2^{charm} even at $\mathcal{O}(\alpha_s^1)$. In other prescriptions, the tree process $\gamma + c \to c + g$ and the one loop process $\gamma + c \to c$ must be computed with non-zero charm mass, and this results in a complicated expression.[20] In the SACOT scheme, the charm mass can be set to zero so that the final result for these sub-processes reduces to the very simple massless result.

[§]The general renormalization scheme is laid out in the CWZ paper[12]. The matching of the PDF's at $\mathcal{O}(\alpha_s^1)$ was computed in Ref. [18] and Ref. [19]. The $\mathcal{O}(\alpha_s^2)$ boundary conditions were computed in Ref. [8].

[¶]*Cf.*, Ref. [17] for a detailed discussion.

[‖]See Ref. [16] for a detailed definition, discussion, and comparisons.

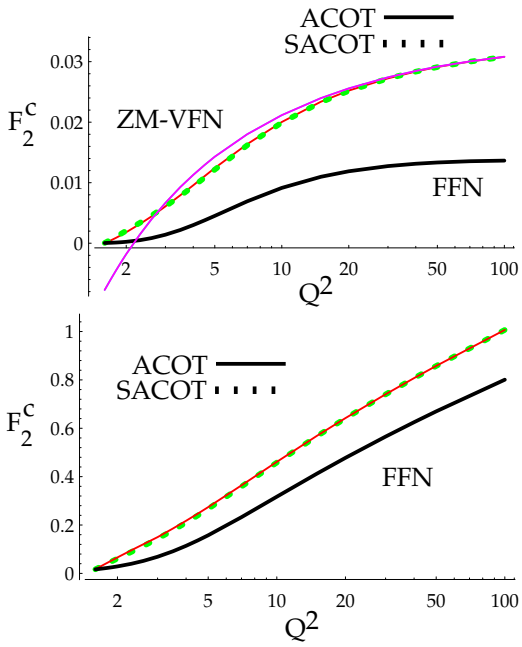

Figure 2. F_2^c as a function of Q^2 in GeV computed to $\mathcal{O}(\alpha_s^1)$ in the ZM-VFN, FFN, ACOT, and SACOT schemes using CTEQ4M PDF's. Fig. a) $x = 0.1$, and Fig. b) $x = 0.001$. Figures taken from Ref. [16].

While the SACOT scheme allows us to simplify the calculation, the obvious question is: does this simplified version contain the full dynamics of the process. To answer this quantitatively, we compare prediction for F_2^{charm} obtained with 1) the SACOT scheme at order α_s^1 with 2) the predictions obtained with the original ACOT scheme, 3) the ZM-VFN procedure in which the charm quark can appear as a parton but has zero mass, and 4) the FFN procedure in which the charm quark has its proper mass but does not appear as a parton. For simplicity, we take $\mu = Q$.

In Fig. 2 we show $F_2^c(x, Q)$ as a function of Q for $x = 0.1$ and $x = 0.001$ using the CTEQ4M parton distributions.[21,22] We observe that the ACOT and SACOT schemes are effectively identical throughout the kinematic range. There is a slight difference observed in the threshold region, but this is small in comparison to the renormalization/factorization μ-variation (not shown). Hence the difference between the ACOT and SACOT results is of no physical consequence. The fact that the ACOT and SACOT match extremely well throughout the full kinematic range provides explicit numerical verification that the SACOT scheme fully contains the physics.

Although we have used the example of heavy quark leptoproduction, let us comment briefly on the implications of this scheme for the more complex case of hadroproduction.[1,23–25] At present, we have cal-

culations for the all the $\mathcal{O}(\alpha_s^2)$ hadroproduction subprocesses such as $gg \to Q\bar{Q}$ and $gQ \to gQ$. At $\mathcal{O}(\alpha_s^3)$ we have the result for the $gg \to gQ\bar{Q}$ sub-processes, but not the general result for $gQ \to ggQ$ with non-zero heavy quark mass. With the SACOT scheme, we can set the heavy quark mass to zero in the $gQ \to ggQ$ sub-process and thus make use of the simple result already in the literature.** This is just one example of how the SACOT has the practical advantage of allowing us to extend our calculations to higher orders in the perturbation theory. We now turn to the case of heavy quark production for hadron colliders.

5. Heavy Quark Hadroproduction

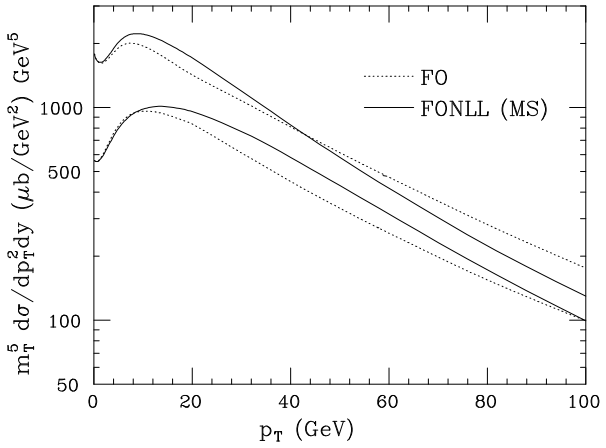

Figure 3. Differential cross section for b-production *vs.* p_T comparing the Fixed-Order (FO) and the Fixed-Order Next-to-Leading-Log (FONLL) result in the $\overline{MS}$ scheme. The bands are obtained by varying independently the renormalization and factorization scales. The cross section is scaled by m_T^5 with $m_T = \sqrt{m_b^2 + p_T^2}$, and $\sqrt{s} = 1800\ GeV$, $m_b = 5\ GeV$, $y = 0$, with CTEQ3M PDF's. Figure taken from Cacciari, Greco, and Nason, Ref. [27].

There has been notable progress in the area of hadroproduction of heavy quarks. The original NLO calculations of the $gg \to b\bar{b}$ subprocess were performed by Nason, Dawson, and Ellis [23], and by Beenakker, Kuijf, van Neerven, Meng, Schuler, and Smith[24]. Recently, Cacciari and Greco[26] have used a NLO fragmentation formalism to resum the heavy quark contributions in the limit of large p_T; the result is a decreased renormalization/factorization scale variation in the large p_T region. The ACOT scheme was applied to the hadroproduction case by Olness, Scalise, and Tung.[25] More recently, the NLO fragmentation formalism of Cacciari and Greco has been merged with the massive FFN calculation of Nason, Dawson, and Ellis by Cacciari, Greco, and Nason,[27]; the result is a calculation which matches the FFN calculation at low p_T, and takes advantage of the NLO fragmentation formalism in the high p_T region, thus yielding good behavior throughout the full p_T range. This is displayed in Fig. 3 where we see that this Fixed-Order Next-to-Leading-Log (FONLL) calculation displays reduced scale variation in the large p_T region, and matches on the the massive NLO calculation in the small p_T region. Further details can be found in the report of the LHC Workshop *b-production group*.††

6. W + Heavy Quark Production

PDF Set	Mass (GeV)	LO	WQQ	NLO
CTEQ1M	m_c=1.7	96	20	161
MRSD0'	m_c=1.7	81	20	138
CTEQ3M	m_c=1.7	83	20	141
CTEQ3M	m_b=5.0	0.17	9.09	9.33

Table 3
The W + charm-tagged one-jet inclusive cross section in pb for LO, $W+Q\bar{Q}$, and NLO (including the $W+Q\bar{Q}$ contribution) using different sets of parton distribution functions. Table is taken from Ref. [28].

The precise measurement of W plus heavy quark ($W+Q$) events provides an important information on a variety of issues. Measurement of $W+Q$ allows us to test NLO QCD theory at high scales and investigate questions about resummation and heavy quark PDF's. For example, if sufficient statistics are available, $W+charm$ final states can be used to extract information about the strange quark distribution. In an analogous manner, the $W+bottom$ final states are sensitive to the charm PDF; furthermore, $W+bottom$ can fake Higgs events, and are also an important background for sbottom ($\tilde{b}$) searches.

The cross sections for W plus tagged heavy quark jet were computed in Ref. [28], and are shown in Table 3.

**For a related idea, see the fragmentation function formalism of Cacciari and Greco[26] in the following section.

††The LHC Workshop *b-production group* is organized by Paolo Nason, Giovanni Ridolfi, Olivier Schneider, Giuseppe Tartarelli, Vikas Pratibha, and the report is currently in preparation. The webpage for the *b-production group* is located at http://home.cern.ch/n/nason/www/lhc99/

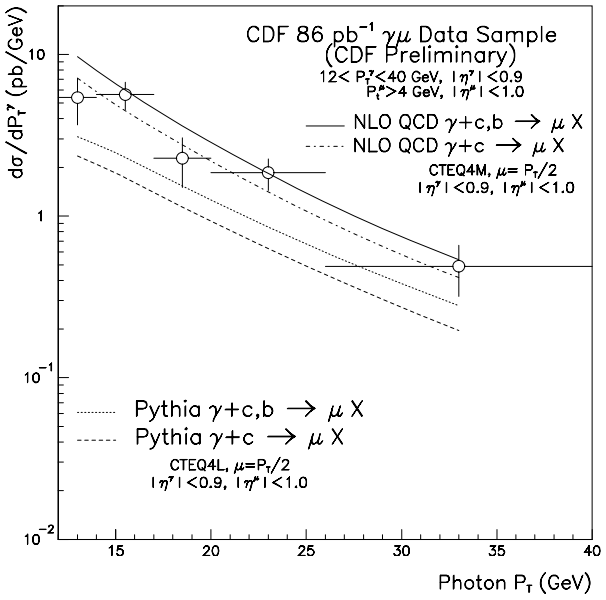

Figure 4. Differential $d\sigma/dp_T^\gamma$ for γ plus tagged heavy quark production as compared with Pythia and the NLO QCD results. Figure taken from Ref. [29]. NLO QCD calculations from Ref. [30].

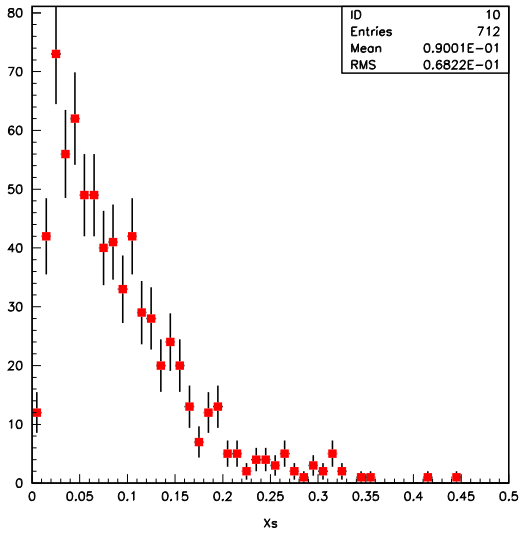

Figure 5. Distribution of $Events/0.01$ *vs.* x of the s-quarks which contribute to the $s + W \to c$ process. Figure taken from Ref. [31].

Note that this process has a large K-factor, and hence comparison between data and theory will provide discerning test of the NLO QCD theory. While the small cross sections of these channels hindered analysis in Run I, the increased luminosity in Run II can make this a discriminating tool. For example, Run I provided minimal statistics on W+Q, but there was data in the analogous neutral current channel γ+Q. The NLO QCD cross sections for γ plus heavy quark were computed in Ref. [30]. Fig. 4 displays preliminary Tevatron data from Run I and the comparison with both the PYTHIA Monte Carlo and the NLO QCD calculations; again, note the large K-factor. If similar results are attainable in the charged current channel at Run II, this would be revealing.

Extensive analysis the W+Q production channels were performed in Working Group I: "QCD tools for heavy flavors and new physics searches," and we can make use of these results to estimate the precision to which the strange quark distribution can be extracted. We display Fig. 5 (taken from the WGI report[31]) which shows the distribution in x of the s-quarks which contribute to the W+c process.[‡‡] This figure indicates that there will good statistics in an x-range comparable to that investigated by neutrino DIS experiments;[2,3] hence, comparison with this data should provide an important test of the strange quark sea and the underlying mechanisms for computing such processes.

7. The Strange Quark Distribution

A primary uncertainty for W+*charm* production discussed above comes from the strange sea PDF, $s(x)$, which has been the subject of controversy for sometime now. One possibility is that new analysis of present data will resolve this situation prior to Run II, and provide precise distributions as an input the the Tevatron data analysis. The converse would be that this situation remains unresolved, in which case new data from Run II may help to finally solve this puzzle.

The strange distribution is directly measured by dimuon production in neutrino-nucleon scattering.[†] The basic sub-process is $\nu N \to \mu^- cX$ with a subsequent charm decay $c \to \mu^+ X'$.

The strange distribution can also be extracted indirectly using a combination of charged ($W^\pm$) and neutral (γ) current data; however, the systematic uncertainties involved in this procedure make an accurate determination difficult.[32] The basic idea is to use the relation

$$\frac{F_2^{NC}}{F_2^{CC}} = \frac{5}{18}\left\{1 - \frac{3}{5}\,\frac{(s+\bar{s}) - (c+\bar{c}) + ...}{q+\bar{q}}\right\} \quad (1)$$

[‡‡]For a detailed analysis of this work including selection criteria, see the report of Working Group I: "QCD Tools For Heavy Flavors And New Physics Searches," as well as Ref. [31].

[†]Presently, there are a number of LO analyses, and one NLO analysis.[2,3]

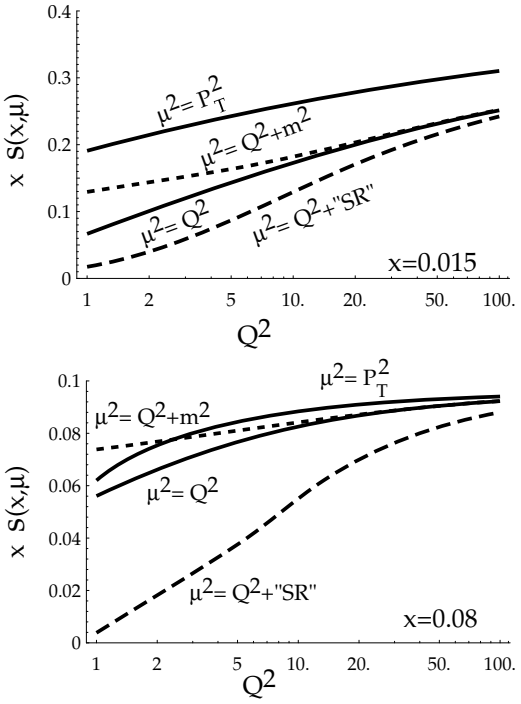

Figure 6. Variation of $x\,s(x,\mu)$ for three choices of μ, and also with a "SR" (slow-rescaling) type correction: $x \to x(1+m_c^2/Q^2)$.

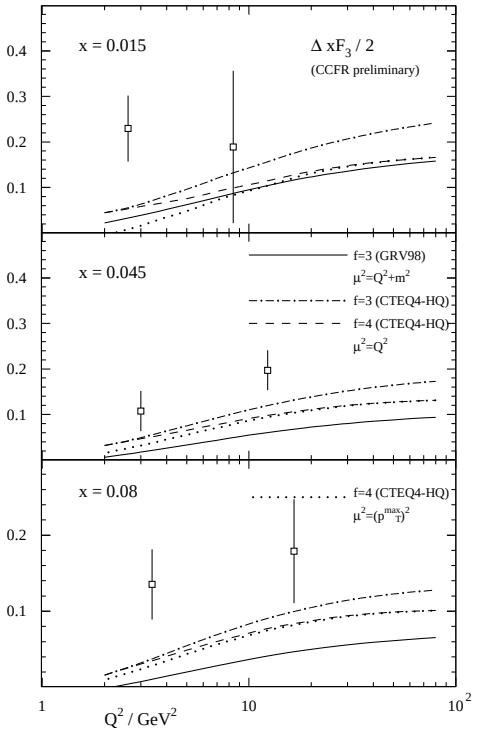

Figure 7. $\Delta xF_3/2$ *vs.* Q^2 for three choices of x. Calculations provided by S. Kretzer.

to extract the strange distribution. This method is complicated by a number of issues including the xF_3 component which can play a crucial role in the small-x region—precisely the region where there has been a long-standing discrepancy.

The structure functions are defined in terms of the neutrino-nucleon cross section via:

$$\frac{d^2\sigma^{\nu,\bar\nu}}{dx\,dy} = \frac{G_F^2 ME}{\pi}\left[F_2(1-y) + xF_1y^2 \pm xF_3y(1-\frac{y}{2})\right]$$

It is instructive to recall the simple leading-order correspondence between the F's and the PDF's:‡

$$\begin{aligned} F_2^{(\nu,\bar\nu)N} &= x\left\{u+\bar u+d+\bar d+2s+2c\right\} \\ xF_3^{(\nu,\bar\nu)N} &= x\left\{u-\bar u+d-\bar d\pm 2s\mp 2c\right\} \end{aligned} \tag{2}$$

Therefore, the combination ΔxF_3:

$$\Delta xF_3 = xF_3^{\nu N} - xF_3^{\bar\nu N} = 4x\{s-c\} \tag{3}$$

can be used to probe the strange sea distribution, and to understand heavy quark (charm) production. This information, together with the exclusive dimuon events, may provide a more precise determination of the strange quark sea.

To gauge the dependence of ΔxF_3 upon various factors, we first consider $xs(x,\mu)$ in Fig. 6, and then the full NLO ΔxF_3 in Fig. 7; this allows us to see the connection between ΔxF_3 and $xs(x,\mu)$ beyond leading order. In Fig. 6 we have plotted the quantity $xs(x,\mu)$ *vs.* Q^2 for two choices of x in a range relevant to the the dimuon measurements. We use three choices of the μ^2 scale: $\{Q^2, Q^2+m_c^2, P^2_{T_{max}}\}$. The choices Q^2 and $Q^2+m_c^2$ differ only at lower values of Q^2; the choice $P^2_{T_{max}}$ is comparable to Q^2 and $Q^2+m_c^2$ at $x=0.08$ but lies above for $x=0.015$. The fourth curve labeled Q^2+"SR" uses $\mu^2=Q^2$ with a "slow-rescaling" type of correction which (crudely) includes mass effects by shifting x to $x(1+m_c^2/Q^2)$; note, the result of this correction is significant at large x and low Q^2.

In Fig. 7 we have plotted the quantity $\Delta xF_3/2$ for an isoscalar target computed to order α_s^1. We display three calculations for three different x-bins relevant to strange sea measurement. 1) A 3-flavor calculation us-

‡To exhibit the basic structure, the above is taken the limit of 4 quarks, a symmetric sea, and a vanishing Cabibbo angle. Of course, the actual analysis takes into account the full structure.[32]

ing the GRV98[33] distributions,[§] and $\mu = \sqrt{Q^2 + m^2}$. 2) A 3-flavor calculation using the CTEQ4HQ distributions, and $\mu = Q$. 3) A 4-flavor calculation using the CTEQ4HQ distributions, and $\mu = Q$.

The two CTEQ curves show the effect of the charm distribution, and the GRV curve shows the effect of using a different PDF set. Recall that the GRV calculation corresponds to a FFN scheme.

The pair of curves using the CTEQ4HQ distributions nicely illustrates how the charm distribution $c(x, \mu^2)$ evolves as $\ln(Q^2/m_c^2)$ for increasing Q^2; note, $c(x, \mu^2)$ enters with a negative sign so that the 4-flavor result is below the 3-flavor curve. The choice $\mu = Q$ ensures the 3- and 4-flavor calculation coincide at $\mu = Q = m_c$; while this choice is useful for instructive purposes, a more practical choice might be $\mu \sim \sqrt{Q^2 + m^2}$, *cf.*, Sec. 2, and Ref. [17].

For comparison, we also display preliminary data from the CCFR analysis.[32] While there is much freedom in the theoretical calculation, the difference between these calculations and the data at low Q values warrants further investigation.

8. Conclusions and Outlook

A detailed understanding of heavy quark production and heavy quark PDF's at the Tevatron Run II will require analysis of fixed-target and HERA data as well as Run I results. Comprehensive analysis of the combined data set can provide incisive tests of the theoretical methods in an unexplored regime, and enable precise predictions that will facilitate new particle searches in a variety of channels. This document serves as a progress report, and work on these topics will continue in preparation for the Tevatron Run II.

This work is supported by the U.S. Department of Energy, the National Science Foundation, and the Lightner-Sams Foundation.

REFERENCES

1. F. Abe *et al.* [CDF Collaboration], Phys. Rev. Lett. **71**, 2396 (1993); F. Abe *et al.* [CDF Collaboration], Phys. Rev. Lett. **71**, 500 (1993); B. Abbott *et al.* [D0 Collaboration], hep-ex/9907029.
2. J. Yu [CCFR / NuTeV Collaboration], hep-ex/9806030; A. O. Bazarko *et al.* [CCFR Collaboration], Z. Phys. **C65**, 189 (1995); T. Adams *et al.* [NuTeV Collaboration], hep-ex/9906037.
3. P. Vilain *et al.* [CHARM II Collaboration], Eur. Phys. J. **C11**, 19 (1999).
4. J. Breitweg *et al.* [ZEUS Collaboration], Eur. Phys. J. **C12**, 35 (2000); C. Coldewey [H1 and ZEUS Collaborations], Nucl. Phys. Proc. Suppl. **74**, 209 (1999).
5. M. E. Hayes and M. Kramer, J. Phys. G **G25**, 1477 (1999).
6. S. Frixione, M. L. Mangano, P. Nason and G. Ridolfi, hep-ph/9702287. Heavy Flavours II, ed. by A.J. Buras and M. Lindner, World Scientific. pp.609-706.
7. E. Laenen, S. Riemersma, J. Smith, W.L. van Neerven, Nucl. Phys. **B392** (1993) 162; Phys. Rev. **D49** (1994) 5753.
8. M. Buza, Y. Matiounine, J. Smith, R. Migneron, W.L. van Neerven, Nucl. Phys. **B472** (1996) 611; M. Buza, Y. Matiounine, J. Smith, and W. L. van Neerven, Phys. Lett. **B411** (1997) 211; Nucl. Phys. **B500** (1997) 301; Eur. Phys. J. C1, 301,1998.
9. A. Chuvakin, J. Smith, W.L. van Neerven, hep-ph/9910250; hep-ph/0002011; A. Chuvakin, J. Smith, hep-ph/9911504.
10. F.I. Olness, S.T. Riemersma, Phys. Rev. **D51** (1995) 4746.
11. F. Olness, W.K. Tung, Nucl. Phys. **B308** (1988) 813; M. Aivazis, F. Olness, W.K. Tung, Phys. Rev. **D50** (1994) 3085; M. Aivazis, J.C. Collins, F. Olness, W.K. Tung, Phys. Rev. **D50** (1994) 3102.
12. J. Collins, F. Wilczek, and A. Zee, *Phys. Rev.* **D18**, 242 (1978).
13. J.C. Collins, Phys. Rev. **D58** (1998) 094002.
14. R.S. Thorne, R.G. Roberts, Phys. Lett. **B421** (1998) 303; Phys. Rev. **D57** (1998) 6871.
15. A.D. Martin, R.G. Roberts, W.J. Stirling, R.S. Thorne, Eur. Phys. J. C4, 463, 1998.
16. M. Krämer, F. Olness, D. Soper, hep-ph/0003035.
17. C. Schmidt, hep-ph/9706496; J. Amundson, C. Schmidt, W. K. Tung, X. Wang, MSU preprint, in preparation; J. Amundson, F. Olness, C. Schmidt, W. K. Tung, X. Wang, FERMILAB-CONF-98-153-T, Jul 1998.
18. J.C. Collins, W.-K. Tung *Nucl. Phys.* **B278**, 934 (1986).
19. S. Qian, ANL-HEP-PR-84-72; UMI-85-17585.
20. S. Kretzer, I. Schienbein Phys. Rev. **D56** (1997) 1804; Phys. Rev. **D58** (1998) 094035; Phys. Rev. **D59** (1999) 054004.
21. H. L. Lai *et al.*, Phys. Rev. **D55** (1997) 1280; hep-ph/9903282.
22. H. L. Lai and W.-K. Tung, Z. Phys. **C74**, 463 (1997).
23. P. Nason, S. Dawson and R. K. Ellis, Nucl. Phys. **B327**, 49 (1989). P. Nason, S. Dawson and

[§]The scale choice $\mu = \sqrt{Q^2 + m^2}$ for the 3-flavor GRV calculation precisely cancels the collinear strange quark mass logarithm in the coefficient function thereby making the coefficient function an exact scaling function, *i.e.* independent of μ^2.

R. K. Ellis, Nucl. Phys. **B303**, 607 (1988).
24. W. Beenakker, W. L. van Neerven, R. Meng, G. A. Schuler and J. Smith, Nucl. Phys. **B351**, 507 (1991). W. Beenakker, H. Kuijf, W. L. van Neerven and J. Smith, Phys. Rev. **D40**, 54 (1989).
25. F. I. Olness, R. J. Scalise and W. Tung, Phys. Rev. **D59**, 014506 (1999)
26. M. Cacciari and M. Greco, Nucl. Phys. **B421**, 530 (1994).
27. M. Cacciari, M. Greco, and P. Nason, hep-ph/9803400, J. High Energy Phys. **05**, 007 (1998).
28. W. T. Giele, S. Keller and E. Laenen, Nucl. Phys. Proc. Suppl. **51C**, 255 (1996); Phys. Lett. **B372**, 141 (1996); hep-ph/9408325.
29. S. Kuhlmann [CDF Collaboration], FERMILAB-CONF-99-165-E, *Prepared for 7th International Workshop on Deep Inelastic Scattering and QCD (DIS 99), Zeuthen, Germany, 19-23 Apr 1999.*
30. B. Bailey, E. L. Berger and L. E. Gordon, Phys. Rev. **D54**, 1896 (1996).
31. R. Demina, J. D. Lykken, K. T. Matchev and A. Nomerotski, hep-ph/9910275.
32. U. K. Yang *et al.* [CCFR-NuTeV Collaboration], hep-ex/9906042.
33. M. Glück, E. Reya and A. Vogt, Eur. Phys. J. **C5**, 461 (1998).

PARTON DENSITIES FOR HEAVY QUARKS

J. Smith[†]

C.N. Yang Institute for Theoretical Physics, SUNY at Stony Brook, Stony Brook, NY 11794-3840

Abstract

We compare parton densities for heavy quarks.

Reactions with incoming heavy (c,b) quarks are often calculated with heavy quark densities just like those with incoming light mass (u,d,s) quarks are calculated with light quark densities. The heavy quark densities are derived within the framework of the so-called zero-mass variable flavor number scheme (ZM-VFNS). In this scheme these quarks are described by massless densities which are zero below a specific mass scale μ. The latter depends on m_c or m_b. Let us call this scale the matching point. Below it there are n_f massless quarks described by n_f massless densities. Above it there are n_f+1 massless quarks described by n_f+1 massless densities. The latter densities are used to calculate processes with a hard scale $M \gg m_c, m_b$. For example in the production of single top quarks via the weak process $q_i + b \to q_j + t$, where q_i, q_j are light mass quarks in the proton/antiproton, one can argue that $M = m_t$ should be chosen as the large scale and m_b can be neglected. Hence the incoming bottom quark can be described by a massless bottom quark density.

The generation of these densities starts from the solution of the evolution equations for n_f massless quarks below the matching point. At and above this point one solves the evolution equations for $n_f + 1$ massless quarks. However in contrast to the parameterization of the x-dependences of the light quarks and gluon at the initial starting scale, the x dependence of the heavy quark density at the matching point is fixed. In perturbative QCD it is defined by convolutions of the densities for the n_f quarks and the gluon with specific operator matrix elements (OME's), which are now know up to $O(\alpha_s^2)$ [1]. These matching conditions determine both the ZM-VFNS density and the other light-mass quark and gluon densities at the matching points. Then the evolution equations determine the new densities at larger scales. The momentum sum rule is satisfied for the $n_f + 1$ quark densities together with the corresponding gluon density.

[†]Work supported in part by the NSF grant PHY-9722101

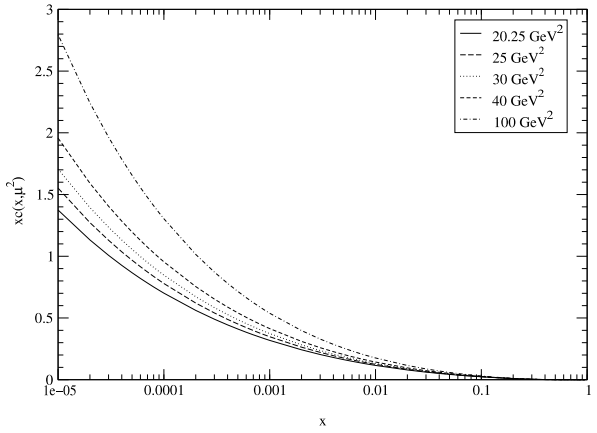

Figure 1. The charm quark density $xc_{\rm NNLO}(5, x, \mu^2)$ in the range $10^{-5} < x < 1$ for $\mu^2 = 20.25$, 25, 30, 40 and 100 in units of $({\rm GeV/c}^2)^2$.

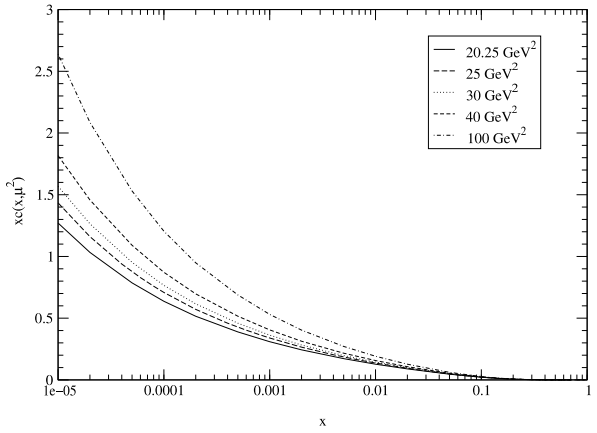

Figure 2. Same as Fig. 1 for the NLO results from MRST98 set 1.

Parton density sets contain densities for charm and bottom quarks, which generally directly follow this approach or some modification of it. The latest CTEQ densities [2] use $O(\alpha_s)$ matching conditions. The x dependencies of the heavy c and b-quark densities are zero at the matching points. The MRST densities [3] have more complicated matching conditions designed so that the derivatives of the deep inelastic structure functions F_2 and F_L with regard to Q^2 are continuous at the matching points. Recently we have provided another set of ZM-VFNS densities [4], which are based

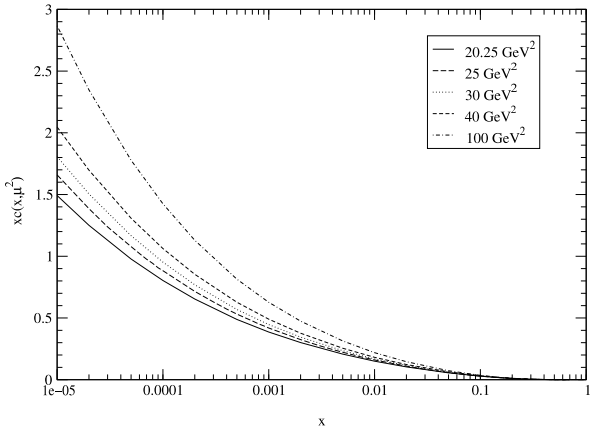

Figure 3. Same as Fig. 1 for the NLO results from CTEQ5HQ.

on extending the GRV98 three-flavor densities in [5] to four and five-flavor sets. GRV give the formulae for their LO and NLO three flavor densities at very small scales. They never produced a c-quark density but advocated that charm quarks should only exist in the final state of production reactions, which should be calculated from NLO QCD with massive quarks as in [6]. We have evolved their LO and NLO densities across the matching point $\mu = m_c$ with $O(\alpha_s^2)$ matching conditions to provide LO and NLO four-flavor densities containing massless c-quark densities. Then these LO and NLO densities were evolved between $\mu = m_c$ and $\mu = m_b$ with four-flavor LO and NLO splitting functions. At this new matching point the LO and NLO four-flavor densities were then convoluted with the $O(\alpha_s^2)$ OME's to form five-flavor sets containing massless b-quarks. These LO and NLO densities were then evolved to higher scales with five-flavor LO and NLO splitting functions. Note that the $O(\alpha_s^2)$ matching conditions should really be used with NNLO splitting functions to produce NNLO density sets. However the latter splitting functions are not yet available, so we make the approximation of replacing the NNLO splitting functions with NLO ones.

In this short report we would like to compare the charm and bottom quark densities in the CS, MRS and CTEQ sets. We concentrate on the five-flavor densities, which are more important for Tevatron physics. In the CS set they start at $\mu^2 = m_b^2 = 20.25$ GeV^2. At this scale the charm densities in the CS, MRST98 (set 1) and CTEQ5HQ sets are shown in Figs. 1 – 3 respectively. Since the CS charm density starts off neg-

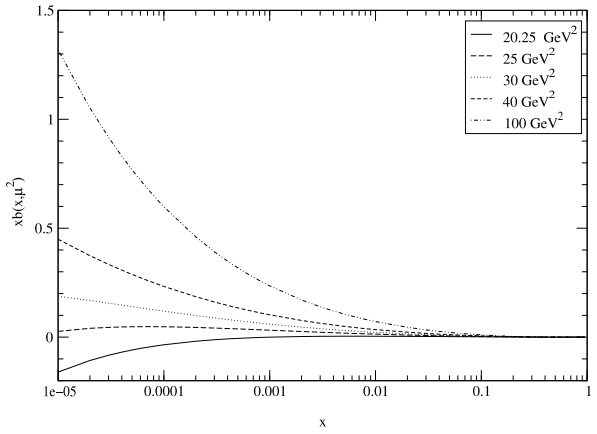

Figure 4. The bottom quark density $xb_{\rm NNLO}(5, x, \mu^2)$ in the range $10^{-5} < x < 1$ for $\mu^2 = 20.25$, 25, 30, 40 and 100 in units of $({\rm GeV/c}^2)^2$.

ative for small x at $\mu^2 = m_c^2 = 1.96$ GeV^2 it evolves less than the corresponding CTEQ5HQ density. At larger μ^2 all the CS curves in Fig. 1 are below those for CTEQ5HQ in Fig. 3 although the differences are small. In general the CS c-quark densities are more equal to those in the MRST (set 1) in Fig. 2.

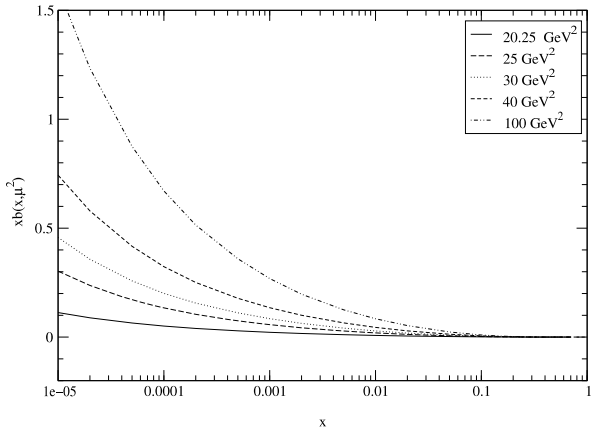

Figure 5. Same as Fig. 4 for the NLO results from MRST98 set 1.

At the matching point $\mu^2 = 20.25$ GeV^2 the b-quark density also starts off negative at small x as can be seen in Fig.4, which is a consequence of the explicit form of the OME's in [1]. At $O(\alpha_s^2)$ the OME's have nonlogarithmic terms which do not vanish at the matching point and yield a finite function in x, which is the boundary value for the evolution of the b-quark density. This negative start slows down the evolution of the b-quark density at small x as the scale μ^2 increases. Hence the CS densities at small x in Fig. 4 are smaller than the MRST98 (set 1) densities in Fig. 5 and the CTEQ5HQ densities in Fig. 6 at the same values of μ^2. The differences between the sets are still small, of the order of five percent at small x and large μ^2. Hence it should not really matter which set is used to calculate cross sections for processes involving incoming b-quarks at the Tevatron.

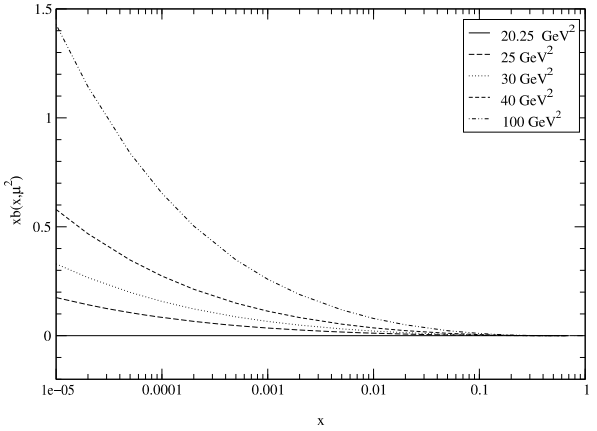

Figure 6. Same as Fig. 4 for the NLO results from CTEQ5HQ.

We suspect that the differences between these results for the heavy c and b-quark densities are primarily due to the different gluon densities in the three sets rather to than the effects of the different boundary conditions. This could be checked theoretically if both LO and NLO three-flavor sets were provided by MRST and CTEQ at small scales. Then we could rerun our programs to generate sets with $O(\alpha_s^2)$ boundary conditions. However these inputs are not available. We note that CS uses the GRV98 LO and NLO gluon densities, which are rather steep in x and generally larger than the latter sets at the same values of μ^2. Since the discontinuous boundary conditions suppress the charm and bottom densities at small x, they enhance the gluon densities in this same region (in order that the momentum sum rules are satisfied). Hence the GRV98 three flavour gluon densities and the CS four and five

flavor gluon densities are generally significantly larger than those in MRST98 (set 1) and CTEQ5HQ. Unfortunately experimental data are not yet precise enough to decide which set is the best one. We end by noting that all these densities are given in the $\overline{\rm MS}$ scheme.

REFERENCES

1. M. Buza, Y. Matiounine, J. Smith, W.L. van Neerven, Eur. Phys. J. **C1**, 301 (1998).
2. H.L. Lai, J. Huston, S. Kuhlmann, J. Morfín, F. Olness, J. Owens, J. Pumplin, W.K. Tung, hep-ph/9903282.
3. A.D. Martin, R.G. Roberts, W.J. Stirling and R. Thorne, Eur. Phys. J. **C4**, 463 (1998).
4. A. Chuvakin, J. Smith, hep-ph/9911504, to be published in Phys. Rev. D.
5. M. Glück, E. Reya and A. Vogt, Eur. Phys. J. **C5**, 461 (1998).
6. E. Laenen, S. Riemersma, J. Smith and W.L. van Neerven, Nucl. Phys. **B392**, 162 (1993); ibid. 229 (1993); S. Riemersma, J. Smith and W.L. van Neerven, Phys. Lett. **B347**, 43 (1995); B.W. Harris and J. Smith, Nucl. Phys. **B452**, 109 (1995).

CONSTRAINTS ON THE GLUON DENSITY FROM LEPTON PAIR PRODUCTION

E. L. Berger[a,‡] and M. Klasen[b,§].

a) HEP Theory Group, Argonne National Laboratory, 9700 South Cass Avenue, Argonne, IL 60439, USA; b) II. Institut für Theoretische Physik, Universität Hamburg, Luruper Chaussee 149, D-22761 Hamburg, Germany

Abstract

The hadroproduction of lepton pairs with mass Q and finite transverse momentum Q_T is described in perturbative QCD by the same partonic subprocesses as prompt photon production. We demonstrate that, like prompt photon production, lepton pair production is dominated by quark-gluon scattering in the region $Q_T > Q/2$. This feature leads to sensitivity to the gluon density in kinematical regimes accessible in collider and fixed target experiments, and it provides a new independent method for constraining the gluon density.

1. Introduction

The production of lepton pairs in hadron collisions $h_1h_2 \to \gamma^* X; \gamma^* \to l\bar{l}$ proceeds through an intermediate virtual photon via $q\bar{q} \to \gamma^*$, and the subsequent leptonic decay of the virtual photon. Traditionally, interest in this Drell-Yan process has concentrated on lepton pairs with large mass Q which justifies the application of perturbative QCD and allows for the extraction of the antiquark density in hadrons [1].

Prompt photon production $h_1h_2 \to \gamma X$ can be calculated in perturbative QCD if the transverse momentum Q_T of the photon is sufficiently large. Because the quark-gluon Compton subprocess is dominant, $gq \to \gamma X$, this reaction provides essential information on the gluon density in the proton at large x [2]. Unfortunately, the analysis suffers from fragmentation, isolation, and intrinsic transverse momentum uncertainties. Alternatively, the gluon density can be constrained from the production of jets with large transverse momentum at hadron colliders [3], but the information from different experiments and colliders is ambiguous.

[‡]Supported by the U.S. Department of Energy, Division of High Energy Physics, under Contract W-31-109-ENG-38.
[§]Supported by Bundesministerium für Bildung und Forschung under Contract 05 HT9GUA 3, by Deutsche Forschungsgemeinschaft under Contract KL 1266/1-1, and by the European Commission under Contract ERBFMRXCT980194.

In this paper we demonstrate that, like prompt photon production, lepton pair production is dominated by quark-gluon scattering in the region $Q_T > Q/2$. This realization means that new independent constraints on the gluon density may be derived from Drell-Yan data in kinematical regimes that are accessible in collider and fixed target experiments but without the theoretical and experimental uncertainties present in the prompt photon case.

In Sec. 2, we review the relationship between virtual and real photon production in hadron collisions in next-to-leading order QCD. In Sec. 3 we present our numerical results, and Sec. 4 is a summary.

2. Next-to-leading order qcd formalism

In leading order (LO) QCD, two partonic subprocesses contribute to the production of virtual and real photons with non-zero transverse momentum: $q\bar{q} \to \gamma^{(*)}g$ and $qg \to \gamma^{(*)}q$. The cross section for lepton pair production is related to the cross section for virtual photon production through the leptonic branching ratio of the virtual photon $\alpha/(3\pi Q^2)$. The virtual photon cross section reduces to the real photon cross section in the limit $Q^2 \to 0$.

The next-to-leading order (NLO) QCD corrections arise from virtual one-loop diagrams interfering with the LO diagrams and from real emission diagrams. At this order $2 \to 3$ partonic processes with incident gluon pairs (gg), quark pairs (qq), and non-factorizable quark-antiquark ($q\bar{q}_2$) processes contribute also. Singular contributions are regulated in n=4-2ϵ dimensions and removed through $\overline{\rm MS}$ renormalization, factorization, or cancellation between virtual and real contributions. An important difference between virtual and real photon production arises when a quark emits a collinear photon. Whereas the collinear emission of a real photon leads to a $1/\epsilon$ singularity that has to be factored into a fragmentation function, the collinear emission of a virtual photon yields a finite logarithmic contribution since it is regulated naturally by the photon virtuality Q. In the limit $Q^2 \to 0$ the NLO virtual photon cross section reduces to the real photon cross section if this logarithm is replaced by a $1/\epsilon$ pole. A more detailed discussion can be found in [4].

The situation is completely analogous to hard photoproduction where the photon participates in the scattering in the initial state instead of the final state. For real photons, one encounters an initial-state singularity that is factored into a photon structure function. For virtual photons, this singularity is replaced by a logarithmic dependence on the photon virtuality Q [5].

A remark is in order concerning the interval in Q_T in which our analysis is appropriate. In general, in two-scale situations, a series of logarithmic contributions will arise with terms of the type $\alpha_s^n \ln^n(Q/Q_T)$. Thus, if either $Q_T >> Q$ or $Q_T << Q$, resummations of this series must be considered. For practical reasons, such as event rate, we do not venture into the domain $Q_T >> Q$, and our fixed-order calculation should be adequate. On the other hand, the cross section is large in the region $Q_T << Q$. In previous papers [4], we compared our cross sections with available fixed-target and collider data on massive lepton-pair production, and we

were able to establish that fixed-order perturbative calculations, without resummation, should be reliable for $Q_T > Q/2$. At smaller values of Q_T, non-perturbative and matching complications introduce some level of phenomenological ambiguity. For the goal we have in mind, viz., contraints on the gluon density, it would appear best to restrict attention to the region $Q_T \geq Q/2$, but below $Q_T >> Q$.

3. Predicted cross sections

In this section we present numerical results for the production of lepton pairs in $p\bar{p}$ collisions at the Tevatron with center-of mass energy $\sqrt{S}$ = 1.8 and 2.0 TeV. We analyze the invariant cross section $Ed^3\sigma/dp^3$ averaged over the rapidity interval -1.0 < y < 1.0. We integrate the cross section over various intervals of pair-mass Q and plot it as a function of the transverse momentum Q_T. Our predictions are based on a NLO QCD calculation [6] and are evaluated in the $\overline{\rm MS}$ renormalization scheme. The renormalization and factorization scales are set to $\mu = \mu_f = \sqrt{Q^2 + Q_T^2}$. If not stated otherwise, we use the CTEQ4M parton distributions [7] and the corresponding value of Λ in the two-loop expression of α_s with four flavors (five if $\mu > m_b$). The Drell-Yan factor $\alpha/(3\pi Q^2)$ for the decay of the virtual photon into a lepton pair is included in all numerical results.

In Fig. 1 we display the NLO QCD cross section for lepton pair production at the Tevatron at $\sqrt{S}$ = 1.8 TeV as a function of Q_T for four regions of Q. The regions of Q have been chosen to avoid resonances, *i.e.* between 2 GeV and the J/ψ resonance, between the J/ψ and the Υ resonances, above the Υ's, and a high mass region. The cross section falls both with the mass of the lepton pair Q and, more steeply, with its transverse momentum Q_T. No data are available yet from the CDF and D0 experiments. However, prompt photon production data exist to $Q_T \simeq 100$ GeV, where the cross section is about 10^{-3} pb/GeV^2. It should be possible to analyze Run I data for lepton pair production to at least $Q_T \simeq 30$ GeV where one can probe the parton densities in the proton up to

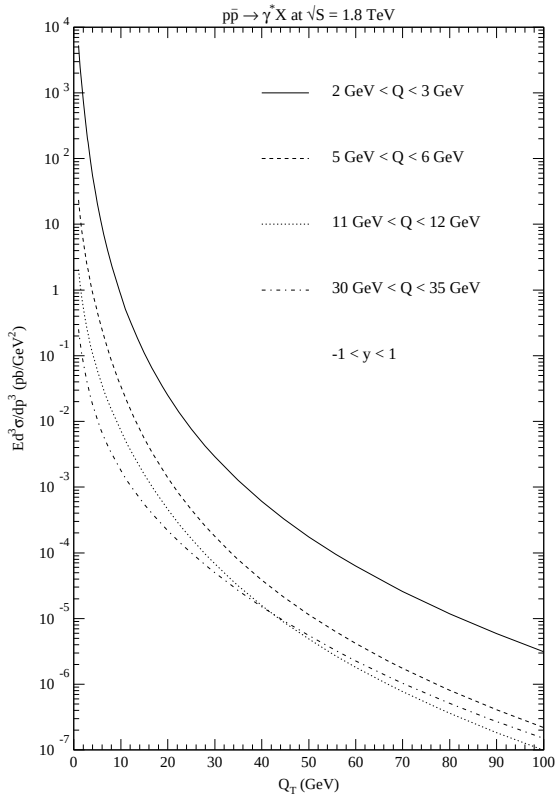

Figure 1. Invariant cross section $Ed^3\sigma/dp^3$ as a function of Q_T for $p\bar{p} \to \gamma^* X$ at $\sqrt{S}$ = 1.8 TeV in non-resonance regions of Q. The cross section falls with the mass of the lepton pair Q and, more steeply, with its transverse momentum Q_T.

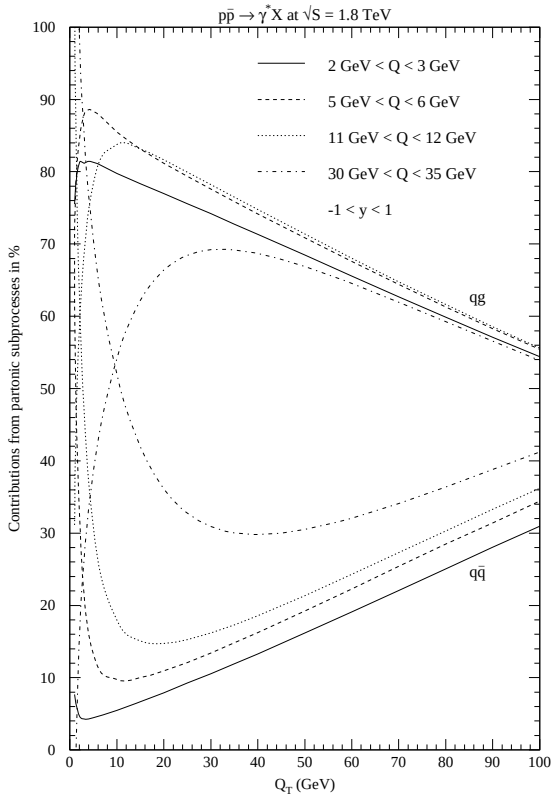

Figure 2. Contributions from the partonic subprocesses qg and $q\bar{q}$ to the invariant cross section $Ed^3\sigma/dp^3$ as a function of Q_T for $p\bar{p} \to \gamma^* X$ at $\sqrt{S}$ = 1.8 TeV. The qg channel dominates in the region $Q_T > Q/2$.

$x_T = 2Q_T/\sqrt{S} \simeq 0.03$. The UA1 collaboration measured the transverse momentum distribution of lepton pairs at $\sqrt{S} = 630$ GeV up to $x_T = 0.13$ [8], and their data agree well with our theoretical results [4].

The fractional contributions from the qg and $q\bar{q}$ subprocesses through NLO are shown in Fig. 2. It is evident that the qg subprocess is the most important subprocess as long as $Q_T > Q/2$. The dominance of the qg subprocess diminishes somewhat with Q, dropping from over 80 % for the lowest values of Q to about 70 % at its maximum for $Q \simeq 30$ GeV. In addition, for very large Q_T, the significant luminosity associated with the valence dominated $\bar{q}$ density in $p\bar{p}$ reactions begins to raise the fraction of the cross section attributed to the $q\bar{q}$ subprocesses. Subprocesses other than those initiated by the $q\bar{q}$ and qg initial channels are of negligible import.

We update the Tevatron center-of-mass energy to Run II conditions ($\sqrt{S} = 2.0$ TeV) and use the latest global fit by the CTEQ collaboration (5M). Figure 3 demonstrates that the larger center-of-mass energy increases the invariant cross section for the production of lepton pairs with mass 5 GeV $< Q <$ 6 GeV by 5 % at low $Q_T \simeq 1$ GeV and 20 % at high $Q_T \simeq 100$ GeV. In addition, the expected luminosity for Run II of 2 fb^{-1} should make the cross section accessible to $Q_T \simeq 100$ GeV or $x_T \simeq 0.1$. This extension would constrain the gluon density in the same regions as prompt photon production in Run I.

Next we present a study of the sensitivity of collider and fixed target experiments to the gluon density in the proton. The full uncertainty in the gluon density is not known. Here we estimate this uncertainty from the variation of different recent parametrizations. We choose the latest global fit by the CTEQ collaboration (5M) as our point of reference [3] and compare results to those based on their preceding analysis (4M[7]) and on a fit with a higher gluon density (5HJ) intended to describe the CDF and D0 jet data at large transverse momentum. We also compare to results based on

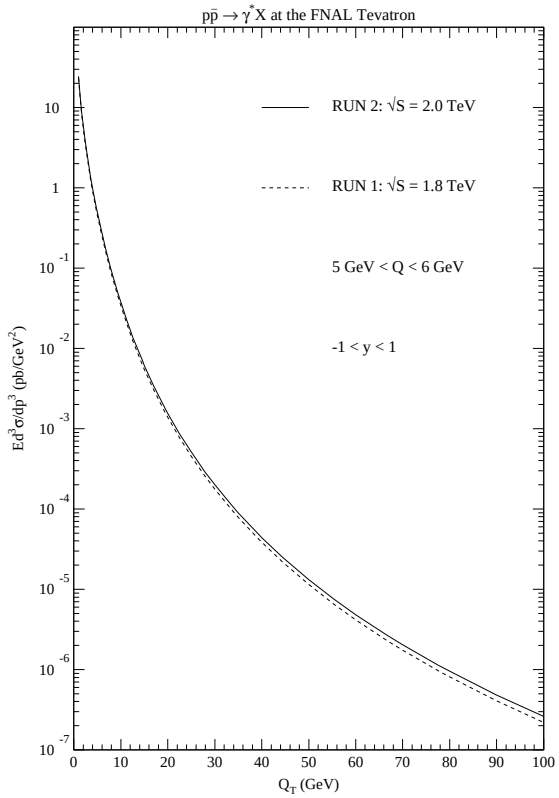

Figure 3. Invariant cross section $Ed^3\sigma/dp^3$ as a function of Q_T for $p\bar{p} \to \gamma^* X$ and two different center-of-mass energies of the Tevatron (Run 1: $\sqrt{S} =$ 1.8 TeV, Run 2: $\sqrt{S} = 2.0$ TeV). The cross section for Run 2 is 5 to 20 % larger, depending on Q_T.

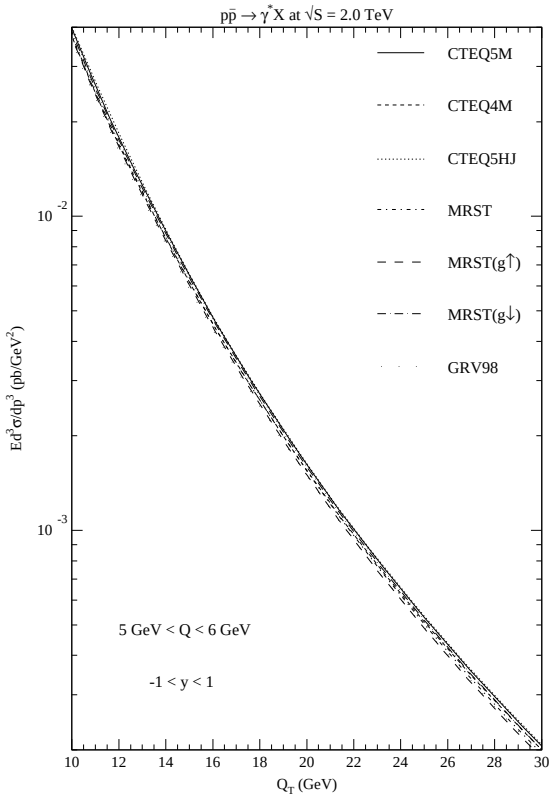

Figure 4. Invariant cross section $Ed^3\sigma/dp^3$ as a function of Q_T for $p\bar{p} \to \gamma^* X$ at $\sqrt{S} = 2.0$ TeV in the region between the J/ψ and Υ resonances. The largest differences from CTEQ5M are obtained with GRV98 at low Q_T (minus 10 %) and with MRST(g↑) at large Q_T (minus 7 %).

global fits by MRST [2], who provide three different sets with a central, higher, and lower gluon density, and to GRV98 [9]*.

In Fig. 4 we plot the cross section for lepton pairs with mass between the J/ψ and Υ resonances at Run II of the Tevatron in the region between $Q_T = 10$ and 30 GeV ($x_T = 0.01 \ldots 0.03$). For the CTEQ parametrizations we find that the cross section increases from 4M to 5M by 2.5 % ($Q_T = 30$ GeV) to 5 % ($Q_T = 10$ GeV) and from 5M to 5HJ by 1 % in the whole Q_T-range. The largest differences from CTEQ5M are obtained with GRV98 at low Q_T (minus 10 %) and with MRST(g↑) at large Q_T (minus 7%).

The theoretical uncertainty in the cross section can be estimated by varying the renormalization and factorization scale $\mu = \mu_f$ around the central value $\sqrt{Q^2 + Q_T^2}$. Figure 5 shows this variation for $p\bar{p} \to \gamma^* X$ at $\sqrt{S} = 2.0$ TeV in the region between the J/ψ and Υ resonances. In the interval $0.5 < \mu/\sqrt{Q^2 + Q_T^2} < 2$ the dependence of the cross section on the scale $\mu = \mu_f$ drops from $\pm 15\%$ (LO) to the small value $\pm 2.5\%$ (NLO). The K-factor ratio (NLO/LO) is approximately 2, as one might expect naively.

A similar analysis for Fermilab's fixed target experiment E772 [11] is shown in Fig. 6. In this experiment, a deuterium target is bombarded with a proton beam of momentum $p_{\rm lab} = 800$ GeV, *i.e.* $\sqrt{S} = 38.8$ GeV. The cross section is averaged over the scaled longitudinal momentum interval $0.1 < x_F < 0.3$. In fixed target experiments one probes substantially larger regions of x_T than in collider experiments. Therefore one expects greater sensitivity to the gluon distribution in the proton. We find that use of CTEQ5HJ increases the cross section by 7 % (26 %) w.r.t. CTEQ5M at $Q_T = 3$

*In this set a purely perturbative generation of heavy flavors (charm and bottom) is assumed. Since we are working in a massless approach, we resort to the GRV92 parametrization for the charm contribution [10] and assume the bottom contribution to be negligible.

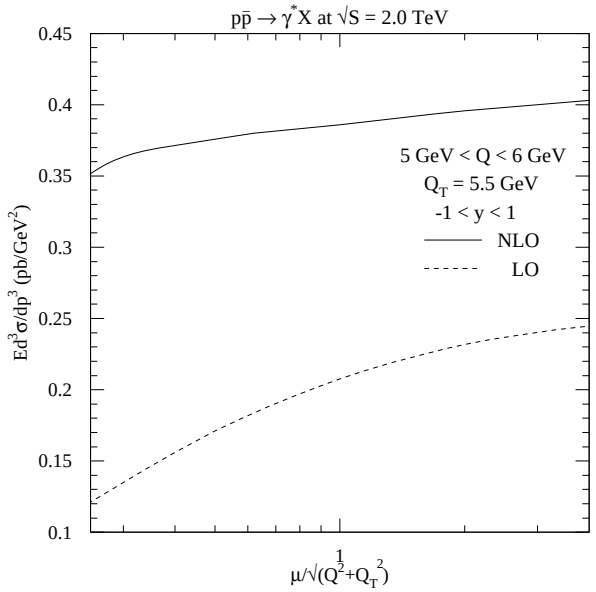

Figure 5. Invariant cross section $Ed^3\sigma/dp^3$ as a function of the renormalization and factorization scale $\mu = \mu_f$ for $p\bar{p} \to \gamma^* X$ at $\sqrt{S} = 2.0$ TeV in the region between the J/ψ and Υ resonances and $Q_T = 5.5$ GeV. In the interval $0.5 < \mu/\sqrt{Q^2+Q_T^2} < 2$ the dependence of the cross section on the scale $\mu = \mu_f$ drops from $\pm 15\%$ (LO) to $\pm 2.5\%$ (NLO). The K-Factor (NLO/LO) is approximately 2.

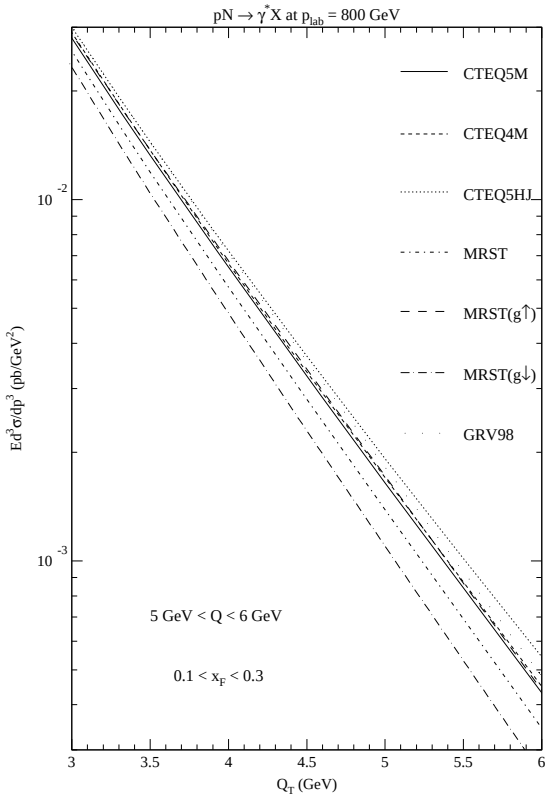

Figure 6. Invariant cross section $Ed^3\sigma/dp^3$ as a function of Q_T for $pN \to \gamma^* X$ at $p_{\rm lab} = 800$ GeV. The cross section is highly sensitive to the gluon distribution in the proton in regions of x_T where it is poorly constrained in current analyses.

GeV ($Q_T = 6$ GeV) and by 134 % at $Q_T = 10$ GeV. With MRST(g↓) the cross section drops relative to the CTEQ5M-based values by 17 %, 40 %, and 59 % for these three choices of Q_T.

Figure 7 shows the variation of the fixed target cross section on the renormalization and factorization scale $\mu = \mu_f$. In the interval $0.5 < \mu/\sqrt{Q^2+Q_T^2} < 2$ the dependence decreases from $\pm 49\%$ (LO) to $\pm 37\%$ (NLO). An optimal scale choice might be $\mu = \mu_f = \sqrt{Q^2+Q_T^2}/4$, where the points of Minimal Sensitivity (maximum of NLO) and of Fastest Apparent Convergence (LO=NLO) nearly coincide. At $\mu = \mu_f = \sqrt{Q^2+Q_T^2}$, the K-factor ratio is 2.6. The NLO cross section turns negative at the lowest scale shown $\mu = \mu_f = \sqrt{Q^2+Q_T^2}/8 \simeq 1$ GeV, a value too low to guarantee perturbative stability.

4. Summary

The production of Drell-Yan pairs with low mass and large transverse momentum is dominated by gluon initiated subprocesses. In contrast to prompt photon production, uncertainties from fragmentation, isolation, and intrinsic transverse momentum are absent. The hadroproduction of low mass lepton pairs is therefore an advantageous source of information on the parametrization and size of the gluon density. The increase in luminosity of Run II increases the accessible region of x_T from 0.03 to 0.1. The theoretical uncertainty has been estimated from the scale dependence of the cross sections and found to be very small for collider experiments.

Acknowledgment

It is a pleasure to thank L. E. Gordon for his collaboration.

REFERENCES

1. S.D. Drell and T. Yan, Phys. Rev. Lett. **25** (1970) 316.
2. A.D. Martin, R.G. Roberts, W.J. Stirling and

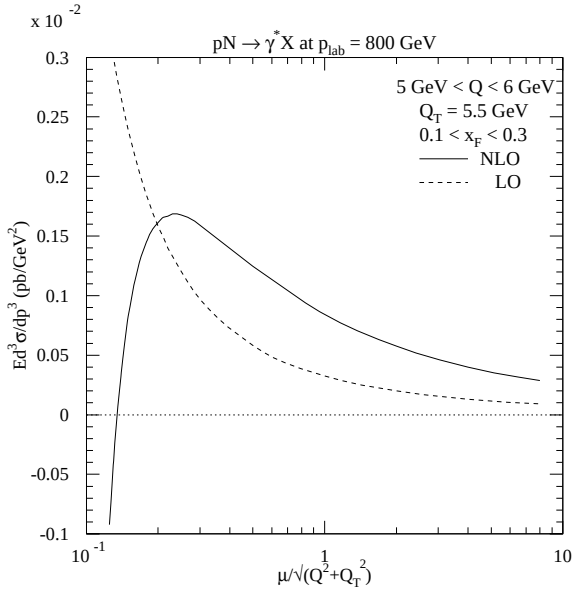

Figure 7. Invariant cross section $Ed^3\sigma/dp^3$ as a function of the renormalization and factorization scale $\mu = \mu_f$ for $pN \to \gamma^* X$ at $p_{\rm lab} = 800$ GeV. In the interval $0.5 < \mu/\sqrt{Q^2 + Q_T^2} < 2$ the dependence of the cross section on the scale μ drops from $\pm 49\%$ (LO) to $\pm 37\%$ (NLO).

R.S. Thorne, Eur. Phys. J. **C4** (1998) 463, hep-ph/9803445, and hep-ph/9907231.

3. H.L. Lai *et al.* [CTEQ Collaboration], hep-ph/9903282.
4. E.L. Berger, L.E. Gordon and M. Klasen, Phys. Rev. **D58** (1998) 074012, hep-ph/9803387; E. L. Berger and M. Klasen, hep-ph/9906402.
5. M. Klasen, G. Kramer and B. Pötter, Eur. Phys. J. **C1** (1998) 261, hep-ph/9703302.
6. P.B. Arnold and R.P. Kauffman, Nucl. Phys. **B349** (1991) 381.
7. H.L. Lai *et al.*, Phys. Rev. **D55** (1997) 1280, hep-ph/9606399.
8. C. Albajar *et al.* [UA1 Collaboration], Phys. Lett. **209B** (1988) 397.
9. M. Glück, E. Reya and A. Vogt, Eur. Phys. J. **C5** (1998) 461, hep-ph/9806404.
10. M. Glück, E. Reya and A. Vogt, Z. Phys. **C53** (1992) 127.
11. P.L. McGaughey *et al.* [E772 Collaboration], Phys. Rev. **D50** (1994) 3038.

CONCLUSION: MANIFESTO

Our goal in this conclusion is not to summarize each of the individual contributions, but to introduce simple guidelines, a "Manifesto", for Run II analysis [†]:

- Each analysis should provide a way to calculate the Likelihood for their data, the probability of the data given a theory prediction.
- The likelihood information should be stored permanently and made available.

The current practice is generally to take experimental data, correct for acceptance and smearing and compare the result to the theoretical predictions. In many cases, the acceptance and smearing corrections depend on the theoretical prediction and thus the practice may lead to uncontrolled uncertainties. Data are generally presented as tables of central values with one-sigma standard deviation. That information is clearly not enough to reconstruct the Likelihood when the uncertainties are not Gaussian distributed. Hence the first guideline of our Manifesto to provide a way to calculate the likelihood, the probability of the data given a theory. The likelihood contains all the information about the experiment and is the basis for any analysis. It should consist of a code and necessary input tables of "data". The code can be as simple as a χ^2 calculation when all the appropriate conditions are met, but will be significantly more involved in the general case, see [2]. The likelihood function should be stored in a format which remains valid for several decades. This means ASCII format for data and simplicity in the code. This is important if we want the experimental data to remain useful even as theoretical calculations evolve. If the experimental results are not tied to theory as it stands in the year 2001, they we will be able to continue to use them, even as the theory evolves from NLO to NNLO to resummed calculation.

The likelihood functions should be stored in a central repository and treated in the same fashion as papers[‡]. This is important because Collaboration evolve over time and eventually disappear.

Note that the burden is of course not just on the experimental side. Theoreticians need to provide predictions with understood theoretical uncertainties over a defined kinematic range. Numerical calculations should be made more efficient. Codes are usually written with the anticipation that they will be run a few times with a few different PDFs. One can anticipate that if the goal to extract uncertainties for the PDFs

[†] clearly this manifesto could be applied to any experiment

[‡] Auxiliary files in the FNAL preprints database may be one location or Web pages

from data is to be reached that these codes will have to be run many orders of magnitude more. Event generators are preferable as they allow a better match to experimental cuts and the possibility of comparison of smeared theory to raw data. A central repository for the theoretical code would also be very helpful.

In this series of workshops several groups reported significant progress towards extracting PDFs from data with uncertainties [2,3]. Note also that other groups, not connected to this workshop [4], have reported results on PDF uncertainties since this workshop started. We are therefore optimistic that realistic PDF uncertainties will be available from several groups by the start of Run II at the Tevatron.

Progress has also been made on the study of the best way to present data [5] for Run II. Clearly, the use of the Run II Tevatron data to their full potential will require planning and care through a collaborative effort between phenomenologists and experimentalists.

REFERENCES

1. S. Alekhin, hep-ph/9611213, recently published in Eur. Phys. J. **C10** (1999) 395-403.
2. W. Giele, S. Keller, D. Kosower, 'Parton Distribution Uncertainties'.
3. R. Brock *et al.*, these proceedings.
4. M. Botje, DESY-99-038, NIKHEF-99-011, hep-ph/9912439.
5. R. Hirosky, 'Experimental uncertainties and their distributions in the inclusive jet cross section'.

Report of the Working Group on Diffractive Physics and Color Coherence

Conveners: Michael Albrow[a], Andrew Brandt[b], Alfred Mueller[c], Carl Schmidt[d]

[a]Fermi National Accelerator Laboratory, Batavia, IL, 60510

[b]University of Texas, Arlington, TX 76019

[c]Columbia University, New York, NY 10027

[d]Michigan State University, East Lansing, MI 48824

Introduction to Diffractive Physics at Run II

Conveners: Michael Albrow[a], Andrew Brandt[b], Alfred Mueller[c], Carl Schmidt[d]

[a]Fermi National Accelerator Laboratory, Batavia, IL, 60510

[b]University of Texas, Arlington, TX 76019

[c]Columbia University, New York, NY 10027

[d]Michigan State University, East Lansing, MI 48824

1. Diffraction

The word "diffraction" covers a rather large class of events at colliders and fixed target machines. The central thread in all the processes one calls diffractive is a rapidity gap (where no particles are produced) which is large enough to guarantee that no flavor or color quantum numbers are exchanged between the colliding particles. Thus, for example at a proton-antiproton collider the reaction $p+\bar{p} \to p^* + \bar{p}^*$ is diffractive if the particles (or jets) making up the p^* and the particles (or jets) making up the $\bar{p}^*$ are separated by a rapidity gap ΔY which is large enough to guarantee that the flavor and color quantum numbers of p^* are the same as p and those of $\bar{p}^*$ the same as $\bar{p}$. $\Delta Y \geq 3$ is a common criterion for such a gap size. The physics being studied varies considerably according to the type of diffraction and so we separate our discussion into (somewhat arbitrary) categories and attempt to highlight the physics issues in each of these categories. The emphasis here is physics at Fermilab, but there are often complementary reactions at HERA. The contrast and comparison between diffraction at these two colliders yields much more insight than the study of diffraction at either collider in isolation.

2. Soft Diffraction

Regge Theory gives a good description of two-body and quasi-two-body reactions, including diffraction, at ISR energies and below. This Regge picture continues to describe total and elastic cross sections through collider energies. However, it is known from studies of elastic and total cross sections of proton-proton and proton-antiproton scattering that the unitarity limit (blackness) has been reached for central impact parameter collisions. It is then somewhat of a mystery why the simple Regge pole picture, a picture only valid far from unitarity limits, works so well for total and elastic scattering. Soft diffraction adds a new piece of information here. Although the Regge pole picture fits the total and elastic cross sections at collider energies it does not work for diffraction [1,2]. The growth in the diffraction cross section is much less rapid through the collider energy region than predicted by fits at ISR energies and below. This fits nicely with the picture that central collisions are unitarity saturating but become weaker with increasing impact parameter. Let's see qualitatively how this looks.

A high energy proton is a state having many degrees of freedom which are built out of quarks and gluons. Schematically one may write

$$|\psi_{\rm proton}\rangle = \sum_i |\psi_i\rangle c_i \qquad (1)$$

where i labels a state in terms of the fundamental degrees of freedom and where $\sum_i |c_i|^2 = 1$. From studying elastic and total cross sections we know that $S(b)|\psi_{proton}\rangle$ is small when b, the impact parameter, is small where S is the S-matrix for elastic reactions. This means that $S(b)|\psi_i\rangle$ is small at central impact parameters for all i having non-negligible c_i. This in turn gives equal inelastic and elastic cross sections because the T-matrix defined by

$$T(b) = i(1 - S(b)) \qquad (2)$$

becomes equal to i at small impact parameters. Diffraction occurs when $S(b)|\psi_i\rangle$ is zero for some configurations, i, and far from zero for other configurations. In such a case the "shadow" of the inelastic collisions is not just the proton state but a wide variety of other states as well, that is diffractive states. Below ISR energies the proton is not black at any impact parameter and the shadow of these inelastic events is both elastic scattering and diffractive production. Here Regge theory works well. As one goes through the ISR region and into collider energies, central impact parameter collisions are becoming black and these regions contribute more strongly to elastic scattering

and give much less diffraction than at lower energies. Diffraction comes from those impact parameters where the S-matrix is changing from strong to relatively weak interactions. The Regge picture (pomeron exchange) now does not work because a single pomeron cannot properly describe a region where $S \approx 0$. In Regge language one needs multiple pomeron exchange for small impact parameter collisions and this considerably complicates the whole Regge picture and robs it of much of its predictive power.

Thus we qualitatively understand the behavior of the soft diffractive cross section. Attempts to make this explanation more quantitative are hampered by the lack of control over nonperturbativie QCD, but there are interesting phenomenological attempts in terms of multiple pomeron exchange [8] (absorption) and a suggestion that the "pomeron flux" may in some sense need to be renormalized as one reaches unitarity limits [1,2].

3. Hard Diffraction

We have seen that soft diffraction comes about at impact parameters corresponding to the transition from the region where $S = 0$ to the region where $S = 1$. This should also be the case for hard diffraction at Fermilab, while new elements come into diffraction at HERA, partly because a virtual photon is weakly interacting, and partly because a virtual photon is not quite a "state."

The motivation for looking at hard diffraction is clear. Unbiased hard interactions probe the parton structure of the proton and tell how many quarks and gluons are in a proton. In hard diffraction one probes the quark and gluon structure of diffraction itself. This is often described in a picturesque language as saying that hard diffraction studies the quark and gluon distribution of the pomeron [2–4] In a typical Fermilab diffractive reaction

$$\text{proton(p)} + \text{antiproton } (\bar{p}) \rightarrow \text{proton } (p') + X$$

with a large rapidity gap between p' and X one often pictures the process as $p \rightarrow p'+$ pomeron followed by the reaction

$$\text{pomeron } (p - p') + \text{antiproton}(\bar{p}) \rightarrow X.$$

If there are jets in X then this reaction can be used to study the parton structure of the pomeron and the antiproton in a standard way. This picture is a little suspect because we have already seen that in low impact parameter reaction a single pomeron does not dominate diffractive reactions. Also it is far from clear in what sense a pomeron can be treated as an incoming state. Nevertheless, it is clear that hard diffraction does study what partons are involved in diffractive reactions, and one may consider the whole description in terms of the structure of the pomeron as simply a picturesque language for describing the quark and gluon structure of diffraction. Similar hard diffraction can be studied at HERA [5] with the reaction

$$\text{proton}(p)+\text{photon } (Q) \rightarrow \text{proton}(p') + X$$

with, again, a rapidity gap between p' and the particles making up X.

Comparing hard diffraction at Fermilab and HERA gives a disagreement between the pomeron structure function of about an order of magnitude [3]. This is strong evidence for factorization breaking with HERA distributions much larger than the corresponding Fermilab ones. This result is not unexpected, and the cause is the same as that leading to the slowing of the growth of soft diffraction. Namely the pomeron is not really a universal object. In pomeron language there should be many pomeron exchanges occurring at Fermilab because unitarity bounds are being reached. The hard part of the reaction then does measure properties of this exchange. At HERA the exchange is much simpler because deep inelastic scattering is a point-like probe and it is this probe itself which is one of the scatterers initiating the reaction. Also in deep inelastic scattering one can view the virtual photon as turning into a quark-antiquark pair before the scattering. This quark-antiquark pair then scatters on the proton and both elastic and diffractive scattering of this pair will be counted as diffractive events in deep inelastic scattering. Thus there is no suppression of diffraction of HERA events at central impact parameter in contrast to what happens at Fermilab.

The nature of diffraction at HERA and at Fermilab is fundamentally different. In neither case have theorists been able to frame the discussion in sharp enough terms to make good use of the large amount of data which is already available and that which can be expected in Run II. Thus in the case of Fermilab it is certainly true that hard diffraction tells us something about the partonic structure of diffraction. But, to what extent are we probing the diffraction that occurs in soft processes at Fermilab, and to what extent is the hard process creating or modifying the diffraction? That is, what properties of diffraction are universal? Similar issues hold at HERA where one might say that large Q^2 diffraction is determining a particular event rather than measuring any particular property of a universal quantity, the pomeron.

In fact it may be that the focus on viewing diffractive hard scattering as probing a preexisting object is misleading. In particular another point of view has proved very successful in understanding and correlat-

ing diffraction and small-x structure functions in a low to moderate Q^2 regime at HERA. In this picture one chooses a frame where the virtual photon breaks up into a quark-antiquark pair before the scattering. Then the process is quark-antiquark pair scattering on a proton. If the scattering is inelastic then the process contributes to the inelastic part of F_2. If the scattering is elastic then the process contributes to the diffractive part of F_2. Thus, here, hard diffraction is the shadow of inelastic events. A rather simple model proposed by Goelec-Biernat and Wüsthoff incorporates unitarity limits (saturation) for the small-x scattering of moderate spatial-sized quark-antiquark pairs along with the probability that a photon will breakup into a pair of a certain size. This model comfortably describes moderate Q^2 deep inelastic scattering, F_2, and diffraction in a semiquantitative way which matches well with theoretical ideas of saturation and dense gluon systems. It is a great challenge to theorists to invent a comparably well-motivated model to deal with hard diffraction at Fermilab.

4. Rapidity Gaps Between Jets

There is a special class of diffractive events which have been pioneered at Fermilab in which one looks for events with a sizeable rapidity gap and where there is a hard jet on either side of the gap. For a gap size $\Delta Y \geq 3$ such events constitute about 1% of all two-jet events at Fermilab and about 10% of all two-jet events at HERA.

There is a good QCD motivation for studying such events. The basic hard process is elastic quark-antiquark (or gluon-gluon) scattering at large momentum transfer and at large rapidity. This seems a good place to measure the BFKL pomeron. However, for the rapidity gap to be present it is also necessary that the spectator parts of the colliding proton and antiproton not produce particles in the rapidity gap. The probability that the latter happens is called the "survival probability" of the gap and is estimated to be about 10% at Fermilab [8]. From the BFKL pomeron point of view the most unfortunate part of the data is the fact that the percentage of gap events decreases when one goes from a center of mass energy of 630 GeV to 1800 GeV. At Fermilab the 1800 GeV runs should be predominately gluon jets while at 630 GeV quarks should dominate the hard scattering. The BFKL contribution (at comparable rapidity gaps) to the gap fraction should be enhanced for hard gluon scattering by a factor of $(\frac{N_c}{C_F})^2 = (\frac{9}{4})^2$ as compared to hard quark scattering. Thus we might expect the gap fraction to grow as one goes from 630 GeV to 1800 GeV while in fact the gap fraction decreases by a factor of 2.

What has gone wrong [9]? The most likely problem is that the survival probability also has an energy dependence [8] and that the survival probability is decreasing between 630 and 1800 GeV. It may be that there are still important contributions from secondary trajectories and that the BFKL pomeron is not dominating the hard scattering. Oderda and Sterman [10] have a variant on rapidity gaps where one requires less than a certain amount of transverse energy be emitted in the gap. This allows the QCD calculation, including color non-singlet exchanges, to be done reliably, but it does not eliminate the difficult survival probability questions. It would be interesting to analyze the data in the Oderda-Sterman way to see if the survival probabilities become significantly larger, and even more importantly, to see if the survival probability becomes energy independent.

There is a very simple picture, the "color evaporation" picture, which qualitatively describes the data [11,12]. Here one takes the hard scattering scattering to be given by a single hard gluon exchange. For example in $p + \bar{p} \to QX + \bar{Q}Y$ one views the X as the remnant of p after the quark Q is taken out and Y the remnant of $\bar{p}$ after $\bar{Q}$ is taken out. Q and $\bar{Q}$ are the (in this case quark) jets being measured. Thus X is a $\underline{3}\times\underline{3}$ representation of color $SU(3)$ while Q, $\bar{Q}$, and Y are $\underline{3}$, $\underline{3}^*$, and $\underline{3}^* \times \underline{3}^*$ representations respectively. The final state color singlet structure is then formed just by counting the ways in which the color representations can be combined into singlets. For example, Q and X have 27 different color states of which only one of them is a singlet. It is necessary to take this singlet in order to have a color singlet state on one side of the rapidity gap. These simple counting rules give reasonable numbers for the gap fractions and predict a decreasing gap fraction as one goes from 630 GeV to 1800 GeV because of the color counting change when Q and $\bar{Q}$ are replaced by gluons.

The color evaporation model is an interesting picture and may be a good hint about how the dynamics is working. However, without a stronger underlying QCD framework it will remain an intriguing curiosity. It is an important challenge to see if a QCD dynamical framework can be developed which leads to something like the color evaporation model.

5. BFKL Searches

There has been an important activity at Fermilab, at HERA and at LEP trying to measure the BFKL pomeron intercept. In the Fermilab analysis the reaction is

$$\text{proton}(p) + \text{antiproton}\ (\bar{p}) \to \text{jet}(k_1) + \text{jet}(k_2) + X$$

where $k_{1\perp}$ and $k_{2\perp}$ are greater than 20 GeV, and where $k_1/p = x_1$ and $k_2/\bar{p} = x_2$ are fixed to be the same at 630 and 1800 GeV. If one takes the ratio

$$R = \frac{\sigma_{2jet}(1800)}{\sigma_{2jet}(630)}$$

then BFKL predicts

$$R = \sqrt{\frac{\Delta Y(630)}{\Delta Y(1800)}} exp\{(\alpha_P - 1)[\Delta Y(1800) - \Delta Y(630)]\}.$$

ΔY is the rapidity interval between the two jets, but this is a purely inclusive measurement so there are no survival probability worries. At HERA one of the jets is replaced by the virtual photon and a similar formula holds. At LEP one simply measures the energy dependence of virtual photon-virtual photon scattering. Each of the accelerators have strong and weak points. The LEP analysis is certainly the cleanest, but so far there is a marginal amount of data. The Fermilab DØ experiment has very robust jets but $\Delta Y(630)$ is only about 2.4 and one may worry that this is not yet large enough for BFKL dominance. At HERA the jets have a rather small $k_\perp$ and the worry is that the jet cross section has not been properly identified.

Perhaps the surprising result [18] is that both Fermilab and HERA suggest that α_P is near 1.5, close to the leading order BFKL calculation. The present theoretical prejudice is that α_P will likely turn out to be nearer 1.25-1.3 when, and if, the dust settles over attempts to give a reliable answer for the higher order corrections. What is perhaps even more striking is that the BFKL evolution seems to be so prominent in this inclusive reaction while it appears to be completely masked by other effects in the more exclusive rapidity gap analysis.

Monte Carlo calculations [19] incorporating BFKL evolution suggest that BFKL effects should be suppressed by various kinematic and non-asymptotic effects. Is there another explanation of the strong small x growth seen in the Fermilab dijet data and the HERA forward jet data, or are the Monte Carlos over-compensating non-leading factors as perhaps the next-to-leading analytic calculations are doing? Much remains to be understood.

6. Run II Diffraction Prospects

Improved understanding of this new field of hard diffraction, requires new detectors for tagging and measuring scattered protons. In Ref [3], new results from a short data taking period with the CDF Roman pot spectrometer, show some of the possibilities of this new sub-detector. In Run II, this detector will be available for the whole run, and will be more fully exploited. The CDF Run II plans, including addition of new forward calorimeters and gap veto counters are outlined in Ref. [20].

DØ is in the process of installing a new Forward Proton Detector (FPD) (see Ref. [21]). This sub-detector consists of nine independent spectrometers which will maximize the acceptance for scattered protons *and* anti-protons. The FPD will be fully integrated into the DØ triggering and data acquisition systems and will provide unprecedented samples of hard diffractive events of all types.

Double pomeron exchange is the most intriguing process that can be studied with these new detectors [14], and there were many talks on this subject at the workshop [22]. In this process both the incoming proton and anti-proton are scattered but remain intact, and a massive central system may be produced. At the Tevatron objects with a mass of more than 100 GeV could be produced. With both arms instrumented it would be possible to measure both the proton and anti-proton using the FPD, and jets (for example) using the central calorimeter. This allows the kinematics of the event to be fully determined.

In addition, CDF can expand on its "gap+track" double pomeron results in Run I, where they tag an anti-proton and a gap. Although, these events are not gold-plated like the DØ double-tagged events, the acceptance penalty of tagging with both proton and anti-proton is avoided, and are thus the data sample is larger. DØ, of course can study both types of events, and combine the results to gain a deeper understanding of this process. Both collaborations will also be able to exploit double gap events as done by DØ in Run I [4], which will be especially valuable for rare events.

Measurement of hard double pomeron exchange would help determine the pomeron structure and provide unique information on the pomeron flux. Double pomeron exchange would have a normalization proportional to the square of the flux factor, unlike other hard diffractive processes. In addition, this process has been proposed as a trigger for Higgs production at the LHC, with optimistic assumptions [15], it might be possible to observe a handful of Higgs events via this mechanism during Tevatron Run II [17]. While this may be unlikely, these would be spectacular events with only the decay products of the Higgs in the central detector, and a proton and an anti-proton in the forward pot spectrometers. In any case, knowledge gained at the Tevatron would indicate if this approach is worth pursuing at the LHC.

Double pomeron interactions are also an ideal place to look for glueball production (bound states of gluons) and states with exotic quantum numbers, and the clean event topologies would make them easier to detect [14,

16,17].

In conclusion, the Run II outlook for hard diffraction and related topics appears to be quite bright and will require the best efforts of the experimental collaborations along with a recently invigorated theoretical community to finally unravel the mysterious pomeron.

REFERENCES

1. M. Convery, "CDF results on double diffraction".
2. K. Goulianos, "Diffractive parton densities".
3. K. Hatakeyama, "Diffractive dijets at CDF".
4. A. Brandt, "DØ Rapidity Gap Studies".
5. C. Royon, "QCD analysis of the diffractive structure functions measured at HERA and factorization breaking at Tevatron".
6. A. Solodsky, "Diffractive heavy flavor production at CDF".
7. M. Wang, "Diffractively produced charm final states in pp interactions at 800 GeV/c".
8. E. Levin, "Cost of Survival for Large Rapidity Gaps".
9. B. Cox, "Is BFKL ruled out by the Tevatron gaps between jets data?".
10. G. Sterman, "Interjet Energy and Color Flow".
11. E. Gregores, "Color Evaporation Induced Rapidity Gaps".
12. R. Engel and J. Ranft, "Monte Carlo simulation of color singlet exchange between jets".
13. M. Strikman, "Hard color coherent phenomena".
14. J. Pumplin, "Double Pomeron Physics in Run II".
15. E. Levin, "Higgs and Heavy Quarks Diffractive Production".
16. D. Kharzeev, "Diffractive Production of Glueballs".
17. M. Albrow, "Glueballs and Exclusive Hadron Production at the Tevatron".
18. R. Peschanski and C. Royon, "A determination of pomeron intercepts at colliders".
19. L. Orr, "BFKL Monte Carlo for Dijet Production at Hadron Colliders".
20. K. Goulianos, "Run 2 plans for hard diffraction studies in CDF".
21. A. Brandt, "The DØ Forward Proton Detector".
22. Working Group VI Web page, http://www.pa.msu.edu/~schmidt/soft.html.

Diffractive Parton Densities

K. GOULIANOS, The Rockefeller University, 1230 York Avenue, New York, NY 10021, USA.

We present a phenomenological model of hard diffraction in which the structure of the Pomeron is derived from the structure of the parent hadron. Predictions for diffractive deep inelastic scattering are compared with data.

The inclusive and diffractive deep inelastic scattering (DIS) cross sections are proportional to the corresponding F_2 structure functions of the proton,

Inclusive DIS $\quad \frac{d^2\sigma}{dx\,dQ^2} \propto \frac{F_2^h(x,Q^2)}{x}$

where

Diffractive DIS $\quad \frac{d^3\sigma}{d\xi\,dx\,dQ^2} \propto \frac{F_2^{D(3)}(\xi,x,Q^2)}{x}$

h and $D(3)$ indicate, respectively, a *hard* structure function (at scale Q^2) and a 3-variable diffractive structure function (integrated over t). The latter depends not only on the hard scale Q^2, but also on the *soft* scale, $\langle M_T \rangle \sim 1$ GeV, which is the relevant scale for the formation of the gap.

The only marker of the rapidity gap is the variable ξ. We therefore postulate that the rapidity gap probability is proportional to the *soft* parton density at ξ and write the DDIS (diffractive DIS) cross section as

$$\frac{d^3\sigma}{d\xi dx dQ^2} \propto \frac{F_2^h(x,Q^2)}{x} \times \frac{F_2^s(\xi)}{\xi} \otimes \xi\text{−norm}$$

where the symbolic notation "$\otimes$ ξ−norm" is used to indicate that the ξ probability is normalized. Since $x = \beta\xi$, the normalization over all available ξ values involves not only F_2^s but also F_2^h, breaking down factorization. It is therefore prudent to write the DDIS cross section in terms of β instead of x, so that the dependence of F_2^h on ξ is shown explicitly:

$$\frac{d^3\sigma}{d\xi d\beta dQ^2} \propto \frac{1}{\beta}\left[F_2^h(\beta\xi,Q^2) \times \frac{F_2^s(\xi)}{\xi} \otimes \xi\text{−norm}\right]$$

The term in the brackets represents the DDIS structure function $F_2^{D(3)}(\xi,\beta,Q^2)$.

In the next step, we seek guidance from the scaling behavior of the soft single-diffractive (sd) differential cross section [1,2],

$$\frac{d\sigma_{sd}}{dM^2} \propto \frac{1}{(M^2)^{1+\epsilon}} \quad \text{(no } s\text{-dependence!)}$$

which in terms of ξ takes the form

$$\frac{d\sigma_{sd}}{d\xi} \propto \underbrace{\frac{1}{s^{2\epsilon}}\,\frac{1}{\xi^{1+2\epsilon}}}_{\text{gap probability}} \times (s')^{\epsilon}$$

where $s' \equiv M^2$ is the s-value of the diffractive sub-system. Noting that ξ is related to the associated rapidity gap by $\Delta Y = \ln\frac{1}{\xi}$, and that the integral $\int_{(s_\circ/s)}^{1} \frac{1}{s^{2\epsilon}}\frac{d\xi}{\xi^{1+2\epsilon}} = constant$, the above equation may be viewed as representing the product of the total cross section at the sub-system energy multiplied by a *normalized* rapidity gap probability. In analogy with this experimentally established behavior, we factorize $F_2^{D(3)}(\xi,\beta,Q^2)$ into $F_2^h(\beta,Q^2)$, the sub-energy DIS cross section, times a normalized gap probability:

$$F_2^{D(3)}(\xi,\beta,Q^2) = P_{gap}(\xi,\beta,Q^2) \times F_2^h(\beta,Q^2)$$

The gap probability is therefore given by

$$P_{gap}(\xi,\beta,Q^2) = F_2^h(\beta\xi,Q^2) \times \frac{F_2^s(\xi)}{\xi} \times N(s,\beta,Q^2)$$

The normalization factor, $N(s,\beta,Q^2)$, is obtained from the following equation, using $\xi_{min} = Q^2/s$,

$$N^{-1}(s,\beta,Q^2) = \frac{1}{f_q}\int_{\xi_{min}}^{1} F_2^h(\beta\xi,Q^2) \times \frac{F_2^s(\xi)}{\xi} d\xi$$

f_q is the quark fraction of the hard structure and is used here because only quarks participate in DIS.

At small x ($\leq\sim$ 0.1), the structure functions F_2^h and F_2^s are represented well by the power law expressions [3] $F_2^h(x,Q^2) = A^h/x^{\lambda_h(Q^2)}$ and $F_2^s(\xi) = A^s/\xi^{\lambda_s}$. Using these forms we obtain

$$N^{-1}(s,\beta,Q^2) = \frac{1}{f_q}\left[\frac{A^h}{\beta^{\lambda_h}}\,\frac{A^s}{\lambda_h+\lambda_s}\,\left(\frac{\beta s}{Q^2}\right)^{\lambda_h+\lambda_s}\right]$$

$$F_2^{D(3)}(\xi,\beta,Q^2) = \frac{1}{\xi^{1+\lambda_h+\lambda_s}} \times f_q(\lambda_h+\lambda_s)\,\left(\frac{Q^2}{\beta s}\right)^{\lambda_h+\lambda_s} \times \frac{A^h}{\beta^{\lambda_h}}$$

Since in DDIS x is always smaller than ξ, the above form of $F_2^{D(3)}$, derived for small x, should be valid for all x when ξ is small; it should also be valid for all $\beta(= x/\xi)$. We therefore expect $F_2^{D(3)}$ to have the following ξ and β dependence at small ξ:

$$F_2^{D(3)}(\xi,\beta,Q^2)|_{\beta,Q^2} \propto \frac{1}{\xi^{1+n}} \qquad n = \lambda_h(Q^2) + \lambda_s$$

$$F_2^{D(3)}(\xi,\beta,Q^2)|_{\xi,Q^2} \propto \frac{1}{\beta^m} \qquad m = 2\lambda_h(Q^2) + \lambda_s$$

The HERA (non-diffractive) DIS measurements [3] yield $\lambda_s \approx 0.1$, which is in agreement with the value of $\epsilon = \alpha(0) - 1 = 0.104$ [4], where $\alpha(0)$ is the intercept of the Pomeron trajectory at t=0. In the Q^2 range of 10-50 GeV^2, where the DDIS data are concentrated, these measurements yield $\lambda_h \approx 0.3$. Using these values we obtain $n = 0.4$ and $m = 0.7$. We therefore expect

$$\text{Prediction:} \quad F_2^{D(3)} \propto \frac{1}{\xi^{1.4}} \times \frac{1}{\beta^{0.7}}$$

We observe the following features:

Factorization

Our prediction exhibits factorization between ξ and β, in agreement with HERA results at small ξ.

ξ-dependence

In the Regge framework, the ξ-dependence of $F_2^{D(3)}$ is expected to have the "Pomeron flux" form $\sim 1/\xi^{1+n}$ with $n = 2\epsilon = 0.2$, independent of Q^2. In the Q^2 range of 10-50 GeV^2, the HERA experiments find that n is ≈ 0.4 and has a small Q^2 dependence, in agreement with our prediction of $n = \lambda_h(Q^2) + \lambda_s$.

β-dependence

The predicted form $1/\beta^m$ for $F_2^{D(3)}$ is valid in the region of (fixed) small ξ and high Q^2, where the x-distribution of $F_2(x,Q^2)$ has the form $A^h/x^{\lambda_h(Q^2)}$. As there are no data points at strictly fixed ξ, we have selected the following set of five points at $Q^2 = 45$ GeV^2 and $\xi \approx 0.01$ from Ref. [5] with which to compare the measured values of $F_2^{D(3)}$ with our prediction:

β	x	$\xi = x/\beta$	$\xi \cdot F_2^{D(3)} \pm stat \pm syst$
0.10	0.00133	0.0133	$0.0384 \pm 0.0066 \pm 0.0030$
0.20	0.00237	0.0118	$0.0406 \pm 0.0061 \pm 0.0026$
0.40	0.00421	0.0105	$0.0215 \pm 0.0046 \pm 0.0016$
0.65	0.00750	0.0115	$0.0240 \pm 0.0054 \pm 0.0026$
0.90	0.00750	0.0083	$0.0088 \pm 0.0041 \pm 0.0005$

The following parameters are used in the calculation of $F_2^{D(3)}$: $\sqrt{s} = 280$ GeV, $\xi = 0.01$, $Q^2 = 45$ GeV^2, $\lambda_s = 0.1$, $\lambda_h = 0.3$, $f_q = 0.4$ [7], and $A^h = 0.2$; the latter was evaluated from $F_2(Q^2 = 50, x = 0.00133) = 1.46$ [6] assuming a $\frac{A^h}{x^{0.3}}$ dependence. In figure 1, our prediction for $\xi \cdot F_2^{D(3)}(\beta)$ versus β is compared with the data. The observed agreement both in shape and normalization is satisfactory, particularly since no free parameters are used in the calculation.

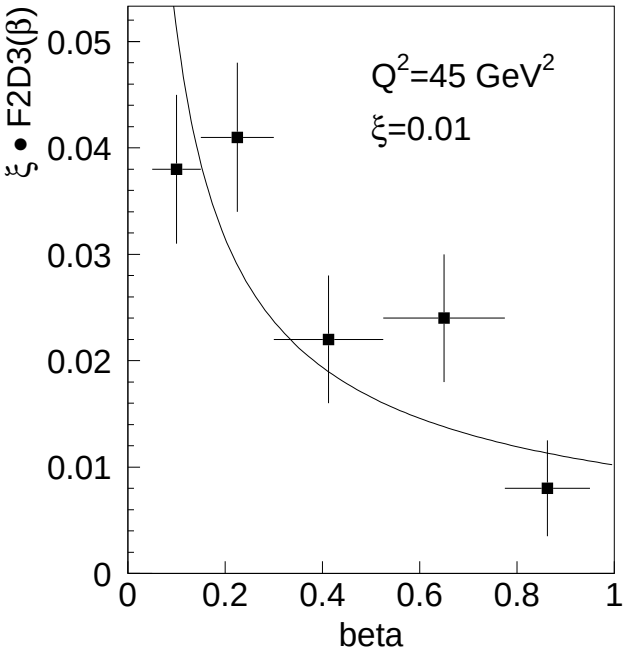

Figure 1. Predicted β dependence of $\xi \times F_2^{D(3)}(\xi,\beta,Q^2)$ for $\xi = 0.01$ and $Q^2 = 45$ GeV^2 (solid curve) compared with measured values (points) obtained from Ref. [5]

REFERENCES

1. K. Goulianos, Phys. Lett. **B358**, 379 (1995); **B363**, 268 (1995).
2. K. Goulianos and J. Montanha, Phys. Rev. **D 59**, 114017 (1999).
3. ZEUS Collaboration, *ZEUS Results on the Measurement and Phenomenology of F2 at Low x and Low Q^2* (Fig. 7), contribution to ICHEP98, Vancouver, Canada.
4. R.J.M. Covolan, J. Montanha and K. Goulianos, Phys. Lett. **B 389**, 176 (1996).
5. C. Adloff *et al.*, H1 Collaboration, Z. Phys. **C 76**, 613 (1997).
6. T. Ahmed *et al.*, H1 Collaboration, Nuc. Phys. **B 439**, 471 (1995).
7. T. Affolder *et al.*, CDF Collaboration, *Observation of Diffractive Beauty Production at the Fermilab Tevatron*, to be published in Phys. Rev. Letters.

CDF Results on Double Diffraction

M. E. Convery [a]

[a]The Rockefeller University, 1230 York Avenue, New York, NY 10021, USA

The double-diffractive cross section is measured for $\bar{p}p$ interactions which produce a central rapidity gap with width $\Delta\eta > 3$ at $\sqrt{s} = 1800$ and 630 GeV. Comparisons are made to predictions from Regge theory based on the triple Pomeron amplitude and factorization and to previous measurements.

Double-diffractive (DD) events are characterized by the exchange of a color singlet with the quantum numbers of the vacuum, the Pomeron, causing both incident hadrons to dissociate. The dissociated hadrons produce diffractive mass clusters along their initial direction, while, since the exchanged object does not radiate as, for example, a colored object would, the region in between the clusters is empty of particles.

Hard double diffraction (Fig. 1a) has previously been studied in events with rapidity gaps between jets. The fraction of dijet events with $1.8 < |\eta^{jet1,jet2}| < 3.5$, $\eta^{jet1}\eta^{jet2} < 0$, and $E_T^{jet1,jet2} > 20$ GeV at $\sqrt{s} = 1800$ GeV due to color singlet exchange (CSE) was found to be [1]

$$R_{JGJ}(1800) = [1.13 \pm 0.12(stat) \pm 0.11(syst)]\%,$$

and for jets with $E_T^{jet1,jet2} > 8$ GeV at $\sqrt{s} = 630$ GeV [2]

$$R_{JGJ}(630) = [2.7 \pm 0.7(stat) \pm 0.6(syst)]\%,$$

so that the CSE fraction at 630 GeV is greater than that at 1800 GeV by a factor of

$$R(630)/R(1800) = 2.4 \pm 0.7(stat) \pm 0.6(syst).$$

The distribution of the CSE fraction as a function of the rapidity separation between the jets was seen to drop as the jets reached the edges of the acceptance. No dependence was observed of the CSE fraction on mean dijet E_T or on jet x, determined from the E_T and η of the jets as $x_i = e^{|\eta_i|}E_T^i/\sqrt{s}$.

We have studied soft double diffraction (Fig. 1b) by looking for central rapidity gaps in minimum-bias events which have hits in the Beam-Beam Counters (BBC's). We looked for gaps which overlap $\eta = 0$ rather than the largest gap anywhere in the detector because the latter method is more likely to be biased by inefficiencies in the calorimeters. The η of the track or calorimeter tower above a given threshold with the smallest $|\eta|$ for $\eta > 0$ ($\eta < 0$) is defined to be $\eta_{max(min)}$. Events with the lowest-$|\eta|$ particle in the BBC, $3.2 < |\eta| < 5.9$, are assigned $|\eta_{max(min)}| \equiv 3.3$. The data

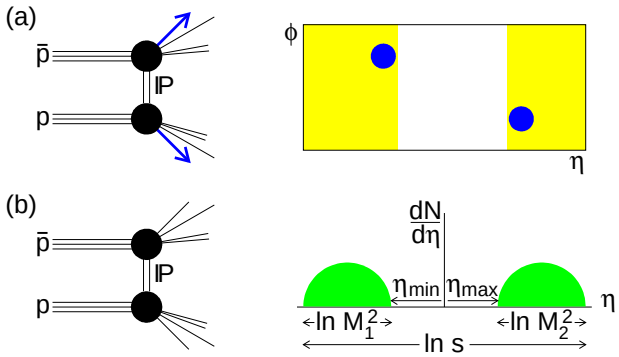

Figure 1. A double-diffractive interaction in which a Pomeron ($I\!P$) is exchanged in a $\bar{p}p$ collision at center-of-mass energy $\sqrt{s}$, (a) with a hard scattering producing jets on opposite sides of a rapidity gap, and (b) producing diffractive masses M_1 and M_2 separated by a rapidity gap of width $\eta_{max} - \eta_{min}$.

are compared to non-diffractive (ND), single-diffractive (SD), and DD Monte Carlo (MC) simulated events as a function of η_{max} and $-\eta_{min}$ (not shown). Structure due to different thresholds and efficiencies in the calorimeter is visible, e.g., at the interface between the plug and forward calorimeters at $\eta \sim 2.4$.

Figure 2 shows histograms of the data and MC as a function of $\Delta\eta^0 = \eta_{max} - \eta_{min}$. The SD contribution is fixed by known cross sections and the fraction of events passing the BBC trigger in the MC. The ND and DD contributions are determined as follows. The DD and non-DD MC distributions are normalized to give the number of events observed in the data in the region $\Delta\eta^0 < 0.8$ (dominantly ND) and $\Delta\eta^0 > 3$ (dominantly DD). The DD MC uses the differential cross sections from Regge theory based on the triple Pomeron amplitude and factorization. The agreement between data and MC seen in Fig. 2 shows that Regge theory appears to correctly predict the mass dependence, as was also observed by the H1 collaboration [3]. Note that the fluctuations in the $\Delta\eta^0$ distribution are due to structure in the calorimeter and are followed closely

by the MC because of careful calibrations derived to match MC particle p_T's to observed calorimeter E_T's.

We find cross sections at $\sqrt{s} = 1800$ (630) GeV by measuring $\sigma_{DD}\mathcal{A}$, where $\mathcal{A}$ is the detector acceptance for triggering on diffractive mass clusters. Preliminary calculations from MC yield $\mathcal{A} = (48.7 \pm 8.4)\%$ [$(61.4 \pm 6.8)\%$], and

$$\sigma_{DD}(\sqrt{s} = 1800 \text{ GeV}, \Delta\eta^0 \geq 3) = 4.71 \pm 0.02(\text{stat})^{+0.92}_{-0.90}(\text{syst}) \text{ mb},$$

$$\sigma_{DD}(\sqrt{s} = 630 \text{ GeV}, \Delta\eta^0 \geq 3) = 4.32 \pm 0.01(\text{stat})^{+0.54}_{-0.76}(\text{syst}) \text{ mb}.$$

The cross sections for all gaps of width $\Delta y > 2.3$, corresponding to the SD coherence limit of $\xi < 0.1$, can be obtained by extrapolation using the differential cross section shape from Regge theory, and are greater by a factor of 1.72 (1.67) at $\sqrt{s} = 1800$ (630) GeV. The resulting cross sections are shown in Fig. 3 along with results from UA5 [4] and other cross sections at lower energies [5,6], most of which were derived from exclusive measurements using factorization relations. The DD cross sections measured by CDF are an order of magnitude smaller than what is predicted using Regge theory, but are in general agreement with the renormalized gap model [7],

The improved plug calorimeters and proposed mini-plug detectors for CDF in Run II will allow a better measurement of the DD cross section and hard DD dijet production, including better resolution of gaps and jets out to $\eta \approx 5.5$.

REFERENCES

1. F. Abe *et al.*, (CDF Collaboration), Phys. Rev. Lett. **80**, 1156 (1998).
2. F. Abe *et al.*, (CDF Collaboration), Phys. Rev. Lett. **81**, 5278 (1998).
3. C. Adloff *et al.*, (H1 Collaboration), Z. Phys. C **74**, 221 (1997).
4. R. E. Ansorge *et al.*, (UA5 Collaboration), Z. Phys. C **33**, 175 (1986).
5. C. Conta *et al.*, Nucl. Phys. B **175**, 97 (1980).
6. A. Givernaud *et al.*, Nucl. Phys. B **152**, 189 (1979) and references therein.
7. K. Goulianos, Phys. Lett. B **358**, 379 (1995).

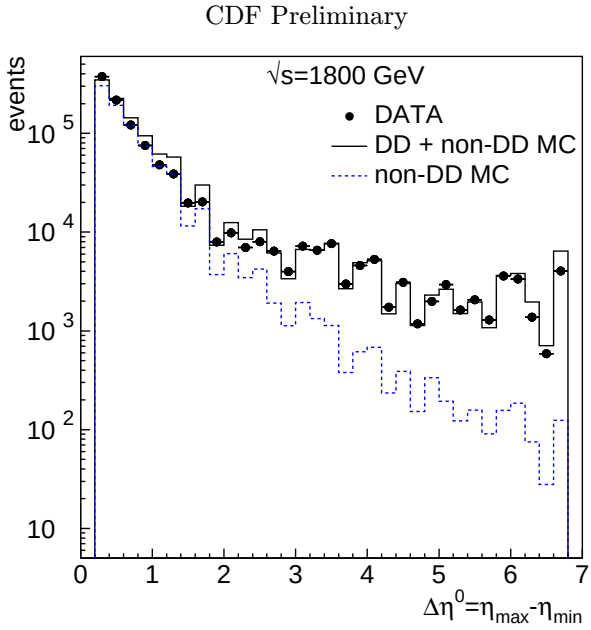

Figure 2. The number of events as a function of $\Delta\eta^0 = \eta_{max} - \eta_{min}$ for 1800 GeV data, and for DD + non-DD and only non-DD MC-generated events.

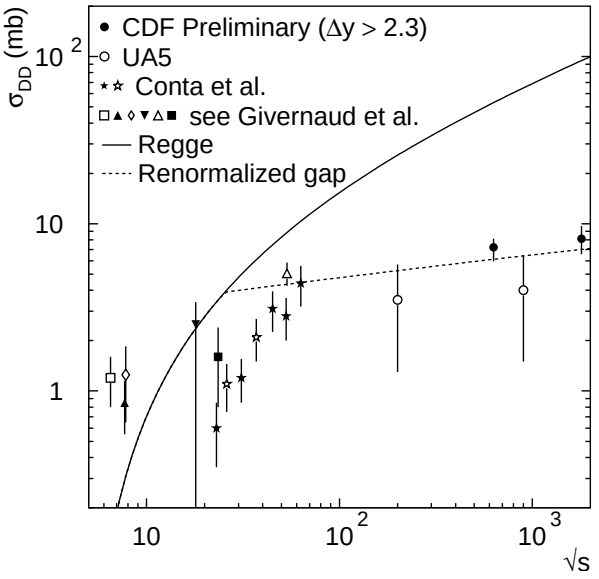

Figure 3. The total DD cross section versus $\sqrt{s}$ compared with predictions from standard Regge theory based on the triple-Pomeron amplitude and factorization (dashed curve) and from the renormalized gap model (solid curve).

Diffractive Dijets at CDF

Ken-ichi Hatakeyama[a]

[a]The Rockefeller University, 1230 York Avenue, New York, NY 10021, USA

We report results obtained from a study of Roman Pot triggered events with a leading antiproton of beam momentum fraction $0.905 < x_F < 0.975$ and 4-momentum transfer squared $|t| < 3$ GeV^2, produced in $\bar{p}p$ collisions at $\sqrt{s} = 1800$ GeV. Using events which contain two jets with transverse energy $E_T^{jet} > 7$ GeV, the diffractive structure function of the antiproton is evaluated and compared with expectations based on results obtained at HERA.

We have studied diffractive dijet events produced in $\bar{p}p$ collisions, which are characterized by two jets with high transverse energy and a leading (anti)proton accompanied by a rapidity gap. The rapidity gap, defined as a region of pseudorapidity devoid of particles, is associated with the exchange of a Pomeron ($I\!P$), which is a color-singlet state with vacuum quantum numbers. In this framework, diffractive dijet events produced in $\bar{p}p$ collisions can be expressed as, $\bar{p} + p \to [\bar{p}' + I\!P] + p \to \bar{p}' + \mathrm{Jet}_1 + \mathrm{Jet}_2 + X$.

Previously, the CDF collaboration studied diffractive W-boson, dijet and $\bar{b}b$ productions [1,2]. In these analyses, diffractive production is tagged by the requirement of a forward rapidity gap. The observed rates of diffractive W-boson, dijet and $b\bar{b}$ productions were found to be significantly lower than predictions based on factorization, while such models describe well the diffractive DIS and photoproduction data obtained at HERA [3,4]. The breakdown of factorization observed in the rate comparisons raises the question of whether the β-distribution is also process dependent, where β is the momentum fraction of the struck parton in the Pomeron. In this analysis, we measure the diffractive structure function of the antiproton, and compare it with expectations based on the diffractive parton densities obtained in diffractive DIS experiments at HERA [4].

The diffractive data used in this analysis were collected by triggering an antiproton detected in three Roman Pot (RP) spectrometers. The beam momentum fraction $x_F = 1 - \xi$ and the four momentum squared t of the detected antiproton were reconstructed from the X-Y RP track position, the position of the event vertex, and the machine transport matrix. The non-diffractive (ND) data were collected with a minimum bias (MB) trigger which required a coincidence of hits on two beam-beam counters (BBC). From these two data samples, we select diffractive and ND dijet events with two jets of $E_T > 7$ GeV.

Figs. 1(a) and 1(b) show the RP acceptance and a lego plot of the inclusive diffractive event sample as a function of ξ and t, respectively. The fraction of dijet events in the inclusive diffractive events is shown as a function of ξ in Fig. 1(c) and t in Fig. 1(d). The fraction is found to increase linearly with increasing ξ, but no significant t dependence is observed, in agreement with the UA8 result [5] which showed a flat t dependence in the region $0.9 < |t| < 2.3$. The jet E_T distributions fall faster with E_T in the diffractive events than in the ND. The diffractive dijets are boosted away from the leading antiproton in η, and are more back-to-back in ϕ than the ND.

In leading order QCD, the cross section ratio, $R(x)$, of the diffractive to ND dijet productions represents the ratio of the diffractive to ND effective structure functions defined as $F_{JJ}^{(D)}(x) = x\{g^{(D)}(x) + \frac{4}{9}\sum_i [q_i^{(D)}(x) + \bar{q}_i^{(D)}(x)]\}$. Thus, the diffractive structure may be obtained by multiplying the "known" ND structure by $R(x)$. The x, the momentum fraction of struck parton in the antiproton, is evaluated from the jets (including a third jet if $E_T^{jet3} > 5$ GeV) as, $x = \sum_{i=1,2(3)} E_T^{(i)} e^{-\eta^{(i)}}/(2p_0^{\bar{p}})$. Fig. 2 shows the ratio $R(x)$ of the diffractive dijet events to the ND dijet events for six ξ bins of width $\Delta\xi = 0.01$, where the two data samples are normalized to the same luminosity. The distributions are fitted well by the form $R(x) = R_0(x/0.0065)^{-r}$, with similar slopes for all ξ bins in the region $10^{-3} < x < 0.5\xi_{min}$.

The diffractive structure function can be determined by multiplying the measured $R(x)$ by the known ND structure function. By changing the variable from x to β $(= x/\xi)$, we obtain the diffractive structure function $F_{JJ}^D(\beta)$, shown in Fig. 3. This structure function is compared to that extracted by the H1 collaboration from diffractive DIS measurements using a QCD analysis [4]. The dashed (dotted) line in Fig. 3 is obtained from H1 diffractive parton densities derived with fit 2 (fit 3), scaled down by a factor of 20. The measured diffractive structure function does not agree with expectations from the H1 results both in normalization and shape. Summed over all β, the discrepancy in nor-

malization is about a factor of 10, in general agreement with predictions based on the renormalized Pomeron flux model [6].

In Run 2, the Roman Pot spectrometers will be placed closer to the antiproton beam, which will enable us to extend our measurement to lower ξ values. In addition, the improved plug calorimeters, two proposed miniplug calorimeters and a set of beam shower counters (BSC) to tag forward rapidity gaps will provide the basis for improved studies in hard diffraction.

REFERENCES

1. F. Abe *et al*, Phys. Rev. Lett. **78**, 2698 (1997); **79**, 2636 (1997)
2. F. Affolder *et al*, FERMILAB-PUB-99/229-E. Submitted to Phys. Rev. Lett. Aug. 7, 1999.
3. M. Derrick *et al*, Z. Phys. **C 68**, 569 (1995); Phys. Lett. **B 356**, 129 (1995).
4. C. Adloff *et al.*, Z. Phys. **C 76**, 613 (1997); Eur. Phys. J. **C 6**, 421 (1999).
5. A. Brandt *et al.* Phys. Lett. **B 298**, 417 (1992).
6. K. Goulianos, Phys. Lett. **B 356**, 379 (1995); **B 363**, 268 (1995).

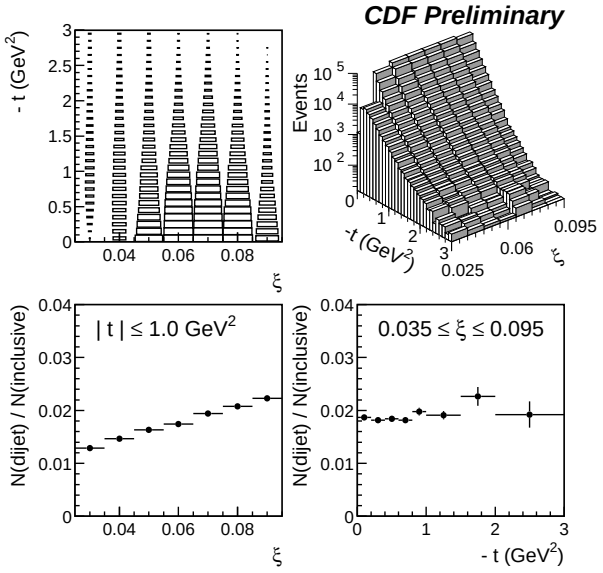

Figure 1. Distributions versus ξ and t: (a) Roman Pot acceptance; (b) inclusive diffractive event sample; (c) ratio of dijet to inclusive diffractive events versus ξ and (d) versus t.

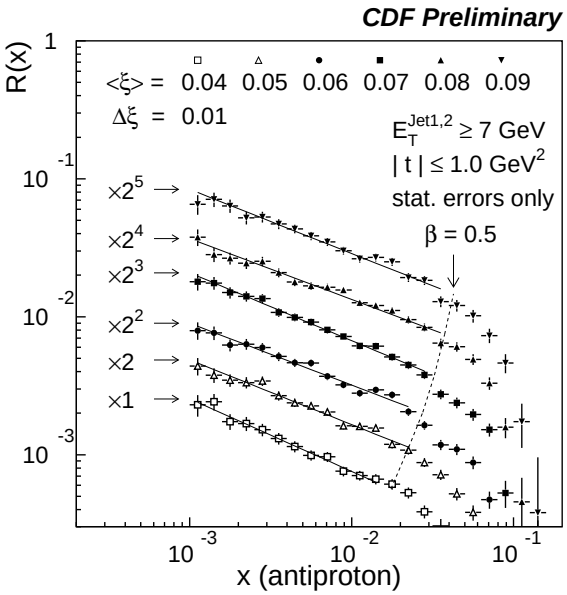

Figure 2. Ratio of diffractive to non-diffractive dijet event rates as a function of x (momentum fraction of struck parton in antiproton). The solid lines are fits to the form $R(x) = R_0(x/0.0065)^{-r}$ for $\beta < 0.5$, where $\beta = x/\xi_{min}$.

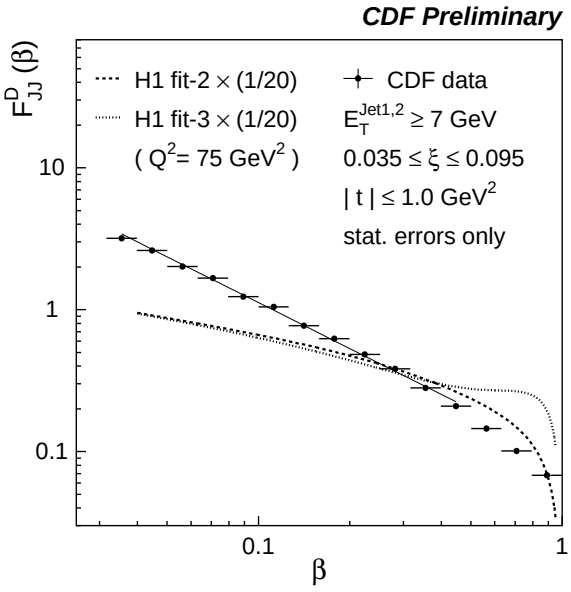

Figure 3. The β distribution from the data (points) and fit (solid line), compared with expectations from the diffractive parton densities of the proton from H1 fit 2 (dashed) and fit 3 (dotted) scaled down by a factor of 20.

DØ Rapidity Gap Studies

Andrew Brandt (DØ Collaboration)[a]

[a]University of Texas at Arlington, P.O. Box 19059, Arlington, TX 76019

DØ Run I Rapidity Gap studies are briefly described.

1. Hard Diffraction Introduction

Inelastic diffractive collisions are responsible for 10–15% of the $\overline{p}p$ total cross section and have been described by Regge theory through the exchange of a pomeron. Diffractive events are characterized by the absence of significant hadronic particle activity over a large region of rapidity or pseudorapidity. This empty region is called a rapidity gap and can be used as an experimental signature for diffraction. Recent interest in diffraction has centered on the possible partonic nature of the pomeron in the framework of quantum chromodynamics (QCD), as suggested by Ingelman and Schlein [1]. Hard single diffraction (HSD), which combines diffraction and a hard scatter (such as jet or W-boson production), can be used to study the properties of the pomeron.

The pomeron's partonic nature was first inferred by the UA8 experiment [2]. Recent analyses of diffractive jet production [3–5] and diffractive W-boson production [6] are consistent with a predominantly hard gluonic pomeron, but measured rates at the Fermilab Tevatron are several times lower than predictions based on data from the DESY ep collider HERA [7].

Current analyses in DØ on diffractive W-boson exchange, double pomeron exchange (central jets with a forward and a backward rapidity gap), and diffractive jet production all attempt to provide new insight into the nature of the pomeron and diffractive interactions. Here we present new measurements from the most mature of these analyses, diffractive jet production.

2. Diffractive Jet Production

In the DØ detector [8], jets are measured with the uranium/liquid-argon calorimeters using a fixed-cone algorithm. The jets are corrected using standard DØ routines for jet-energy scale [9], except that there is no subtraction of energy from spectator parton interactions, since these are unlikely for diffractive events. To identify rapidity gaps, we measure the number of tiles containing a signal in the LØ forward scintillator arrays ($n_{\mathrm{L}\emptyset}$), and towers ($\Delta\eta \times \Delta\phi = 0.1 \times 0.1$) above threshold in the calorimeters (n_{CAL}).

For $\sqrt{s}$ = 630 and 1800 GeV, we use triggers which required at least two jets with transverse energy $E_T > 12$ or 15 GeV to study the dependence of the gap fraction on jet location. The forward jet triggers required the two leading jets to both have $\eta > 1.6$ (or $\eta < -1.6$), while the central jet triggers had an offline requirement of $|\eta| < 1.0$. The events in the final data samples all have a single $\overline{p}p$ interaction requirement, a vertex position within 50 cm of the center of the interaction region, and two leading jets that satisfy standard quality criteria [10].

The $n_{\mathrm{L}\emptyset}$ versus n_{CAL} distributions are shown in Fig. 1. For forward jet events, these quantities are defined by the η region on the side opposite the two leading jets, while for central jet events they are defined by the forward η interval that has the lower multiplicity. The distributions display a peak at zero multiplicity ($n_{\mathrm{CAL}} = n_{\mathrm{L}\emptyset} = 0$), in qualitative agreement with expectations for a diffractive component in the data.

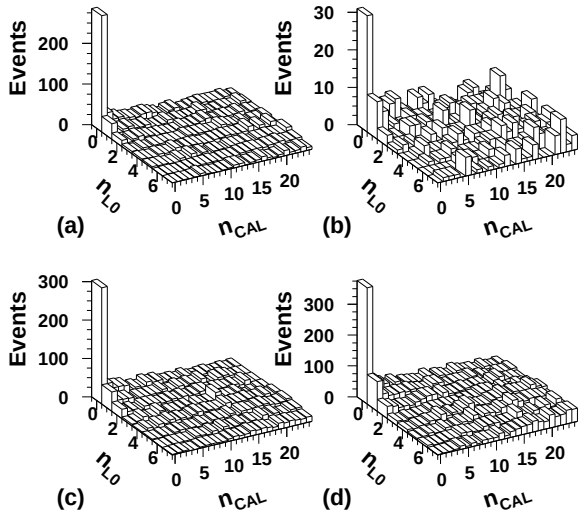

Figure 1. Multiplicity distributions at $\sqrt{s} = 1800\,\mathrm{GeV}$ for (a) forward and (b) central jet events, and at $\sqrt{s} = 630\,\mathrm{GeV}$ for (c) forward and (d) central jet events.

Table 1
The measured and predicted gap fractions and their ratios.

Gap Fractions Sample	Data	Hard Gluon	Flat Gluon	Soft Gluon	Quark
1800 GeV $\|\eta\| > 1.6$	$(0.65 \pm 0.04)\%$	$(2.2 \pm 0.3)\%$	$(2.2 \pm 0.3)\%$	$(1.4 \pm 0.2)\%$	$(0.79 \pm 0.12)\%$
1800 GeV $\|\eta\| < 1.0$	$(0.22 \pm 0.05\%$	$(2.5 \pm 0.4)\%$	$(3.5 \pm 0.5)\%$	$(0.05 \pm 0.01)\%$	$(0.49 \pm 0.06)\%$
630 GeV $\|\eta\| > 1.6$	$(1.19 \pm 0.08)\%$	$(3.9 \pm 0.9)\%$	$(3.1 \pm 0.8)\%$	$(1.9 \pm 0.4)\%$	$(2.2 \pm 0.5)\%$
630 GeV $\|\eta\| < 1.0$	$(0.90 \pm 0.06)\%$	$(5.2 \pm 0.7)\%$	$(6.3 \pm 0.9)\%$	$(0.14 \pm 0.04)\%$	$(1.6 \pm 0.2)\%$
Ratios of Gap Fractions					
630/1800 $\|\eta\| > 1.6$	1.8 ± 0.2	1.7 ± 0.4	1.4 ± 0.3	1.4 ± 0.3	2.7 ± 0.6
630/1800 $\|\eta\| < 1.0$	4.1 ± 0.9	2.1 ± 0.4	1.8 ± 0.3	3.1 ± 1.1	3.2 ± 0.5
1800 $\|\eta\| > 1.6/\|\eta\| < 1.0$	3.0 ± 0.7	0.88 ± 0.18	0.64 ± 0.12	$30. \pm 8.$	1.6 ± 0.3
630 $\|\eta\| > 1.6/\|\eta\| < 1.0$	1.3 ± 0.1	0.75 ± 0.16	0.48 ± 0.12	$13. \pm 4.$	1.4 ± 0.3

The gap fraction is extracted from a two-dimensional fit to the lego plot of $n_{\mathrm{L}\emptyset}$ versus n_{CAL}. Table 1 shows the gap fractions obtained for the four event samples. Uncertainties are dominated by those on the fit parameters. Table 1 shows that the gap fractions at $\sqrt{s} = 630$ GeV are larger than gap fractions at $\sqrt{s} = 1800\,\mathrm{GeV}$ and that gap fractions for forward jets are larger than for central jets. Table 1 also lists predicted gap fractions for several possible pomeron structure functions.

We compare the data to Monte Carlo (MC) simulations using the hard diffractive event generator POMPYT [11]. In POMPYT, a pomeron is emitted from the proton with a certain probability (called the flux factor [1]), and has a structure functions $s(\beta)$, where β is the fractional momentum of the pomeron carried by the hard parton. We used the standard Donnachie-Landshoff flux factor [12] in this analysis and compare our data to several typical structure function choices. In each case, the gap fraction is defined as the cross section for jet events with a rapidity gap based on POMPYT divided by the jet cross section from PYTHIA [13]. Many uncertainties, such as the choice of proton parton densities, cancel in the ratio. The MC values are corrected for diffractive events that fail the gap selection criteria.

Monte Carlo gap fractions are shown in Table 1. The systematic uncertainties are dominated by the difference in energy scale between data and MC. We observe that rates for harder gluon structures are far higher than supported by data, while the quark structure is in reasonable agreement with the data. The quark structure, however, has previously been shown to predict an excessive rate of diffractive W-Bosons [6].

A hard gluonic pomeron is capable of describing previous measurements [3–6], if combined with a flux factor that decreases with increasing $\sqrt{s}$ [14]. The ratios of gap fractions shown in the lower half of Table 1 provide new information, since the flux factor cancels for the same $\sqrt{s}$, and dependence on the flux factor is reduced for different $\sqrt{s}$. The ratios for jets with $|\eta| > 1.6$ to jets with $|\eta| < 1.0$ show clear disagreement between the data and predictions for a hard-gluon pomeron structure, despite this cancellation. A gluon-dominated pomeron containing both soft and hard components, combined with a reduced flux factor, could describe all the data samples.

REFERENCES

1. G. Ingelman and P. Schlein, Phys. Lett. B **152**, 256 (1985).
2. A. Brandt *et al.* (UA8 Collaboration), Phys. Lett. B **297**, 417 (1992).
3. F. Abe *et al.* (CDF Collaboration), Phys. Rev. Lett. **79**, 2636 (1997).
4. J. Breitweg *et al.* (ZEUS Collaboration), Eur. Phys. J. **C5**, 41 (1998) and references therein.
5. C. Adloff *et al.* (H1 Collaboration), Eur. Phys. J. **C6**, 421 (1999).
6. F. Abe *et al.* (CDF Collaboration), Phys. Rev. Lett. **78**, 2698 (1997).
7. L. Alvero, J.C. Collins, J. Terron and J. Whitmore, Phys. Rev. D **59**, 74022 (1999).
8. S. Abachi *et al.* (DØ Collaboration), Nucl. Instrum. Methods Phys. Res. A **338**, 185 (1994).
9. B. Abbott *et al.* (DØ Collaboration), Nucl. Instrum. Methods Phys. Res. A **424**, 352 (1999).
10. B. Abbott *et al.* (DØ Collaboration), Phys. Rev. Lett. **82**, 2451 (1999).
11. P. Bruni and G. Ingelman, DESY 93-187, 1993 (unpublished).We used a modified version of 2.6.
12. A. Donnachie and P.V. Landshoff, Nucl. Phys. B **303**, 634 (1988).
13. H.-U. Bengtsson and T. Sjöstrand, Comp. Phys. Comm. **46**, 43 (1987); T. Sjöstrand, CERN-TH.6488/92. We used version 5.7.
14. K. Goulianos, Phys. Lett. B **358**, 379 (1995).

QCD Analysis of the Diffractive Structure Functions Measured at HERA and Factorization Breaking at the Tevatron

C. Royon [a]

[a]DAPNIA/SPP, Commissariat à l'Energie Atomique, Saclay,
F-91191 Gif-sur-Yvette Cedex

The 1994 data published by the H1 collaboration are compared with models based on Regge phenomenology. The $x_{I\!P}$ dependence of the data can be described in a model based on the exchange of a dominant diffractive (pomeron) trajectory with additional sub-leading reggeon contributions. The dynamics of the Pomeron structure is studied within the framework of perturbative QCD and new parton distributions are obtained. These parton distributions will allow a direct test of factorization breaking at Tevatron.

1. Regge parameterization

The 1994 data are first investigated in the framework of a Regge phenomenological model [1]. The 1994 data are subjected to a fit in which a single factorizable trajectory ($I\!P$) is exchanged such that:

$$F_2^{D(3)}(Q^2,\beta,x_{I\!P}) = f_{I\!P/p}(x_{I\!P}) F_2^{I\!P}(Q^2,\beta) \ . \qquad (1)$$

In this parameterization, $F_2^{I\!P}$ can be interpreted as the structure function of the pomeron [4]. The value of $F_2^{I\!P}$ is treated as a free parameter at each point in β and Q^2. The pomeron flux takes a Regge form with a linear trajectory $\alpha_{I\!P}(t) = \alpha_{I\!P}(0) + \alpha'_{I\!P} t$, such that

$$f_{I\!P/p}(x_{I\!P}) = \int_{t_{cut}}^{t_{min}} \frac{e^{B_{I\!P} t}}{x_{I\!P}^{2\alpha_{I\!P}(t)-1}} \mathrm{d}t \ , \qquad (2)$$

where $|t_{min}|$ is the minimum kinematically allowed value of $|t|$ and $t_{cut} = -1$ GeV^2 is the limit of the measurement. The value of $\alpha_{I\!P}(0)$ is a free parameter and $B_{I\!P}$ and $\alpha'_{I\!P}$ are taken from hadron-hadron data [1]. The fit with a single trajectory does not give a good description of the data in the same way as it is observed at $Q^2 = 0$ [2] that secondary trajectories in addition to the pomeron are required to describe diffractive ep data.

A much better fit is obtained when both a leading ($I\!P$) and a sub-leading ($I\!R$) trajectory are considered in the same way as in formula (1), where the values of $F_2^{I\!P}$ and $F_2^{I\!R}$ are treated as free parameters at each point in β and Q^2, $\alpha_{I\!P}(0)$ and $\alpha_{I\!R}(0)$ being two free parameters. The flux factor for the secondary trajectory takes the same form as equation (2), with $B_{I\!R}$, and $\alpha'_{I\!R}$ again taken from hadron-hadron data [1]. This fit yields to the following value of $\alpha_{I\!P}(0) = 1.203 \pm 0.020$ (stat.) $\pm$ 0.013 (syst.)$^{+0.030}_{-0.035}$ (model) [1] and is significantly larger than values extracted from soft hadronic data ($\alpha_{I\!P} \sim$ 1.08). The quality of the fit is similar if interference between the two trajectories is introduced.

2. QCD fits and the structure of the Pomeron

It has been suggested that the Q^2 evolution of the Pomeron structure function may be understood in terms of parton dynamics from perturbative QCD where parton densities are evolved according to DGLAP [3] equations [4,1], using the GRV parameterization for $F_2^{I\!R}$ [5].

For the pomeron, a quark flavor singlet distribution ($zS_q(z,Q^2) = u + \bar{u} + d + \bar{d} + s + \bar{s}$) and a gluon distribution ($zG(z,Q^2)$) are parameterized in terms of coefficients $C_j^{(S)}$ and $C_j^{(G)}$ at $Q_0^2 = 3$ GeV^2 such that :

$$zS(z,Q^2=Q_0^2) \left[\sum_{j=1}^{n} C_j^{(S)} \cdot P_j(2z-1)\right]^2 \cdot e^{\frac{a}{z-1}} \qquad (3)$$

$$zG(z,Q^2=Q_0^2) \left[\sum_{j=1}^{n} C_j^{(G)} \cdot P_j(2z-1)\right]^2 \cdot e^{\frac{a}{z-1}} \qquad (4)$$

where $z = x_{i/I\!P}$ is the fractional momentum of the pomeron carried by the struck parton, $P_j(\zeta)$ is the j^{th} member in a set of Chebyshev polynomials, which are chosen such that $P_1 = 1$, $P_2 = \zeta$ and $P_{j+1}(\zeta) = 2\zeta P_j(\zeta) - P_{j-1}(\zeta)$. Some details about the fits can be found in Reference [7].

A sum of $n = 3$ orthonormal polynomials is used so that the input distributions are free to adopt a large range of forms for a given number of parameters. The exponential factor is needed to ensure a correct convergence close to z=1.

The trajectory intercepts are fixed to $\alpha_{I\!P} = 1.20$ and $\alpha_{I\!R} = 0.62$. Only data points of H1 with $\beta \leq 0.65$, $M_X > 2$ GeV and $y \leq 0.45$ are included in the fit in order to avoid large higher twist effects and the region that may be most strongly affected by a non zero value of R, the longitudinal to transverse cross-section ratio.

3. Results of the QCD fits

The resulting parton densities of the Pomeron are presented in figure 1. As it was noticed in the 1994 F_2^D paper [1], we find two possible fits quoted here as fit 1 and fit 2. Each fit shows a large gluonic content. The quark contribution is quite similar for both fits, but the gluon distribution tends to be quite different at high values of z. This can be easily explained as no data above $z = 0.65$ are included in the fits. Thus there is no constraint from the data at high z. The quark densities is on the contrary more constrained in this region with the DGLAP evolution. Both fits show similar χ^2 (the χ^2 per degree of freedom is about 1.2)*. Adding the 1995 data points into the fits also allows to get a better constraint on initial parton densities at $Q_0^2 = 3$ GeV^2 compared to the fits performed with 1994 data points alone. For the gluon density presented in figure 1, we have determined that $\frac{\delta G}{G} \simeq 25\%$ for z below 0.6.

The result of the fit is presented in figure 2 together with the experimental values for 1994 data points ; we see on this figure the good agreement of the QCD prediction and the data points, which supports the validity of description of the Pomeron in terms of partons following a QCD dynamics.

We have also tried to extend the QCD fits to lower Q^2 (below 3 GeV^2) using the 1995 F_2^D measurement. The χ^2 of the fit turns out to increase ($\chi^2/ndf = 1.6$, adding 35 low Q^2 points to the 171 points) [8]. This can be illustrated in figure 2 of Reference [8] where changes of slopes of scaling violations for Q^2 below and above 3 GeV^2 can be seen. It may indicate that breaking of perturbative QCD has already occurred in this region.

The idea would then to use these parton distributions and to compare with the measurements at Tevatron in order to study factorization breaking. The roman pots which will be available in the D0 experiment at Run II will allow a direct comparison with the results obtained from the HERA parton distributions. It will be possible to know where factorization breaking takes place at Tevatron, e.g. is it at low or high β?

4. Acknowledgments

The results described in the present contribution come from a fruitful collaboration with H. Jung and L. Schoeffel.

*Fit 2 is a bit disfavored compared to fit 1 (its χ^2 by degree of freedom is 1.3 compared to 1.2 for fit 1) and is quite instable: changing a little the parameters modifies the gluon distribution at high z.

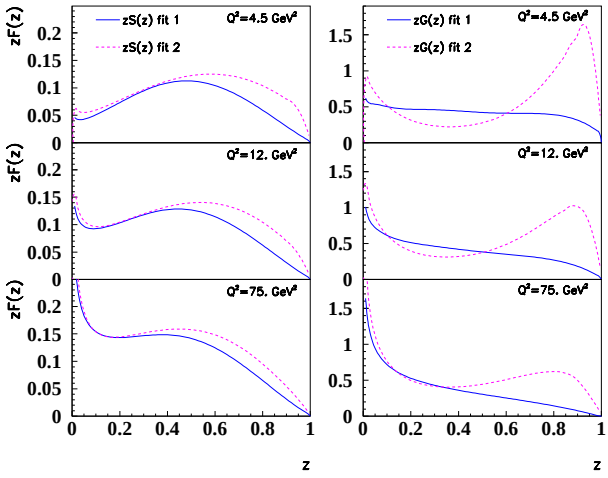

Figure 1. Quark flavor singlet (zS, left) and gluon (zG, right) distributions of the pomeron deduced as a function of z, the fractional momentum of the pomeron carried by the struck parton, from the fit on 1994 data points with $Q^2 \geq 4$ GeV^2. Two possible fits labelled as fit 1 and fit 2 are found ($\chi^2/ndf = 1.2$ for fit 1,and $\chi^2/ndf = 1.3$ for fit 2 with statistical errors only).

REFERENCES

1. H1 Collab., C.Adloff et al., Z. Phys. C76 (1997) 613.
2. H1 Collab., C. Adloff et al., Z. Phys. C74 (1997) 221.
3. G.Altarelli, G.Parisi, Nucl. Phys. B126 (1977) 298. V.N.Gribov, L.N. Lipatov, Sov. J. Nucl. Phys. 15 (1972) 438 and 675.
4. G. Ingelman, P. Schlein, Phys. Lett. B152 (1985) 256.
5. M. Glück, E. Reya, A. Vogt, Z. Phys. C53 (1992) 651.
6. V.S.Fadin, E.A.Kuraev, L.N.Lipatov Phys. Lett. B60 (1975) 50.
   I.I.Balitsky, L.N.Lipatov, Sov. J. Nucl. Phys. 28 (1978) 822.
7. L.Schoeffel, N.I.M.A423 (1999) 439.
8. C.Royon for the H1 collaboration, talk given at the DIS99 conference, Zeuthen (Allemagne), 19-23/04/99, preprint hep-ph/9908216

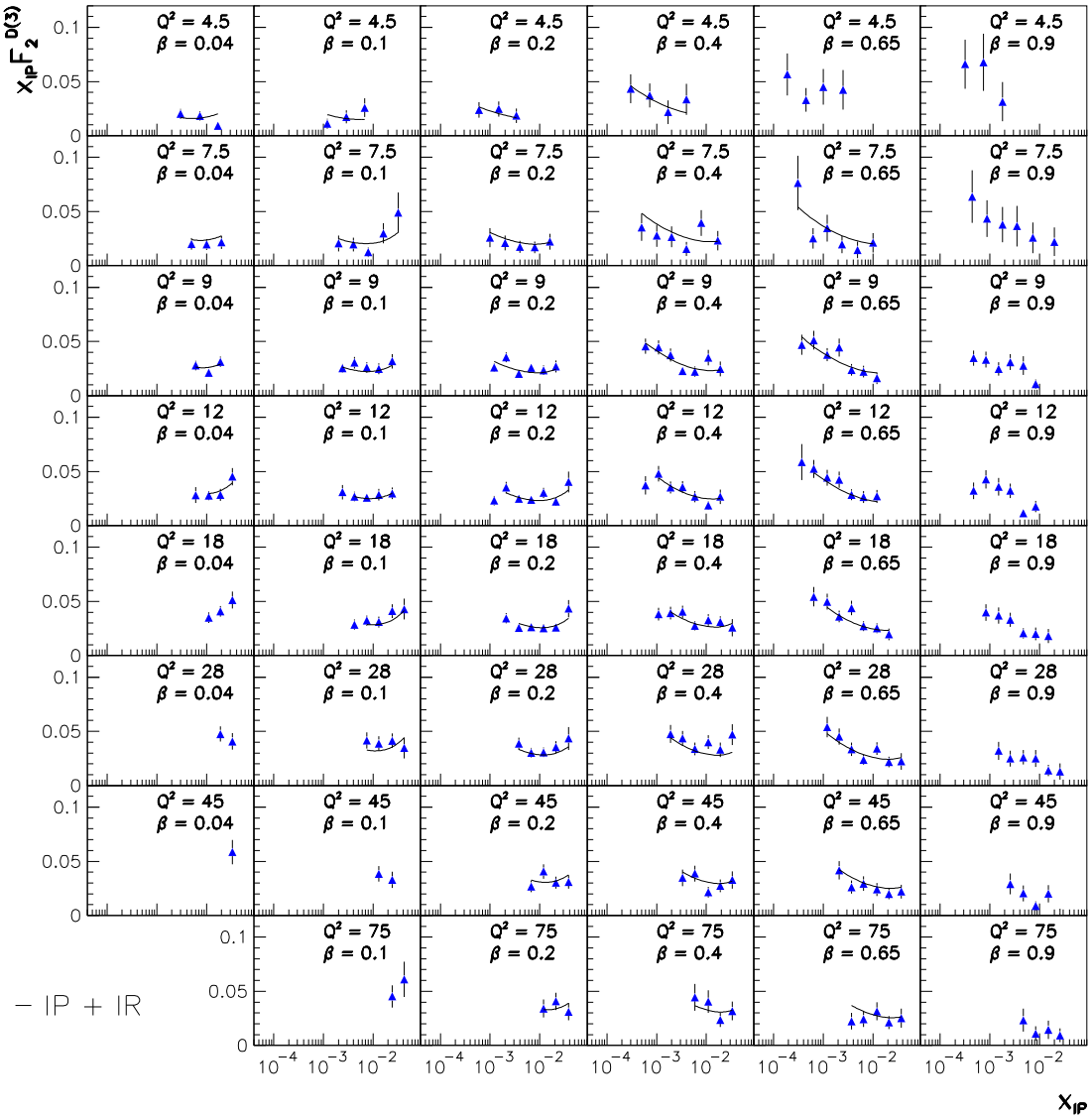

Figure 2. The H1 data points on $x_{I\!P} F_2^{D(3)}$ (1994) are shown with the result of the QCD fit described in the text; the result of the fit is drawn only in bins included in the minimization procedure.

Diffractive Heavy Flavor Production at CDF

Andrei Solodsky [a]

[a]The Rockefeller University, 1230 York Avenue, New York, NY 10021

We report results of diffractive production of heavy flavors, charm and beauty, from CDF.

We extended our studies of diffractive processes to diffractive heavy flavor production, charm and beauty, to probe directly the gluon content of the pomeron. Our diffractive beauty [1] production measurement is based on identifying a high transverse momentum electron with $E_T > 9.5$ GeV and $|\eta| < 1.1$, from the semi-leptonic b-quark decay, produced in single diffraction dissociation, $p+\bar{p} \to p/\bar{p}+b(\to e+X')+X$. Each event is required to have a jet consisting of at least two tracks in addition to the electron candidate.

First, we extract a diffractive signal from the obtained event sample and then estimate the b-quark fraction separately in the diffractive and total event samples.

As in our diffractive dijet[2] and W [3] analyses, the diffractive signal is extracted by counting BBC hits, N_{BBC}, and adjacent forward calorimeter towers, N_{CAL}, with $E > 1.5$ GeV. Figure 1(a) shows the correlation between N_{BBC} and N_{CAL} for both the positive and negative η sides of the detector, i.e. two entries per event. The (0,0) bin contains 100 events. We evaluate the non-diffractive content of the (0,0) bin from the distribution of events along the diagonal of Fig. 1(a), with $N_{BBC} = N_{CAL}$, shown in Fig. 1(b) by extrapolating a fit to the data of bins (2,2) to (9,9) to bin (0,0). This yields 24.4±5.5 non-diffractive background events in the (0,0) bin.

Figures 1(c) and 1(d) show the electron E_T and η distribution, respectively, for the diffractive (points) and total (histogram) event samples. In Fig. 1(d), the sign of η of diffractive events with a gap at positive η was changed, so that the gap always appears at negative η. While the E_T spectra show no significant difference, the diffractive η distribution is shifted away from the gap relative to the symmetric distribution of the total event sample, in agreement with the single diffraction event topology.

In addition to events from b-quark decays, the data contain events from charm decays and background. The background is mainly due to electrons from residual photon conversions and to hadrons faking electrons.

We use two methods to extract the fraction of beauty events in the data. In the first method, we fit the electron momentum component perpendicular to the jet axis, $p_T^{e/jet}$, which depends on the mass of the parent quark, with the sum of four templates: photon conversions, fake electrons from hadrons, charm and beauty. This fit yields a beauty fraction of (42.9±0.4)% [(38±14)%] for the total [diffractive] event sample. The second method uses the impact parameter of the electron track, which is defined as the minimum distance between the primary vertex and the electron track in the $r-\phi$ plane and depends on both the mass and the lifetime of the parent quark. A fit to the impact parameter distribution using four templates, as above, yields $(47.7 \pm 0.4)\%$ $[(38 \pm 14)\%]$ for our two data samples.

The average of the results of both methods yields $73371 \pm 485(stat) \pm 7774(syst)$ $[44.4 \pm 10.2(stat) \pm 4.7(syst)]$ beauty events for the total [diffractive] event sample. The difference between the results of the two methods is assigned as systematic uncertainty. After subtracting the 24% non-diffractive background estimated from the fit in Fig. 1(b), there remain $33 \pm 10(stat) \pm 5(syst)$ diffractive beauty events. Correcting the diffractive event yield for single-vertex selection cut efficiency (0.26 ± 0.01), and for the detector live-time acceptance (0.77 ± 0.07) due to noise or beam associated background, we obtain $165 \pm 50(stat) \pm 29(syst)$ diffractive beauty events.

The diffractive to total b-quark production ratio obtained from the above numbers is $R_{b\bar{b}}^{gap} = [0.23 \pm 0.07(stat) \pm 0.05(syst)]\%$. The rapidity gap acceptance for events generated using POMPYT Monte Carlo with a flat pomeron structure, which is favored by HERA measurements [4,5], and a gluon to quark ratio of 0.7±0.2, as reported in ref. 3, is found to be 0.37±0.02. Dividing $R_{b\bar{b}}^{gap}$ by this value yields a diffractive to total production ratio of

$$R_{b\bar{b}} = [0.62 \pm 0.19(stat) \pm 0.14(syst)]\% \ (\xi < 0.1).$$

POMPYT with the standard pomeron flux and a flat (hard) pomeron structure consisting of purely gluons or quarks yields $R_{b\bar{b}}$ of 10.4%(11.6%) and 0.92%(1.02%), respectively. The ratio D of the measured $R_{b\bar{b}}$ fraction to that predicted by POMPYT depends on the gluon fraction f_g of the pomeron. This dependence is shown in Fig. 2, where D is plotted as a function of f_g along with published results from ZEUS

and CDF measurements [2,3]. For each measurement the two curves show the 1σ bounds. The black cross and shaded ellipse represent the best fit and 1σ contour of a least square two-parameter fit to the three CDF results. The fit yielded $D_{CDF} = 0.19 \pm 0.04$ and $f_g^{CDF} = 0.54^{+0.16}_{-0.14}$, in agreement with the results we obtained from the W and dijet rates, namely $D = 0.18 \pm 0.04$ and $f_g = 0.7 \pm 0.2$ [2]. The value of D_{CDF} is significantly smaller than the ZEUS result. The discrepancy between the HERA and Tevatron D-values represents a breakdown of factorization. The observed discrepancy is in general agreement with predictions based on the renormalized pomeron flux model [6].

We also searched for diffractive J/ψ production in a sample of central ($|\eta| < 1.1$) dimuons. For J/ψ reconstruction we required a pair of opposite charge muons with $p_T > 2$ GeV/c and invariant mass close to the J/ψ mass. The technique we used to extract the diffractive signal is identical to that used in our previous studies. Preliminary results of this analysis, before correcting for the gap acceptance A, give a ratio of diffractive to non-diffractive J/ψ production of

$$R_{J/\psi} \times A = [0.36 \pm 0.07]\%.$$

In spite of the fact that all diffractive processes studied at CDF are differently sensitive to the quark and gluon content of the pomeron, the obtained ratios of diffractive to non-diffractive production are all of the same order of magnitude, $\sim 1\%$. This indicates that the structure of the pomeron probed in single diffraction events is not very different from the structure of the proton.

REFERENCES

1. T. Affolder *et al.*, submitted to Phys. Rev. Lett.
2. F. Abe *et al.*, Phys. Rev. Lett. **79**, 2636 (1997).
3. F. Abe *et al.*, Phys. Rev. Lett. **78**, 2698 (1997).
4. M. Derrick *et al.*, Z. Phys. **C 68**, 569 (1995); Phys. Lett. **B 356**, 129, (1995); *Eur. Phys. J.* A **6**, 43 (1999).
5. T. Ahmed *et al.*, Phys. Lett. **B 348**, 681, (1995); C. Adloff *et al.*, Z. Phys. **C 76**, 613 (1997).
6. K. Goulianos, Phys. Lett. **B 358**, 379, (1995); **B 363**, 268 (1995).

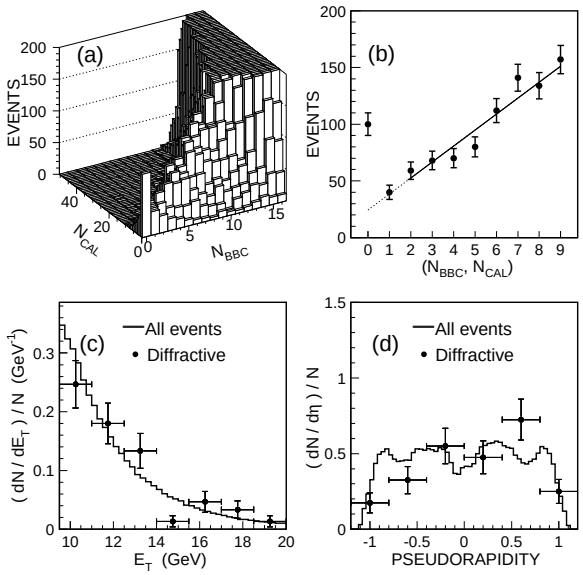

Figure 1. (a) Beam-beam counter multiplicity, N_{BBC}, versus forward calorimeter tower multiplicity, N_{CAL}; (b) multiplicity distribution along the diagonal with $N_{BBC} = N_{CAL}$ in the plot in (a); (c) electron p_T and (d) pseudorapidity for the diffractive (points) and total (histogram) event samples.

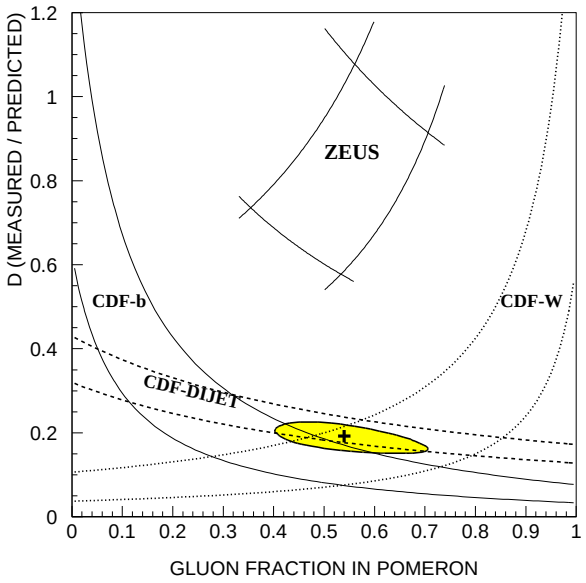

Figure 2. The ratio D of measured to predicted diffractive rates as a function of the gluon content of the pomeron.

Diffractively Produced Charm Final States in pp Interactions at 800 GeV/c

M.H.L.S. Wang [a,e], M.C. Berisso[a], D.C. Christian [b], J. Félix [c], A. Gara [d], E. Gottschalk[b], G. Gutiérrez[b], E.P. Hartouni [e], B.C. Knapp[d], M.N. Kreisler[a,e], S. Lee[a], K. Markianos[a], G. Moreno[c], M.A. Reyes[c], M. Sosa[c], A. Wehmann[b], D. Wesson[a]

[a]University of Massachusetts, Amherst, Massachusetts 01003, USA

[b]Fermilab, Batavia, Illinois 60510, USA

[c]Universidad de Guanajuato, León, Guanajuato, México

[d]Columbia University, Nevis Laboratories, Irvington, New York 10533, USA

[e]Lawrence Livermore National Laboratory, Livermore, California 94551, USA

We report the observation of charm final states produced by the diffractive dissociation reaction $pp \to pX$ at a c.m. energy of $\sqrt{s} = 40$ GeV. Signals are observed for the decay modes $D^{*+} \to D^0(K^-\pi^+)\pi^+$ and $D^{*-} \to \overline{D^0}(K^+\pi^-)\pi^-$. Our results are based on analysis of data representing over 50% of the 5.5 billion events acquired by experiment E690 in the Fermilab fixed target run of 1991.

1. Experiment

Experiment E690 was a fixed target experiment that investigated diffractive pp interactions using an 800 GeV/c proton beam incident on a fixed liquid hydrogen target. The E690 detector was made up of a beam spectrometer system and a multi-particle spectrometer. The beam spectrometer system consisted of two separate spectrometers– an incoming beam spectrometer which detected the incident beam proton and an outgoing beam spectrometer which measured the forward or scattered beam proton. Together they allowed measurement of the momentum difference between the beam proton and the fast, outgoing proton. The multi-particle spectrometer, on the other hand, which was made up of 6 drift chambers, a time-of-flight (TOF) system and a Cerenkov counter for particle identification, measured the particles produced by the interaction of the beam proton in the LH_2 target.

During the run, events were written to tape when they met the following requirements:

1. An incident beam proton in the incoming beam spectrometer.
2. A fast proton in the outgoing beam spectrometer.
3. At least one extra charged track in the main spectrometer.

By the end of the fixed target run in 1991, E690 had acquired about 5.5 billion events meeting these requirements. The number of events used for this analysis was about 2.8 billion events, representing over half of the entire data sample.

2. Charm selection

In the search for diffractive charm, the charm decay mode $D^* \to D^0(K\pi)\pi$ was used due to its low Q value (where $Q = M(K\pi\pi) - M(K\pi) - M(\pi)$) which provided a valuable signature for reducing combinatorial backgrounds. The following criteria were used to select charm candidates from the E690 data sample:

1. At least 3 tracks with the appropriate charges to form a $K\pi\pi$ invariant mass combination.
2. Track assigned as the K from the D^0 decay must have Cerenkov identification consistent with a K.
3. Track assigned as the π from the D^0 decay must have Cerenkov identification consistent with a π.
4. $1.810\ GeV/c^2 < M(K\pi\pi) < 2.210\ GeV/c^2$.
5. $|Q - .00583\ GeV/c^2| < .0005\ GeV/c^2$.
6. Only for the D^{*+}: TOF identification for slow π from the D^* decay consistent with a π.

3. Results

Applying all of these cuts to the 2.8 billion events used for this analysis resulted in 446 events for the D^{*+} and 4,916 events (without the TOF requirement for the slow π) for the the D^{*-}. Fitting a Gaussian plus a linear background to the invariant $K\pi\pi$ mass distributions of the events meeting these requirements provided an estimate of 45 events for the D^{*+} and 157 events for the D^{*-}. To select diffractive events, the

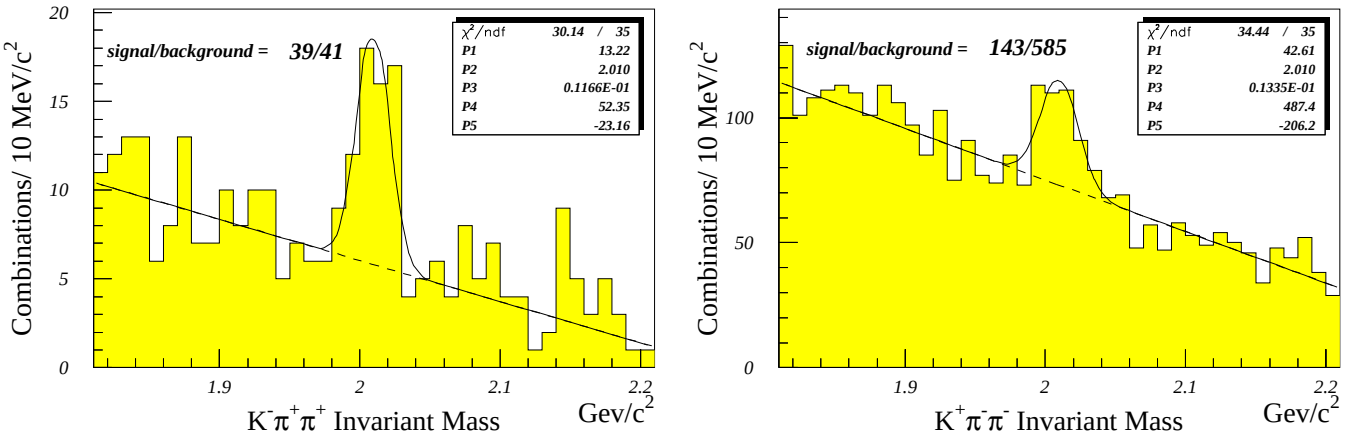

Figure 1. Invariant $K\pi\pi$ mass distributions for D^{*+} and D^{*-} events meeting the coherence condition, $x_F > 0.85$, fitted to a Gaussian plus a linear background

coherence condition [1] was imposed requiring the x_F of the fast, outgoing proton to be greater than 0.85. With this additonal requirement, fits to the $K\pi\pi$ mass distributions shown in Figure 1 yielded 39 events for the D^{*+} and 143 events for the D^{*-}. A plot of the rapidity y (where $y = \frac{1}{2}ln(\frac{E+P_L}{E-P_L})$) is shown in Figure 2 for the D^{*+}, the scattered proton, and the Y system where Y represents all the particles in the X system excluding the D^* in a single diffractive reaction of the type $pp \to p_{fast}X(D^*Y)$. This plot shows a rapidity gap of nearly 5 units between the D^* and the fast, outgoing proton p_{fast} which is characteristic of a single diffractive interaction.

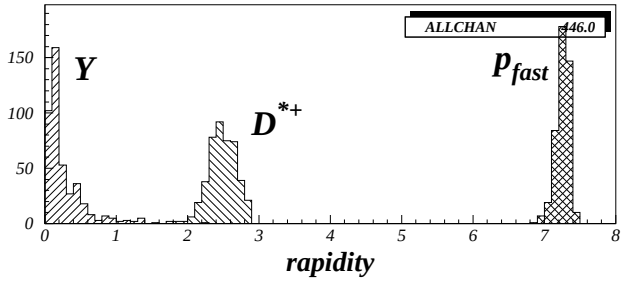

Figure 2. Rapidity plot of the D^*, Y system, and p_{fast} for $D^{*+} \to D^0(K^-\pi^+)\pi^+$ events

4. Conclusion

In conclusion, after analyzing over half of the entire E690 data sample, we observe signals of 39 events in the $D^{*+} \to \overline{D^0}(K^-\pi^+)\pi^+$ channel and 143 events in the $D^{*-} \to \overline{D^0}(K^+\pi^-)\pi^-$ channel meeting the coherence condition of $x_F > 0.85$ for the fast, outgoing proton. To our knowledge this is the first observation of open charm production in single diffractive pp interactions. A search conducted by a previous experiment, FNAL E653, found no evidence for diffractively produced charm in $p - Si$ interactions [2] resulting in an upper limit of $\sigma_{diff}(c\overline{c}) < 26\ \mu b$ for $p - Si$. If we assume that the dependence of the cross section σ on the atomic weight A goes like $\sigma \propto A^{2/3}$, this upper limit translates to $\sigma_{diff}(c\overline{c}) < 2.8\ \mu b$ in the case of pp interactions at 800 GeV/c. Preliminary cross section estimates based on the E690 results using some crude assumptions and models yielded figures consistent with this upper limit.

REFERENCES

1. K. Goulianos, Phys. Rep. 101 (1983) 170.
2. K. Kodama et al., Phys. Lett. B 316 (1993) 188.

Cost of Survival for Large Rapidity Gaps

Eugene Levin [a] [b]

[a] HEP Department, School of Physics, Tel Aviv University, Tel Aviv 69978, ISRAEL

[b] Physics Department, Brookhaven National Laboratory, Upton, NY 11973 - 5000, USA

In this note we report on calculations of the survival probability of the large rapidity gap (LRG) processes and its energy behaviour.

1. INTRODUCTION

In this note we consider the reaction

$$p + p \longrightarrow \tag{1}$$

$X_1 + jet_1(y_1, p_{1,t} \ll \mu) + [LRG] + jet_2(p_{2,t} \ll \mu) + X_2$,

where LRG denotes the large rapidity gap between produced particles and X corresponds to a system of hadrons with masses much smaller than the total energy.

The story of LRG processes started from Refs. [1–3], where it was noticed that these processes give us a unique way to measure high energy asymptotic at short distances. Indeed, at first sight the experimental observable

$$f_{gap} \;=\; \frac{\sigma(\;dijet\;\;production\;\;with\;\;LRG\;)}{\sigma_{inclusive}(\;dijet\;\;production\;)} \tag{2}$$

is directly related to the so called "hard" Pomeron exchange. However, this is not the case and the factor (survival probability $\langle |\; S\; |^2 \rangle$ appears between the "hard" Pomeron exchange and the experimental observable.

$$f_{gap} = \frac{\sigma(LRG)}{\sigma(INCL)} = \langle S^2 \rangle \frac{|\;P\;|^2}{|\;G\;|^2}$$

Actually, this factor $\langle |\; S\; |^2 \rangle$ is a product of two survival probabilities

$$\langle |\; S\; |^2 \rangle = \tag{3}$$

$\langle |\; S_{bremsstrahlung}(\Delta y = |y_1 - y_2|\; |^2 \rangle \times \langle |\; S_{spectators}(s)\; |^2 \rangle$

which have different meanings.

1. $\langle |\; S_{bremsstrahlung}\; |^2 \rangle$ is *probability that the LRG will not be filled by emission of bremsstrahlung gluons from partons, taking part in the "hard" interaction* (see fig 1-a). This factor is certainly important and has been calculated in pQCD in Refs. [4,5,10]. We are not going to discuss it here;

2. $\langle |\; S_{spectator}|\; |^2 \rangle$ is related to *probability that every parton with* $x_i > x_1$ *will have no inelastic interaction with any parton with* $x < x_2$ (see fig. 1-b). The situation with our knowledge of this survival probability is the main goal of this paper.

2. Q & A

Q: Have we developed a theory for $\langle |\; S_{spectators}\; |^2 \rangle$?

A: No, there are only models on the market (see Refs. [6–10]).

Q: Can we give a reliable estimates for the value of $\langle |\; S_{spectator}\; |^2 \rangle$?

A: No, we have only rough estimates based on the Eikonal - type models.

Q: Can we give a reliable estimates for the energy behaviour of $\langle |\; S_{spectator}\; |^2 \rangle$?

A: No, but we understood that $\langle |\; S_{spectator}\; |^2 \rangle$ could steeply decreases with energy.

Q: Why are you talking about $\langle |\; S_{spectator}\; |^2 \rangle$ if you can do nothing ?

A: Because dealing with models we learned what questions we should ask experimentalists to improve our estimate and what problems we need to solve theoretically to provide reliable estimates.

3. EIKONAL-TYPE MODELS

3.1. Eikonal model

In eikonal model we assumed that the correct degrees of freedom at high energies are hadrons, and, therefore, the scattering amplitude is diagonal in the hadron basis. Practically, it means [6] that we assume that

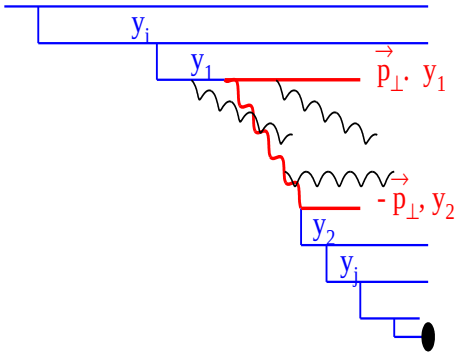

Fig.1-a

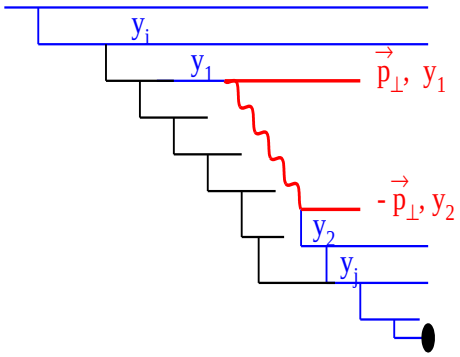

Fig. 1 -b

Figure 1. *Two sources of survival probability: (a) emission of gluons from the partons taking parts in "hard" interaction and (b) emission due to "soft" interaction of spectator quarks (partons).*

the ratio σ^{SD}/σ^{el} ' $\ll 1$. In this model the unitarity constraint looks simple, namely,

$$Ima_{el}(s,b) = \mid a_{el}(s,b) \mid^2 + G_{in}(s,b) \ , \qquad (4)$$

which has solution in terms of arbitrary real function - opacity $\Omega(s,b)$:

$$a_{el} = i\left[1 - e^{-\frac{\Omega(s,b)}{2}}\right] ; \qquad (5)$$

$$G_{in}(s,b) = 1 - e^{-\Omega(s,b)} ; \qquad (6)$$

$$\Omega(s,b) = \nu(s)\, e^{-\frac{b^2}{R^2(s)}} ; \qquad (7)$$

where Eq. (7) is Pomeron-like parameterization that has been used for numerical estimates. The formula

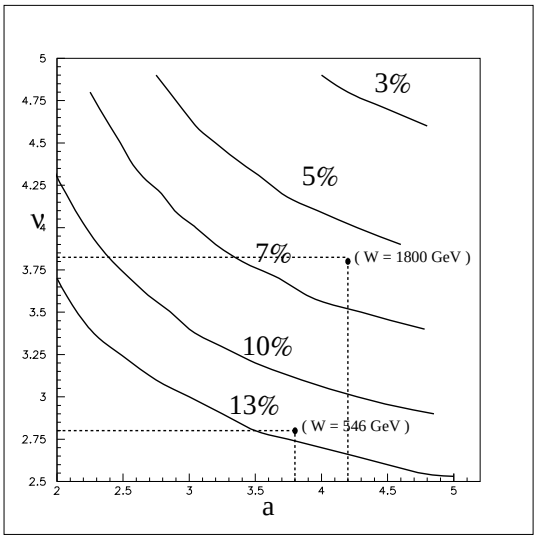

Figure 2. *Survival probability in the eikonal model.*

for survival probability looks as [3] [6]

$$<\mid S \mid^2> = \frac{\int d^2b e^{-\frac{b^2}{R_H^2}} e^{-\Omega(s,b)}}{\int d^2b e^{-\frac{b^2}{R_H^2}}} \qquad (8)$$

where R_H^2 is radius for the hard processes. In Ref. [6] the values of R_H^2 and $R^2(s)$ were discussed in details. The main observation is that the experimental value of the ration σ^{el}/σ_{tot} depends only on the value of ν. This gives us a way to find the value of ν directly from the experimental data. The result is plotted in Fig.2 and shows both the small value of the survival probability and its sharp energy dependence.

3.2. Three channel model.

The assumption that σ^{SD}/σ^{el} ' $\ll 1$ is in contradiction with the experimental data, therefore, it is interesting to generalize the eikonal model to include processes of the diffractive dissociation. It was done in Ref.[7], where the rich diffractive final state was described by one wave function orthogonal to the hadron

$$\Psi_{hadron} = \alpha\,\Psi_1 + \beta\,\Psi_2 \ ; \quad \Psi_D = -\beta\,\Psi_1 + \alpha\,\Psi_2 \ , \qquad (9)$$

where $\alpha^2 + \beta^2 = 1$. The scattering amplitude is diagonal with respect functions $\Psi_{1,2}$ and we used Eq. (5)-Eq. (7) -type parameterization to describe it. The result of our calculation is given in Fig.3.

4. CONCLUSIONS

The experimentally observed value of the survival probability appear naturally in these two models.

The parameters that have been used are in agreement with the more detailed fit of the experimental data.

It turns out that the scale of $\langle \mid S_{spectator} \mid^2 \rangle$ is given by ratios $R_{el} = \frac{\sigma_{el}}{\sigma_{tot}}$, $R_{SD} = \frac{\sigma_{SD}}{\sigma_{tot}}$ and $R_{DD} = \frac{\sigma_{DD}}{\sigma_{tot}}$, but not the ratio $R_D = \frac{\sigma_{el} + \sigma_{SD} + \sigma_{DD}}{\sigma_{tot}}$, which does not show any energy dependence.

The further measurement all ratios mentioned above will specify the model and will provide a better predictions for the survival probability. For example, new data on R_{DD} [11] will specify the value of β which will lead to more definite predictions for $\langle \mid S_{spectator} \mid^2 \rangle$ (see Fig. 3).

Acknowledgements:

I am very grateful to A. Gotsman and U. Maor for encouraging optimism and their permanent efforts in hard business of survival of LRG.

REFERENCES

1. Yu.L. Dokshitser, V. Khoze and S.I. Troyan, Sov. J. Nucl. Phys. 46 (1987) 116.
2. Yu.L. Dokshitser, V.A. Khoze and T. Sjostrand, Phys. Lett. B274 (1992)116.
3. J.D. Bjorken, Phys. Rev. D45 (1992) 4077; D47 (1993) 101.
4. A.D. Martin, M.G. Ryskin and V.A. Khoze, Phys. Rev. D56 (1997) 5867; Phys. Lett. B401 (1997) 330.
5. G. Oderda and G. Sterman, Phys. Rev. Lett. 81 (1998) 359; Talk at ISMD'99, Providence,RI, 9-13 Aug 1999, `hep-ph/9910414`;
6. E. Gotsman, E. Levin and U. Maor, Phys. Rev. D48 (1993) 2097; Nucl. Phys. B493 (1997) 354; Phys. Lett. B438 (1998) 229.
7. E. Gotsman, E. Levin and U. Maor, Phys. Rev. D60 (1999) 094011; Phys. Lett. B438 (1998) B452 (1999) 387, B438 (1998) 229.
8. R.S. Fletcher, Phys. Rev. D48 (1993) 5162; Phys. Lett. B320 (1994) 373.
9. A. Rostovtsev and M.G. Ryskin, Phys. Lett. B390 (1997) 375).
10. E. Levin, A.D. Martin and M.G. Ryskin. J. Phys. G25 (1999) 1507.
11. K. Goulianos, talk at this WS.

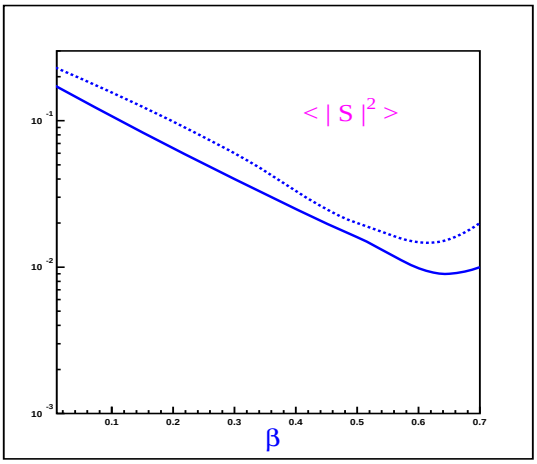

Fig.3-a

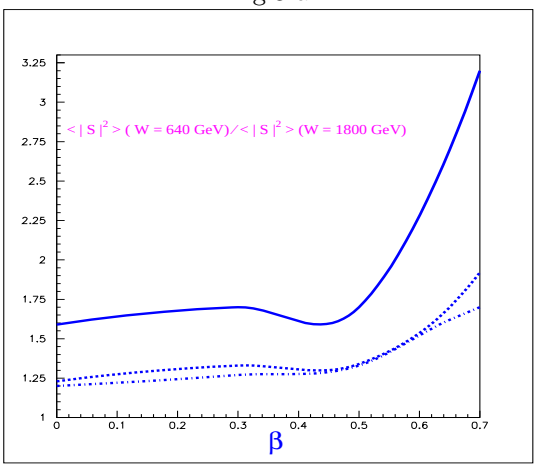

Fig. 3-b

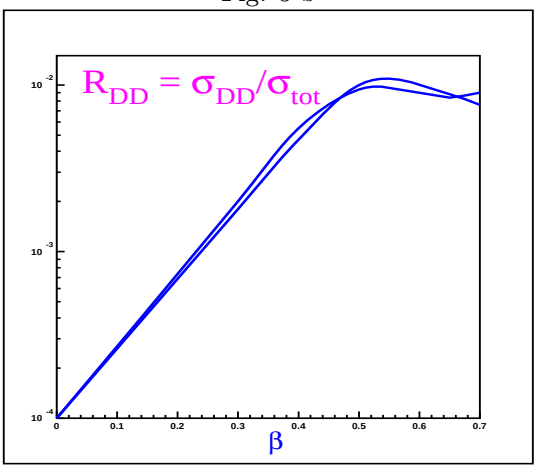

Fig. 3-c

Figure 3. *The value of survival probability (Fig.3-a), its energy dependence (Fig.3-b) and prediction for the ratio of double diffraction dissociation to the total cross section (Fig.3-c) versus β.*

Is BFKL ruled out by the Tevatron Gaps between Jets Data?

B.E. Cox, J.R. Forshaw[a] and L. Lönnblad[b]

[a]Department of Physics and Astronomy, University of Manchester, Manchester, M13 9PL, England.

[b]Dept. of Theoretical Physics 2, Sölvegatan 14A, S-223 62 Lund, Sweden.

We have performed a detailed phenomenological investigation of the hard colour singlet exchange process observed at the Tevatron in events that have a large rapidity gap between outgoing jets. We include the effects of multiple interactions to obtain a prediction for the gap survival factor. Comparing the data on the fraction of gap events with the prediction from BFKL pomeron exchange we find agreement provided that a constant value of α_s is used in the BFKL calculation. Moreover, the value of α_s is in line with that extracted from measurements made at HERA.

1. Introduction

Events with large rapidity gaps in the hadronic final state and a large momentum transfer across the gap, characterized by the presence of a hard jet on each side of the gap, have been observed in both $p\bar{p}$ collisions at the Tevatron [1–4] and in γp collisions at HERA [5,6]. Such events are unexpected in standard Regge phenomenology since the cross section is predicted to fall as $\sim s^{-\alpha|t|}$, where $\alpha \simeq 0.25$ GeV^{-2}, whilst events with $|t| > 1000$ GeV^2 are routinely observed at the Tevatron. Clearly some other explanation must be sought. Uniquely in diffractive physics, high-t events are amenable to the use of perturbative QCD since the gap producing mechanism is squeezed to small distances [7]. Such calculations have been carried out within the leading logarithmic approximation of BFKL [8] by Mueller and Tang [9], and it is the aim of this talk to present comparisons of these calculations with the latest data from the Tevatron. The situation is greatly complicated by the possibility that rapidity gaps formed by whatever process can be destroyed by multiple interactions between spectator partons in the colliding hadrons. Detailed comparisons made and conclusions drawn from any dynamic model of high-t rapidity gap formation must therefore include a careful treatment of such physics. In this analysis, we use a model implemented in the PYTHIA Monte Carlo generator to simulate the effects of multi-parton interactions.

2. DØ data versus the BFKL pomeron

The analysis presented here was stimulated to some extent by the recent DØ measurements [2] of the fraction of dijet events containing a large rapidity gap as a function of E_{T2}, the E_T of the second hardest jet, and the rapidity difference between the two leading jets, $\Delta\eta$. The DØ results are shown in figure 1. Jets are found using a cone algorithm [10,11] with cone radius 0.7 and the `OVLIM` parameter set to 0.5. The inclusive dijet sample is defined by the following cuts:

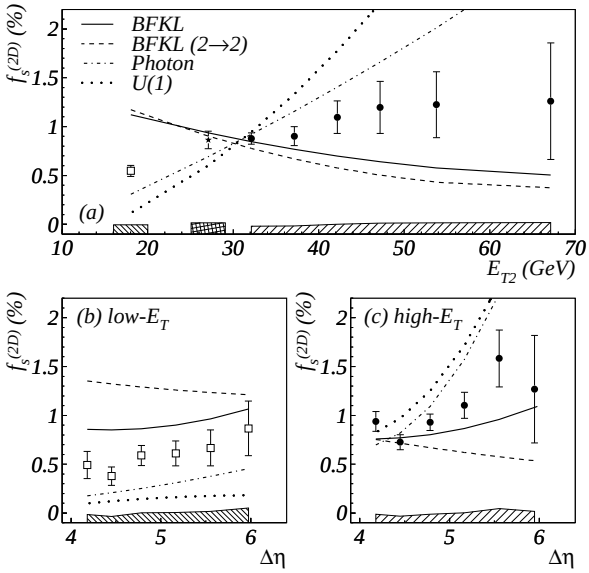

Figure 1. DØ data compared with a BFKL calculation. Plot from [2].

- $|\eta_1|, |\eta_2| > 1.9$, i.e. jets are forward or backward
- $\eta_1\eta_2 < 0$, i.e. opposite side jets
- $E_{T2} > 15$ GeV
- $\Delta\eta > 4$, i.e. jets are far apart in rapidity.

The sub-sample of gap events is obtained by employing the further cut that there be no particles emitted in the central region $|\eta| < 1$ with energy greater than 300 MeV. The BFKL curve is clearly ruled out by the data. The DØ BFKL curves are based on the

calculation of Mueller and Tang implemented into the standard HERWIG 5.9 release [12,22]. In particular, the asymptotic cross-section of [9] is used; in the limit $y \equiv \Delta\eta \gg 1$,

$$\frac{d\sigma(qq \to qq)}{dt} \approx (C_F \alpha_s)^4 \frac{2\pi^3}{t^2} \frac{\exp(2\omega_0 y)}{(7\alpha_s C_A \zeta(3) y)^3} \qquad (1)$$

where $\omega_0 = \omega(0) = C_A(4\ln 2/\pi)\alpha_s$. The α_s^4 in the pre-factor runs with $-t$ according to the two-loop beta function, $\omega_0 = 0.3$ and the α_s in the denominator $= 0.25$. The falling of the BFKL curve with increasing E_{T2} is driven by the running of the coupling in the pre-factor since the gap fraction goes like $\sim \alpha_s^4/\alpha_s^2$.

3. Key issues

In this analysis, we choose somewhat different parameters. We also use the full Mueller Tang calculation without the asymptotic approximation. This is also available in HERWIG 5.9 [23] and is available from the authors. We choose to fix $\alpha_s = 0.17$. To leading logarithmic accuracy α_s is simply an unknown parameter. Higher order corrections will indeed cause the coupling to run, however it is not clear how this should be done in a consistent way. In this paper we restrict ourselves to the leading logarithmic approximation and treat the coupling as a free parameter. Moreover, we are guided by recent HERA data on the double dissociation process [13] which can be described by the leading logarithmic BFKL formalism with $\alpha_s = 0.17$. We also note that a fixed coupling constant was needed in order to explain the high-t data on $p\bar{p}$ elastic scattering via three gluon exchange [14]. Furthermore, NLO corrections suggest a fixed value for the leading eigenvalue of the BFKL equation, $\omega(0)$, [15] which in turn suggests the use of a fixed coupling in the LLA kernel.

4. Underlying events and gap survival

As mentioned above, it is critical in any estimate of gap formation rates to take into account the possibility that gaps can be destroyed by secondary scatters, which may be perturbative or non-perturbative, between spectator partons in the colliding hadrons. Several models are available [16–18], but it would be fair to say that all are as yet in a early stage of development and are not tuned to $p\bar{p}$ data. We choose the model as implemented in PYTHIA 6.127 [17]. Here the probability to have several parton-parton interactions in the same collision is modeled using perturbative QCD. The probability for additional interactions is not fixed but varies according to an impact-parameter picture, where central collisions are more likely to have multiple interactions. The partons in the proton are assumed

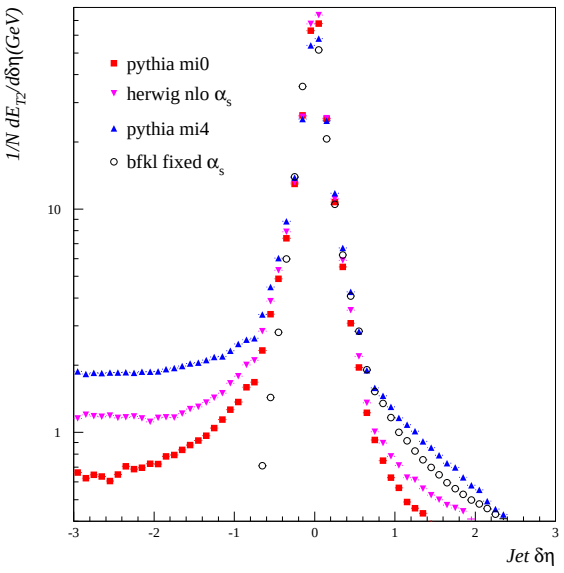

Figure 2. Jet η profiles

to be distributed according to a double-Gaussian as described in [19,17]. There are several parameters in this model and we have used the default setting for each.* Our strategy is to generate high-t photon exchange events (hard BFKL pomeron exchange has not been implemented in PYTHIA) with and without multiple interactions, and take the percentage change in the number of rapidity gap events, defined as in the DØ analysis, as the gap survival factor. We find that gap survival in this model is to first order independent of E_T^{jet} and $\Delta\eta$, i.e. it can be treated as a multiplicative factor. The gap survival factor $\mathcal{S}$ does vary strongly with centre of mass energy, which is not unexpected since the number density of partons in the colliding hadrons, and therefore the probability of having a secondary scatter, increases with energy. In summary, we find $\mathcal{S}(1800\text{ GeV}) = 22\%$, $\mathcal{S}(630\text{ GeV}) = 35\%$. Full details can be found in [20].

A key point to notice is the interplay between gap survival and underlying event : multiple interactions also give rise to the so-called jet pedestal and underlying event effects. This means that the jets measured in hadron-hadron collisions cannot be compared directly to e.g. predictions from fixed order perturbation theory. In Figure 2 we show jet profiles obtained from PYTHIA with (mi4) and without (mi0) multiple inter-

*Setting the switch `MSTP(82)=4` in PYTHIA , with everything else default, will give the model as we have used it.

actions (and with $|\delta\phi| < 0.7$). The proton remnant is at $\delta\eta > 0$. It is clear that multiple interactions introduce a jet pedestal of more than 1 GeV of E_T per unit rapidity. For comparison, also shown is the jet pedestal from HERWIG . We note that HERWIG predicts a greater amount of energy outside the jet cone than PYTHIA without multiple interactions. Again, a full discussion of these differences can be found in [20].

In the DØ jet measurements the excess E_T from the underlying event is taken into account by correcting the jet E_T using minimum bias data. In particular, the correction is determined by looking at the E_T flow in regions away from the jets. The correction is made by subtracting approximately 1 GeV from the E_T of each reconstructed jet [21]. In particular, in the gap fraction measurement, this subtraction is performed for all jets, including those in gap events. But, requiring a large rapidity gap also selects events without multiple interactions, where the jet pedestal is absent, or at least much smaller; multiple interactions destroy gaps, and therefore a gap event *cannot have* a multiple interaction. Since jet cross sections fall faster than $1/E_T^4$, such a correction can decrease the measured jet rate by up to 30% for 18 GeV jets. Our contention therefore is that the jets in gap events should not be corrected for underlying event, and therefore the gap fraction should rise less steeply with E_T than in figure 1.

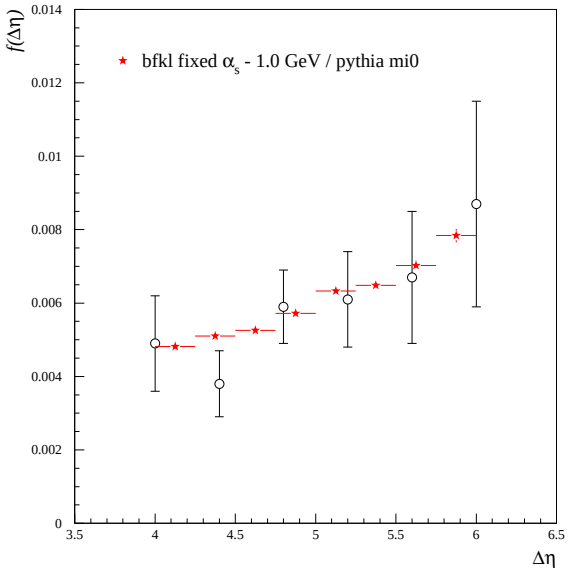

Figure 3. Gap fraction as a function of $\Delta\eta$ compared to the DØ data

5. Gap fractions

Figures 3 and 4 show our results for the gap fractions as functions of $\Delta\eta$ and E_{T2} respectively. The stars are the HERWIG BFKL simulation with fixed $\alpha_s = 0.17$, with 1 GeV subtracted from each jet in order to simulate the DØ underlying event correction and the open circles are the DØ data. The gap fractions are constructed using a standard PYTHIA QCD simulation without colour singlet exchange, and without multiple interactions. We have used both CTEQ2M and CTEQ3M parton distribution functions [24,25], and have found the differences to be small. Our philosophy is that the DØ data have been corrected for the effects of multiple interactions in non-singlet exchange events, and we should therefore generate none, whereas we must undo the erroneous correction to the colour singlet sample. The combination of fixing α_s and correcting the gap events erroneously for multiple interactions produces the rise of the gap fraction at low jet E_T. The solid circles show the gap fraction using a running α_s in the BFKL sample. Even with the underlying event correction, this sample is unable to fit the data. The overall normalisation of the simulated gap fractions is multiplied by a factor of 0.6. That this is a reasonable thing to do can be appreciated once it is realized that our results have not been fitted to the data and that the overall normalization is acutely sensitive to the magnitude of α_s. Furthermore, the overall normalization of the BFKL cross-section is uncertain since, within the leading logarithmic approximation, one does not know a priori the scale at which to evaluate the leading logarithms. Given these points, we conclude that the DØ data are in agreement with the leading order BFKL result. Figure 5 shows our result for the gap fraction as a function of $\Delta\eta \equiv 2\eta^*$ compared to the CDF data [4]. Note that CDF do not attempt to correct their jets to include the effect of an underlying event. We therefore generate the PYTHIA non-singlet sample with multiple interactions (labelled mi4), and do not perform the 1 GeV / jet subtraction from the HERWIG BFKL sample. In this plot, our theory points are obtained using a renormalization factor of unity (compared to 0.6 in the DØ case). We then find reasonable agreement with the data except at the larger values of η^* where we are quite unable to explain a fall in the η^* distribution. Recall however that DØ do not see a fall at large $\Delta\eta$. Further clarification of the situation will require an increase in statistics.

We have also computed the ratio of the gap fractions at 630 GeV and 1800 GeV. We find that, even including gap survival effects, $R(630/1800) \sim 1$ at the

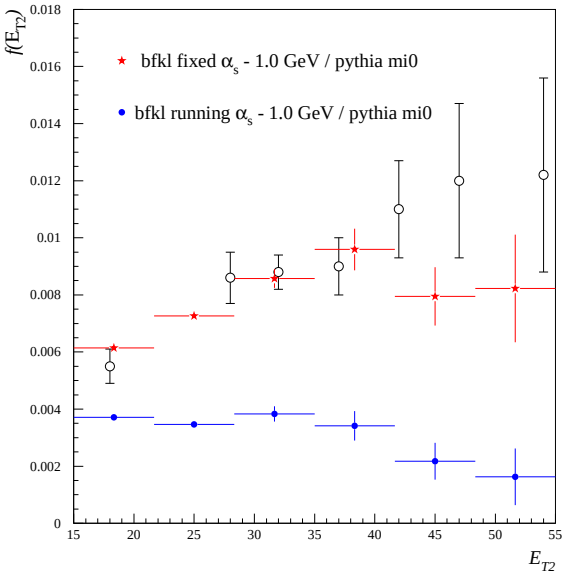

Figure 4. Gap fraction as a function of E_{T2} compared to the DØ data

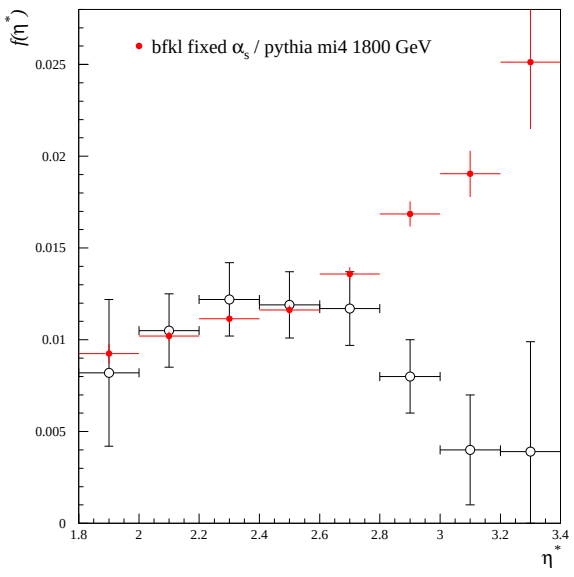

Figure 5. Gap fraction compared to the CDF data

parton level. When hadronization effects are taken into account, however, we find that the ratio rises significantly to ~ 3, with a strong dependence on $\Delta\eta$. DØ find $R(630/1800) = 3.4 \pm 1.2$ [2], and CDF find $R(630/1800) = 2.4 \pm 0.9$. In the DØ case the effect may be attributed to the different parton x ranges of the 630 GeV and 1800 GeV measurements (although we note that the CDF result is calculated at fixed x). The restriction $x < 1$ forces the gap and non-gap cross-sections to fall to zero at some maximum $\Delta\eta$, $\Delta\eta_{\rm max}$. Now, the colour connection that exists between the jets in the non-gap sample drags the jets closer together in rapidity. This has a small effect away from $\Delta\eta_{\rm max}$ (since the $\Delta\eta$ spectrum is roughly flat) however as $\Delta\eta \to \Delta\eta_{\rm max}$ it leads to a more rapid vanishing of the non-gap cross-section than occurs in the gap cross-section. This effect, combined with the fact that $\Delta\eta_{\rm max}(630\ {\rm GeV}) < \Delta\eta_{\rm max}(1800\ {\rm GeV})$, leads to an enhancement of the measured 630 GeV gap fraction at large $\Delta\eta$ at the hadron level, and hence the larger value of $R(630/1800)$.

6. Conclusions and future possibilities

We have explicitly demonstrated that the Tevatron data on the gaps-between-jets process at both 630 GeV and 1800 GeV are in broad agreement with the predictions obtained using the leading order BFKL formalism. However, we are not able to explain the behaviour of the CDF gap fraction at large $\Delta\eta$. Agreement is obtained using the same fixed value of $\alpha_s = 0.17$ as was used to explain the recent HERA data on high-t double diffraction dissociation.

Care must be taken in the interpretation of our findings, however. The BFKL formalism itself suffers from being evaluated only to leading logarithmic accuracy. The uncertainties of the overall normalization which follow will not be removed until an understanding of BFKL dynamics at non-zero t beyond the leading logarithmic approximation in achieved.

An understanding of the effects of underlying event and its impact on gap survival is crucial to the interpretation of the gaps between jets data, and indeed diffractive data as a whole.

As pointed out in [9,20], the gap fraction defined in terms of a region void of hadronic activity is not strictly infrared safe. A better observable would be to define a gap to be a region that does not contain any jets with transverse momenta above some perturbatively large scale. Work along these lines has also been performed in [26].

One major disadvantage of the gaps between jets process arises from the need to measure both jets since this limits the reach in rapidity. In [27], it was suggested to focus instead on the double dissociation sam-

ple (the gaps between jets events form a subsample of this generally much larger sample). By dropping the requirement to observe jets one not only gains in rapidity reach and statistics but also from the reduced systematics associated with this more inclusive observable.

Acknowledgements

We should like to thank Andrew Brandt, Dino Goulianos, Mark Hayes, Mike Seymour and Torbjörn Sjöstrand for helpful discussions. This work was supported by the EU Fourth Framework Programme 'Training and Mobility of Researchers', Network 'Quantum Chromodynamics and the Deep Structure of Elementary Particles', contract FMRX-CT98-0194 (DG 12-MIHT). BC would like to thank the UK's Particle Physics and Astronomy Research Council for support.

REFERENCES

1. S. Abachi et al (DØ Collaboration), Phys. Rev. Lett. **72** (1994) 2332; Phys. Rev. Lett. **76** (1996) 734.
2. B. Abbott et al (DØ Collaboration), Phys. Lett. **B81** (1998) 189.
3. F. Abe et al (CDF Collaboration), Phys. Rev. Lett. **74** (1995) 855;
   Phys. Rev. Lett. **80** (1998) 1156.
4. F. Abe et al (CDF Collaboration), Phys. Rev. Lett. **81** (1998) 5278.
5. M. Derrick et al (ZEUS Collaboration), Phys. Lett. **B369** (1996) 55.
6. H1 Collaboration, "Rapidity gaps between jets in Photoproduction at HERA", contribution to the International Europhysics Conference on High Energy Physics, Jerusalem, Israel (1997).
7. J.R. Forshaw and P.J. Sutton, Euro. Phys. J. **C14** (1998) 285.
8. I. Balitsky and L.N. Lipatov, Sov. J. Nucl. Phys. 28 (1978) 822.
9. A. H. Mueller and W. -K. Tang, Phys. Lett. **B284** (1992) 123.
10. S.D. Ellis, private communication to the OPAL Collaboration; D.E. Soper and H.-C. Yang, private communication to the OPAL Collaboration; L.A. del Pozo, University of Cambridge PhD thesis, RALT-002 (1993); R. Akers et al (OPAL Collaboration), Z. Phys. **C63** (1994) 197.
11. F. Abe et al (CDF Collaboration), Phys. Rev. **D45** (1992) 1448.
12. G. Marchesini et al, Comp. Phys. Comm. **67** (1992) 465.
13. H1 Collaboration, "Double Diffraction Dissociation at large $|t|$ in Photoproduction at HERA", contribution to the 29th International Conference on High-Energy Physics ICHEP98, Vancouver, Canada, 1998;
    B. E. Cox, "Double Diffraction Dissociation at large $|t|$ from H1", contribution to the DIS99 Workshop, Zeuthen, Germany (1999) `hep-ph/9906203`.
14. A. Donnachie and P. V. Landshoff, Z. Phys. **C2** (1979) 55, erratum-ibid **C2** (1979) 372; Phys. Lett. **B387** (1996) 637.
15. S. J. Brodsky et al, "The QCD Pomeron with Optimal Renormalisation", SLAC-PUB-8037, IITAP-98-010, `hep-ph/9901229`.
16. E. Gotsman, E. Levin, U. Maor, Phys. Lett. B438 (1998) 229; Phys. Rev. D60 (1999)
17. PYTHIA version 6.127, program and manual, T. Sjöstrand, Comput. Phys. Comm. **82** (1994) 74.
18. J. M. Butterworth, J. R. Forshaw and M. H. Seymour, Zeit. für Phys. C72 (1996) 637-646.
19. T. Sjöstrand and M. van Zijl, Phys. Rev. **D36** (1987) 2019
20. B.E.Cox, J.R. Forshaw, L.Lönnblad, JHEP10(1999)023.
21. B. Abbott et al (DØ Collaboration), Nucl. Instrum. Methods **A424** (1999) 352.
22. J. M. Butterworth, M. E. Hayes, M. H. Seymour and L. E. Sinclair, "Rapidity gaps between jets", in the proceedings of the Workshop 'Future Physics at HERA', eds. G. Ingelman, A. de Roeck and R. Klanner, DESY (1996).
23. M. E. Hayes, University of Bristol PhD Thesis (1997).
24. H. L. Lai et al, Phys. Rev. **D55** (1997) 1280.
25. H. Plothow-Besch, "PDFLIB User's Manual", W5051 PDFLIB, 1997.07.02, CERN-PPE; Int. J. Mod. Phys. **A10** (1995) 2901.
26. G. Oderda and G. Sterman, Phys. Rev. Lett. 81, 3591 (1998).
27. B. E. Cox and J. R. Forshaw, Phys. Lett. **B434** (1998) 133-140.

Interjet Energy and Color Flow

George Sterman[a]

[a]C.N. Yang Institute for Theoretical Physics
SUNY, Stony Brook, NY 11794-3840, USA

Rapidity gap events are conventionally defined by requiring no particle production in a gap region. In the case of dijet events, the distribution of energy, $E_{\rm gap}$, that flows into the interjet region is calculable in perturbative QCD nearly down to $E_{\rm gap} = 0$, and sheds light on the role of color exchange in hard scattering. Distributions are calculable for $E_{\rm gap}$ as a function of scattering angle, momentum transfer and gap width. The concept of a hard color singlet exchange is clarified.

1. GAPS AND COLOR FLOW

A compelling heuristic principle suggests that the exchange of gluons in a color singlet state produces little radiation even when the scattering produces jets at high p_T [1]. The correspondence has such currency that dijet gap events are routinely termed "color singlet exchange". This insight, however, has been difficult to implement in perturbative terms. After all, gluons of any energy carry octet color charge, so that there is no unique way of defining color exchange in a finite amount of time [2]. On the other hand, it takes a very short time to radiate a hard gluon, and once radiated, it cannot be reabsorbed on the basis of soft color rearrangements at very long times.

1.1. Two-gluon vs. Soft Color Models

The simplest short-distance model for dijet gaps is based on two-gluon exchange [1]. In a two-gluon model, the gap is usually filled by spectator interactions, up to a "survival probability", P_S, which may be estimated [1,3] from low-p_T diffractive scattering to be of order one tenth. Denoting the probability for hard color-singlet exchange as f_1, the fraction of gap events becomes

$$f_{\rm gap} = f_1 \, P_S \, . \tag{1}$$

If we estimate $f_1 \sim \mathcal{O}(\alpha_s(p_T)/\pi) \sim 0.1$, we predict gap events at the one percent level, and this is what is seen experimentally [4–7]. This analysis would lead us to expect more gap events from gluon-gluon than quark-quark scattering, because of the larger color factors in exchange graphs between gluons. This expectation was tested by comparing 630 and 1800 GeV data from the Tevatron, because at fixed p_T the role of gluon-gluon scattering increases with the overall center-of-mass energy. The proportion of gap events, however, decreased, rather than increased, with the energy.

In the soft color approach [8], normally presented as an alternative to the two-gluon model, the underlying hard scattering is treated at lowest order, which for gap events is primarily single-gluon, color octet exchange. The gap probability is determined by counting possible color exchanges, assuming all to be equally likely, up to an overall survival factor (rather larger than 1/10). Because gluons have more color states than quarks, they are correspondingly less likely to produce gap events. The soft color model then naturally leads to fewer gap events as the energy, and hence the role of gluons, increases.

1.2. Energy Flow

A third approach is a perturbative QCD formalism for rapidity gaps, made possible by redefining gaps in terms of an energy flow, $E_{\rm gap}$, rather than particle multiplicity [9]. The resulting cross sections can be treated via standard factorization theorems. In this formulation, if $E_{\rm gap} \gg \Lambda_{\rm QCD}$ the cross section is perturbatively calculable. In addition, when $p_T \gg E_{\rm gap} \gg \Lambda_{\rm QCD}$, the gap cross sections have two perturbative scales, and logarithms in their ratio can be resummed by renormalization group methods.

Resummation in $\ln(E_{\rm gap}/p_T)$ allows us to probe color flow at short distances, and to generalize the concept of hard color singlet exchange.

The dijet cross section at measured $E_{\rm gap} \gg \Lambda_{\rm QCD}$ falls into the class of inclusive jet cross sections that can be written in factorized form:

$$\frac{d\sigma}{dE_{\rm gap}\, d\cos\hat\theta}\,(\Delta y) \;=\; \sum_{f_A, f_B} \phi_{f_A/p} \otimes \phi_{f_B/\bar p} \otimes \sum_{f_C, f_D} \frac{d\hat\sigma^{(\rm f)}}{dE_{\rm gap}\, d\cos\hat\theta}\,(\Delta y) \; , \tag{2}$$

with the $\phi_{f/h}$ parton distributions, evaluated at the scale of the dijet momentum transfer. The partonic cross section $d\hat\sigma^{(\rm f)}/dE_{\rm gap}\, d\cos\hat\theta$ is a hard scattering function, starting with the Born cross section at lowest order (cf. the soft color model). The index f denotes the partonic hard scattering $f_A + f_B \to f_C + f_D$. The cross section depends on the dijet pair rapidity y_{JJ}, the partonic center-of-mass (c.m.) energy

squared $\hat{s}$, the partonic c.m. scattering angle $\hat{\theta}$, with $-\frac{\hat{s}}{2}\left(1-\cos\hat{\theta}\right)=\hat{t}$, and Δy, the gap size as a rapidity interval.

2. INTERJET ENERGY DISTRIBUTION

To leading logarithm in $E_{\rm gap}/\sqrt{-\hat{t}}$, the gap energy dependence is of the form

$$\frac{d\hat{\sigma}^{(\rm f)}}{dE_{\rm gap}\,d\cos\hat{\theta}}\,(\Delta y) \;=\; \sum_{\beta\gamma}\,\tilde{\sigma}_{\beta\gamma}(\hat{\theta}) \times\frac{E_{\gamma\beta}}{E_{\rm gap}}\,\left[\ln\left(\frac{E_{\rm gap}}{\Lambda}\right)\right]^{E_{\gamma\beta}-1}\,\left[\ln\left(\frac{\sqrt{-\hat{t}}}{\Lambda}\right)\right]^{-E_{\gamma\beta}}\,. \quad (3)$$

In this expression, β and γ label the color exchange at short distances, contained in $\bar{\sigma}$, in a color tensor basis that diagonalizes a perturbative anomalous dimension matrix. The exponents $E_{\gamma\beta}$ are given in terms of the eigenvalues, $\lambda_\beta=(\alpha_s/\pi)\lambda_\beta^{(1)}$, of this matrix by

$$E_{\gamma\beta}\left(\hat{\theta},\Delta y\right)=\frac{2}{\beta_0}\,\left[\lambda^{(1)*}_\gamma,+\hat{\lambda}^{(1)}_\beta\right]\,, \quad (4)$$

with $\beta_0=11N_c/3-2n_f/3$. The color exchange with smallest eigenvalue thus dominates the behavior of the cross section in the limit $E_{\rm gap}/p_T\to 0$.

The concept of a dominant eigenvalue generalizes conventional hard singlet exchange, because the eigenvectors of the anomalous dimension matrix are linear combinations of elements in the basis of t-channel color transfers. The coefficients depend, in general, on the jet scattering angle. Eq. (3) thus leads to a detailed set of predictions for dijet data with measured interjet energy flow.

Explicit anomalous dimension eigenvalues λ_α for quark and gluon processes may be found in Ref. [10]. The overlap of the dominant eigenvector with hard color singlet exchange grows in the direction of forward scattering for all partonic processes, so that in the Regge limit, $-\hat{t}/\hat{s}\to 0$, $\hat{t}$ fixed, the dominant color exchange becomes purely color singlet [11]. In addition, the eigenvalues for gluon-gluon scattering are larger than those for processes involving quarks. This makes it harder for gluon-gluon hard scattering to produce rapidity gaps, for much the same reasons as in the soft color model: the size of the eigenvalue λ_α is related to the number of color states available. At low interjet energy, however, the smallest eigenvalue for quark-antiquark scattering is actually less than unity in absolute value, and produces a small upturn in the interjet energy distribution in predictions based on Eq. (3) [9]. This is the "hard singlet exchange" observed by CDF and D0 [4,5]. Gap events defined by vanishing particle multiplicity in the interjet region are counted in this excess. The perturbative predictions for such events must be diluted, as usual, by corrections associated with spectator interactions, which, according to the factorization formalism, are suppressed only by powers of $\Lambda_{\rm QCD}/E_{\rm gap}$, and which therefore become important for small $E_{\rm gap}$. We have in Eqs. (2)-(4), however, a set of predictions for the full range of $E_{\rm gap}$.

3. SUMMARY

Energy flow analysis makes possible a quantitative study of radiation in interjet regions, and gives a perturbative meaning to short-distance color exchange, generalizing both the two-gluon and soft color models. On the basis of this analysis, gaps in dijet events come from a compound structure, predominantly, but not purely, singlet in the hard scattering [9,10]. Many qualitative results, including the relative suppression of dijet gaps for gluon-gluon scattering, are consistent with the successes of the soft color model. The perturbative analysis offers a systematic set of differential predictions for energy flow, as a function of momentum transfer, flavor and interjet rapidity interval.

REFERENCES

1. J.D. Bjorken, Phys. Rev. D **47**, 101 (1993).
2. R. Oeckl and D. Zeppenfeld, Phys. Rev. D **58** 014003 (1998), hep-ph/9801257.
3. E. Gotsman, E. Levin and U. Maor, Phys. Lett. B **309**, 199 (1993); Phys. Lett. B **452** 387 (1999) hep-ph/9901416.
4. F. Abe *et al.* (CDF Collaboration) Phys. Rev. Lett. **74**, 855 (1995); Phys. Rev. Lett. **80**, 1156 (1998).
5. S. Abachi *et al.* (D0 Collaboration) Phys. Rev. Lett. **76**, 734 (1996).
6. B. Abbott *et al.* (D0 Collaboration) Phys. Lett. B **440** 189 (1998); F. Abe *et al.* (CDF Collaboration) Phys. Rev. Lett. **81** 5278 (1998).
7. M. Derrick *et al.* (ZEUS Collaboration), Phys. Lett. B **369**, 55 (1996).
8. O.J.P. Eboli, E.M. Gregores and F. Halzen, Phys. Rev. D **58** 114005 (1998).
9. G. Oderda and G. Sterman, Phys. Rev. Lett. **81** 3591 (1998), hep-ph/9806530.
10. G. Oderda, Stony Brook report ITP-SB-98-70, Mar 1999, hep-ph/9903240.
11. V. Del Duca end W.-K. Tang, Phys. Lett. B **312**, 225 (1993).

Color Evaporation Induced Rapidity Gaps

O. J. P. Éboli[a*], E. M. Gregores[a], and F. Halzen[b]

[a]Instituto de Física Teórica, Universidade Estadual Paulista
Rua Pamplona 145, 01405–900, São Paulo – SP, Brazil

[b]Department of Physics, University of Wisconsin
Madison, WI 53706, USA

We show that soft color rearrangement of final states can account for the appearance of rapidity gaps between jets. In the color evaporation model the probability to form a gap is simply determined by the color multiplicity of the final state. This model has no free parameters and reproduces all data obtained by the ZEUS, H1, DØ, and CDF collaborations.

1. Introduction

The inclusion of soft color interactions between the dynamical partons leads to a parameter–free calculation of the formation rate of rapidity gaps. The idea is extremely simple. A rapidity gap occurs whenever final state partons form color singlet clusters separated in rapidity. As the partons propagate within the hadronic medium, they exchange soft gluons which modify the string configuration. The probability to form a rapidity gap is then determined by the color multiplicity of the final states formed by the dynamical partons, and nothing else. All data obtained by ZEUS, H1, DØ, and CDF collaborations are reproduced when this color structure of the interactions is superimposed on the usual perturbative QCD calculation for the production of the hard jets. We pointed out [1] that this soft color mechanism is identical to the color evaporation mechanism [2] for computing the production rates of heavy quark pairs produced in color singlet onium states, like J/ψ. Moreover, we also suggested that the soft color model could provide a description for the production of rapidity gaps in hadronic collisions [1].

The success of the color evaporation model to explain the data on quarkonium production is unquestionable [3]. We showed [5] that the straightforward application of the color evaporation approach to the string picture of QCD readily explains the formation of rapidity gaps between jets at the Tevatron and HERA colliders.

2. Color Counting Rules

In the color evaporation scheme for calculating quarkonium production, it is assumed that all color configurations of the quark pair occur with equal probability. We propose that the same color counting applies to the final state partons in high E_T jet production. In complete analogy with quarkonium, the production of high energy jets is a two–step process where a pair of high E_T partons is perturbatively produced at a scale E_T, and hadronize into jets at a scale of order Λ_{QCD} by stretching color strings between the partons and spectators. The strings subsequently hadronize. Rapidity gaps appear when a cluster of dynamical partons, *i.e.* interacting partons or spectators, form a color singlet. As before, the probability for forming a color singlet cluster is inversely proportional to its color multiplicity.

The soft color procedure is obvious in a specific example: let us calculate the gap formation probability for the subprocesses $p\bar{p} \to Q^V \bar{Q}^V \to Q\bar{Q}XY$, where Q^V stands for u or d valence quark, and X (Y) is the diquark remnant of the proton (antiproton). The final state is composed of the X ($\mathbf{3}\otimes\mathbf{3}$) color spectator system with rapidity $\eta_X = +\infty$, the Y ($\overline{\mathbf{3}} \otimes \overline{\mathbf{3}}$) color spectator system with $\eta_Y = -\infty$, one $\mathbf{3}$ parton j_1, and one $\overline{\mathbf{3}}$ parton j_2. It is the basic assumption of the soft color scheme that by the time these systems hadronize, any color state is equally likely. One can form a color singlet final state between X and j_1 since $\mathbf{3} \otimes \mathbf{3} \otimes \mathbf{3} = \mathbf{10} \oplus \mathbf{8} \oplus \mathbf{8} \oplus \mathbf{1}$, with probability 1/27. Because of overall color conservation, once the system $X \otimes j_1$ is in a color singlet, so is the system $Y \otimes j_2$. Moreover, to form a rapidity gap these systems ($j_1 \otimes X$ and $j_2 \otimes Y$) must not overlap in rapidity space. In this configuration, the color strings linking the remnant and the parton will not hadronize in the region between the two jets. We have thus produced two jets separated by a rapidity gap using the color counting rules which form the basis of the color evaporation scheme for calculating quarkonium production.

3. Rapidity Gaps at HERA

The differential cross section has two sources of gap events: color evaporation gaps ($d\sigma^{gap}_{c\epsilon m}$) and background gaps ($d\sigma^{gap}_{bg}$). In our model, the gap cross sec-

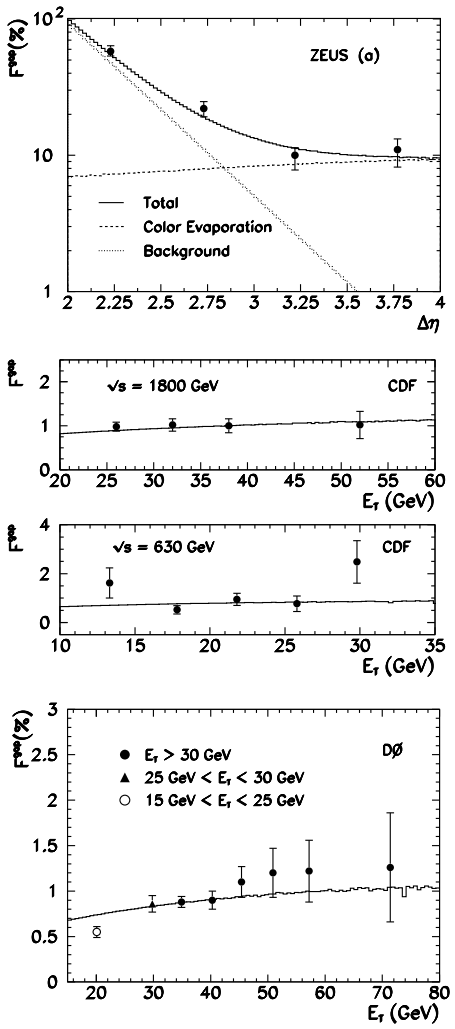

Figure 1. Frequency of events with rapidity gap between jets as a function of the gap size $\Delta\eta$ in γp collisions, and as function of the jets transverse energy in $p\bar{p}$ collisions.

tion is the weighted sum over resolved events, $d\sigma^{gap}_{cem} = \sum_N F_N \; d\sigma^N_{res}$, with gap probability F_N for the different processes. Background gaps are formed when the region of rapidity between the jets is devoid of hadrons because of statistical fluctuation of ordinary soft particle production. Their rate should fall exponentially as the rapidity separation $\Delta\eta$ between the jets increases. We parametrize the background gap probability as $F_{bg}(\Delta\eta) = e^{b(2-\Delta\eta)}$, where b is a constant. The background gap cross section is then written as $d\sigma^{gap}_{bg} = F_{bg}(\Delta\eta) d\sigma^{jets} - d\sigma^{gap}_{cem})$.

The gap frequency $F^{gap}(\Delta\eta) = d\sigma^{gap}/d\sigma^{jets}$ is shown in the figure, where we depict the contributions of the color evaporation mechanism and the background.

4. Rapidity Gaps at Tevatron

The color evaporation model prediction for the gap production rates in $p\bar{p}$ collisions is analogous to the one in $p\gamma$ interactions, with the obvious replacement of the photon by the antiproton, represented as a $\bar{\mathbf{3}} \otimes \bar{\mathbf{3}} \otimes \bar{\mathbf{3}}$ system.

The distributions presented by CDF are normalized to unity on average. Therefore our predictions do not exhibit any free parameter to be adjusted. In the figure we compare our predictions with CDF results of the gap fraction as a function of the jets transverse energy. To compare with DØ results we assumed an *ad-hoc* survival probability of 30%.

We can also compare the ratio $R = F^{gap}_{630}/F^{gap}_{1800}$ with the experimental result. DØ has measured this fraction for jets with $E_T > 12$ GeV for both energies, and they found $R = 3.4 \pm 1.2$; we predict $R = 2.5 \pm 0.5$. On the other hand, CDF measured this ratio using different values for E_T^{min} at 630 GeV and 1800 GeV; they obtained $R = 2.0 \pm 0.9$ while we obtained $R = 2.0 \pm 0.4$ for the same kinematical arrangement.

5. Conclusion

In summary, the occurrence of rapidity gaps between hard jets can be understood by simply applying the color evaporation scheme for calculating quarkonium production to the conventional perturbative QCD calculation of the production of hard jets. The agreement between data and this model is impressive.

REFERENCES

1. J. Amundson, O. J. P. Éboli, E. M. Gregores, and F. Halzen, Phys. Lett. B**372**, 127 (1996).
2. H. Fritzsch, Phys. Lett. B**67**, 217 (1977); F. Halzen, Phys. Lett. B**69**, 105 (1977).
3. R. Gavai *et al.*, Int. J. Mod. Phys. A**10**, 3043 (1995); J. Amundson, O. J. P. Éboli, E. M. Gregores, and F. Halzen, Phys. Lett. B**390**, 323 (1997); O. J. P. Éboli, E. M. Gregores, and F. Halzen, Phys. Lett. B**395**, 113 (1997); *ibidem* **451**, 241 (1999); *idem*, Phys. Rev. D **60**, 117501 (1999).
4. O. J. P. Éboli, E. M. Gregores, and F. Halzen, Phys. Rev. D**58**, 114005 (1998).
5. O. J. P. Éboli, E. M. Gregores, and F. Halzen, MADPH-99-1135, Aug 1999, `hep-ph/9908374`.

Monte Carlo Simulation of Color Singlet Exchange Between Jets

R. Engel[a] and J. Ranft[b]

[a]University of Delaware, Bartol Research Institute, Newark, DE 19716, USA

[b]Physics Dept. Universität Siegen, D–57068 Siegen, Germany

1. Introduction

Rapidity gaps between jets are an ideal configuration for searching for new-physics signatures [1]. They also provide a clean environment for testing the dynamics of perturbative QCD in Regge limit [2]. The large rapidity difference between the jets together with the transverse momentum of the two back-to-back pointing jets ensure that the center of mass energy of the hard process is much greater than its typical hard scale. In literature, alternative calculations have been proposed for such processes including the approximation of the n-gluon exchange by a BFKL pomeron [2,3] and soft color recombination (evaporation) [4,5]. Both models predict different dependences of the rapidity gap event fraction on the width of the rapidity gap and on the jet transverse momentum.

In this paper we shall calculate the experimentally observable cross section for color singlet exchange between jets using a detailed Monte Carlo simulation of both parton-parton interactions producing rapidity gaps and non-perturbative processes giving rise to the "underlying event". We use the model PHOJET [6,7] which treats perturbative QCD effects such as hard parton-parton scattering and parton showers as well as non-perturbative effects like soft hadronic interactions. This model is based on the Dual Parton Model [8] in its two-component version [9].

2. Implementation of color evaporation model

To describe events with color singlet exchange between jets within the PHOJET Monte Carlo, we implement a soft color reconnection (SCR) model [4,5,10]. The simplest hard q–q event, where SCR leads to a rapidity gap between two jets is an event with just one single hard valence–quark – valence–quark scattering. In normal events in the Dual Parton Model we get two color strings each being stretched between one scattered quark and the diquark of the other hadron. Large rapidity gaps are exponentially suppressed in such events. However, SCR can cause a color transfer due to the exchange of soft gluons resulting in a color configuration where the strings connect the hard scattered quark and the diquark of the same hadron. These are events with might lead to hadronic final states with a large rapidity gap between two jets. In PHOJET, we use the following probabilities of color singlet exchange $F_{qq} : F_{qg} : F_{gg} = 1/9 : 1/24 : 1/64$ [4].

In most of the hard scattering events we have a non-negligible contribution from the underlying event, mainly resulting from spectator interactions. Thus, even if a rapidity gap appears in one of the partonic collisions, the gap might be filled by hadrons produced in another parton-parton interaction. Furthermore, hard parton radiation (initial and final state radiation) can change the size of rapidity gaps considerably. Both effects are simulated in our Monte Carlo calculation which includes QCD parton showers and multiple soft and hard interactions as implemented in PHOJET. This means that the probability for the gap survival [1] is calculated in detail.

3. Comparison to data

Both the D0 and CDF collaborations have published data on dijet production with rapidity gaps [11–17]. In the following we will concentrate on the D0 data [14]. Further comparisons of our calculations with data can be found in [18–20].

D0 [14] uses at $\sqrt{s} = 1800$ GeV two different triggers. With the high $E_\perp$ trigger (we refer to this in short as D0–h) they find opposite side ($\eta^{\rm jet1} \times \eta^{\rm jet2} < 0$) dijets with $E_\perp^{\rm jet-2} > 30$ GeV and $|\eta^{\rm jet}| > 2$. The pseudorapidity gap is at $|\eta| < 1.3$. With this the fraction of JgJ events is found to be $R_{\rm JgJ-D0-h} = ({\rm JgJ})/({\rm JJ}) = (0.94 \pm 0.04(stat) \pm 0.12(syst))$.

With the low $E_\perp$ trigger (we refer to this in short as D0–l) they find at $\sqrt{s} = 1800$ GeV opposite side ($\eta^{\rm jet1} \times \eta^{\rm jet2} < 0$) dijets with $E_\perp^{\rm jet-2} > 12$ GeV and $|\eta^{\rm jet}| > 2$. The pseudorapidity gap is at $|\eta| < 1.3$. With this the fraction of JgJ events is found to be $R_{\rm JgJ-D0-l} = ({\rm JgJ})/({\rm JJ}) = (0.54 \pm 0.06(stat) \pm 0.16(syst))$. In PHOJET we find with the D0 triggers $R_{\rm JgJ-PHOJET-D0-h} = 1.06\%$, $R_{\rm JgJ-PHOJET-D0-l} = 0.45\%$. Here the background JgJ events with only an accidental gap were subtracted. These PHOJET results

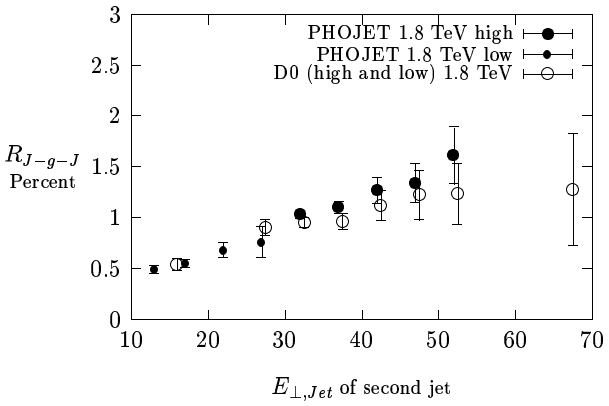

Figure 1. The change of R_{JgJ} with the $E_{\perp}^{\mathrm{jet2}}$ of he next to leading jet. Data from the D0 Collaboration are compared to the PHOJET results obtained with SCR.

are fully consistent with the experimental data. The same is found comparing to the 630 GeV data and to the CDF data. The change of R_{JgJ} with the $E_{\perp}^{\mathrm{jet2}}$ of the second leading jet was studied by the D0 Collaboration [14]. A modest rise of the color singlet fraction with $E_{\perp}^{\mathrm{jet2}}$ was found. In Fig. 1 we compare the PHOJET results on R_{JgJ} with these data. The PHOJET predictions exhibit a $E_{\perp}^{\mathrm{jet2}}$ dependence being compatible with the data. The D0 Collaboration [14] also studied for the D0–h and D0–l triggers the dependence of R_{JgJ} on $\Delta\eta = |\eta^{\mathrm{jet1}} - \eta^{\mathrm{jet2}}|$. For both triggers a slight rise of R_{JgJ} with $\Delta\eta$ was found which is well described by the PHOJET simulations (not shown here). It is important to notice that our calculation does not only describe the rise of R_{JgJ} with $E_{\perp}^{\mathrm{jet2}}$ and $\Delta\eta$, but also reproduces the absolute sizes of R_{JgJ} without free parameters.

We also compared the pseudorapidity distributions of charged hadrons of events passing the D0–h and D0–l triggers with and without gap. The remarkable feature of this comparison is, that the opposite side jet trigger without the gap requirement selects events with much higher rapidity distribution (particle multiplicity) than typically found in minimum bias events. We interpret this in the following way. With the jet trigger events are selected with an exceptional large number of soft and hard multiple interactions and parton emissions.

4. Rapidity gap survival probability

The rapidity gap survival probability $\langle |S|^2 \rangle$ was originally defined by Bjorken [1]. In a series of recent papers, Gotsman, Levin and Maor [21–23] use a eikonal model to calculate the energy dependence of $\langle |S|^2 \rangle$. For example, they obtain in $p\bar{p}$ collisions at 630 (1800) GeV values of 16.3% (5.6 %) [22]. The eikonal model used in PHOJET is a two-channel model which differs certainly from the one used by Gotsman et al., but the gap survival probability as contained in the PHOJET Monte Carlo events is calculated in a rather analogous way. We can use the JgJ events and JJ events obtained from PHOJET for given trigger conditions to give the gap survival probability according to PHOJET.

In the PHOJET Monte Carlo we can subdivide the hard scattering events into g–g, g–q and q–q scatterings. We calculate (not shown here) for the D0–h and D0–l triggers the fractions or weights W_{JJ}^{i} for i = g–g, g–q and q–q events for JJ events (without gap trigger), W_{JgJ}^{i} for JgJ events obtained with SCR and W_{JgJbg}^{i} for background JgJ events (obtained without SCR). We find, that q–q scattering dominates the JgJ events, but g–q and g–g scattering contributes also.

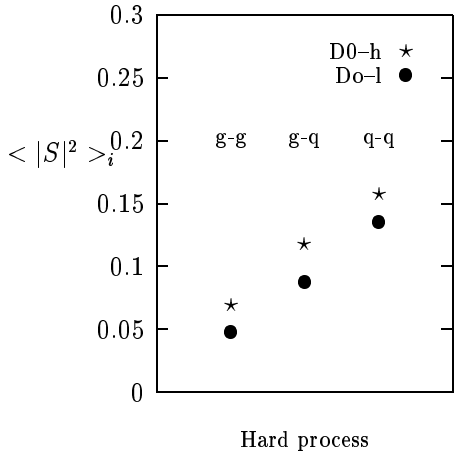

Figure 2. The gap survival probabilities $\langle |S|^2 \rangle_i$ according to PHOJET given separately for i = g–g, g–q and q–q events and for the D0–h and D0–l triggers.

Starting from the JJ and JgJ weights W_{JJ}^{i} and W_{JgJ}^{i} (i = g–g, g–q and q–q) and the SCR probabilities F_i we work out the gap survival probabilities according to PHOJET. We obtain the gap survival probabilities as follows

$$\langle |S|^2 \rangle_i = \frac{W_{JgJ}^{i}}{W_{JJ}^{i} F_i}. \qquad (1)$$

$W_{JJ}^{i} F_i$ is the probability to have two jets corresponding to the given trigger without gaps and furthermore a gap between the two jets due to SCR. Most of the

gaps are filled by soft or hard multiple interactions and or parton showering, therefore $W^i_{J_gJ}$ is considerably smaller than $W^i_{J_J F_i}$. In Fig. 2 we plot for the D0–h and D0–l triggers at $\sqrt{s} = 1800$ GeV the $\langle|S|^2\rangle_i$ obtained. We find values larger than but roughly consistent to the calculation by Gotsman et al. [22]. However, in contrast to the assumptions used in [1,22], we find a slight dependence of the gap survival probability on the trigger conditions resulting in a smaller $\langle|S|^2\rangle_i$ for the D0–l trigger. Furthermore, we find $\langle|S|^2\rangle_i$ to depend on the hard scattering process with $\langle|S|^2\rangle_{q-q}$ larger than $\langle|S|^2\rangle_{g-g}$ and $\langle|S|^2\rangle_{g-q}$.

5. Concluding remarks

The processes implemented in PHOJET allow us to study hard and soft diffraction in many channels. Here we have been able to demonstrate, that the PHOJET model supplemented with the soft color recombination mechanism describes remarkably well the data from the TEVATRON on color singlet exchange between jets. Besides of finding a good agreement with the D0 and CDF data we are able in addition to study many features of the model, which would be useful to verify in the experiments.

We hope that the PHOJET tool and more TEVATRON data in Run II on color singlet exchange and on hard and soft single diffraction and central diffraction could help to answer important questions: (i) Is soft color recombination the correct mechanism to describe color singlet exchange processes between jets? Could this mechanism be responsible for other features of diffractive processes as well? (ii) Can hard diffraction consistently be described by pomeron structure functions? What is the best pomeron structure function?

Acknowledgements

One of the authors (R.E.) is supported by U.S. Department of Energy grant DE-FG02 91ER 40626.

REFERENCES

1. J. D. Bjorken: Phys. Rev. D47 (1993) 101
2. A. H. Mueller and W. K. Tang: Phys. Lett. B284 (1992) 123
3. B. Cox, J. R. Forshaw and L. Lönnblad: JHEP 10 (1999) 023
4. O. J. P. Eboli, E. M. Gregores and F. Halzen: Phys. Rev. D58 (1998) 114005
5. O. J. P. Eboli, E. M. Gregores and F. Halzen: MADPH-99-1135, (hep-ph/9908374), 1999
6. R. Engel: Z. Phys. C66 (1995) 203
7. R. Engel and J. Ranft: Phys. Rev. D54 (1996) 4244
8. A. Capella, U. Sukhatme, C. I. Tan and J. Trân Thanh Vân: Phys. Rep. 236 (1994) 225
9. P. Aurenche, F. W. Bopp, A. Capella, J. Kwieciński, M. Maire, J. Ranft and J. Trân Thanh Vân: Phys. Rev. D45 (1992) 92
10. J. F. Amundson, O. J. P. Eboli, E. M. Gregores and F. Halzen: Phys. Lett. B372 (1996) 127
11. D0 Collab.: S. Abachi et al.: Phys. Rev. Lett. 72 (1994) 2332
12. D0 Collab.: S. Abachi et al.: Phys. Rev. Lett. 76 (1996) 734
13. D0 Collab.: S. Abachi et al.: Phys. Rev. D53 (1996) 6000
14. D0 Collab.: B. Abbott et al.: Phys. Lett. B440 (1998) 189
15. CDF Collab.: F. Abe et al.: Phys. Rev. Lett. 74 (1995) 855
16. CDF Collab.: F. Abe et al.: Phys. Rev. Lett. 80 (1998) 1156
17. CDF Collab.: F. Abe et al.: Phys. Rev. Lett. 81 (1998) 5278
18. R. Engel and J. Ranft: (hep-ph/9711383), in Proceedings of The Int. Symposium on Near Beam Physics, Fermilab, Sept. 22-24, 1997, 1997
19. F. W. Bopp, R. Engel and J. Ranft: (hep-ph/9803437), Proceedings of LAFEX Int. School on High-Energy Physics (LISHEP98), Session C: Workshop on Diffractive Physics, Rio de Janeiro, Brazil, 16-20 Feb. 1998, 1998
20. R. Engel and J. Ranft: Proceedings of the 4th Workshop on Small-x and Diffractive Physics, Fermilab Sept. 1998, p. 255, 1998
21. E. Gotsman, E. M. Levin and U. Maor: Phys. Lett. B309 (1993) 199
22. E. Gotsman, E. Levin and U. Maor: Phys. Lett. B438 (1998) 229
23. E. Gotsman, E. Levin and U. Maor: Phys. Rev. D60 (1999) 094011

Hard Color Coherent Phenomena

M. Strikman[a]

[a]PSU, University Park, PA16802

We consider hard color coherent phenomena which can be probed at FNAL collider.

1. Introduction

During the last few years a number of hard color coherent phenomena was discovered which can be legitimately calculated in QCD: pion dissociation into 2 jets observed in [1] is consistent with predictions of [2], HERA data for exclusive production of mesons in DIS initiated by longitudinally polarized photons are consistent with predictions of [3]. These processes allow both to study the interaction of small color dipoles with hadrons at high energies and hence probe break down of the DGLAP approximation as well as to study hadron wave functions in the minimal Fock space configurations.

2. Hard exclusive diffraction

2.1. Diffraction into three jets

It is possible that a nucleon (meson) has a significant amplitude to be in a configuration where valence partons are localized in a small transverse area together with the rest of the partons. These configurations are usually referred to as *minimal* Fock space configurations - $|3q\rangle$ ($|q\bar{q}\rangle$). Hadrons in such a configuration occupy a small transverse area with a larger probability than in the case of non-minimal configurations, because, e.g. the long range pion field is very weak. Therefore, such initial configurations are expected to interact with other hadrons, even at high energy, with a small cross-section. However for the fixed transverse size, b, this cross section is proportional to the gluon density at $Q^2 \sim 10/b^2$ and hence rapidly increases with increase of energy. At sufficiently high energies this growth should be tamed not to violate unitarity constraints, for the recent discussion see [4].

In the case of the "elastic scattering" of such a proton configuration off another proton, this three-quark system with large relative momenta should preferentially diffractively dissociate into a system of three jets with large transverse momenta $p_{Ti} \sim \pi\ b^{-1}$, where b is the transverse size of the minimal configuration. Kinematics of the process is presented at the lego plot of Fig.1.

The production cross-section for the three jets can be estimated to leading order in $(\alpha_s \ln M^2_{3jet})$. As in the case of diffractive vector meson production in deep inelastic scattering, the cross-section is proportional to the square of the gluon density in the nucleon at $x \approx M^2_{3jets}/s$, and virtuality $\sim p^2_{T\ jet}$[5]. The distribution over the fractions of the momentum carried by the jets is proportional to the square of the light cone wave function of the $|3q\rangle$ configuration. Hence the diffraction of a proton into three jets provides important information about the short-distance quark structure of the proton, and also provides unique information about the longitudinal momentum distribution in the $|3q\rangle$ configuration. From an analysis of diffraction data [5,6], numerical estimates for $\sqrt{s} = 2$ TeV lead to a value of the cross-section integrated over everything except a $p_{T\ jet}$ threshold for one jet,

$$\sigma_{3\ jets} \sim (10^{-5} - 10^{-6}) \left(\frac{5\ \text{GeV}}{p_{T\ jet}}\right)^8 \text{mb}. \qquad (1)$$

The probability of the $|3q\rangle$ configuration is estimated using a phenomenological fit to the probability of configurations of different interaction strengths in a nucleon (cf. [5,6]).

Another interesting group of hard processes is proton diffraction into 2 high p_T jets and one collinear jet. These processes are dominated by parton configurations when only 2 quarks in the projectile proton are close to each other, i.e., have large transverse momenta. Such quark configurations are relevant for estimates of proton decay rates. The wave function describing such a configuration can be measured in the double-diffraction process where each of the protons fragments into 3 high p_t jets: $pp \to jet(k_t) + jet(-k_t - q_t) + jet(q_t) + jet(l_t) + jet(-l_t - r_t) + jet(r_t)$.

2.2. Tagged-pion diffraction dissociation

Reactions containing a very forward neutron or a Δ-isobar can be dominated by the scattering off the pion cloud of the nucleon. In this way the proton beam is effectively converted into a pion beam; the leading baryon is effectively a pion tag. A necessary condition that one-pion exchange dominates this process is that the transverse momentum of the forward baryon be small compared to 300 MeV and, in the case of the Δ, that its x_F exceed 0.9. The precise condition is

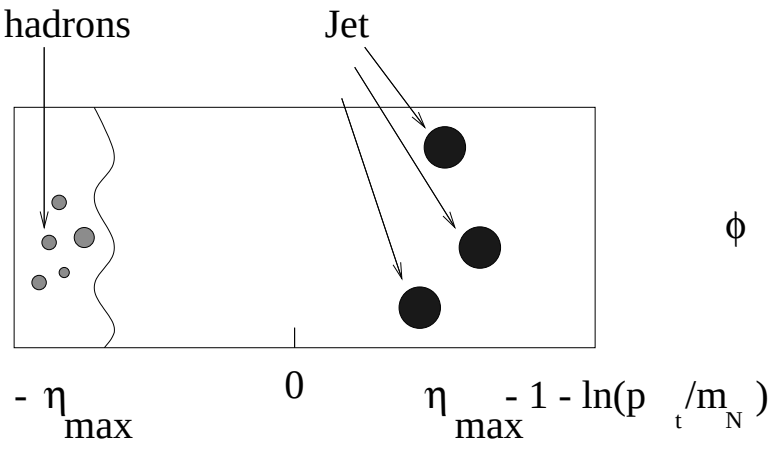

Figure 1. LEGO plot for diffraction of proton into three jets

$$|t| = (\frac{M_B^2}{x_F} - m_N^2)(1 - x_F) + \frac{k_t^2}{x_F} \leq 0.1 \text{ GeV}^2. \qquad (2)$$

One must still deal with absorptive corrections due to the simultaneous interactions of the projectile with a nucleon and a pion. These are expected to be corrections no larger than a factor two.

Two types of processes would be of special interest:

Pion diffraction into two jets:

In analogy with the process of nucleon diffraction into three jets it is expected that a pion can dissociate into two jets in the process $\pi + p \to jet_1 + jet_2 + p$ [7,2] (Fig. 2).

The cross-section for this process has a similar structure [2]: due to the rapid increase of the gluon density with energy one expects the cross-section for pion diffraction into two jets to be much larger than in the case of the fixed target experiment E791 at FNAL which has just reported first evidence for this effect [1].

Two → three hard reactions:

It is also interesting to study large $|t|$ elastic scattering off the pion cloud in a number of reactions [8].

$$pp \to B(p_{T\ B}) + \pi(p_{T\ \pi}) + p(p_{T\ p}), \qquad (3)$$

for $B = N, \Delta$, $x_F(B) \geq 0.9$, $p_{T\ B} \sim 0$, and $p_{T\ \pi} \sim -p_{T\ p} \gg 1$ GeV, which corresponds to the proton elastic scattering off the pion cloud. Although the flux of such pions in the proton is only $\sim 1\%$, at large $|t| \approx p_{T\ p}^2$ the cross-section for elastic πp scattering is expected to be substantially larger than the cross-section for elastic pp scattering. * Hence the cross-sections for reaction (3) and elastic pp scattering at $|t|$ larger than 10 GeV^2 should be comparable.

One may also consider elastic scattering of two pions in processes like

$$pp \to B(p_{T\ B}) + \pi(p_{T\ \pi}) + \pi(p_{T\ \pi'}) + B'(p_{T\ B'}) \qquad (4)$$

for $B, B' = N, \Delta$, $x_B, x_{B'} \geq 0.9$, $p_{T\ B} \sim p_{T\ B'} \sim 0$, and $p_{T\ \pi} \sim -p_{T\ \pi'} \gg 1$ GeV. Again the much slower decrease of the $\pi\pi$ elastic scattering with $|t|$ helps to compensate the small probability of finding both nucleons in configurations with pions.

Many generalizations of such processes can be estimated. These include channels with strange particles in the final state like

$$pp \to (\Lambda K^+, \Sigma^+ K^0) + p$$

as well as kinematics for which the transverse momentum of the proton is balanced by a baryon, not a meson. Such processes are of interest, both for the study of high-energy scattering and for the structure of color correlations in hadrons, especially in relation to the question of intrinsic strangeness in nucleons, see e.g. [10]. Note that at sufficiently large $|t|$, where the colliding-hadron configurations are sufficiently small for the applicability of perturbative QCD, new factorization relations are expected to be valid relating these processes with analogous exclusive DIS processes.

3. Diffractive hard factorization

In difference from the case of deep inelastic scattering there is no reason for applicability of the factor-

*The high-energy data on large $|t|$ πp elastic scattering [9] are consistent with this expectation.

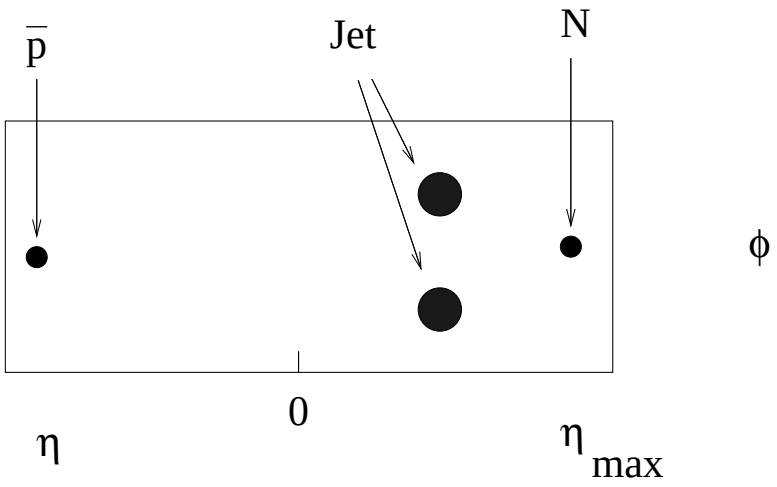

Figure 2. LEGO plot for the tagged 2 jet production

ization theorem for diffractive scattering. Hence it is convenient to represent the measured cross-section as a factorizing cross-section times a suppression factor:

$$\sigma_{\rm true} = \sigma_{\rm fact}(x_N, x_{I\!P}) \times S(x_{I\!P}, t, s). \qquad (5)$$

Estimates of the value of S typically give a value $S \sim \frac{1}{10}$.

S may actually be a slowly varying, but rather complicated function of initial energy, $x_{I\!P}$, t, and x_N. For example, one can expect that it will decrease with an increase of $\sigma_{tot}(pp)$ (stronger spectator effects), increase with increasing $|t|$ (selection of more weakly interacting configurations in the intact nucleon [11]), and increase as x_N becomes large (due to a selection of smaller size configurations in N) (N is the nucleon which diffracted inelastically).

It would be also interesting to study diffraction to inelastic low-mass final states B in the process:

$$p(p_1) + p(p_2) \to (\mathrm{jet}_1 + \mathrm{jet}_2 + X) + B \qquad (6)$$

which may select configurations with an interaction strength rather different from the average one. Several examples of interesting channels are the aforementioned $B = n\pi^+, p\pi^+\pi^-$ and ΛK^+, each of which can be studied as a function of p_T of the produced jets for fixed $t \sim 0$. A hard factorization combined with Regge factorization would lead to

$$\frac{\sigma(p(p_1) + p(p_2) \to (\mathrm{jet}_1 + \mathrm{jet}_2 + X) + B)}{\sigma(p(p_1) + p(p_2) \to (\mathrm{jet}_1 + \mathrm{jet}_2 + X) + p)} = \frac{\sigma(p(p_1) + p(p_2) \to p + B)}{\sigma(p(p_1) + p(p_2) \to p + p)} \qquad (7)$$

It is natural to expect that at least for large enough p_T this factorization would be broken, with the cross-section of diffractive jet production in the inelastic diffraction channel substantially enhanced compared to the expectations of Eq. (7).

REFERENCES

1. D. Ashery, e-Print Archive: hep-ex/9910024
2. L. Frankfurt, G.A. Miller, and M. Strikman, Phys. Lett. **B304** 1 (1993).
3. S. J. Brodsky, L. Frankfurt, J. F. Gunion, A. H. Mueller and M. Strikman, Phys. Rev. **D50** (1994) 3134.
4. L. Frankfurt and M. Strikman, hep-ph/9907221, in Proceedings of DIS99.
5. L. Frankfurt and M. Strikman, hep-ph/9806536,In DIS98, Deep inelastic scattering and QCD, 77-93.
6. L. L. Frankfurt, G. A. Miller and M. Strikman, Ann. Rev. of Nucl. and Part. Phys. **44** (1994) 501.
7. G. Bertsch, S.J. Brodsky, A.S. Goldhaber, J. Gunion, Phys. Rev. Lett. **47**, 297 (1981).
8. L. Frankfurt, M. Strikman, in Proceedings of Baryons'95, Edi. B. F. Gibson, P. D. Barnets, J. B. McClelland, W. Weise, World Scientific, 1996, p.211.
9. R. Rubinstein *et al.*, Phys. Rev. **D30** (1984) 1413.
10. S. J. Brodsky, J. Ellis, M. Karliner Phys. Lett. **206B**: 309, 1988
11. L. Frankfurt and M. Strikman, Phys. Rev. Lett. **63**, 1914 (1989), Erratum, ibid. **64**, 815, (1990).

Double Pomeron Physics in Run II

Jon Pumplin[a]

[a]Department of Physics and Astronomy, Michigan State University, East Lansing, MI 48824

A "normal" event at the Tevatron produces ~ 0.3 hadron resonances per unit of $\Delta\eta \times \Delta\phi$. Hence in a region of length Δy, one expects $\sim 0.3 \times 2\pi \times \Delta y$ of them. Naively assuming no correlations, i.e., a Poisson distribution in the number, leads to the probability $\approx e^{-2.0\,\Delta y}$ of zero particles: a rapidity gap. A much more sophisticated argument from Regge theory also predicts the gap probability to be suppressed exponentially, albeit with a smaller coefficient: $\sigma_{\rm gap} \approx e^{2\,(\alpha_R - 1)\,\Delta y} \approx e^{-1.0\,\Delta y}$ based on the vector meson Regge intercepts α_ρ, α_ω near 0.5 .

But rapidity gap cross sections are actually *not* suppressed exponentially in this way. Fitting the multiplicity distribution in a region $> 2-3$ units in rapidity, using a smooth distribution such as negative binomial or generalizations thereof, reveals an excess at zero multiplicity which is the rapidity gap cross section. The pomeron can be defined operationally as the thing that makes rapidity gaps. We must keep our minds open, however, to the possibility that there may be more than one kind of pomeron — e.g., the classical "soft" pomeron may be different from the pomeron that operates when there is a large momentum transfer t at one end of the gap; or when there is a large momentum transfer $p_\perp$ across the gap.

Roman pots that detect p or $\bar{p}$ very close to the beam directions can be used to study rapidity gaps according to the kinematic relation

$$\xi = 1 - x_p = \sum \sqrt{p_\perp^2 + m^2}\, e^y / \sqrt{s}\ .$$

For example if a $\bar{p}$ is observed with a momentum fraction $x_p = 0.98$, no pions with $p_\perp > 0.3\,\mathrm{GeV}$ can appear at $y > 4.7$, so there is a gap > 2.8 between any such pion and the leading proton which is at $y = 7.5$. The Roman pot method of observing gaps has several advantages: it allows us to study pure $\bar{p}$ going in the beam direction instead of an unknown mixture of $\bar{p}$ and $\bar{p}^*$; it allows measurement of the momentum transfer squared t; and if Roman pots can be placed both forward and backward, important azimuthal angular correlations between the forward and backward p and $\bar{p}$ can be observed. It will be important to see if final state properties change with t (or $t_{\rm forward}$ and $t_{\rm backward}$). It is also important to study how large the non-diffractive contamination is for, say, $x < 0.95$. Perhaps one could also get a handle on this by comparing forward protons with forward neutrons as HERA, using the Zeus forward neutron detector.

Double pomeron exchange (DPE) will be studied in Tevatron Run II in reactions of the form $p\,\bar{p} \to p\,X\,\bar{p}$. A variety of centrally produced systems X are worthy of study:

1. **X = soft, inclusive:** The fully differential cross section is $d\sigma/dt_1\,dt_2\,dy_1\,dy_2$, where t_1, t_2 are the 4-momentum transfers to the quasi-elastically scattered p and $\bar{p}$, and y_1, y_2 are the inside edges of the gaps. This cross section is integrated over t_1 and t_2 in the absence of Roman pots. The measurement can be compared with predictions based on measurements of single diffractive scattering by assuming Regge factorization.

2. **X = soft, exclusive:** Low multiplicity final states in DPE are a prime hunting ground for glueball states, since X automatically has isospin 0 and is made more-or-less from gluons [1]. In this case, azimuthal correlations with the quasi-elastic p and $\bar{p}$ can be particularly significant [2]. The absence of large $p_\perp$ presents a challenge for triggering on these final states, but low multiplicity and the presence of the gaps and/or Roman pot triggers should make it possible.

3. **X = hard, inclusive:** Dijet production in DPE [4] has already been measured in Run I; but Run II offers, along with improved accuracy and the push to higher jet p_t, the possibility to study the dependence on momentum transfers to the p and $\bar{p}$. It should also be possible to measure the fraction of the jets that are $b\bar{b}$.

4. **X = hard, exclusive:** It is possible that some simple heavy quark systems can be produced exclusively in DPE [3]. A promising candidate to search for is the $b\bar{b}$ state $\chi_{b1}(1P)$, which has a mass of $9.892\,\mathrm{GeV}$. It decays with a 35% branching ratio to $\gamma\,\Upsilon(1S)$, with subsequent decay $\Upsilon \to \ell^+\ell^-$ with 10% branching ratio ($\ell = e$ or μ). This would have a remarkable signature:

nothing but $\ell^+\ell^-\gamma$ in the entire central detector. Although the rate will surely be small, the transverse momenta of several GeV along with the large quiet regions in the detector should be sufficient to make triggering possible. Meanwhile the large Q^2 scale offers the hope of attempting to calculate the cross section in pQCD. Depending on how the pomeron really works, exclusive processes may turn out to be very strongly suppressed by the condition that in spite of the large Q^2 scale, no extra soft gluons are radiated.

The quantum number selection rules for the production of exclusive $b\bar{b}$ states are as follows. The pomeron is believed to have the same internal quantum numbers as the vacuum, so the state X produced by the "collision" of two pomerons must have $I = 0$ and $C = +$. The pomeron is an even-signature Regge trajectory, so it has spin and parity $J^P = 0^+, 2^+, 4^+, \ldots$; but when two of these are combined with the orbital angular momentum of the collision, all J^P values become allowed for X. For the purposes of a DPE experiment, $\chi_{b1}(1P)$ ($m = 9.892$, $J^{PC} = 1^{++}$) and $\chi_{b2}(1P)$ ($m = 9.913$, $J^{PC} = 2^{++}$) are the most promising because of their large (35%, 22%) branching ratios into $\gamma\,\Upsilon(1S)$. As a control experiment, the states $\Upsilon(1S)$ and $\Upsilon(2S)$ should not be produced in DPE, because they have odd charge conjugation.

One could also look for $\Upsilon\Upsilon$ or $\psi\psi$ exclusive states, or even $\gamma\psi$ [5], in DPE.

Finally, an important experimental problem to be addressed is how to study gap physics in the presence of multiple $p\bar{p}$ collisions at the higher luminosity of Run II. Presumably the main tool will be to make use of scheduled or unscheduled running in which the luminosity is not in fact very high. For jet physics, the Roman pot method permits gap studies even when the gap cannot be observed directly because it is filled in by multiple interactions.

At the LHC, very high luminosity will make conventional rapidity gap physics impossible. With the help of Tevatron Run II, we should begin to think about whether similar physics can be done by a looser but more enforceable criterion of no *minijets* instead of no particles in a "gap" region. Since jet multiplicities are much less than particle multiplicities, this can only work if the required length Δy to define a gap is made larger.

As a final comment, backgrounds to DPE — along with some important questions regarding underlying events in jet physics — would benefit from an improved study of "minimum bias" physics, along the lines of what was done long ago and at a lower energy in the UA(5) experiment. Results from that experiment are still being used in the absence of measurements at $\sqrt{s} = 1.8\,\text{TeV}$. This is another important topic to clean up before the LHC, where fluctuations from a large number of multiple interactions will be important.

REFERENCES

1. F.E. Close and G.A. Schuler, hep-ph/9905305; WA102 Collaboration, hep-ph/9908253, hep-ex/9909013, hep-ph/9907302.
2. N. Kochelev, hep-ph/9902203; N.I. Kochelev, T. Morii, A.V. Vinnikov, hep-ph/9903279; A. Kirk, O. Villalobos Baillie, hep-ph/9811230.
3. J. Pumplin, Phys. Rev. D47, 4820 (1993) (hep-ph/9301216).
4. J. Pumplin, Phys. Rev. D52, 1477 (1995) (hep-ph/9412381); A. Berera and J. C. Collins, Nucl. Phys. B474, 183 (1996) (hep-ph/9509258); A.D. Martin, M.G. Ryskin, and V.A. Khoze, Phys. Rev. D56, 5867 (1997) (hep-ph/9705258); A. Berera hep-ph/9910405.
5. Jia-Sheng Xu and Hong-An Peng, hep-ph/9811416.

Higgs and Heavy Quarks Diffractive Production

Eugene Levin [a] [b]

[a] HEP Department, School of Physics, Tel Aviv University, Tel Aviv 69978, ISRAEL

[b] Physics Department, Brookhaven National Laboratory, Upton, NY 11973 - 5000, USA

In this note we give the highest of reasonable estimates for the value of cross section of the double Pomeron Higgs meson production and suggest a new mechanism for heavy quark diffractive production which will dominate at the Tevatron energies.

1. INTRODUCTION

In this note we consider three reactions

$$p + p \longrightarrow p + [LRG] + H + [LRG] + p \; ; \quad (1)$$

$$p + p \longrightarrow X_1 + [LRG] + H + [LRG] + X_2 \; ; \quad (2)$$

$$p + p \longrightarrow b + \bar{b} + X + [LRG] + p \; ; \quad (3)$$

where LRG denotes the large rapidity gap between produced particles and X corresponds to a system of hadrons with masses much smaller than the total energy. The first two reactions are so called double Pomeron production of Higgs meson while the third is the single diffraction production of bottom - antibottom pair.

The goals of this note are the following:

1. To give the highest from reasonable estimates for the cross sections of reactions Eq. (1) and Eq. (2) ;

2. To summarize all uncertainties which we see in doing these estimates ;

3. To show that there is a new mechanism of diffractive heavy quark production (Eq. (3)) which is suppressed in DIS and dominates in hadron-hadron collision at the Tevatron ;

4. To estimate the value of the cross section of reaction Eq. (3) due to this new mechanism and to show that all attempts to compare the diffraction dissociation in hadron-hadron collisions and DIS[1] look unreliable without a detail experimental study of this process at Fermilab.

2. DOUBLE POMERON HIGGS PRODUCTION

2.1. Inclusive Higgs production

Inclusive Higgs production has been studied in many details [2–4] for the Tevatron energies. The main source for Higgs is gluon-gluon fusion which gives $\sigma(GG \to H) = 1pb$ for Higgs with mass $M_H = 10\,GeV$ [4]. The reference point for our estimates is the cross section of Higgs production due to W and Z fusion which is equal to $\sigma(WW(ZZ) \to H) = 0.1pb$ [4]. In this process we also expect the two LRG [3] and in some sense this is a competing process for reactions of Eq. (1) and Eq. (2).

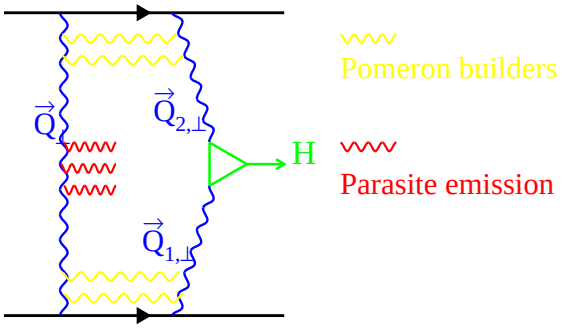

Figure 1. *Double Pomeron Higgs production in QCD*

2.2. Double Pomeron Higgs production is a "soft" process !!!

Let us estimate the simplest digram for the DP Higgs production, namely, Fig.1 without any of s-channel gluons. This diagram leads to the amplitude

$$M(qq \to qHq) = \quad (4)$$

$$\frac{2}{9}\, 2\, g_H \int \frac{d^2Q_\perp}{Q^2_\perp\, Q^2_{1,\perp}\, Q^2_{2,\perp}}\, 4\alpha_S(Q^2_\perp)\, (\vec{Q}_{1,\perp} \cdot \vec{Q}_{2,\perp})\,.$$

For reaction of Eq. (1), $|t_1| = |\vec{Q}_\perp - \vec{Q}_{1,\perp}| \approx |t_2| = |\vec{Q}_\perp - \vec{Q}_{2,\perp}| \approx 2/B_{el}$ and therefore,

$$M(q + q \to q + H + q) \propto \int \frac{d^2Q_\perp}{Q^4_\perp}. \quad (5)$$

Eq. (5) has an infrared divergence that is regularized by the size of the colliding hadrons. In other words, one can see that the simplest diagrams shows that DP Higgs production is a typical "soft" process.

2.3. The more the gluons the more the problems...

In Fig.1 one can see that we have two sets of gluon which play a different role. The first one is the gluons that connect t-channel lines. Their contribution increases the value of cross section [5–8]

$$\frac{d\sigma_P(pp \to ppH)}{dy}|_{y=0} = \tag{6}$$

$$\frac{4\,g_H^2}{16^2\,\pi^3}\int dt_1 dt_2 g_{Pp}^2 g_{Pp}^2\, e^{\frac{B_{el}(s/M_H^2)}{2}(t_1+t_2)}\left(\frac{s}{M_H^2}\right)^{2\,\Delta_P}$$

Eq. (6) can be rewritten in the form

$$\frac{d\sigma_P(pp \to ppH)}{dy}|_{y=0} = \tag{7}$$

$$\frac{16}{\pi}\,\sigma(GG \to H)\left(\frac{\sigma_{el}(s/M_H^2)}{\sigma_{tot}(s/M_H^2)}\right)^2$$

which is convenient for numeric estimates. However, first we need to find the value of $\sigma(GG \to H) = g_H^2$. In inclusive production the value of g_H^2 has been calculated [9]

$$g_H^2 = \sqrt{2} G_F \alpha_S^2(M_H^2) N^2/9\pi^2. \tag{8}$$

However, I think that the scale of α_S for our process is not the mass of Higgs but the "soft" scale ($\alpha_S(Q_0^2)$ with $Q_0^2 \approx 1\,GeV^2$). Indeed, using BLM procedure [10] we can include the bubbles with large number of light quarks only in t-channel gluon line which carry the "soft" transverse momenta. This gives a sizable effect in numbers, since $\sigma(GG \to H)$ for $M_H = 100\,GeV$ is equal to 1.16 pb ($\alpha_S(M_H^2)$) and to 20 pb ($\alpha_S(Q_0^2)$). Taking the last value we have

$$\frac{d\sigma_P(pp \to ppH)}{dy}|_{y=0} = 2pb \tag{9}$$

This is our maximal value since all other effects related to gluon emission suppressed the value of the cross section.

2.4. Cost of survival

Actually, we have to multiply the cross section of Eq. (9) by two factors to obtain the estimate for the experimental cross section

$$\frac{d}{\sigma}(pp \to ppH)dy|_{y=0} \tag{10}$$

$$= S^2_{spect} S^2_{par} \frac{d\sigma_P(pp \to ppH)}{dy}|_{y=0}$$

The first factor is the probability that there is no inelastic interaction of the spectators in our process. I The situation with calculation of this factor has been reported in this workshop [11] and the conclusion is that this factor $S^2_{spect} = 0.07 \div 0.13$ at the Tevatron energies. The discussion for double Pomeron processes you can find in Ref. [12]

The second factor in Eq. (10) describe the probability that there is no parasite emission in Fig.1 which leads to a process with hadrons in central rapidity region which do not come from the Higgs decay. The generic formula for S^2_{par} is

$$S^2_{spect} = e^{-<N_G(\Delta y = ln(M_H^2/s_0)>} \tag{11}$$

where $< N_G(\Delta y) >$ is the mean number of gluon in interval Δy. In pQCD this number is large [13] $< N_G(\Delta y) \approx 8$ which leads to very small cross section for Higgs production. For "soft" double Pomeron production we can estimate the value of $< N_G(\Delta y)$ assuming that the hadron production is two stage process: (i) production of mini jet with $p_t \approx 2 - 3GeV$ and (ii) minijet decay in hadrons which can be taken from $e^+e^- \to hadrons$ process. Finally,

$$< N_G(\Delta y) >= \frac{N_{hadrons}}{N(one \quad minijet)} \approx 2 \div 3\,, \tag{12}$$

which gives $S^2_{parasite \quad emission} \approx 0.1$.

2.5. God loves the brave !!!

Finally, we have

$$\frac{d\sigma(pp \to ppH)}{dy}|_{y=0} = 0.02pb \tag{13}$$

We can increase the cross section, measuring reaction of Eq. (2). Its cross section is equal to

$$\frac{d\sigma(pp \to X_1 X_2 H)}{dy}|_{y=0} = \tag{14}$$

$$\frac{d\sigma(pp \to ppH)}{dy}|_{y=0}\left(\frac{\sigma^{SD}\cdot B_{el}(\sqrt{s}/M_H)}{4\,\sigma_{el}\cdot B_{DD}(\sqrt{s}/M_H)}\right)^2 =$$

$$3 - 4\frac{d\sigma(pp \to ppH)}{dy}|_{y=0} = 0.06 \div 0.08pb$$

2.6. Sensitive issues

Eq. (13) and Eq. (14) are our results. I firmly believe that they give the maximum values of the cross sections which we could obtain from reasonable estimates. However, I would like to summarize the most sensitive points in our estimates:

1. The scale for running coupling QCD constant in cross section of Higgs production. We took the "soft" scale for our estimates. However, it is a point which needs more discussion and even more it looks in contradiction with our feeling, as I have realized during our last meeting. My argument is the BLM procedure but more discussions are needed;

2. We took S^2_{spect} for double Pomeron processes the same as for "hard" LRG process. The justification for this is eikonal type model [12], but it could be different opinions as well as direct experimental data;

3. The estimates for S^2_{par} is very approximate and we need to work out better theory for this suppression.

3. DIFFRACTIVE HEAVY QUARK PRODUCTION

The main observation is that there are two contributions for heavy quark diffractive production (see Eq. (3)): (i) the first is so called Ingelman-Schlein mechanism [15] which described by Fig.2-a and (ii) the second one is closely related to coherent diffraction suggested in Ref. [16] and which corresponds to Fig. 2-b. The estimates of both of them have been discussed in Ref. [14]. The main conclusion is that the main contribution for the Tevatron energies stems from CD (see also [17,18] while the IS mechanism leads to the value of the cross section in one order [14,19] less than CD one. on the other hand in DIS the CD contribution belongs to the high twist and because of that it is rather small [14,17].

Our conclusion is very simple. At the Tevatron we has a good chance to measure a new contribution to "hard" diffraction which is small in DIS. The typical values of the cross section is

$$\frac{d\sigma}{dY} = \int_{p_t^{min}}^{\infty} dp_t^2 \int_{-\infty}^{+\infty} d\Delta y \int_0^{\infty} dq_t^2 \frac{d\sigma}{dY d\Delta y dq_t^2 dp_t^2}$$

$$\approx 10^{-4} \div 10^{-10} \quad for \quad p_{t,min} = 5 \div 50\ GeV \tag{15}$$

One can find all details in Ref. [14].

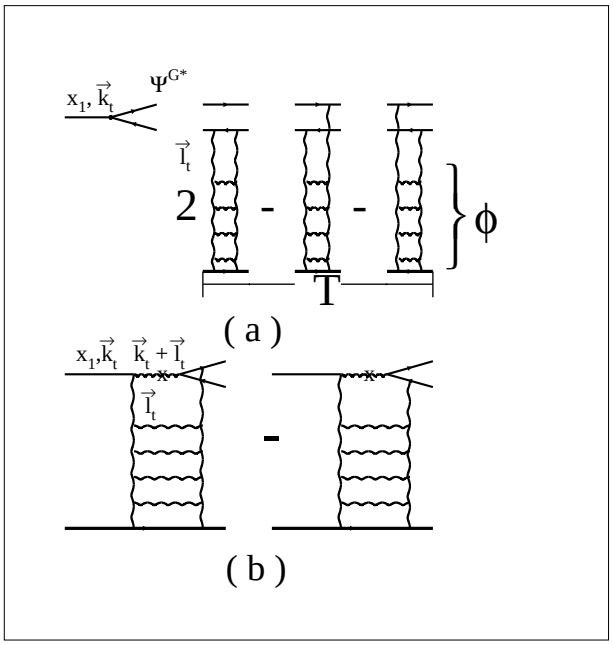

Figure 2. *The contributions for diffractive Higgs production: (a) Ingelman-Schlein mechanism and (b) Coherent diffraction*

REFERENCES

1. L. Alvero, J.C. Collins and J.J. Whitmore, PSU-TH-200,hep-ph/9806340;
   L. Alvero, J.C. Collins, J. Terron and J.J. Whitmore, Phys. Rev. D59 (1999) 074022.
2. Z. Kunszt and W.J. Stirling, Aachen ECFA WS, p.428, 1990.
3. Yu.L. Dokshitzer,V.A. Khoze and T. Sjostrand, Phys. Lett. B274 (1992) 116.
4. A.Strange,W. Marciano and S. Willenbrock, Phys. Rev. D49 (1994) 1354.
5. A. Bialas and P.V. Landshoff, Phys. Lett. B256 (1991) 540.
6. B. Muller and Alec J. Schramm, Nucl. Phys. A523 (1991) 677.
7. J-R Cudell and Oscar F. Hernandez, Nucl. Phys. B471 (1996) 471.
8. V. Barger, R.J.N.Phillips and D.Zeppenfeld, Phys. Lett. B346 (1995) 106.
9. S. Dawson, Nucl. Phys. B359 (1991) 283; A. Djouadi, M. Spira and P. Zerwas, Phys. Lett. B264 (1991) 440.
10. S.J. Brodsky, P. Lepage and P. B. Mackenzie, Phys.Rev. D28 (1983) 228.
11. E. Levin, talk at this WS.
12. E. Gotsman, E. Levin and U. Maor, Phys.Lett. B353 (1995) 526.
13. A.D. Martin, M.G. Ryskin and V.A. Khoze, Phys.Rev. D56 (1997) 5867; Phys.Lett. B401 (1997) 330.

14. G. Alves, E. Levin and A. Santoro, Phys. Rev. DD55 (1997) 2683.
15. G. Ingelman and P. Schlein, Phys. Lett. B152 (1985) 256.
16. J. Collins, L. Frankfurt and M. Strikman, Phys. Lett. B307 (1993) 161.
17. D. E. Soper, Talk at DIS'97, hep-ph/9707384.
18. M. Wüsthoff and A.D. Martin, hep-ph/9909362.
19. F. Yuan and K.-T. Chao, hep-ph/9810340; hep-ph/9811285.

Diffractive Production of Glueballs

Dmitri Kharzeev[a]

[a]Physics Department and RIKEN-BNL Research Center, Brookhaven National Laboratory, Upton NY 11973, USA

This contribution is based on the work with John Ellis [1], in which we link the unexpected azimuthal dependence of the production of scalar glueball candidate observed recently by the WA91 and WA102 Collaborations to the broken scale invariance of QCD.

Confinement and the non-Abelian structure of QCD imply the existence of bound states of gluons. Clearly, finding and recognizing such glueball states is very important. One intriguing possibility is to identify the observed $f_0(1500)$ state with the lightest scalar glueball [2]. To verify the gluonic nature of this state, one has to check in particular if the mechanisms of its production are consistent with those expected for glueball states. This suggests in particular that one looks for its production in gluon-rich environments. It was suggested long time ago [3] that the glueballs should be produced copiously in the central production process

$$pp \to p_f X p_s \tag{1}$$

This may be dominated by double-Pomeron exchange when the final-state protons carry large fractions of the initial-state proton momenta in the centre-of-mass frame. In fixed-target experiments, this requires the presence of fast (p_f) and slow (p_s) protons in the final state.

Recently, a big step in the investigation of this process has been taken by the WA91 and WA102 Collaborations, which have reported remarkable kinematical dependences of central meson production [4,5]. Specifically, it was observed [5] that the the production of glueball candidates depends strongly on the relative transverse momenta of the final-state protons p_f and p_s. The variable suggested in [5,6] was the difference between the transverse momenta $\vec{p\prime}_t$ and $\vec{q\prime}_t$ of the final-state protons:

$$dP_t = |\vec{p_t}\prime - \vec{q_t}\prime|. \tag{2}$$

The dependence of central meson production on this variable appears to be very non-trivial: namely, it was found that at small dP_t the production of glueball candidates, in particular the $f_0(1500)$, was significantly enhanced over the production of conventional $\bar{q}q$ mesons. It was proposed [6] that this remarkable feature of central production could be related to the intrinsic structure of glueball states, and that the selection of events with small dP_t could act effectively as a glueball filter. So far, no dynamical explanation of this important empirical observation has been suggested, so the challenge for theory is to understand the dynamics behind this glueball filter.

We have proposed [1] the following form for the coupling responsible for scalar glueball production in Pomeron-Pomeron collisions:

$$Ł \sim \Theta(x) G_a^{\mu\nu}(x) G^a_{\mu\nu}(x), \tag{3}$$

In momentum space, this coupling leads to an amplitude that is proportional to the square of the scalar product of the four-momenta of the colliding gluons g_1 and g_2:

$$\begin{aligned} \mathcal{M} &\sim (g_1.g_2 g^{\mu\nu} - g_1^\mu g_2^\nu)(g_1.g_2 g_{\mu\nu} - g_{1\mu} g_{2\nu}) \\ &\sim (g_1.g_2)^2. \end{aligned} \tag{4}$$

This form of the coupling, and the Pomeron flux factors, imply [1] that the production of the scalar glueball should be most efficient when the two protons scatter in parallel directions in the transverse plane, in agreement with the experimental observations.

Our findings support the idea that the azimuthal dependence in double diffractive production provides a valuable way to single out the scalar glueballs and to understand their properties. It would be extremely interesting to extend these studies to collider energies, where the dominance of the Pomeron exchange is much better justified.

REFERENCES

1. J. Ellis and D. Kharzeev, hep-ph/9811222.
2. For a review, see R. Landua, Ann. Rev. Nucl. Part. Sc. 46 (1997) 351.
3. D. Robson, Nucl. Phys. B 130 (1977) 328; Phys. Lett. B66 (1977) 267.
4. D. Barberis et al., WA91 Collaboration, Phys. Lett. B388 (1996) 853.
5. D. Barberis et al., WA102 Collaboration, Phys. Lett. B397 (1997) 339; A. Kirk et al., WA102 Collaboration, hep-ph/9810221.

6. F.E. Close and A. Kirk, Phys. Lett. B397 (1997) 333.

Glueballs and Exclusive Hadron Production at the Tevatron

Michael G. Albrow[a]

[a]Fermilab, USA

The study of *low mass* hadronic systems in double pomeron exchange processes is completely virgin territory at the Tevatron. These are events with the p and $\bar{p}$ at Feynman $x_F \geq 0.997$ or so, with central masses less than a few GeV and large rapidity gaps in both forward directions. Important physics topics are (a) to search for glueball states G by the exclusive process $p\bar{p} \to pG\bar{p}$ (b) to measure exclusive hyperon-antihyperon production up to $\Omega^-\bar{\Omega}^+$ (c) to search for exclusive χ_c and χ_b production (d) to search for events with an unusually large or small ratio of charged hadrons to π^o (DCC = disoriented chiral condensate?). These studies would all extend our understanding of QCD to the low-Q^2 domain. I discuss briefly how they could be carried out in CDF and DØ .

1. DOUBLE POMERON EXCHANGE

Double pomeron exchange, DPE, events [1] contain two large rapidity gaps, where by "large" is meant not exponentially damped on a scale of order one unit of rapidity. A region $\Delta\eta$ (or better Δy) as large as (say) 4 units with no hadrons is dominated by pomeron, P, exchange in the t-channel, with little background from other processes (non-diffractive or reggeon exchange). The "pomeron" is a colorless but strongly interacting entity with the quantum numbers of the vacuum: No charge, no isospin, positive parity, C-parity and G-parity. Probably at low $|t|$ and Q^2 it is predominantly two or more gluons in a colorless combination. Probing it with virtual photons at HERA [2], and observing diffractive W production at the Tevatron [3], demonstrate a $q\bar{q}$ component at large Q^2.

The total rapidity range of a $p\bar{p}$ collision is $\Delta y = ln\frac{s}{m_p^2}$, which was 8.4 at the CERN ISR ($\sqrt{s} = 63$ GeV), 13.0 at the $Sp\bar{p}S$ ($\sqrt{s} = 630$ GeV), and is 15.3 at the Tevatron ($\sqrt{s} = 2000$ GeV). $\Delta y = 6.9$ (7.4) at the fixed target experiments WA102 [4] (E690 [5]) with $p_{beam} = 450$ (800) GeV/c. At the colliders if we restrict ourselves to events with all central hadrons in $|\eta| \leq 1.5$ ($155^o \geq \theta \geq 25^o$) where they can be well measured, the forward rapidity gaps exceed 2.7 at the ISR and 6.1 at the Tevatron. The AFS experiment at the ISR [6] showed very little non-DPE background in central $\pi^+\pi^-$ production. Gaps exceeding 6 units at the Tevatron will have negligible background from non-pomeron exchange *.

2. GLUEBALL PHYSICS

At this workshop Barnes [7], Kharzeev [10] and Pumplin [11] also discussed hadron spectroscopy in double pomeron exchange processes. There are different ways of thinking about the *exclusive* process $p\bar{p} \to pG\bar{p}$ with G a central gluonium or glueball state. (D.Robson [12] first suggested this channel.) One is to note that any hadrons or hadron pairs with the quantum numbers of the vacuum will be present as virtual states in the vacuum and they can be made real by the collision of two hadrons, whose role is essentially to allow 4-momentum to be conserved. (What is the spectrum of these states, for specific quantum numbers?) Another is to consider the fusion of a colorless pair (or triplet) of gluons from each beam particle, noting that the gluon density rises rapidly as $x_{Bjorken}$ becomes very small. Yet another is to note that glueball states, like all hadrons, must couple to the pomeron and if the quantum numbers are right the process will proceed by $PP \to G$. Allowed quantum numbers are $I = 0, C = +$ but any J^P [11]. The advantage of the *exclusive* process is clear: Glueballs are probably being produced with a high cross section in inelastic collisions but when the multiplicity is high the combinatorial background is overwhelming. In exclusive production there is **no** combinatorial background.

For this physics one would like to select events with 2, 4 or possibly 6 well measured charged particles in the central detectors. Particle identification (π, K, p) is important both for reconstructing the mass and checking that the overall charge, strangeness, and baryon number are zero. Additional neutral particles (γ, π^o, K_L^o, n) may be looked for and either used in the final state combination or used to reject non-exclusive events. The list of interesting final states is long and fairly obvious, including $\pi^+\pi^-, K^+K^-, K_S^oK_S^o, p\bar{p}, \Lambda\bar{\Lambda}, \phi\phi, 4\pi, \pi\pi KK, KKKK$, etc. The mass resolution when the charged tracks are all measured is very good, typically 10 MeV. It would be good to be able to use the electromagnetic calorimetry to measure neutral states like $\eta\eta \to 4\gamma$ but I suspect this is very difficult to trigger on, the

*I assume no *Odderon* exchange. That could be looked for by the exclusive production of a central ω or ϕ with $I^GJ^{PC} = 0^-1^{--}$.

backgrounds would be high and the mass resolution poor. However I have not done a study of this.

3. HYPERON AND OTHER PAIRS

At the Axial Field Spectrometer at the ISR exclusive central $p\bar{p}$ pairs were observed [6] with masses from 2 GeV to 2.8 GeV. With only 64 events there were no significant structures. (WA102 [4] also reported no significant structures with more events but more non-DPE background.) The total cross section for $pp \to pp\bar{p}p$ with the central p and $\bar{p}$ having $|\eta| \leq 1.5$ is 40±20 nb which, if s-independent[†], would correspond to a rate of 4 Hz at $L = 10^{32} cm^{-2} s^{-1}$. Actually with that luminosity and 36 bunches ($\Delta t = 396 ns$) the fraction of inelastic collisions that occur in isolation (therefore useful for gap physics) is only about 13%. The optimum luminosity for gap physics is when $< n >= 1$, at $L \approx 5 \times 10^{31} cm^{-2} s^{-1}$, and the fraction of events that occur singly is then 37%. So perhaps one could get thousands of events in an hour of special running, along with other channels that could come with the same trigger (say 2 or 4 central charged particles). This estimate is assuming full $|t|$ coverage and should be multiplied by the t-acceptance if it is limited.

If proton pairs are produced by DPE we must also have hyperon pairs $Y\bar{Y}$ produced. Just using charged particles, and allowing for displaced vertices, one can measure pairs of $\Lambda, \Xi^-, \Xi(1530), \Omega^-$ and maybe even Λ_c. Using γ and π^o other pairs like Σ^o, Σ^+ and Ξ^o become accessible. Why would one want to do this? The wealth of data possible can be used to measure the coupling of all these baryons to the pomeron, and relate them to elastic and total cross sections ... does the phenomenology hang together? How do the $Y\bar{Y}$ mass spectra depend on Y, and on t_1, t_2 if they are measured. If one measures also meson pair production ($\phi\phi$) how do the cross sections compare at the same mass (2-quarks vs 3-quarks)? With hyperon pairs one can measure polarizations and hence study spin-spin correlations which might reveal interesting things about the spin of the pomeron (are there correlations with $t_1, t_2, \Delta\phi(p\bar{p})$)? When $K^o\bar{K}^o$ pairs are produced are they $K^o_s K^o_s$ and $K^o_L K^o_L$ or sometimes $K^o_S K^o_L$, and is the answer dependent on $M_{K\bar{K}}$? If both kaons were to decay to $\pi^+\pi^-$ is there a correlation between their decay times as there is in ϕ decay?

[†]The cross section should be s-independent for $\alpha_P(0) = 1.0$, whereas it falls with s for reggeon exchange $\alpha_R(0) < 1.0$.

4. HYBRIDS, HEAVY MESONS, AND HIGGS

There can be a very interesting spectroscopy of, possibly narrow, hybrid states $b\bar{b}g$ [7] [13]. Those with the allowed quantum numbers (DPE is a *Quantum Number Filter*) will be produced exclusively; e.g. one gluon from each beam proton fuse $gg \to g$ and another make $gg \to b\bar{b}$.

Also we should search for the 0^+0^{++} χ_c and χ_b states; the latter decays to $\Upsilon\gamma$ to $\mu^+\mu^-\gamma$. One very interesting reason to study isolated central χ_b production is because it may instruct us about a possible *Higgs* production (discovery?) channel [8]. In the former case two gluons fuse to form the χ_b, and another soft gluon is exchanged between the two beam particles to leave them colorless and unexcited. (This is called non-factorisable double pomeron exchange, NFDP.) Measuring this cross section will enable us to better estimate the similar process where the two gluons (low p_T but $p_L \approx p_{beam} - \frac{M_H}{2}$) make a Higgs via a top-quark loop, and another soft gluon sorts out the color. The process is then $p\bar{p} \to pH\bar{p}$. Measuring the outgoing $x_F \approx 0.94$ beam particles in precision roman pot detectors (this requires dipole spectrometers on both sides to get to $|t| = t_{min}$) the missing mass resolution can be much better than the effective mass resolution of the $H \to b\bar{b}$ jet pair. . Neither CDF nor DØ have the apparatus for this but if the signal estimates and (DPE/QCD $b - \bar{b}$ dijet) backgrounds are encouraging then it could be done [9].

Studies of meson pairs may be extendable to the charm sector; the masses of D and D_s are little above the Ω mass, and there are exclusive decay modes e.g. $KK\pi$ with branching fractions around 9% and 5% respectively. Unfortunately exclusive $B\bar{B}$ pairs are probably unobtainable.

All these processes, systematically studied, will clearly tell us a lot about the nature of diffraction/pomerons, in addition to the hybrid or meson spectroscopy itself.

5. DISORIENTED CHIRAL CONDENSATES etc.

High energy cosmic ray events have been observed with either an anomalously large ratio of charged hadrons:γ/e (Centauros; one striking event has a ratio 49:1) or a very small ratio (Anticentauro; one event has 1 charged track and 32 γ's in an η, ϕ circle of radius 0.7). Such events have been interpreted [14] as manifestations of a "Disoriented Chiral Condensate". No accelerator experiments have seen anomalous tails on the charged:neutral ratio [15]. No searches have yet been made in the central region of DPE events.

It is worthwhile making a search, because as I have said for low-t, low Q^2 (no jets) events the pomeron might be dominated by just gluons. In that case this would be the first study of high mass ($\approx$ 50 GeV) "isotropic" events where the initial state is (to some degree) purely gluonic. One would trigger on gap-X-gap events, anti-select on jets, construct the ratio $\Sigma_{p_T}(charged\ tracks)$: $\Sigma_{E_T}(electromagnetic\ cal)$ and study the tails (with a single vertex, rejecting cosmics, etc.).

High charged multiplicity events, DCC candidates or not, can be analysed for Bose-Einstein correlations, which can be used to measure the radius of the particle emission (separately for pions and kaons, if identified ... also for K^o_s if there are enough of them per event) in both the longitudinal and transverse directions. The K/π ratio is another interesting quantity to study either in a sample of DCC candidate events or in other special classes of events. Note that the AFS experiment [6] found, for 2-central tracks, R$[K^+K^-/\pi^+\pi^-]$ above 1.0 just above the $K\bar{K}$ threshold, but this is probably a manifestation of the prominent $f_o(970)$ resonance.

6. EXPERIMENTAL CONSIDERATIONS

CDF and DØ have some complementary aspects for this physics and it would be best to have both experiments producing results, for cross checks where they overlap. DØ will have the apparent advantage of having roman pots (quadrupole spectrometers) on both the p and the $\bar{p}$ side, while CDF only has a dipole pot spectrometer on the $\bar{p}$ side. So DØ can tag both beam particles and measure their t and ϕ, which CDF cannot. Very interesting dependences of the central mass spectra ($\pi^+\pi^-$) on the relative azimuth $\Delta\phi$ have been observed [16] at $\sqrt{s}$ = 28 GeV/c. Are these dependences due to regge exchanges which will die away with $\sqrt{s}$? DØ will pay a fairly severe rate penalty $\approx 10^{-4}$ for double tagging, because $|t_{min}| \approx 0.5 - 0.6$ GeV^2 on each side. Even when both p and $\bar{p}$ are detected, the *missing mass* resolution is O(GeV); the spectroscopy is done by reconstructing the effective mass of the central system. The CDF approach is to ignore the forward p and $\bar{p}$, allowing them to go down the beam pipe, which gives acceptance for all $|t|$. CDF can trigger on rapidity gaps on both sides, and to make this possible have installed *Beam Shower Counters (BSC)* where possible around the beam pipe (just in front of the low-β quadrupoles, before and after the electrostatic separators, and on the $\bar{p}$ side just before the Roman Pots at 56 m). CDF hopes to install also *Miniplug Calorimeters* for $3.5 \leq |\eta| \leq 5.5$ ($\theta \leq 3^o$) and in this region there are also the *Cerenkov Luminosity Counters (CLC)* which count charged particles from the interaction region. All of these in veto will give rapidity gaps of 4 units on each side. It might be advantageous to require even larger gaps by (in CDF) vetoing on energy in the plug calorimeter (which has an $\eta\phi$ geometry) with $|\eta| \geq 2.0$ ... after all one cannot measure tracks well there. DØ could, I believe, make a similar trigger. These "2-gap" triggers will be *very* effective at vetoing multiple interactions. Of course some positive requirement (more than the beam crossing signal X_0) is also needed. This could be made in principal, in CDF or DØ , by requiring a minimal energy E in the complementary central region; above noise levels but as low as possible. CDF has the more attractive possibility of using its time-of-flight (*TOF*) barrel (216 ϕ-segments of fast scintillator) to trigger on a central charged particle multiplicity of 2,4 or 6 particles. (Actually the trigger would probably be only able to use ϕ segments of 15° for technical reasons.) The tracks which hit the *TOF* barrel are full length and very well measured. Most will also be identified: The *TOF* gives 2σ separation of π and K to 1.6 GeV/c, and the *Central Outer Tracker (COT)* will measure dE/dx to 10% which will provide further information on π, K, p identification.

The best way of implementing this physics program in CDF and DØ is probably to set up a trigger table based on two forward gaps and the various central requirements. One wants in addition the same central requirements with one or no forward gaps required, but with large prescaling factors to compensate for the much higher rates. These samples are used to measure cross sections and estimate the signal:background (multiplicity = 0 tails of non-diffractive events). Ideally one would like this trigger table to give a rate of about 50 Hz at $L = 5.10^{31} cm^{-2} s^{-1}$, and to take 3-4 hours of test data at such a luminosity (or at a lower luminosity if the trigger cross section is higher). These 0.5-1.0 million events should be analysed both for their own physics and to refine triggers. This should be enough to whet our appetite for the most promising and interesting channels, and either to take more dedicated running towards the end of stores or to include this as a fraction of the "QCD bandwidth".

7. CONCLUSION

There is a great deal of new physics to study with low mass exclusive central states in DPE at the Tevatron. The hardware should exist (the CDF Miniplugs should be approved!) and the fraction of additional integrated dead-time needed is negligible.

REFERENCES

1. See e.g. M.G. Albrow, Double Pomeron Exchange from the ISR to the SSC, Nucl. Phys. B (Proc.Supp.) **12**, 291 (1990) and references therein.
2. M. Derrick et al. (ZEUS), Phys. Lett. **B315**, 481 (1993); T. Ahmed et al.(H1), Nucl. Phys. **B429**, 477 (1994).
3. F. Abe et al. (CDF), Phys. Rev. Lett. **78**, 2698 (1997); L. Coney (DØ), Observation of Diffractive W Production at DØ , APS Meeting, Atlanta GA, March 1999.
4. See e.g. D. Barberis et al. (WA102), Phys. Lett. **B432**, 436 (1998) for $DPE \to \phi\phi$; D.Barberis et al., Phys. Lett. **B446**, 342 (1999) for $p\bar{p}$ and $\Lambda\bar{\Lambda}$, and other WA102 papers.
5. M.A. Reyes et al., Phys. Rev. Lett. **81**, 4079 (1998); M. Sosa et al., Phys. Rev. Lett. **83**, 913 (1999) (E690).
6. T. Akesson et al. (AFS,R807), Nucl.Phys. **B264**, 154 (1986).
7. Ted Barnes, Glueballs and Exotics in QCD, talk at this workshop.
8. A. Bialas and P.V. Landshoff, Phys. Lett. **B256**, 540 (1991); D. Kharzeev and E. Levin, hep-ph/0005311 and references therein.
9. M. Albrow,D. Litvintsev,P. Murat and A. Rostovtsev, Run II SUSY Higgs Workshop proc. (http://fnth37.fnal.gov/susy.html) pp 87-89.
10. Dmitri Kharzeev, Diffractive Production of Glueballs, these proceedings.
11. Jon Pumplin, Double Pomeron Physics in Run II, these proceedings.
12. D. Robson, Nucl. Phys. **B130**, 328 (1977).
13. See e.g. P.R. Page,E.S. Swanson and A.P. Szczepaniak, Phys. Rev. **D59**:034016 (1999).
14. J.D. Bjorken, Int. J. Mod. Phys. **A7**, 4189 (1992).
15. For a CDF limit, see P. Melese, Proc.XI Topical Workshop on $p\bar{p}$ Collider Physics, Padova, Italy (1996). FERMILAB-Conf-96/205-E.
16. D. Barberis et al. (WA102), Phys. Lett. **B397**, 339 (1997), F. Close, A. Kirk and G. Schuler, Phys. Lett. **B477**, 13 (2000).

A Determination of Pomeron Intercepts at Colliders

R. Peschanski [a] C. Royon [b]

[a]CEA, Service de Physique Theorique, CE-Saclay, F-91191 Gif-sur-Yvette Cedex

[b]DAPNIA/SPP, Commissariat à l'Energie Atomique, Saclay,
F-91191 Gif-sur-Yvette Cedex

A method allowing for a direct comparison of data with theoretical predictions is proposed for forward jet production at HERA and Mueller-Navelet jets at Tevatron. An application to the determination of the *effective* Pomeron intercept in the BFKL-LO parameterization from $d\sigma/dx$ data at HERA leads to a good fit with a significantly higher *effective* intercept, $\alpha_P = 1.43 \pm 0.025(stat.) \pm 0.025(syst.)$, than for proton (total and diffractive) structure functions. It is however less than the value of the pomeron intercept using dijets with large rapidity intervals obtained at Tevatron. We also evaluate the rapidity veto contribution to the higher order BFKL corrections. We suggest to measure the dependence of the dijet cross-sections as a function of the jet transverse energies as a signal for BFKL pomeron at Tevatron.

1. Forward jet cross-section at HERA

The study of forward jets at colliders is considered as the milestone of QCD studies at high energies, since it provides a direct way of testing the perturbative resummations of soft gluon radiation. More precisely, the study of one forward jet (w.r.t. the proton) in an electron-proton collider [1] seems to be a good candidate to test the energy dependence of hard QCD cross-sections. It is similar to the previous proposal of studying two jets separated by a large rapidity interval in hadronic colliders [2], for which only preliminary results are available [3]. This test is also possible in γ^*-γ^* scattering [4] but here the statistics and the energy range are still insufficient to get a reliable determination of the physical parameters for hard QCD cross-sections. Indeed, the proposed (and favored for the moment being) set-up [1] is to consider jets with transverse momentum k_T of the order of the photon virtuality Q allowing to damp the QCD evolution as a function of k_T (DGLAP evolution [5]) in favor of the evolution in energy at fixed k_T (BFKL evolution [6]).

In contrast to full Monte-Carlo studies we want to focus on the jet cross section $d\sigma/dx$ observable itself, by a consistent treatment of the experimental cuts and minimizing the uncertainties for that particular observable. Let us remark that our approach is not intended to provide a substitution to the other methods, since the Monte-Carlo simulations have the great merit of making a set of predictions for various observables. Hence, our method has to be considered as complementary to the others and dedicated to a better determination of the *effective* Pomeron intercept using the $d\sigma/dx$ data. As we shall see, it will fix more precisely this parameter, but it will leave less constrained other interesting parameters, such as the cross-section normalization.

The cross-section for forward jet production at HERA in the dipole model reads [10]:

$$\frac{d^{(4)}\sigma}{dxdQ^2dx_Jdk_T^2d\Phi} = \frac{\pi N_C \alpha^2 \alpha_S(k_T^2)}{Q^4 k_T^2}\ f_{eff}(x,\mu_f^2)$$
$$\Sigma e_Q^2 \int_{\frac{1}{2}-i\infty}^{\frac{1}{2}+i\infty} \frac{d\gamma}{2i\pi}\left(\frac{Q^2}{k_T^2}\right)^\gamma \exp\{\epsilon(\gamma,0)Y\} \times$$
$$\times \quad \left[\frac{h_T(\gamma)+h_L(\gamma)}{\gamma}(1-y) + \frac{h_T(\gamma)}{\gamma}\frac{y^2}{2}\right] \qquad (1)$$

where

$$Y = \ln\frac{x_J}{x} \qquad (2)$$
$$\epsilon(\gamma,p) = \bar{\alpha}\left[2\psi(1) - \psi(p+1-\gamma) - \psi(p+\gamma)\right] \qquad (3)$$
$$f_{eff}(x,\mu_f^2) = G(x,\mu_f^2) + \frac{4}{9}\Sigma(Q_f + \bar{Q_f}) \qquad (4)$$
$$\mu_f^2 \sim k_T^2\ , \qquad (5)$$

are, respectively, Y the rapidity interval between the photon probe and the jet, $\epsilon(\gamma,p)$ the BFKL kernel eigenvalues, f_{eff} the effective structure function combination, and μ_f the corresponding factorization scale. The main BFKL parameter is $\bar{\alpha}$, which is the (fixed) value of the effective strong coupling constant in LO-BFKL formulae. Note that we gave the BFKL formula not including the azimuthal dependence as we will stick to the azimuth-independent contribution with the dominant $\exp\{\epsilon(\gamma,0)Y\}$ factor.

The so-called "impact factors" h_T, h_L

$$\begin{pmatrix} h_T \\ h_L \end{pmatrix} = \frac{\alpha_S(k_T^2)}{3\pi\gamma}\frac{(\Gamma(1-\gamma)\Gamma(1+\gamma))^3}{\Gamma(2-2\gamma)\Gamma(2+2\gamma)}\frac{1}{1-\frac{2}{3}\gamma} \begin{pmatrix} (1+\gamma)(1-\frac{\gamma}{2}) \\ \gamma(1-\gamma) \end{pmatrix}\ , \qquad (6)$$

are obtained from the k_T factorization properties [15] of the coupling of the BFKL amplitudes to external hard probes. The same factors can be related to the photon wave functions [16,14] within the equivalent context of the QCD dipole model [17].

Our goal is to compare as directly as possible the theoretical parameterization (1) to the data which are collected in experiments [7,8]. The crucial point is how to take into account the experimentally defined kinematic cuts [7,8].

The main problem to solve is to investigate the effect of these cuts on the determination of the integration variables leading to a prediction for $d\sigma/dx$ from the given theoretical formula for $d^{(4)}\sigma$ as given in formula (1). The effect is expected to appear as bin-per-bin *correction factors* to be multiplied to the theoretical cross-sections for average values of the kinematic variables for a given x-bin before comparing to data (e.g. fitting the cross-sections) [9].

The experimental correction factors have been determined using a toy Monte-Carlo designed as follows. We generate flat distributions in the variables k_T^2/Q^2, $1/Q^2$, x_J, using reference intervals which include the whole of the experimental phase-space (the Φ variable is not used in the generation since all the cross-section measurements are ϕ independent). In practice, we get the correction factors by counting the numbers of events which fulfill the experimental cuts given in Table **I** for each x-bin. The correction factor is obtained by the ratio to the number of events which pass the experimental cuts and the kinematic constraints, and the number of events which fullfil only the kinematic constraints,i.e. the so-called reference bin. The correction factors are given in reference [9].

We perform a fit to the H1 and ZEUS data with only two free parameters. these are the *effective* strong coupling constant in LO BFKL formulae $\bar{\alpha}$ corresponding to the *effective* Lipatov intercept $\alpha_P = 1 + 4\log 2\bar{\alpha}N_C/\pi$, and the cross-section normalization. The obtained values of the parameters and the χ^2 of the fit are given in Table **III** for a fit to the H1 and ZEUS data separately, and then to the H1 + ZEUS data together.

The χ^2 of the fits have been calculated using statistical error only and are very satisfactory (about 0.6 *per point* for H1 data, and 1. *per point* for ZEUS data). We give both statistical and systematic errors for the fit parameters. The values of the Lipatov intercept are close to one another and compatible within errors for the H1 and ZEUS sets of data, and indicate a preferable medium value ($\alpha_P = 1.4 - 1.5$). We also notice that the ZEUS data have the tendency to favour a higher exponent, but the number of data points used in the fit is much smaller than for H1, and the H1 data are also at lower x. The normalization is also compatible between ZEUS and H1. The fit results are shown in Figure 1 and compared with the H1 and ZEUS measurements.

Table 1
Fit results.

fit	$\bar{\alpha}$	α_P
H1	0.17 ± 0.02 ± 0.01	1.44 ± 0.05 ± 0.025
ZEUS	0.20 ± 0.02 ± 0.01	1.52 ± 0.05 ± 0.025
H1+ZEUS	0.16 ± 0.01 ± 0.01	1.43 ± 0.025 ± 0.025
D0	0.24 ± 0.02 ± 0.02	1.65 ± 0.05 ± 0.05
fit	Norm.	$\chi^2(/dof)$
H1	29.4 ± 4.8 ± 5.2	5.7 (/9)
ZEUS	26.4 ± 3.9 ± 4.7	2.0 (/2)
H1+ZEUS	30.7 ± 2.9 ± 3.5	12.0 (/13)

2. Comparison with Tevatron results

The final result of our new determination of the effective pomeron intercept is $\alpha_P = 1.43 \pm 0.025$ (stat.) ± 0.025 (syst.). Our method allows a direct comparison of the intercept values with those obtained in other experimental processes, i.e. $\gamma^*\gamma^*$ cross-sections at LEP [4], jet-jet cross-sections at Tevatron at large rapidity intervals [3], F_2 and F_2^D proton structure function measurements [12–14].

Let us compare our results with the effective intercept we obtain from recent preliminary dijet data obtained by the D0 Collaboration at Tevatron [3]. The measurement consists in the ratio $R = \sigma_{1800}/\sigma_{630}$ where σ is the dijet cross-section at large rapidity interval $Y \sim \Delta\eta$ for two center-of-mass energies (630 and 1800 GeV), $\Delta\eta_{1800} = 4.6$, $\Delta\eta_{630} = 2.4$. The experimental measurement is $R = 2.9 \pm 0.3$ (stat.) ± 0.3 (syst.). Using the Mueller-Navelet formula [2], this measurement allows us to get a value of the effective intercept for this process

$$R = \frac{\int_{\frac{1}{2}-i\infty}^{\frac{1}{2}+i\infty} \frac{d\gamma}{2i\pi\gamma(1-\gamma)} e^{\epsilon(\gamma,0)\Delta\eta_{1800}}}{\int_{\frac{1}{2}-i\infty}^{\frac{1}{2}+i\infty} \frac{d\gamma}{2i\pi\gamma(1-\gamma)} e^{\epsilon(\gamma,0)\Delta\eta_{630}}}. \quad (7)$$

We get α_P=1.65 ± 0.05 (stat.) ± 0.05 (syst.), in agreement with the value obtained by D0 using a saddle-point approximation [3] (see Table 1). This intercept is higher than the one obtained in the forward jet study.

Formula (7) is obtained after integration over the jet transverse energies at 630 and 1800 GeV, E_{T_1}, E_{T_2}. We

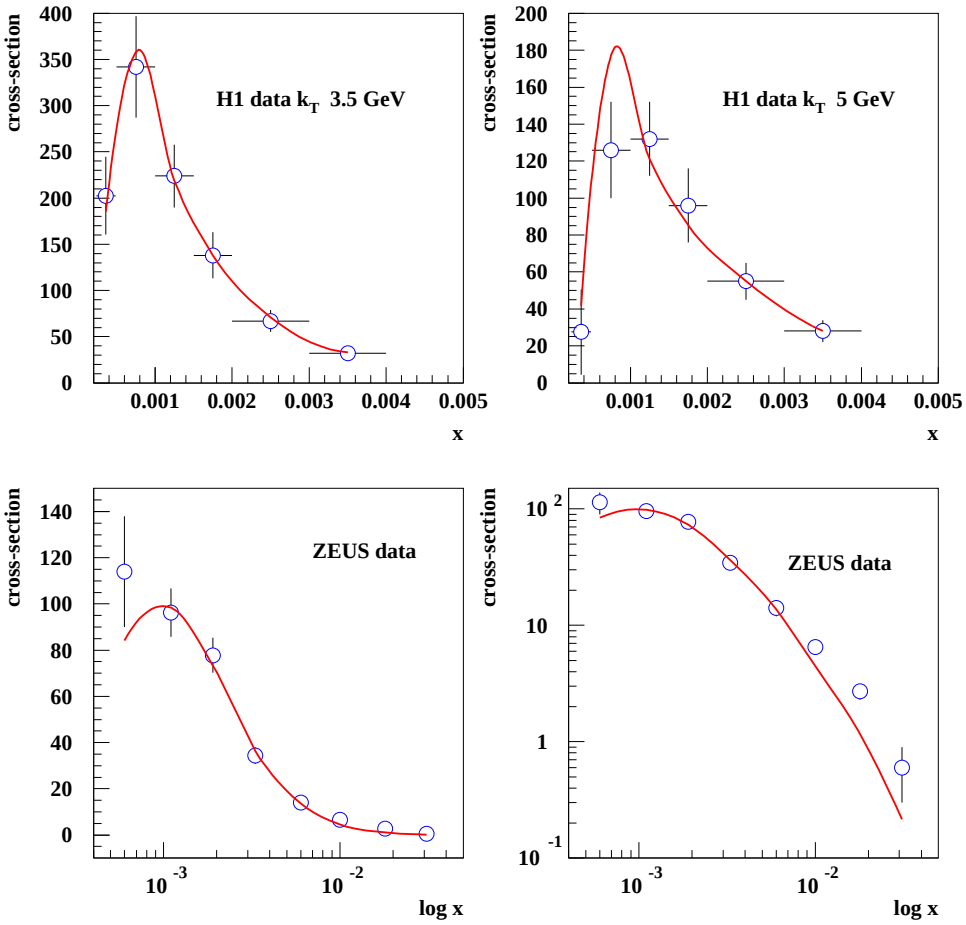

Figure 1. The H1 data ($k_T > 3.5$ GeV, $k_T > 5$ GeV), and the ZEUS data are compared with the result of the fit. ZEUS data are also displayed in logarithmic scales in vertical coordinates to show the discrepancy at high x values.

note that the non integrated formula

$$R(E_{T_1}/E_{T_2}) = \frac{\int_{\frac{1}{2}-i\infty}^{\frac{1}{2}+i\infty} \frac{d\gamma}{2i\pi} \left(\frac{E_{T_1}}{E_{T_2}}\right)^{2\gamma} e^{\epsilon(\gamma,0)\Delta\eta_{1800}}}{\int_{\frac{1}{2}-i\infty}^{\frac{1}{2}+i\infty} \frac{d\gamma}{2i\pi} \left(\frac{E_{T_1}}{E_{T_2}}\right)^{2\gamma} e^{\epsilon(\gamma,0)\Delta\eta_{630}}} \quad (8)$$

shows a sizeable dependence on E_{T_1}/E_{T_2}, which could be confronted with experiment. Let us show both the integrated and E_{T_1}/E_{T_2} dependent cross-sections in Figure 2.

The question arises to interpret the different values of the effective intercept. It could reasonably come from the differences in higher order QCD corrections for the BFKL kernel and/or in the impact factors depending on the initial probes (γ^* vs. jets). In order to evaluate the approximate size of the higher order BFKL corrections, we will use their description in terms of rapidity veto effects [18]. In formula (1), we replace $\exp(\epsilon(\gamma,0)Y)$ by

$$\Sigma_{n=0}^{\infty}\ \theta(Y-(n+1)b)\ \frac{[\epsilon(\gamma,0)\ (Y-(n+1)b)]^n}{\Gamma(n+1)}\ . \quad (9)$$

The Heaviside function θ ensures that a BFKL ladder of n gluons occupies $(n+1)b$ rapidity interval where b parametrises the strength of NLO BFKL corrections. The value of the leading order intercept is fixed to $\alpha_p = 1.75(\alpha_S(Q^2 = 10) = 0.28)$, where $Q^2 = 10$ GeV^2 is inside the average range of Q^2 in the forward jet measurement. The fitted value of the b parameter obtained using the forward jet data is found to be 1.28 $\pm$ 0.08 (stat.) $\pm$ 0.02 (syst.). Imposing the same value of α_P with Tevatron data gives b=0.21 $\pm$ 0.11 (stat.) $\pm$ 0.11 (syst.). Note that the theoretical value of b for the NLO BFKL kernel is expected to be of the order 2.4, which is also compatible with the result obtained for the $\gamma^*\gamma^*$ cross-section. A contribution from the NLO impact factors is not yet known, and could perhaps explain the different values of b.

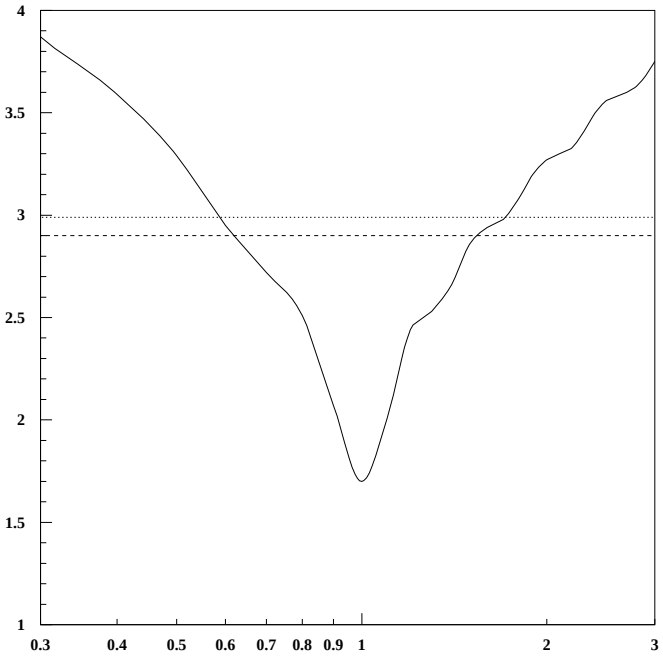

Figure 2. E_{T_1}/E_{T_2} dependence of the dijet cross-section ratio. E_{T_1}/E_{T_2} is given in the horizontal axis, and R in vertical axis. In full line is given the non integrated $R(E_{T_1}/E_{T_2})$ (see formula (8)), in dotted line, the integrated R (formula (7) and in dashed line, the saddle point approximation of R [2], for the fitted value of α_P (see table 1).

3. Conclusion

To summarize our results, using a new method to disentangle the effects of the kinematic cuts from the genuine dynamical values we find that the effective pomeron intercept of the forward jet cross-sections at HERA is $\alpha_P = 1.43 \pm 0.025$ (stat.) $\pm$0.025 (syst.). It is much higher than the soft pomeron intercept, and, among those determined in hard processes, it is intermediate between $\gamma^*\gamma^*$ interactions at LEP and dijet productions with large rapidity intervals at Tevatron, where we get α_P=1.65 $\pm$ 0.05 (stat.) $\pm$ 0.05 (syst.).

Looking for an interpretation of our results in terms of higher order BFKL corrections expressed by rapidity gap vetoes b between emitted gluons, we find a value of b =1.3 at HERA, and 0.21 at Tevatron. The HERA value is sizeable but less than the theoretically predicted [11] value for the NLO BFKL kernel (b =2.4). The Tevatron value is compatible with zero. The observed dependence in the process deserves further more precise studies [19].

We suggest to measure the dependence of the dijet cross-sections as a function of the jet transverse energies as a signal for BFKL pomeron at Tevatron run II. The Mueller Navelet jet study would also benefit from a lower energy run at the end of Run II to allow a normalization independence of the intercept determination and BFKL tests.

4. Acknowledgments

R.P. acknowledges supports by the EU Fourth Framework Programme 'Training and Mobility of Researchers', Network 'Quantum Chromodynamics and the Deep Structure of Elementary Particles', contract FMRX-CT98-0194 (DG 12 - MIHT).

REFERENCES

1. A.H. Mueller, *Nucl. Phys.* **B** (Proc. Suppl.) 18C (1991) 125.
2. A.H. Mueller and H. Navelet, *Nucl. Phys.* **B282** (1987) 107.
3. A. Goussiou, for the D0 collaboration, *Dijet Cross section at large s/Q^2 in $\bar{p}p$ Collisions*, presented at the 'International Europhysics Conference On High-Energy Physics' (EPS-HEP 99), Tampere, Finland, July, 1999.
4. S.Brodsky, V.S. Fadin, V.T. Kim, L.N. Lipatov, G.B. Pivovarov, *JETP Lett.* **70** (1999) 155; M. Boonekamp, A. De Roeck, C. Royon, S. Wallon, *Nucl.Phys.* **B555** (1999) 540, for a recent review and references, Ch. Royon, *BFKL signatures at a linear collider*, invited talk given at the International Workshop on Linear Colliders (LCWS99), April 28- May 5, Sitges (Spain), hep-ph/9909295.
5. G. Altarelli and G. Parisi, *Nucl. Phys.* **B126** 18C (1977) 298; V.N. Gribov and L.N. Lipatov, *Sov. Journ. Nucl. Phys.* (1972) 438 and 675; Yu.L. Dokshitzer, *Sov. Phys. JETP.* **46** (1977) 641.
6. L.N. Lipatov, *Sov. J. Nucl. Phys.* **23** (1976) 642; V.S. Fadin, E.A. Kuraev and L.N. Lipatov, *Phys. lett.* **B60** (1975) 50; E.A. Kuraev, L.N. Lipatov and V.S. Fadin, *Sov. Phys. JETP* **44** (1976) 45, **45** (1977) 199; I.I. Balitsky and L.N. Lipatov, *Sov. J. Nucl. Phys.* **28** (1978) 822.
7. H1 Collaboration, C. Adloff et al. *Nucl. Phys.* **B538** (1999) 3.
8. ZEUS Collaboration, J. Breitweg et al. *Eur. Phys. J.* **C6** (1999) 239.
9. G. Contreras, R. Peschanki, C. Royon, hep-ph/0002057, to appear.
10. J. Bartels, A. De Roeck, M. Loewe, *Zeit. für Phys.* **C54** (1992) 921; W-K. Tung, *Phys. lett.* **B278** (1992) 635; J. Kwiecinski, A.D. Martin, P.J. Sutton, *Phys.Rev.* **D46** (1992) 921.
11. V.S. Fadin and L.N. Lipatov *Phys. Lett.* **B429** (1998)127; M. Ciafaloni *Phys. Lett.* **B429** (1998) 363; M. Ciafaloni and G. Camici *Phys. Lett.* **B430** (1998) 349.
12. H. Abramowicz, *Diffraction and the Pomeron* Contribution to the 19th International Symposium on Lepton and Photon Interactions at High-Energies (LP 99), Stanford, California, 9-14 Aug 1999, hep-ph/0001054.
13. H. Navelet, R. Peschanski, Ch. Royon, *Phys. Lett.* **B366** (1995) 329. H. Navelet, R. Peschanski, Ch. Royon, S. Wallon, *Phys. Lett.* **B385** (1996) 357.
14. S. Munier, R. Peschanski, Ch. Royon, *Nucl. Phys.* **B534** (1998) 297.
15. S. Catani, M. Ciafaloni, F. Hautmann, *Nucl. Phys.* **B366** (1991) 135. J.C. Collins, R.K. Ellis, *Nucl. Phys.* **B360** (1991) 3. E.M. Levin, M.G. Ryskin, Yu. M. Shabelskii, A.G. Shuvaev, *Sov. J. Nucl. Phys.* **53** (1991) 657.
16. J.D. Bjorken, J. Kogut and D. Soper, *Phys. Rev.* **D3** (1971) 1382. N.N. Nikolaev, B.G. Zakharov, *Zeit. für. Phys.* **C49** (1991) 607; *Phys. Lett.* **B332** (1994) 184.
17. A.H. Mueller, *Nucl. Phys.* **B415** (1994) 373; A.H. Mueller and B. Patel, *Nucl. Phys.* **B425** (1994) 471; A.H. Mueller, *Nucl. Phys.* **B437** (1995) 107.
18. L.N. Lipatov, talk presented at the 4th Workshop on Small-x and Diffractive Physics, FNAL, September 1998, C. Schmidt, *Phys. Rev.* **D60** (1999) 074003, J. Forshaw, D.A. Ross, A. Sabio Vera, *Phys. Lett.* **B455** (1999) 273-282.
19. V.T. Kim, L.N. Lipatov, R. Peschanski, G. Pivovarov, C. Royon, in progress.

BFKL Monte Carlo for Dijet Production at Hadron Colliders

Lynne H. Orr[a] and W.J. Stirling[b]

[a]Department of Physics and Astronomy, University of Rochester
Rochester NY 14627-0171

[b]Departments of Physics and Mathematical Sciences, University of Durham,
Durham DH1 3LE, UK

The production of jet pairs at large rapidity difference at hadron colliders is potentially sensitive to BFKL physics. We present the results of a BFKL Monte Carlo calculation of dijets at the Tevatron. The Monte Carlo incorporates kinematic effects that are absent in analytic BFKL calculations; these effects significantly modify the behavior of dijet cross sections.

1. MONTE CARLO APPROACH TO BFKL

Fixed-order QCD perturbation theory fails in some asymptotic regimes where large logarithms multiply the coupling constant. In those regimes resummation of the perturbation series to all orders is necessary to describe many high-energy processes. The Balitsky-Fadin-Kuraev-Lipatov (BFKL) equation [1] performs such a resummation for virtual and real soft gluon emissions in such processes as dijet production at large rapidity difference in hadron-hadron collisions. BFKL resummation gives [2] a subprocess cross section that increases with rapidity difference as $\hat{\sigma} \sim \exp(\lambda\Delta)$, where Δ is the rapidity difference of the two jets with comparable transverse momenta p_{T1} and p_{T2}.

Experimental studies of these processes have recently begun at the Tevatron $p\bar{p}$ and HERA ep colliders. Tests so far have been inconclusive; the data tend to lie between fixed-order QCD and analytic BFKL predictions. However the applicability of analytic BFKL solutions is limited by the fact that they implicitly contain integrations over arbitrary numbers of emitted gluons with arbitrarily large transverse momentum: there are no kinematic constraints included. Furthermore, the implicit sum over emitted gluons leaves only leading-order kinematics, including only the momenta of the 'external' particles. The absence of kinematic constraints and energy-momentum conservation cannot, of course, be reproduced in experiments. While the effects of such constraints are in principle sub-leading, in fact they can be substantial and should be included in predictions to be compared with experimental results.

The solution is to unfold the implicit sum over gluons and to implement the result in a Monte Carlo event generator [3,4]. This is achieved as follows. The BFKL equation contains separate integrals over real and virtual emitted gluons. We can reorganize the equation by combining the 'unresolved' real emissions — those with transverse momenta below some minimum value (chosen to be small compared to the momentum threshold for measured jets) — with the virtual emissions. Schematically, we have

$$\int_{virtual} + \int_{real} = \int_{virtual+real,unres.} + \int_{real,res.} \qquad (1)$$

We perform the integration over virtual and unresolved real emissions analytically. The integral containing the resolvable real emissions is left explicit.

We then solve by iteration, and we obtain a differential cross section that contains a sum over emitted gluons along with the appropriate phase space factors. In addition, we obtain an overall form factor due to virtual and unresolved emissions. The subprocess cross section is

$$d\hat{\sigma} = d\hat{\sigma}_0 \times \sum_{n\geq 0} f_n \qquad (2)$$

where f_n is the iterated solution for n real gluons emitted and contains the overall form factor. It is then straightforward to implement the result in a Monte Carlo event generator. Because emitted real (resolved) gluons appear explicitly, conservation of momentum and energy, as well as evaluation of parton distributions, is based on exact kinematics for each event. In addition, we include the running of the strong coupling constant. See [3] for further details.

2. DIJET PRODUCTION AT HADRON COLLIDERS

At hadron colliders, the BFKL increase in the dijet subprocess cross section with rapidity difference Δ is unfortunately washed out by the falling parton distribution functions (pdfs). As a result, the BFKL prediction for the total cross section is simply a less steep falloff than obtained in fixed-order QCD, and tests of this prediction are sensitive to pdf uncertainties. A

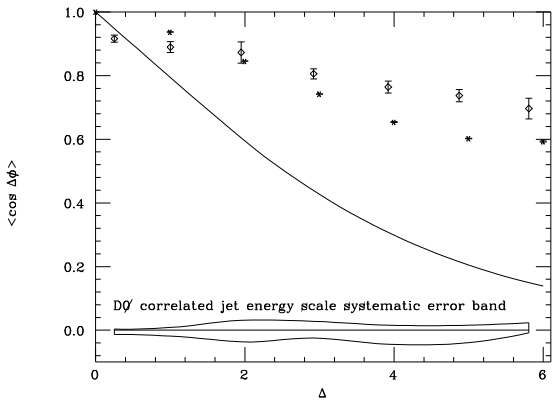

Figure 1. The azimuthal angle decorrelation in dijet production at the Tevatron as a function of dijet rapidity difference Δ, for jet transverse momentum $p_T > 20$ GeV. The analytic BFKL solution is shown as a solid curve and a preliminary DØ measurement [6] is shown as diamonds. Error bars represent statistical and uncorrelated systematic errors; correlated jet energy scale systematics are shown as an error band.

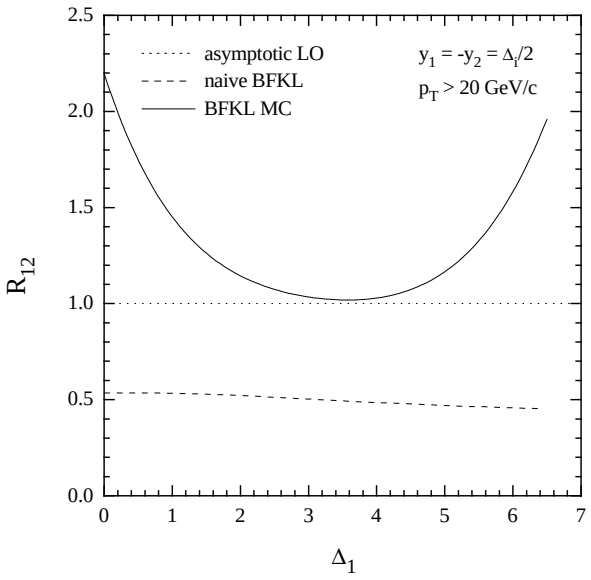

Figure 2. The ratio R_{12} of the dijet cross sections at the two collider energies $\sqrt{s}_1 = 630$ GeV and $\sqrt{s}_2 = 1800$ GeV, as defined in the text. The curves are: (i) the BFKL MC predictions (solid curve), (ii) the 'naive' BFKL prediction (dashed curve), and (iii) the asymptotic QCD leading-order prediction (dotted curve) $R_{12} = 1$.

more robust prediction is obtained by noting that the emitted gluons give rise to a decorrelation in azimuth between the two leading jets.[5,3] This decorrelation becomes stronger as Δ increases and more gluons are emitted. In lowest order in QCD, in contrast, the jets are back-to-back in azimuth and the (subprocess) cross section is constant, independent of Δ.

This azimuthal decorrelation is illustrated in Figure 1 for dijet production at the Tevatron $p\bar{p}$ collider [3], with center of mass energy 1.8 TeV and jet transverse momentum $p_T > 20$ GeV. The azimuthal angle difference $\Delta\phi$ is defined such that $\cos\Delta\phi = 1$ for back-to-back jets. The solid line shows the analytic BFKL prediction. The BFKL Monte Carlo prediction is shown as crosses. We see that the kinematic constraints result in a weaker decorrelation due to suppression of emitted gluons, and we obtain improved agreement with preliminary measurements by the DØ collaboration [6], shown as diamonds in the figure.

In addition to studying the azimuthal decorrelation, one can look for the BFKL rise in dijet cross section with rapidity difference by considering ratios of cross sections at different center of mass energies at fixed Δ. The idea is to cancel the pdf dependence, leaving the pure BFKL effect. This turns out to be rather tricky [8], because the desired cancellations occur only at lowest order. Therefore we consider the ratio

$$R_{12} = \frac{d\sigma(\sqrt{s}_1, \Delta_1)}{d\sigma(\sqrt{s}_2, \Delta_2)} \qquad (3)$$

with Δ_2 defined such that $R_{12} = 1$ in QCD lowest-order. the result is shown in Figure 2, and we see that the kinematic constraints strongly affect the predicted behavior, not only quantitatively but sometimes qualitatively as well. More details can be found in [8].

3. CONCLUSIONS

In summary, we have developed a BFKL Monte Carlo event generator that allows us to include the subleading effects such as kinematic constraints and running of α_s. We have applied this Monte Carlo to dijet production at large rapidity separation at the Tevatron. We found that kinematic constraints, though nominally subleading, can be very important. In particular they lead to suppression of gluon emission, which in turn suppresses some of the behavior that is considered to be characteristic of BFKL physics. It is clear therefore that reliable BFKL tests can only be performed using predictions that incorporate kinematic constraints.

REFERENCES

1. L.N. Lipatov, Sov. J. Nucl. Phys. **23** (1976) 338; E.A. Kuraev, L.N. Lipatov and V.S. Fadin, Sov. Phys. JETP **45** (1977) 199; Ya.Ya. Balitsky and L.N. Lipatov, Sov. J. Nucl. Phys. **28** (1978) 822.
2. A.H. Mueller and H. Navelet, Nucl. Phys. **B282** (1987) 727.
3. L.H. Orr and W.J. Stirling, Phys. Rev. **D56** (1997) 5875.
4. C.R. Schmidt, Phys. Rev. Lett. **78** (1997) 4531.
5. V. Del Duca and C.R. Schmidt, Phys. Rev. **D49** (1994) 4510; W.J. Stirling, Nucl. Phys. **B423** (1994) 56; V. Del Duca and C.R. Schmidt, Phys. Rev. **D51** (1995) 215; V. Del Duca and C.R. Schmidt, Nucl. Phys. Proc. Suppl. **39BC** (1995) 137; preprint DESY 94-163 (1994), presented at the 6th Rencontres de Blois, Blois, France, June 1994.
6. DØ Collaboration: S. Abachi *et al.*, Phys. Rev. Lett. **77** (1996) 595; DØ Collaboration: presented by Soon Yung Jun at the Hadron Collider Physics XII Conference, Stony Brook, June 1997.
7. L.H. Orr and W.J. Stirling, Phys. Lett. **B436** (1998) 372.
8. L.H. Orr and W.J. Stirling, Phys. Lett. **B429** (1998) 135.

Run 2 Plans for Hard Diffraction Studies in CDF

K. GOULIANOS, The Rockefeller University, 1230 York Avenue, New York, NY 10021, USA.

We summarize briefly the CDF proposal for "Further Studies in Hard Diffraction and Very Forward Physics with CDF in Run II" and discuss the present status of the proposed detectors.

A program has been proposed for studies of hard diffraction and very forward physics with CDF in Run 2, which requires adding to CDF three detector components (see Fig. 1):

1) A Roman Pot Spectrometer (RPS) to detect leading antiprotons.

2) Two MiniPlug (MP) calorimeters covering the pseudorapidity region $3.5 < |\eta| < 5.5$ to detect particles and jets and measure their energies.

3) A set of Beam Shower Counters (BSC) positioned around the beam pipe at four (three) locations along the $\bar{p}$ (p) beam direction to tag rapidity gaps within $5.5 < |\eta| < 7.5$.

The Roman Pot Spectrometer will be the one used in Run 1C. It consists of X-Y scintillation fiber detectors placed in three Roman Pots located at a distance of 57 m downstream in the $\bar{p}$ direction. The detectors have a position resolution of $\pm 100\,\mu m$, which makes possible a $\sim 0.1\%$ measurement of the $\bar{p}$ momentum. In Run 1C, the $\bar{p}$-beam was behind the proton beam, as viewed from the RPS side. An inverted polarity (with respect to Run I) of the electrostatic beam separators will enable us to move the RPS detectors closer to the $\bar{p}$-beam and thereby gain acceptance at small $|t|$ down to $\xi \equiv 1 - x_F(\bar{p}) = 0.03$ (at larger $|t|$ lower ξ values can be reached with good acceptance).

The MiniPlugs will be placed within the holes of the muon toroids (see Fig. 2). They consist of layers of lead plates immersed in liquid scintillator (Fig. 3). The signal is guided by 1 mm dia. WLS fibers strung through holes in the plates, as shown, to be read out by multi-cannel PMT's. The "tower" structure, defined by the way the fibers are grouped to be read out, is shown in Fig. 4. A full depth ($\sim 30\,rl$) MiniPlug prototype has been constructed and tested in high energy muon, electron and pion beams with excellent results [1,2]. As of December 1999, the final Miniplug design has been completed, the vessels and all mechanical parts have been fabricated, a prototype lead plate of the final design (laminated with reflective aluminum) has been procured, and several Hamamatsu R5900-M16 PMT's have been acquisitioned and tested.

Beam Shower counters are rings of scintillation counters "hugging" the beam pipe. In stations #1 the rings are segmented into four quadrants, and in the other stations into two. As of December 1999, all 18 counters are ready for installation.

The physics topics to be addressed include:

Hard single diffraction

W, b, J/ψ and dijet production; dependence of the cross section on ξ and t; third-jet activity in jet production; extraction of the pomeron structure function.

Soft and hard double diffraction

(central rapidity gaps)

Dependence of cross section of dijet events with a rapidity gap between jets on jet E_T and jet η separation and comparison with predictions from BFKL and other models; measurement of the differential soft double diffraction cross section and comparison with phenomenological predictions; relationship between gap fractions in minimum bias and dijet events.

Double pomeron exchange (DPE)

Measurement of dijet cross section in events with a DPE topology (pomeron-pomeron collisions); extraction of the diffractive proton structure function from DPE dijet events and comparison with the diffractive antiproton structure measured in single diffraction (test of factorization); measurement of soft DPE cross section (test of soft factorization); connection between soft and hard diffractive processes; opportunities for new physics in exclusive DPE channels.

Small-x/large-x physics:

Measurement of proton parton distribution functions in the range $4 \times 10^{-5} < x < 0.8$; x_{max} can be measured as a function of the E_T scale down to E_T of 5 GeV.

Centauros and Disoriented Chiral Condensates

The signature for Centauros/DχCs is multiparticle clusters of large $dN/d\eta$ with abnormal charge to neutral ratios.

REFERENCES

1. S. Bagdasarov, K. Goulianos, A. Maghakian and Q. Wang, *Test-beam results of a prototype position sensitive towerless calorimeter*, Nucl. Instrum. Meth. **A 372** (1995) 117-124.
2. K. Goulianos and S. Lami, *Performance of a prototype position sensitive towerless calorimeter*, Nucl. Instrum. Meth. **A 430** (1999) 34-47.

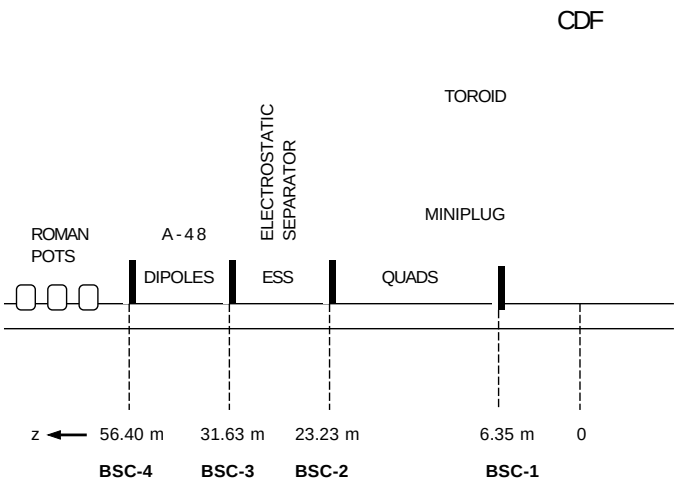

Figure 1. Location of the Beam Shower Counter stations along the $\bar{p}$ direction on the West side of CDF (not to scale). On the East side only the first three BSC stations will be installed, as there is no room for BSC-4.

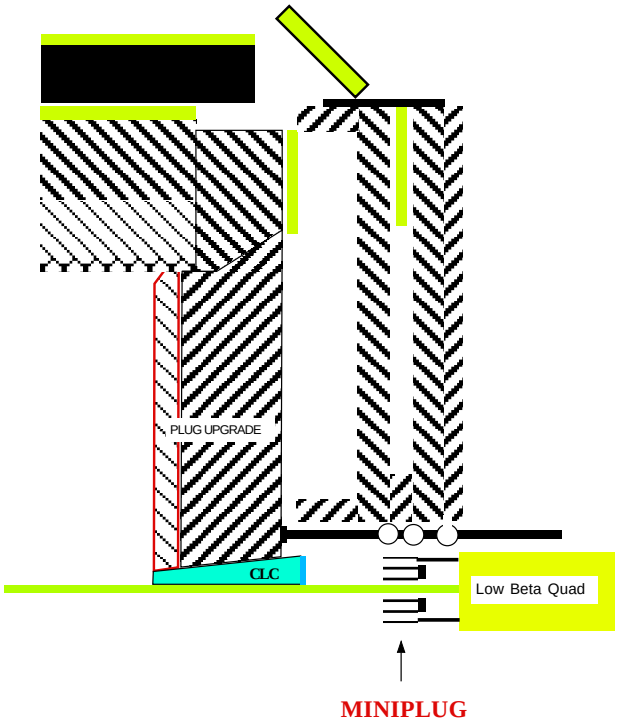

Figure 2. Schematic drawing showing a MiniPlug hanging from two beams supported on one end by the plug and on the other by the toroid (not to scale). This scheme allows for moving the toroids and/or the plug while the MiniPlug remains stationary.

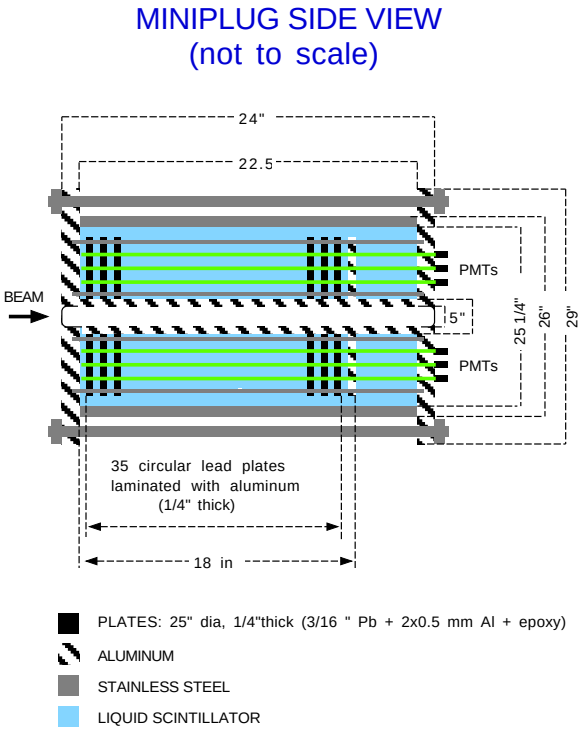

Figure 3. Schematic side view of a Miniplug.

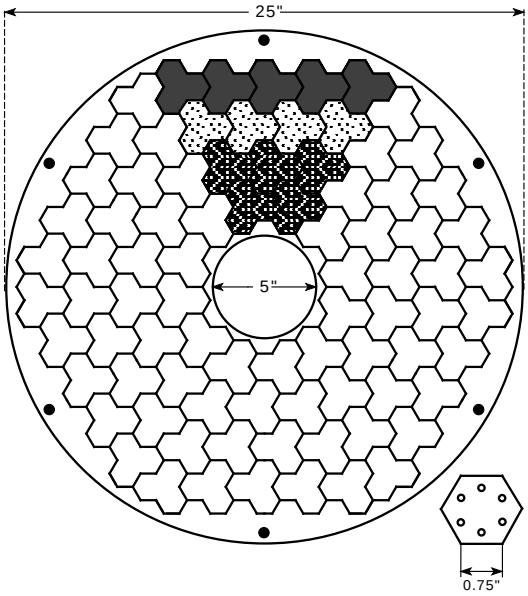

Figure 4. Proposed MiniPlug lead plate. The design is based on a hexagon geometry. Each hexagon has six holes, with a WLS fiber inserted in each hole. The six fibers of a hexagon are grouped together and are viewed by one MCPMT channel. There are 252 hexagons in each MiniPlug viewed by 18 16-channel MCPMTs. The MCPMT outputs are added in groups of 3 to form 84 calorimeter "towers".

The DØ Forward Proton Detector

Andrew Brandt (DØ Collaboration)[a]

[a]University of Texas at Arlington, P.O. Box 19059, Arlington, TX 76019

The Run II DØ Forward Proton Detector is described.

1. Hard Diffraction

One of the most interesting new results from Tevatron Run I was the existence of large rapidity gaps in events with a hard scattering. CDF and DØ published several papers on events with a central rapidity gap between jets [1,2] and have several more papers either published or in preparation on related topics, including diffractive production of jets [3,4], W and Z bosons [5,6], and b quarks [7]. Improved understanding of the new field of hard diffraction, which probes otherwise inaccessible details of the strong force and vacuum excitation, requires new detectors for tagging and measuring scattered protons.

2. The Forward Proton Detector

The DØ Forward Proton Detector (FPD) [8] consists of momentum spectrometers which make use of accelerator magnets along with points measured on the track of the scattered proton to calculate the proton's momentum and scattering angle. Tracks are measured using scintillating fiber detectors (a prototype detector is shown in Fig. 1) located in vacuum chambers positioned in the Tevatron tunnel 20–60 meters upstream and downstream of the central DØ detector. The vacuum chambers were built in Brazil and will be installed in the Tevatron in August 2000. One of the completed Roman pot castles is shown in Figure 2. The scintillating fiber detectors will be assembled at the University of Texas at Arlington.

Figure 3 shows the layout of the FPD. In the center of the diagram is the DØ detector (not to scale). The dipole spectrometer consists of two scintillating fiber detectors located after the Tevatron dipole magnets (D) about 57 meters downstream of the interaction point on the outgoing $\bar{p}$ arm, and measures anti-protons that have lost a few per cent of the beam momentum (and are thus deflected out of the beam envelope and into the detector located on the radial inside of the Tevatron ring). The detectors comprising the quadrupole spectrometers are located adjacent to the electrostatic beam separators (S) on both the proton (P) and anti-proton (A) sides and use the low beta quadrupole magnets (Q) as the primary analyzing magnets. They have acceptance for a large range of proton (anti-proton) momenta and angles.

Figure 1. A photograph of the prototype scintillating fiber detector.

Each of the nine independent spectrometers consists of a pair of detectors, both in the same plane: above, below, to the right, or to the left of the beam. This combination of spectrometers maximizes the acceptance for protons and anti-protons given the available space for locating the detectors. Particles traverse thin steel windows at the entrance and exit of each Roman pot (the stainless steel vessel that houses the detector). The pots are remotely controlled and can be moved close to the beam (within a few mm) during stable beam conditions and retracted otherwise. The scintillating fiber detectors are read out by multi-anode photomultiplier tubes and are incorporated into the standard DØ triggering and data acquisition system.

The FPD project has proceeded well and is expected to be ready for the start of Run II, although final funding for the phototubes and trigger electronics has not yet been secured. The FPD will allow new insight into an intriguing class of events that are not currently understood within the Standard Model. It allows us

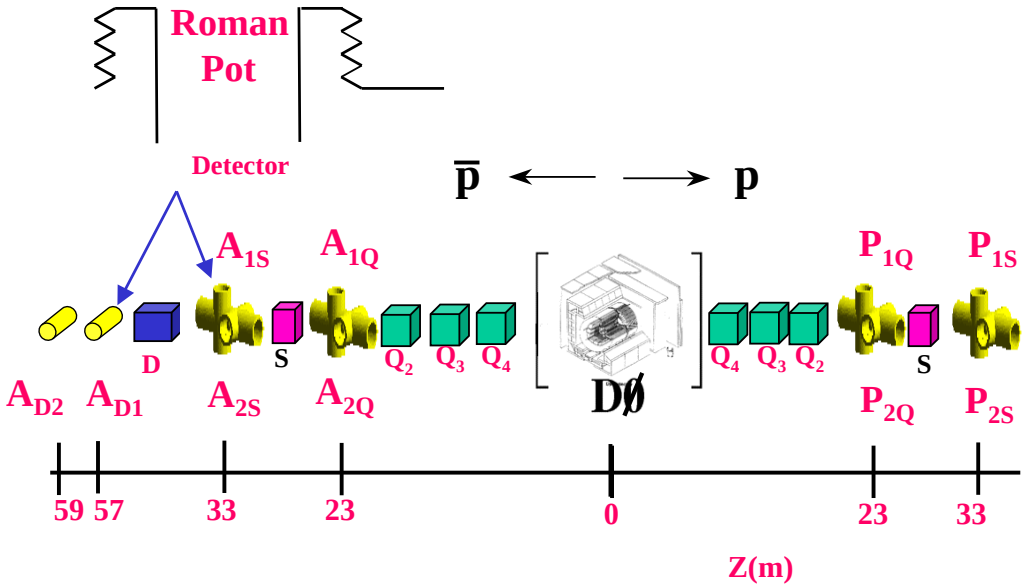

Figure 3. The layout of the Roman pot stations and Tevatron components comprising the Forward Proton Detector as described in the text (not drawn to scale).

Figure 2. A completed Roman pot castle at Fermilab along with project leaders Alberto Santoro (left) and Andrew Brandt.

to trigger directly on events with a scattered proton, anti-proton, or both, along with activity in the DØ detector. In addition to improved studies of recently discovered hard diffractive processes, the new detector will allow a search for glueballs and exotic phenomena. The FPD will also provide improved luminosity measurements, which are an important component to all DØ analyses.

REFERENCES

1. S. Abachi *et al.* (DØ Collaboration), Phys. Rev. Lett. **72**, 2332 (1994);
   Phys. Rev. Lett. **76**, 734 (1996);
   B. Abbott *et al.* (DØ Collaboration), Phys. Lett. B **440** 189 (1998).
2. F. Abe *et al.* (CDF Collaboration), Phys. Rev. Lett. **74**, 855 (1995);
   Phys. Rev. Lett. **80**, 1156 (1998);
   Phys. Rev. Lett. **81**, 5278 (1998).
3. F. Abe *et al.* (CDF Collaboration), Phys. Rev. Lett. **79**, 2636 (1997); K. Hatakeyama (CDF Collaboration), *Proceedings of the XXXVth Rencontres de Moriond* (2000).
4. B. Abbott *et al.* (DØ Collaboration), Hep-ex 9912061, Submitted to Phys. Rev. Lett.
5. F. Abe *et al.* (CDF Collaboration), Phys. Rev. Lett. **78**, 2698 (1997).
6. L. Coney (DØ Collaboration), "Observation of Diffractive W Boson Production at DØ," APS Meeting, Atlanta, Georgia, March 1999.
7. T. Affolder *et al.* (CDF Collaboration), Phys. Rev. Lett. **84**, 232 (2000).
8. DØ Collaboration, "Proposal for a Forward Proton Detector at DØ" (presented by A. Brandt to the Fermilab PAC, 1997); A. Brandt *et al*, Fermilab PUB–97-377.